Metal Oxides Series

Magnetic, Ferroelectric, and Multiferroic Metal Oxides

Edited by

Biljana D. Stojanovic
Institute for Multidisciplinary Research, University of Belgrade, Belgrade, Serbia

Series Editor
Ghenadii Korotcenkov

Elsevier
Radarweg 29, PO Box 211, 1000 AE Amsterdam, Netherlands
The Boulevard, Langford Lane, Kidlington, Oxford OX5 1GB, United Kingdom
50 Hampshire Street, 5th Floor, Cambridge, MA 02139, United States

Notices

Knowledge and best practice in this field are constantly changing. As new research and experience broaden our understanding, changes in research methods, professional practices, or medical treatment may become necessary.

Practitioners and researchers must always rely on their own experience and knowledge in evaluating and using any information, methods, compounds, or experiments described herein. In using such information or methods they should be mindful of their own safety and the safety of others, including parties for whom they have a professional responsibility.

To the fullest extent of the law, neither the Publisher nor the authors, contributors, or editors, assume any liability for any injury and/or damage to persons or property as a matter of products liability, negligence or otherwise, or from any use or operation of any methods, products, instructions, or ideas contained in the material herein.

British Library Cataloguing-in-Publication Data
A catalogue record for this book is available from the British Library

Library of Congress Cataloging-in-Publication Data
A catalog record for this book is available from the Library of Congress

ISBN: 978-0-12-811180-2

Publisher: Matthew Deans
Acquisition Editor: Kayla Dos Santos
Editorial Project Manager: Andrae Akeh
Production Project Manager: Omer Mukthar
Cover Designer: Miles Hitchen

Typeset by MPS Limited, Chennai, India

Contents

Biomedical applications

20

Drago M. Djordjevic[1], *Sasa T. Cirkovic*[1] *and Dusanka S. Mandic*[2]
[1]University of Belgrade, Belgrade, Serbia, [2]MADU Clinic, Belgrade, Serbia

20.1 Introduction

Natural magnetic particles can be found everywhere. Metals and metal oxides are the primary magnetic materials. Magnetic particles and nanoparticles (1−100 nm) can be divided into magnetic metal oxides, pure magnetic metals, and magnetic composites [1]. Magnetic metal oxide particles (biological, artificial) are the most represented magnetic particles on Earth.

Biological magnetic oxides include primarily enormous amounts of sediments in the water and land that contain particles of metal oxides in Earth's material. Only small amounts of metal iron oxide particles are formed from magnetosomes, which represent special organelles in bacteria [2]. Throughout nature, microorganisms are known to synthesize iron oxide nanoparticles (IONPs) through intra- and extracellular mineralization processes [3].

Iron oxide particles are present in a wide range of biological species. An integral part of natural minerals are iron (Fe) oxides: magnetite (Fe_3O_4), hematite (α-Fe_2O_3), and maghemite (γ-Fe_2O_3) [4], as well as greigite (Fe_3S_4) and various ferrites [$MO \cdot Fe_2O_3$, where M = cobalt (Co), nickel (Ni), magnesium (Mg), manganese (Mn), zinc (Zn), and O = oxide] that are crystallized by living organisms under ambient conditions [5]. The most common iron storage protein ferritin $(FeOOH)n$, which contains magnetic nanoparticles, is present in almost every cell of plants and animals including humans [6]. The human brain contains over 10^8 magnetic nanoparticles of Fe_3O_4−γ-Fe_2O_3 per gram of tissue [6].

Magnetism is a minor sense that has been used for navigation from magnetotaxic bacteria, insects, fishes, and birds to mammals that is realized by magnetic particles [7]. All of these organisms contain an aggregate of magnetic particles mainly attached to nerve cells [8]. Sensitivity to electrical field is another minor sense in some sharks, rays, dolphins, duck-billed platypuses, and salt and fresh water fish [7].

Biomineralization in living organisms leads to inorganic−organic nanocomposite formation of hybrid nanomaterials [5]. The formation of inorganic crystals in the process of biomineralization is genetically controlled by organic biomolecules [9], and presumably incorporated in the genome of higher organisms, including humans [10]. Interactions between metal-containing particles, biopolymers (proteins, nucleic acids, polysaccharides), and cells are crucial in enzymatic catalysis, biomineralization, and many biological processes [11].

Artificial magnetic oxides are synthesized on the bases of biogenic magnetic particles with a tendency to use the properties of these particles not only for material sciences but also for natural sciences. According to all major stages of transformation

Magnetic, Ferroelectric, and Multiferroic Metal Oxides. DOI: http://dx.doi.org/10.1016/B978-0-12-811180-2.00020-7

of metal atoms (particle size > metal atom > cluster > nanoparticle > colloid > bulk metal) [11], metal oxides are synthesized in size, shape, and properties suitable for use in biomedical purpose. Especially important is synthesis and use of magnetic nanoparticles or nanostructures, as well as their interactions with biological magnetic materials and biopolymers [12–14].

20.2 Biomedical applications of magnetic oxides

Among a wide range of the magnetic nanomaterials used in biomedicine are nanoparticles of magnetic metals, simple and complex magnetic oxides, and magnetic alloys or composites. In particular, the widespread applications have iron, cobalt, nickel, chromium (e.g., $MgCr_{0.9}Fe_{11}O_4$), titanium alloys, and iron oxide (ferrite) (e.g., barium (Ba) ferrite ($BaFe_{12}O_{19}$), $CoFe_2O_4$, and $ZnO/ZnFe_2O_4$) [1]. Iron oxides have multiple applications in various fields of biomedicine. Lesser significance used other magnetic oxides. Lanthanides metals and oxides have more and more usage in many fields of biomedicine.

In biomedicine, mainly used are magnetic alloys and polymer nanocomposites, which represent magnetic nanoparticles in a polymer inorganic or organic matrix [3,6]. The most magnetic nanoparticles for biomedical applications are comprised of iron oxide-based nanocrystalline structures of magnetite and/or maghemite encased or coated with organic stabilizers and organic or inorganic coatings (metal or nonmetal) [15] in a core-shell, matrix, and core-shell-core structures [16]. However, novel nanoparticles with advanced magnetic properties have different compositions. Bimagnetic materials include a combination of IONPs and other magnetic inorganic materials in a core-shell architecture [3]. They involve transition metal ferrite (MFe_2O_4) nanoparticles, where M is a divalent metal ion (M = Mn, Co, Zn, Ni, Fe, Cu, etc.) [3], while others are metal alloys such as iron cobalt (FeCo) [6,15], iron platinum (FePt) [3,6,15], iron silver (FeAg), or iron gold (FeAu) nanoparticles [1,4].

Biomedical applications of magnetic oxide nanomaterials, especially nanoparticles, can be classified according to their application inside or outside the body (in vivo, in vitro). In medicine, nanoparticles are usually used as components of (1) magnetic liposomes (liposomes with combination of ferromagnetic iron oxide and other magnetic or paramagnetic ions) [17]; and (2) ferrofluids: (a) surfacted (iron oxide coated with shell of surfactant molecule) and (b) ionic-cationic or anionic (iron oxide coated with electric shell) [14].

Some of the main possible applications of magnetic nanoparticles in biomedicine and health care are summarized in Table 20.1 [18–41].

20.2.1 Magnetic oxide sensors

Sensors are devices that detect and measure a physical and chemical stimulus. The sensors primarily consist of sensing elements (e.g., different biorecognition

Table 20.1 Biomedical and health care applications of magnetic nanoparticles [18–41]

	Applications of magnetic nanoparticles
Biomedical	Information technology [18] (e.g., ferrites for microwave 1–100 GHz applications [19]), printed electronics [4], nanoelectronics and magnetooptics [20], nanoelectronics, and nanoelectromechanical systems [21]. Magnetic/thermoresponsive technology [22]. Magnetic nanoparticles technology [23]. Medical instrumentation [24], machine tool positioning, and for rotation and speed sensing in devices [25]. Nanocoatings [23,24]. Magnetic macro- and nanosensors, and consumer electronics [25]. Biosensors (electrochemical sensors, immunosensors, optical (surface plasmon resonance) biosensors, DNA or RNA sensors) [3]. Flexible electronics (flexible magnetic field sensors, biomedical flexible appliances, and artificial devices like robotics) [26]. Magnetic particle (particularly coated with liposomes [4]—magnetic liposomes targeted liposomal delivery systems) [17] for molecular biology investigations [6], fluorescent biological labels [17,21,23], biorecognition (antibodies, aptamers, or antibiotics) [27], specific capture of targeted biomolecules [3], drug delivery and gene delivery [1,17,21,23]. Biomedical imaging [23]: contrast agents (MRI, etc.) [1,6,17,23,28], contrast enhancement [17,28], color imaging [28]. Cell sorting [28]. Drug discovery [23]. Biotechnology [21,29]. Agriculture, food, and cosmetics [30]. In vitro application: diagnostic (selection and separation, magnetorelaxometry and magneto-optical relaxation [31]; bioseparation (DNA, antibody, protein, gene, enzyme, cell, virus, and bacteria) [32], and magnetic based biosensors [1,14,16,32]; catalysis applications [33]; magnetic immunoassay [23]). Bioanalytics (analytical target signal, fluorescence techniques [33], imaging) [17], probing of DNA structure [17], biodetection and selectively separation of biomaterials (cells, proteins, genes, and pathogens) [3,14,17,23]. Blood purification [14]. Models to predict the in vivo behavior of nanoparticles for drug delivery [34]. In vivo targeted drug delivery (including control by superconducting magnetic force [14,16,35]), magnetic contrast agents in MRI [14], and hyperthermia [14,16] or thermoablation agents [32]; MRI of enzyme activity, tracking of labeled dendritic cells and macrophages cells, monitoring stem cell migration [36]. Cellular therapy (e.g., cell labeling [1,33], cell separation and handling of cells, purifying cell population, transfection (magnetofection), tissue repair [1,4,33], diseases of the musculoskeletal system, severe inflammation, disability, and pain) [4], gene therapy [6,23], tumor destruction via heating (magnetic hyperthermia) [1,3,17,23]. Immunomagnetic methods in cell biology and cell separation, and in pure medical application [1,6,17]. Engineering [37], genetic and tissue engineering [1,23,38].

(*Continued*)

Table 20.1 (Continued)

	Applications of magnetic nanoparticles
Health care	Magnetic cooling and heating systems [28]. Smartphone-based medical diagnosis system [39]. Diagnostic imaging (contrast enhancement in MRI, magnetic particle imaging) [2,14,23]; multimode nanoprobes (fluorescent magnetic, etc.) [1,21]. Theranostics [32]. Therapeutic in vivo applications of magnetic carriers, target specific drug delivery [1,3,6,14,21,23] (including painkillers, cancer gene therapy [17,21,23], magnetic hyperthermia [14], and detoxification) [30]; MRI contrast agents [1,3,23] and delivery of therapeutic radioisotopes [17]; therapeutic targets in (cancer and tumor) chemotherapy and radiotherapy (including nanoneedles) [1]; nanoscale biosensors and imaging [1,4,32]; nanocoatings on surfaces [24] including implants [40]; nanocarrier for vaccination and antimicrobial activities [4,17,29,30]; medical implant infection control [40]. Solid lipid nanoparticles in drug delivery and research; nanophotothermolysis for the treatment of cancer, hepatitis B virus, and many other viruses; delivering antigens for a particular disease into the blood stream; and preventing aging of the skin [4]. Biomechanical applications [41]. Regenerative medicine [1,14,21,30,38].

Abbreviations: *DNA*, deoxyribonucleic acid; *MRI*, magnetic resonance imaging; *RNA*, ribonucleic acid.

elements) and a range of transducers (e.g., electrochemical, magnetic, optical, and acoustic) to translate the stimulus (recognition) into physical (e.g., electrical) signals [42]. They are generally classified as (1) electric, magnetic, electromagnetic wave sensors; (2) heat, temperature sensors; (3) optical sensors; (4) physical (mechanical displacement) sensors; and (5) chemical sensors [42].

Magnetic field sensors are sensors that are used to transform magnetic or magnetically coded information into electrical signals (magnetic transducers). Magnetic nanoparticles, clusters, and partially thin films are used as magnetic field sensors. Magnetic sensors are mainly based on the same working principle: the change of magnetic moment, change of temperature, or magnetoelasticity that create the medium in which they are immersed [43]. In biomedical applications, the medium can be a fluid such as blood, the cerebrospinal fluid, or a culture medium or organic tissue.

Natural biological sensors (biosensors) are found in all biological species in the form of magnetic particles such as ferromagnetic iron oxides (magnetite, maghemite) and sulphides (greigite) [5]. Magnetic particles are the basis of the navigation system of living beings responsible for their behavior and orientation in relation to the Earth's magnetic field lines, including seasonal migrations over long distances [7,44]. The human brain and other organs [10] also contain biogenic magnetite [6,44], which is important for the interactions with the external magnetic/electromagnetic fields (MFs/EMFs) [12,13].

The behavior of the magnetic materials that absorb or emit heat in magnetizing or demagnetizing processes is called magnetocaloric effect (MCE) [45]. Many nanoparticles of biologic origin take part in sustainability of thermodynamic balance in organisms like magnetite, maghemite, and greigite, because MCE is inherent physical property of all magnetic materials [46].

Artificial magnetic field sensors are devices that detect or measure the magnetic field in a medium. They are measuring the magnitude of the field or the vector component of the field. Magnetic nanoparticles, clusters, and partially thin films are used as magnetic field sensors [47,48]. Sensors mostly serve for other applications; for example, magnetoresistive sensors are mainly used as reading heads in the computer industry for biomedical purposes, superconducting quantum interference device (SQUID) sensors for biomagnetic applications, inductive sensors on resonance principle for medical applications [49], and magnetocaloric sensors for temperature changes in the medium [50]. In addition to nuclear magnetic resonance (NMR), detection methods of homogeneous biosensing cover inductive coils, Hall sensors, magnetoresistive sensors, SQUID sensors, and optical sensors [51].

Caloric sensors are sensors that register changes in environment temperature, and then switch on specific thermodynamic triggers for reversible decrease or increase of temperature. They are working on the principle of reversible thermal effects, which are activated in solids by magnetic, electric, or stress fields (magnetocaloric, electrocaloric, and elastocaloric effect) [50]. Magnetocaloric sensors are made of magnetocaloric materials, which show reversible temperature changes in response to the changes of applied magnetic field [46,52]. All magnetic materials express MCE, but the intensity depends on the characteristics of each material [53].

Magnetic field sensors are generally divided into two large groups: vector sensors and scalar sensors. Vector sensors are magnetometers specialized in measuring low magnetic fields (<1 mT) and gaussmeters specialized in measuring high magnetic fields (>1 mT) [54]. Magnetometer sensors are (1) SQUID; (2) magnetoresistive; (3) fiber-optic; (4) fluxgate; (5) inductive [54]; (6) magnetoimpedance; (7) resonance; (8) cholographic; and (9) others (spintronic sensors, sensors prepared by using a microelectromechanical system technology, etc.) [49]. Gaussmeter's sensors are (1) Hall; (2) magnetoresistive; (3) magnetodiode; (4) magnetotransistors [54]; and (5) others. Scalar sensors include proton precession and optically pumped sensors [54].

Almost all types of sensors can be used in biomedicine, but five types of sensors dominate in biomedical applications: Hall sensors (high magnetic fields), magnetoresistive sensors (medium magnetic fields), flux-gate sensors (small magnetic fields), SQUID sensors, and magnetoimpedance sensors [55] (very small magnetic fields) [49]. From an application point of view, most of them represent a separate group consisting of biosensors: (1) electrochemical biosensors (label-based and label-free enzyme sensors, DNA sensors, and nanomaterial-based labels vs nanomaterial-modified sensors) [56]; (2) optical biosensors (surface plasmon resonance and fluorescence from evanescent wave excitation); and (3) acoustic biosensors [57]. Particularly important are biosensors for noninvasive detections and measurements of biological parameters in media other than blood [58], nanosized

biosensors or nanobiosensors (1−100 nm) [59], and wearable sensors for biomedical applications [42].

A complete new generation of flexible and wearable devices was developed based on sensors, which are completely autonomous with ultrathin and flexible modules navigation, body tracking, and relative position monitoring systems [26]. Such appliances are required for soft robotics; functional medical implants; and epidermal, imperceptible, and transient electronics [26]. These applications include real-time monitoring of artificial joints or valves of the heart to diagnose early stages of dysfunctions [26].

Modern refrigeration technology is highly efficient technology friendly to the environment, based on use of MCE or electrocaloric effect [60]. It is used in all fields of biomedicine, from research activities to numerous useful applications. Its vital application can be prenatal (sperm banks), throughout lifespan (storing food, biomedicine), and after end of life (storing human organs, tissues, or whole bodies). Without refrigeration technology many activities or procedures in biology or medicine would not be possible, like cold storing of sampled materials (biomaterial, tissues, organs), organ transplantation, cryosurgery, normal functioning of magnetic resonance imaging (MRI), or comfortable working conditions in laboratories, operating rooms, or intensive care units.

Stimuli-responsive polymers are macromolecules mainly composed of magnetic metallopolymer nanocomposites (mostly ferromagnetic metal particles) that change their properties in response to a various stimuli: (1) small change in temperature (thermally responsive polymers); (2) electric or magnetic field (electroresponsive polymers, light/photoresponsive polymers); (3) pH (pH-sensitive polymers); (4) molecular stimuli; (5) mechanical stress; (6) combinations of different stimuli; and (7) others [14]. These "smart" materials are called smart polymers [14] and are used as high-density information media, materials for permanent magnets, magnetic cooling systems, and for production of magnetic sensors [28] as well as in medicine as microfluidic devices, pulsatile drug release systems, bioadhesion mediators, and motors/actuators [14]. Materials made of thermosensitive polymers, which can perform local cooling, are increasingly applied in control of transfer and release of drugs, hormones, and biomedical substances (e.g., antiinflammatory and antiproliferative agents, glues, and others from the surface of the implant) to the specified locations in the body, as in control of state of implant coating [52]. Magnetic materials with large MCE values make magnetic hyperthermia, causing local heating, which is used for cancer treatment [52]. Such materials could be used in any situation where there is necessity for common hypothermia, as in the case of treating patients with super-refractory convulsive status epilepticus (resistant to general anesthesia), by induced hypothermia (32°C−34°C for 24 h) [61].

The future creation of all types of sensors of flexible and wearable sensor networks is associated with wearable sensing or wearable computing goals to create body sensor network systems and electronic textiles as a particular class of wireless sensor networks for continuous healthcare services (e.g., medical monitoring and communication in emergency situations) [42].

20.2.2 Magnetic oxide labels

Detection of biomarkers in vitro and in vivo by magnetic particle labels is a central focus of biomedical research and applications. There are two main types of labeling: *direct labeling* (by nanoparticles and chemical agents), and *indirect labeling* (by genetic incorporation of reporter genes) [62].

Direct labeling mostly use contrast agents in form of nanoparticles and radionuclides; rarely use chemical agents which have larger dimensions than nanoparticles. Direct labeling refers to nonspecific internalization of agent (contrast medium or fluorescent probe), which can be visualized (by radiotracer) in special cell population that is examined, or on specific linking of agents to target molecules, which can be short term and followed radiologically (e.g., paramagnetic nanoparticles for MRI) [63].

Direct labeling is exogenous labeling with MRI-based contrast agents or radioisotopes for positron emission computed tomography (PET)/single-photon emission computed tomography (SPECT) imaging [62,64]. Magnetic nanoparticles convenient for MRI include (1) ultra-small ($<$50 nm) and superparamagnetic ($>$50 nm) iron oxide nanoparticle (USPIONP and SPIONP)-based T_2 contrast agents (i.e., ferucarbotran, ferumoxytol, ferumoxtran-10, ferumoxsil, feruglose, and very small superparamagnetic iron oxide particles (VSOP) coated with citrate (VSOP-C184) for USPIONs vs ferumoxides, ferucarbotran for SPIONs) [62,64–66]; and (2) paramagnetic gadolinium (Gd)-filled microcapsules and liposomes, perfluorocarbon nanoparticle- or manganese (Mn) particle-based T_1 contrast agents [62,64,66].

Magnetic nanoparticles serve as labels for monitoring biological binding reactions, which can be measured by magnetorelaxometry and magnetooptic relaxation devices [31]. Larger particles like liposomes are very convenient flexible carriers for contrast agents, whose phospholipid surface can be modified with various molecules such as polyethylene glycol, antibodies, metal chelates, and radioisotopes (positron emission and single photon radionuclides) [67].

Radionuclide labeling includes use of adequate (MRI, PET/SPECT) radionuclides (e.g., gallium-67 (^{67}Ga), indium-111 (^{111}In), technetium-99m (^{99m}Tc), oxygen-15 (^{15}O)) [62].

According to radiolabeling methods, there are two categories of radiolabeled IONPs: (1) chelator-based radiolabeled IONPs (e.g., ^{99m}Tc-labeled IONPs, ^{111}In- and iodine-125 (^{125}I)-labeled IONPs, copper-64 (^{64}Cu)- and gallium-68 (^{68}Ga)-labeled IONPs); and (2) chelator-free radiolabeled IONPs (e.g., fluorine-18 (^{18}F)- and carbon-11 (^{11}C)-labeled IONPs, arsenic [*As (* = 71, 72, 74, 76)]- and germanium-69 (^{69}Ge)-labeled IONPs, ^{64}Cu- and zirconium-89 (^{89}Zr)-labeled IONPs) [68].

Nanoparticles are used as important radionuclide carriers because of their physicochemical properties, enormous possibility for surface modification (functionalization), great linking capacity, biological stability, and compatibility [69]. Surface modification is carried out with inorganic and organic coatings for biomedical application. After labeling with radionuclide functionalized nanostructures, nanoparticles can serve as candidates for molecular imaging (MRI, PET, or SPECT) [64,69].

Indirect labeling consider using genetically modified cells to express reporter genes by coding proteins which generate imaging signals, often under interaction with molecular sample or substrate which the cells take [62]. Reporter genes inserted in genome express surface proteins, channels, storage proteins, receptors, or enzymes, which are detectable or (which) bind detectable samples [62], visible with fluorescence or bioluminescence imaging (e.g., luciferase activity) [63].

Indirect labeling is genetic labeling, which refers to stable insertion of reporter genes whose expression correlates with molecular processes during examination, or is specific for a given cell population, with possible radiological long-term proliferation follow-up [63]. However, insertion of a reporter gene, whose expression is examined in vivo as a biomarker of tumor cells, limits use of this method in preclinical studies because of genetic modification of the cell population [63].

Cell labeling is performed adequately by the techniques used for in vivo cell imaging. For in vivo cell imaging with MRI usually paramagnetic nanoparticles of iron oxide are used [63,64]; gadolinium chelates or manganese chelates are used, and also used for radionuclide labeling (e.g., ^{99m}Tc, ^{111}In, ^{64}Cu) [63]. Radionuclide labeled substances are used as contrast agents by binding radionuclides through a chelating agent to targeted components, including antibodies, antibody fragments, peptides, proteins, oligonucleotides, or receptor ligands [69].

Cell labeling and monitoring enables insight in a normal and pathological state of cells, tissues, and organs; making diagnoses, prescribing therapy; and following its course. Direct labeling helps the assessment of an illness's course and response to therapy [63]. This labeling also helps in vivo investigation of the role of health and ill cells in mechanisms of genesis and development of pathological process, stopping it with adequate therapy, and follow-up treatment efficiency [63]. Indirect genetic labeling, on the other hand, gives more detailed, intracellular insight, but only in ex vivo active processes in cells [63]. Together, direct and indirect labeling enable complex analysis of the whole state of an organism, necessary for follow-up of the regression of an illness's course, treatment efficiency, and eventual therapy correction.

20.2.3 Magnetic oxide contrast agents

Magnetic contrast agents (media) are pharmaceutical substances that are used to enhance contrast between structures or fluids in the body for the purpose of biomedical imaging. With support of contrast agents the differences between healthy and ill tissue can be determined, in order to the assess state of functionality of organs or the bloodstream after insertion of mediums. At a cellular level, molecular imaging is defined as "in vivo visualization, characterization and measurement of biological processes at the molecular and cellular levels in humans and other living systems" [70]. According to the chemical composition, magnetic contrast agents can be divided into nonorganic, organic, and mixed, or in natural and artificial agents.

The contrast media in biomedical imaging is classified according to the use of imaging modalities. In general, molecular imaging modalities include optical

bioluminescence (optical fluorescence or fluorescence imaging), ultrasound, magnetic resonance techniques, and tomographic techniques [68].

Magnetic contrast agents are used in many classical biomedical techniques:

1. NMR and related techniques (MRI, functional MRI (fMRI), NMR spectroscopy (MRS), magnetic resonance spectroscopic imaging (MRSI))
2. X-ray computed tomography (CT)
3. Γ-ray positron emission tomography (PET)
4. Single photon emission computed tomography (SPECT)
5. Others techniques [69].

NMR and similar techniques (MRI, MRS, and MRSI) are relatively harmless, because they emit nonionizing radiation, as opposed to CT, PET, and SPECT, which emit ionizing radiation.

All contrast agents can be used for research, diagnostic, or therapeutic purposes. Some contrast agents can also be radiopharmaceutical agents, and can be used alone or as part of a diagnostic system.

20.2.3.1 Magnetic contrast agents of nuclear magnetic resonance imaging and related techniques

The MRI is a noninvasive imaging method that is used for function and structure visualization of live biological systems from molecules, cells, tissues, and organs to whole organisms for the purpose of research, diagnostics, and therapy or their special combination (theranostics) [71]. The fMRI is a variant of MRI, which provides real-time images of the metabolic activity or response of the human brain areas to external stimuli using, for example, blood-oxygen-level dependent contrast [72].

For biomedical purpose two groups of magnetic contrast agents apply: (1) metal-based contrast agents; and (2) chemical exchange saturation transfer (CEST) contrast agents [73].

Metal-based contrast agents can be alkaline earth metal-based, transition metal-based (e.g., iron oxide, manganese complex, and copper complex) [74], and lanthanide-based complex (e.g., gadolinium (Gd), dysprosium (Dy), and ytterbium (Yb) complex) [75]. CEST MRI contrast agents can be exogenous and endogenous [73].

Contrast agents that are used in MRI (paramagnetic, superparamagnetic, and ferromagnetic) are divided into four major groups: (1) two classical (positive (bright signal) T_1-weighted and negative (dark signal) T_2-weighted [64,76]) and one additional T_2 exchange relaxation (T_{2ex}) [77]; and (2) two new groups (two CEST: diamagnetic CEST (diaCEST) and paramagnetic CEST (paraCEST; lanthanide is the source of paramagnetism)) and one hyperpolarized molecules (e.g., carbon-13 (^{13}C) MRI or hyperpolarized ^{13}C MRS/I (MR spectroscopy/spectroscopic imaging)) [77].

Complementary combinations of various types of materials (e.g., fluorescent molecules and radioisotopes) allow nanoparticle dual imaging as well as development of the new types of contrast agents that are used in emerging imaging technologies. Magnetic nanoparticles for T_1-T_2 MRI, MRI-optical, and MRI−PET/SPECT

dual-modal imaging can serve as nontraditional multimode imaging agents such as (1) magnetic particle imaging (MPI-MRI dual-modal imaging); (2) magneto-motive ultrasound (US) imaging (MMUS)-US dual-modal imaging; and (3) magneto-photoacoustic imaging (MPA)-US dual-modal imaging [78].

Magnetic MRI contrast agents can be divided into (1) extracellular contrast agents; (2) blood pool contrast agents (intravascular agents); (3) targeted contrast agents; (4) responsive contrast agents; and (5) CEST and paraCEST MRI contrast agents [76].

20.2.3.2 Magnetic contrast agents of X-ray computed tomography

X-ray CT magnetic contrast agents are often applied in biomedicine. Most frequently used contrast-generating elements are iodine (I), gold (Au), and bismuth (Bi); less commonly used are barium (Ba), bromine (Br), tantalum (Ta), platinum (Pt), ytterbium (Yb), yttrium (Y), gadolinium (Gd), wolfram (W), dysprosium (Dy), and lutecium (Lu) [67].

Lanthanide-based contrast agents are the most frequently used in CT, especially Gd chelates. Ytterbium-based nanoparticulate contrast agents usually also include Ba-, Bi-, Au-, Pt-, and Ta-based nanoparticles [79].

Metal-based contrast agents are less frequently used than lanthanides like copolymeric nanoparticles of iron oxides, zinc, copper [80], Au, and silver (Ag) [79,80]. Dextran-coated bismuth−iron oxide nanohybrid contrast agents are also synthesized for in vivo CT and MR imaging [81].

Other metallic contrast agents include in vitro and in vivo use of basic elements like Ba (e.g., $BaSO_4$), Bi (e.g., Bi_2S_3), Ta (e.g., Ta_2O_5) [79,80], and Pt (e.g., FePt) [82].

Various combinations of elements are used for the dual-modal imaging, for example, core/shell Fe_3O_4/TaO_x nanoparticles as a bifunctional agent for CT and MRI [83].

20.2.3.3 Magnetic contrasts of positron emission tomography

A large number of classical and new (nanostructured and others) contrast agents are used in PET for preclinical and clinical purposes. The most commonly used PET radioisotopes (radionuclides) are ^{11}C, nitrogen-13 (^{13}N), ^{15}O, ^{18}F, ^{64}Cu, ^{68}Ga, rubidium-82 (^{82}Rb), and holmium-166 (^{166}Ho) [84]; less commonly used are arsenic-72 (^{72}As) and ^{89}Zr [85].

Magnetic nanoparticles, especially IONPs, are in development as MRI contrast agents, but also in iron oxide-based PET/MR dual applications [86] for detection of many disorders and diseases. Contrast agents for NMR and MRI can be achieved by labeling a variety of PET isotopes (e.g., ^{11}C, ^{18}F, ^{64}Cu, ^{68}Ga, ^{69}Ge, ^{72}As, and ^{89}Zr) and SPECT isotopes (e.g., ^{99m}Tc, iodine-123 (^{123}I) or ^{125}I, and ^{111}In) to water-soluble IONPs [68].

Radionuclide (e.g., ^{99m}Tc, ^{111}In, ^{64}Cu) cell labeling is used ex vivo for labeling tumor cells, lymphocytes, dendritic cells, and monocytes in PET and SPECT

examinations [63]. Iodine-124 (^{124}I) radiolabeled IONPs are developed for optical/PET/MR modality tumor imaging [86]. ^{89}Zr radiolabeled nanoparticles are explored for PET oncological imaging and indium-120 (^{120}In) for colon carcinoma imaging [86]. Gold nanoshell with ^{64}Cu radiolabeling [86] and SPIONs with multiple radioisotopes (e.g., ^{64}Cu, ^{68}Ga, ^{89}Zr, and ^{69}Ge) [66] were used for multimodality theranostics [66,86].

20.2.3.4 Magnetic contrasts of single photon emission computed tomography

SPECT is a nuclear biomedicine technology that deals with preclinical and clinical monitoring of the distribution, kinetics, and targeting of radiolabeled organic and nonorganic molecules into tomographic (two- or three-dimensional) images. SPECT is very similar to PET in its use of radioactive tracer and detection of γ-rays, because it emits only a single γ-ray during decay of a radioisotope that is measured directly, unlike PET, which records pairs of γ-rays that are emitted and measured indirectly [84].

Target-specific SPECT radioisotopes can be divided into two main parts: a targeting biomolecule (e.g., peptide, antibody fragment, vitamin) and a γ-radiation emitting radionuclide (e.g., ^{99m}Tc, ^{111}In) [87]. Most radionuclides consist of metallic radioisotopes. In successive processes of conjugation, radiolabeling, and target binding, bifunctional chelator links to the targeting biomolecule and radiometal that form a target-specific radiobioconjugate that binds to the targeting structure [87].

The most commonly used radioisotopes for SPECT imaging are ^{99m}Tc, ^{111}In, ^{67}Ga, and ^{123}I [87]. The most commonly used therapy/SPECT isotopes are lutetium-177 (^{177}Lu), rhenium-186 (^{186}Re), rhenium-188 (^{188}Re), copper-67 (^{67}Cu), and iodine-131 (^{131}I) [86]. Less commonly used isotopes are ^{125}I, tin-117m (^{117m}Sn), and radiolanthanides gadolinium-159 (^{159}Gd), samarium-153 (^{153}Sm), ^{166}Ho, thallium-201 (^{201}Tl), and itrium-90 (^{90}Y).

Among the metallic radioisotopes, SPECT imaging ^{99m}Tc is the most widely applied radioisotope of diagnostic agents [66,87]. Among all nonmetallics, the most used isotope is ^{123}I; less used are ^{125}I and ^{131}I [87].

The SPIONs have been labeled with multiple radioisotopes for both SPECT and PET (e.g., ^{99m}Tc, ^{125}I, ^{111}In, and ^{131}I) [66]. The USPIONs are conjugated by arginylglycylaspartic acid (RGD) peptides and labeled by ^{99m}Tc (^{99m}Tc-USPION-RGD) in order to be successively used for molecular imaging as a targeting probe for SPECT imaging, dual-contrast (T_1/T_2-weighted) MRI, and dual-modality (MRI/SPECT) imaging of tumor angiogenesis [64].

The SPECT radionuclides may be used alone or in combination with other radionuclides, depending on the nature of the examination.

The SPECT tracer media are used for (1) biomolecule labeling [88]; (2) biodistribution [89]; (3) bioassay [88]; (4) tissue imaging [90]; (5) diagnostic applications [87,88]; (6) therapeutic applications [87] (including targeted radiotherapy [84] and radioimmunotherapy [87]); and (7) theranostics [32,66].

20.2.4 Magnetic oxide diagnostics and therapy applications

Medical application of magnetic oxides in human and veterinary medicine is widespread in numerous medical fields.

In human medicine, magnetic oxides are used in many fields: (1) microbiology (e.g., magnetic IONPs can stimulate or inhibit microbial growth [29]); (2) dentistry (e.g., dental repair and dental implants [1], secure dentures, or prostheses) [14,91,92]; (3) orthopedy (e.g., bone repair and bone implants) [1,93]; (4) cardiology (e.g., activation of artificial heart valves by permanent magnets [94], self-controlled nanovalves [14]); (5) neurology (e.g., provide communication and mobility [95,96]); (6) surgery (e.g., navigating within the brain [14]); (7) gynecology (e.g., magnetic intrauterine devices for contraception [15]); (8) oncology (e.g., magnetic fluid (nanoparticles) hyperthermia—iron oxide (SPIONs and others ferrofluids) and transition metal nanoparticles [97], tumor destruction and detoxification [3,17,30]); (9) radiology (diagnostic imaging [1,2,6,64], deliver therapeutic radioisotopes [17] and therapeutic targets in chemotherapy [1,4]); and (10) physical medicine and rehabilitation (e.g., treatment of various diseases [98]; aid feeble muscles in the eyelids or bladder [94], guiding catheters through the body with permanent magnets [14,94]).

In veterinary medicine, magnetic oxides are used much less frequently than in human medicine. Their use is mainly for applications of contrast agents in veterinary radiology, therapeutic agents in veterinary oncology (e.g., electrochemotherapy and gene therapy), [99] and veterinary physical medicine and rehabilitation (e.g., healing a horse's injury) [100].

Magnetic oxides are used in human and veterinary medicine for diagnostic and therapeutic purposes, including assistive technology as a special type of therapy.

20.2.4.1 Medical diagnostics

Medical diagnostics use a multitude of devices, appliances, handy tools, and other equipment that contain magnetic oxide materials.

1. **Electrodiagnostics**

   Electrodiagnostics is based on the registration of bioelectric fields in certain areas of the body and cover electrodiagnostic techniques and electrodiagnostic testing for research and clinical purposes. Registration is performed by metallic or nonmetallic electrodes, both noninvasive (sensor patches) and invasive (needles).

   Electrodiagnostic techniques include many procedures such as electrocardiography, electroencephalography, electrogastrography, spirometry, audiometry, and electrodermal activity (measurement of changes in skin conductance).

   Electrodiagnostic testing measures electrical activity of muscles and nerves and typically consists of needle electromyography and electroneurography (or nerve conduction studies for motor and sensory nerves), including long latency reflex testing (F-waves) [101]. Somatosensory evoked potentials, magnetic stimulation motor evoked potentials, and autonomic testing are rarely used [101].

2. **Magnetodiagnostics**
   Magnetic field diagnostics is based on the registration of biomagnetic fields for research and clinical purposes such as magnetoencephalography, magnetospinography, magnetoneurography, magnetoretinography, magnetocardiography, magnetomyography, magnetic impurity detection (magnetopneumography), magnetic susceptometry (liver iron measurement), and magnetogastrography [102].
   Magnetic trackers are used for biological detection (e.g., pathogens or other targeted biomolecules such as DNA, RNA, antibodies, and metabolites), determine the position of medical tools inside the body (e.g., endoscope, colonoscope, and biopsy needle), and to observe biomechanical motions [103]. An external magnetic field can exert on the particle the force at range of 10^{-12} to 10^{-9} newtons, which represent the typical levels that cells experience in vivo [23].

20.2.4.2 Medical therapy

Magnetic oxides are widely used in various fields of medical therapy, especially in physical medicine and rehabilitation as electrotherapy, magnetotherapy, and assistive technology.

1. **Electrotherapy versus electrophysical agents**
   Electrotherapy includes delivery and therapeutic application of electrical and possibly also electromagnetic energies emitted by various sources [104]. Electrophysical agents have the wider concept involving ultrasound, light, vibration, and various heat therapies [104]. Together they are divided into three main subgroups: electrical stimulation, thermal modalities, and nonthermal modalities [104].
2. **Magnetotherapy**
   Magnetotherapy involves therapeutic application of MF/EMF modalities emitted by various sources: from the simplest such as magnetophores and elastic magnetic stripes (made of iron oxides [98] or lanthanides) to the most complex such as MF/EMF-emitting devices (magnetic devices) [13]. Therapeutic modalities of MFs/EMFs can be classified into the following groups: (1) static/permanent MFs; (2) low-frequency sine waves; (3) pulsed EMFs; (4) pulsed radio-frequency fields; (5) magnetic/electric stimulation; (6) millimeter waves; and (7) electroporation and nanoelectroporation [13].
3. **Assistive technology**
   Assistive technology devices are used in physical medicine and rehabilitation for communication disorders, mobility impairments, ergonomics and prevention of secondary injuries, hearing impairments, visual impairments, and cognitive/learning disabilities [105].

20.2.5 Other magnetic oxide techniques and applications

In biomedicine, besides the already mentioned techniques, mainly magnetic separation and magnetic tweezers are in use.

20.2.5.1 Magnetic separation

Magnetic separation is the technique for the extraction of magnetic particles from nonmagnetic materials. For bioseparation processes, the magnetic nanoparticles usually are coated with various polymeric materials [1]. By using magnetic

particles, the magnetic separation method is used for sensitive and reliable capture of specific proteins, genetic material, and other biomolecules [17]. The magnetic separation is the technique of sorting specific biological targets based on magnetically labeled surfaces and is used in a wide range of applications from in vitro diagnostics to cell-based therapies in vivo. Possible therapy includes extracorporeal magnetic separation-based blood purification due to rapid and selective removal of disease-causing compounds from whole blood [106].

The magnetic separation uses the magnetic field gradient-induced magnetophoresis, which can be either toward (positive magnetophoresis) or away (negative magnetophoresis) from the magnetic source due to separate particles and cells based on the difference in physical properties [107]. Positive magnetophoresis refers to magnetic particles or magnetically tagged cells, and negative magnetophoresis to diamagnetic particles and cells in magnetic fluids [107].

20.2.5.2 Magnetic tweezers

Magnetic tweezers are techniques of biological micromanipulators that use the magnetic force on superparamagnetic or ferromagnetic particles performed by gradients in an applied magnetic field [72,94]. They belong to single-molecule techniques that allow research of the behavior of individual biological molecules in solution in real time [108]. These are molecule techniques for determination of functions of various enzymes at a molecular level by exerting forces on individual proteins [109] that are used to monitor the mechanical properties of nucleic acids and their interactions with the proteins [108].

An important feature of magnetic tweezers is their ability to apply torque while maintaining a constant stretching force [108] and their ability to quickly and accurately twist macromolecules [110]. Magnetic tweezers offer an appropriate tool for handling two or more DNAs [110]. This can be easily achieved by increasing the amount of DNA during its attachment to magnetic particles [110]. NonDNA applications of magnetic tweezers include a number of other noninvasive applications such as protein folding, rotating protein assemblies, cellular cortical stiffness, cellular mechanotransduction processes, and intracellular transport [110].

References

[1] X. Li, J. Wei, K.E. Aifantis, Y. Fan, Q. Feng, F.-Z. Cui, et al., Current investigations into magnetic nanoparticles for biomedical applications, J. Biomed. Mater. Res. Part A 104A (2016) 1285−1296.

[2] W. Andrä, U. Häfeli, R. Hergt, R. Misri, Application of magnetic particles in medicine and biology, in: H. Kronmüller, S. Parkin (Eds.), Handbook of Magnetism and Advanced Magnetic Materials, vol. 4, Novel Materials, John Wiley & Sons, Ltd, Chichester, 2007, pp. 1−33.

[3] W. Wu, C.Z. Jiang, V.A.L. Roy, Designed synthesis and surface engineering strategies of magnetic iron oxide nanoparticles for biomedical applications, Nanoscale (2016). Available from: http://dx.doi.org/10.1039/c6nr07542h.

[4] A. Ali, H. Zafar, M. Zia, I. Ul Haq, A.R. Phull, J.S. Ali, et al., Synthesis, characterization, applications, and challenges of iron oxide nanoparticles, Nanotechnol. Sci. Appl. 9 (2016) 49–67.
[5] A.D. Pomogailo, V.N. Kestelman, Chemical methods of metal–polymer nanocomposite production, Metallopolymer Nanocomposites, Springer-Verlag Berlin, 2005, pp. 135–236.
[6] S.P. Gubin, Introduction, in: S.P. Gubin (Ed.), Magnetic Nanoparticles, Wiley-VCH Verlag GmbH & Co. KGaA, Weinheim, 2009, pp. 1–23.
[7] T.A. Waigh, The senses, The Physics of Living Processes: A Mesoscopic Approach, first ed., John Wiley & Sons, Ltd, Chichester, 2014, pp. 541–554.
[8] R.K. Hobbie, B.J. Roth, Biomagnetism, Intermediate Physics for Medicine and Biology, fifth ed., Springer International Publishing Switzerland, Cham, 2015, pp. 213–238.
[9] A.D. Pomogailo, V.N. Kestelman, Nanobiocomposites, Metallopolymer Nanocomposites, Springer-Verlag, Berlin, 2005, pp. 377–422.
[10] O. Strbak, P. Kopcansky, I. Frollo, Biogenic magnetite in humans and new magnetic resonance hazard questions, Meas. Sci. Rev. 11 (3) (2011) 85–91.
[11] A.D. Pomogailo, V.N. Kestelman, Nanoparticles in materials chemistry and in the natural sciences (introduction), Metallopolymer Nanocomposites, Springer-Verlag, Berlin, 2005, pp. 3–24.
[12] D.M. Djordjevich, S.R. De Luka, I.D. Milovanovich, S. Janković, S. Stefanović, S. Vesković-Moračanin, et al., Hematological parameters' changes in mice subchronically exposed to static magnetic fields of different orientations, Ecotoxicol. Environ. Saf. 81 (2012) 98–105.
[13] M.S. Markov, Benefit and hazard of electromagnetic fields, in: M.S. Markov (Ed.), Electromagnetic Fields in Biology and Medicine, Taylor & Francis Group, LLC, Boca Raton, 2015, pp. 15–28.
[14] S.F. Medeiros, A.M. Santos, H. Fessi, A. Elaissari, Stimuli-responsive magnetic particles for biomedical applications, Int. J. Pharm 403 (2011) 139–161.
[15] C. Bárcena, A.K. Sra, J. Gao, Applications of magnetic nanoparticles in biomedicine, in: J.P. Liu, E. Fullerton, O. Gutfleisch, D.J. Sellmyer (Eds.), Nanoscale Magnetic Materials and Applications, Springer Science+Business Media, LLC, Springer Dordrecht, 2009, pp. 591–626.
[16] M.R. Ghazanfari, M. Kashefi, S.F. Shams, M.R. Jaafari, Perspective of Fe_3O_4 nanoparticles role in biomedical applications, Biochem. Res. Int. 2016 (2016), Article ID 7840161. http://dx.doi.org/10.1155/2016/7840161.
[17] V.N. Nikiforov, E. Yu Filinova, Biomedical Applications of Magnetic Nanoparticles, in: S.P. Gubin (Ed.), Magnetic Nanoparticles, Wiley-VCH Verlag GmbH & Co. KGaA, Weinheim, 2009, pp. 393–455.
[18] S. Mørup, M.F. Hansen, Superparamagnetic particles, in: H. Kronmüller, S. Parkin (Eds.), Handbook of Magnetism and Advanced Magnetic Materials, vol. 4, Novel Materials, John Wiley & Sons, Ltd, Chichester, 2007, pp. 1–18.
[19] S. Tumanski, Magnetic materials, Handbook of Magnetic Measurements, CRC Press/Taylor & Francis Group, Boca Raton, 2011, pp. 117–158.
[20] G.B. Khomutov, Y.A. Koksharov, Organized ensembles of magnetic nanoparticles: preparation, structure, and properties, in: S.P. Gubin (Ed.), Magnetic Nanoparticles, Wiley-VCH Verlag GmbH & Co. KGaA, Weinheim, 2009, pp. 117–195.
[21] A. Masotti, A. Caporali, Preparation of magnetic carbon nanotubes (Mag-CNTs) for biomedical and biotechnological applications, Int. J. Mol. Sci. 14 (2013) 24619–24642.

[22] L. Chen, X. Wang, W. Lu, X. Wua, J. Li, Molecular imprinting: perspectives and applications, Chem. Soc. Rev. (2016). Available from: http://dx.doi.org/10.1039/c6cs00061d.
[23] A. Aseri, S.K. Garg, A. Nayak, S.K. Trivedi, J. Ahsan, Magnetic nanoparticles: magnetic nano-technology using biomedical applications and future prospects, Int. J. Pharm. Sci. Rev. Res. 31 (2) (2015) 119−131, 20.
[24] D.V. Louzguine-Luzgin, Bulk metallic glasses and glassy/crystalline materials, in: A. Zhukov (Ed.), Novel Functional Magnetic Materials: Fundamentals and Applications, Springer International Publishing Switzerland, 2016, pp. 396−440.
[25] S.A. Solin, L.R. Ram-Mohan, Geometry-driven magnetoresistance, in: H. Kronmüller, S. Parkin (Eds.), Handbook of Magnetism and Advanced Magnetic Materials, volume 5, Spintronics and Magnetoelectronics, John Wiley & Sons, Ltd, Chichester, 2007, pp. 1−21.
[26] M. Melzer, J.I. Mönch, D. Makarov, Y. Zabila, G.S. Cañón Bermúdez, D. Karnaushenko, et al., Wearable magnetic field sensors for flexible electronics, Adv. Mater. 27 (2015) 1274−1280.
[27] C. Wang, J. Wang, P. Li, Z. Rong, X. Jia, Q. Ma, et al., Sonochemical synthesis of highly branched flower-like Fe_3O_4@SiO_2@Ag microcomposites and their application as versatile SERS substrates, Nanoscale (2016). Available from: http://dx.doi.org/10.1039/c6nr07295j.
[28] G.I. Dzhardimalieva, A.D. Pomogailo, A.S. Rozenberg, M. Leonowicz, Magnetic metallopolymer nanocomposites: preparation and properties, in: S.P. Gubin (Ed.), Magnetic Nanoparticles, Wiley-VCH Verlag GmbH & Co. KGaA, Weinheim, 2009, pp. 59−85.
[29] R. Dinali, A. Ebrahiminezhad, M. Manley-Harris, Y. Ghasemi, A. Berenjian, Iron oxide nanoparticles in modern microbiology and biotechnology, Crit. Rev. Microbiol. (2016). Available from: http://dx.doi.org/10.1080/1040841X.2016.1267708.
[30] K.S. Siddiqi, A. Ur Rahman, Tajuddin, A. Husen, Biogenic fabrication of iron/iron oxide nanoparticles and their application, Nanoscale Res. Lett. 11 (2016) 498.
[31] L. Trahms, Biomedical applications of magnetic nanoparticles, in: S. Odenbach (Ed.), Colloidal Magnetic Fluids, Basics, Development and Application of Ferrofluids, Springer, Berlin, 2009, pp. 327−358.
[32] W. Wu, Z. Wu, T. Yu, C. Jiang, Woo-Sik Kim, Recent progress on magnetic iron oxide nanoparticles: synthesis, surface functional strategies and biomedical applications, Sci. Technol. Adv. Mater. 16 (2015) 023501, 43pp.
[33] A. Akbarzadeh, M. Samiei, S. Davaran, Magnetic nanoparticles: preparation, physical properties, and applications in biomedicine, Nanoscale Res. Lett. 7 (2012) 144.
[34] P. Chetprayoon, M. Matsusaki, U. Yokoyama, T. Tejima, Y. Ishikawa, M. Akashi, Use of three-dimensional arterial models to predict the in vivo behavior of nanoparticles for drug delivery, Angew. Chem. Int. Ed. 55 (2016) 4461−4466.
[35] M. Muralidhar, M. Murakami, Superconductivity in oxides: from processing to applications, in: M. Lorenz, M.S. Ramachandra Rao, T. Venkatesan, E. Fortunato, P. Barquinha, R. Branquinho, et al., (Eds.), The 2016 oxide electronic materials and oxide interfaces roadmap, *J. Phys. D: Appl. Phys.* **49**, 2016, 433001 (53pp): pp. 23−24.
[36] M. Colombo, S. Carregal-Romero, M.F. Casula, L. Gutiérrez, M.P. Morales, I.B. Böhm, et al., Biological applications of magnetic nanoparticles, Chem. Soc. Rev. 41 (2012) 4306−4334.
[37] V.A. L'vov, V.A. Chernenko, J.M. Barandiaran, Magnetic shape memory materials with improved functional properties: scientific aspects, in: A. Zhukov (Ed.), Novel

Functional Magnetic Materials: Fundamentals and Applications, Springer International Publishing Switzerland, 2016, pp. 1–40.
[38] B.D. Plouffe, S.K. Murthy, L.H. Lewis, Fundamentals and application of magnetic particles in cell isolation and enrichment, Rep. Prog. Phys. 78 (1) (2015) 016601.
[39] T. Takamura, P.J. Ko, J. Sharma, R. Yukino, S. Ishizawa, A. Sandhu, Magnetic-particle-sensing based diagnostic protocols and applications, Sensors 15 (2015) 12983–12998.
[40] J. Coffel, E. Nuxoll, Magnetic nanoparticle/polymer composites for medical implant infection control, J. Mater. Chem. B (2015). Available from: http://dx.doi.org/10.1039/c5tb01540e.
[41] R. Riemer, A. Shapiro, Biomechanical energy harvesting from human motion: theory, state of the art, design guidelines, and future directions, J. Neuroeng. Rehabil. 8 (2011) 22.
[42] C. Crean, C. McGeough, R. O'Kennedy, Wearable biosensors for medical applications, in: S. Higson (Ed.), Biosensors for Medical Applications, Woodhead Publishing Limited, Cambridge, 2012, pp. 301–330.
[43] G. Rivero, M. Multigner, J. Spottorno, Magnetic sensors for biomedical applications, in: K. Kuang (Ed.), Magnetic Sensors - Principles and Applications, InTech, Rijeka, 2012, pp. 125–150.
[44] V.A.M. Brabers, Ferrimagnetic insulators, in: H. Kronmüller, S. Parkin (Eds.), Handbook of Magnetism and Advanced Magnetic Materials, vol. 4, Novel Materials, John Wiley & Sons, Ltd, Chichester, 2007, pp. 1–19.
[45] J.R. Sun, B.G. Shen, F.X. Hu, Magnetocaloric effect and materials, in: J.P. Liu, E. Fullerton, O. Gutfleisch, D.J. Sellmyer (Eds.), Nanoscale Magnetic Materials and Applications, Springer Science+Business Media, LLC, Springer Dordrecht, 2009, pp. 441–483.
[46] V.K. Pecharsky, K.A. Gschneidner Jr., Magnetocaloric materials, in: H. Kronmüller, S. Parkin (Eds.), Handbook of Magnetism and Advanced Magnetic Materials, volume 4, Novel Materials, John Wiley & Sons, Ltd, Chichester, 2007, pp. 1–15.
[47] V. Kuncser, P. Palade, A. Kuncser, S. Greculeasa, G. Schinteie, Engineering magnetic properties of nanostructures via size effects and interphase interactions, in: V. Kuncser, L. Miu (Eds.), Size Effects in Nanostructures, Basics and Applications, Springer-Verlag, Berlin, 2014, pp. 169–237.
[48] M.D. Glinchuk, A.V. Ragulya, V.A. Stephanovich, Ferroics, Nanoferroics, Springer Science+Business Media, Dordrecht, 2013, pp. 1–32.
[49] S. Tumanski, Modern magnetic field sensors – a review, Prz. Elektrotechniczny. R. 89 (2013) NR 10/2013.
[50] V.K. Pecharsky, J. Cui, D.D. Johnson, (Magneto)caloric refrigeration: is there light at the end of the tunnel? Phil. Trans. R. Soc. A 374 (2016) 20150305.
[51] A.-Y. Chang, M.S.-C. Lu, A CMOS magnetic microbead- based capacitive biosensor array with on-chip electromagnetic manipulation, Biosens. Bioelectron. 45 (2013) 6–12.
[52] A.M. Tishin, Y.I. Spichkin, V.I. Zverev, P.W. Egolf, A review and new perspectives for the magnetocaloric effect: new materials and local heating and cooling inside the human body, Int. J. Refrig. (2016), http://dx.doi.org/10.1016/j.ijrefrig.2016.04.020.
[53] J.Q. Zhao, C.L. Zhang, Y.G. Nie, H.F. Shi, E.J. Ye, Z.D. Han, et al., Tunable magnetostructural phase transition and magnetocaloric effect in $Mn_{1-x}Ni_{1-x}Co_{2x}Si_{1-x}Ge_x$ system, J. Alloys Compd. 698 (2017) 7–12.
[54] U.C. Inan, Design and Implementation of Magnetic Field Sensors for Biomedical Applications, A Thesis Submitted to The Graduate School of Natural and Applied

Sciences of Middle East Technical University, Middle East Technical University, Department of Electrical and Electronics Engineering, Ankara, 2015. http://etd.lib.metu.edu.tr/upload/12618588/index.pdf

[55] K. Mohri, T. Uchiyama, L.V. Panina, M. Yamamoto, K. Bushida, Recent advances of amorphous wire CMOS IC magneto-impedance sensors: innovative high-performance micromagnetic sensor chip, J. Sens. 2015 (2015), Article ID 718069. http://dx.doi.org/10.1155/2015/718069.

[56] A.J. Veloso, X.R. Cheng, K. Kerman, Electrochemical biosensors for medical applications, in: S. Higson (Ed.), Biosensors for Medical Applications, Woodhead Publishing Limited, Cambridge, 2012, pp. 3–40.

[57] C. Parsajoo, J.-M. Kauffmann, M. Elkaoutit, Biosensors for drug testing and discovery, in: S. Higson (Ed.), Biosensors for Medical Applications, Woodhead Publishing Limited, Cambridge, 2012, pp. 233–262.

[58] L. Micheli, D. Moscone, G. Palleschi, Biosensors for non-invasive measurements, in: S. Higson (Ed.), Biosensors for Medical Applications, Woodhead Publishing Limited, Cambridge, 2012, pp. 263–300.

[59] J.C. Claussen, J. Shi, C.S. Rout, M.S. Artiles, M.M. Roushar, M.C. Stensberg, et al., Nano-sized biosensors for medical applications, in: S. Higson (Ed.), Biosensors for Medical Applications, Woodhead Publishing Limited, Cambridge, 2012, pp. 65–102.

[60] M.A. Hamad, Magnetocaloric effect in Sr_2FeMoO_6/Ag composites, Process. Appl. Ceram. 9 (1) (2015) 11–15.

[61] S. Legriel, V. Lemiale, M. Schenck, J. Chelly, V. Laurent, F. Daviaud, et al., Hypothermia for neuroprotection in convulsive status epilepticus, for the HYBERNATUS Study Group N. Engl. J. Med. 375 (2016) 2457–2467.

[62] A.V. Naumova, M. Modo, A. Moore, C.E. Murry, J.A. Frank, Clinical imaging in regenerative medicine, Nat. Biotechnol. 32 (8) (2014) 804–818.

[63] L. Ottobrini, C. Martelli, G. Lucignani, Imaging cell trafficking in cancer research, in: X. Chen (Ed.), Molecular Imaging Probes for Cancer Research, World Scientific Publishing, Co., Pte. Ltd., Singapore, 2012, pp. 905–948.

[64] S. Xue, C. Zhang, Y. Yang, L. Zhang, D. Cheng, J. Zhang, et al., ^{99m}Tc-labeled iron oxide nanoparticles for dual-contrast (T_1/T_2) magnetic resonance and dual-modality imaging of tumor angiogenesis, J. Biomed. Nanotechnol. 11 (2015) 1027–1037.

[65] D. Couto, M. Freitas, F. Carvalho, E. Fernandes, Iron oxide nanoparticles: an insight into their biomedical applications, Curr. Med. Chem. 22 (2015) 1808–1828.

[66] S. Goel, C.G. England, F. Chen, W. Cai, Positron emission tomography and nanotechnology: a dynamic duo for cancer theranostics, Adv. Drug Deliv. Rev. (2016). Available from: http://dx.doi.org/10.1016/j.addr.2016.08.001.

[67] N. Lee, S.H. Choi, T. Hyeon, Nano-sized CT contrast agents, Adv. Mater. 25 (2013) 2641–2660.

[68] F. Ai, C.A. Ferreira, F. Chen, W. Cai, Engineering of radio labeled iron oxide nanoparticles for dual modality imaging, WIREs Nanomed. Nanobiotechnol. 8 (2016) 619–630.

[69] W.-K. Rhim, M. Kim, K.L. Hartman, K.W. Kang, J.-M. Nam, Radionuclide-labeled nanostructures for in vivo imaging of cancer, Nano Converg 2 (2015) 10. Available from: http://dx.doi.org/10.1186/s40580-014-0041-3.

[70] D.A. Mankoff, A definition of molecular imaging, J. Nucl. Med. 48 (2007) 18N–21N.

[71] O.L. Gobbo, K. Sjaastad, M.W. Radomski, Y. Volkov, A. Prina-Mello, Magnetic nanoparticles in cancer theranostics, Theranostics 5 (11) (2015) 1249–1263.

[72] T.A. Waigh, Experimental techniques, The Physics of Living Processes: A Mesoscopic Approach, first ed., John Wiley & Sons, Ltd, Chichester, 2014, pp. 357–433.

[73] J. Kim, Y. Wu, Y. Guo, H. Zheng, P.Z. Sun, A review of optimization and quantification techniques for chemical exchange saturation transfer (CEST) MRI toward sensitive in vivo imaging, Contrast Media Mol. Imaging 10 (3) (2015) 163–178.
[74] D. Pan, S.D. Caruthers, A. Senpan, C. Yalaz, A.J. Stacy, G. Hu, et al., Synthesis of nanoQ, a copper-based contrast agent, for high-resolution magnetic resonance imaging characterization of human thrombus, J. Am. Chem. Soc. 133 (24) (2011) 9168–9171.
[75] H.U. Rashid, K. Yu, J. Zhou, Lanthanide(III) chelates as MRI contrast agents: a brief description, J. Struct. Chem. 54 (1) (2013) 223–249.
[76] G.P. Yan, L. Robinson, P. Hogg, Magnetic resonance imaging contrast agents: overview and perspectives, Radiography 13 (2007) e5–e19.
[77] S. Sinharay, M.D. Pagel, Advances in magnetic resonance imaging contrast agents for biomarker detection, Annu. Rev. Anal. Chem. 9 (2016) 95–115.
[78] T.-H. Shin, Y. Choi, S. Kim, J. Cheon, Recent advances in magnetic nanoparticle-based multi-modal imaging, Chem. Soc. Rev. 44 (2015) 4501–4516.
[79] Y. Liu, K. Ai, L. Lu, Nanoparticulate X-ray computed tomography contrast agents: from design validation to in vivo applications, Acc. Chem. Res. 45 (10) (2012) 1817–1827.
[80] H. Lusic, M.W. Grinstaff, X-ray computed tomography contrast agents, Chem. Rev. 113 (3) (2013). Available from: http://dx.doi.org/10.1021/cr200358s.
[81] P.C. Naha, A.A. Zaki, E. Hecht, M. Chorny, P. Chhour, E. Blankemeyer, et al., Dextran coated bismuth–iron oxide nanohybrid contrast agents for computed tomography and magnetic resonance imaging, J. Mater. Chem. B (2014). Available from: http://dx.doi.org/10.1039/c4tb01159g.
[82] R.M. Taylor, T.C. Monson, R.R. Gullapalli, Influence of carbon chain length on the synthesis and yield of fatty amine-coated iron-platinum nanoparticles, Nanoscale Res. Lett 9 (2014) 306, http://www.nanoscalereslett.com/content/9/1/306.
[83] S. Sheng-Nan, W. Chao, Z. Zan-Zan, H. Yang-Long, S.S. Venkatraman, X. Zhi-Chuan, Magnetic iron oxide nanoparticles: synthesis and surface coating techniques for biomedical applications, Chin. Phys. B. 23 (3) (2014) 037503. Available from: http://dx.doi.org/10.1088/1674-1056/23/3/037503.
[84] F.-M. Lu, Z. Yuan, PET/SPECT molecular imaging in clinical neuroscience: recent advances in the investigation of CNS diseases, Quant Imaging Med. Surg. 5 (3) (2015) 433–447.
[85] X. Sun, W. Cai, X. Chen, Positron emission tomography imaging using radiolabeled inorganic nanomaterials, Acc. Chem. Res. 48 (2) (2015) 286–294.
[86] Y. Liu, M.J. Welch, Nanoparticles labeled with positron emitting nuclides: advantages, methods, and applications, Bioconjug. Chem. 23 (4) (2012) 671–682.
[87] C. Müller, R. Schibli, Single photon emission computed tomography tracer, in: O. Schober, B. Riemann (Eds.), Molecular Imaging in Oncology, Springer-Verlag Berlin, 2013, pp. 65–105.
[88] S.A. Albu, S.A. Al-Karmi, A. Vito, J.P.K. Dzandzi, A. Zlitni, D. Beckford-Vera, et al., I-tetrazines and inverse-electron-demand Diels – Alder chemistry: a convenient radioiodination strategy for biomolecule labeling, screening, and biodistribution studies, Bioconjug. Chem. 27 (1) (2016) 207–216.
[89] M. Bączyk, Radioisotope therapy of bone metastases, Nucl. Med. Rev. 14 (2) (2011) 96–104.
[90] T.A. Henderson, The diagnosis and evaluation of dementia and mild cognitive impairment with emphasis on SPECT perfusion neuroimaging, CNS Spectr. 17 (2012) 176–206.

[91] P. Ceruti, S.R. Bryant, J.-H. Lee, M.I. MacEntee, Magnet-retained implant-supported overdentures: review and 1-year clinical report, J. Can. Dent. Assoc. 76 (2010) a52.
[92] R. Raghavan, M. Ramzi, R. Kumar P, P.A. Shajahan, J. Usman, S. Balakrishnan, Magnets in complete dentures, Int. J. Oral Health Dent. 1 (3) (2015) 133–137.
[93] M. Mazaheri, N. Eslahi, F. Ordikhani, E. Tamjid, A. Simchi, Nanomedicine applications in orthopedic medicine: state of the art, Int. J. Nanomed. 10 (2015) 6039–6054.
[94] J.M.D. Coey, Special topics, Magnetism and Magnetic Materials, Cambridge University Press, Cambridge, 2009, pp. 542–579.
[95] S.T. Carmichael, Emergent properties of neural repair: elemental biology to therapeutic concepts, Ann. Neurol. 79 (2016) 895–906.
[96] Y. Suzuki, Mental health services and related factors in health care of traumatic brain injury survivors, Cogent Med 4 (2017) 1273568, http://dx.doi.org/10.1080/2331205X.2016.1273568.
[97] P. Kandesar, P. Chikode, S. Sabale, Perspective of magnetic fluid hyperthermia (MFH) for the treatment of tumor, J. Tumor Res. 2 (1) (2016) 111.
[98] A.Ž. Ilić, S. Ćirković, D.M. Djordjevic, S.R. De Luka, I.D. Milovanovich, A.M. Trbovich, et al., Analytical description of two-dimensional magnetic arrays suitable for biomedical applications, IEEE Trans. Magn. 49 (12) (2013) 5656–5663.
[99] M. Cemazar, T. Kotnik, G. Sersa, D. Miklavcic, Electroporation for electrochemotherapy and gene therapy, in: M.S. Markov (Ed.), Electromagnetic Fields in Biology and Medicine, Taylor & Francis Group, LLC, Boca Raton, 2015, pp. 395–413.
[100] R. Parker, M.S. Markov, Electromagnetic fields in the treatment of tendon injury in human and veterinarian medicine, in: M.S. Markov (Ed.), Electromagnetic Fields in Biology and Medicine, Taylor & Francis Group, LLC, Boca Raton, 2015, pp. 433–452.
[101] T. Schelle, Electrodiagnostic testing of the peripheral nerves, in: G. Penkert, J. Böhm, T. Schelle (Eds.), Focal Peripheral Neuropathies: Imaging, Neurological, and Neurosurgical Approaches, Springer-Verlag, Berlin, 2015, pp. 25–56.
[102] S. Tumanski, Magnetic field measurements and their applications, Handbook of Magnetic Measurements, CRC Press/ Taylor & Francis Group, Boca Raton, 2011, pp. 335–382.
[103] H.-X. Peng, F. Qin, M.-H. Phan, Giant magnetoimpedance sensors and their applications, Ferromagnetic Microwire Composites: From Sensors to Microwave Applications, Springer International Publishing Switzerland, 2016, pp. 99–117.
[104] T. Watson, Electrotherapy, in: S.B. Porter (Ed.), Tidy's Physiotherapy, fifteenth ed., Elsevier Ltd, Edinburgh, 2013, pp. 417–455.
[105] C. Bodine, Computer assistive devices and environmental controls, in: D.X. Cifu (Ed.), Braddom's Physical Medicine and Rehabilitation, fifth ed., Elsevier, Inc, Philadelphia, 2016, pp. 407–423.
[106] I.K. Herrmann, A.A. Schlegel, R. Graf, W.J. Stark, B. Beck-Schimmer, Magnetic separation-based blood purification: a promising new approach for the removal of disease-causing compounds? J. Nanobiotechnol. 13 (2015) 49.
[107] Y. Zhou, X. Xuan, Diamagnetic particle separation by shape in ferrofluids, Appl. Phys. Lett. 109 (2016) 102405.
[108] J. Lipfert, M. Lee, O. Ordu, J.W.J. Kerssemakers, N.H. Dekker, Magnetic tweezers for the measurement of twist and torque, J. Vis. Exp. 87 (2014) e51503.
[109] A.S. Adhikari, J. Chai, A.R. Dunn, Multiplexed single-molecule force proteolysis measurements using magnetic tweezers, J. Vis. Exp. 65 (2012) e3520.
[110] R. Sarkar, V.V. Rybenkov, A guide to magnetic tweezers and their applications, Front. Phys. 4 (2016) 48.

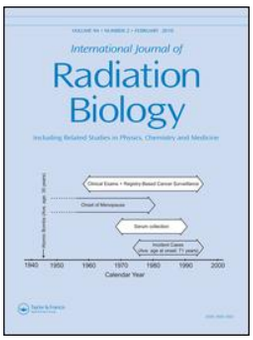

International Journal of Radiation Biology

ISSN: 0955-3002 (Print) 1362-3095 (Online) Journal homepage: http://www.tandfonline.com/loi/irab20

Modulation of rat synaptosomal ATPases and acetylcholinesterase activities induced by chronic exposure to the static magnetic field

Marko Dinčić, Danijela Z. Krstić, Mirjana B. Čolović, Jelena Nešović Ostojić, Sanjin Kovačević, Silvio R. De Luka, Drago M. Djordjević, Saša Ćirković, Predrag Brkić & Jasna Todorović

To cite this article: Marko Dinčić, Danijela Z. Krstić, Mirjana B. Čolović, Jelena Nešović Ostojić, Sanjin Kovačević, Silvio R. De Luka, Drago M. Djordjević, Saša Ćirković, Predrag Brkić & Jasna Todorović (2018): Modulation of rat synaptosomal ATPases and acetylcholinesterase activities induced by chronic exposure to the static magnetic field, International Journal of Radiation Biology

To link to this article: https://doi.org/10.1080/09553002.2018.1518611

Published online: 21 Sep 2018.

INTERNATIONAL JOURNAL OF RADIATION BIOLOGY
https://doi.org/10.1080/09553002.2018.1518611

Taylor & Francis
Taylor & Francis Group

ORIGINAL ARTICLE

Modulation of rat synaptosomal ATPases and acetylcholinesterase activities induced by chronic exposure to the static magnetic field

Marko Dinčić[a], Danijela Z. Krstić[b], Mirjana B. Čolović[c], Jelena Nešović Ostojić[a], Sanjin Kovačević[a], Silvio R. De Luka[a], Drago M. Djordjević[a], Saša Ćirković[d], Predrag Brkić[e] and Jasna Todorović[a]

[a]Institute of Pathological Physiology, Faculty of Medicine, University of Belgrade, Belgrade, Serbia; [b]Institute of Medical Chemistry, Faculty of Medicine, University of Belgrade, Belgrade, Serbia; [c]Department of Physical Chemistry, Vinča Institute of Nuclear Sciences, University of Belgrade, Belgrade, Serbia; [d]Institute of Physics, University of Belgrade, Belgrade, Serbia; [e]Institute of Physiology, Faculty of Medicine, University of Belgrade, Serbia

ABSTRACT

Purpose: It is considered that exposure to static magnetic fields (SMF) may have both detrimental and therapeutic effect, but the mechanism of SMF influence on the living organisms is not well understood. Since the adenosine triphosphatases (ATPases) and acetylcholinesterase (AChE) are involved in both physiological and pathological processes, the modulation of Na^+/K^+-ATPase, ecto-ATPases and AChE activities, as well as oxidative stress responses were followed in synaptosomes isolated from rats after chronic exposure toward differently oriented SMF.

Material and methods: Wistar albino rats were randomly divided into three experimental groups (six animals per group): Up and Down group - exposed to upward and downward oriented SMF, respectively, and Control group. After 50 days, the rats were sacrificed, and synaptosomes were isolated from the whole rat brain and used for testing the enzyme activities and oxidative stress parameters.

Results: Chronic exposure to 1 mT SMF significantly increased ATPases, AChE activities, and malondialdehyde (MDA) level in both exposed groups, compared to control values. The significant decrease in synaptosomal catalase activity (1.48 ± 0.17 U/mg protein) induced by exposure to the downward oriented field, compared to those obtained for Control group (2.60 ± 0.29 U/mg protein), and Up group (2.72 ± 0.21 U/mg protein).

Conclusions: It could be concluded that chronic exposure to differently oriented SMF increases ATPases and AChE activities in rat synaptosomes. Since brain ATPases and AChE have important roles in the pathogenesis of several neurological diseases, SMF influence on the activity of these enzymes may have potential therapeutic importance

ARTICLE HISTORY
Received 13 April 2018
Revised 21 May 2018
Accepted 9 July 2018

KEYWORDS
Static magnetic field; ATPases; acetylcholinesterase; malondialdehyde; catalase; hydroperoxidases

1. Introduction

There is growing interest for examining the effects of static magnetic fields (SMFs) on biological systems due to the development of artificial SMFs. Permanent magnets and electromagnetic coils, magnetic resonance imaging, magnetic levitation for transportation are examples of artificial SMFs. It is considered that exposure to these fields may have both detrimental and therapeutic effect (Repacholi and Greenebaum 1999; Jajte et al. 2002; Rosen 2003b; Lahbib et al. 2014; Luo et al. 2016; Dornelles et al. 2017), and accordingly, clear understanding of the mechanisms of SMF influence on the living organisms is necessary. A large number of SMF effects may be explained on the basis of diamagnetic anisotropic properties of molecules, such as lipids and proteins. Furthermore, results show that SMF exposure induces the reorientation of membrane phospholipids and it leads to deformation and modulation of membrane-bound molecules activity (Rosen 2003b; De Nicola et al. 2006; Nuccitelli et al. 2006; Wang et al. 2009). Therefore, investigating the influence of SMF on membrane-bound enzymes is important for understanding effects of SMF.

Adenosine triphosphatases (ATPases) and acetylcholinesterase (AChE) are membrane-bound enzymes involved in both physiological and pathological processes (Colovic et al. 2013; al-Rashida and Iqbal 2014; de Lores Arnaiz and Ordieres 2014). The main role of Na^+/K^+-ATPase (EC 3.6.1.37) is the maintenance of electrochemical gradient across the cell membranes by regulating the entry of K^+, along with the exit of Na^+ from cells. This essential enzyme is important for the generation and propagation of membrane potentials, the regulation of cell volume and cytoplasmic Ca^+ concentration, as well as the releasing of excitatory neurotransmitters. It is thought that brain Na^+/K^+-ATPase activity is altered during development and aging, and in diseases, such as epilepsy, Alzheimer's disease (AD), and

CONTACT Danijela Z. Krstić danijela.krstić@med.bg.ac.rs Institute of Medical Chemistry, Faculty of Medicine, University of Belgrade, Višegradska 26, 11 000, Belgrade, Serbia; Marko Dinčić dincic89@yahoo.com Institute of Pathological Physiology, Faculty of Medicine, University of Belgrade, Dr Subotica 1 11 000, Belgrade, Serbia

Color versions of one or more of the figures in the article can be found online at www.tandfonline.com/irab

depression (Liguri et al. 1990; Xiong and Stringer 2000; Gamaro et al. 2003; Reime Kinjo et al. 2007). The ecto-nucleotide triphosphate diphosphohydrolases (E-NTPDases, ecto-ATPases) are family of eight different isoenzymes which hydrolyze extracellular adenine nucleotides (ATP, ADP), in the presence of divalent cations (Ca^{2+} or Mg^{2+}). These enzymes probably play a role in many pathological conditions such as cancer development, epilepsy, ischemia and demyelination (Gendron et al. 2002; al-Rashida and Iqbal 2014; Lee et al. 2015). Therefore, molecules that affect ecto-ATPase represent potential therapeutic agent for these diseases. Acetylcholinesterase (AChE, EC 3.1.1.7) is a serin hydrolase accountable for degradation of the neurotransmitter acetylcholine (ACh) into choline and acetic acid in neuromuscular junctions and cholinergic synapses. Additionally, AChE is the target enzyme for molecules with reversible and irreversible inhibitory effect. Reversible AChE inhibitors are therapeutic agents for diagnosis and/or treatment of various disorders, on the other hand, irreversible AChE inhibitors are very potent toxic agents (Colovic et al. 2013).

There is evidence which suggests that SMF induce an imbalance between prooxidants and antioxidants in the body (Elferchichi et al. 2015; Ghodbane, Ammari, et al. 2015). However, there is, also, the study that does not support these assertions (Pawłowska-Góral et al. 2016). Reactive oxygen species (ROS) as intermediate products of oxygen reduction are highly reactive molecules which interact with target macromolecules. This interaction can lead to cell damage and death. Protection from ROS effects can be accomplished by antioxidants. Catalase (CAT; EC 1.11.1.6) as enzymatic antioxidant plays a crucial role in the cell antioxidant defense by conversion of H_2O_2 to O_2 and water. Levels of ROS and lipid peroxidation marker - malondialdehyde (MDA), as well as catalase activity are good markers of oxidative stress in various tissues, including nerve tissue.

The influence of SMF on nervous system has been investigated for a long time. Results obtained in different experimental models show the effects of SMF on neuroprotective mechanisms (Gao et al. 2010), excitability of neurons (Rosen 2003a; Coots et al. 2004), brain cells differentiation (Prasad et al. 2017), as well as cell morphology (Teodori et al. 2006). However, the mechanisms of SMF action on this system are still unclear. A large number of in vitro and in vivo studies suggest that short-term exposure to SMF does not produce any adverse health impact (Hiraoka et al. 1992; Repacholi and Greenebaum 1999; Sakurai et al. 2009); however, long-term exposure to SMF may have both potential therapeutic and adverse health effects (Elferchichi et al. 2007; Chae and Kim 2017; Dornelles et al. 2017; Medina-Fernandez et al. 2018). In addition, investigations show that the upward and downward oriented magnetic fields have different effects on experimental models (Djordjevich et al. 2012). Although the biological effects of SMF have been investigated for many years, the whole mechanisms of these fields on living organisms are still not well understood. In order to elucidate the mechanisms of static magnetic field on nervous system, the aim of this study was to examine the influence of chronic continuous exposure to 1 mT SMF of different orientation (upward and downward) on the activities of ATPases and AChE, as well as oxidative stress response (catalase activity, and the concentrations of hydroperoxides and MDA) in rat brain synaptosomes.

2. Material and methods

2.1. Chemicals

All reagents and chemicals were of high-purity grade and used as purchased without further purification. Acethylthiocholine iodide (AcSChI), 5,5′-dithio-bis-2-nitrobenzoic acid (DTNB), adenosinetriphosphate (ATP), ethylenediaminetetraacetic acid disodium salt dihydrate (EDTA), bovine serum albumin were obtained from Sigma-Aldrich (Munich, Germany). PeroxiDetect Kit for hydroperoxide determination was also purchased from Sigma. Thiobarbituric acid (TBA), H_2O_2 (33%), sodium hydroxide (NaOH), hydrochloric acid (HCl), n-butanol and other medium assay chemicals (magnesium chloride, Tris-HCl, sodium chloride, potassium chloride, stannous chloride, potassium hydrogen phosphate ($K_2HPO_4 \times 3H_2O$), ammonium molybdate) were purchased from Merck (Darmstadt, Germany).

2.2. Ethics statement

This study was carried out in strict accordance with the Animal Welfare Act of the Republic of Serbia (Official Gazette of the Republic of Serbia No. 41/09), Directive 2010/63/EU on the Protection of Animals Used for Scientific Purposes, and the Guide for the Care and Use of Laboratory Animals (National Research Council, 8th ed., Washington, USA). The methodology used in our investigation was approved by the Ethical Commission for the Welfare Protection of Experimental Animals (Faculty of Medicine, University of Belgrade).

2.3. Animals

Male Wistar albino rats six weeks old and 250–350 g weight were used. The animals ($n = 18$) were obtained from Military Medical Academy Research Facility (Belgrade, Serbia), and were kept in Plexiglas cage $48 \times 37.5 \times 21$ cm under controlled laboratory conditions (constant temperature $22 \pm 1^{\circ}$C, humidity of $65 \pm 1\%$, 12 h light/dark cycle) with free access to food and water. The weight of the rats was measured before the start of experiment and was followed up each day through the course of the experiment.

2.4. Static magnetic fields system

SMF was generated by placing Magnetic Deep Unipolar Oriented Field (MADU Strips) (Figure 1) (The Mihailo Pupin Institute, Belgrade, Serbia; patent number YU 48907/02, Republic of Serbia Intellectual Property Office, Belgrade, Serbia; patent number WO 99/60581, World Intellectual Property Organization, Brussels, Belgium, EU) under Plexiglas cages as described before (Ilic et al. 2013; De Luka et al. 2016) (Figure 2(a,b)).

2.5. Experimental design

The animals were randomly divided into three experimental groups (six animals in each group):

- I: Control
- II: Up
- III: Down

The animals in first group were housed in the Plexiglas cages without MADU stripes and were exposed only to naturally occurring SMF of negligible intensity (for Belgrade 0.048 mT, 61° 44′ inclination). The animals in II and III group were exposed to the upward and downward oriented SMF, respectively. All experimental animals were continuously exposed to SMF. At the end of the experiment, after 50 days, the animals were sacrificed by guillotine (Harvard Apparatus, Holliston, USA). The brains were rapidly excised and kept on ice-cold glass until synaptosomal preparation. The period of 50 days was chosen, because chronic toxicity studies last from one to three months, during which period hematological, biochemical and urinalysis assays could give an insight into biological responses to certain substance or exposure. We wanted to be sure that our animals were chronically exposed to SMF and therefore, a period of 50 days was selected.

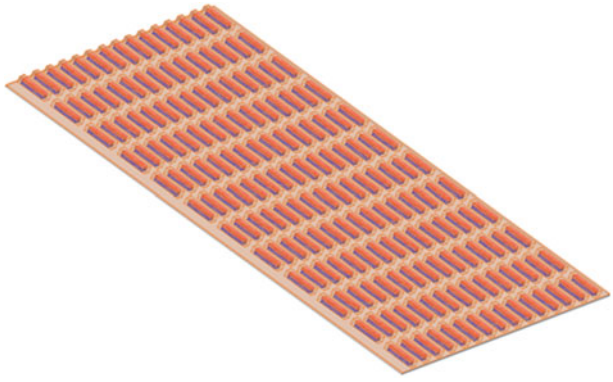

Figure 1. Graphic presentation of MADU stripe (43 × 23 cm). The L type MADU stripe contains ferromagnetic rods made of barium ferrite embedded in a plastic sheet. The size of each rod is 4.8 mm ×24.4 mm ×4.8 mm. The magnetic axes of the rods are vertical and equally directed.

2.6. Synaptosomal preparation

Synaptosomes were isolated from the whole rat brain using the method as described before (Cohen et al. 1977; Towle and Sze 1983). The brain tissues were homogenized in 10 ml 0.32 M sucrose containing 10 mM Tris-HCl pH 7.4. Then, the homogenates were centrifuged at 1000 × g for 10 min at 4 °C, and the supernatants were transferred to new tubes. The remaining pellets were resuspended in the homogenization buffer and centrifuged as before. Two supernatant fractions were combined and centrifuged at 10000 × g for 20 min at 4 °C. The precipitated synaptosomal pellets were resuspended in 3 ml of the buffered 0.32 M sucrose, and used for further analysis.

2.7. Acetylcholinesterase assay

The AChE activity was measured using Ellman's procedure (Ellman et al. 1961). A mixture composed of 20 μl synaptosomal preparation, 590 μl phosphate buffer (50 mM, pH 8) and 20 μl DTNB (10 mM) as a chromogenic reagent was prepared. The mixture was preincubated for 10 min at 37 °C, and the enzyme reaction was started by addition of AcSChI as the enzyme substrate. The yellow colored product formed in thiocholineiodide reaction with DTNB was determined spectrophotometrically at 412 nm (Perkin Elmer Lambda 35 UV-VIS, Shelton, USA). All experiments were made in triplicates. The activity of AChE was expressed as ΔA/(min × mg protein).

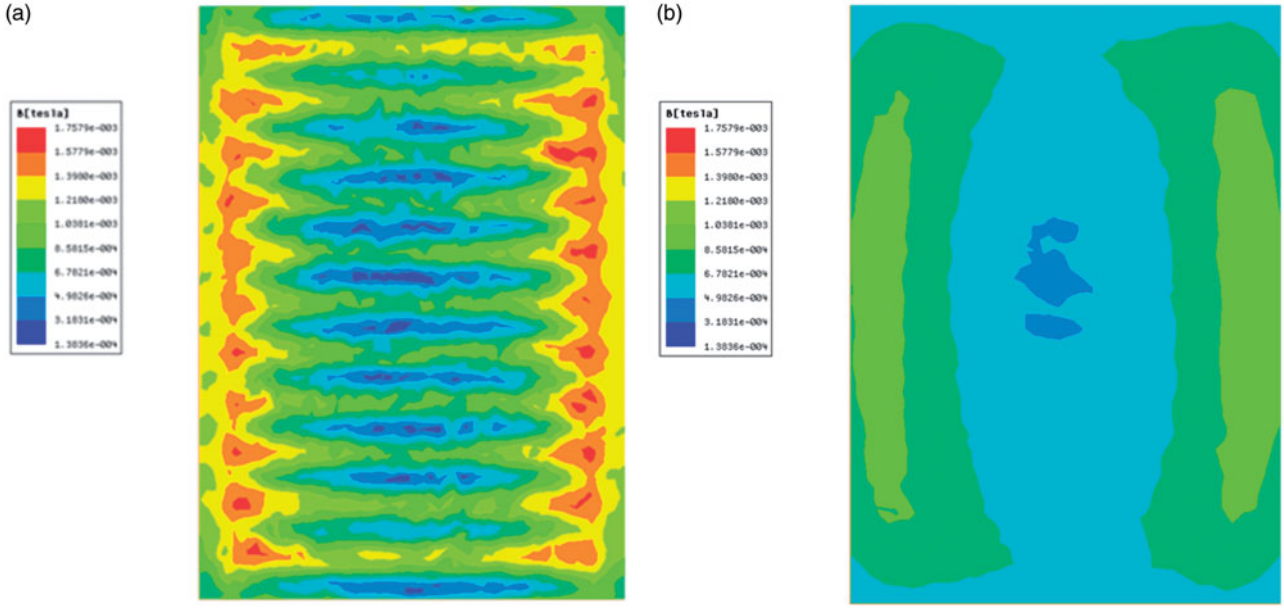

Figure 2. (a) Magnetic flux density at 30 mm above the ferromagnetic rods. The magnetic flux density variation in horizontal planes obtained using the finite-element calculations. Mean magnetic flux density in the experimental volume is obtained by averaging within the *z*-ranges of interest. (b) Magnetic flux density at 50 mm above the ferromagnetic rods.

2.8. ATPase assay

The specific activity of total ATPase was determined in a standard reaction medium (200 μl), containing 50 mM Tris-HCl (pH 7.4), 100 mM NaCl, 20 mM KCl, 5 mM $MgCl_2$, 2 mM ATP and 25 μl synaptosomal preparation. Assay for ecto-ATPase activity contained 50 mM Tris-HCl (pH 7.4), 5 mM $MgCl_2$, 1 mM oubain, 2 mM ATP and 25 μl synaptosomal preparation. After preincubation for 10 min at 37 °C, the reaction was initiated by addition of ATP and stopped after 10 min by adding 22 μl ice cold of 3 M $HClO_4$ and immediate cooling on ice. The concentration of liberated orthophosphate (Pi) from the hydrolysis of ATP was determined by modified spectrophotometric method (Vasic et al. 1999). The activity obtained in the presence of ouabain was attributed to ecto-ATPases activity. Na^+/K^+-ATPase activity was calculated by subtracting the ecto-ATPase activity from the total ATPase activity. The activities of Na^+/K^+-ATPase and ecto-ATPase were expressed as μmolPi/(h × mg protein).

2.9. Lipid peroxidation assay

The extent of lipid peroxidation was evaluated as the concentration of thiobarbituric acid reactive product malondialdehyde (MDA) by using the method of Aruoma (Aruoma et al. 1989). 0.5 ml of synaptosomal preparation was mixed with 0.5 ml of TBA in 0.05 M NaOH and 0.5 ml of HCl (25%). The mixture was placed in glass tubes and heated in boiling water for 10 min. After cooling, chromogen was extracted in 3 ml n-butanol, and organic phase was separated by centrifugation at 2000 × g for 10 min. The absorbance of the organic phase was read spectrophotometrically at 532 nm (Perkin Elmer Lambda 35 UV-VIS, Shelton, USA). 1,1,3,3′-tetraethoxy propane (in the range 0–20 nmol) was used to obtain standard curve. MDA level was expressed as nmol MDA/mg protein.

2.10. Catalase assay

Catalase activity was measured by the H_2O_2 degradation assay (Weissman 1976). This assay involves the change in absorbance at 240 nm, for 5 min, due to catalase dependent decomposition of H_2O_2. Catalase activity was expressed as U/mg protein. One unit (U) of catalase activity was defined as 1 μmol of H_2O_2 consumed/min.

2.11. Determination of hydroperoxides concentration

Hydroperoxides concentration was measured by using commercial PeroxiDetect Kit (Sigma-Aldrich, Munich, Germany). The procedure is based on the fact that peroxides oxidize Fe^{2+} to Fe^{3+} at pH 9. A colored adduct formed in the reaction between the Fe^{3+} ion and xylenol orange was determined spectrophotometrically, at 560 nm. The concentration of hydroperoxides in synaptosomal preparation was expressed as nmol peroxide/ml.

2.12. Determination of protein concentration

Protein concentration was measured by Lowry's method (Lowry et al. 1951) using bovine serum albumin (in the range 0–10 mg/ml) as a standard.

2.13. Statistical analysis

All data are expressed as the mean ± standard error of the mean (S.E.M). A statistical analysis of each of the parameters of interest was carried out using analysis of variance (One-way ANOVA). When a significant F value ($p<.05$) was obtained, post hoc test (Tukey HSD for multiple comparisons) was used. The statistical calculations were performed using GraphPad Prism for Windows (Version 7.0, GraphPad Software, La Jolla California, USA).

3. Results

3.1. General habits of animals

No changes in behavior regarding sleeping and feeding of the animals could be detected. The animals did not show any significant differences in body weights (all changes in body weight were in line with the timeframe of monitoring). Additionally, the animals did not have any changes in the appearance of the skin and mucosa.

3.2. The influence of differently oriented static magnetic field on Na^+/K^+-ATPase and ecto-ATPase activity in synaptosomes

The influence of chronic exposure to differently oriented SMF on the activity of synaptosomal Na^+/K^+-ATPase is presented in Figure 3. The obtained results (Figure 3) show that activity of Na^+/K^+-ATPase increases in both Up (5.26 ± 0.56 μmolPi/(hxmg protein)) and Down group (3.61 ± 0.59 μmolPi/(hxmg protein)) when compared to Control group (1.67 ± 0.16 μmolPi/(hxmg protein) $p<.001$ and $p<.05$, respectively). However, there was no difference in Na^+/K^+-ATPase activity (Figure 3) among the Up and Down group ($p>.05$).

Similar results were obtained for the activity of synaptosomal ecto-ATPase (Figure 4). The activity of ecto-ATPase in the Up group (22.38 ± 1.59 μmolPi/(hxmg protein)) was significantly higher ($p<.001$) when compared to the Control group (5.83 ± 0.33 μmolPi/(hxmg protein); additionally, ecto-ATPase activity in the Down group (26.62 ± 1.91 μmolPi/(hxmg protein)) was significantly increased ($p<.001$) when compared to the Control group (5.83 ± 0.33 μmolPi/(hxmg protein).

3.3. Effect of downward and upward static magnetic field on synaptosomal AChE activity

AChE activity in synaptosomes exposed to SMF and control group are shown in Figure 5. The AChE activity in the Up group (8.60 (6.86–11.17) ΔA/(minxmg protein)) and the Down group (7.91 (6.41–10.20) ΔA/(minxmg protein)) was

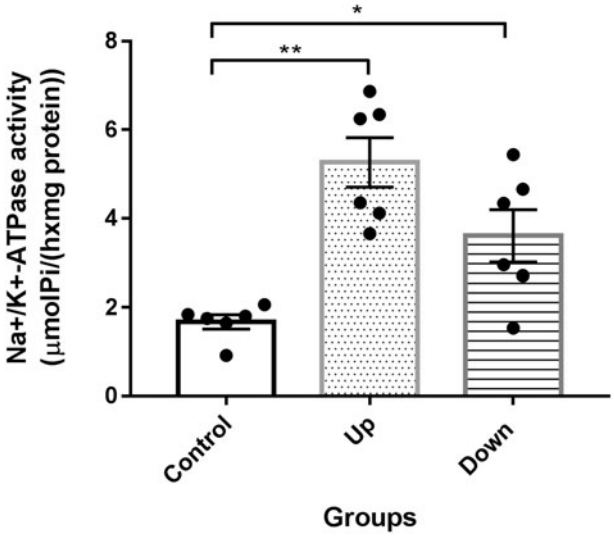

Figure 3. The influence of SMF chronic continuous exposure to 1 mT oriented upwards and downward on the activity of Na^{+}/K^{+}-ATPase in rat brain synaptosomes. Bars represent mean ± S.E.M; *$p<.05$; **$p<.001$.

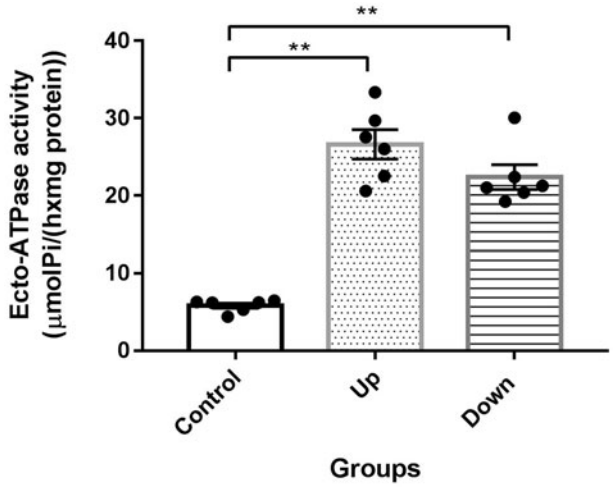

Figure 4. Effect of SMF either orientation on synaptosomal ecto-ATPase activity. Bars represent mean ± S.E.M; **$p<.001$.

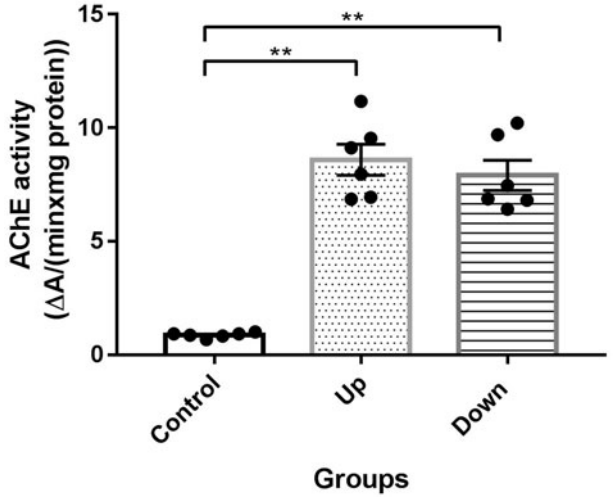

Figure 5. The activity of AChE in synaptosomes of exposed and control group animals. Values are mean ± S.E.M; **$p<.001$.

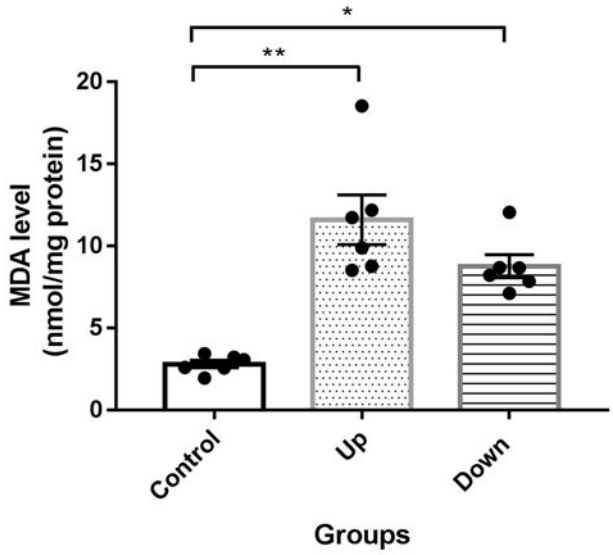

Figure 6. MDA level in synaptosomes of exposed and control group animals. Values are mean ± S.E.M; *$p<.05$; **$p<.001$.

significantly higher ($p<.05$) comparing the Control group (0.89 (0.67–1.01) ΔA/(minxmg protein)) (Figure 5).

3.4. The influence of upward and downward static magnetic field on lipid peroxidation

The effect of upward and downward SMF exposure on the level of MDA, as marker of lipid peroxidation, is shown in Figure 6. In the Up group there was a significant increase ($p<.001$) in MDA level (11.60 ± 1.51 nmol/mg protein); also there was a significant rise ($p<.05$) in the Down group (8.75 ± 0.70 nmol/mg protein) when compared to the Control group (2.80 ± 0.22 nmol/mg protein) (Figure 4). There was no difference in MDA level (Figure 6) among the exposed groups ($p>.05$).

3.5. The influence of upward and downward static magnetic field on catalase activity

The influence of differently oriented SMF exposure on the activity of CAT as antioxidant enzyme is presented in Figure 7. Obtained results show a significant decrease ($p<.01$) in the activity of synaptosomal CAT in animals exposed to the downward oriented SMF (1.48 ± 0.17 U/mg protein) when compared to those exposed to the upward oriented field (2.72 ± 0.21 U/mg protein). Also, when compared to Control group (2.60 ± 0.29 U/mg protein) there was a significant ($p<.01$) decrease of activity in the Down group (Figure 7). However, there was no difference in CAT activity among the Up and Control group ($p>.05$) (Figure 7).

3.6. The influence of upward and downward static magnetic field on hydroperoxides concentration

Hydroperoxides concentration in rats exposed to SMF of different orientation is shown in Figure 6. Chronic exposure to upward and downward oriented SMF did not induce

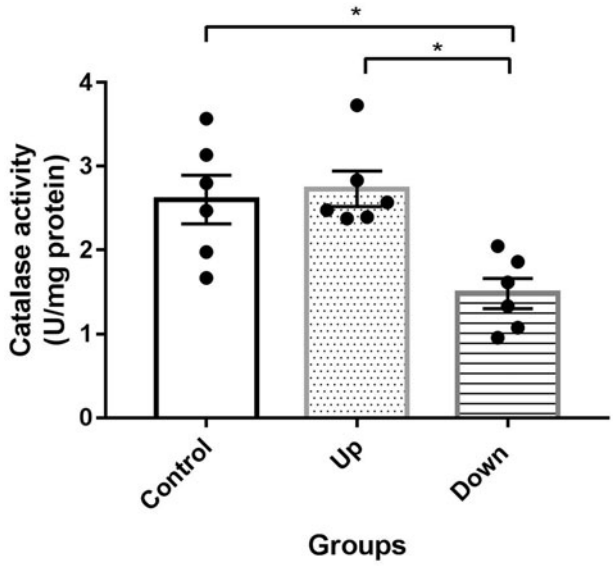

Figure 7. Synaptosomal CAT activity in rats exposed (Up, Down) or not exposed (Control) to SMF of different orientation for 50 days. Data are expressed as mean ± S.E.M; *p<.01.

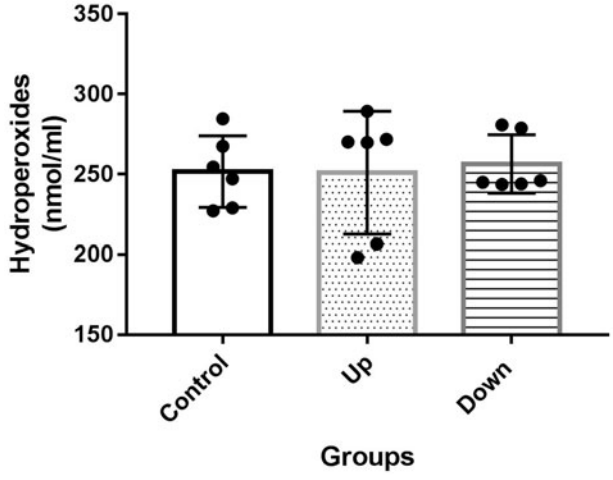

Figure 8. Synaptosomal concentration of hydroperoxides in rats exposed (Up, Down) or not exposed (Control) to SMF of different orientation for 50 days. Data are expressed as mean ± S.E.M.

statistically significant change of the hydroperoxides concentration in both groups (p>.05) comparing to the control animals (Figure 8).

4. Discussion

Sources of SMFs are commonly ranging from specialized (audio speakers, battery operated motors, microwave ovens) to highly trivial (such as refrigerator magnets), and the fields they produce are from few μT to few mT (Hashish et al. 2008). Numerous studies (Engstrom et al. 2002; Dini and Panzarini 2010; Markov 2011) suggest the existence of 'biological windows' representing combinations of amplitude, frequency of exposure and exposure duration within which the optimal response is observed. For SMFs several windows have been reported, such as 0.5–2 mT, 15–20 mT and 45–50 mT. Since exposure to such moderate SMFs occurs more frequently than to strong or ultrastrong fields, we preformed our experiment to such artificially generated moderate magnetic field that belongs to proposed 'biological window'. Magnetic orientation seems to play an important role in biological responses to SMFs, however, the available results are scarce and unconvincing. The only conclusive outcome could be found in studies which explored seed germination and root growth. This phenomenon of plant movement in response to SMF is known as magnetotropism. However, similar findings were rarely shown in animals.

The results found in the published literature on the SMF influence on ATPases and AChE activities, as well as on markers of oxidative stress, are scarce and conflicting (Stegemann et al. 1993; Okano 2008). Also, there is a large volume of studies describing the importance of these enzymes and oxidative stress in either pathogenesis or treatment of diverse diseases (Liguri et al. 1990; Ohnishi et al. 2015; Gonzalez-Gonzalez et al. 2017). Magnetic fields have been studied as potential therapeutics in various neurological disorders; however, mechanisms of action are not well understood (Janicak and Dokucu 2015; Smith and Stinear 2016). Therefore, the influence of SMF on ATPases and AChE activities, and, also, on oxidative stress markers could probably explain some of the mechanisms of SMF action on nervous system.

In this study, we have shown that chronic 50 days continuous exposure to moderate intensity SMF (1 mT) of either orientation has induced significant increase of ATPases and AChE activities. Increasing activities of ATPases and AChE may help us to understand some of the effects of SMF. The study of Leenen et al. (1994) demonstrated that brain Na^+/K^+-ATPase plays a role in blood pressure regulation; increased level of blood pressure is associated with depressed activity of this enzyme. Furthermore, in the analysis of SMF effects on spontaneously hypertensive rats, Tasic et al. (2017) found that moderate intensity SMF (16 mT for the period of 30 days) affects low-frequency spectral component of systolic blood pressure variability which reflects sympathetic outflow to resistance vessels. The same study showed reduced plasma concentration of noradrenalin by half, thus both findings strongly suggest that SMF reduces peripheral resistance. The increased activity of Na^+/K^+-ATPase obtained in our experiment could be, therefore, considered as a compensatory response to decreased blood pressure. Recent work of Nikolic et al. (2013) demonstrated an increase in Na^+/K^+-ATPase activity after short-term exposure to moderate intensity SMF (10 mT for 15 min). They showed that SMF induced redistribution of the Na^+/K^+ pump from intracellular compartments toward plasma membrane. Their study revealed increased expression of the Na^+/K^+ pump α-subunit in the plasma membrane area with concomitant decrease in the cytoplasm. The rise in the activity of Na^+/K^+ pump is probably mediated by phosphorylation and dephosphorylation signaling pathways which regulate expression and functional properties of Na^+/K^+-ATPase in the plasma membrane. Previous study (Rosen 2003b) reported that SMF exposure induced the reorientation of membrane lipids as diamagnetic anisotropic molecules.

ATPases are membrane-spanning proteins and any change in the lipid component of the membrane will directly affect the catalytic potential of these enzymes.

The other roles of Na^+/K^+-ATPase have been shown in the pathophysiology of depression (Yu et al. 2013), in the protection of hippocampal slice culture neurons from hypoxia-hypoglycemia (Tian et al. 2008), and an improvement in patients with acute ischemic stroke after exposure to SMF (Xie and Zhang 2012). Both fluoxetine, as a therapeutic drug for depression, and SMF increase the activity of Na^+/K^+-ATPase, therefore SMF is used in depressed patient's treatment. The same explanation was offered for protection of neurons exposed to ischemia and their subsequent recovery after SMF exposure. By knowing that SMF induces increase in Na^+/K^+-ATPase activity, we may begin to understand the beneficial effects of a therapeutically applied magnetic field on the nervous system, moreover since Na^+/K^+-ATPase shows an essential similarity among neurons of diverse animal species.

The main physiological role of ecto-ATPases is to control the extracellular nucleotide levels by hydrolysis ATP and ADP to AMP. A number of researchers have reported that these nucleotides and their nucleoside product adenosine control diverse physiological and pathological actions in body (Ribeiro et al. 2002; Spanevello et al. 2009). However, this signal molecule in high concentration may induce cell damage by increasing the intracellular calcium levels (Sperlagh and Illes 2014) and, also, plays an important role in neurotransmission of pain (Gendron et al. 2002). Since SMF is used in the treatment of pain, one can speculate that the increasing activity of ecto-ATPase could represent the mechanism of SMF action in the pain therapy. The results obtained in our study can only strengthen the assumption of protective role of static magnetic field. The present study demonstrated that downward and upward SMF lead to increase of AChE activity. This finding is in agreement with the study of Hamdy et al. (2014) which showed that AChE activity was significantly increased in whole brain homogenates of mice exposed to combination of SMF and time-varying (electromagnetic) field (3 mT for one-third weeks). Contrary to these results, Ravera et al. (2010) suggested that magnetic fields (0.74 mT) caused a decreased AChE activity. Takeshige and Sato (Takeshige and Sato 1996) suggested that 130 mT SMF exposure enhanced release of acetylcholine (ACh). The increase in AChE activity in our study could thus be the compensatory response to increased ACh. Taken together, all these results of the influence of SMF on biological systems should be interpreted with great caution with regard to animal species, field's orientation and intensity, type and period of exposure to SMF.

Our results show that exposure to SMF increased synaptosomal MDA concentration, which is a marker of lipid peroxidation. These findings are in concurrence with previously published results about increased MDA concentration following the exposure to SMF (128 mT 1 h/day for 5 days) (Ghodbane, Lahbib, et al. 2015). However, we found that SMF of either orientation did not induce alteration in hydroperoxides concentration in both exposed groups. Whereas the reorientation of membrane lipids after SMF exposure had been previously confirmed (Rosen 2003b), we may hypothesize that this reorientation exposed lipid molecules to physiologically produced radical oxygen species (ROS) within the cell, which resulted in elevated concentrations of MDA in both groups. With unchanged hydroperoxides concentration, the MDA rise is for certain not the consequence of increased ROS burden.

In this study, we found an interesting effect, depending on SMF orientation, on the activity of catalase (CAT). Downward oriented SMF caused a decreased activity of CAT, while upward oriented SMF did not induce change in the enzymatic activity. Earlier study (Amara et al. 2009) showed that subchronic exposure to SMF (128 mT, 1 h/day during 30 consecutive days) decreased CAT activity in various organs. Catalase catalyzes the decomposition of hydrogen peroxide to water and oxygen. Since there was no increase in hydroperoxides concentration in this study we can attribute our results to specific effects of differently oriented SMF to activity of examined enzyme, which are shown for the first time. Future examination of the expression of catalase could reveal the exact effect of differently oriented static magnetic field.

5. Conclusions

In conclusion, we can say that chronic exposure to differently oriented SMF increases ATPases and AChE activities in rat synaptosomes. Since brain ATPases and AChE have important roles in the pathogenesis of several neurological diseases, SMF influence on the activity of these enzymes may have potential therapeutic importance. Our results encourage the research for the proper use of static magnetic field in the treatment of various, mainly neurological, disorders, but simultaneous increase in MDA concentration and decrease in catalase activity, force us to conclude that further studies are needed to elucidate the real nature of SMF effects.

Disclosure statement

No potential conflict of interest was reported by the authors.

Notes on contributors

Marko Dinčić, MD is PhD student employed as teaching assistant at Institute of Pathophysiology, Faculty of Medicine, University of Belgrade, Serbia. His research activities are focused on the physiological and toxicological studies using different in vitro and in vivo model systems.

Danijela Krstić obtained her BSc., MSc. and PhD in biochemistry from the Faculty of Chemistry, University of Belgrade, Serbia. Working as an Associate Professor in the Institute of Medical Chemistry, School of Medicine, University of Belgrade. The topics of her research activities are enzymology, enzyme inhibition and toxic effects of different (organic or inorganic) pharmacologically and physiologically active compounds. She published (author or coauthor) more than 40 scientific papers in international journals.

Mirjana B. Čolović, PhD (ORCID ID https://orcid.org/0000-0001-5037-9985), a research associate has been emoloyed at Department of Physical Chemistry, Vinča Institute of Nuclear Sciences, University of Belgrade, Serbia, from 2005. Her research activities are in the field of enzymology, toxicology, biosensors, physiologically active compounds and their interaction with biomolecules. She has published 36 papers in impacted international journals, 4 chapters in books, 3 articles in national scientific journals, and over 60 abstracts in international and national scientific meetings. She served as a reviewer in over 20 international journals and 9 international projects.

Jelena Nešović Ostojić received the M.D., M.Sc., and Ph.D. degrees from the Faculty of Medicine, University of Belgrade, Belgrade, Serbia, in 2000, 2005, and 2009. She is currently an Associate Professor of pathophysiology at the Faculty of Medicine, University of Belgrade. Over 15 years of experience in medical research. Performed basic science research in the field of electrophysiology; can apply appropriate techniques of conventional electrophysiology; research interests are physiology, biophysics and pharmacology of epithelial and excitable membranes. Currently engaged in three areas of research: electrophysiology (epithelial and excitable membranes), static magnetic field (animal models), pathogenesis of acute and chronic renal failure (animal models).

Sanjin Kovačević received the M.D. degree from the Faculty of Medicine, University of Belgrade, Belgrade, Serbia. Three years of experience in the field of medical research and teaching at the Department of Pathophysiology, Faculty of Medicine, University of Belgrade, Serbia. Assistant in Laboratory for intracellular electrophysiology and a PhD candidate focused in Physiological Sciences. Currently focused on researching the role of potassium channels in proximal tubule transport processes and the influence of tissue oxygenation on pathophysiological processes in acute renal failure. Also, shows interests in sports medicine and static magnetic field.

Silvio R. De Luka was born in Belgrade, Serbia. He received the M.D. degree, M.Sc. degree in neurochemistry, and Ph.D. degree in neurology from the Faculty of Medicine, University of Belgrade, Belgrade, Serbia. He is currently an Associate Professor of pathophysiology at the Faculty of Medicine, University of Belgrade. His current research interests include static magnetic field, trace elements, and biomarkers of aging.

Drago M. Djordjević received the M.D., M.Sc., and Ph.D. degrees from the University of Belgrade, Belgrade, Serbia, in 1982, 1995, and 2008, respectively, as well as completed his residency in physical medicine and rehabilitation there in 1991. He is currently an Associate Professor with the Institute of Pathophysiology, Faculty of Medicine, University of Belgrade. His current research interests include pathobiology, biophysics, biomaterials, biomedical applications of magnetic nanomaterials, magnetobiology, bioelectromagnetism, quantum biology, and quantum medicine.

Saša Ćirković received the B.S., M.S., and Ph.D. degrees in electrical engineering from the University of Belgrade, Belgrade, Serbia, in 1989, 2001, and 2009, respectively. He was with GTE, Vinča Institute of Nuclear Sciences, and Innovation Center of School of Electrical Engineering, University of Belgrade. He is currently a Research Assistant Professor at the Institute of Physics, University of Belgrade, Belgrade, Serbia. His current research interests include accelerator physics and technology, bioengineering, biophysics, and bioinformatics.

Predrag Brkić obtained his M.D., MSc. and PhD from the Faculty of Medicine, University of Belgrade, Serbia. Predrag Brkic obtained his Specialist in Sport Medicine and Sub specialist in Baromedicine, Postgraduate School of Medicine, University of Belgrade. Working as an Assistant Professor in the Department of Medical Physiology, Faculty of Medicine, University of Belgrade. Member of domestic and international professional organizations. Organizer and Member of Organizing Boards of several domestic and international.

Jasna Todorović was born in Serbia. She received the M.D. degree and M.Sc. degree in neuroendocrinology. Her Ph.D. degree is from pathoendocrinology from the Faculty of Medicine, University of Belgrade, Belgrade, Serbia. She is currently an Assistant Professor at pathophysiology at the Faculty of Medicine, University of Belgrade. Her current research interests include pathoendocrinology, static magnetic field, and electrophysiology.

Funding

This work was supported by Ministry of Education, Science and Technological Development of the Republic of Serbia (projects no. 175081 and 172023).

References

al-Rashida M, Iqbal J. 2014. Therapeutic potentials of ecto-nucleoside triphosphate diphosphohydrolase, ecto-nucleotide pyrophosphatase/phosphodiesterase, ecto-5′-nucleotidase, and alkaline phosphatase inhibitors. Med Res Rev. 34:703–743.

Amara S, Douki T, Garel C, Favier A, Sakly M, Rhouma KB, Abdelmelek H. 2009. Effects of static magnetic field exposure on antioxidative enzymes activity and DNA in rat brain. Gen Physiol Biophys. 28: 260–265.

Aruoma OI, Halliwell B, Laughton MJ, Quinlan GJ, Gutteridge JM. 1989. The mechanism of initiation of lipid peroxidation. Evidence against a requirement for an iron(II)-iron(III) complex. Biochem J. 258:617–620.

Chae K-S, Kim Y-H. 2017. Potential impact of geomagnetic field in transcranial magnetic stimulation for the treatment of neurodegenerative diseases. Front Hum Neurosci. 11:478.

Cohen RS, Blomberg F, Berzins K, Siekevitz P. 1977. The structure of postsynaptic densities isolated from dog cerebral cortex. I. Overall morphology and protein composition. J Cell Biol. 74:181–203.

Colovic MB, Krstic DZ, Lazarevic-Pasti TD, Bondzic AM, Vasic VM. 2013. Acetylcholinesterase inhibitors: pharmacology and toxicology. CN. 11: 315–335.

Coots A, Shi R, Rosen AD. 2004. Effect of a 0.5-T static magnetic field on conduction in guinea pig spinal cord. J Neurol Sci. 222:55–57.

de Lores Arnaiz GR, Ordieres MG. 2014. Brain Na(+), K(+)-ATPase activity in aging and disease. Int J Biomed Sci. 10:85–102.

De Luka SR, Ilić AŽ, Janković S, Djordjevich DM, Ćirković S, Milovanovich ID, Stefanović S, Vesković-Moračanin S, Ristić-Djurović JL, Trbovich AM. 2016. Subchronic exposure to static magnetic field differently affects zinc and copper content in murine organs. Int J Radiat Biol. 92:140–147.

De Nicola M, Cordisco S, Cerella C, Albertini MC, D'Alessio M, Accorsi A, Bergamaschi A, Magrini A, Ghibelli L. 2006. Magnetic fields protect from apoptosis via redox alteration. Ann N Y Acad Sci. 1090:59–68.

Dini L, Panzarini E. 2010. The influence of a 6 mT static magnetic field on apoptotic cell phagocytosis depends on monocyte/macrophage differentiation. Exp Biol Med (Maywood). 235:1432–1441.

Djordjevich DM, De Luka SR, Milovanovich ID, Janković S, Stefanović S, Vesković-Moračanin S, Cirković S, Ilić AŽ, Ristić-Djurović JL, Trbovich AM. 2012. Hematological parameters' changes in mice subchronically exposed to static magnetic fields of different orientations. Ecotoxicol Environ Saf. 81:98–105.

Dornelles EB, Goncalves BD, Schott KL, Barbisan F, Unfer TC, Glanzner WG, Machado AK, Cadona FC, Azzolin VF, Montano MAE, et al. 2017. Cytotoxic effects of moderate static magnetic field exposure on human periphery blood mononuclear cells are influenced by Val16Ala-MnSOD gene polymorphism. Environ Sci Pollut Res Int. 24: 5078–5088.

Elferchichi M, Abdelmelek H, Sakly M. 2007. Effects of sub-acute exposure to static magnetic field on iron status and hematopoiesis in rats. Turk J Haematol. 24:54–68.

Elferchichi M, Maaroufi K, Ammari M, Sakly M, Abdelmelek H. 2015. Effects of combined ferrous sulfate administration and exposure to static magnetic field on brain oxidative stress and emotional behavior. Arch Ital Biol. 153:37–45.

Ellman GL, Courtney KD, Andres V, Jr, Feather SRM. 1961. A new and rapid colorimetric determination of acetylcholinesterase activity. Biochem Pharmacol. 7:88–95.

Engstrom S, Markov MS, McLean MJ, Holcomb RR, Markov JM. 2002. Effects of non-uniform static magnetic fields on the rate of myosin phosphorylation. Bioelectromagnetics. 23:475–479.

Gamaro GD, Streck EL, Matte C, Prediger ME, Wyse AT, Dalmaz C. 2003. Reduction of hippocampal Na+, K+-ATPase activity in rats subjected to an experimental model of depression. Neurochem Res. 28: 1339–1344.

Gao F, Wang S, Guo Y, Wang J, Lou M, Wu J, Ding M, Tian M, Zhang H. 2010. Protective effects of repetitive transcranial magnetic stimulation in a rat model of transient cerebral ischaemia: a microPET study. Eur J Nucl Med Mol Imaging. 37:954–961.

Gendron FP, Benrezzak O, Krugh BW, Kong Q, Weisman GA, Beaudoin AR. 2002. Purine signaling and potential new therapeutic approach: possible outcomes of NTPDase inhibition. Curr Drug Targets. 3: 229–245.

Ghodbane S, Ammari M, Lahbib A, Sakly M, Abdelmelek H. 2015. Static magnetic field exposure-induced oxidative response and caspase-independent apoptosis in rat liver: effect of selenium and vitamin E supplementations. Environ Sci Pollut Res Int. 22:16060–16066.

Ghodbane S, Lahbib A, Ammari M, Sakly M, Abdelmelek H. 2015. Does static magnetic field-exposure induced oxidative stress and apoptosis in rat kidney and muscle? Effect of vitamin E and selenium supplementations. Gen Physiol Biophys. 34:23–32.

Gonzalez-Gonzalez FJ, Chandel NS, Jain M, Budinger GRS. 2017. Reactive oxygen species as signaling molecules in the development of lung fibrosis. Transl Res. 190:61–68.

Hamdy HA, Mahmoud BF, Shalaby TE, El-Sharkawy AM, Farag IM. 2014. Effect of static and alternating magnetic fields on acetylcholinesterase and monoamine oxidase activities in the brain of mice. J Invest Biochem. 3:133–137.

Hashish AH, El-Missiry MA, Abdelkader HI, Abou-Saleh RH. 2008. Assessment of biological changes of continuous whole body exposure to static magnetic field and extremely low frequency electromagnetic fields in mice. Ecotoxicol Environ Saf. 71:895–902.

Hiraoka M, Miyakoshi J, Li YP, Shung B, Takebe H, Abe M. 1992. Induction of c-fos gene expression by exposure to a static magnetic field in HeLaS3 cells. Cancer Res. 52:6522–6524.

Ilic AZ, Cirkovic S, Djordjevic DM, De Luka SR, Milovanovich ID, Trbovich AM, Ristic-Djurovic JL. 2013. Analytical description of two-dimensional magnetic arrays suitable for biomedical applications. IEEE Trans Magn. 49:5656–5663.

Jajte J, Grzegorczyk J, Zmyślony M, Rajkowska E. 2002. Effect of 7 mT static magnetic field and iron ions on rat lymphocytes: apoptosis, necrosis and free radical processes. Bioelectrochemistry. 57:107–111.

Janicak PG, Dokucu ME. 2015. Transcranial magnetic stimulation for the treatment of major depression. Neuropsychiatr Dis Treat. 11: 1549–1560.

Lahbib A, Ghodbane S, Sakly M, Abdelmelek H. 2014. Vitamins and glucose metabolism: The role of static magnetic fields. Int J Radiat Biol. 90:1240–1245.

Lee S-Y, Fiene A, Li W, Hanck T, Brylev KA, Fedorov VE, Lecka J, Haider A, Pietzsch H-J, Zimmermann H, et al. 2015. Polyoxometalates-potent and selective ecto-nucleotidase inhibitors. Biochem Pharmacol. 93: 171–181.

Leenen FH, Harmsen E, Yu H. 1994. Dietary sodium and central vs. peripheral ouabain-like activity in Dahl salt-sensitive vs. salt-resistant rats. Am J Physiol. 267:H1916–H1920.

Liguri G, Taddei N, Nassi P, Latorraca S, Nediani C, Sorbi S. 1990. Changes in Na+, K(+)-ATPase, Ca2(+)-ATPase and some soluble enzymes related to energy metabolism in brains of patients with Alzheimer's disease. Neurosci Lett. 112:338–342.

Lowry OH, Rosebrough NJ, Farr AL, Randall RJ. 1951. Protein measurement with the Folin phenol reagent. J Biol Chem. 193:265–275.

Luo Y, Ji X, Liu J, Li Z, Wang W, Chen W, Wang J, Liu Q, Zhang X. 2016. Moderate intensity static magnetic fields affect mitotic spindles and increase the antitumor efficacy of 5-FU and Taxol. Bioelectrochemistry. 109:31–40.

Markov MS. 2011. How living systems recognize applied electromagnetic fields. Environmentalist. 31:89–96.

Medina-Fernandez FJ, Escribano BM, Padilla-Del-Campo C, Drucker-Colin R, Pascual-Leone A, Tunez I. 2018. Transcranial magnetic stimulation as an antioxidant. Free Radic Res 1:9.

Nikolic L, Bataveljic D, Andjus PR, Nedeljkovic M, Todorovic D, Janac B. 2013. Changes in the expression and current of the Na+/K+ pump in the snail nervous system after exposure to a static magnetic field. J Exp Biol. 216:3531–3541.

Nuccitelli S, Cerella C, Cordisco S, Albertini MC, Accorsi A, De Nicola M, D'Alessio M, Radogna F, Magrini A, Bergamaschi A, et al. 2006. Hyperpolarization of plasma membrane of tumor cells sensitive to antiapoptotic effects of magnetic fields. Ann N Y Acad Sci. 1090: 217–225.

Ohnishi T, Yanazawa M, Sasahara T, Kitamura Y, Hiroaki H, Fukazawa Y, Kii I, Nishiyama T, Kakita A, Takeda H, et al. 2015. Na, K-ATPase α3 is a death target of Alzheimer patient amyloid-β assembly. Proc Natl Acad Sci USA. 112:E4465–E4474.

Okano H. 2008. Effects of static magnetic fields in biology: role of free radicals. Front Biosci. 13:6106–6125.

Pawłowska-Góral K, Kimsa-Dudek M, Synowiec-Wojtarowicz A, Orchel J, Glinka M, Gawron S. 2016. Effect of static magnetic fields and phloretin on antioxidant defense system of human fibroblasts. Environ Sci Pollut Res Int. 23:14989–14996.

Prasad A, Teh DBL, Blasiak A, Chai C, Wu Y, Gharibani PM, Yang IH, Phan TT, Lim KL, Yang H, et al. 2017. Static magnetic field stimulation enhances oligodendrocyte differentiation and secretion of neurotrophic factors. Sci Rep. 7:6743.

Ravera S, Bianco B, Cugnoli C, Panfoli I, Calzia D, Morelli A, Pepe IM. 2010. Sinusoidal ELF magnetic fields affect acetylcholinesterase activity in cerebellum synaptosomal membranes. Bioelectromagnetics. 31: 270–276.

Reime Kinjo E, Arida RM, Mara de Oliveira D, da Silva Fernandes MJ. 2007. The Na+/K+ ATPase activity is increased in the hippocampus after multiple status epilepticus induced by pilocarpine in developing rats. Brain Res. 1138:203–207.

Repacholi MH, Greenebaum B. 1999. Interaction of static and extremely low frequency electric and magnetic fields with living systems: health effects and research needs. Bioelectromagnetics. 20:133–160.

Ribeiro JA, Sebastiao AM, de Mendonca A. 2002. Adenosine receptors in the nervous system: pathophysiological implications. Prog Neurobiol. 68:377–392.

Rosen AD. 2003. Effect of a 125 mT static magnetic field on the kinetics of voltage activated Na + channels in GH3 cells. Bioelectromagnetics. 24:517–523.

Rosen AD. 2003. Mechanism of action of moderate-intensity static magnetic fields on biological systems. Cbb. 39:163–173.

Sakurai T, Terashima S, Miyakoshi J. 2009. Effects of strong static magnetic fields used in magnetic resonance imaging on insulin-secreting cells. Bioelectromagnetics. 30:1–8.

Smith MC, Stinear CM. 2016. Transcranial magnetic stimulation (TMS) in stroke: Ready for clinical practice? J Clin Neurosci. 31:10–14.

Spanevello R, Mazzanti CM, Schmatz R, Bagatini M, Stefanello N, Correa M, Kaizer R, Maldonado P, Mazzanti A, Graça DL, et al. 2009. Effect of vitamin E on ectonucleotidase activities in synaptosomes and platelets and parameters of oxidative stress in rats experimentally demyelinated. Brain Res Bull. 80:45–51.

Sperlagh B, Illes P. 2014. P2X7 receptor: an emerging target in central nervous system diseases. Trends Pharmacol Sci. 35:537–547.

Stegemann S, Altman KI, Muhlensiepen H, Feinendegen LE. 1993. Influence of a stationary magnetic field on acetylcholinesterase in murine bone marrow cells. Radiat Environ Biophys. 32: 65–72.

Takeshige C, Sato M. 1996. Comparisons of pain relief mechanisms between needling to the muscle, static magnetic field, external qigong and needling to the acupuncture point. Acupunct Electrother Res. 21:119–131.

Tasic T, Djordjevic DM, De Luka SR, Trbovich AM, Japundzic ZN. 2017. Static magnetic field reduces blood pressure short-term variability and enhances baro-receptor reflex sensitivity in spontaneously hypertensive rats. Int J Radiat Biol. 93:527–534.

Teodori L, Albertini MC, Uguccioni F, Falcieri E, Rocchi MB, Battistelli M, Coluzza C, Piantanida G, Bergamaschi A, Magrini A, et al. 2006. Static magnetic fields affect cell size, shape, orientation, and membrane surface of human glioblastoma cells, as demonstrated by electron, optic, and atomic force microscopy. Cytometry A. 69:75–85.

Tian D, Dmitrieva RI, Doris PA, Crary JF, Sondhi R, Sacktor TC, Bergold PJ. 2008. Protein kinase M zeta regulation of Na/K ATPase: a persistent neuroprotective mechanism of ischemic preconditioning in hippocampal slice cultures. Brain Res. 1213:127–139.

Towle AC, Sze PY. 1983. Steroid binding to synaptic plasma membrane: differential binding of glucocorticoids and gonadal steroids. J Steroid Biochem. 18:135–143.

Vasic V, Jovanovic D, Krstic D, Nikezic G, Horvat A, Vujisic L, Nedeljkovic N. 1999. Prevention and recovery of CuSO4-induced inhibition of Na+/K+ -ATPase and Mg2+ -ATPase in rat brain synaptosomes by EDTA. Toxicol Lett. 110:95–104.

Wang Z, Sarje A, Che PL, Yarema KJ. 2009. Moderate strength (0.23-0.28 T) static magnetic fields (SMF) modulate signaling and differentiation in human embryonic cells. BMC Genomics. 10:356.

Weissman SM. 1976. Red cell metabolism. A manual of biochemical methods. 2nd edition. Yale J Biol Med. 49:310–311.

Xie Y, Zhang T. 2012. Repetitive transcranial magnetic stimulation improves consciousness disturbance in stroke patients: a quantitative electroencephalography spectral power analysis. Neural Regen Res. 7: 2465–2472.

Xiong ZQ, Stringer JL. 2000. Sodium pump activity, not glial spatial buffering, clears potassium after epileptiform activity induced in the dentate gyrus. J Neurophysiol. 83:1443–1451.

Yu JJ, Zhang Y, Wang Y, Wen ZY, Liu XH, Qin J, Yang JL. 2013. Inhibition of calcineurin in the prefrontal cortex induced depressive-like behavior through mTOR signaling pathway. Psychopharmacology (Berl). 225:361–372.

Design and Optimization of Electromagnets for Biomedical Experiments With Static Magnetic and ELF Electromagnetic Fields

Jasna L. Ristić-Djurović, Slavica S. Gajić, *Graduate Student Member, IEEE*, Andjelija Ž. Ilić, *Member, IEEE*, Nebojša Romčević, Drago M. Djordjevich, Silvio R. De Luka, Alexander M. Trbovich, Vesna Spasić Jokić, and Saša Ćirković

***Abstract*—With the expanding usage of various devices, which emit static and extremely low-frequency magnetic fields, increases the number of biomedical reports on their influence as well as demand for suitable experimental exposure systems. Experimental setups range from permanent magnets through Helmholtz coils to solenoids; however, almost all of them provide relatively weak magnetic fields of up to 10 mT. Widespread use of devices such as MR scanners imposes intentional as well as unintentional exposure to stronger fields. A typical solenoid produces stronger although less homogeneous field than the most commonly used experimental equipment composed of sets of coaxial coils. In order to provide scalable, relatively strong, low-varying field within experimental volume that is large enough for *in vivo* as well as *in vitro* experiments modified solenoids are considered. Variation of the field was reduced by modifying the shape and size of solenoid's cross section. Modified solenoids were modeled analytically, numerically, and as a prototype. Solenoid geometries were optimized for maximal field performance and minimal power consumption. The optimal modified solenoids scalable to desired sizes of the experimental volume and values of maximal magnetic induction intensities are offered. The suggested solenoid modification method can decrease field variation as much as 10.6 times.**

Manuscript received May 22, 2017; revised September 21, 2017; accepted October 10, 2017. Date of publication November 13, 2017; date of current version February 13, 2018. This work was supported by the Ministry of Education, Science and Technological Development of Serbia under Grant III-45003 and Grant III-41019. *(Corresponding author: Saša Ćirković.)*

J. L. Ristić-Djurović, A. Ž. Ilić, N. Romčević, and S. Ćirković are with the Institute of Physics, University of Belgrade, Belgrade 11080, Serbia (e-mail: jasna@stanfordalumni.org; andjelijailic@ieee.org; romcevi@ipb.ac.rs; kosjera@ipb.ac.rs).

S. S. Gajić is with the Faculty of Technical Sciences, University of Novi Sad, Novi Sad 21000, Serbia, and also with University of Banja Luka, Banja Luka 78000, Bosnia and Herzegovina (e-mail: slavica.savic@etfbl.net).

D. M. Djordjevich, S. R. De Luka, and A. M. Trbovich are with the Department of Pathological Physiology, School of Medicine, University of Belgrade, Belgrade 11000, Serbia (e-mail: dragodj@med.bg.ac.rs; de_luka@eunet.rs; alexander.m.trbovich@gmail.com).

V. Spasić Jokić is with the Faculty of Technical Sciences, University of Novi Sad, Novi Sad 21000, Serbia (e-mail: svesna@uns.ac.rs).

This paper has supplementary downloadable multimedia material available at http://ieeexplore.ieee.org provided by the authors. This material is 12.4 MB in size.

Color versions of one or more of the figures in this paper are available online at http://ieeexplore.ieee.org.

Digital Object Identifier 10.1109/TIE.2017.2772158

***Index Terms*—Biomedical engineering, exposure systems, modeling, optimization, solenoids.**

I. Introduction

THERE is a rising interest among scientific community in static to extremely low-frequency (ELF) magnetic fields and their influence on life. For example, it has been shown that this nonionizing radiation affects cancer and immune system [1]–[3], cardiovascular system [4]–[6], bones [7], central nervous system [8]–[11], reproductive system [12], and cellular system [13]. The mechanisms of action of electromagnetic fields on living organisms include those commonly regarded as macroscopic as well as those at the level of molecules and elementary particles. Namely these can be magnetic forces and torques, induced currents, magneto-hydrodynamic forces and pressures, interference with ion fluxes across cell membrane, electromagnetic properties of organic molecules, and impact on rates and yields of chemical reactions [14]–[19]. A critical review implied that numerous biomedical studies do not devote sufficient attention to exposure characterization [20] and, consequently, the reported effects cannot be related with certainty to the declared exposure. In addition, animal movement in some *in vivo* experiments may cause ambiguities regarding the exposure conditions, which can be avoided if the experimental setup provides equal exposure conditions throughout the experimental volume.

In numerous studies, experiments were performed *in vitro* on human or animal tissues as well as *in vivo* on human volunteers or with animals, and using wide variety of experimental setups with permanent magnets, Helmholtz coils, Merritt coils, and solenoids. In addition to the exposure systems used to perform experiments in [1]–[5], [7], [9], [11], [21], several more are described in [6] and [22]–[31]. Excluding the experiment performed inside an MR scanner [21], and the solenoid whose inner radius is smaller than 20–30 mm [2], [30], and [31], in the cited references the value of the magnetic induction used was smaller than 10 mT. Namely, in the exposure systems described in [1], [3], [22], [23], and [28], the magnetic induction ranges from 3.6 to 9 mT, whereas the values reported in [4], [7], [9], [11], [25], [27], and [29] are between 0.1 and 1 mT.

With the expanding usage of the devices that can be associated with relatively weak electromagnetic fields, such as for

example, mobile phones and electronic article surveillance systems, or magnetic resonance imaging systems, which produce stronger ELF fields, concerns about the safety and dosimetry increase as well, see, for example, [32]–[37]. In addition, the results of the experiments performed in an MR scanner [21], and in a cyclotron magnet [38], [39], indicate that strong static magnetic fields cause significant effects. Homogeneous [38]–[40] as well as inhomogeneous [41], [42] static magnetic fields were shown to initiate biomedical changes, and, surprisingly, differently oriented fields produced different effects [38], [39], [42]. As a result, inevitable questions on the threshold levels of the field; on how the effects depend on the field level, homogeneity, and direction; and on the reversibility of the effects arose. Answers to these questions require further experimenting, preferably with an exposure system designed for the purpose, which can provide scalable homogeneous ELF magnetic field with relatively strong peak value inside an experimental volume large enough to accommodate *in vivo* as well as *in vitro* experiments.

The magnetic inductions stronger than 10 mT directed the primary shape of the needed exposure system towards a solenoid. Since coils have numerous and very diverse applications [43]–[45], much research has been done to study, improve, and optimize their performance [46]–[49]. For our intended biomedical application, uniformity of the field inside a typical solenoid is not sufficient and needs improvement. Enhancement of field uniformity was obtained in [50] by using copper plates and flux concentrating rings to modify a solenoid with experimental volume of 125 cm^3 and in [51] by adjusting the Helmholtz coils dimensions. The larger number of windings and smaller coil size of the outer coils were successfully used to increase homogeneity of relatively weak fields produced by the sets of circular and square coaxial coils, as described in [24] and [26], respectively. Here, an idea similar to the one used in a set of coaxial coils with outer coils having larger number of windings and smaller radius is applied to a solenoid. With the aim to account for the field decrease towards the ends of a typical solenoid, the number of windings at solenoid's ends and towards its axis is increased. Further, solenoids modified in such a way are considered as classes defined by the ratios of solenoid dimensions, rather than designing a particular exposure system that has unique size. Scaling of the obtained results provides an optimized modified solenoid that can be used as an initial model in designing experimental setups for a variety of desired experiments, i.e., for different values of desired field intensities and experimental volume sizes.

II. Calculation

When designing a particular experimental setup one is often facing a number of specific technical requirements and choices related to spools, holders, supports, wire profile, winding, etc., that differ for different designs. Consequently, influence of additional equipment on solenoid performances depends on the specifics of an experimental setup design. Effects of fabrication deformations on the magnetic field of the high-field circular Helmholtz coil systems and its uniformity were analyzed mathematically in [50] and shown to be of the order of a few percent. In order to avoid restrictions of a single, particular exposure system or corrections related to a specific, realistic, practical solenoid, that result, for example, from fabrication deformations and imperfections, in the first approximation we considered an ideal thick solenoid with a homogeneous cross section. Magnetic induction along the axis of a solenoid is derived by decomposing a solenoid into a set of very thin, i.e., single layer solenoids, and further into circular current loops (see Fig. 1). Using the Biot−Savart law

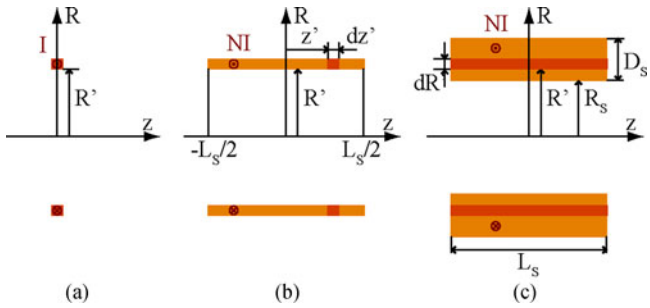

Fig. 1. Coordinate systems and vertical cross sections of (a) circular current loop, (b) thin, single-layer solenoid, and (c) solenoid.

$$\overrightarrow{dB} = \frac{\mu_0}{4\pi}\frac{I\overrightarrow{dl}\times\hat{r}}{r^2} \tag{1}$$

the z-component of magnetic induction corresponding to a wire segment dl, at the axis of a current loop with radius R' and current I, depicted in Fig. 1(a), becomes

$$dB_a = \frac{\mu_0 I}{4\pi}\frac{R'dl}{\left(R'^2+z^2\right)^{3/2}}. \tag{2}$$

Since the radial field components cancel out, the magnetic induction along the z-axis is obtained by integrating dB_a along the circumference of the current loop, i.e.,

$$B_a = \oint dB_a = \frac{\mu_0 I}{2}\frac{R'^2}{\left(R'^2+z^2\right)^{3/2}}. \tag{3}$$

N current loops each carrying current I positioned at $z' \in [-L_S/2,\ L_S/2]$ form a thin, single-layered solenoid shown in Fig. 1(b). If a thin solenoid with length L_S carries the current NI, then the solenoid's segment whose length is dz' carries the current $dz'NI/L_S$. Therefore, the part of thin solenoid's field, which corresponds to a loop with width dz', positioned at $z = z'$ is

$$dB_b = B_a\left(z-z'\right)\frac{Ndz'}{L_S} = \frac{\mu_0 NI}{2L_S}\frac{R'^2dz'}{\left(R'^2+(z-z')^2\right)^{3/2}}. \tag{4}$$

After integration over the thin solenoid's length, the expression for the magnetic field along the axis of a thin solenoid is

obtained to be

$$B_b = \int_{z'=-L_S/2}^{z'=L_S/2} dB_b = \frac{\mu_0 NI}{2L_S}\int_{-L_S/2}^{L_S/2}\frac{R'^2 dz'}{\left(R'^2+(z-z')^2\right)^{3/2}} = \frac{\mu_0 NI}{2L_S}\left(\frac{z+L_S/2}{\sqrt{R'^2+(z+L_S/2)^2}}-\frac{z-L_S/2}{\sqrt{R'^2+(z-L_S/2)^2}}\right). \quad (5)$$

A thin solenoid, shown in Fig. 1(b), represents a dR' thick layer of a solenoid depicted in Fig. 1(c); therefore, magnetic field along the axis of a solenoid is composed of magnetic fields corresponding to thin solenoids, i.e.,

$$dB_c = B_b\frac{dR'}{D_S} = \frac{\mu_0 NI}{2L_S D_S}\left(\frac{(z+L_S/2)\,dR'}{\sqrt{R'^2+(z+L_S/2)^2}}-\frac{(z-L_S/2)dR'}{\sqrt{R'^2+(z-L_S/2)^2}}\right). \quad (6)$$

Factor dR'/D_S takes into account that current NI is distributed over the area $L_S{\cdot}dR'$ in the very thin solenoid in Fig. 1(b), and over $L_S \cdot D_S$ in the solenoid in Fig. 1(c). Substitution for current density $J = NI/(L_S D_S)$ and integration over the solenoid thickness, i.e.,

$$B_c = \frac{\mu_0 J}{2}\left((z+L_S/2)\int_{R_S}^{R_S+D_S}\frac{dR'}{\sqrt{R'^2+(z+L_S/2)^2}} - (z-L_S/2)\int_{R_S}^{R_S+D_S}\frac{dR'}{\sqrt{R'^2+(z-L_S/2)^2}}\right) \quad (7)$$

provide the analytical formula for the magnetic induction, B_S, along the axis of a solenoid with the inner radius R_S, length L_S, and thickness D_S, i.e., $B_c = B_S(z,\ L_S,\ D_S,\ R_S)$. After carrying out the integrals, we obtain

$$B_S(z, L_S, D_S, R_S) = \frac{\mu_0 J}{2}\cdot\left((z+L_S/2)\ \ln\left|\frac{R_S+D_S+\sqrt{(R_S+D_S)^2+(z+L_S/2)^2}}{R_S+\sqrt{R_S{}^2+(z+L_S/2)^2}}\right| - (z-L_S/2)\ln\left|\frac{R_S+D_S+\sqrt{(R_S+D_S)^2+(z-L_S/2)^2}}{R_S+\sqrt{R_S{}^2+(z-L_S/2)^2}}\right|\right). \quad (8)$$

The derived formula quantitatively expresses the dependence that magnetic induction along the axis of a solenoid is maximal in the solenoid's center and that it decreases towards each of solenoid's ends. For example, the darker pattern in Fig. 2(a) emphasizes the cross section of a 60-cm-long and 6-cm-thick solenoid with the inner radius of 25 cm, whereas the corresponding magnetic field induction calculated using (8) and the current density of $J = 2.5\ \mathrm{A/mm^2}$ is given as the darker curve in Fig. 2(b). In general, the described field can be flattened if the thickness of the solenoid is increased at its ends. For example, if the additional wire windings form the shaped lid on each end of the solenoid, whose cross section is indicated by the lighter color in Fig. 2(a), the resulting field along the solenoid axis becomes almost ideally flat, see lighter curve in Fig. 2(b). The shape of additional wire windings required for the depicted field flattening was determined using numerical integration and an iterative procedure.

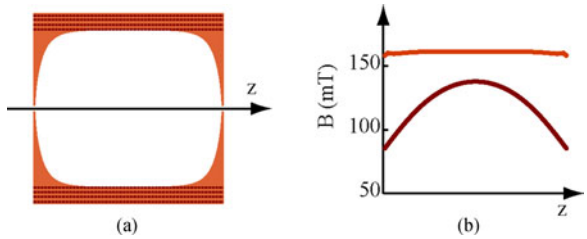

Fig. 2. Field flattening along solenoid axis. (a) The darker pattern emphasizes cross section of a 60-cm-long and 6-cm-thick solenoid with the inner radius of 25 cm. The additional wire windings form the shaped lid on each end of the solenoid. (b) The magnetic induction along the solenoid axis for the solenoid without and with the additions is depicted by the darker and lighter line, respectively. The induction current density is taken to be $J = 2.5\ \mathrm{A/mm^2}$.

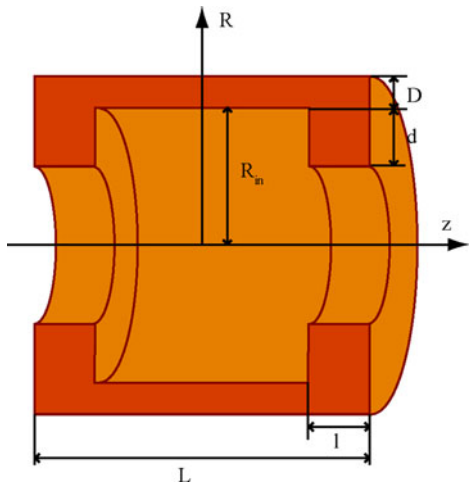

Fig. 3. Modified solenoid dimensions. The length and the thickness of the basic solenoid are taken to be L and D, respectively, whereas the corresponding measures of the additional solenoids are l and d, respectively. The inner radius of the modified solenoid R_{in} is defined as the inner radius of the basic solenoid. The cylindrical coordinate system is used throughout. For analytical and numerical modeling purposes, the cross section of the solenoid is assumed to be homogeneous.

The shape of a modified solenoid that provides a constant value of magnetic induction along the axis inside the solenoid would be quite difficult to wind. In addition, the volume needed for biomedical experiments can be shorter than the solenoid length. Consequently, although it is desirable that the flat section of the field is as long as possible, it is not necessary that it covers complete length of the solenoid. Therefore, the ideal additions with elaborate shape were replaced by two simple solenoids added at inner ends of the basic solenoid, as shown in Fig. 3. The length and thickness of the basic solenoid are taken to be L and D, whereas the corresponding measures of the additional solenoids are l and d, respectively. The inner radius of the modified solenoid, R_{in}, is defined as the inner radius of the basic solenoid.

In order to enable comparison of different modified solenoids the same induction current density of 2.72 A/mm^2 is used in all examples. This value corresponds to the maximal current density of 3 A/mm^2 and the wire winding fill factor of 0.907. Therefore the fields obtained in all examples are the strongest available; for weaker fields, induction current should be adequately scaled.

With the aim to enable use of the obtained results in designing wide range of solenoids the results are scaled to a desired size of experimental volume using R_{in} as a scaling factor. However, the specific examples are given for a realistic size suitable for *in vivo* experiments with rodents. Namely, the experimental volume radius of 25 cm accommodates up to four small standard size cages for mice or one medium standard size cage that houses mice or rats.

III. Results and Discussion

A. Analytical Modeling

As can be seen from Fig. 3, the modified solenoid is a union of three regular solenoids. Therefore, the magnetic induction of the modified solenoid B is the sum of the magnetic induction of the basic solenoid, B_B, and of the two additional solenoids attached to the inner ends of the basic solenoid B_{A1} and B_{A2}, i.e.,

$$B(z, L, D, l, d, R_{in}) = B_B + B_{A1} + B_{A2}. \quad (9)$$

Consequently, the analytical expression for the magnetic induction along the axis of the modified solenoid becomes

$$\begin{aligned} B(z, L, D, l, d, R_{in}) &= B_S(z, L, D, R_{in}) \\ &+ B_S\left(z + \frac{L}{2} - \frac{l}{2}, l, d, R_{in} - d\right) \\ &+ B_S\left(z - \frac{L}{2} + \frac{l}{2}, l, d, R_{in} - d\right) \end{aligned} \quad (10)$$

where L, D, l, d, and R_{in} are defined in Fig. 3 and B_S is defined with (8). This expression was used to study the influence of the modified solenoid dimensions on the strength and flatness of its field.

With the increase of the additional solenoids' size, the shape of the field along solenoid axis transforms from a curve with a maximum at $z = 0$ to a curve with two local maximums and a minimum at $z = 0$. This transition is illustrated in Fig. 4 by using fixed values for all the parameters of the modified solenoid except the additional solenoids' thickness, d. Namely, magnetic induction along the solenoid axis B was calculated for $L = 50$ cm, $D = 5$ cm, $R_{in} = 25$ cm, $l = 3$ cm and the seven values of d. The field flatness is maximal for $d = 14.5$ cm, whereas the field level, $B_0 = B(z = 0)$ increases with the increase in d. Although not shown, the increase of the additional solenoids' length l produces qualitatively the same field shape evolution.

The two parameters chosen to quantitatively describe the field are B_0, the magnetic induction at $z = 0$, and Δz, the length of the z-axis segment along which the magnetic induction deviation is smaller than 0.5% of B_0, i.e., along which $\Delta B/B_0 < 0.5\%$. Field quality, described by these two parameters, depends on all five dimensions that define the size of a modified solenoid.

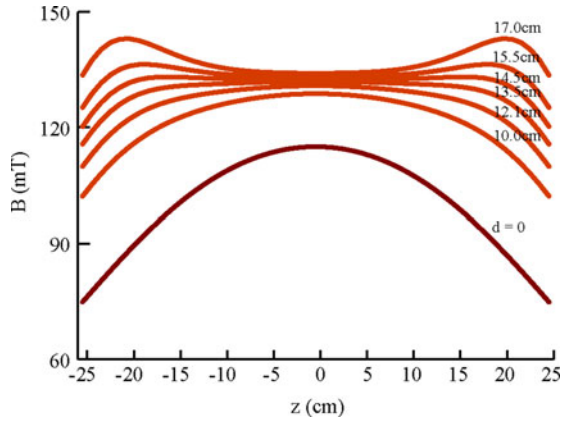

Fig. 4. Field shape dependence on additional solenoids' thickness. Magnetic induction along the solenoid axis B was calculated for $L = 50$ cm, $D = 5$ cm, $R_{in} = 25$ cm, $l = 3$ cm, and seven values of d. The field flatness has a maximum for $d = 14.5$ cm, whereas the field level $B_0 = B(z = 0)$ increases with the increase in d.

Modified solenoids are divided into classes by scaling all the data to R_{in}. The influence of the additional solenoid size is investigated firstly, and the results are given in Fig. 5 for nine subclasses defined by three fixed values of $L/R_{in} = 2.4$, 2.0, and 1.6 and $D/R_{in} = 0.4$, 0.2, and 0.04. The field level B_0/R_{in} increases with the increase in D/R_{in}, L/R_{in}, d/R_{in}, as well as l/R_{in}, as can be seen in the upper nine graphs in Fig. 5. D/R_{in} is the most influential by far, whereas the effect of the remaining three parameters is very weak. The quantitative values are available in supplementary materials. $\Delta z/R_{in}$, depends strongly on l/R_{in} as well as on d/R_{in}, and its large values are restricted to the narrow set of $(d/R_{in}, l/R_{in})$ pairs depicted with the bright area in the bottom nine graphs in Fig. 5. The area below and to the left of large $\Delta z/R_{in}$ corresponds to field shapes, $B(z)$, with one extremum, whereas the field shapes with three extrema are above and to the right of the bright area in the lower nine graphs in Fig. 5.

Δz is smaller than L; however, Δz expressed as percentage of L is smaller than when it is represented as a percentage of the z-dimension of space available inside a modified solenoid. This is because the z-dimension of experimental volume in a modified solenoid is smaller than L, namely it is equal to $L - 2l$. Even if this decrease of experimental volume is not taken into account, in a modified solenoid, Δz can be increased as much as 7.5 times for $L/R_{in} = 2.0$ and $D/R_{in} = 0.04$ or at least 6.4 times for $L/R_{in} = 1.6$ and $D/R_{in} = 0.4$, when compared to a solenoid without additions.

In order to validate applicability of the described approach, the results are compared with the results obtained by a more exact calculation. The field components around a circular current loop in the point with coordinates z and R in the cylindrical coordinate system are given in [52] as

$$\begin{aligned} d^2 B_R = &\frac{C(z - z')}{2\alpha^2 \beta R} \\ &\times \left[\left(R'^2 + R^2 + (z - z')^2\right) E(k^2) - \alpha^2 K(k^2)\right] \end{aligned}$$

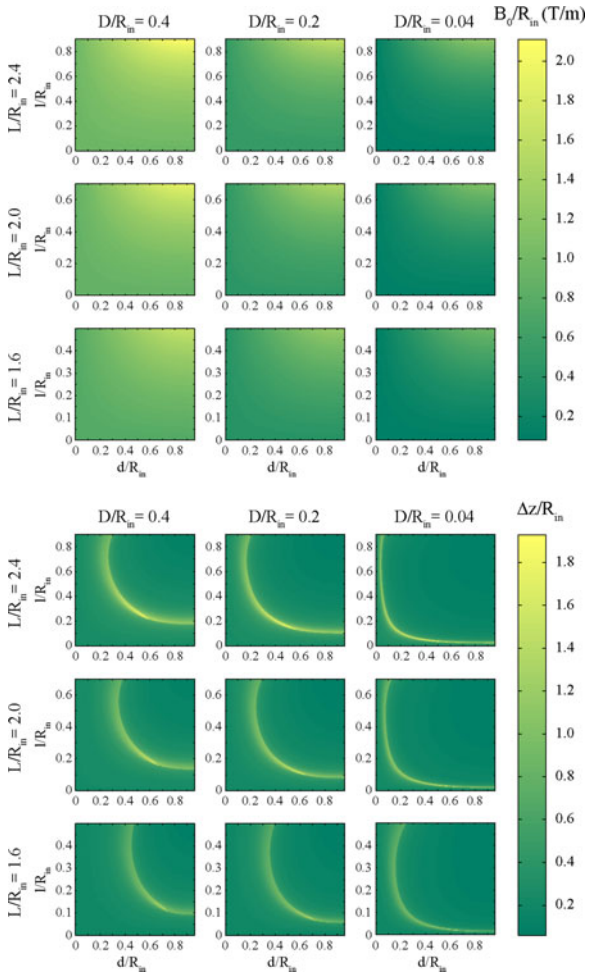

Fig. 5. Dependence of field properties on solenoid size. Graphs in the same row of graphs correspond to the solenoids with the same L/R_{in}, whereas those in the same column all have the same D/R_{in}, as is indicated in row and column headings. The field level B_0, i.e., the magnetic induction at $z = 0$, increases with the increase in L/R_{in}, D/R_{in}, d/R_{in}, as well as l/R_{in}, and it is the most sensitive on D/R_{in}. Δz represents the z-axis segment along which the magnetic induction deviation is smaller than 0.5% of B_0, i.e., $\Delta B/B_0 < 0.5\%$. $\Delta z/R_{\text{in}}$ depends strongly on l/R_{in} as well as on d/R_{in}, and its large values are restricted to the narrow set of $(d/R_{\text{in}}, l/R_{\text{in}})$ pairs depicted with bright areas in the lower set of nine graphs. The $\Delta z/R_{\text{in}}$ dependence on L/R_{in} and D/R_{in} is not as pronounced, although the dependence on D/R_{in} is the stronger of the two. Each graph is given as a MATLAB file as a supplementary material.

$$d^2B_z = \frac{C}{2\alpha^2\beta} \times \left[\left(R'^2 - R^2 - (z-z')^2\right) E\left(k^2\right) + \alpha^2 K\left(k^2\right)\right] \tag{11}$$

where $\alpha^2 = R'^2 + R^2 + (z-z')^2 - 2RR'$, $\beta^2 = R'^2 + R^2 + (z-z')^2 + 2RR'$, $k^2 = 1 - \alpha^2/\beta^2$, $C = \mu_0 J \mathrm{d}R'\mathrm{d}z'/\pi$, E and K are the elliptic integrals, R' is the loop radius, and z' is its axial position. The field in each point of the entire axial cross section of experimental volume is obtained by numerical integration of (11) over the modified solenoid windings. Computed magnetic fields are used to determine ΔS, the area of experimental volume cross section inside which field deviation is smaller than 0.5%.

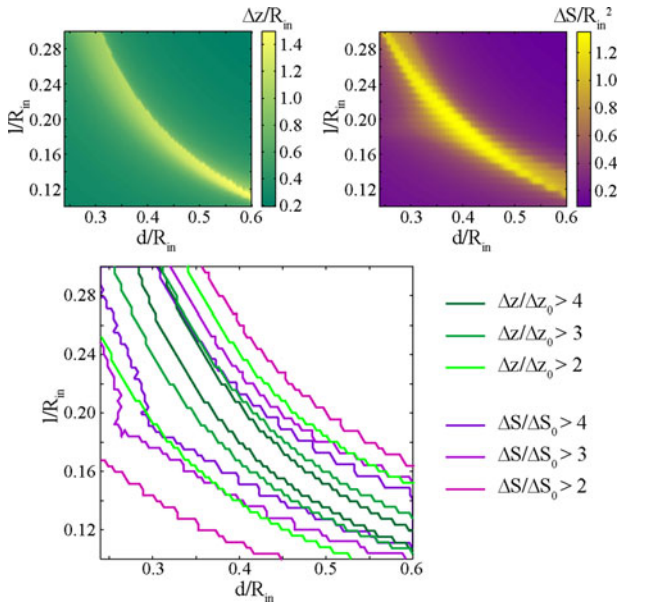

Fig. 6. Comparison between Δz and ΔS approach. ΔS is the area of axial cross section with the field deviation of 0.5%, similarly to Δz, the axial segment along which B deviates less than 0.5%. The data corresponds to modified solenoids with $L/R_{\text{in}} = 2$ and $D/R_{\text{in}} = 0.2$. The computer time needed for ΔS data given in the upper right graph was more than 1850 times larger than for Δz data in the upper left graph. The values Δz_0 and ΔS_0 correspond to unmodified solenoid. The lower graph shows that conditions expressed with Δz are more restrictive.

The comparison between Δz and ΔS approach illustrated in Fig. 6 is performed on the modified solenoid class defined with $L/R_{\text{in}} = 2$ and $D/R_{\text{in}} = 0.2$. This class is represented by the central graphs in both lower and upper part of Fig. 5. The considered ranges of additional solenoid dimensions in Fig. 6 are smaller, and the field calculation step sizes are twice as large as those in Fig. 5. Nevertheless the results presented in the upper right graph in Fig. 6 took 4087 s computer time on Intel Core i7-2670QM 2.20 GHz processor with 8 GB of RAM. The lower graph in Fig. 6 shows that restrictions expressed using Δz are more rigorous than when ΔS is used. The described more exact calculation of the field in the entire experimental volume is used to illustrate effects of solenoid modifications on field uniformity in Fig. 7. Further analysis is performed using Δz because it is more rigorous and much less computer-time-consuming than the ΔS approach.

For a biomedical experiment, it is preferred that conditions in the experimental volume are equal as well as that the ranges of available values of input parameters are as broad as possible. In the case of the modified solenoid, these conditions become demand for large Δz as well as B_0. In addition to the biomedical requirements, an engineering condition for low power consumption is considered. The Ohmic losses are calculated as

$$P = \rho_{\text{Cu}} 2\pi R_m S J^2 = \rho_{\text{Cu}} \pi J^2 \left((2R_{\text{in}} + D) LD + 2(2R_{\text{in}} - d) ld\right) \tag{12}$$

where ρ_{Cu} is the copper resistivity, R_m is the mean radius of solenoid windings, and S is the surface of solenoid cross section. The biomedical need for large B_0 as well as Δz, and engineering desire for small electrical power consumption can

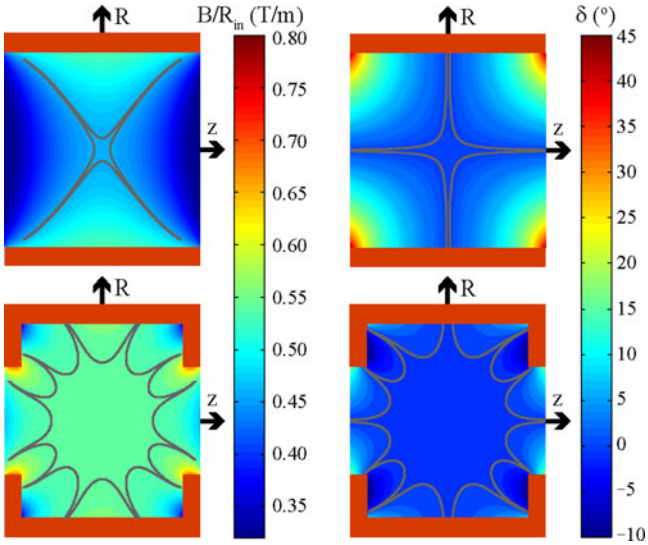

Fig. 7. Field uniformity. Parameters B/R_{in} and $\delta = \arctan(B_r/B_z)$ are given for the unmodified and modified solenoids with $L/R_{\text{in}} = 2$ and $D/R_{\text{in}} = 0.2$ in the upper and lower pair of graphs, respectively. For the modified solenoid $l/R_{\text{in}} = 0.168$ and $d/R_{\text{in}} = 0.44$. The gray lines indicate the area with 0.5% deviation, i.e., with $0.9975 \leq B/B_0 \leq 1.0025$ and $|B_r/B_z| \leq 0.005/0.995$. Modification of the solenoid increased the depicted areas 10.6 and 6.1 times for B/R_{in} and δ, respectively.

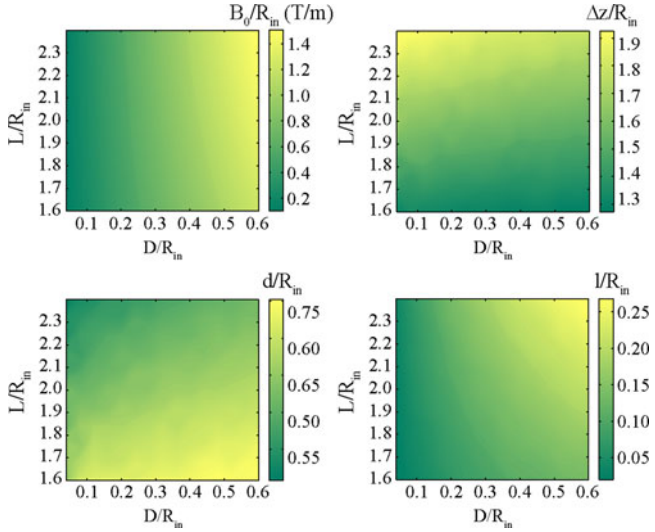

Fig. 8. Optimal solenoids. For each pair of values of L/R_{in} and D/R_{in}, the depicted optimal B_0/R_{in} and optimal $\Delta z/R_{\text{in}}$, as well as the size of the additional solenoids, i.e., l/R_{in} and d/R_{in}, which produce them, were determined so that the optimization criterion is met. The optimization criterion combines biomedical need for large B_0 as well as Δz, and engineering desire for small electrical power consumption. Consequently, the optimization criterion was that the expression $(B_0/\overline{B_0})\,(\Delta z/\overline{\Delta z})\,(\overline{P}/P)$ is maximal within the considered ranges of l/R_{in} and d/R_{in}. The optimal B_0/R_{in}, given in the left upper graph, increases with the increase of L/R_{in} as well as D/R_{in}; however, it is much more sensitive on D/R_{in}. The optimal $\Delta z/R_{\text{in}}$ increases with L/R_{in} and decreases with D/R_{in}, the value of L/R_{in} being much more influential, as can be seen from the upper left graph. The optimal additional solenoids' length, l/R_{in}, and width, d/R_{in}, which correspond to a particular basic solenoid size, L/R_{in} and D/R_{in}, as well as to the optimal B_0/R_{in} and $\Delta z/R_{\text{in}}$, determined through the optimization procedure are given in the lower left and lower right graph, respectively. The numerical values of the presented data are available in the supplementary materials where each graph is given as a MATLAB file.

be summarized in different expressions for optimization functions and criterions. For example, for optimization functions $(B_0/\overline{B_0})\,(\Delta z/\overline{\Delta z})\,(\overline{P}/P)$ and $B_0/\overline{B_0} + \Delta z/\overline{\Delta z} - P/\overline{P}$ the optimization criterion is that the function has its maximum within the considered ranges of d/R_{in} and l/R_{in}. Normalization to the values $\overline{B_0}$, $\overline{\Delta z}$, and $\overline{P}$, averaged over the considered ranges of l/R_{in} and d/R_{in}, was performed in order to prevent favoring of the variables with larger values. When either of the two optimization functions was applied to the results in Fig. 5 that correspond to $L/R_{\text{in}} = 2$ and $D/R_{\text{in}} = 0.2$, the optimal values $B_0/R_{\text{in}} = 0.5207\,\text{T/m}$, $\Delta z/R_{\text{in}} = 1.584$, and $P = 0.4165\,\text{W/cm}^3$, corresponding to $l/R_{\text{in}} = 0.1$ and $d/R_{\text{in}} = 0.64$ were obtained. This optimization could be perceived as adjusting the additional solenoid size l and d, in order to get the most out of the basic solenoid defined with L and D, i.e., in order to achieve the optimal results in the form of the optimal field and power.

The optimization procedure described on the example $L/R_{\text{in}} = 2$ and $D/R_{\text{in}} = 0.2$, was repeated for 315 additional pairs of L/R_{in} and D/R_{in} using the optimization function $(B_0/\overline{B_0})\,(\Delta z/\overline{\Delta z})\,(\overline{P}/P)$ and its maximum as the optimization criterion. For each pair of values of L/R_{in} and D/R_{in}, the optimal B_0/R_{in} and optimal $\Delta z/R_{\text{in}}$, as well as the size of the additional solenoids, i.e., l/R_{in} and d/R_{in}, which produce them, were determined so that the optimization criterion is met. The values for L/R_{in} and D/R_{in} were taken from the set [1.6, 2.4] with the step size $\Delta L/R_{\text{in}} = 0.08$ and [0.04, 0.6] with the step size $\Delta D/R_{\text{in}} = 0.04$, respectively. The dependences of the obtained optimized B_0/R_{in} and $\Delta z/R_{\text{in}}$ on the size of the basic solenoid, i.e., on L/R_{in} as well as D/R_{in}, are given in the two upper graphs in Fig. 8. The two lower graphs in Fig. 8 give the corresponding optimal additional solenoids' size, i.e., the values of l/R_{in} and d/R_{in}, which enable the optimal performance. The optimal B_0/R_{in}, given in the upper left graph in Fig. 8, increases with the increase of L/R_{in} as well as D/R_{in}; however, it is much more sensitive on D/R_{in}. The optimal $\Delta z/R_{\text{in}}$ increases with L/R_{in} and decreases with D/R_{in}, the value of L/R_{in} being much more influential, as can be seen from the upper right graph in Fig. 8. The exact values of the data presented in Fig. 8 can be read from the MATLAB figure files provided in supplementary materials.

When choosing the optimal size of a modified solenoid for a particular experiment, the inner radius, R_{in}, as well as the needed Δz is determined from the size of the experimental volume. The determined value of $\Delta z/R_{\text{in}}$ defines the curve $L_1/R_{\text{in}}(D/R_{\text{in}})$ in the upper right graph, whereas the desired value of B_0/R_{in} defines the curve $L_2/R_{\text{in}}(D/R_{\text{in}})$ in the upper left graph in Fig. 8. The intersection of $L_1/R_{\text{in}}(D/R_{\text{in}})$ and $L_2/R_{\text{in}}(D/R_{\text{in}})$ gives the values for L/R_{in} and D/R_{in}, which further, in the bottom part of Fig. 8, lead to the corresponding l/R_{in} and d/R_{in} needed for the optimal performance.

The results given in Figs. 5 and 8 can be used for designing a modified solenoid suitable for smaller or larger experimental volumes. One should keep in mind that the calculations were performed for ideal cases; therefore, the values of B_0 and Δz achievable in a realistic modified solenoid should be expected to be somewhat different from predicted. Note that scaling factor for the Ohmic losses P is R_{in}^3.

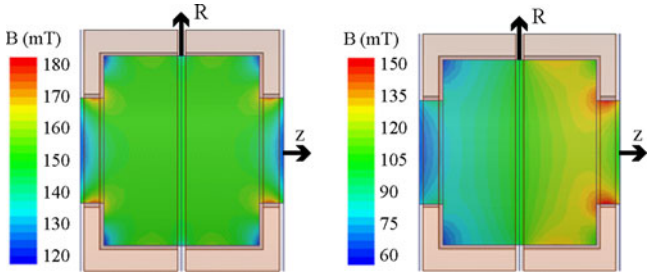

Fig. 9. Numerical model of modified solenoid. To enable placement of samples into the experimental volume, the modified solenoid is divided along the $z = 0$ plane in two identical parts. The halves are pulled apart by 2 cm to provide space for holders of opening and closing mechanism. The inner layer of 1 cm is left for chamber wall, thermal insulation, etc. For the numerical modeling purposes, the spool is taken to be of plexiglass. The coil dimensions are $R_{in} = 26$ cm, $L/2 = 25$ cm, $D = 6$ cm, $l = 4.3$ cm, and $d = 11.1$ cm. In the left plot, each half was powered by $NI = 53\,780$ A, which corresponds to $J = 2.72\,\mathrm{A/mm^2}$. In the right plot, the two halves of the model are powered independently. The left and right half was powered by $NI_{left} = 25$ kA and $NI_{right} = 50$ kA, respectively. Asymmetric powering provides control over the field gradient as well as intensity.

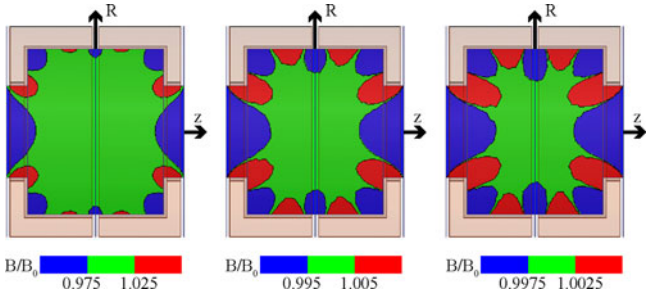

Fig. 10. Field quality. Deviation of the obtained field is small not only along the *z*-axis but in the whole experimental volume, as well. The 5%, 1% and 0.5% deviation regions shown in the left, middle, and right solenoid cross section correspond to $R_{5\%} = 19$ cm, $z_{5\%} = \pm 19$ cm, $R_{1\%} = 15$ cm, $z_{1\%} = \pm 13.4$ cm and $R_{0.5\%} = 15$ cm, $z_{0.5\%} = \pm 10.6$ cm, which is 69.8%, 38.8%, and 30.7% of the experimental area defined with $R_{exp} = 25$ cm, $z_{exp} = \pm 20.7$ cm, respectively.

B. Numerical Modeling

If a modified solenoid is to be used as an exposure system, numerous technical aspects, such as for example, positioning of samples in the experimental volume, appropriate experimental conditions in terms of temperature, noise, or light, must be considered. In order to provide space for the mechanical solutions to the mentioned technical problems, geometry of the modified solenoid was adjusted. To provide access to the experimental volume the solenoid is divided along the plane $z = 0$ into movable halves. In order to make room for a coating layer, thermal insulation, holders and supporters, the inner radius of the solenoid was increased by 1 cm to $R_{in} = 26$ cm and its halves are separated by a 2-cm-wide gap, as depicted in Fig. 9. Equation (10) was modified to account for these changes and the optimization method described in Section III-A was performed with the required field level value $B_0 = 150$ mT. The analytically obtained optimal dimensions of the modified solenoid were further adjusted to extend the flat-field region to the off-axis area. The additional solenoids produce two local maximums in an off-axis field of the modified solenoid close to $R = R_{in}$. Therefore, instead of adopting the optimal solenoid parameters, which place the flattest $B(z)$ at $R = 0$, it is better if the field curve along the axis has a single maximum (see Fig. 4). This moves the flattest field dependence on z off-axis, i.e., at $R \neq 0$, and improves the overall radial flatness of the field. The model as well as the field obtained by numerical modeling in the solenoid interior is shown in Fig. 9. For the numerical modeling purposes, the spool is taken to be of plexiglass. The modified solenoid dimensions are taken to be $R_{in} = 26$ cm, $L/2 = 25$ cm, $D = 6$ cm, $l = 4.3$ cm, and $d = 11.1$ cm. Each half of the modified solenoid shown in the left part of Fig. 9 was powered by $NI = 53\,780$ A, which corresponds to $J = 2.72\,\mathrm{A/mm^2}$.

Uniformity of the obtained field is illustrated in Fig. 10 by the areas within which field deviates for less than 5%, 1%, and 0.5%. The smoothness of the lines along the borders of the depicted region decreases with the decrease of the field variation requirement in accordance with the numerical simulation error. The obtained variation of the field is very small not only along the z-axis but in the whole experimental volume, as well. The 5%, 1%, and 0.5% deviation regions shown in the left, middle, and right solenoid cross section in Fig. 10 correspond to $R_{5\%} = 19.5$ cm, $z_{5\%} = \pm 18$ cm; $R_{1\%} = 18$ cm, $z_{1\%} = \pm 13$ cm; and $R_{0.5\%} = 15.5$ cm, $z_{0.5\%} = \pm 11$ cm, which are 67.8%, 45.2%, and 33% of the experimental area defined with $R_{exp} = 25$ cm, $z_{exp} = \pm 20.7$ cm, respectively.

In order to compare our results with those of the most widely used coil systems described in [24], the overall experimental volume dimension, V, and uniformity region corresponding to 1% field deviation, $U_{1\%}$, were used. For our example of the modified solenoid these parameters were calculated to be $V = 0.650\,(D_{exp})^3$ and $U_{1\%} = 0.374\,(D_{exp})^2$, where D_{exp} is experimental volume diameter and is equal to 50 cm. In our case the ratio $V/U_{1\%} = 1.7\,D_{exp}$, which is smaller than $2.0\,D_{exp}$, the value corresponding to the Lee-Whiting coil system, shown to be the second best of the seven coil systems compared in [24]. The best, i.e., the smallest value of $V/U_{1\%} = 1.5\,D_{exp}$ corresponds to the Tetracoil system [24], whereas for all other compared systems this value is larger than 3.

The necessity to physically divide modified solenoid in two identical parts in order to enable access to the experimental volume, made independent powering of the two halves of the model shown in Fig. 9 easily feasible. Since, the method of independent powering of two halves was successfully used to significantly broaden the application scope of another device designed for ion beam acceleration facilities [53], it seemed worthwhile to check if the operation of a modified solenoid would undergo a similar benefit. The left and right half of the model was powered by $NI_{left} = 25$ kA and $NI_{right} = 50$ kA, respectively and the results are given in the right part of Fig. 9. As expected, the obtained field is not homogenous; however, asymmetric powering produced magnetic induction gradient, which enables experimenting with the influence of the completely controllable electromagnetic field. Namely, availability of two input parameters, i.e., induction currents for the left and right half of the solenoid, NI_{left} and NI_{right}, enables adjustment of B_0 as well as of the gradient $\Delta B/\Delta z$ to the desired values.

Fig. 11. Prototype of modified solenoid. The dimensions of modified solenoid prototype are $R_{in} = 6$ cm, $L = 12.2$ cm, $D = 0.66$ cm, $l = 1.76$ cm, $d = 1.1$ cm. It is winded using a 1-mm-diameter copper wire (1.1 mm with coating), and it has 979 turns. Its resistance, inductivity, and mass are measured to be 9 Ω, 68.37 mH, and 3.6 kg, respectively. The spool thickness is 5 mm.

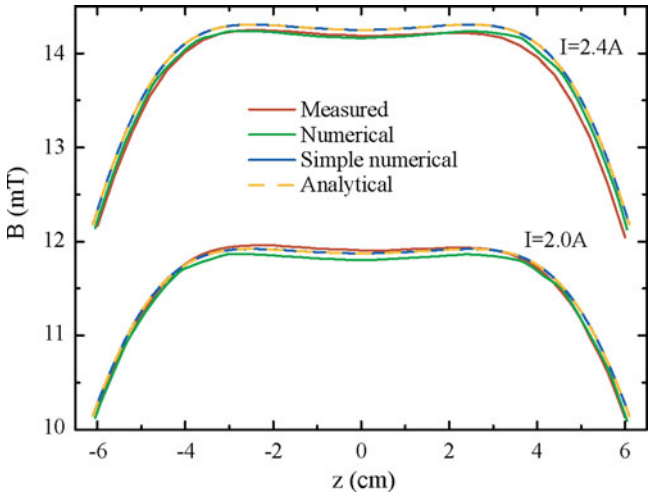

Fig. 12. Comparison of analytical, simple numerical, numerical, and measured field. The modified solenoid prototype is powered by the current source. The comparison is given for current values of 2 A and 2.4 A. Small deviation between the analytical and measured fields justifies the use of (10) in the presented modified solenoid analysis.

C. Prototype

The proposed method of solenoid modification and obtained results are experimentally verified by a prototype whose photograph is given in Fig. 11. The prototype geometry was restricted by the size of field measuring equipment and minimal spool thickness to $R_{in} - d > 3.7$ cm and thus does not correspond to the optimal values given in Fig. 8. The graph similar to those in the lower part of Fig. 5 that corresponds to $L/R_{in} = 2.0$ and $D/R_{in} = 0.11$ is used to choose $l/R_{in} = 0.18$ and $d/R_{in} = 2.9$. The dimensions are chosen having in mind wire size of 1.1 mm.

Magnetic fields along the axis of the prototype obtained by four different methods are compared in Fig. 12. The field obtained using (10) does not differ from the one obtained by numerical integration of (12) and they are labeled as analytical and simple numerical, respectively. The electrical current density in these calculations is taken to be $J = 0.821I$, where I is the value of current used to power the prototype. Numerical modeling of the prototype included its spool as well as the aluminum tube used for probe positioning during field measurements. The numerical model of the prototype is excited by $979I$ Ampere-turns. The field along the axis of the prototype is measured with a digital teslameter (DTM-151, Group3 Technology, Auckland, New Zealand) with the resolution of 0.002 mT. As can be seen from Fig. 12, all four fields agree reasonably well. Within the range $|z| \leq 4.4$, the maximal relative error between the analytical and measured fields is 0.46% and 1.36% for $I = 2$ A and $I = 2.4$ A, respectively. Therefore, the use of analytical method defined by (10) in the presented analysis of modified solenoids is credible.

IV. Conclusion

The modified solenoid was proposed as a new experimental device for biomedical research with relatively strong static as well as ELF magnetic fields. To obtain improved uniformity of the field throughout experimental volume, a typical solenoid was modified using the methods employed to sets of coils for the same purpose [24], [26]. To the best of our knowledge, depending on the size of the needed experimental volume, the maximal obtained field levels were as much as two orders of magnitude larger than those reported for other described exposure systems, whereas the obtained field uniformity is comparable to the best of those listed in [24]. The proposed method of solenoid modification by adding extra windings at its ends and toward its axis can increase the length of the low-field variation segment along the experimental volume axis as much as 7.5 times. The area of low field variation in the axial cross section of experimental volume can be enlarged as much as 10.6 times when compared to the one in unmodified solenoid.

Since suggested modifications in the form of additional wire windings are in the interior of a typical solenoid, they may cause inconvenience in accessing the experimental volume. Therefore, the possibility to achieve field homogenization with modifications added to the outer surface of a solenoid is worth exploring.

References

[1] T. Lin, L. Wan, X. Qi, W. Shi, and J. Lin, "A moderate static magnetic field enhances TRAIL-induced apoptosis by the inhibition of Cdc2 and subsequent downregulation of survivin in human breast carcinoma cells," *Bioelectromagnetics*, vol. 35, pp. 337–346, 2014.

[2] S. Yamaguchi, M. Ogiue-Ikeda, M. Sekino, and S. Ueno, "Effects of magnetic stimulation on tumors and immune functions," *IEEE Trans. Magn.*, vol. 41, no. 10, pp. 4182–4184, Oct. 2005.

[3] K. Zhang, W. Chen, T. Bu, H. Qi, R. Sun, and X. He, "Decreased P-glycoprotein is associated with the inhibitory effects of static magnetic fields and cisplatinon K562 cells," *Bioelectromagnetics*, vol. 35, pp. 437–443, 2014.

[4] S. Barzelai, A. Dayan, M. S. Feinberg, R. Holbova, S. Laniado, and M. Scheinowitz, "Electromagnetic field at 15.95–16 Hz is cardio protective following acute myocardial infarction," *Ann. Biomed. Eng.*, vol. 37, pp. 2093–2104, 2009.

[5] Y. Li *et al.*, "Low strength static magnetic field inhibits the proliferation, migration, and adhesion of human vascular smooth muscle cells in a restenosis model through mediating integrins β1-FAK, Ca^{2+} signaling pathway," *Ann. Biomed. Eng.*, vol. 40, pp. 2611–2618, 2012.

[6] M. Misakian, A. S. Sheppard, D. Krause, M. E. Frazier, and D. L. Miller, "Biological, physical, and electrical parameters for in vitro studies with ELF magnetic and electric fields: A primer," *Bioelectromagnetics*, vol. 14, no. S2, pp. S1–S73, 1993.

[7] F. Tao *et al.*, "The correlation between dielectric properties and microstructure of femoral bone in rats with different bone qualities," *Ann. Biomed. Eng.*, vol. 42, pp. 1238–1249, 2014.

[8] X.-L. Chen *et al.*, "Analysis of human brain exposure to low-frequency magnetic fields: A numerical assessment of spatially averaged electric fields and exposure limits," *Bioelectromagnetics*, vol. 34, pp. 375–384, 2013.

[9] V. Di Lazzaro *et al.*, "A consensus panel review of central nervous system effects of the exposure to low-intensity extremely low-frequency magnetic fields," *Brain Stimul.*, vol. 6, pp. 469–476, 2013.

[10] A. Legros, P. Gaillot, and A. Beuter, "Transient effect of low-intensity magnetic field on human motor control," *Med. Eng. Phys.*, vol. 28, pp. 827–836, 2006.

[11] I. Tasset, A. Pérez-Herrera, F. J. Medina, Ó. Arias-Carrión, R. Drucker-Colín, and I. Túnez, "Extremely low-frequency electromagnetic fields activate the antioxidant pathway Nrf2 in a Huntington's disease-like rat model," *Brain Stimul.*, vol. 6, pp. 84–86, 2013.

[12] D. Geng *et al.*, "Effects of electromagnetic field of UHV transmission lines exposure on testis tissue in mice," *IEEE Trans. Magn.*, vol. 45, no. 10, pp. 4853–4856, Oct. 2009.

[13] H.-W. Cho, S.-N. Kim, K. K. Kim, K. Kim, and K.-J. Kim, "Pulsed electromagnetic fields stimulate cellular proliferation in different types of cells," *IEEE Trans. Magn.*, vol. 52, no. 7, Jul. 2016, Art. no. 5000604, doi: 10.1109/TMAG.2016.2520980.

[14] A. D. Rosen, "Mechanism of action of moderate-intensity static magnetic fields on biological systems," *Cell Biochem. Biophys.*, vol. 39, pp. 163–173, 2003.

[15] J. F. Schenck, "Safety of strong, static magnetic fields," *J. Magn. Reson. Imaging*, vol. 12, pp. 2–19, 2000.

[16] S. Johnsen and K. J. Lohmann, "Magnetoreception in animals feature article," *Phys. Today*, vol. 61, no. 3, pp. 29–35, 2008.

[17] B. Brocklehurst and K. A. McLauchlan, "Free radical mechanism for the effects of environmental electromagnetic fields on biological systems," *Int. J. Radiat. Biol.*, vol. 69, pp. 3–24, 1996.

[18] C. T. Rodgers, "Magnetic field effects in chemical systems," *Pure Appl. Chem.*, vol. 81, no. 1, pp. 19–43, 2009.

[19] K. Maeda *et al.*, "Magnetically sensitive light-induced reactions in cryptochrome are consistent with its proposed role as a magnetoreceptor, " *Proc. Natl. Acad. Sci. USA*, vol. 109, no. 13, pp. 4774–4779, 2012.

[20] A. P. Colbert *et al.*, "Static magnetic field therapy: A critical review of treatment parameters," *Evid.-Based Complement. Alternat. Med.*, vol. 6, pp. 133–139, 2009.

[21] T. Yamamoto, Y. Nagayama, and M. Tamura, "A blood-oxygenation-dependent increase in blood viscosity due to a static magnetic field," *Phys. Med. Biol.*, vol. 49, pp. 3267–3277, 2004.

[22] M. Capstick, P. Schär, D. Schuermann, A. Romann, and N. Kuster, "ELF exposure system for live cell imaging," *Bioelectromagnetics*, vol. 34, pp. 231–239, 2013.

[23] A. Fujita, Y. Kawahara, S. Inoue, and H. Omori, "Development of a higher power intermediate-frequency magnetic field exposure system for in vitro studies," *Bioelectromagnetics*, vol. 31, pp. 156–163, 2010.

[24] G. Gottardi, P. Mesirca, C. Agostini, D. Remondini, and F. Bersani, "A four coil exposure system (tetracoil) producing a highly uniform magnetic field," *Bioelectromagnetics*, vol. 24, pp. 125–133, 2003.

[25] R. Lodato, C. Merla, R. Pinto, S. Mancini, V. Lopresto, and G. A. Lovisolo, "Complex magnetic field exposure system for in vitro experiments at intermediate frequencies," *Bioelectromagnetics*, vol. 34, pp. 211–219, 2013.

[26] R. Merritt, C. Purcell, and G. Stroink, "Uniform magnetic field produced by three, four, and five square coils," *Rev. Sci. Instrum.*, vol. 54, pp. 879–882, 1983.

[27] I. Montanari, "Optimal design of a system for large in vivo experiments on the effects of 50-Hz magnetic fields," *IEEE Trans. Magn.*, vol. 39, no. 3, pt. 2, pp. 1823–1826, May 2003.

[28] J. Schuderer, W. Oesch, N. Felber, D. Spät, and N. Kuster, "In vitro exposure apparatus for ELF magnetic fields," *Bioelectromagnetics*, vol. 25, pp. 582–591, 2004.

[29] T. Shigemitsu *et al.*, "A newly designed and constructed 20 kHz magnetic field exposure facility for in vivo study," *Bioelectromagnetics*, vol. 30, pp. 36–44, 2009.

[30] V. Novickij, A. Grainys, J. Novickij, and A. Lucinskis, "Programmable pulsed magnetic field system for biological applications," *IEEE Trans. Magn.*, vol. 50, no. 11, Nov. 2014, Art. no. 5101004. doi: 10.1109/TMAG.2014.2323336

[31] P. Rastogi, R. L. Hadimani, and D. C. Jiles, "Investigation of coil designs for transcranial magnetic stimulation on mice," *IEEE Trans. Magn.*, vol. 52, no. 7, Jul. 2016, Art.ID. 5200404. doi: 10.1109/TMAG.2015.2514064

[32] J. F. Bakker *et al.*, "Children and adults exposed to low-frequency magnetic fields at the ICNIRP reference levels: theoretical assessment of the induced electric fields," *Phys. Med. Biol.*, vol. 57, pp. 1815–1829, 2012.

[33] C. Calderón *et al.*, "Assessment of extremely low frequency magnetic field exposure from GSM mobile phones," *Bioelectromagnetics*, vol. 35, pp. 210–221, 2014.

[34] M. A. Fuentes, A. Trakic, S. J. Wilson, and S. Crozier, "Analysis and measurements of magnetic field exposures for healthcare workers in selected MR environments," *IEEE Trans. Biomed. Eng.*, vol. 55, no. 4, pp. 1355–1364, Apr. 2008.

[35] M.-C. Gosselin, S. Kühn, and N. Kuster, "Experimental and numerical assessment of low-frequency current distributions from UMTS and GSM mobile phones," *Phys. Med. Biol.*, vol. 58, pp. 8339–8357, 2013.

[36] I. Laakso, S. Kännälä, and K. Jokela, "Computational dosimetry of induced electric fields during realistic movements in the vicinity of a 3 T MRI scanner," *Phys. Med. Biol.*, vol. 58, pp. 2625–2640, 2013.

[37] P. Roivainen, T. Eskelinen, K. Jokela, and J. Juutilainen, "Occupational exposure to intermediate frequency and extremely low frequency magnetic fields among personnel working near electronic article surveillance systems," *Bioelectromagnetics*, vol. 35, pp. 245–250, 2014.

[38] I. D. Milovanovich *et al.*, "Homogenous static magnetic field of different orientation induces biological changes in sub-acutely exposed mice," *Environ. Sci. Pollut. Res.*, vol. 23, pp. 1584–1597, 2016. doi: 10.1007/s11356-015-5109-z

[39] D. Todorović *et al.*, "Estimation of changes in fitness components and antioxidant defense of Drosophila subobscura (Insecta, Diptera) after exposure to 2.4 T strong static magnetic field," *Environ. Sci. Pollut. Res.*, vol. 22, no. 7, pp. 5305–5314, 2015. doi: 10.1007/s11356-014-3910-8

[40] S. Amara *et al.*, "Effects of static magnetic field exposure on antioxidative enzymes activity and DNA in rat brain," *Gen. Physiol. Biophys.*, vol. 28, no. 3, pp. 260–265, 2009.

[41] A. Csillag *et al.*, "Exposure to inhomogeneous static magnetic field beneficially affects allergic inflammation in a murine model," *J. R. Soc. Interface*, vol. 11, p. 20140097, 2014.

[42] D. M. Djordjevich *et al.*, "Hematological parameters' changes in mice subchronically exposed to static magnetic fields of different orientations," *Ecotoxicol. Environ. Saf.*, vol. 81, pp. 98–105, 2012.

[43] H. Jo and H. Cha, "Sequence control verification of a central solenoid converter for nuclear fusion reactors by using a hardware-in-the-loop," *IEEE Trans. Ind. Electron.*, vol. 64, no. 9, pp. 6864–6873, Sep. 2017. doi: 10.1109/TIE.2017.2686305.

[44] X. Zhao, L. Li, J. Song, C. Li, and X. Gao, "Linear control of switching valve in vehicle hydraulic control unit based on sensorless solenoid position estimation," *IEEE Trans. Ind. Electron.*, vol. 63, no. 7, pp. 4073–4085, Jul. 2016.

[45] K. J. Smith, D. J. Graham, and J. A. Neasham, "Design and optimization of a voice coil motor (VCM) with a rotary actuator for an ultrasound scanner," *IEEE Trans. Ind. Electron.*, vol. 62, no. 11, pp. 7073–7078, Nov. 2015.

[46] Q. Deng *et al.*, "Frequency-dependent resistance of Litz-wire square solenoid coils and quality factor optimization for wireless power transfer," *IEEE Trans. Ind. Electron.*, vol. 63, no. 5, pp. 2825–2837, May 2016.

[47] M. W. Kennedy, S. Akhtar, J. A. Bakken, and R. E. Aune, "Empirical verification of a short-coil correction factor," *IEEE Trans. Ind. Electron.*, vol. 61, no. 5, pp. 2573–2583, May 2014.

[48] V. Prasanth and P. Bauer, "Distributed IPT systems for dynamic powering: Misalignment analysis," *IEEE Trans. Ind. Electron.*, vol. 61, no. 11, pp. 6013–6021, Nov. 2014.

[49] I. Dülk and T. Kovácsházy, "Parameter estimation in linear electromagnetic devices," *IEEE Trans. Ind. Electron.*, vol. 62, no. 6, pp. 3619–3628, Jun. 2015.

[50] D. E. Bordelon *et al.*, "Modified solenoid coil that efficiently produces high amplitude AC magnetic fields with enhanced uniformity for biomedical applications," *IEEE Trans. Magn.*, vol. 48, no. 1, pp. 47–52, Jan. 2012.

[51] R. Beiranvand, "Effects of the winding cross section shape on the magnetic field uniformity of the high field circular Helmholtz coil systems," *IEEE Trans. Ind. Electron.*, vol. 64, no. 9, pp. 7120–7131, Sep. 2017. doi: 10.1109/TIE.2017.2686302

[52] J. Simpson, J. Lane, C. Immer, and R. Youngquist, "Simple analytic expressions for the magnetic field of a circular current loop," *NASA Technical Report*, 2001. [Online]. Available: https://ntrs.nasa.gov/archive/nasa/casi.ntrs.nasa.gov/20010038494.pdf

[53] J. L. Ristić-Djurović, S. Ćirković, and A. Ž. Ilić, "Magnet with uncoupled combined functions," *IEEE Trans. Nucl. Sci.*, vol. 60, no. 6, pt. 2, pp. 4618–4626, 2013.

Jasna L. Ristić-Djurović received the B.S. degree in electrical engineering from the University of Belgrade, Belgrade, Serbia, in 1987, the M.S. degree in applied physics from Columbia University, New York, NY, USA, in 1989, and the Ph.D. degree in electrical engineering from Stanford University, Stanford, CA, USA, in 1993.

She is currently a Research Professor at the Institute of Physics, University of Belgrade, Belgrade. Her current research interests include wave–particle interactions in Earth's magnetosphere and accelerator physics, applied electromagnetics, biophysics, bioengineering, bioinformatics, and spectroscopy.

Slavica S. Gajić (GS'15) was born in Mrkonjić Grad, Bosnia and Herzegovina, in 1986. She received the B.Sc. and M.Sc. degrees in electronic and telecommunication engineering from the University of Banja Luka, Banja Luka, Bosnia and Herzegovina. She is currently working toward the Ph.D. degree in energy, electronic, and telecommunication engineering at the University of Novi Sad, Novi Sad, Serbia.

Since 2010, she has been a Teaching Assistant at the University of Banja Luka. Her current research interests include digital signal and image processing and electromagnetics.

Andjelija Ž. Ilić (S'01–M'04) received the Dipl.Ing. degree from the University of Belgrade, Belgrade, Serbia, in 1998, the M.Sc. degree from University of Massachusetts Dartmouth, MA, USA, in 2004, and the Ph.D. degree from University of Belgrade, Belgrade, Serbia, in 2010, all in electrical engineering.

She is currently an Assistant Research Professor with the Institute of Physics, University of Belgrade. She was a Postdoctoral Research Associate with the University of Westminster, London, U.K., during 2013–2014. She has authored or coauthored 27 international journal papers and numerous conference papers. Her current research interests include all the topics in applied and computational electromagnetics.

Dr. Ilić was the recipient of the 2006 Young Scientist and the 2014 Best Paper ETRAN Awards, as well as the "Prof. Aleksandar Marinčić" Award given annually by the IEEE MTT Serbia chapter, for the best journal paper in 2016.

Nebojša Romčević received the B.S. degree in electrical engineering and M.S. and Ph.D. degrees in physics from the University of Belgrade, Belgrade, Serbia, in 1987, 1991, and 1997, respectively.

He is currently a Research Professor at the Institute of Physics, University of Belgrade, Belgrade, Serbia, where he is also a Professor at the School of Electrical Engineering. He is the founder of Kristal infiz Ltd., innovative company devoted to technology and knowledge transfer from science to industry. His current research interests include experimental research in the field of spectroscopy (Raman, X-ray, and FTIR) on semiconductors (bulk crystals, thin films, and nanodimensional systems).

Drago M. Djordjevich received the M.D., M.Sc., and Ph.D. degrees from the University of Belgrade, Belgrade, Serbia, in 1982, 1995, and 2008, respectively, as well as completed his residency in physical medicine and rehabilitation there in 1991.

He is currently an Associate Professor with the Institute of Pathophysiology, School of Medicine, University of Belgrade. His current research interests include pathobiology, biophysics, biomaterials, biomedical applications of magnetic nanomaterials, magnetobiology, bioelectromagnetism, quantum biology, and quantum medicine.

Silvio R. De Luka was born in Belgrade, Serbia, in 1967. He received the M.D. degree, M.Sc. degree in neurochemistry, and Ph.D. degree in neurology from the School of Medicine, University of Belgrade, Belgrade, Serbia, in 1992, 2000, and 2008, respectively.

He is currently an Associate Professor of pathophysiology at the School of Medicine, University of Belgrade. His current research interests include static magnetic field, trace elements, and biomarkers of aging.

Alexander M. Trbovich was born in Yugoslavia in 1966. He received the M.D. degree from University of Belgrade School of Medicine, Belgrade, Serbia, in 1991, and the Ph.D. degree in pathology, cellular and molecular biology from Boston University School of Medicine, Boston, MA, USA, in 2000.

He is currently an Associate Professor of pathophysiology and a Research Professor with the School of Medicine, University of Belgrade, Belgrade, Serbia. His current research interests include bioelectromagnetism and aging.

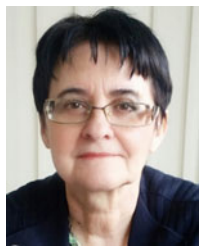

Vesna Spasić Jokić received the B.Sc., M.Sc., and Ph.D. degrees in electrical engineering from the School of Electrical Engineering, University of Belgrade, Belgrade, Serbia, in 1978, 1986, and 1994, respectively.

She is a tenured Professor with the Faculty of Technical Sciences, University of Novi Sad. She is also with the International Atomic Energy Agency as an expert in the field of nuclear knowledge management. She has authored or coauthored more than 200 international journal papers, books and chapters in international monographs, conference papers, and international projects.

Saša Ćirković received the B.S., M.S., and Ph.D. degrees in electrical engineering from the University of Belgrade, Belgrade, Serbia, in 1989, 2001, and 2009, respectively.

He was with GTE, Vinča Institute of Nuclear Sciences, and Innovation Center of School of Electrical Engineering, University of Belgrade. He is currently a Research Assistant Professor at the Institute of Physics, University of Belgrade, Belgrade, Serbia. His current research interests include accelerator physics and technology, bioengineering, biophysics, and bioinformatics.

International Journal of Radiation Biology

ISSN: 0955-3002 (Print) 1362-3095 (Online) Journal homepage: http://www.tandfonline.com/loi/irab20

Subchronic exposure to static magnetic field differently affects zinc and copper content in murine organs

Silvio R. De Luka, Andjelija Ž. Ilić, Saša Janković, Drago M. Djordjevich, Saša Ćirković, Ivan D. Milovanovich, Srdjan Stefanović, Slavica Vesković-Moračanin, Jasna L. Ristić-Djurović & Alexander M. Trbovich

To cite this article: Silvio R. De Luka, Andjelija Ž. Ilić, Saša Janković, Drago M. Djordjevich, Saša Ćirković, Ivan D. Milovanovich, Srdjan Stefanović, Slavica Vesković-Moračanin, Jasna L. Ristić-Djurović & Alexander M. Trbovich (2016): Subchronic exposure to static magnetic field differently affects zinc and copper content in murine organs, International Journal of Radiation Biology, DOI: 10.3109/09553002.2016.1135266

To link to this article: http://dx.doi.org/10.3109/09553002.2016.1135266

Published online: 05 Feb 2016.

INTERNATIONAL JOURNAL OF RADIATION BIOLOGY, 2016
http://dx.doi.org/10.3109/09553002.2016.1135266

Taylor & Francis
Taylor & Francis Group

RESEARCH ARTICLE

Subchronic exposure to static magnetic field differently affects zinc and copper content in murine organs

Silvio R. De Luka[a]*, Andjelija Ž. Ilić[b]*, Saša Janković[c], Drago M. Djordjevich[a], Saša Ćirković[b], Ivan D. Milovanovich[a], Srdjan Stefanović[c], Slavica Vesković-Moračanin[c], Jasna L. Ristić-Djurović[b] and Alexander M. Trbovich[a]

[a]Department of Pathological Physiology, School of Medicine, University of Belgrade, Belgrade, Serbia; [b]Institute of Physics, University of Belgrade, Zemun-Belgrade, Serbia; [c]Institute of Meat Hygiene and Technology, Belgrade, Serbia

ABSTRACT

Purpose Static magnetic fields (SMF) have been widely used in research, medicine and industry. Since zinc and copper play an important role in biological systems, we studied the effects of the subchronic continuous SMF exposure on their distribution in murine tissues.

Materials and methods For 30 days, mice were exposed to inhomogeneous, vertical, downward or upward oriented SMF of 1 mT averaged intensity with spatial gradient in vertical direction.

Results SMF decreased the amount of copper and zinc in liver. In brain, zinc levels were increased and copper levels were decreased. In spleen, zinc content was reduced, while copper amount remained unchanged.

Conclusions Subchronic exposure to SMF differently affected copper and zinc content in examined organs, and the changes were more pronounced for the downward oriented field. The outcome could be attributed to the protective, rather than the harmful effect of SMF.

ARTICLE HISTORY
Received 22 June 2015
Accepted 30 October 2015

KEYWORDS
Inhomogeneous SMF of different orientation; zinc; copper; brain; liver; spleen

Introduction

Elements, such as zinc (Zn) and copper (Cu), play important roles in biological processes. An essential micronutrient to nutritionists, zinc represents a constituent of enzymes and other proteins to biochemists, whereas to environmentalists and marine biologists, free zinc in water is regarded a toxic pollutant (Frederickson et al. 2005, Witeska and Kosciuk 2013). Zinc deficiency is associated with anorexia and alterations of the epidermal, gastrointestinal, central nervous, immune, skeletal and reproductive systems (Tapiero and Tew 2003). Zinc is crucial for normal development and function of cells mediating innate immunity, neutrophils and natural killer (NK) cells. It induces the production of metallothionein, an excellent scavenger of hydroxyl radical ($OH^{\bullet}$) (Prasad 2008), and may also play a relevant part in the control of both cell proliferation and mitosis (Wolford et al. 2010). It is a component of many transcription factors and proteins that control the cell cycle and can inhibit apoptosis (Chasapis et al. 2012).

Copper is a redox-active essential trace element that is predominantly used by organisms living in oxygen-rich environments and in such environments it fluctuates between the oxidized Cu^{2+} and reduced Cu^{1+} states (Turski and Thiele 2009). Copper is required for functioning of over 30 proteins, including superoxide dismutase, ceruloplasmin, lysyl oxidase, cytochrome-c-oxidase, tyrosinase and dopamine-β-hydroxylase (Rana 2008). Cu ions participate in DNA synthesis and cell proliferation. Central nervous system (CNS) development and function is particularly dependent on copper metabolism and homeostasis. In excess of cellular needs, it can lead to the generation of reactive oxygen species (ROS) or to the displacement of other metal cofactors from their natural ligands.

All living organisms are continually exposed to the Earth's magnetic field (geomagnetic field, GMF) ranging from 0.02–0.07 mT, although environmental fields from 0.01–0.1 mT can be recorded, depending on the geographic location and presence of magnetic materials in the vicinity (Repacholi and Greenebaum 1999). In recent years static magnetic fields (SMF) have been widely used in research, medicine and industry (Yamaguchi-Sekino et al. 2011, László et al. 2012, Mészáros et al. 2013, Lahbib et al. 2014). Moderate intensity SMF, between 1 mT and 1 T, can produce considerable effects on biological systems (Rosen 2003), yet for a large part of this intensity range research data is insufficient. We focus here on the average SMF intensity of about 1 mT for two reasons. Firstly, there is scarce data on the biological effects of moderate SMF at the lower end of the intensity range. It is known from previous in vitro experiments that the low-field effect (LFE) threshold falls into this intensity range, with its exact value dependent upon a number of factors (Brocklehurst

CONTACT Prof. Alexander M. Trbovich aleksandar.trbovic@mfub.bg.ac.rs, alexander.m.trbovich@gmail.com Department of Pathological Physiology, School of Medicine, University of Belgrade, Dr Subotića 9, 11000 Belgrade, Serbia
*These authors made equal contributions to the paper and, thus, share first authorship.

and McLauchlan 1996, Maeda et al. 2012). At field values below the LFE threshold, including the GMF, SMF affects biochemical reactions by increasing the proportion of free radicals surviving longer and diffusing into the surroundings, whereas exactly the opposite happens for SMF values above the threshold. Secondly, SMF of 1 mT has been shown to cause interference with cardiac pacemakers and implantable cardioverter-defibrillators at a distance of up to 24 cm (Ryf et al. 2008), raising a question about other possible effects on biological processes having lower interaction thresholds. Inhomogeneous SMF has been employed in this study, motivated by the recent investigations suggesting possible significance of local SMF gradients, in addition to the SMF intensity, in the effects produced on biological systems (László et al. 2007, Djordjevich et al. 2012, Vergallo et al. 2013). With our exposure set-up, lateral SMF gradients are almost negligible and the vertical SMF gradient is dominant. Field intensity decreases nearly as a linear function of height above the set-up. Also, gradient SMF can more truthfully than a homogeneous SMF mimic real life exposures of organisms to electromagnetic devices and SMF sources.

The effects of inhomogeneous, vertically decreasing, SMF on Zn and Cu distribution in different mouse tissues (brain, liver and spleen) have been investigated. The incentive for this particular choice of tissues has been the presence of trace elements in these tissues. Copper is most abundant in brain and liver, while zinc is most abundant in liver (Allen et al. 2006). Additionally, in respect to zinc, we decided to choose brain over kidney because of enormous importance of zinc for brain function. Spleen has been selected, since the SMF effect on spleen was obtained in previous studies (Hashish et al. 2008, Djordjevich et al. 2012).

Theoretical background

Direct mechanisms of action of SMF on the living systems include the magnetic forces and torques, motion-induced currents in tissues, presence of ferrimagnetic particles in an organism, SMF acting on a flux of ions across the cell membrane, diamagnetic anisotropy of organic molecules, magnetohydrodynamic forces and pressures, and SMF affecting the rates and yields of chemical reactions (Schenck 2000, Rosen 2003). Only three of the mechanisms remain plausible when considering the GMF, which also applies to other very weak SMF sources, as explained in detail by Johnsen and Lohmann (2008). These are the ferrimagnetism, electromagnetic induction and SMF effects on chemical reactions through the radical pair mechanism (RPM).

It has long been disputed that the weak SMF, being below the thermodynamic threshold of k_BT associated with the random thermal energy, can exhibit significant effects on biological systems. In statistical mechanics, probability of a state with energy E is proportional to $\exp(-E/k_BT)$, implying that any weak SMF effect cannot be thermodynamic in origin and cannot affect the position of a system equilibrium. Biological systems, however, usually operate on the verge of equilibrium or oscillate about the equilibrium (Brocklehurst and McLauchlan 1996). The fact that the kinetic processes and chemical reactions in an organism can be influenced by SMF is what matters in this case.

The RPM arises from the existence of spin angular momentum, an intrinsic property of elementary particles. Electrons, protons and neutrons belong to fermions, particles that have half-integer spin. Distribution of fermions over energy states is described by the Fermi-Dirac statistics and as such it obeys the Pauli exclusion principle, stating that no two identical fermions can simultaneously occupy the same quantum state. For an electron in an atom or a molecule, quantum state is determined by its energy, orbital angular momentum, magnetic moment and spin (spin up or spin down). General form of equations, describing the electron spin evolution, would have to take into account all of the degrees of freedom and all of the mutual interactions of the system constituents. Fortunately, the quantum chemists have succeeded in treating the time evolution of the electron spin and spatial coordinates separately, introducing a number of empirical parameters. Numerical models of different complexity are used in calculations, whereas the semi-classical vector model is excellent for the qualitative RPM illustration (Brocklehurst and McLauchlan 1996, Rodgers 2009). Excitation occurring in a complex molecule AB, where A and B are joined by an electron-pair bond, leads to the transfer of an electron into a different quantum state and from A to B, thus forming a spin-correlated radical pair A and B. In the bound state the two electrons have had the opposite spins ($\uparrow\downarrow$), forming a singlet state with total spin equal to zero. If the radical pair (RP) recombines before A and B separate due to diffusion, which is called the geminate cage recombination, the singlet product (SP) is formed. If the RP constituents separate definitely, an escape product (EP) is formed. If the re-encounter occurs at a later time, there is a possibility of the secondary geminate recombination. However, the electron spins that remain antiparallel for a short time after the RP formation, due to the short separation of electrons resulting in a strong exchange interaction between electron spins, soon begin to differ in their precession frequencies and phases of precession as well. Under the influence of molecular hyperfine interactions, the RP undergoes the singlet to triplet ($S\leftrightarrow T$) interconversion, with the secondary recombination possible only from the singlet spin state of the RP. The hyperfine interaction, made up of two contributions – magnetic moment coupling and spin coupling, couples the unpaired electron spin with the internal magnetic field from the spins of magnetic nuclei. A detailed account of kinetics of reactions involving RP, along with the explanations of hyperfine, exchange and Zeeman interactions, has been given by Rodgers (2009).

Spin evolution between singlet and triplet states ($S\leftrightarrow T$ interconversion) is affected by the externally applied magnetic fields, modifying the yields of reaction products SP and EP and consequently leading to the magnetic field effects (MFE). Three triplet spin states, of the total spin equal to one and differing in the total spin projections (+1, 0, or −1), were degenerate in energy at zero magnetic field. In the presence of an external magnetic field, energy levels change by the energy of the magnetic moment of an atom in the field, leading to the spectral line splitting into several components designated as the Zeeman effect. The Zeeman interaction occurs between

the unpaired electron spins on each radical and an external magnetic field; along with the hyperfine interactions it forms the hyperfine mechanism responsible for weak field MFE, up to about 50 mT (Rodgers 2009). In higher fields, the Δg-mechanism dominates, due to the different magnetic moments of the two radicals in RP and thus somewhat different g-tensors of the two radicals linking the field intensity with the produced Zeeman interaction. Due to a typical RP lifetime of 10 ns to 1 μs, the RPM is expected to act similarly for the SMF and the low-frequency fields up to about 1 MHz (Rodgers 2009).

Much more than the thermal energy k_BT is required for the generation of the RP. It has to be supplied prior to and independently of the RPM action, as a result of photochemical excitation, low-dose radiation exposure, thermolytic bond cleavage, etc. Additionally, RP are intrinsically widely present in biological systems, as reactants or products of usual biochemical reactions. Experimental confirmation of the biological MFE due to the RPM has been obtained for cryptochrome/photolyase protein family (Maeda et al. 2012, Evans et al. 2015). As pointed out by Brocklehurst and McLauchlan (1996), freely diffusing RP tend to be highly reactive and undiscriminating in their reactions and the MFE are expected to be small. Reactions involving single radicals become SMF dependent mostly through the effect of change of radical concentration, eventually leading to the change in the rate of reaction.

With regard to the trace elements, Zn and Cu, investigated here, possible target for the RPM action has to be a chemical reaction involving free radicals. Among their other roles, Zn and Cu are the constituents of Cu/Zn superoxide dismutase (CuZn-SOD), an enzyme that catalyses the metabolism of the superoxide radical ($^{\bullet}O_2^-$) into hydrogen peroxide (H_2O_2) and oxygen (O_2), thus belonging to the ROS scavengers. CuZn-SOD is a metalloprotein, in which the Zn ion contributes to the structural stability (Roberts et al. 2007), whereas the Cu^{2+} ion directly participates in the catalytic mechanism of CuZn-SOD:

$$\text{SOD-Cu}^{2+} + {}^{\bullet}O_2^- \rightarrow \text{SOD-Cu}^{1+} + O_2;$$

$$\text{SOD-Cu}^{1+} + {}^{\bullet}O_2^- + 2H^+ \rightarrow \text{SOD-Cu}^{2+} + H_2O_2.$$

As the CuZn-SOD binds the superoxide byproducts of metabolism to produce H_2O_2, that has to be further catalyzed into water and oxygen, both the diminished or highly increased activity of CuZn-SOD can be harmful to an organism. It is the balance of CuZn-SOD, as well as the balance between Cu and Zn, that is the prerequisite for the first step of antioxidant defense in nearly all living cells exposed to oxygen. In the excess of Cu^{2+}, copper-initiated reaction between H_2O_2 and CuZn-SOD results in the formation of $^{\bullet}OH$ (Sato et al. 1992, Ramirez et al. 2009). The aforementioned $^{\bullet}O_2^-$, H_2O_2, and $^{\bullet}OH$ are the biologically most relevant ROS, an unavoidable consequence of aerobic metabolism, also involved in cell signaling mechanisms and immune response (Dröge 2002, Sies 2014). Often the case with metalloprotein cofactors, both Cu and Zn belong to the transition metals, their atomic numbers being 29 and 30, and abbreviated electron configurations $[Ar]4s^13d^{10}$ and $[Ar]4s^23d^{10}$, respectively. Therefore, Cu, which due to its easy interconversion between Cu^{2+} and Cu^{1+} (Cu(II) and Cu(I)) plays a major catalytic role, has an unpaired electron spin both in its atomic state and as a Cu^{2+} ion. Moreover, Cu^{2+} ion is paramagnetic due to its $[Ar]3d^9$ electron configuration. Taken all into account, cyclic redox reactions involving the superoxide dismutase could be sensitive to the externally applied SMF. This is suggested by the recent investigations of the SMF effect on ROS scavenger enzymes (Amara et al. 2006, 2009), albeit with the much stronger SMF of 128 mT. It is of interest to investigate possible MFE on these enzymes at different field strengths in the weak to moderate SMF range.

Materials and methods

Experimental animals

Male Swiss-Webster 6-month-old mice, obtained from the Military Medical Academy Animal Research Facility (Belgrade, Serbia), were maintained on a nutritionally and energetically adequate diet (21% protein, 62% carbohydrate, 5% fat, 0.25% vitamin premix, 2.25% mineral mixture; Veterinarski zavod, Subotica, Serbia) for 30 days. The animals were housed in cages with five animals per cage in a temperature-controlled room (19 ± 1 °C) with a 12 h light-dark cycle. All animals were matched for initial body weight and were weighed at weekly intervals.

All experimental protocols involving animals were reviewed and approved by the University of Belgrade, Faculty of Medicine Experimental Animals Ethics Committee. Furthermore, all experiments were conducted in accordance with the procedures described in the National Institutes of Health Guide for Care and Use of Laboratory Animals (Washington, DC, USA), as well as the US-NIH guidelines for the conduction of magnetic field experiments on animals.

Static magnetic field

Experimental SMF was produced by the specialized medical device patented under the name MADU stripe (Mandić 1999). Primarily intended for use in physical therapy and rehabilitation, MADU stripes consist of small permanent magnets embedded into an elastic rubber stripe or sheet. We use the type L MADU stripe, which resembles a sheet due to the five rows of ferromagnetic rods ($BaFe_{12}O_{19}$), four rods per each row, with the magnetic axes of the rods all in the same direction perpendicular to the stripe. Accordingly with the dimensions of the cages, three MADU stripes type L were placed under each cage, as shown in Figure 1, to ensure optimal SMF coverage.

Detailed analysis of the general case of two-dimensional magnetic arrays is published (Ilić et al. 2013). That work describes in great detail the SMF produced by the type L MADU stripe, utilized here as an exposure setup. Analytical expressions and particularities of the finite element calculations, along with the SMF measurements, are presented. The SMF calibration procedure utilizes field values measured on a 9×9.75 mm grid, at eight heights above the MADU stripe, to determine the SMF scaling factor proportional to the remanent magnetization of ferromagnetic rods.

Were the magnetic axes of the neighboring rods oriented in the opposite directions, SMF would be predominantly parallel to the sheet's surface and confined to a thin layer above it. The same direction of all magnetic axes, on the contrary, produces SMF perpendicular to the MADU sheet's surface, much

stronger and extending several centimeters from the surface. As shown in Figure 1, using the two vertical cross sections of the cage, SMF decrease with height is dominant in comparison with its variation in the horizontal planes due to the discrete positions of individual magnets. Right on top of each individual magnet, at height $z = 0$ m, maximal magnetic flux density is 98 mT. Figure 2 shows the magnetic flux density in four planes parallel to the MADU surface at the heights 5, 10, 20 and 30 mm.

Given the relatively dense placement of the stripe's magnetic rods in respect to the size of the animals, as well as that the mice were freely moving, magnetic field and its vertical gradient were averaged in horizontal planes first. Further averaging is performed over the volume between the horizontal planes $z = 20$ mm and $z = 50$mm, resulting in mean magnetic flux density and its mean gradient of 1.23 mT and 0.02 T/m, respectively. Field decrease is almost linear from $z = 20$ mm to $z = 50$ mm. The summary of the relevant SMF parameters, required for the complete SMF description (Colbert et al. 2009), is given in Table 1.

Experimental design

The effects of the subchronic continuous exposure to SMF were studied for both the upward oriented and the downward oriented SMF. The experiment was performed on the Earth's Northern hemisphere; therefore, the vertical GMF component was directed downwards and our SMF had the same or opposite direction in respect to the GMF. Mice were randomly divided into three groups (control and two experimental groups), each containing 10 animals. Since the magnets embedded in the MADU stripes cannot be removed or turned off, instead of sham exposure, the first experimental group, which served as a control, was exposed to the measured ambient magnetic field of 40 μT intensity. The second experimental group was exposed to the upward oriented SMF (Up group), and the third experimental group was exposed to the downward oriented SMF (Down group). Note that the magnetic field above MADU stripes was measured. It is the sum of the MADU stripe SMF and the ambient magnetic field, the latter comprising only 3.25% of the total exposure field.

Except for the SMF, all three groups of experimental animals were kept under the same conditions. The animal Plexiglas cages were separated out by 10 cm, which was enough to avoid magnetic interference. Three MADU stripes of appropriate orientation, generating either upward or downward oriented SMF, were placed under the cages of the Up and Down groups for the entire duration of the experiment, i.e., continuously for 30 days. Food consumption was measured daily and body mass weekly. In the animal facilities, where animals were kept, all cages were marked with a code. A person in charge of feeding and wellbeing of animals was the only person aware of presence of magnets below some cages, but she did not know the code. At the end of the exposure, mice were transferred to the laboratory where tissues were collected for analyses that were performed blindly. Tissues were put in samples that were coded and analyzed by researchers who were not cognizant of group sample origin.

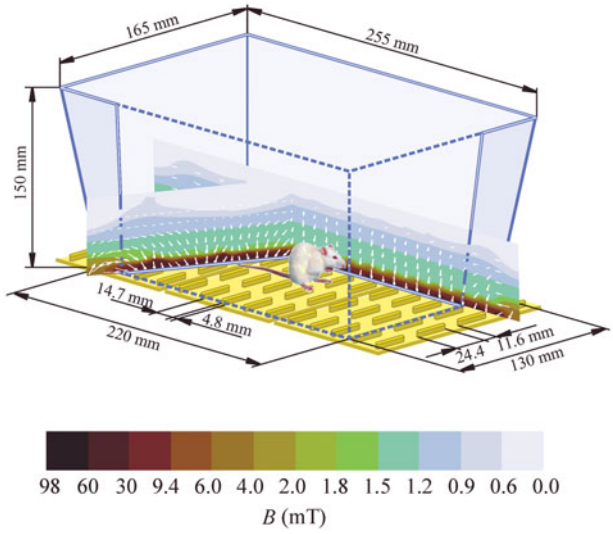

Figure 1. Experimental animal in cage with MADU stripes below. Static but spatially dependent magnetic field acts on animals moving freely within the experimental volume. The SMF distribution in vertical planes is shown for the two vertical cross sections of the cage. The first one coincides with the middle of the space between the two rows of ferromagnetic rods, while the second cross section is given at an angle of 60° in respect to the first one. The SMF intensity, indicated by different colors (shades of gray), varies much more with height than in the horizontal planes. The magnetic lines of force are almost vertical everywhere except at the edges of the stripes and the magnetic field can be characterized as vertically declining (Ilić et al. 2013).

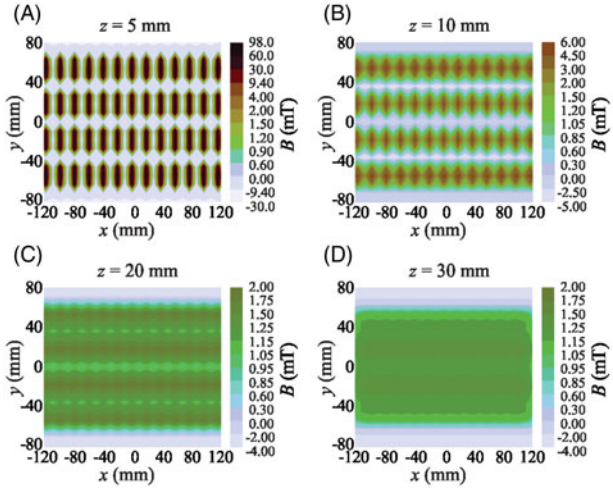

Figure 2. SMF variation in horizontal planes above the MADU type L stripes. Matrix arrangement of individual magnets produces the slowly decreasing SMF. Panels A, B, C, and D, show field variation in the planes parallel to the MADU surface. Detailed magnetic field description as well as more data is given by Ilić et al. (2013).

Table 1. Ten SMF dosage parameters (Colbert et al. 2009).

Magnet materials	Barium hexaferrite, $BaFe_{12}O_{19}$
Magnet dimensions	$W \times L \times H = 4.8 \times 24.4 \times 4.8$ mm^3
Pole configuration	Same magnetic axes direction
Measured field strength	1–2 mT (magnet axis)
Frequency of application	Continuous application
Duration of application	30 days
Site of application	Whole body exposure
Magnet support device	Elastic rubber stripe
Target tissue	Brain, liver, spleen
Distance from the magnet surface	20–50 mm

Determination of copper and zinc

In order to determine the content of Zn and Cu in brain, liver, and spleen of the experimental animals, samples were microwave digested (ETHOS TC, Milestone S.r.l., Sorisole, Italy) according to manufacturer's recommendations. Tissue of interest (0.5 g) was treated with 8 ml of nitric acid (HNO_3) and 2 ml of hydrogen peroxide (30% H_2O_2); temperature program was as follows: 5 min from room temperature (20 °C) to 180 °C, then 10 min hold at 180 °C. After cooling, samples were transferred with deionized water in 50 ml volumetric flask. Analyses were carried out on atomic absorption spectrometer 'SpectrAA 220' (Varian, Palo Alto, CA, USA) according to Varian Atomic Absorption Spectrometers (AAS) Analytical Methods. Analytical quality control was achieved by analyzing certified reference material BCR-186 (Community Bureau of Reference – BCR, Brussels, Belgium), which is lyophilized pig kidney for determining trace elements (Institute for Reference Materials and Measurements, Geel, Belgium). Replicate analyses were undertaken within the range of certified values. Zinc and copper values were expressed as μg of Zn/Cu per mg of dried analyzed tissue.

Statistical analysis

Findings reported at this time correspond to a single subchronic continuous SMF exposure experiment. Each of the three experimental groups consisted of the same number of 10 animals per group. Except for the exposure SMF, experimental conditions were identical for all three groups. Simultaneous exposure was carried out while in the same facilities, and the subsequent analyses were performed blindly. Data is presented, in Figures 3 and 4, as mean ± SEM. Statistical analysis was performed using the SPSS Statistics software for Windows, version 16.0 (SPSS, Chicago, IL). Differences among groups were evaluated by the one-way ANOVA, followed by the Fischer's LSD test. The level of significance was set at $p < 0.05$.

Results

Experimental animals were, on average, exposed to 1 mT SMF, continuously, for the period of 30 days. Compared to the control group (13.36 ± 0.14 μg/mg), the animals in the Up group (14.46 ± 0.42 μg/mg) had statistically higher levels of Zn in brain tissue. The Zn increase in brain was even more pronounced in the Down group (15.00 ± 0.20 μg/mg). Brain Zn values in experimental groups are shown in Figure 3.

As for brain copper, the SMF produced significant decrease in both Up (3.66 ± 0.09 μg/mg) and Down (3.08 ± 0.09 μg/mg) groups, compared to the control group (4.25 ± 0.08 μg/mg). Even more, the level of Cu in the Down group was significantly decreased compared to the Up group. The brain Cu values for the three experimental groups are shown in Figure 4.

Zinc content in liver (Figure 3), as well as liver copper (Figure 4), decreased significantly following the exposure to 1 mT SMF. Specifically, zinc in the Up (46.07 ± 0.61 μg/mg) and Down (46.82 ± 0.75 μg/mg) groups experienced a drop of about 20% when compared to the control group

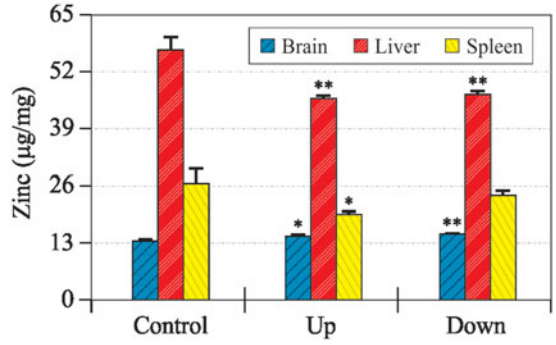

Figure 3. Zinc content in murine organs after exposure to SMF of different (Up and Down) orientation for 30 days. Data represent the mean ± SEM. *$p < 0.05$ compared to control; **$p < 0.01$ compared to control.

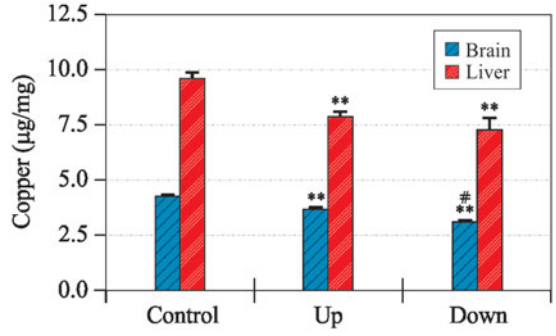

Figure 4. Copper values in murine organs after exposure to SMF of different (Up and Down) orientation for 30 days. Data represent the mean ± SEM. **$p < 0.01$ compared to control; #$p < 0.01$ compared to Up.

(56.89 ± 3.30 μg/mg). Similarly, the liver Cu in the Up group was 7.88 ± 0.22 μg/mg and in the Down group was 7.33 ± 0.48 μg/mg, whereas for the control group it was 9.59 ± 0.30 μg/mg.

Exposure to the SMF for 30 days produced significant decrease in Zn content in spleen in the Up group (19.40 ± 0.78 μg/mg), while in the Down group (23.70 ± 1.20 μg/mg) decrease was not statistically significant (Figure 3). The control group zinc amounted to 26.48 ± 3.32 μg/mg. The copper levels in spleen were low (1.14 ± 0.81 μg/mg), disallowing for the precise determination of statistical differences between any two of the three groups of animals; therefore this data is not shown.

Discussion

The research data focusing on trace elements distribution after exposure to SMF is scarce (Salem et al. 2005, Miryam et al. 2010, Aida et al. 2014, Zhang et al. 2014). The impact to biological activities of imbalance in these elements, as well as the likelihood of being affected by magnetic fields, motivates further effort in this direction.

Numerous studies (Pourahmad et al. 2001, 2003, Tassabehji et al. 2005, Vanlandingham et al. 2005, Rana 2008, Annabi et al. 2013, Nunes et al. 2014, Waheed et al. 2014) showed toxic effects induced by Cu overload in tissues. Excess copper can, instead of iron, serve as a catalyst in Fenton-like reactions,

resulting in the production of ROS, responsible for lipid peroxidation in membranes, direct oxidation of proteins and cleavage of DNA and ribonucleic (RNA) molecules (Tapiero et al. 2003). A recent study (Singh et al. 2013) showed that in aging mice, accumulation of Cu in brain was associated with increased amyloid beta (Aβ) production and neuroinflammation. The pathological production of $^{\bullet}OH$ from H_2O_2 and CuZn-SOD due to excess copper might play a role in Alzheimer's disease as well (Multhaup et al. 1997). Similar mechanism is known to be associated with the familial amytrophic lateral sclerosis, resulting from CuZn-SOD gene mutations that lead to the zinc deficiency (Roberts et al. 2007).

Large amounts of zinc are normally present in the brain. Ten percent of the total brain zinc is localized to the lumen of glutamate containing synaptic vesicles, that may be released on excitation and may play role in modulation of synaptic signaling (Tapiero and Tew 2003). The dominant effect of zinc in the normal brain is to reduce excitability, thereby functioning as an endogenous anticonvulsant (Frederickson et al. 2005). The converse treatment, which involves intracranial administration of zinc salts, is directly cytolethal and proconvulsive. Since low Zn levels inhibit cell growth as well as division, and increase the possibility of seizures, whereas high Zn levels are toxic, cells must maintain cellular zinc content within a narrow window, which is estimated to be in a low picomolar range. Toxicity develops when the zinc concentration rises to nanomolar levels (Bozym et al. 2010).

Our results showed increased brain concentration of Zn upon exposure to SMF, as well as a decrease in the amount of brain Cu. From the standpoint of atomic physics, different result of the SMF influence on Zn and Cu could be attributed in part to their electron configurations. Zinc is diamagnetic with completely filled 3d orbital and no unpaired electron spins both in its atomic state and as a Zn^{2+} ion which is often a cofactor in complex molecules. In its atomic state, Cu is diamagnetic with completely filled 3d orbital and an unpaired spin in $4s^1$, whereas as a Cu^{2+} ion it becomes paramagnetic with an unpaired electron spin in 3d orbital. Therefore, Cu is much more likely to be directly affected by the externally applied SMF than Zn, whereas Zn can be affected indirectly through the chemical reactions involving Cu and possibly ROS. Moreover, in certain chemical reactions Zn and Cu act together, for example as cofactors in the CuZn-SOD, and any change in one or the other can influence the other one in the opposite way. In some disorders, for example, Zn deficiency and the excess of Cu can reinforce each other leading to the disruption of homeostasis (Dröge 2002, Roberts et al. 2007). It is important to assess whether these effects of 1 mT SMF on Zn and Cu are mostly beneficial, adversarial, or could be both depending on a situation.

Moderate increase in brain Zn could lead to anticonvulsive effect of Zn with preservation of its regulatory function for healthy brain (Sterman et al. 1986, Elsas et al. 2009). However, zinc dysregulation is implicated as a contributing factor in two types of neuropathology: Alzheimer's disease and the so-called 'excitotoxicity' that injures neurons. It is widely accepted that free zinc in the extracellular fluid induces amyloid deposition and early-phase clinical trials indicate that zinc chelation inhibits Aβ-plaque deposition (Ritchie et al. 2003). On the other hand, while Cu and Fe binding to Aβ induce O_2-dependent H_2O_2 production and toxicity, co-incubation with zinc inhibits H_2O_2 production (Cuajungco and Faget 2003). Therefore, Zn^{2+} loading into plaque may represent an attempt at protective homeostatic response against Alzheimer's disease, where plaques form as the result of a more robust Zn antioxidant response to the underlying oxidative attack. Also, the Aβ in the plaques has been redox-silenced by the high concentrations of zinc, whereas the diffuse and soluble Aβ accumulations within the brain would be a source of H_2O_2 and oxidative damage (Frederickson and Bush 2001). Decreased Cu, as long as its level is sufficient to maintain normal brain functioning of exposed animals, protects the brain from oxidative injury or premature apoptosis. The increase of zinc in our experiment was diminutive, yet statistically significant, which, along with the decrease of copper, suggests probable protective effect against neuroinflammation.

Liver, as well as the brain, is an organ extremely vulnerable to the disturbed Cu metabolism and homeostasis. An observed decrease in liver Cu acts protectively against the ROS production, again if its level is still sufficient. We have also demonstrated the SMF induced decrease of Zn in the liver of exposed animals. A number of cited studies showed deleterious effects of zinc deficiency (Sullivan et al. 1980, Dardenne 2002). However, it was also shown (Phillips et al. 1996) that excess of zinc induced severe progressive cholestasis in children. Since the decrease of zinc concentration in liver of exposed animals was not very large, we can speculate that it did not disturb zinc homeostasis, but rather protected liver from possible damage. Interestingly, previous study of combined subchronic exposure to 128 mT SMF and Zn supplementation showed increased metallothionein synthesis in liver that has been suspected to control metal homeostasis and to maintain cell survival in response to various stimuli such as oxidative stress (Salem et al. 2005). As discussed for the RPM, weak SMF and moderately strong SMF can actually produce the opposite biological effects.

Studies performed on the Zn-deficient mice showed depressed responses to both the T-lymphocyte-dependent and the T-lymphocyte-independent antigens, as well as the decreased NK cell activity (Dardenne 2002). It cannot be stated with certainty if the observed decrease of zinc in the spleen in the Up group is sufficient to produce the above responses.

Conclusion

In our subchronic SMF exposure experiment, brain, liver and spleen were analyzed for Cu and Zn content. Specific changes were observed in the Cu and Zn content in examined organs, which presumably could be attributed to protective, rather than harmful effects of SMF. A decrease of copper in brain and liver, along with the increase of zinc in brain could, probably, represent positive consequences of the SMF exposure. It is worth pointing out that combined effect of decreased copper and increased zinc in brain was more statistically pronounced in the Down group. Potential employment of the SMF exposure against metal overload, instead of the standard chelator therapy, is a promising assumption adding to the importance of the observed results. Further studies with

chronic exposure and different SMF intensities could give better insight in the observed changes.

Acknowledgements

This study was supported by the grants No III-41013, No III-41019 and No III-45003 from the Ministry of Education, Science and Technological Development, Government of Serbia.

Disclosure statement

The authors report no conflict of interest. The authors alone are responsible for the content and writing of the paper.

Funding information

No funding body had any involvement in the preparation or content of this article or in the decision to submit it for publication.

References

Aida L, Soumaya G, Myriam E, Mohsen S, Hafedh A. 2014. Effects of static magnetic field exposure on plasma element levels in rat. Biol Trace Elem Res 160:67–72.

Allen KJ, Buck NE, Cheah DMY, Gazeas S, Bhathal P, Mercer JFB. 2006. Chronological changes in tissue copper, zinc and iron in the toxic milk mouse and effects of copper loading. BioMetals 19:555–564.

Amara S, Abdelmelek H, Garrel C, Guiraud P, Douki T, Ravanat JL, Favier A, Sakly M, Ben Rhouma K. 2006. Effects of subchronic exposure to static magnetic field on testicular function in rats. Arch Med Res 37:947–952.

Amara S, Douki T, Garel C, Favier A, Sakly M, Rhouma KB, Abdelmelek H. 2009. Effects of static magnetic field exposure on antioxidative enzymes activity and DNA in rat brain. Gen Physiol Biophys 28:260–265.

Annabi A, Said K, Messaoudi I. 2013. Heavy metal levels in gonad and liver tissues – effects on the reproductive parameters of natural populations of *Aphanius fasciatus*. Environ Sci Poll Res 20:7309–7319.

Bozym RA, Chimienti F, Giblin LJ, Gross GW, Korichneva I, Li Y, Libert S, Maret W, Parviz M, Frederickson CJ, Thompson RB. 2010. Free zinc ions outside a narrow concentration range are toxic to a variety of cells in vitro. Exp Biol Med 235:741–750.

Brocklehurst B, McLauchlan KA. 1996. Free radical mechanism for the effects of environmental electromagnetic fields on biological systems. Int J Radiat Biol 69:3–24.

Chasapis CT, Loutsidou AC, Spiliopoulou CA, Stefanidou ME. 2012. Zinc and human health: An update. Arch Toxicol 86:521–534.

Colbert AP, Wahbeh H, Harling N, Connelly E, Schiffke HC, Forsten C, Gregory WL, Markov MS, Souder JJ, Elmer P, King V. 2009. Static magnetic field therapy: A critical review of treatment parameters. Evid-Based Complement Alternat Med 6:133–139.

Cuajungco MP, Faget KY. 2003. Zinc takes the central stage: Its paradoxical role in Alzheimer's disease. Brain Res Rev 41:44–56.

Dardenne M. 2002. Zinc and immune function. Eur J Clin Nutr 56:S20–23.

Djordjevich DM, De Luka SR, Milovanovich ID, Janković S, Stefanović S, Vesković-Moračanin S, Ćirković S, Ilić AŽ, Ristić-Djurović JL, Trbovich AM. 2012. Hematological parameters' changes in mice subchronically exposed to static magnetic fields of different orientations. Ecotoxicol Environ Saf 81:98–105.

Dröge W. 2002. Free radicals in the physiological control of cell function. Physiol Rev 82:47–95.

Elsas SM, Hazany S, Gregory WL, Mody I. 2009. Hippocampal zinc infusion delays the development of after discharges and seizures in a kindling model of epilepsy. Epilepsia 50:870–879.

Evans EW, Dodson CA, Maeda K, Biskup T, Wedge CJ, Timmel CR. 2015. Magnetic field effects in flavoproteins and related systems. Interface Focus 3:20130037.

Frederickson CJ, Bush AI. 2001. Synaptically released zinc: Physiological functions and pathological effects. BioMetals 14:353–366.

Frederickson CJ, Koh JY, Bush AI. 2005. The neurobiology of zinc in health and disease. Nat Rev Neurosci 6:449–462.

Hashish AH, El-Missiry MA, Abdelkader HI, Abou-Saleh RH. 2008. Assessment of biological changes of continuous whole body exposure to static magnetic field and extremely low frequency electromagnetic fields in mice. Ecotoxicol Environ Saf 71:895–902.

Ilić AŽ, Ćirković S, Djordjevic DM, De Luka SR, Milovanovich ID, Trbovich AM, Ristić-Djurović JL. 2013. Analytical description of two-dimensional magnetic arrays suitable for biomedical applications. IEEE Trans Magn 49:5656–5663.

Johnsen S, Lohmann KJ. 2008. Magnetoreception in animals feature article. Phys Today 61:29–35.

Lahbib A, Ghodbane S, Sakly M, Abdelmelek H. 2014. Vitamins and glucose metabolism: The role of static magnetic fields. Int J Radiat Biol 90:1240–1245.

László J, Reiczigel J, Székely L, Gasparics A, Bogár I, Bors L, Rácz B, Gyires K. 2007. Optimization of static magnetic field parameters improves analgesic effect in mice. Bioelectromagnetics 28:615–627.

László JF, Farkas P, Reiczigel J, Vágó P. 2012. Effect of local exposure to inhomogeneous static magnetic field on stomatological pain sensation – a double-blind, randomized, placebo-controlled study. Int J Radiat Biol 88(5):430–438.

Maeda K, Robinson AJ, Henbest KB, Hogben HJ, Biskup T, Ahmad M, Schleicher E, Weber S, Timmel CR, Hore PJ. 2012. Magnetically sensitive light-induced reactions in cryptochrome are consistent with its proposed role as a magnetoreceptor. Proc Natl Acad Sci USA 109:4774–4779.

Mandić D, Patent No. (WO1999060581) Surface magnetised elastic magnetic strip and application. Available at: http://patentscope.wipo.int/search/en/WO1999060581

Mészáros S, Tabák AG, Horváth C, Szathmári M, László JF. 2013. Influence of local exposure to static magnetic field on pain perception and bone turnover of osteoporotic patients with vertebral deformity – a randomized controlled trial. Int J Radiat Biol 89:877–885.

Miryam E, Aida L, Samira M, Mohsen S, Hafedh A. 2010. Effects of acute exposure to static magnetic field on ionic composition of rat spinal cord. Gen Physiol Biophys 29:288–294.

Multhaup G, Ruppert T, Schlicksupp A, Hesse L, Beher D, Masters CL, Beyreuther K. 1997. Reactive oxygen species and Alzheimer's disease. Biochem Pharmacol 54:533–539.

Nunes B, Capela RC, Sergio T, Caldeira C, Goncalves F, Correia AT. 2014. Effects of chronic exposure to lead, copper, zinc and cadmium on biomarkers of the European eel, *Anguilla Anguilla*. Environ Sci Poll Res 21:5689–5700.

Phillips MJ, Ackerley CA, Superina RA, Filler RM, Roberts EA, Levy GA. 1996. Excess zinc associated with severe progressive cholestasis in Cree and Ojibwa-Cree children. The Lancet 347:866–868.

Pourahmad J, Ross S, O'Brien PJ. 2001. Lysosomal involvement in hepatocyte cytotoxicity induced by Cu^{2+} but not Cd^{2+}. Free Radical Biol Med 30:89–97.

Pourahmad J, O'Brien PL, Jokar F, Daraei B. 2003. Carcinogenic metal induced sites of reactive oxygen species formation in hepatocytes. Toxicol In Vitro 17:803–810.

Prasad AS. 2008. Zinc in human health: Effect of zinc on immune cells. Mol Med 14:353–357.

Ramirez DC, Gomez-Mejiba SE, Corbett JT, Deterding LJ, Tomer KB, Mason RP. 2009. Cu,Zn-superoxide dismutase-driven free radical modifications: Copper- and carbonate radical anion-initiated protein radical chemistry. Biochem J 417:341–353.

Rana SVS. 2008. Metals and apoptosis: Recent developments. J Trace Elem Med Biol 22:262–284.

Repacholi MH, Greenebaum B. 1999. Interaction of static and extremely low frequency electric and magnetic fields with living systems: Health effects and research needs. Bioelectromagnetics 20:133–160.

Ritchie CW, Bush AI, Mackinnon A, Macfarlane S, Mastwyk M, MacGregor L, Kiers L, Cherny R, Li QX, Tammer A, Carrington D, Mavros C, Volitakis I, Xilinas M, Ames D, Davis S, Beyreuther K, Tanzi RE, Masters CL. 2003. Metal-protein attenuation with iodochlorhydroxyquin (Clioquinol) targeting Aβ amyloid deposition and toxicity in Alzheimer disease: A pilot phase 2 clinical trial. Arch Neurol 60:1685–1691.

Roberts BR, Tainer JA, Getzoff ED, Malencik DA, Anderson SR, Bomben VC, Meyers KR, Karplus PA, Beckman JS. 2007. Structural characterization of

zinc-deficient human superoxide dismutase and implications for ALS. J Mol Biol 373:877–890.
Rodgers CT. 2009. Magnetic field effects in chemical systems. Pure Appl Chem 81:19–43.
Rosen AD. 2003. Mechanism of action of moderate-intensity static magnetic fields on biological systems. Cell Biochem Biophys 39:163–173.
Ryf S, Wolber T, Duru F, Luechinger R. 2008. Interference of neodymium magnets with cardiac pacemakers and implantable cardioverter-defibrilators: An in vitro study. Technol Health Care 16:13–18.
Salem A, Hafedh A, Rached A, Mohsen S, Khemais BR. 2005. Zinc prevents hematological and biochemical alterations induced by static magnetic field in rats. Pharmacol Rep 57:616–622.
Sato K, Akaike T, Kohno M, Ando M, Maeda H. 1992. Hydroxyl radical production by H_2O_2 plus Cu,Zn-superoxide dismutase reflects the activity of free copper released from the oxidatively damaged enzyme. J Biol Chem 267:25371–25377.
Schenck JF. 2000. Safety of strong, static magnetic fields. J Magn Reson Imaging 12:2–19.
Sies H. 2014. Role of metabolic H_2O_2 generation: Redox signalling and oxidative stress. J Biol Chem 289:8735–8741.
Singh I, Sagare AP, Coma M, Perlmutter D, Gelein R, Bell RD, Deane RJ, Zhong E, Parisi M, Ciszewski J, Kasper RT, Deane R. 2013. Low levels of copper disrupt brain amyloid-β homeostasis by altering its production and clearance. Proc Natl Acad Sci USA 110:14771–14776.
Sterman M, Shouse M, Fairchild M, Belsito O. 1986. Kindled seizure induction alters and is altered by zinc absorption. Brain Res 383:382–386.
Sullivan JF, Jetton MM, Hahn HKJ, Burch RE. 1980. Enhanced lipid peroxidation in liver microsomes of zinc-deficient rats. Am J Clin Nutr 33:51–56.
Tapiero H, Townsend DM, Tew KD. 2003. Trace elements in human physiology and pathology. Copper. Biomed Pharmacother 57:386–398.
Tapiero H, Tew KD. 2003. Trace elements in human physiology and pathology: Zinc and metallothioneins. Biomed Pharmacother 57:399–411.
Tassabehji NM, VanLandingham JW, Levenson CW. 2005. Copper alters the conformation and transcriptional activity of the tumor suppressor protein p53 in human HepG2 cells. Exp Biol Med (Maywood) 230:699–708.
Turski ML, Thiele DJ. 2009. New roles for copper metabolism in cell proliferation, signaling and disease. J Biol Chem 284:717–721.
VanLandingham JW, Tassabehji NM, Somers RC, Levenson CW. 2005. Expression profiling of p53-target genes in copper-mediated neuronal apoptosis. Neuromolecular Med 7:311–324.
Vergallo C, Dini L, Szamosvölgyi Z, Tenuzzo BA, Carata E, Panzarini E, László JF. 2013. In vitro analysis of the anti-inflammatory effect of inhomogeneous static magnetic field-exposure on human macrophages and lymphocytes. PLoS One 8:e72374.
Waheed S, Kamal A, Malik RN. 2014. Human health risk from organ-specific accumulation of toxic metals and response of antioxidants in edible fish species from Chenab River, Pakistan. Environ Sci Poll Res 21:4409–4417.
Witeska M, Kosciuk B. 2013. The changes in common carp blood after short-term zinc exposure. Environ Sci Poll Res 10:284–286.
Wolford JL, Chishti Y, Jin Q, Ward J, Chen L, Vogt S, Finney L. 2010. Loss of pluripotency in human embryonic stem cells directly correlates with an increase in nuclear zinc. PLoS One 5:1–7.
Yamaguchi-Sekino S, Sekino M, Ueno S. 2011. Biological effects of electromagnetic fields and recently updated safety guidelines for strong static magnetic fields. Magn Reson Med Sci 10:1–10.
Zhang J, Ding C, Shang P. 2014. Alterations of mineral elements in osteoblast during differentiation under hypo, moderate and high static magnetic fields. Biol Trace Elem Res 162:153–157.

Environmental Toxicology and Pharmacology 92 (2022) 103853

Contents lists available at ScienceDirect

Environmental Toxicology and Pharmacology

journal homepage: www.elsevier.com/locate/etap

Distinct fatty acid redistribution and textural changes in the brain tissue upon the static magnetic field exposure

Andjelija Ž. Ilić [a,1], Silvio R. de Luka [b,1], Tamara B. Popović [c], Jasmina Debeljak-Martačić [c], Milica Kojadinović [c], Saša Ćirković [a], Jasna L. Ristić-Djurović [a], Alexander M. Trbovich [b,*]

[a] Institute of Physics Belgrade, University of Belgrade, Pregrevica 118, Zemun, Belgrade, Serbia
[b] Department of Pathological Physiology, Faculty of Medicine, University of Belgrade, Dr. Subotića 9, 11000 Belgrade, Serbia
[c] Institute for Medical Research, University of Belgrade, Centre of Excellence in Nutrition and Metabolism, Tadeuša Košćuška 1, Belgrade 11000, Serbia

ARTICLE INFO

Keywords:
Vertical homogeneous static magnetic field (SMF) of different orientations
Brain fatty acids (FA)
Thin liquid chromatography (TLC) and gas liquid chromatography (GC)
Fractal (dimension/lacunarity) and multifractal analysis
Histograms of the local fractal dimension distributions
Gray level co-occurrence matrix (GLCM) statistical features

ABSTRACT

We observed different outcomes upon the subacute exposure to the 128 mT highly homogeneous static magnetic field (SMF) when its orientation was (i) aligned with the vertical component of the geomagnetic field; (ii) in the opposite direction. We employed the fatty acids (FA) composition and digital image analyses (DIA) to provide insights into the underlying processes and examine the possible weak SMF effects. Swiss-Webster male mice were whole-body exposed for 1 h/day over five days. Brain tissue's thin liquid chromatography resulted in brain FA composition, indicating a possible sequence of changes due to the SMF exposure. Quantitative DIA accurately assessed different image parameters. Delicate textural changes were revealed in the group where pathohistological or biochemical alterations have not been detected. DIA-based biological markers seem to be very promising for studying delicate tissue changes, which results from the high sensitivity and wide availability of DIA.

1. Introduction

Over the past two decades, significant evidence has been collected about the interaction of static magnetic fields (SMF) with living organisms (Kim et al., 2010; Yu and Shang, 2014; De Luka et al., 2016; Piszczek et al., 2021; Kthiri et al., 2019) as well as with the cell and tissue samples (Dini and Panzarini, 2010; Kimsa-Dudek et al., 2018). In some cases, beneficial effects have been observed (Lv et al., 2021; Kimsa-Dudek et al., 2018; Chiu et al., 2007), opening the possibility to use the SMF in biomedicine apart from their use in magnetic resonance imaging (Bongers et al., 2018; Yamaguchi-Sekino et al., 2014). On the other side, studies of the potentially adverse effects of the magnetic fields (MF), including the SMF (Amara et al., 2007; Ghodbane et al., 2011; Çelik et al., 2015; Zhang et al., 2016; Bongers et al., 2018), call for further investigations in order to avoid any potentially harmful effects. The presence of MF in everyday life and possible occupational exposures (Zhang et al., 2016; Bongers et al., 2018) additionally motivate such investigations.

The present study continues our previous investigation on the effects on tissues and organs of moderate-intensity static magnetic field (Milovanovich et al., 2016). Magnetic fields (MF) of low and moderate intensity have been shown to affect biological systems considerably (Amara et al., 2007; Kroupová et al., 2007; Torres-Duran et al., 2007; Kim et al., 2010; Martínez-Sámano et al., 2010; Ghodbane et al., 2011; Calabrò, 2016; De Luka et al., 2016; Mouhoub et al., 2018). Different effects have been observed based on the cell or tissue type, magnetic field strength, and exposure durations. Kroupová et al. (2007) observed effects at the cytoskeleton level of the 2 mT low frequency MF (50 Hz), indicating that cell death, apoptosis, has been induced. Calabrò studied acute (4 h) exposure of the neuronal-like cells to the similar MF (50 Hz, 1 mT), explaining the results by the mechanism of protein aggregation combined with an increase in hydrogen bonding. Both low frequency MF and SMF have been linked with effects at the level of particular organs and tissues (Kim et al., 2010; Martínez-Sámano et al., 2010; Torres-Duran et al., 2007; Milovanovich et al., 2016; De Luka et al., 2016). Exposure to a 128 mT horizontal SMF has been studied in (Amara et al., 2007; Elferchichi et al., 2011; Ghodbane et al., 2011). Metabolic alterations were observed upon the 128 mT SMF exposure for 1 h per

* Correspondence to: Faculty of Medicine (BU), Dr. Subotića 9, Belgrade 11000, Serbia.
E-mail addresses: alexander.m.trbovich@gmail.com, aleksandar.trbovic@mfub.bg.ac.rs (A.M. Trbovich).
[1] These authors contributed equally to this work and, thus, share the first authorship

https://doi.org/10.1016/j.etap.2022.103853
Received 13 October 2021; Received in revised form 24 January 2022; Accepted 16 March 2022
Available online 19 March 2022

day during 15 consecutive days (Elferchichi et al., 2011). On the other side, zinc supplementation was found to minimize oxidative damage induced by the 128 mT SMF (1 h per day during 30 consecutive days) in rat tissues (Amara et al., 2007). The oxidative stress most probably resulted from free radical production due to the SMF exposure. Ghodbane et al., 2011 reached similar conclusions regarding the interaction between the 128 mT SMF (1 h per day during 5 consecutive days) and selenium. Selenium is important for a number of physiological processes, including the elimination of reactive oxygen species (ROS) and the modulation of redox-sensitive enzyme cascades. Its levels in the kidney, muscle, and brain were decreased upon the SMF exposure and restored by selenium supplementation. Although the mechanisms of influence are still not completely understood, the non-thermal SMF effects are believed to be mediated through the radical pair mechanism (RPM) or the voltage-gated calcium channels activation (Pall, 2018; Piszczek et al., 2021; De Luka et al., 2016; Barnes and Greenebaum, 2018). De Luka et al., 2016 presented the theoretical background on the RPM, emphasizing the activity of antioxidant enzymes and possible effects on the distribution of antioxidant trace elements (Zn, Se, Cu) in different tissues. Barnes and Greenebaum, 2018 additionally considered the role of feedback in biological systems. It has also been shown that MF and SMF exposure can induce tissue and lipid profile changes (Milovanovich et al., 2016; Torres-Duran et al., 2007; Elferchichi et al., 2011; Mouhoub et al., 2018).

We decided to assess the moderate-intensity (128 mT) vertical SMF influence on mice brain tissue at three levels by employing (i) classical histological approach where two independent pathologists read the tissue slides, (ii) biochemical approach in which a fatty acids (FA) composition was determined, and (iii) digital image analysis (DIA) approach where tissue slides were analyzed by various mathematical morphometric and statistical textural methods. Different effects were previously observed based on the SMF orientation (Milovanovich et al., 2016; Tian et al., 2018; Yang et al., 2021). A possible explanation is that living organisms are adapted to environmental conditions, including the geomagnetic field (GMF). It has been demonstrated that the long-term GMF deprivation (GMF vertical component kept below 20 nT) affected the concentration of Fe, Mn, Cu, and Cr in the hair of experimental animals (Tombarkiewicz, 2008). In our case, the two SMF orientations corresponded to increased vertical MF component in the GMF direction and to reversed total vertical MF (the opposite direction).

The FA composition determination (biochemical approach) is expected to identify a possible sequence of changes towards the observed effects. Being low-cost and widely available, biochemical tests are routinely used to support medical conclusions. On the other side, histopathology is the “gold standard” for the vast majority of diagnoses because most of the diseases can be defined by microscopic features. As the next step in tissue analyses, DIA uses histological micrographs to evaluate the modifications in a fully quantitative manner. DIA provides an unbiased quantitative assessment of the intensity of changes, including minor or early-stage changes (Kroupová et al., 2007; Tan et al., 2015; Tomaszewska et al., 2015; Ghosh et al., 2018; Manera et al., 2021), unnoticed during the histological examination. Different DIA tools extract information on different image parameters. Since the SMF effects could be weak, it is interesting to cross-compare different DIA parameters and check on their agreement. It would allow us to understand better the observed impacts of differently oriented SMF on the brain. The recognition of the pathological processes in their very early stages is the incentive to introduce and use highly accurate analyses.

2. Materials and methods

2.1. Experimental design

Male Swiss-Webster mice, 23 ± 3 g on average, 9–10 weeks old, were obtained from the Military Medical Academy Animal Research Facility (Belgrade, Serbia) and placed in Plexiglas cages with tap water and pelleted food available ad libitum. The number of animals per cage was four or five. All experimental protocols were approved by the University of Belgrade, Faculty of Medicine Experimental Animals Ethics Committee, and conducted according to procedures described in the Directive 2010/63/EU of the European Parliament and of the Council of 22 Sep 2010 on the protection of animals used for scientific purposes, and procedures described in the National Institutes of Health Guide for Care and Use of Laboratory Animals (Washington, DC, USA).

The experimental animals were divided randomly into three groups (9 mice per group), kept under the same conditions. The animals in the first experimental group were whole-body exposed, for 1 h/day over five days, to the 128 mT SMF in the direction opposite to the vertical GMF component at the experimental location (denoted as Up group). In the second experimental group (designated as the Down group), the whole-body exposure was to the downward oriented 128 mT SMF for 1 h/day over five days (aligned with the vertical GMF component). In the third group (denoted as the Control group), animals were placed inside the exposure system while it was turned off for 1 h/day over five days and were sham-exposed. Animals were sacrificed by exsanguinations in ketamine (100 mg/kg i.p.) anesthesia after the treatment.

2.2. Exposure system description

When studying the effects of SMF exposures, a frequent problem is an insufficiently homogeneous SMF that was applied to the specimens or even the lack of information on the SMF uniformity (Colbert et al., 2009). The attainment of the very homogeneous SMF of moderate or strong intensity typically requires large magnetomotive forces and enclosed volumes such as the interior of solenoids (Ilić et al., 2014) and modified solenoids (Ristić-Djurović et al., 2018b). However, for this experiment, we were able to produce the highly homogeneous SMF of 128 mT magnetic flux density using the ferromagnetic structure of the VINCY Cyclotron (Milovanovich et al., 2016), which was under construction. The fully assembled and operative but still accessible ferromagnetic structure allowed the employment of a strong SMF as an experimental tool.

The SMF between the two poles of the VINCY Cyclotron, which is a straight sector isochronous cyclotron, is highly homogeneous in the sector regions and in the valley regions. In the vicinity of sector edges, it changes abruptly, and the SMF gradient is high. However, the used Plexiglas cages were sized 35.5 cm-by-20.5 cm and 19.0 cm high, which allowed their placement in the middle of the cyclotron valley and inside the circle of radius 80 cm (from the cyclotron center), avoiding the stray field components at radii larger than 84 cm. The main coil current was set to 36.5 A to produce the 128 mT magnetic flux density without using trim coils. The magnetic flux density during the experiments was monitored using the miniature ($14 \times 5 \times 2$ mm^3) Hall probe MPT-141, which enabled high measurement precision. Under these conditions, the desired SMF was attained with less than 0.68% variation throughout the experimental volume, which is considered highly homogeneous, enabling the true whole-body exposures. For the Control group, zero magnetic flux density with all coil currents set to zero was used.

The vertical component of GMF in the northern hemisphere is directed downward, i.e., in the same direction as gravity. According to the measurements conducted at the Geophysical Institute of Grocka (Serbia), (44.6° N, 20.8° E), the geomagnetic flux density during the experiments, (44.7° N, 20.6° E), was on the order of 47,6 μT, 47,6 μT, making an angle of about 28.5° with the vertical. The vertical component was on the order of 41,9 μT.41,9 μT.

2.3. Histological analysis and digitalized micrographs

Brain tissues fixation in 10% formaldehyde (water solution) lasted for 24 h prior to embedding the tissues in paraffin. The 5 μm thick sections of the frontal cortex were put on slides and stained with haematoxylin/eosin (Bio-Optica, Milan, Italy; MP Biomedicals LLC, Illkirch

Cedex, France, respectively). Analysis of stained sections was performed independently by two pathologists using the light microscope Olympus BX41 (Tokyo, Japan). Digitalized micrographs were produced by the two pathologists using a digital camera Sony Exwave HAD, model SSC-DC50AP (Tokyo, Japan). The images were acquired at 400 × magnification, using a 40 × (N.A. 0.65) objective along with an eyepiece of 10 × magnification. Immunohistochemical (IHC) analysis was carried out with the mouse anti-human antibodies against CD 3 (A0452, Dako, Denmark), CD 15 (M3631, clone Carb 3, Dako, Denmark), and CD 20 (NCL-L-CD20-L26, clone L26, Leica Novocastra, Germany). After the 1 hr exposure of tissue to primary antibodies, slides were rinsed with water, and the secondary antibody was added. Detection was carried out using the horseradish peroxidase kit (EnVision FLEX K8000, Dako, Denmark). CD 3 is a marker for T lymphocytes, CD 20 is a marker for B lymphocytes, and CD 15 is a marker for granulocyte lineage.

Digitalized micrographs (Fig. 1) had to be prepared for the planned DIA analyses, as described in detail in the Supplement on DIA Methodology. The monochromatic images were converted into grayscale, pixels with intensity below the intensity threshold were singled out using the local Niblack thresholding, and the binary outlines were found, as illustrated in Fig. 2**a**. Grayscale micrographs (Fig. 2**b**) were used for textural analysis by the modified fractal dimension, multifractal analysis, and computing the statistical parameters of the gray level co-occurrence matrices (GLCM), as described in the Supplement. The binary outlines (Fig. 2**c**) were used in the standard fractal analysis and multifractal analysis. DIA performed repeated calculations for each of the five considered micrographs per group, selected by the pathologists as the most representative of the typical tissue appearance in each group.

2.4. Biochemical analysis

For biochemical analyses, we used the entire mice brains (around 0.5 g) without the tips of the frontal cortex, which were cut off and saved for histological analysis. We employed a solvents system (chloroform/methanol 2:1 and butylated hydroxytoluene) to extract total lipids. In the end, we added water (0.2 volumes), and following centrifugation, the upper phase was removed. Then it was processed with solvent systems: methanol/benzene (2:1), acetone/benzene (2:1), and ethanol/benzene (2:1). Afterward, chloroform and hexane were used to prepare the sample for thin liquid chromatography (TLC). To isolate the phospholipid fraction from the extracted lipids, one-dimensional TLC was used with a neutral lipid solvent system of hexane-diethyl ether acetic acid (87:2:1, v/v). Previously, we described the process of fatty acid methyl esters extraction and preparation and their gas chromatography (GC) analysis (Popovic et al., 2009). To compare sample peak retention times, we used authentic standards (Sigma Chemical Co, St. Louis, MO, USA) and/or the PUFA-2 standard mixture (Supelco Inc., Bellefonte, PA, USA) allowing identification of individual FAs methyl esters (Folch et al., 1957).

2.5. Statistical analysis

In planning the experiment, statistical power calculations led to a sample size of seven to nine animals per group. We used nine samples per group, indicated as highly accurate even for the weak effects (Ristić-Djurović et al., 2018a). We performed the statistical analysis of obtained data using the SPSS for Windows software, v.16.0 (SPSS, Chicago, IL, USA). We used one-way ANOVA followed by the post hoc Tukey test to evaluate the differences among groups. The level of significance was set at $p < 0.05$.

2.6. Fractal analysis

The fractal analysis allows non-integer dimensionality in assessing the structural complexity of objects under study. It is well suited for studying structures of natural origin. It has been confirmed as a powerful method in the study of anatomy (Den Buijs et al., 2006; Karperien and Jelinek, 2016; Captur et al., 2017) and classification of cells and tissues (Smith et al., 1996; Al Kadi and Watson 2008; Lopes and Betrouni, 2009; Manera et al., 2021).

Fractal dimension is a parameter describing the increase in complexity of a fractal measure, $\mu(l)$, with scale, l, (Smith et al., 1996; Lopes and Betrouni, 2009):

$$\mu(l) = Al^{D}, \tag{1}$$

(A – prefactor, D – fractal dimension). The normalized grid size for a grid cell length l, and an entire set perimeter L, equals $\varepsilon = l/L$. For a grid cell size ε, and $N(\varepsilon)$ grid cells needed to cover an object, the fractal dimension (D_b) is approximately found using

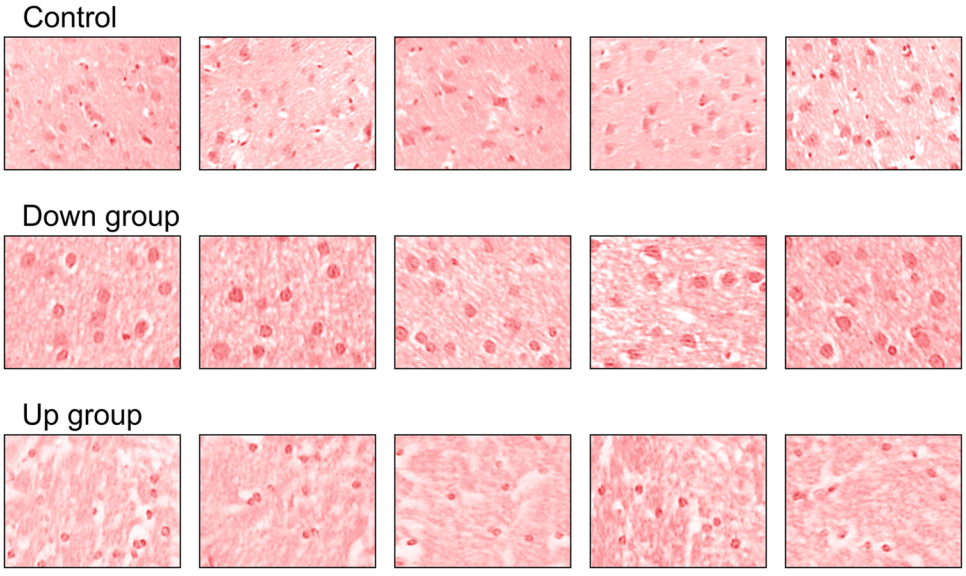

Fig. 1. Typical micrographs of tissue section slides. Histological analysis confirmed the brain edema in observed neurons in eight out of nine animals exposed to the upwards oriented SMF (Up group) compared to the sham (Control) and Down groups.

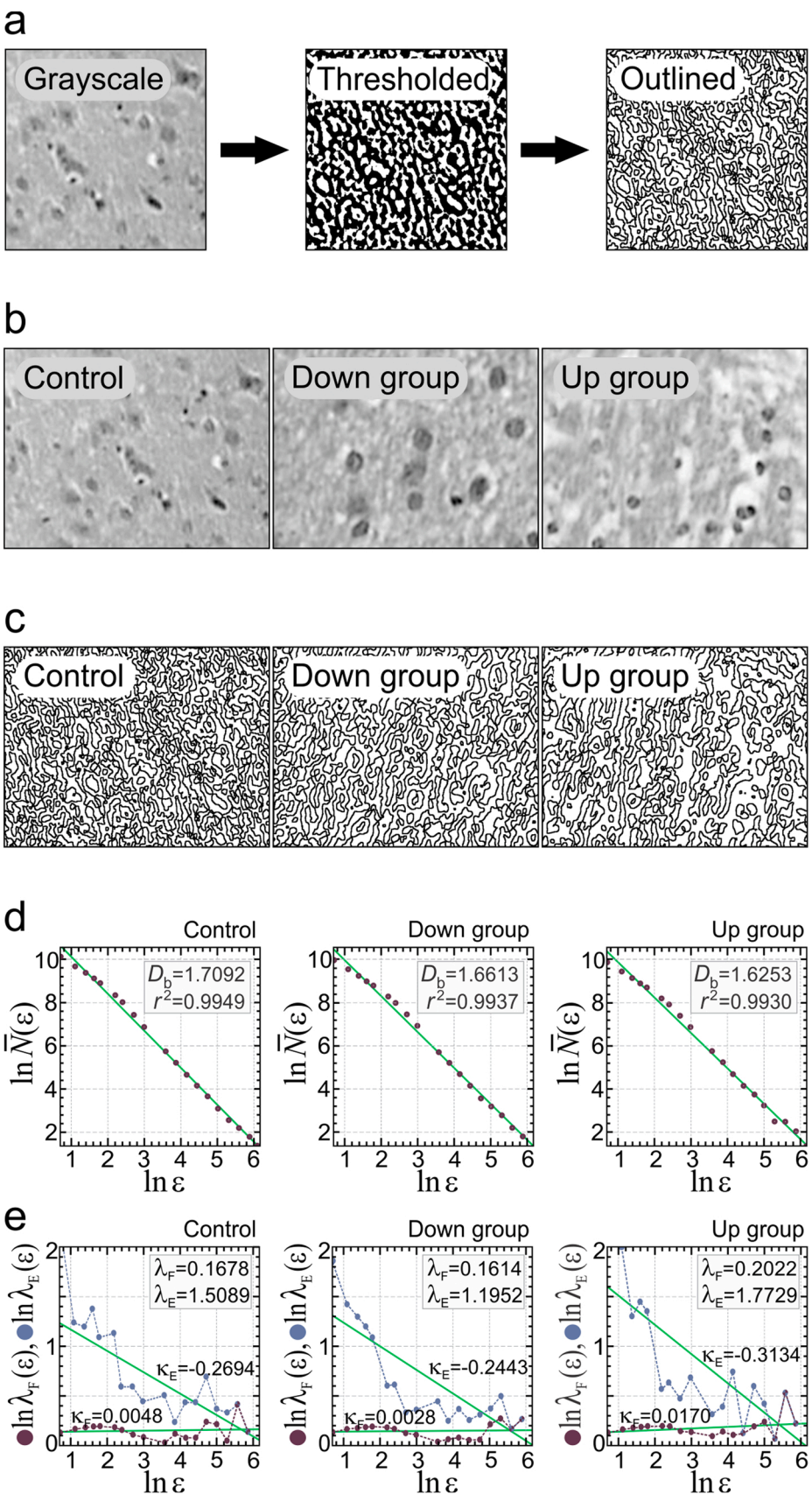

Fig. 2. Fractal analysis – fractal dimension (D_b) and pixel mass lacunarity ($\lambda_F(\varepsilon)$,$\lambda_E(\varepsilon)$) calculation. (**a**) Micrograph preparation included grayscale conversion, applying a threshold to single out entities of interest, and obtaining contours by outlining. (**b**) Grayscale micrographs were used in textural fractal analysis and the GLCM analysis. (**c**) Binary outlines were used in the fractal and multifractal analyses. (**d**) Fitting the regression lines to the data points is used in determining the fractal dimension, D_b, with data linearity described by the correlation coefficients, r^2 (straight line: $r^2 = 1.0$). (**e**) We used the lacunarity based on the foreground pixels, $\lambda_F(\varepsilon)$, more sensitive to the local changes in data (Table 3), rather than $\lambda_E(\varepsilon)$, which includes the empty grid cells.

$$D_b = -\lim_{\varepsilon \to 0} \frac{\ln N(\varepsilon)}{\ln \varepsilon}. \quad (2)$$

We used the software ImageJ (NIH, Bethesda, MD, USA), and the FracLac plugin for ImageJ (A. Karperien, Charles Sturt University, Australia) in all calculations. The least square regression lines were fitted to the (ε, $N(\varepsilon)$) data (Fig. 2**d**), with the correlation coefficients, r^2, showing the wellness of the fit. We also determined the mass moments (Smith et al., 1996), allowing the calculation of fractal lacunarity, $\lambda(\varepsilon)$. The first-order mass moment, $M(\varepsilon)$, and the higher-order mass moments, for m points enclosed in a patch of size ε with probability$P(m, \varepsilon)$, were calculated as

$$M(\varepsilon) = \sum_m mP(m,\varepsilon),\ M^q(\varepsilon) = \sum_m m^q P(m,\varepsilon). \quad (3)$$

Previously, $P(m, \varepsilon)$ was normalized to give $\sum_m P(m,\varepsilon) = 1$. The fractal dimension D_m was estimated as the positive slope of a regression line fit to the (ε, $M(\varepsilon)$) data. Using $M(\varepsilon)$ and $M^2(\varepsilon)$, we calculated the fractal lacunarity, $\lambda(\varepsilon)$:

$$\lambda(\varepsilon) = \frac{\langle M^2(\varepsilon)\rangle - \langle M(\varepsilon)\rangle^2}{\langle M(\varepsilon)\rangle^2}, \quad (4)$$

where the angle brackets, $\langle\cdot\rangle$, denote the mathematical expectation (average). Fitting the regression lines was used to avoid the influence of higher-order moments on the results (Fig. 2**e**).

Digitalized brain tissue micrographs were sized 700-by-528 px^2. We used twelve randomly positioned grids (offsets) per grid size to reduce the grid positioning effects. The following grid sizes (in pixels) were used in all analyses: $\varepsilon \in$ {2, 3, 4, 5, 6, 9, 11, 15, 20, 36, 48, 64, 85, 114, 152, 203, 270, 360}.

2.7. Multifractal analysis

The success of the fractal analysis in the study of biomedical phenomena is very much owed to the multiplicative processes in an organism, leading to the multifractal structure of proteins and protein aggregations (Yang et al., 2009; Foderà et al., 2013), as well as the genetic sequences (Moreno et al., 2011). Such processes are also responsible for cell growth and differentiation. Multifractal analysis (Den Buijs et al., 2006; Smith et al., 1996; Gould et al., 2011; Stošić and Stošić, 2006) additionally allows the calculation of the higher-order moments, $\chi(q)$, and generalized fractal dimensions, D_q:

$$\chi(q) = \sum_i P_i^q,\ D_q = \lim_{\varepsilon \to 0}\left(\frac{1}{q-1}\frac{\ln \chi(q)}{\ln \varepsilon}\right), \quad (5)$$

q denoting the order, $P_i = P(i, \varepsilon)$ the probabilities (size ε, i-th cell measure). For $q = 0$, one obtains the standard fractal dimension (also called the capacity dimension). Fig. 3**b** shows (q, D_q) curves. The Legendre transform of (q, $\tau(q)$), with $\tau(q)$ the partition function parameter, gives a multifractal spectrum (Fig. 3**a**), representing a span of fractal dimensions encountered in the analyzed data. The narrower spectra indicate more uniform data.

$$\tau(q) = (q-1)D_q = q\alpha(q) - f(\alpha(q)), \quad (6a)$$

$$\alpha(q) = \frac{\mathrm{d}}{\mathrm{d}q}[(q-1)D_q], \quad (6b)$$
$$f(\alpha(q)) = q\alpha(q) - (q-1)D_q$$

2.8. Spatial fractal dimension distribution analysis

Another method, particularly useful in the investigation of textural data, is to perform local analyses of fractal dimensions and to determine their spatial distribution. Micrographs were divided uniformly into the smaller patches, with each of the patches characterized by an averaged fractal dimension over that patch. We used binary outlines to perform structural textural analysis (Smith et al., 1996) (Fig. 2**c,** Fig. 4**a**), and grayscale images to perform grayscale textural analysis (Sarkar and Chaudhuri, 1992) (Fig. 2**b,** Fig. 4**b**). The modified fractal analysis (pixels scaled by their intensity) is useful mostly for the extraction of micrograph sub-regions (Al-Kadi and Watson, 2008), or spatial distribution of mean local properties. We determined the distribution histograms and the corresponding Gaussian fits.

2.9. Gray level co-occurrence matrix (GLCM) textural analysis

The second group of DIA methods, which we used, extracted the textural features using the GLCM (Haralick et al., 1973; Kulaseharan et al., 2019; Tan et al., 2015; Wu et al., 2013). The term co-occurrence relates to the spatial dependence of gray level pixel intensities. An N_g-by-N_g GLCM was obtained, for N_g gray level intervals, per a single spatial arrangement of two pixels in an image (displacement vector, d / displacement angle, θ). An in-house created code varied the displacement, $d = 1$ to $d = 64$, for $\theta \in \{0°, 45°, 90°, 135°\}$.

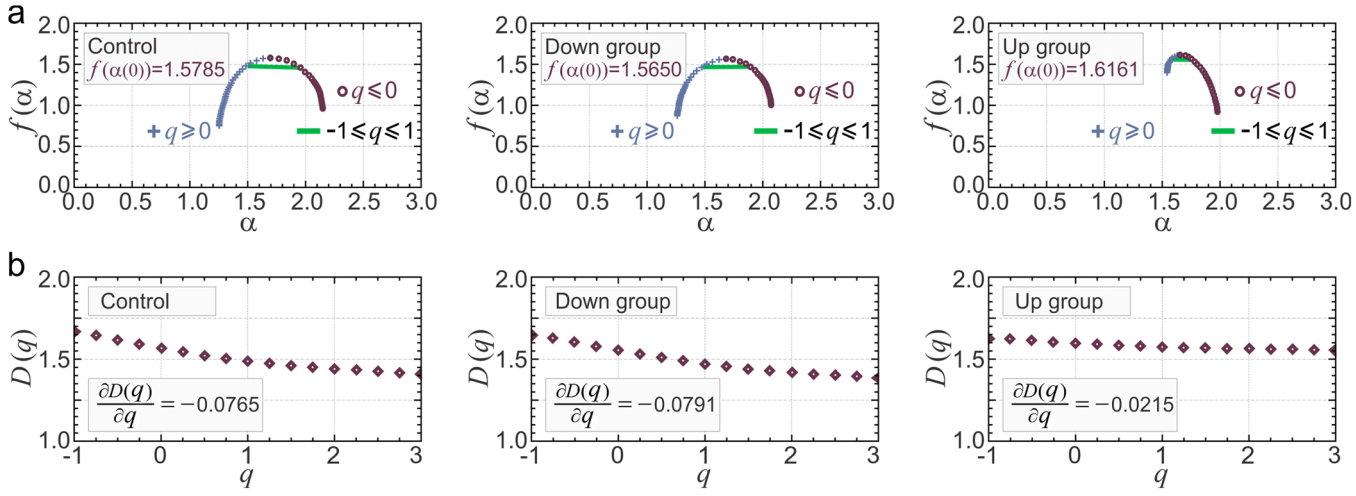

Fig. 3. The multifractal analysis yields the span of generalized dimensions, $D(q)$, describing the multiplication and scaling rules for the interwoven data subsets. (**a**) Multifractal spectra give the span of fractal dimensions, $f(\alpha)$, encountered in an image, versus the dimensions of related data subsets, α. Narrowing of the multifractal spectrum in the Up group is related to the less pronounced multifractality and underlying processes that are less random, often linked to a decrease in physiological variability. (**b**) Generalized dimensions, $D(q)$, as a function of order q, correspond to the higher-order moments of the probability distribution.

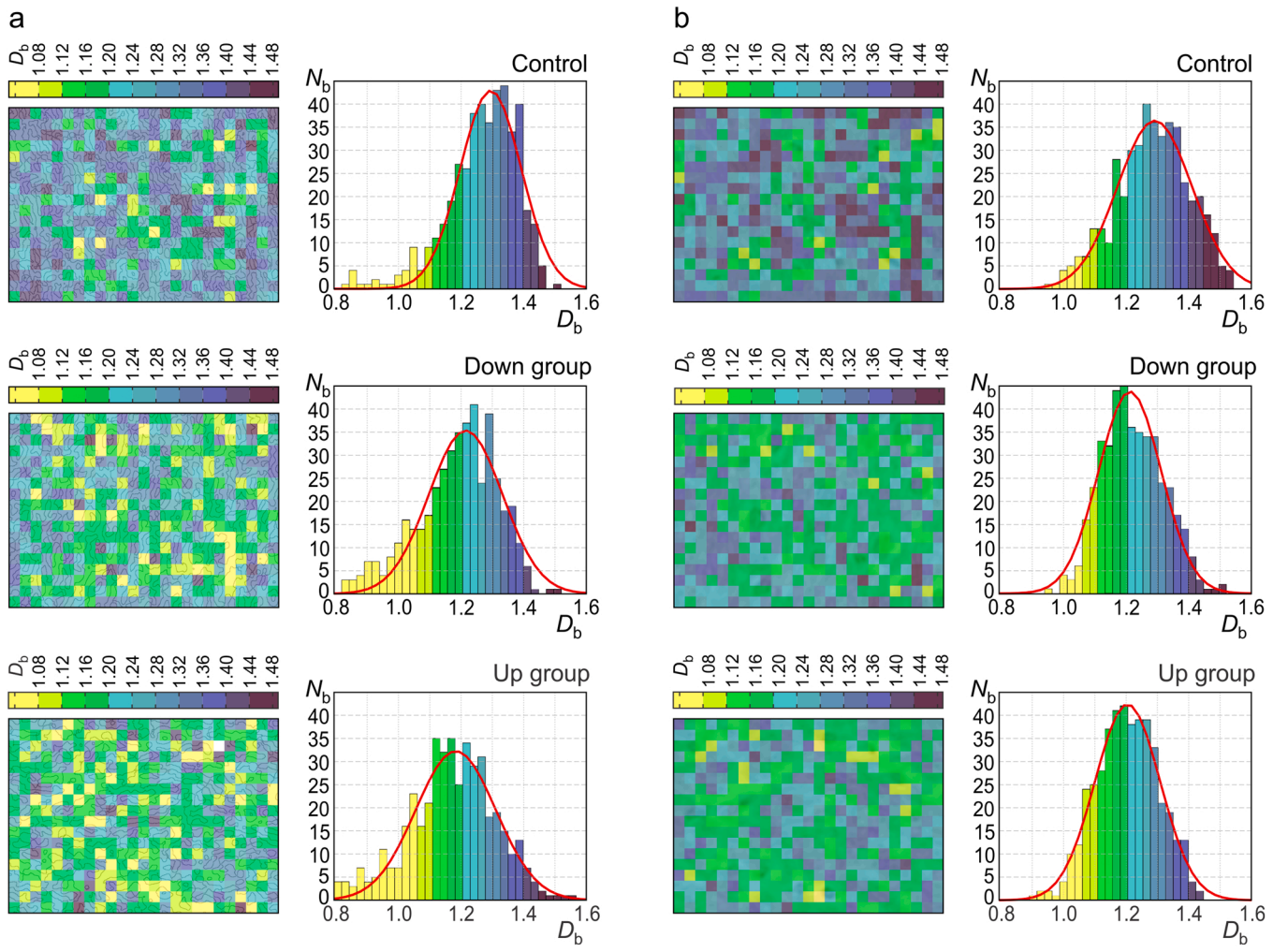

Fig. 4. Spatial distribution of local fractal dimensions. Histograms of D_b showing counts, N_b, of local fractal dimensions. (**a**) Structural textural analysis used binary outlines to determine fractal parameters. (**b**) Grayscale textural analysis used all image pixels, scaled by the normalized grayscale intensity, showing statistical changes in the boundaries of objects as well as in the surrounding medium. We observed statistically significant shifts of the fractal dimension distributions towards the lower D_b values for both SMF exposed groups using both types of analysis.

Statistical measures (features) used were contrast, energy, and homogeneity. The contrast is obtained by

$$f_C = \sum_{n=0}^{Ng-1} n^2 \left\{ \sum_{i=1}^{Ng} \sum_{j=1}^{Ng} p(i,j) \,|\, |i-j| = n \right\} \tag{7}$$

The energy or the angular second moment (ASM) is sensitive to a displacement angle. It is obtained as

$$f_E = \sum_{i=1}^{Ng} \sum_{j=1}^{Ng} p(i,j)^2. \tag{8}$$

The homogeneity, also called the inverse difference moment, is calculated as

$$f_H = \sum_{i=1}^{Ng} \sum_{j=1}^{Ng} \frac{p(i,j)}{1+|i-j|}. \tag{9}$$

For larger pixel displacements, d, the GLCM features approach certain asymptotic values. Relying solely on the tonal and textural statistical properties, the GLCM analysis gives very good results regardless of the type of data being analyzed or its origin.

3. Results

3.1. Histological and biochemical analyses

Histological analysis conclusively confirmed the existence of brain edema in 89% of animals exposed to the upwards oriented SMF (Up group), whereas in the Down group, the samples were classified as normal. Typical tissue micrographs are presented in Fig. 1. The observed differences were statistically significant for the Up group when compared to the Down and Control (sham) groups ($p < 0.05$).

The FA profile of brain phospholipids significantly differed in the Up group only compared to sham and Down groups, as shown in Table 1 and Table 2. Palmitoleic acid (C16:1) significantly increased ($p < 0.05$) in the Up group, compared to the other two groups, while stearic acid (C18:0) decreased ($p < 0.01$), also, when compared to sham and Down groups. Arachidonic (20:4 n-6) and oleic acid (18:1 n-9) increased significantly ($p < 0.05$) in the Up group when compared to the brains of unexposed animals, but not in comparison with the Down group. As for docosatetraenoic acid (22:4 n-6), commonly known as adrenic acid: it significantly increased ($p < 0.05$) in the Up group, compared to both sham and the Down group.

Table 1
Fatty acid profile of brain phospholipids (mean ± SD)[§].

Fatty acids (%) in brain	Control	Down group	Up group
16:0 palmitic acid	27.45 ± 1.99	26.74 ± 1.29	25.79 ± 1.66
16:1 palmitoleic acid	0.47 ± 0.09 *	0.44 ± 0.03 #	0.54 ± 0.09 *,#
18:0 stearic acid	27.58 ± 2.46 **	27.00 ± 1.05 ##	24.89 ± 1.17 **,##
18:1 n9 oleic acid	17.53 ± 2.12 *	17.73 ± 0.96	19.39 ± 1.38 *
18:1 n7 vaccenic acid	3.85 ± 0.43	3.90 ± 0.23	4.35 ± 0.62
18:2 linoleic acid	0.52 ± 0.07	0.55 ± 0.04	0.58 ± 0.08
18:3 n3 α-linolenic acid	0.029 ± 0.002	0.036 ± 0.002	0.020 ± 0.001
20:3 dihomo-γ-linolenic acid	0.61 ± 0.04	0.69 ± 0.12	0.61 ± 0.06
20:4 arachidonic acid	6.75 ± 0.69 *	6.96 ± 0.35	7.44 ± 0.56 *
20:5 eicosapentaenoic acid	0.07 ± 0.01	0.07 ± 0.01	0.07 ± 0.02
22:4 adrenic acid	2.21 ± 0.33 *	2.15 ± 0.17 #	2.30 ± 0.26 *,#
22:5 docosapentaenoic acid	0.19 ± 0.04	0.15 ± 0.02	0.17 ± 0.03
22:6 docosahexaenoic acid	12.72 ± 1.25	13.54 ± 0.91	13.86 ± 1.27

§ One way ANOVA, post hoc Tukey's test; * $p < 0.05$; ** $p < 0.01$ – compared to Control; # $p < 0.05$; ## $p < 0.01$ – between groups.

Table 2
Brain polyunsaturated / monounsaturated fatty acids (mean ± SD)[§].

Substrate	Control	Down group	Up group
SFA – saturated fatty acids	55.03 ± 3.85 **	53.75 ± 1.14	50.62 ± 2.34 **
MUFA – monounsaturated fatty acids	21.87 ± 2.46 *	22.08 ± 0.89	24.29 ± 1.75 *
PUFA – polyunsaturated fatty acids	23.10 ± 2.14	24.17 ± 1.38	25.09 ± 1.98
n-6 – omega 6 polyunsaturated fatty acids[a]	10.08 ± 1.03	10.37 ± 0.46	10.95 ± 0.79
n-3 – omega 3 polyunsaturated fatty acids[b]	13.02 ± 1.29	13.80 ± 0.95	14.13 ± 1.28
n-6 / n-3 – ratio of omega 6 to omega 3 PUFA[c]	0.78 ± 0.06	0.75 ± 0.03	0.78 ± 0.04
Δ9 desaturase – enzyme[d]	0.65 ± 0.05 *	0.66 ± 0.05 #	0.78 ± 0.07 *,#
Elongase – enzyme[e]	1.01 ± 0.08	1.01 ± 0.07	0.97 ± 0.06
Δ6 desaturase – enzyme[f]	1.20 ± 0.18	1.26 ± 0.22	1.06 ± 0.18
Δ5 desaturase – enzyme[g]	11.17 ± 1.27	10.35 ± 2.10	12.23 ± 1.44

§ One way ANOVA, post hoc Tukey's test; * $p < 0.05$; ** $p < 0.01$ – compared to Control; # $p < 0.05$ – between groups. [a] characterized by a double bond in the n-6 position; [b] characterized by a double bond three atoms away from the terminal methyl group; [c] balance between dietary fatty acids which can influence inflammation and cardiovascular health; [d] enzyme catalyzing the synthesis of monounsaturated fatty acids; [e] enzyme catalyzing the carbon chain extension; [f] enzyme converting PUFA precursors (α-linolenic and linoleic acid) to their respective metabolites; [g] enzyme metabolizing dihomo-γ-linolenic acid to arachidonic acid.

3.2. Fractal analysis

Typical examples of the obtained D_b data, based on the five most representative micrographs in each group with twelve repeated calculations, are shown in Fig. 2**d** along with the corresponding regression lines. Table 3 lists the resulting averaged fractal dimensions, $\overline{D}_b$, and standard deviations, σ_{D_b}. The correlation coefficients, r^2, close to unity confirm almost linear data (Table 3). Fractal dimensions for the Down group and Control differed significantly, by 1.1% ($p < 0.05$), while the decrease of $\overline{D}_b$ in the Up group was highly significant (2.4%, $p < 0.001$). As a variation moment, lacunarity depends more on the range of grid sizes; Fig. 2**e** shows both $\lambda_F(\varepsilon)$, excluding the zero-pixel grid cells, and $\lambda_E(\varepsilon)$, including all grid cells. Table 3 lists the mean lacunarity based on foreground pixels, $\overline{\lambda}_F(\varepsilon)$, and its standard deviation, σ_λ. An increasing trend of 4.0% and a decreasing trend of 4.3% were observed for the Down and Up groups, respectively. Such a result corresponds to a presence of larger textural gaps in the Down group and more homogeneous tissue texture in the Up group. The lacunarity change with respect to Control was not statistically significant; however, the difference between the Down and Up group was ($p = 0.002$) (Table 3).

3.3. Multifractal analysis

We performed the multifractal spectra calculations for two types of binary images. In the first case, we used the Niblack method of local image thresholding, based on the local mean and standard deviation of pixels inside the window of radius R ($R = 16$ px). In that way, local details are being outlined while avoiding the effects of non-uniform

Table 3
Box counting fractal dimension and pixel mass lacunarity (mean, SD).

Experimental group	$\overline{D}_b$	σ_{D_b}	r^2_{min}	r^2_{max}	D_b	$\Delta\overline{D}_b$ (%)*	Percentile p *	$\overline{\lambda}_F$	σ_λ	$\Delta\overline{\lambda}_F$ (%)*
Control	1.6982	0.0413	0.9918	0.9956	1.6819	–	–	0.1602	0.0211	–
Down group	1.6790	0.0385	0.9910	0.9944	1.6420	–1.13	0.0291	0.1666	0.0233	4.00
Up group	1.6572	0.0427	0.9911	0.9945	1.6417	–2.41	$1.5{\cdot}10^{-7}$	0.1533	0.0191	–4.28

*Relative changes in fractal dimension and lacunarity, as well as percentile p, were calculated with respect to the Control group data.
($\overline{D}_b$– mean fractal dimension, σ_{D_b}– standard deviation of f.d., $[r^2_{min}, r^2_{max}]$ – interval of obtained linearity coefficients, D_b – fractal dimension best fit, $\Delta\overline{D}_b$– percent change with respect to sham(control), p – statistical significance of $\Delta\overline{D}_b$, $\overline{\lambda}_F$– mean fractal lacunarity, σ_λ– standard deviation for lacunarity, $\Delta\overline{\lambda}_F$ – percent change of mean lacunarity).

Table 4
Generalized fractal dimensions from multifractal analysis.

Image thresholding	Local (Niblack $R = 16$ px) thresholding *			Global thresholding (IsoData) **		
Experimental group	**Control**	**Down group**	**Up group**	**Control**	**Down group**	**Up group**
Capacity dimension, D_0	1.8656	1.8655	1.8127	1.5785	1.5650	1.6161
Information dimension, D_1	1.8653	1.8639	1.8125	1.4850	1.4652	1.5893
Correlation dimension, D_2	1.8653	1.8639	1.8125	1.4296	1.4035	1.5753
Triplet correlation dim., D_3	1.8652	1.8633	1.8112	1.3943	1.3688	1.5686

* Data is shown for the example images given in Fig. 2c. ** Data is shown for the Fig. 2b images, after the IsoData thresholding.

background (Fig. 2**c**). Such binary outlines were all classified as monofractal, with fractal dimensions of example images given in the first three columns of Table 4. To assess the possible multifractal scaling in the original micrographs, we also automatically converted grayscale images (Fig. 2**b**) to binary using the default method, where a single global threshold corresponds to a midpoint between the average intensity of pixels lighter than a threshold and the average intensity of pixels darker than a threshold (IsoData method). We used the same grid sizes, ε, as in the standard fractal analysis in both cases. The utilized range of exponents, q, was from –10 to 10, with the $\Delta q = 0.25$ step. The right part of Table 4 shows generalized fractal dimensions for the second case for the same example micrographs. The optimized multifractal spectra are shown in Fig. 3**a**, revealing the multifractal scaling. Relative spectral spans, for $|q| \leq 1$, equaled 13.9% (Control), 13.7% (Down), and 4.2% (Up group). Accordingly, the slope of the curve of generalized dimensions was almost four times lower for the Up group than for the other two groups (Fig. 3**b**). On average, the slope of the $D(q)$ curves was –0.0653 (Control), –0.0605 (Down group), –0.0208 (Up group). The difference between the Control and Down group is significant ($p < 0.05$), while the observed change for the Up group is highly significant ($p < 10^{-9}$). Such behavior is much less multifractal than the one in the Control and Down group. It is interesting to note the differences in fractal dimensions when a global threshold is applied, neglecting the fine local details of the tissue structure. On average, capacity dimension, $D(0)$, was 1.47 ± 0.04, 1.63 ± 0.04, 1.70 ± 0.04, for the Control, Down group, and Up group, respectively.

3.4. Spatial local Db distribution analysis

Original micrograph heights were reduced to 504 px, and these were divided into a total of 450 sub-regions sized 28-by-28 px^2. Grid sizes $\varepsilon \in \{6, 7, 8, 10, 11, 13, 15, 18, 21\}$ px were used to calculate local fractal dimensions and to obtain the relative unit sub-region variations (Fig. 4). Calculated local fractal dimensions are lower than those obtained on the entire images, as only the data points for small ε were used to fit the regression lines (please see the upper left corners in Fig. 2**d**). In the grayscale textural analysis, scaling grayscale pixel intensities were normalized to the [0.0 1.4] interval, to facilitate a comparison of data with the structural textural analysis. Histograms of the spatial distribution of D_b were formed and fitted with the Gaussian curves (Table 5). The mean sub-region fractal dimension of the binary outlines was lower in the Down and Up groups compared with the Control, which was also

Table 5
Histograms of local fractal dimension distributions (fitted data).

Structural textural analysis of binary outlines						
Experimental group	(μ_B, σ_B)	$\overline{N}_B$	$\overline{\mu}_B$	μ_{Bci} (95% Conf.b.)	$\Delta\overline{N}_B$ (%)*	$\Delta\overline{\mu}_B$ (%)*
Control	(1.2980, 0.1395)	33.64	1.2780	[1.2470, 1.3080]	–	–
	(1.2900, 0.1328)					
	(1.2590, 0.1618)					
	(1.2680, 0.1619)					
	(1.2750, 0.1508)					
Down group	(1.2150, 0.1495)	30.55	1.2174	[1.2000, 1.2350]	9.18	4.74
	(1.2240, 0.1599)					
	(1.2100, 0.1602)					
	(1.2180, 0.1770)					
	(1.2200, 0.1713)					
Up group	(1.2260, 0.1648)	25.95	1.1948	[1.1650, 1.2390]	22.86	6.51
	(1.1790, 0.1931)					
	(1.1970, 0.2001)					
	(1.1850, 0.1983)					
	(1.1870, 0.1869)					
Grayscale textural analysis (pixels scaled by the normalized intensity)						
Experimentalgroup	(μ_G, σ_G)	$\overline{N}_G$	$\overline{\mu}_G$	μ_{Gci} (95% Conf.b.)	$\Delta\overline{N}_G$ (%)*	$\Delta\overline{\mu}_G$(%)*
Control	(1.2949, 0.1667)	25.21	1.2614	[1.2268, 1.3047]	–	–
	(1.2715, 0.1709)					
	(1.2379, 0.1830)					
	(1.2421, 0.1646)					
	(1.2608, 0.1744)					
Down group	(1.2384, 0.1264)	32.80	1.2200	[1.2060, 1.2252]	30.11	3.28
	(1.2141, 0.1271)					
	(1.2149, 0.1425)					
	(1.2146, 0.1331)					
	(1.2180, 0.1251)					
Up group	(1.2117, 0.1431)	31.394	1.1956	[1.1612,1.2218]	24.51	5.22
	(1.1708, 0.1343)					
	(1.1952, 0.1366)					
	(1.1934, 0.1234)					
	(1.2071, 0.1439)					

* Relative changes in the peak counts and mean fractal dimensions were calculated with respect to the Control group data.

followed by widening of the histogram and lowering the peak histogram count $\overline{N}_B$ (Fig. 4**a**). Similarly, the local fractal dimension as a result of the grayscale textural analysis was lower in the Down and Up groups when compared with the Control (Fig. 4**b**). Table 5 shows mean peak counts and fractal dimensions, along with the 95% confidence bounds of the fractal distributions, μ_{Bci} and μ_{Gci}. The local fractal dimension decrease was more pronounced for the Up group. The shift in the data distributions, however, was statistically significant ($p < 0.05$) in both cases (structural binary and textural analysis).

3.5. GLCM analysis

The dependence of the three considered GLCM features on the pixel displacement is shown in Fig. 5. Our analysis for four displacement angles, 0°, 45°, 90°, and 135°, demonstrated the absence of the direction-dependent features; therefore, we used GLCM features averaged for four angles. For larger displacements, d, the GLCM features approach certain asymptotic values, as listed in Fig. 5 for $d = 40$ px. Mean values for the Control, Down, and Up groups are depicted by thick solid lines, whereas the standard deviations are shown as lighter regions about the means. We observed the increase of contrast, f_C, with respect to the Control, amounting to 40% for the Down group and 66% for the Up group. For displacements, $d > 42$ px, the increase of contrast in the Down group was statistically significant ($p = 0.048$), whereas for the Up group, it was very significant ($p = 0.002$). The energy, f_E, and homogeneity, f_H, both decreased for the SMF exposed groups. The energy decrease was 50% for the Down group and 63% for the Up group. It was highly significant ($p < 0.001$), for both groups. The homogeneity decrease was 18% for the Down group and 23% for the Up group, which was highly significant for both groups ($p < 0.001$). The changes of parameters were more pronounced for the Up group, which is consistent with other analyses.

4. Discussion

Tissue changes as a result of the SMF exposures range from very mild to severe. In this particular case, histological analysis confirmed the brain edema when the applied SMF was contrary in orientation to the vertical GMF component at the location of the experiment. Since the results were significant for the Up group only, we were very interested in investigating the possible underlying mechanisms by looking into the alterations in fatty acids, as well as checking on the degree of tissue changes by quantitative analysis of digitalized micrographs. The relationships among the changes in the brain fatty acids composition resulting from the SMF exposure were examined, as well as the structural and textural changes in the brain tissue micrographs. It is important to note that our study examined the effects of SMF on fatty acids *in vivo*, contrary to the majority of other research (Mouhoub et al., 2017; Novitskaya et al., 2006; Tang et al., 2015; Kthiri et al., 2019). Moreover, we managed to show the predominance of proinflammatory fatty acids after exposure to the static magnetic field.

Our previous study (Milovanovich et al., 2016), concerning subacute exposure to a homogenous vertical SMF, showed histological changes in various tissues. Regarding the brains of examined animals, Up group only showed edematous neurons without any sign of inflammation. Given that blood parameters like leukocytes and C-reactive protein remained unchanged in both groups exposed to SMF, we wanted further to analyze the cause for this modification in brain tissue since classical histopathological examination proved insufficient to explain the changes. We hypothesized that the origin of the obtained vasogenic edema under the SMF exposure was the release of vasoactive substances, which increased the permeability of brain blood vessels. We conducted biochemical analyses to examine FA composition in the brain tissue of experimental animals since some fatty acids are precursors of proinflammatory cytokines.

The obtained results showed a striking distinction between the FA compositions in experimental animals exposed to the SMF of different orientations. The results in the Down group did not significantly differ from the Control group ones, while exposure to the upward oriented SMF changed brain FA composition significantly. Exactly in the same experimental group, striking neuronal edema was present (Milovanovich et al., 2016).

The observed edema was probably a consequence of two distinct changes in the FA content – an increase of both oleic and arachidonic acid. The breaking down of the blood-brain barrier and consequential efflux of circulating fluid into brain parenchyma resulted in the development of vasogenic edema. The involvement of arachidonic acid in the formation of vasogenic cerebral edema has been implicated in several studies (Phillis et al., 2006; Bosetti, 2007). By catalytic activity of cyclooxygenase (COX) and lipoxygenase (LOX) enzymes, it is the source of prostanoids and free radicals. However, the other finding is of even more importance. Oleic acid is produced by the desaturation of stearic acid (18:0), and the reaction is catalyzed by the enzyme Δ9 desaturase. In our experiment, stearic acid was decreased in the Up group, while the activity of Δ9 desaturase was increased, as well as the product of this reaction – oleic acid. So, the consumption of stearic acid led to the increased oleic acid content, another probable cause of neuronal swelling. It had been shown that high oleic acid concentrations had been implicated in the development of ARDS, possibly by impairing the alveolar cell Na/K transport (Gonçalves-de-Albuquerque et al., 2015). Even though the mentioned mechanism is not entirely understood, it has been shown that oleic acid possesses the capacity to alter membrane

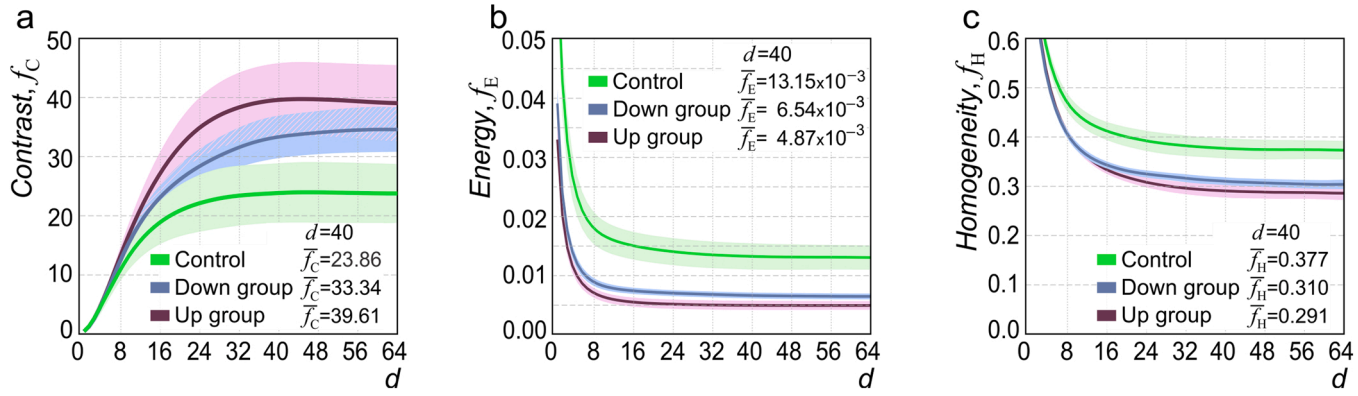

Fig. 5. The GLCM statistical feature analysis (f_C, f_E, f_H). (**a**) The contrast, f_C, quantifies the dynamics of local gray level variations in an image with the increase in distance, d, between the two pixels. (**b**) The energy, f_E, measures textural uniformity, as very few dominant gray level transitions result in higher energy than a large number of small matrix entries. (**c**) The homogeneity, f_H, quantifies the probabilities of matrix entries that are away from the GLCM diagonal. Characteristic asymptotical values are listed on the graphs for $d = 40$ px. Changes were statistically significant for both SMF exposed groups.

fluidity and impede the activity of various transporters, mainly sodium/potassium ionic pump. Membrane fluidity allows the cell to adapt to the altered (patho)physiological conditions and, also, it is vital for housing various enzymes, channels, and receptors. The importance of arachidonic and oleic acid has been stressed in (Gómez Candela et al., 2011) due to the oleic acid influence upon membrane plasticity and fluidity for signal transmission between neurons, which has been shown to be crucial for physical and mental well-being. Furthermore, the stearic/oleic fatty acid ratio represents the saturation index (SI), which decreased in the Up group, suggesting brain injury. Decreased SI is strongly connected to disturbed cellular control over Δ9 desaturase activity (Aclimandos et al., 1992). It also affects membrane fluidity and cell homeostasis. So, the increased concentrations of oleic and arachidonic acids in our study impaired membrane ionic transport and led to sodium intracellular accumulation, followed by the liquid redistribution and subsequent neuronal edema.

The increased content of adrenic acid in the group exposed to upward-oriented SMF compared to sham and the Down groups, is another important finding. Its immediate precursor is arachidonic acid, and it represents the third most abundant polyunsaturated fatty acid (PUFA) in the brain after docosahexaenoic acid and arachidonic acid. It is found mainly in the lipids forming myelin (Galano et al., 2015). The adrenal gland and kidneys are particularly rich in adrenic acid. However, its specific function(s) is not completely understood. Its role in the pathogenesis of Alzheimer's disease has been implicated (Wijendran et al., 2002). It has been shown that the adrenic acid metabolites from endothelial and zona glomerulosa cells led to concentration-dependent relaxations of adrenal cortical arteries (Kopf et al., 2010). Therefore, its metabolites could serve as endogenous factors which can induce hyperpolarization in the adrenal cortex. In that way, adrenic acid could take part in controlling adrenal blood flow. The regulation of vascular tone could be attributed to adrenic acid and its metabolites, mainly in tissues with a significant amount of adrenic acid. This presumed role of adrenic acid in the brain could enhance the formation of vasogenic edema caused by arachidonic acid metabolites. Two recent studies presented conflicting results concerning the role of adrenic acid. The first one (Nababan et al., 2017) showed that adrenic acid could increase the inflammatory process in non-alcoholic fatty liver disease by increasing the expression of various proinflammatory cytokines and, in that way, it could contribute to a disease progression. The other study (Brouwers et al., 2018) presented adrenic acid as a new anti-phlogistic factor in osteoarthritis (OA). The researchers showed that adrenic acid effectively blocked the production of LTB4 by neutrophils. Additionally, adrenic acid enhances macrophages' phagocytic activity, which could be vital for the proper removal of cartilage decomposition products in OA joints. This activity could result in better recovery. Incomplete insight into the function of adrenic acid will postpone our understanding of the obtained results. However, its rise in the Up group following an SMF exposure certainly represents adaptive changes in the brains of exposed animals.

Quantitative analysis of tissue micrographs was performed using three fractal-based approaches and a statistical textural method based on the GLCM. Brain tissue digitalized micrographs were subjected to four types of DIA, in order to extract different descriptors of tissue texture, which were then cross-compared. The obtained results were consistent with the previous analyses, showing highly pronounced changes in the Up group in all cases. DIA methods assessed the degree of histological changes, supporting unbiased analysis of the findings and accurate tracking of pronounced as well as very mild modifications in the SMF exposed tissue. Fractal dimension results revealed a subtle but statistically significant decrease in the Down group in addition to the highly significant modification in the Up group. An increasing trend was noted in the Down group, and a decreasing trend in the Up group, for lacunarity, which is a second-order moment analogous to the coefficient of variation in statistics. Multifractal spectra were significantly narrowed in the Up group, which is typically an indication of reduced physiological variability. Spatial distribution analysis of the binary outlines as well as fine grayscale texture revealed a tissue complexity decrease for both groups exposed to the SMF. Similarly, the GLCM textural features captured statistical differences for both SMF exposed groups. Therefore, SMF exposure also seems to have caused mild structural changes in the Down group, not identified by classical pathohistological examination. In that sense, the employment of the DIA analyses is important for determining and quantifying even the subtle tissue changes upon the SMF exposure.

Different effects of the SMF based on its orientation were observed in several studies, including our previous study (Milovanovich et al., 2016). In (Tian et al., 2018), an upward 0.2–1 T SMF reduced the cell numbers of seven human solid tumor cell lines, while a downward SMF mostly had no statistically significant effect. The authors confirmed similar effects to the tumor growth *in vivo*. The leukemia cells in suspension were inhibited by both SMF orientations, whereas the non-cancer cell lines were not affected. The *in vitro* results were linked with the shape-induced anisotropy, which could be present in adherent cells and not in floating cells in suspension. The molecular mechanisms for *in vivo* effects remained unexplained, although several additional parameters were investigated. In (Yang et al., 2021), a strong 9.4 T SMF was used for *in vitro* and *in vivo* analyses. The tumor growth was significantly inhibited by the upward 9.4 T SMF and not by the downward 9.4 T SMF. Further analyses revealed the inhibition of DNA synthesis by both upward and downward 9.4 T SMF, while no cell death occurred due to 9.4 T SMF exposures. However, a significant increase in the reactive oxygen species (ROS) level was observed only for the upward 9.4 T SMF exposure. The authors hypothesized that the SMF could align DNA chains and exert Lorentz forces on negative charges of DNA. Due to the intrinsic chirality of many biomolecules, including proteins and DNA, the DNA rotation and supercoil tightness would be differentially affected by the two considered SMF orientations (upward and downward) (Yang et al., 2020). In our case, a possible increase in the reactive oxygen species (ROS) could result from altered fatty acids metabolism. Apart from the above hypothesis based on biomolecular structure, we strongly believe that the adaptation of living organisms to environmental conditions could also play some role *in vivo* investigations. Namely, the downward SMF is consistent in orientation with the geomagnetic field (GMF), although it is of much stronger intensity. However, the upward-oriented SMF is in the opposite direction with respect to the vertical GMF component at the experimental location, which could be sensed as a stress factor.

In conclusion, the changes noticed initially by the pathohistological analysis in the experimental group exposed to upward-oriented SMF were further confirmed by the results of the biochemical tests. Given the significance of FAs in the normal functioning of the nervous system, and primarily, the neuroprotective effects of PUFA (Bazinet and Layé, 2014), a more refined insight into the brain's metabolic changes expands our knowledge about the *in vivo* mechanisms of action of moderate SMF. Using the DIA analyses, the observed changes in the group exposed to upward-oriented SMF were quantified. Additionally, subtle initial modifications were revealed in the group exposed to downward oriented vertical SMF, i.e., in the same direction as the vertical geomagnetic field component at the experimental location. Consequently, quantifiable differences have been observed in the brain tissue of animals exposed to the highly homogeneous vertical SMF of different orientations.

CRediT authorship contribution statement

Andjelija Ilić: Conceptualization, Formal analysis, Investigation, Methodology, Software, Project administration, Visualization, Writing – original draft, Writing – review & editing. **Silvio de Luka:** Conceptualization, Writing – original draft, Investigation, Methodology, Writing – review & editing. **Jasna Ristić-Djurović:** Conceptualization, Formal analysis, Resources. **Tamara Popović:** Formal analysis, Investigation, Methodology, Resources, Writing – original draft. **Jasmina Debeljak-**

Martačić: Formal analysis, Investigation. **Milica Kojadinović:** Formal analysis, Investigation. **Saša Ćirković:** Formal analysis, Investigation. **Alexander Trbovich:** Conceptualization, Methodology, Resources, Funding acquisition, Project administration, Supervision, Writing – original draft, Writing – review & editing.

Declaration of Competing Interest

The authors declare that they have no known competing financial interests or personal relationships that could have appeared to influence the work reported in this paper.

Acknowledgments

The authors acknowledge funding provided by the Institute of Physics Belgrade, the Faculty of Medicine, and the Institute for Medical Research, University of Belgrade, through the grants by the Ministry of Education, Science, and Technological Development of the Republic of Serbia. This study was also supported by the grants No III-41013, No III-41019, No III-41030, No III-45003, and 451–03-68/2020–14/200015, from the Ministry of Education, Science and Technological Development of Serbia.

Role of funding source

No funding body had any involvement in the preparation or content of this article or in the decision to submit it for publication.

Appendix A. Supporting information

Supplementary data associated with this article can be found in the online version at doi:10.1016/j.etap.2022.103853.

References

Aclimandos, W.A., Heinemann, D., Kelly, S.B., Sheraidah, G.A.K., Hungerford, J.L., 1992. Erythrocyte stearic to oleic acid ratio in patients with ocular melanoma. Eye 6, 416–419.
Al-Kadi, O.S., Watson, D., 2008. Texture analysis of aggressive and nonaggressive lung tumor CE CT images. IEEE Trans. Biomed. Eng. 55, 1822–1830.
Amara, S., Abdelmelek, H., Garrel, C., Guiraud, P., Douki, T., Ravanat, J.-L., et al., 2007. Zinc supplementation ameliorates static magnetic field-induced oxidative stress in rat tissues. Environ. Toxicol. Pharmacol. 23 (2), 193–197.
Barnes, F., Greenebaum, B., 2018. Role of radical pairs and feedback in weak radio frequency field effects on biological systems. Environ. Res. 163, 165–170.
Bazinet, R.P., Layé, S., 2014. Polyunsaturated fatty acids and their metabolites in brain function and disease. Nat. Rev. Neurosci. 15, 771–785.
Bongers, S., Slottje, P., Kromhout, H., 2018. Development of hypertension after long-term exposure to static magnetic fields among workers from a magnetic resonance imaging device manufacturing facility. Environ. Res. 164, 565–573.
Bosetti, F., 2007. Arachidonic acid metabolism in brain physiology and pathology: Lessons from genetically altered mouse models. J. Neurochem. 102, 577–586.
Brouwers, H., Jonasdottir, H., Kwekkeboom, J., Lopez-Vicario, C., Claria, J., Freysdottir, J., et al., 2018. Adrenic acid as a novel anti-inflammatory player in osteoarthritis. Osteoarthr. Cartil. 26, S126.
Calabrò, E., 2016. Competition between hydrogen bonding and protein aggregation in neuronal-like cells under exposure to 50 Hz magnetic field. Int. J. Radiat. Biol. 92 (7), 395–403.
Captur, G., Karperien, A.L., Hughes, A.D., Francis, D.P., Moon, J.C., 2017. The fractal heart - embracing mathematics in the cardiology clinic. Nat. Rev. Cardiol. 14, 56–64.
Çelik, M.S., Güven, K., Akpolat, V., Akdağ, M.Z., Nazıroğlu, M., Gül-Güven, R., et al., 2015. Extremely low-frequency magnetic field induces manganese accumulation in brain, kidney and liver of rats. Toxicol. Ind. Health 31 (6), 576–580.
Chiu, K., Ou, K., Lee, S., Lin, C., Chang, W., Chen, C., Huang, H., 2007. Static magnetic fields promote osteoblast-like cells differentiation via increasing the membrane rigidity. Ann. Biomed. Eng. 35, 1932.
Colbert, A.P., Wahbeh, H., Harling, N., Connelly, E., Schiffke, H.C., Forsten, C., et al., 2009. Static magnetic field therapy: A critical review of treatment parameters. Evid. Based Complement. Altern. Med. 6, 133–139.
De Luka, S.R., Ilić, A.Ž., Janković, S., Djordjevich, D.M., Ćirković, S., Milovanovich, I.D., et al., 2016. Subchronic exposure to static magnetic field differently affects zinc and copper content in murine organs. Int. J. Radiat. Biol. 92 (3), 140–147.
Den Buijs, J., Bajzer, Ž., Ritman, E.L., 2006. Branching morphology of the rat hepatic portal vein tree: a micro-CT study. Ann. Biomed. Eng. 34, 1420–1428.
Dini, L., Panzarini, E., 2010. The influence of a 6mT static magnetic field on apoptotic cell phagocytosis depends on monocyte/macrophage differentiation. Exp. Biol. Med. 235, 1432–1441.
Elferchichi, M., Mercier, J., Bourret, A., Gross, R., Lajoix, A.D., Belguith, H., et al., 2011. Is static magnetic field exposure a new model of metabolic alteration? Comparison with Zucker rats. Int. J. Radiat. Biol. 87, 483–490.
Foderà, V., Zaccone, A., Lattuada, M., Donald, A.M., 2013. Electrostatics controls the formation of amyloid superstructures in protein aggregation. Phys. Rev. Lett. 111, 108105.
Folch, J., Lees, M., Sloane Stanley, G.H., 1957. A simple method for the isolation and purification of total lipids from animal tissues. J. Biol. Chem. 226, 497–509.
Galano, J.-M., Lee, J.C.-Y., Gladine, C., Comte, B., Le Guennec, J.-Y., Oger, C., Durand, T., 2015. Non-enzymatic cyclic oxygenated metabolites of adrenic, docosahexaenoic, eicosapentaenoic and α-linolenic acids; bioactivities and potential use as biomarkers. Biochim. Biophys. Acta (BBA) 1851, 446–455.
Ghodbane, S., Amara, S., Garrel, C., Arnaud, J., Ducros, V., Favier, A., et al., 2011. Selenium supplementation ameliorates static magnetic field-induced disorders in antioxidant status in rat tissues. Environ. Toxicol. Pharmacol. 31 (1), 100–106.
Ghosh, S., Roy, A., Chakraborty, I., Mukhopadhyay, M., Dasgupta, S., Sarkar, D., 2018. Fractal dimension of erythrocyte membranes: A highly useful precursor for rapid morphological assay. Ann. Biomed. Eng. 46, 1362–1375.
Gómez Candela, C., Bermejo López, L.M., Loria Kohen, V., 2011. Importance of a balanced omega 6/omega 3 ratio for the maintenance of health. Nutritional recommendations. Nutr. Hosp. 26, 323–329.
Gonçalves-de-Albuquerque, C.F., Silva, A.R., Burth, P., Castro-Faria, M.V., Castro-Faria-Neto, H.C., 2015. Acute respiratory distress syndrome: Role of oleic acid-triggered lung injury and inflammation. Mediat. Inflamm. 2015, 260465.
Gould, D.J., Vadakkan, T.J., Poché, R.A., Dickinson, M.E., 2011. Multifractal and lacunarity analysis of microvascular morphology and remodeling. Microcirculation 18 (2), 136–151.
Haralick, R.M., Shanmugam, K., Dinstein, I., 1973. Textural features for image classification. IEEE Trans. Syst. Man. Cybern. 3, 610–621.
Ilić, A.Ž., Ristić-Djurović, J.L., Ćirković, S., Ilić, M.M., Trbovich, A.M., 2014. Experimental electromagnet for in vivo exposure of small animals to ELF electromagnetic fields. Proc. 2nd Int. Conf. Rad. Dosim. Var. Fields Res. (Rad. 2014) 2014, 1–4.
Karperien, A.L., Jelinek, H.F., 2016. Morphology and fractal-based classifications of neurons and microglia. In: Di Ieva, A. (Ed.), The Fractal Geometry of the Brain. Springer, NY, New York, NY, pp. 91–108.
Kim, S., Chung, Y., Lee, C., Chae, J., Juh, R., Jeong, J., 2010. Target-specific rCBF changes induced by 0.3-T static magnetic field exposure on the brain. Brain Res 1317, 211–217.
Kimsa-Dudek, M., Synowiec-Wojtarowicz, A., Derewniuk, M., Gawron, S., Paul-Samojedny, M., Kruszniewska-Rajs, C., Pawłowska-Góral, K., 2018. Impact of fluoride and a static magnetic field on the gene expression that is associated with the antioxidant defense system of human fibroblasts. Chem. Biol. Interact. 287, 13–19.
Kopf, P.G., Zhang, D.X., Gauthier, K.M., Nithipatikom, K., Yi, X.-Y., Falck, J.R., Campbell, W.B., 2010. Adrenic acid metabolites as endogenous endothelium-derived and zona glomerulosa-derived hyperpolarizing factors. Hypertension 55, 547–554.
Kroupová, J., Bártová, E., Fojt, L., Strašák, L., Kozubek, S., Vetterl, V., 2007. Low-frequency magnetic field effect on cytoskeleton and chromatin. Bioelectrochemistry 70, 96–10.
Kthiri, A., Hidouri, S., Wiem, T., Jeridi, R., Sheehan, D., Landouls, A., 2019. Biochemical and biomolecular effects induced by a static magnetic field in *Saccharomyces cerevisiae*: Evidence for oxidative stress. PLoS ONE 14 (1), e0209843.
Kulaseharan, S., Aminpour, A., Ebrahimi, M., Widjaja, E., 2019. Identifying lesions in paediatric epilepsy using morphometric and textural analysis of magnetic resonance images. Neuroimage Clin. 21, 101663.
Lopes, R., Betrouni, N., 2009. Fractal and multifractal analysis: A review. Med. Image Anal. 13 (4), 634–649.
Lv, H., Liu, J., Zhen, C., Wang, Y., Wei, Y., Ren, W., Shang, P., 2021. Magnetic fields as a potential therapy for diabetic wounds based on animal experiments and clinical trials. Cell Prolif. 54 (3), e12982.
Manera, M., Castaldelli, G., Fano, E.A., Giari, L., 2021. Perfluorooctanoic acid-induced cellular and subcellular alterations in fish hepatocytes. Environ. Toxicol. Pharmacol. 81, 103548.
Martínez-Sámano, J., Torres-Durán, P.V., Juárez-Oropeza, M.A., Elías-Viñas, D., Verdugo-Díaz, L., 2010. Effects of acute electromagnetic field exposure and movement restraint on antioxidant system in liver, heart, kidney and plasma of Wistar rats: A preliminary report. Int. J. Radiat. Biol. 86, 1088–1094.
Milovanovich, I.D., Ćirković, S., De Luka, S.R., Djordjevich, D.M., Ilić, A.Ž., Popović, T., et al., 2016. Homogeneous static magnetic field of different orientation induces biological changes in subacutely exposed mice. Environ. Sci. Pollut. Res. 23, 1584–1597.
Moreno, P.A., Vélez, P.E., Martínez, E., Garreta, L.E., Díaz, N., Amador, S., et al., 2011. The human genome: A multifractal analysis. BMC Genom. 12, 506.
Mouhoub, R.B., El May, A., Cheraief, I., Landoulsi, A., 2017. Influence of static magnetic field exposure on fatty acid composition in *Salmonella Hadar*. Microb. Pathog. 108, 13–20.
Mouhoub, R.B., May, El, Boujezza, A., Sethom, I., Feki, M.M., Landoulsi A, M., 2018. Viability and membrane lipid composition under a 57mT static magnetic field in *Salmonella Hadar*. Bioelectrochemistry 122, 134–141.
Nababan, S.H.H., Nishiumi, S., Kawano, Y., Kobayashi, T., Yoshida, M., Azuma, T., 2017. Adrenic acid as an inflammation enhancer in non-alcoholic fatty liver disease. Arch. Biochem. Biophys. 623–624, 64–75.

Novitskaya, G.V., Tserenova, O.A., Kocheshkova, T.K., Novitskii, Y.I., 2006. Effect of alternating magnetic field on the composition and level of lipids in radish seedings. Russ. J. Plant Physiol. 53, 75–84.
Pall, M.L., 2018. Wi-Fi is an important threat to human health. Environ. Res. 164, 405–416.
Phillis, J.W., Horrocks, L.A., Farooqui, A.A., 2006. Cyclooxygenases, lipoxygenases, and epoxygenases in CNS: Their role and involvement in neurological disorders. Brain Res. Rev. 52, 201–243.
Piszczek, P., Wójcik-Piotrowicz, K., Gil, K., Kaszuba-Zwoińska, J., 2021. Immunity and electromagnetic fields. Environ. Res. 200, 111505.
Popovic, T., Ranic, M., Bulajic, P., Milicevic, M., Arsic, A., Vucic, V., Glibetic, M., 2009. Effects of n-3 fatty acids supplementation on plasma phospholipids fatty acid composition in patients with obstructive jaundice – a pilot study. J. Clin. Biochem. Nutr. 45, 370–375.
Ristić-Djurović, J.L., Ćirković, S., Mladenović, P., Romčević, N., Trbovich, A.M., 2018a. Analysis of methods commonly used in biomedicine for treatment versus control comparison of very small samples. Comput. Meth. Prog. Biomed. 157, 153–162.
Ristić-Djurović, J.L., Gajić, S.S., Ilić, A.Ž., Romčević, N., Djordjevich, D.M., De Luka, S.R., et al., 2018b. Design and optimization of electromagnets for biomedical experiments with static magnetic and ELF electromagnetic fields. IEEE Trans. Ind. Electron. 65 (6), 4991–5000.
Sarkar, N., Chaudhuri, B.B., 1992. An efficient approach to estimate fractal dimension of textural images. Pattern Recognit. 25, 1035–1041.
Smith Jr., T.G., Lange, G.D., Marks, W.B., 1996. Fractal methods and results in cellular morphology – dimensions, lacunarity and multifractals. J. Neurosci. Methods 69, 123–136.
Stošić, T., Stošić, B.D., 2006. Multifractal analysis of human retinal vessels. IEEE Trans. Med. Imag. 25, 1101–1107.
Tan, M., Pu, J., Cheng, S., Liu, H., Zheng, B., 2015. Assessment of a four-view mammographic image feature based fusion model to predict near-term breast cancer risk. Ann. Biomed. Eng. 43, 2416–2428.
Tang, J., Alsop, R.J., Schmalzl, K., Epand, R.M., Rheinstädter, M.C., 2015. Strong static magnetic fields increase the gel signal in partially hydrated DPPC/DMPC membranes. Membranes 5 (4), 532–552.
Tian, X., Wang, D., Zha, M., Yang, X., Ji, X., Zhang, L., Zhang, X., 2018. Magnetic field direction differentially impacts the growth of different cell types. Electromagn. Biol. Med. 37 (2), 114–125.
Tomaszewska, E., Winiarska-Mieczan, A., Dobrowolski, P., 2015. The lack of protective effects of tea supplementation on liver and jejunal epithelium in adult rats exposed to cadmium and lead. Environ. Toxicol. Pharmacol. 40 (3), 708–714.
Tombarkiewicz, B., 2008. Effect of long-term geomagnetic field deprivation on the concentration of some elements in the hair of laboratory rats. Environ. Toxicol. Pharmacol. 26 (1), 75–79.
Torres-Duran, P.V., Ferreira-Hermosillo, A., Juarez-Oropeza, M.A., Elias-Viñas, D., Verdugo-Diaz, L., 2007. Effects of whole body exposure to extremely low frequency electromagnetic fields (ELF-EMF) on serum and liver lipid levels, in the rat. Lipids Health Dis. 6, 31.
Wijendran, V., Lawrence, P., Diau, G.-Y., Boehm, G., Nathanielsz, P.W., Brenna, J.T., 2002. Significant utilization of dietary arachidonic acid is for brain adrenic acid in baboon neonates. J. Lipid Res. 43, 762–767.
Wu, H., Sun, T., Wang, J., Li, X., Wang, W., Huo, D., et al., 2013. Combination of radiological and gray level co-occurrence matrix textural features used to distinguish solitary pulmonary nodules by computed tomography. J. Digit. Imag. 26, 797–802.
Yamaguchi-Sekino, S., Nakai, T., Imai, S., Izawa, S., Okuno, T., 2014. Occupational exposure levels of static magnetic field during routine MRI examination in 3 T MR system. Bioelectromagnetics 35, 70–75.
Yang, J.Y., Yu, Z.G., Anh, V., 2009. Clustering structures of large proteins using multifractal analyses based on a 6-letter model and hydrophobicity scale of amino acids. Chaos Solitons Fract. 40 (2), 607–620.
Yang, X., Li, Z., Polyakova, T., Dejneka, A., Zablotskii, V., Zhang, X., 2020. Effect of static magnetic field on DNA synthesis: The interplay between DNA chirality and magnetic field left-right asymmetry. FASEB BioAdv 2, 254–263.
Yang, X., Song, C., Zhang, L., Wang, J., Yu, X., Yu, B., et al., 2021. An upward 9.4 T static magnetic field inhibits DNA synthesis and increases ROS P53 to suppress lung cancer growth. Transl. Oncol. 14 (7), 101103.
Yu, S., Shang, P., 2014. A review of bioeffects of static magnetic field on rodent models. Prog. Biophys. Mol. Biol. 114 (1), 14–24.
Zhang, Y., Zhang, D., Zhu, B., Zhang, H., Sun, Y., Sun, C., 2016. Effects of dietary green tea polyphenol supplementation on the health of workers exposed to high-voltage power lines. Environ. Toxicol. Pharmacol. 46, 183–187.

Received: 23 May 2019 | Revised: 22 July 2019 | Accepted: 23 July 2019

DOI: 10.1002/jrs.5718

RESEARCH ARTICLE

WILEY Journal of RAMAN SPECTROSCOPY

Raman spectroscopy of zinc oxide nanoplatelets modified with ruthenium (II) complexes

Jasna L. Ristić-Djurović[1] | Leunam Fernández-Izquierdo[2,3] | Branka Hadžić[1] | Linnavel Jiménez-Hernández[4] | Alicia M. Díaz-García[3] | Jelena Mitrić[1] | Biljana Babić[1] | Maja Romčević[1] | Saša Ćirković[1] | Nebojša Romčević[1]

[1] Institute of Physics, University of Belgrade, Belgrade, Serbia

[2] Faculty of Chemistry, Pontifical Catholic University of Chile, Santiago, Chile

[3] Bioinorganic Laboratory (LBI), Department of Inorganic and General Chemistry, University of Havana, Havana, Cuba

[4] Institute of Material Science and Technology (IMRE), University of Havana, Havana, Cuba

Correspondence
Jasna L. Ristić-Djurović, Institute of Physics, University of Belgrade, Pregrevica 118, Belgrade, Serbia.
Email: jasna@stanfordalumni.org

Funding information
Serbian Ministry of Education, Science, and Technological Development, Grant/Award Number: III-45003

Abstract

We analyzed and compared the unmodified and three modified zinc oxide nanoplatelet materials. The three components used in zinc oxide modification were the 4,4′-bipyridine and two ruthenium (II) complexes, namely, the *trans*-$[Ru(bpy)(bpyCOO)Cl_2]^{2-}$ and *cis*-$[Ru(bpy)(bpyCOO)Cl_2]^{2-}$. The obtained results revealed that after modification, ZnO nanoplatelets became smaller and embedded in the materials used for the modification. When ZnO was modified with either of the two ruthenium (II) complexes, the interaction between them led to a higher activity of ZnO. The metal-to-ligand charge transfer that was also detected in the two cases of ZnO nanoplatelets modified with the ruthenium (II) complexes caused significant alteration of the Raman spectrum and consequent changes of the optical properties. Various forms of ruthenium (II) complexes were used in several published studies related to dye-sensitized solar cells and biomedicine. The biomedical applications include, for example, the ATP (adenosine-5′-triphosphate) detection, interaction with human serum albumin, DNA analysis, and cancer detection and treatment. The properties of the ZnO nanoplatelets modified with the two ruthenium (II) complexes presented here indicate that it may be worth exploring if the studied materials are applicable in the dye sensitized solar cells and biomedicine. Possible advantage of our results is that they were obtained at room temperature.

KEYWORDS

nanocomposite, semiconductor, spectroscopy

1 | INTRODUCTION

The ruthenium complexes have been often used in research areas related to biomedical applications[1–7] and have emerged as potential candidates for use in dye-sensitized solar cells (DSSCs).[8–13] Compared with conventional inorganic crystals, donor–acceptor substituted organic molecules with nonlinear optical properties have advantages such as the optical damage threshold, lower dielectric constant, fast response time, tunability of optical properties by chemical modification, and low production cost.[14,15] Zinc oxide and TiO_2 are the most commonly used semiconductors in dye-sensitized solar cells. They both have the same electron affinities and almost the same band gap energies; however, ZnO has much higher electron diffusivity, high electron mobility, and large excitation binding energy; it is stable against photo-corrosion and is available at low-cost.[16] Also, ZnO has probably

the richest variety of nanostructures due to a very broad range of synthesis methods.[17] An excellent review of ZnO-based dye-sensitized solar cells is given by Anta et al. as well as by Vittal and Ho.[16,17] Various nanostructures such as nanoparticles, hierarchical aggregates, porous films, nanosheets, nanowires, and tetrapods are most often combined with the ruthenium-based dyes and the iodide/triiodide redox couple. The highest power conversion rate of DSSC with ZnO of 7.5%[18] is lower than the long-standing record of 11.1%[19] and the highest reported so far of 12.3%.[20] In addition to the most commonly investigated use in the solar cells, emerge applications of ruthenium based dyes in other scientific fields, for example, in biomedicine.[1–7] Ruthenium (II) complexes were shown to bind to DNA defects[7] as well as to be a quantitative DNA detectors.[3] Recently, a number of studies have suggested them as a potential photodynamic agents in the cancer therapy,[4–6] live-cell imaging,[21,22] ATP (adenosine-5′-triphosphate) detection,[1] interaction with HSA (human serum albumin),[2] and theranostic applications.[23]

In addition to the DSSC and biomedicine, other fields of application emerge as well. Ruthenium dyes have been successfully used to generate electrostatically stabilized gold colloides,[24] whereas Ru/TiO_2 has been employed as a catalyst in the selective methanation of CO.[25] A number of recent studies are devoted to the materials that incorporate ruthenium, for example, the ruthenium doped ZnO nanorods,[26] amorphous silicon ruthenium thin films embedded with nanocrystals,[27] Ru-doped ZnS quantum dots,[28] ruthenium complexes bound to CdSe nanoparticles,[29] hybrid materials including the Zn (II)-Ru (II) complexes,[30] trinuclear ruthenium complex, Ru-red,[31] and isolated and agglomerated gold nanoparticles functionalized with a ruthenium dye.[24]

The Raman scattering, a sensitive, nondestructive characterization tool, has been used to obtain information about sample quality as well as to analyze specific aspects of lattice dynamics, namely, the isotopic effects, phonon lifetimes, position of doping ions in a host lattice, and presence of impurities that are undetectable by the X-ray analysis.[32,33] In particular, the vibrational properties of ZnO in the form of nanostructured samples and thin films, as well as of the bulk ZnO, were investigated in a number of studies using Raman spectroscopy. The variety of studied ZnO properties include the multiphonon processes, electron–phonon coupling, dopant incorporation, local atomic arrangement, changes in samples with annealing process, and temperature dependence of Raman modes.[34–39]

The aim of the work presented here is to characterize the ZnO nanoplatelets (NPs) modified with the *trans*-[Ru (bpy)(bpyCOO)Cl_2]$^{2-}$ and *cis*-[Ru (bpy)(bpyCOO)Cl_2]$^{2-}$ in order to establish if further investigation of their possible use in the fields of dye-sensitized solar cells and biomedicine is worthwhile. The NPs of ZnO, its combination with 4,4′-bipyridine (4,4′-bpy) as well as with two ruthenium (II) complexes, are characterized using X-ray diffraction (XRD), photoluminescence, and Raman spectroscopy.

2 | MATERIALS AND METHODS

The synthesis of modified ZnO NPs was undertaken by the precipitation method and the 4,4′-bpy as a surfactant. The 4,4′-bpy was used as a bridge in the synthesis of ruthenium (II) complexes, as well. The ruthenium (II) complexes *trans*-[Ru (bpy)(bpyCOO)Cl_2]$^{2-}$and *cis*-[Ru (bpy)(bpyCOO)Cl_2]$^{2-}$ with 2,2′-bipyridine and 2,2′-bipyridine 4,4′-dicarboxilic acid as ligands were obtained as depicted in Fig. 1 and were further adhered to ZnO NPs. The *trans*- and *cis*- ruthenium (II) complexes are abbreviated as SAh and SA, respectively. Consequently, the four studied nanomaterials are ZnO NPs, ZnO NPs–4,4′-bpy, ZnO NPs–SA, and ZnO NPs–SAh. The additions to ZnO NPs, namely, the 4,4′-bpy, SA, and SAh, are shown in Fig. 2.

Scanning electron microscopy (SEM) images of the samples were obtained with the high-resolution electron microscope MIRA3 FEG-SEM, Tescan, using accelerating voltages lower than 20 kV. The samples were prepared for SEM imaging by coating them with an ultrathin gold layer in the SC7620 Mini Sputter Coater, Quorum Technologies.

Structural characteristics of all samples were obtained using the XRD powder technique. Philips PW 1050 diffractometer equipped with a PW 1730 generator was used. All samples were examined under the same conditions, namely, 40 kV × 20 mA, using Ni filtered Co Kα radiation of 0.1778897 nm at room temperature. Measurements were carried out in the 2-hr range of 10–80^{o} with the scanning step of 0.05^{o} and 10 s scanning time per

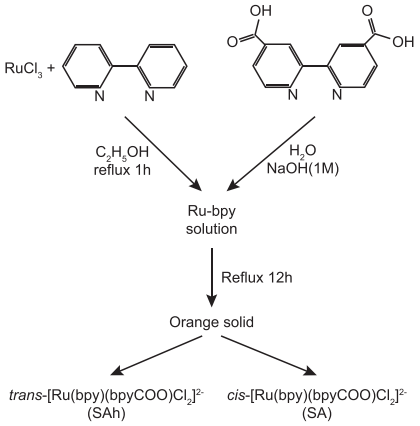

FIGURE 1 Synthesis of ruthenium complexes

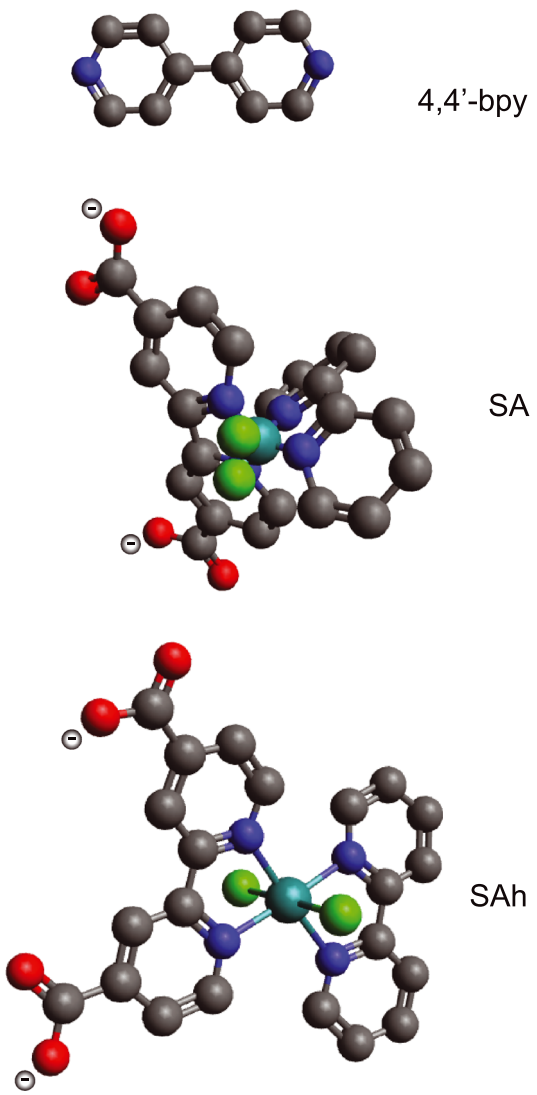

FIGURE 2 Compounds used to modify zinc oxide nanoplatelets. The ZnO nanoplatelets were modified using the 4,4'-bipyridine, as well as ruthenium (II) complexes *cis*-[Ru (bpy)(bpyCOO)Cl_2]$^{2-}$ and *trans*-[Ru (bpy)(bpyCOO)Cl_2]$^{2-}$, further referred to as the 4,4'-bpy, SA, and SAh, respectively [Colour figure can be viewed at wileyonlinelibrary.com]

step. Crystallite size was determined with the XFIT computing program, which is based on the fundamental parameter convolution approach.[40]

The photoluminescence spectrum excited by argon laser line at 514.5 nm was measured at room temperature using the Jobin Yvon model U-1000 monochromator with a conventional photocounting system.

The micro-Raman spectra were taken in the backscattering configuration with the Jobin Yvon T64000 spectrometer, equipped with nitrogen cooled charge-coupled-device detector. As was the case with the photoluminescence spectrum, the 514.5-nm line of an Ar-ion laser was used as the excitation source. The measurements were performed at room temperature using the laser power of 20 mW. All samples were investigated in the spectral range between 100 and 1,700 cm^{-1}.

3 | RESULTS AND DISCUSSION

3.1 | SEM measurements

The representative SEM images of the four studied materials are given in Fig. 3, whereas the sets of images with three values of magnification are provided in Fig. S1 in the Supporting Information. The unmodified ZnO particles can be classified as NPs because their thickness is of the order of 50 nm. This is confirmed by the four examples of NPs whose thickness is equal or smaller than 40 nm, given in the image corresponding to ZnO NPs in Fig. 3. Note that the thickness of 40 nm is somewhat smaller than 50 nm, which is the step size of the scale. The modified ZnO NPs, namely, the ZnO NPs–4,4′-bpy, ZnO NPs–SA, and ZnO NPs–SAh appear to be coated with the material used in the modification, that is, with 4,4′-bpy, SA, and SAh. Further, SA and SAh seem to have caused clustering and agglomeration, which is more pronounced for ZnO NPs–SAh.

3.2 | XRD measurements

The structure of prepared samples was identified using the XRD patterns shown in Fig 4. The diffractograms show intense peaks of ZnO originating from (110), (002), (101), (102), (110), (103), and (112) and confirm that the structures crystallized in the hexagonal wurtzite, P63mc, structure shown in the insert in the top right corner of Fig 4. All the marked peaks are in good agreement with the JCPDS card 36-145. All the other peaks originate from the modifiers. Because 4,4′-bpy was used as a surfactant, ZnO NP sample shows not only the peaks of pure ZnO but the peaks of 4,4′-bpy as well. That is why this diffractogram is very similar to the one that corresponds to ZnO NPs–4,4′-bpy. However, the peaks that correspond to 4,4′-bpy are more intense in the diffractogram of ZnO NPs–4,4′-bpy because in this case 4,4′-bpy was used not only as a surfactant in the synthesis of ZnO but as a capping agent, as well. The ZnO crystallite size is calculated for all the samples and is found to be 35.8, 19.2, 10.6, and 7.5 nm for ZnO NPs, ZnO NPs–4,4′-bpy, ZnO NPs–SA, and ZnO NPs–SAh, respectively. Consequently, the ZnO crystallite size is significantly smaller in the modified material, that is, in the presence of the capping agent. Note that for unmodified ZnO NPs, the particle sizes calculated from the XRD patterns of 35.8 nm agree well with the NP thicknesses found from the SEM images to be of the order of 40 nm. In the case of the modified ZnO

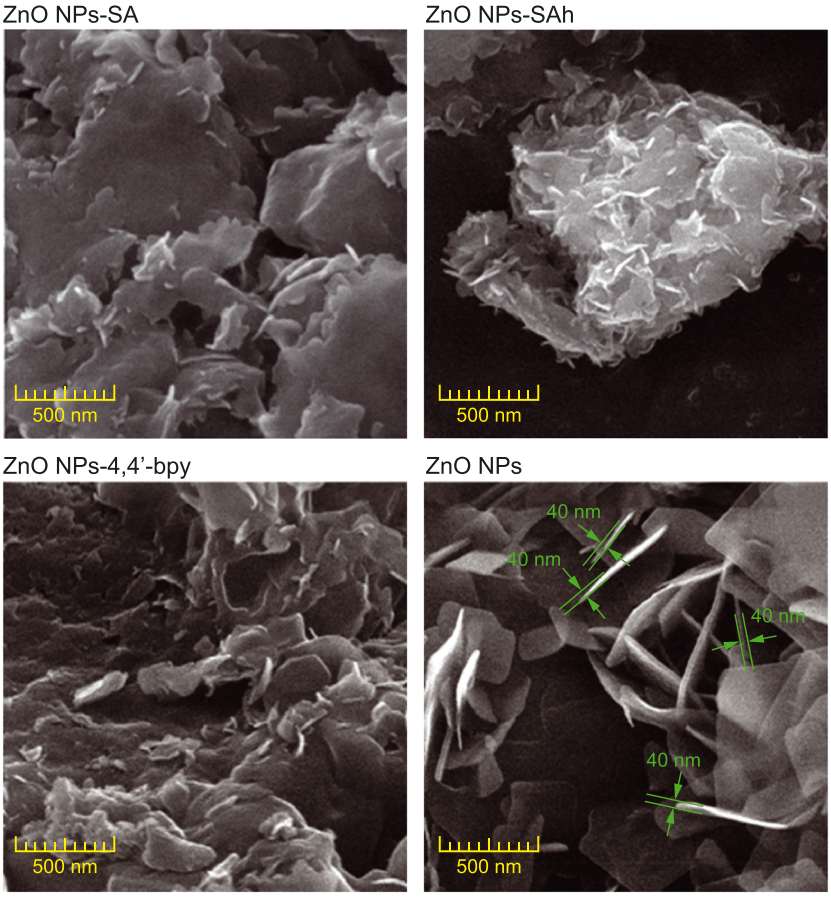

FIGURE 3 Scanning electron microscopy images. The micrographs of the four studied materials are given here with the magnification of 133,000, whereas Fig. S1 contains the micrographs with the magnification values of 55,700 and 267,000, as well. Nanoplatelets of ZnO are about 40 nm thick. In the modified material ZnO NPs are coated with the modifier and are clustered [Colour figure can be viewed at wileyonlinelibrary.com]

NPs, the particle sizes obtained from SEM images are bigger than those calculated by the XRD patterns, which suggests particle aggregation.

3.3 | Photoluminescence measurements

The luminescence spectrum of the four studied samples is given in Fig. 5. Given that our excitation wavelength was 514.5 nm, our study is limited to the broad long-wavelength part of the spectrum. Photoluminescence spectra are often analyzed using the convolution of the Lorentzian functions that are given with

$$I(\omega) = \frac{2A}{\pi} \frac{W}{4(\omega - \omega_c)^2 + W^2}, \quad (1)$$

where I, ω_c, W, and A are the line intensity, position of the maximum, half-width of the peak, and parameter that depends on W, respectively. The measured data depicted with circles in Fig. 5 is approximated with the calculated red curve, which represents the sum of the components each defined with Equation (1) and shown with green lines.

The spectra of ZnO NPs and those modified with 4,4′-bpy can be decomposed into four components positioned at ω_c values of approximately 553, 605, 634, and 678 nm. Various forms of ZnO exhibit two luminescence bands, namely, a short-wavelength band, which is located near the absorption edge, and a broad long-wavelength band, the maximum of which is in the green spectral range.[41] Impurities, zinc vacancies, oxygen vacancies, interstitial zinc ions, oxygen antisites, and transitions from interstitial zinc ions to zinc vacancies as well as a combination of various centers were assumed to be responsible for the green luminescence.[41] In our case, these are described with the Lorentzians positioned at the ω_c values of 605, 634, and 678 nm.

Modification with 4,4′-bpy caused significant enhancement of the relative contribution of the peak at 553 nm, which can be attributed to 4,4′-bpy. This peak is visible in the spectrum of unmodified ZnO NPs because 4,4′-bpy was used as a surfactant in ZnO NPs synthesis.

However, in the spectra of ZnO NPs modified with the ruthenium (II) complexes, ZnO NPs–SA, and ZnO NPs–SAh, the component at 553 nm is not present. Instead, the peak at 678 nm became much stronger and metal-to-ligand charge transfer introduced the component at 737 nm.[42] Consequently, it seems that ZnO in ZnO NPs–SA and ZnO NPs–SAh became more active due to the interaction between ZnO and ruthenium (II) complex. In the spectrum corresponding to ZnO NPs–SAh relative intensity of the peak at 637 nm became larger than

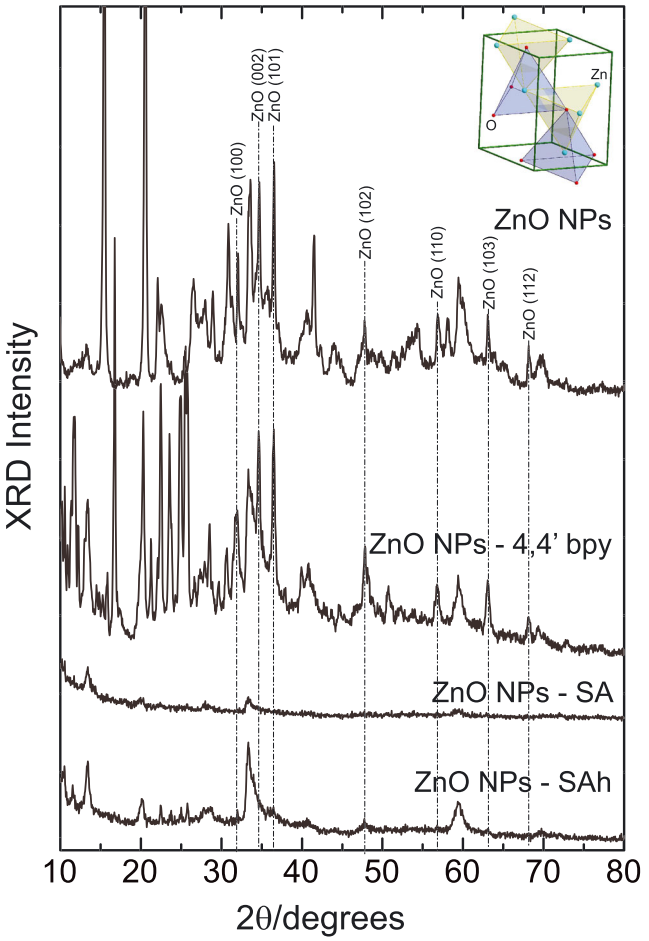

FIGURE 4 X-ray diffraction patterns. The insert shows the structure of the ZnO crystallite, that is, the hexagonal wurtzite, P63mc [Colour figure can be viewed at wileyonlinelibrary.com]

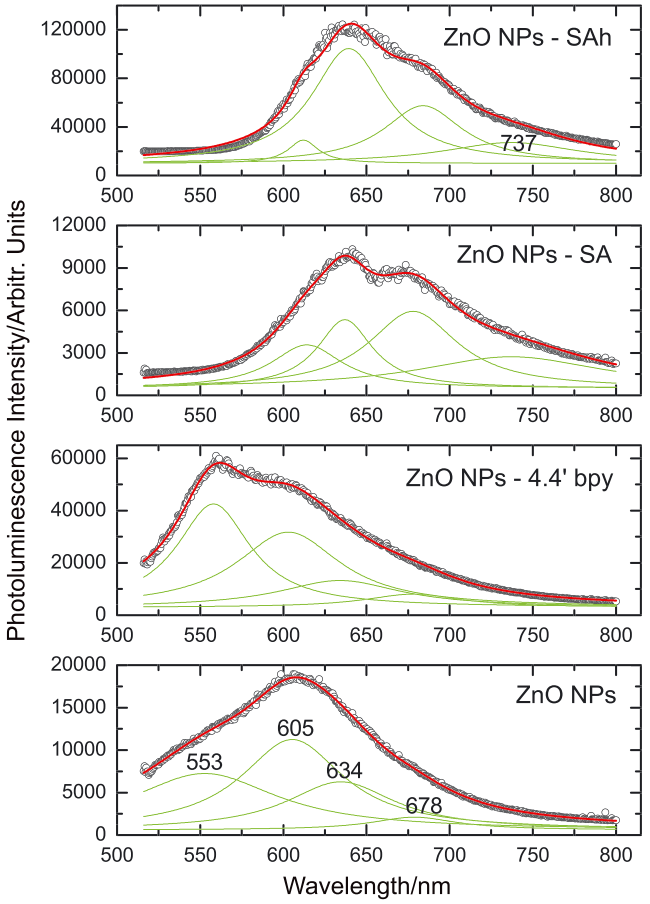

FIGURE 5 Photoluminescence. The photoluminescence spectra of the four analyzed samples were measured at room temperature with the excitation source of 514.5 nm. The measured data depicted with circles are approximated with the calculated thick red line that represents the sum of the Lorentzian components given as the thin green lines. The parameters of each Lorentzian component are given in Table S1 [Colour figure can be viewed at wileyonlinelibrary.com]

was the case in the ZnO NPs–SA spectrum. The fluorescence emission spectra of Ru $(bpy)_3^{2+}$ incorporated in silica gel film studied by Innocenzi et al. seem to have similar structure as our result corresponding to ZnO NPs modified with 4,4'-bpy; however, their structure is centered at 603 nm, whereas ours is located at approximately 554 nm.[42] Table S1 in the Supporting Information gives the parameters of spectral components obtained by decomposing our spectra.

For the five Ru (II) complexes studied by Ji et al. the wavelengths of 594, 626, 626/667/726, 631, and 620 nm were obtained.[43] Note that their third complex has centers located at similar positions as our samples with SA and SAh. With the increase of external hydrostatic pressure, the spectra of two complexes considered by Pannwitz et al. seem to develop similarities with our spectra; however, their peaks are at somewhat larger wavelengths.[44] To the contrary, the spectra of Ru (II) complexes given by Oner et al. in the region above 500 nm exhibit structures centered at somewhat smaller wavelength than is the case with our spectra.[45] The spectra corresponding to all the modified samples are similar to those considered by McConnell et al. with respect to detecting DNA defects.[7] However, in order to obtain peaks, their spectra had to be recorded at 77 K, whereas our spectra were measured at room temperature.

3.4 | Raman spectroscopy

The Raman spectra and peak assignments of the four studied nanomaterials are given in Fig. 6 and Table 1, respectively. In the Raman spectrum of unmodified ZnO NPs the peaks were recorded at 290, 319, 404, 440, 679, 937, 1,048, 1,353, 1,435, and 1,589 cm^{-1}. The peaks at 404 and 440 cm^{-1} are the well-known peaks that are characteristic to ZnO, and they correspond to E_1 (TO) and E_2^{high}, respectively. The peak E_2^{high} is less intense than usually due to a high luminescence of the sample. All

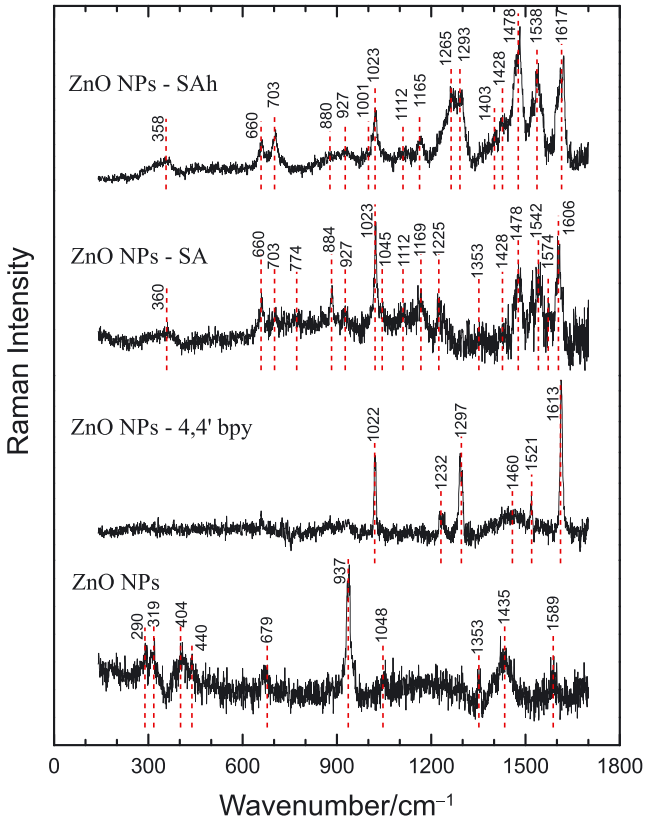

FIGURE 6 Raman spectra. The Raman spectra of the four samples were obtained at room temperature with 514.5-nm excitation source [Colour figure can be viewed at wileyonlinelibrary.com]

the other peaks are the multiphonon peaks or the second harmonics (second order Raman peaks). The obtained results are in good agreement with previously reported results for pure ZnO.[32] The Raman spectra of ZnO are usually taken in the spectral range between 99 and 1,160 cm^{-1} because it is only the multiphonon peaks and second harmonics that exist above 618 cm^{-1}. In our study, the Raman spectra were taken in the wider range due to the peaks expected to correspond to the 4,4′-bpy, SA, and SAh used in the three remaining samples.

When ZnO NPs were modified with 4,4′-bpy, the Raman spectrum changed significantly. Most of the ZnO peaks disappeared and the peaks that correspond to 4,4′-bpy became dominant. The part of our Raman spectrum that can be related to the 4,4′-bpy contains the peaks located at 1,022, 1,232, 1,297, 1,521, and 1,613 cm^{-1} as well as the wide structure centered at approximately 1,460 cm^{-1}. The peak at 1,297 cm^{-1} is the inter-ring stretch (Ω), whereas the peak at 1,613 cm^{-1} is the ring stretch (8a). The peak that represent the ring in-plane deformation (12) is located at 1,022 cm^{-1} in our spectrum; however, in the works of Castellà-Ventura and E. Kassab[46] and Ould-Moussa et al.[47] this peak is positioned at 1,000 and 1,038 cm^{-1}. For our peak at 1,232 cm^{-1} that represent the CH in-plane bend (9a) Castellà-Ventura and E. Kassab[46] reported the experimental peak position at 1,218 cm^{-1} and scaled calculated position of 1,227 and 1,235 cm^{-1}. The peak at 1,521 cm^{-1} representing the CH in-plane bend and ring stretch (19a) is in Castellà-Ventura and E. Kassab[46] given by the experimental value of 1,511 cm^{-1} and scaled calculated value of 1,523 cm^{-1}. The wide structure centered at approximately 1,460 cm^{-1} is a consequence of the three peaks that represent the CH in-plane bend and ring stretch at 1,406 (19b), 1,424 (19b), and 1,487 cm^{-1} (19a).[46] In Castellà-Ventura and E. Kassab[46] and Ould-Moussa et al.[47] there is no information regarding the laser used as an excitation source. Consequently, the discrepancy between their reported peak positions and our measurements may be caused by different excitation sources. In Moissette et al.[48] the infrared laser light of 1,064 nm was used to detect the 4,4′-bpy peaks at 999, 1,075, 1,227, 1,294, 1,508, 1,597, and 1,616 cm^{-1}, which is in good agreement with our peaks. On the other hand, using the laser light of 532 nm, Pérez León et al.[49] reported the 4,4′-bpy peaks at 1,024, 1,273, 1,490, 1,537, and 1,630 cm^{-1} and characterization of the peak at 1,024 cm^{-1} as the ring breathing band. The blue laser light of 488 nm was employed by Rzeźnicka et al.[50] to obtain the 4,4′-bpy peaks at 1,016, 1,337, 1,533, and 1,630 cm^{-1}. With all this in mind it can be concluded that our results corresponding to ZnO NPs–4,4′-bpy show a fairly good agreement with the data found in the literature.

In the Raman spectra of ZnO NPs–SA the existence of peaks that belong to the both phases is evident. In addition to the wide structure at approximately 360 cm^{-1}, there are peaks at 660, 703, 774, 884, 927, 1,023, 1,045, 1,112, 1,169, 1,225, 1,353, 1,428, 1,478, 1,542, 1,574, and 1,606 cm^{-1}. Both phases have several peaks at the very similar positions, causing the peaks at those positions to be wider and asymmetric as well as making the spectral analysis more complex. Note the wide structure whose center is approximately at 360 cm^{-1}. In Hureau et al.[51] the peak at 360 cm^{-1} is reported to correspond to SA. However, ZnO has a multiphonon peak at 333 cm^{-1} and A_1 (TO) peak at 378 cm^{-1}.[32] The asymmetry of our peak at 660 cm^{-1} is a consequence of coexistence of the ZnO multiphonon peak at 660 cm^{-1} as well as the SA peak at 657 cm^{-1}. The peak at 703 cm^{-1} is the multiphonon ZnO peak. The peak at 774 cm^{-1} combines the ZnO multiphonon peak at 773 cm^{-1} and the SA peak at 781 cm^{-1}. The peaks at 884, 927, and 1,023 cm^{-1} are the SA peaks. The peak at 1,045 cm^{-1} consists of the SA peak at 1,031 cm^{-1} and the ZnO multiphonon peak at 1,044 cm^{-1}. The peak at 1,112 cm^{-1} is composed of the ZnO multiphonon peak at 1,105 cm^{-1} and SA peak at 1,114 cm^{-1}, whereas the peak at 1,169 cm^{-1} is a mixture of ZnO multiphonon peak at 1,158 cm^{-1} and SA peak at

TABLE 1 Raman peak assignments

Raman wavenumber/cm^{-1}						
Experimental results						
ZnO NPs	ZnO NPs–4,4′-bpy	ZnO NPs–SA	ZnO NPs–SAh	Reference	Phase	Assignment
290				284[32]	ZnO	B_1^{high}-B_1^{low}
319				333[32]	ZnO	E_1^{high}-E_1^{low}
		360	358	333[32] 306[24], 376[31] 378[32]	ZnO SA/SAh ZnO	E_1^{high}-E_1^{low} Ru–N stretch A_1 (TO)
401				410[32]	ZnO	E_1 (TO)
440				438[32]	ZnO	E_2^{high}
		660	660	657[51] 657[32], 666[32]	SA/SAh ZnO	 TA+LO
679				666[32]	ZnO	TA+LO
		703	703	692[51] 700[32]	SA/SAh ZnO	 LA+TO
		774		773[32] 778[31]	ZnO SA	LA+TO Ru–O
		884	880	896[51]	SA/SAh	
		927	927	934 812[32], 980[32]	SA/SAh ZnO	 LA+LO, 2TO
937				812[32], 980[32]	ZnO	LA+LO, 2TO
			1,001	999[48], 1,000[51]	SAh	
	1,022	1,023	1,023	1,016[50], 1,024[49,51], 1,029[24]	4,4′-bpy/SA/SAh	in-plane def. (12), ring breath
1,048		1,045		1,029[24], 1,031, 1,038[47] 1,044[32]	SA ZnO	ring breath TO+LO
		1,112	1,112	1,105[32] 1,114[51], 1,119[25]	ZnO SA/SAh	2LO C–O–C
		1,169	1,169	1,158[32] 1,169[51]	ZnO SA/SAh	$2A_1$(LO), $2E_1$(LO), 2LO
	1,232	1,225		1,227[48], 1,235[46]	4,4′-bpy/SA	CH in-plane bend (9a)
			1,265	1,264[24], 1,273[51]	SAh	CN stretch
	1,297		1,293	1,290[51], 1,294[48], 1,300[24]	4,4′-bpy/SAh	Inter-ring stretch (Ω), COO stretch
1,353		1,353			ZnO SA	multi-phonon, second order
			1,403	1,401[51]	SAh	
		1,428	1,428	1,424[47]	SA/SAh	CH in-plane bend, ring stretch (19b)
1,435					ZnO	multiphonon, second order
	1,460			1,406[47] 1,424[47]	4,4′-bpy 4,4′-bpy	CH in-plane bend, ring stretch (19b) CH in-plane bend, ring stretch (19b)

(Continues)

TABLE 1 (Continued)

Raman wavenumber/cm^{-1}						
Experimental results						
ZnO NPs	ZnO NPs–4,4′-bpy	ZnO NPs–SA	ZnO NPs–SAh	Reference	Phase	Assignment
				1,487[47]	4,4′-bpy	CH in-plane bend, ring stretch (19a)
		1,478	1,478	1,456[51], 1,477[24], 1,484[51]	SA/SAh	asymmetric CC+CN stretch
	1,521			1,511[47], 1,523[46], 1,531[47]	4,4′-bpy	CH in-plane bend, ring stretch (19a)
		1,542	1,538	1,545[24]	SA/SAh	asymmetric CC+CN stretch
1,589					ZnO	multiphonon, second order
		1,574			SA	
		1,606			SA	
	1,613		1,617	1,614[24], 1,615[51]	SAh	symmetric CC+CN stretch

Abbreviations: 4,4′-bpy: 4,4′-bipyridine; NPs: nanoplatelets.

1,169 cm^{-1}. The peaks at 1,225, 1,353, 1,478, 1,574, and 1,606 cm^{-1} belong to the SA phase. The differences in SA peak positions in our measurements and those reported in Hureau et al.[51] are due to different laser lights used in the two experiments. An excitation sources in Hureau et al.[51] were red and infrared lasers at 632 and 1,064 nm, respectively, compared with 514-nm laser light used in our experiment. The excitation source wavelength may be the reason for the two peaks in our spectra that can be attributed to SA, the very intense peak at 1,542 cm^{-1} and less intense peak at 1,428 cm^{-1}. The peak at 1,542 cm^{-1} is too strong to be the second harmonic of the peak at 774 cm^{-1}.

When compared with the Raman spectrum of ZnO NPs–SA, the spectrum of ZnO NPs–SAh has better signal-to-noise ratio as well as more symmetric peaks. From our experience with other coated nanoparticles, this can be a consequence of the difference in the coating layer thickness. The spectrum has two wide asymmetric structures centered at approximately 358 and 927 cm^{-1} and the peaks at 660, 703, 880, 1,001, 1,023, 1,112, 1,165, 1,265, 1,293, 1,403, 1,428, 1,478, 1,538, and 1,617 cm^{-1}. The wide structures are composed of peaks that belong to both phases, ZnO and SAh. The ZnO peaks at 333 and 378 cm^{-1} and the SAh peak at 360 cm^{-1} form the wide structure centered at approximately 358 cm^{-1}, whereas the wide structure centered at approximately 927 cm^{-1} is composed of the SAh peak at 934 cm^{-1} and the ZnO peak at 980 cm^{-1}. The ZnO peaks at 333 and 980 cm^{-1} are the multiphonon peaks, whereas the peak at 378 cm^{-1} is of the type A_1 (TO). All other peaks in our spectrum belong to the SAh phase and show good agreement with peaks reported in Hureau et al.,[51] namely, the peaks at 657, 692, 896, 1,000, 1,024, 1,114, 1,169, 1,273, 1,290, 1,401, 1,456, 1,484, and 1,615 cm^{-1}. Small differences in peak position are due to different laser lights used as an excitation source. This may also cause the existence of the peaks at 1,428 and 1,538 cm^{-1} in our spectra, whereas in Hureau et al.[51] the existence of peak at 1,456 cm^{-1} is reported.

The fluorescence spectra showed that the excitation wavelength is in the visible light range; therefore, the ZnO NPs modified with the two considered ruthenium (II) complexes can be regarded as prospective candidates for use in energy conversion. Future studies can develop towards applying these materials in DNA analysis. For example, it can be investigated if use of our modified ZnO NPs in altering an electrode of a cell for electrochemiluminescence spectra measurement will prove efficient as was the case with the pristine carbon nanotube that was used by Tang et al.[3] Application of the analyzed materials in detecting DNA defects seems promising because our photoluminescence spectra were recorded at room temperature, whereas those employed for this purpose by McConnell et al.[7] were measured at 77 K.

4 | CONCLUSION

The unmodified zinc oxide nanoplatelets (ZnO NPs) and three modifications of these ZnO NPs were analyzed. The three materials used for the modification were the 4,4′-bpy and the two ruthenium (II) complexes of equal composition but with two different geometries, namely, the *cis* and *trans* geometry. The three modified materials were denoted as ZnO NPs–4,4′-bpy, ZnO NPs–SA (for *cis* geometry), and ZnO NPs–SAh (for *trans* geometry). It was found that in the modified ZnO, the ZnO NPs are smaller and coated with the material used for the modification. The metal-to-ligand charge transfer was detected in the ZnO modified with the SA and SAh ruthenium (II) complexes, which caused significant changes of the Raman spectrum and consequent alteration of the optical properties. Because 4,4′-bpy was used as a surfactant in the synthesis of ZnO NPs as well as in further modification of one of the three studied modified ZnO NPs, the spectral component at 553 nm that corresponds to 4,4′-bpy was detected in the luminescence spectrum of ZnO NPs as well as of ZnO NPs–4,4′-bpy. As expected, this peak is stronger in the spectrum of ZnO NPs–4,4′-bpy, namely, in the case when 4,4′-bpy was used as a modifier as well as a surfactant. In the spectra of ZnO NPs modified with the ruthenium (II) complexes SA and SAh three important changes were detected. Namely, the 4,4′-bpy-related peak at 553 nm disappeared, the peak that corresponds to the metal-to-ligand charge transfer appeared at 737 nm, and the peak at 678 nm that is a characteristics of ZnO became much stronger. Consequently, it seems that the interaction between ZnO and ruthenium (II) caused ZnO to be more active. The obtained results indicate that it can be beneficial to pursue investigation towards the application of the studied materials in the DSSC and DNA analysis.

ACKNOWLEDGEMENTS

This work is financially supported by the Serbian Ministry of Education, Science, and Technological Development (III-45003). The authors thank M. Mitrić and B. Jokić for their help with XRD and SEM measurements.

ORCID

Jasna L. Ristić-Djurović https://orcid.org/0000-0002-5344-1892
Branka Hadžić https://orcid.org/0000-0001-5459-7461
Jelena Mitrić https://orcid.org/0000-0002-1526-3976
Maja Romčević https://orcid.org/0000-0002-5064-175X

REFERENCES

[1] E. Babu, P. Muthu Mareeswaran, A. Ramdass, P. Ramesh, S. Rajagopal, *J. Lumin.* **2016**, *175*, 267.
[2] N. Cacita, S. Nikolaou, *J. Lumin.* **2016**, *169*, 115.
[3] X. Tang, D. Zhao, J. He, F. Li, J. Peng, M. Zhang, *Anal.Chem.* **2013**, *85*, 1711.
[4] S. M. Cloonan, R. B. P. Elmes, M. Erby, S. A. Bright, F. E. Poynton, D. E. Nolan, S. J. Quinn, T. Gunnlaugsson, D. C. Williams, *J. Med. Chem.* **2015**, *58*, 4494.
[5] L. Zeng, P. Gupta, Y. Chen, E. Wang, L. Ji, H. Chao, Z. -S. Chen, *Chem. Soc. Rev.* **2017**, *46*, 5771.
[6] J. Zhang, K. -L. Wong, W. -K. Wong, N. -K. Mak, D. W. J. Kwong, H. -L. Tam, *Org. Biomol. Chem.* **2011**, *9*, 6004.
[7] A. J. McConnell, M. H. Lim, E. D. Olmon, H. Song, E. E. Dervan, J. K. Barton, *Inorg. Chem.* **2012**, *51*, 12511.
[8] S. Shah, I. M. Noor, J. Pitawala, I. Albinson, T. M. W. J. Bandara, B. -E. Mellander, A. K. Arof, *Opt. Mater. Express* **2017**, *7*, 2069.
[9] C. -Y. Huang, C. -F. You, C. -E. Cheng, B. -C. Lei, J. -C. Jhang, F. -C. Yu, C. -S. Chang, F. S. -S. Chien, *Opt. Mater. Express* **2016**, *6*, 1024.
[10] M. A. Gaikwad, M. P. Suryawanshi, P. S. Maldar, T. D. Dongale, A. V. Moholkar, *Opt. Mater.* **2018**, *78*, 325.
[11] S. Kushwaha, L. Bahadur, *J. Lumin.* **2015**, *161*, 426.
[12] O. Wiranwetchayan, W. Promnopas, K. Hongsith, S. Choopun, P. Singjai, S. Thongtem, *Res. Chem. Intermed.* **2016**, *42*, 3655.
[13] K. Sim, S. -J. Sung, S. -N. Park, D. -H. Kim, J. -K. Kang, *Opt. Mater. Express* **2013**, *3*, 739.
[14] J. M. Hales, J. Matichak, S. Barlow, S. Ohira, K. Yesudas, J. L. Bradas, J. W. Perry, S. R. Marder, *Science* **2010**, *19*, 1466.
[15] Y. Li, J. Li, R. Su, J. Cui, *Opt. Mater.* **2013**, *36*, 437.
[16] R. Vittal, K. -C. Ho, *Renewable and Sustainable Energy Reviews* **2017**, *70*, 920.
[17] J. A. Anta, E. Guillén, R. Tena-Zaera, *J. Phys. Chem.* **2017**, *C116*, 11413.
[18] N. Memarian, I. Concina, A. Braga, S. M. Rozati, A. Vomiero, G. Sberveglieri, *Angew. Chem., Int. Ed.* **2011**, *50*, 12321.
[19] Y. Chiba, A. Islam, Y. Watanabe, R. Komiya, N. Koide, L. Han, *Jpn. J. Appl. Phys.* **2006**, *45*, L638.
[20] A. Yella, H. -W. Lee, H. N. Tsao, C. Yi, A. K. Chandiran, M. K. Nazeeruddin, E. W. -G. Diau, C. -Y. Yeh, S. M. Zakeeruddin, M. Grätzel, *Science* **2011**, *334*, 629.
[21] W. -K. Tsui, L. -H. Chung, M. M. -K. Wong, W. -H. Tsang, H. -S. Lo, Y. Liu, C. -H. Leung, D. -L. Ma, S. -K. Chiu, C. -Y. Wong, *Sci. Rep. –UK* **2014**, 09070.
[22] N. Karaoun, A. K. Renfrew, *Chem. Commun.* **2015**, *51*, 14038.
[23] C. R. Cardoso, M. V. S. Lima, J. Cheleski, E. J. Peterson, T. Venâcio, N. P. Farrell, R. M. Carlos, *J. Med. Chem.* **2014**, *57*, 4906.
[24] D. Grasseschi, A. L. A. Parussulo, V. M. Zamarion, R. R. Guimarães, K. Araki, H. E. Toma, *J. Raman Spectrosc.* **2014**, *45*, 758.
[25] L. M. Martínez Tejada, A. Muñoz, M. A. Centeno, J. A. Odriozola, *J. Raman Spectrosc.* **2016**, *47*, 189.

[26] S. Kumar, P. Kaur, C. L. Chen, R. Thangavel, C. L. Dong, Y. K. Ho, J. F. Lee, T. S. Chan, T. K. Chen, B. H. Mok, S. M. Rao, M. K. Wu, *J. Alloy. Compd.* **2014**, *588*, 705.

[27] A. Guo, W. Li, X. Jiang, C. Wang, Y. Jiang, *J. Raman Spectrosc.* **2015**, *46*, 619.

[28] R. Sahraei, F. Mohammadi, E. Soheyli, M. Roushani, *J. Lumin.* **2017**, *187*, 421.

[29] N. Bair, J. M. Hancock, C. J. Simonson, S. W. Thalman, J. S. Colton, M. C. Asplund, R. G. Harrison, *J. Lumin.* **2015**, *158*, 501.

[30] S. S. Chavan, S. B. Pawal, S. R. Lolage, *J. Lumin.* **2017**, *181*, 261.

[31] K. S. Joya, H. J. M. de Groot, *J. Raman Spectrosc.* **2013**, *44*, 1195.

[32] R. Cuscó, E. Alarcón-Lladó, J. Ibáñez, L. Artús, J. Jiménez, B. Wang, M. J. Callahan, *Phys. Rev. B* **2007**, *75*, 165202.

[33] Y. Liu, J. L. MacManus-Driscoll, *Appl. Phys. Letters* **2009**, *94*, 022503.

[34] J. Xu, W. Ji, X. B. Wang, H. Shu, Z. X. Shen, S. H. Tang, *J. Raman Spectrosc.* **1998**, *29*, 613.

[35] H. Zeng, W. Cai, B. Cao, J. Hu, Y. Li, P. Liu, *Appl. Phys. Lett.* **2006**, *88*, 181905.

[36] N. Romčević, R. Kostić, B. Hadžić, M. Romčević, I. Kuryliszin-Kudelska, W. Dobrowolski, U. Narkievicz, D. Sibera, *J. Alloy. Compd.* **2010**, *507*, 386.

[37] M. Millot, J. Gonzalez, I. Molina, B. Salas, Z. Golacki, J. M. Broto, H. Rakoto, M. Gorian, *J. Alloy. Compd.* **2006**, *423*, 224.

[38] R. P. Wang, G. Xu, P. Jin, *Phys. Rev. B* **2004**, *69*, 113303.

[39] R. Y. Sato-Berrú, A. Vázquez-Olmos, A. L. Fernández-Osorio, S. Sotres-Martínez, *J. Raman Spectrosc.* **2007**, *38*, 1073.

[40] R. W. Cheary, A. Coelho, *J. Appl. Cryst.* **1992**, *25*, 109.

[41] P. A. Rodnyi, I. V. Khodyuk, *Opt. Spectrosc.* **2011**, *111*, 776.

[42] P. Innocenzi, H. Kozuka, T. Yoko, *J. Phys. Chem. B* **1997**, *101*, 2285.

[43] S. Ji, W. Wu, W. Wu, P. Song, K. Han, Z. Wang, S. Liu, H. Guo, J. Zhao, *J. Mater. Chem.* **2010**, *20*, 1953.

[44] A. Pannwitz, S. Poirier, N. Blanger-Desmarais, A. Prescimone, O. S. Wenger, C. Reber, *Chem. Eur. J.* **2018**, *24*, 7830.

[45] I. Oner, C. Sahin, C. Varlikli, *Dyes Pigments* **2012**, *92*, 23.

[46] M. Castellà-Ventura, E. Kassab, *J. Raman Spectrosc.* **1998**, *29*, 511.

[47] L. Ould-Moussa, O. Poizat, M. Castellà-Ventura, G. Buntinx, E. Kassab, *J. Phys. Chem.* **1996**, *100*, 2072.

[48] A. Moissette, Y. Batonneau, C. Brémard, *J. Am. Chem. Soc.* **2001**, *123*, 1232.

[49] C. Pérez León, L. Kador, B. Peng, M. Thelakkat, *J. Phys. Chem. B* **2006**, *110*, 8723.

[50] I. I. Rzeźnicka, H. Horino, N. Kikkawa, S. Sakaguchi, A. Morita, S. Takahashi, T. Komeda, H. Fukumura, T. Yamada, M. Kawai, *Surf. Sci.* **2013**, *617*, 1.

[51] M. Hureau, K. S. Smirnov, A. Moissette, H. Jobic, *Phys. Chem. Chem. Phys.* **2014**, *16*, 7562.

SUPPORTING INFORMATION

Additional supporting information may be found online in the Supporting Information section at the end of the article.

How to cite this article: Ristic-Djurovic JL, Fernández-Izquierdo L, Hadzic B, et al. Raman spectroscopy of zinc oxide nanoplatelets modified with ruthenium (II) complexes. *J Raman Spectrosc*. 2019;50:1829–1838. https://doi.org/10.1002/jrs.5718

Computer Methods and Programs in Biomedicine 157 (2018) 153–162

Contents lists available at ScienceDirect

Computer Methods and Programs in Biomedicine

journal homepage: www.elsevier.com/locate/cmpb

Analysis of methods commonly used in biomedicine for treatment versus control comparison of very small samples

Jasna L. Ristić-Djurović[a,*], Saša Ćirković[a], Pavle Mladenović[b], Nebojša Romčević[a], Alexander M. Trbovich[c]

[a] Institute of Physics, University of Belgrade, Pregrevica 118, 11080 Belgrade, Serbia
[b] Faculty of Mathematics, University of Belgrade, Studentski trg 16, 11000 Belgrade, Serbia
[c] Department of Pathological Physiology, School of Medicine, University of Belgrade, Dr Subotića 9, 11000 Belgrade, Serbia

ARTICLE INFO

Article history:
Received 12 June 2017
Revised 4 January 2018
Accepted 24 January 2018

Keywords:
Biomedical statistics
Computer simulation
Errors
Qualitative comparison
Very small samples

ABSTRACT

Background and objective: A rough estimate indicated that use of samples of size not larger than ten is not uncommon in biomedical research and that many of such studies are limited to strong effects due to sample sizes smaller than six. For data collected from biomedical experiments it is also often unknown if mathematical requirements incorporated in the sample comparison methods are satisfied.

Methods: Computer simulated experiments were used to examine performance of methods for qualitative sample comparison and its dependence on the effectiveness of exposure, effect intensity, distribution of studied parameter values in the population, and sample size. The Type I and Type II errors, their average, as well as the maximal errors were considered.

Results: The sample size 9 and the *t*-test method with $p = 5\%$ ensured error smaller than 5% even for weak effects. For sample sizes 6–8 the same method enabled detection of weak effects with errors smaller than 20%. If the sample sizes were 3–5, weak effects could not be detected with an acceptable error; however, the smallest maximal error in the most general case that includes weak effects is granted by the standard error of the mean method. The increase of sample size from 5 to 9 led to seven times more accurate detection of weak effects. Strong effects were detected regardless of the sample size and method used.

Conclusions: The minimal recommended sample size for biomedical experiments is 9. Use of smaller sizes and the method of their comparison should be justified by the objective of the experiment.

1. Introduction

The sample size is an important parameter that must be decided upon when designing a biomedical experiment. There are numerous studies dedicated to the calculation of sample size in general or for a particular type of analysis, see for example [1–7]. Often, sample size calculation is focused on ensuring low probability of wrongly detecting a difference between the treated and the control populations. However, other studies recognize the importance of the power of the test and the underlying chance to wrongly miss a difference between the samples [5–7] or focus on the equivalence tests and their comparison [8,9]. Unfortunately, other restrictions, such as experimenting with animals or laboratory expenses, may influence the implemented sample size [10,11]. In such cases small samples [12–14] or even very small samples need to be considered. Experiments conducted with as little as ten samples are likely to be, at first, thought of as unjustifiable, particularly by non-biomedical scientists. However, when experimenting with cats, dogs, or non-human primates is considered, it becomes easy to understand that even ten samples may be too many. To roughly estimate the usage of small samples, we examined 264 biomedical research papers published in *Nature* from September 2012 through February 2013. It was found that 51% of them used samples whose size is not larger than 10. Further, the samples of size 3, 4, 5, 6, 7, 8, 9, and 10 were used in 72%, 38%, 38%, 40%, 37%, 42%, 32%, and 29% of the studies that used very small samples, respectively. The three most frequent sizes of 3, 8 and 6 are advised in biomedical statistics courses as the number of required repetitions of an experiment, the smallest acceptable sample size in USA, and the smallest acceptable sample size in Europe, respectively. Note that the samples smaller than 6, i.e., smaller than the

* Corresponding author.
E-mail addresses: jasna@stanfordalumni.org (J.L. Ristić-Djurović), sasa.cirkovic@ipb.ac.rs (S. Ćirković), paja@matf.bg.ac.rs (P. Mladenović), romcevi@ipb.ac.rs (N. Romčević), aleksandar.trbovic@mfub.bg.ac.rs (A.M. Trbovich).

https://doi.org/10.1016/j.cmpb.2018.01.026
0169-2607/

smallest acceptable sample size recommended in Europe as well as in USA, were used in 88% of the studies. In the 134 examined studies the very small samples were analyzed using the standard error of the mean (s.e.m.) in 71% of the studies and the standard deviation (s.d.) in 35% of the cases. The *t*-test methods with *p* parameter value of 5%, 1%, and smaller than 1% were used in 64%, 53%, and 54% of the studies, respectively. It can be argued that the considered research papers are not a representative illustration of biomedical research and that the obtained numbers cannot be assumed to reflect small biomedical sample occurrence in general. Nevertheless, they indicate that the frequency of very small sample usage is significant and that the sample sizes as well as the methods used for their comparison are not standardized.

Statistical methods are applicable under precisely defined conditions, for example, that the data distribution is normal, the distribution mean is affected but not its standard deviation, etc. However, in a typical biomedical experiment it is not known whether or not these and alike requirements hold. Examples of biomedical data distributions that do not comply with these requirements are blood pressure [15], blood glucose [16,17], body mass index [18], number of cancer cases [19], banana leaf spot disease [20], as well as the several examples given in [21]. The misinterpretations as well as unrecognized needs and incorrect applications of methods exist despite numerous textbooks in statistics that are tailored to biomedical usage, and the awareness of these issues as well as their importance emerges through papers on statistics published in biomedical journals [22–26]. Several columns [27,28] and lecture papers series referenced by the last lecture [29–31] emphasize the importance of statistical representations and methods used in biomedicine, offer summaries, and discuss some common misinterpretations as well.

Most statistical research papers that consider small samples recognize biomedicine as a field of application; however, many of them assume small samples to be of the order of several tens or not smaller than ten [3,12,14,32,33]. A number of statistical studies offer solutions or modifications of the well-known existing solutions to various types of the two-sample problem, for example [4,34–36].

Regardless of whether the usage of a particular method was mathematically appropriate (i.e., the assumptions of the method were satisfied), we considered and evaluated all the methods for very small sample comparison commonly used by the biomedical scientific community, i.e., the methods relaying on standard deviation of samples, standard error of sample means, and the *t*-test method. For example, the *t*-test method is applicable to data with the normal distribution; however, in our empirical study its performance was evaluated on non-normal data distributions as well. Further, the method that uses standard deviation of the population was investigated since it was suggested as a possible approach to the problem in the original work of Student [37]. In addition, sample range method was considered since an engineer would use this approach when dealing with small samples. To evaluate the performance of the mathematically inappropriate methods we had to use computer simulations and, for the sake of consistency, we also performed virtual experimenting for the methods whose outcomes are mathematically derivable. The performances of the considered methods were evaluated by the percentage of erroneous conclusions that the compared groups do not differ, as well as by the accuracy when reporting a difference between the groups, i.e., by the Type I as well as the Type II error. The overall performance of the methods was conveyed as the average of the two types of error and as the maximal error.

The influence of different variables on the comparison methods' performance was studied, the variables being the type, standard deviations, and difference between means of the distributions from which the data in two compared samples originate, and sample size. The aim was to find the minimal sample size and comparison method that provide desired accuracy as well as to determine the most accurate method of sample comparison for sample sizes smaller than the minimal. An additional preference was that the determined parameters depend neither on the studied effect nor on the data distribution in the population. Our study is focused on very small samples, namely on sample sizes not larger than ten. Consequently, the obtained results do not apply to large clinical studies and other types of scientific investigations where the number of subjects in the samples is in the 100s or 1000s.

2. Methods

To investigate how the results of small sample comparison depend on the distribution of events from which the samples were taken, in particular on the type and standard deviation of the data distribution, we used six data distributions depicted in Fig. 1a. For each of the three considered types of distribution, normal, uniform, and skewed, two values of standard deviations were used, namely normal data distributions, P_N with $\sigma = 2.0$, and P_{N1} with $\sigma = 3.9$; skewed distributions, P_S with $\sigma = 3.0$, and P_{S1} with $\sigma = 5.4$; and uniform distributions, P_U with $\sigma = 2.0$, and P_{U1} with $\sigma = 3.0$. The skewed distributions P_S and P_{S1} are the chi-squared distributions with 4.5 and 14.5 degrees of freedom, respectively. The event distributions were created using Matlab functions `normrnd`, `chi2rnd`, and `unifrnd`. The rationale for normal distributions were the examples of blood glucose distributions reported by Escobedo et al., [16] and Yang et al., [17], whereas skewed distributions were motivated by the examples of blood pressure [15], body mass index [18], cancer [19], and banana disease [20]. Uniform distribution is considered since it is one of the three main types of species dispersion.

To model an ineffective exposure or treatment, the data values representing the treated and the control sample were taken from the same event distribution. The influence of the standard deviation was intended to be extracted from the results corresponding to the same types of data distributions, whereas the pair P_N and P_U which both have $\sigma = 2$, as well as P_S and P_{U1}, which both have $\sigma = 3$, served to extract the influence of the data distribution type.

If it could be applied to the entire population, an effective treatment would have changed the distribution of the observed parameter values. Consequently, if a treatment is effective, the treatment group represents a different population than that of the control group. Therefore, for simulation of an effective treatment, two samples, each represented by a chosen number of studied parameter values, were taken from different data distributions. Four pairs of data distributions were used; namely, P_N and P_{N1}; P_S and P_{S1}; P_U and P_{U1}; and P_N and P_N, see Fig. 1b. For each distribution pair the difference between their means took four values; therefore, the total of 16 cases was considered. For the 12 cases that correspond to the first three pairs of distributions it was assumed that the treatment changes the mean as well as the standard deviation of the data distribution. These examples were meant to illustrate the influence of the distribution type. The four examples with the pair P_N and P_N depict the cases when the data distributions used as sources of the treated and control samples, differ only in their mean. Comparison between the (P_N, P_{N1}) and (P_N, P_N) cases is aimed to single out the influence of the standard deviation of data distribution. The intensity of a treatment was modeled by the extent the data distributions that represent the non-treated and treated groups overlap, and was measured by the difference between distribution means divided by the sum of distribution standard deviations, i.e., by $D = (\mu_2 - \mu_1)/(\sigma_2 + \sigma_1)$. For each pair of data distributions, four effect intensities were considered, weak, $D = 1$, moderate, $D = 1.5$, strong, $D = 2$, and very strong, $D = 3$. Instead of D, parameter $d = (\mu_2 - \mu_1)/\sqrt{\sigma_2^2 + \sigma_1^2}$ is often used to de-

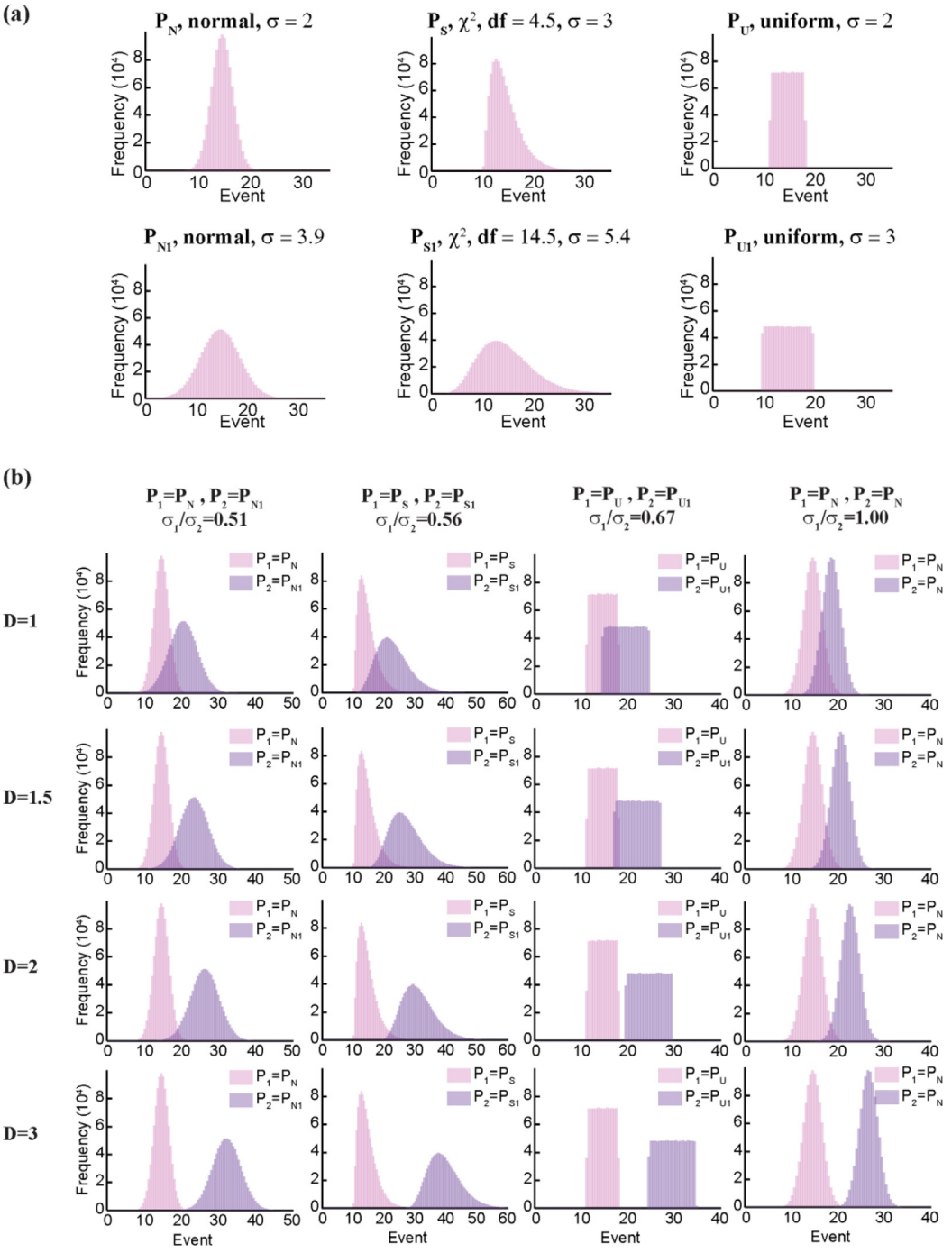

Fig. 1. Event distributions used in virtual experiments. (a) Six data distributions were used to model ineffective treatments. (b) Twelve effective treatments were modeled by four data distribution pairs with different degrees of overlapping defined by $D=(\mu_2-\mu_1)/(\sigma_1+\sigma_2)$, where μ_1 and μ_2 are data distribution means, and σ_1 and σ_2 are their standard deviations.

fine the difference between two distributions. In our examples, the values of d corresponding to $D=1$, 1.5, 2, and 3 were $d=1.3$, 2.0, 2.7, and 4.0 for $(P_1, P_2)=(P_N, P_{N1})$; $d=1.4$, 2.0, 2.7, and 4.1 for $(P_1, P_2)=(P_S, P_{S1})$; $d=1.4$, 2.1, 2.8, and 4.2 for $(P_1, P_2)=(P_U, P_{U1})$; and $d=1.4$, 2.1, 2.8, and 4.2 for $(P_1, P_2)=(P_N, P_N)$, respectively. The cases (P_N, P_N) correspond to the most common assumption in biostatistics of normal distribution whose standard deviation is not affected. The cases with $D=2$ and 3 are the most likely scenarios for all those experiments which report differences with samples smaller than 6. The effect strengths corresponding to $D=1$ and 1.5 were intended to model examples similar to those of blood glucose level, blood pressure, and airborne contamination with bacteria. Namely, the difference between the fasting glucose levels of subjects without and those with diabetes given by Escobedo et al., in [16] has the value of $D=0.92$, the differences between the normal, untreated hypertensive, and treated hypertensive blood pressure seem to be characterized by $D<1.5$ [15], whereas the airborne contaminations with bacteria at the two locations reported by Di Giorgio et al., in [38] differ by $D=1.1$. In all examples the compared data distributions had different standard deviations. Note that the considered 16 cases enabled studying the influence of data distribution type and its standard deviation, as well as of the intensity

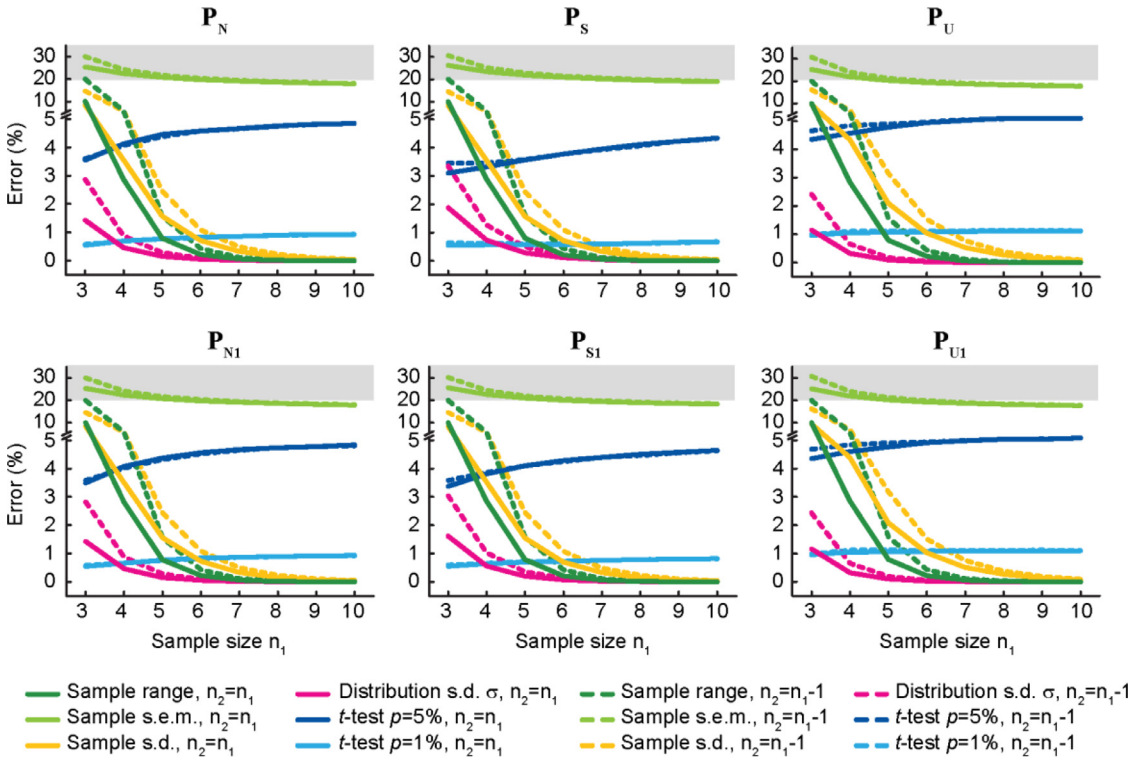

Fig. 2. Performance of methods given as probability of false positive. The position of a graph matches the position of the distribution in Fig. 1a from which the samples were taken, as indicated by the graph title. Each sample pair of size n_1 and n_2 was compared by six methods represented by different colors. The error values above the acceptable value of 20% are shaded. The data distribution type as well as its standard deviation are much less influential than the method of comparison and sample size.

of the applied effect. The test whether or not a pair of samples comes from the same data distribution was performed using six methods: the sample range, sample s.e.m., sample s.d., distribution s.d. σ, *t*-test $p = 5\%$, and *t*-test $p = 1\%$ method. In the first four methods the samples, X_1 and X_2, were taken to differ if the intervals drawn as error bars around their means, m_1 and m_2, did not overlap. The compared intervals were $[\min(X_1), \max(X_1)]$ and $[\min(X_2), \max(X_2)]$; $[m_1 - s_1/\sqrt{n_1}, m_1 + s_1/\sqrt{n_1}]$ and $[m_2 - s_2/\sqrt{n_2}, m_2 + s_2/\sqrt{n_2}]$; $[m_1 - s_1, m_1 + s_1]$ and $[m_2 - s_2, m_2 + s_2]$; and $[m_1 - \sigma, m_1 + \sigma]$ and $[m_2 - \sigma, m_2 + \sigma]$, where s_1 and s_2 are standard deviations of samples X_1 and X_2, n_1 and n_2 are their sizes, whereas σ is standard deviation of the data distribution from which samples X_1 and X_2 were taken. The two remaining methods, the *t*-test methods, were performed with the alpha parameter set to the appropriate value of 5% or 1% and the Matlab built in function `ttest2`, which uses Satterthwaite's approximation for the effective degrees of freedom.

The data populations were created and virtual experiments were performed in Matlab on Intel Core i7-2670QM 2.20 GHz processor with 8 GB of RAM.

3. Results

3.1. Type I error

When reporting a difference between two groups of data, it is important to know the probability that the groups actually come from the same population, i.e., that the difference between them is obtained by chance (false positive). To study the Type I error, ineffective treatments were simulated by drawing both samples within a pair from the same data distribution and the false outcomes of virtual experiments are summarized in Fig. 2. All six described event distributions given in Fig. 1a, were used as a source of sample pairs with the intention to investigate the influence of the type of the data distribution as well as of its standard deviation. To enhance visibility as well as to enable comparison of the testing methods the graphs have *y*-axis break.

For each of the six event distributions the experiments were performed using eight sizes of the first sample, $n_1 = 3$, 4, 5, 6, 7, 8, 9, and 10, and, for each of them, two sizes of the second sample, n_2, one equal to n_1, i.e., $n_2 = n_1$, and the other by one smaller than n_1, i.e., $n_2 = n_1 - 1$, which is depicted by solid and dashed line, respectively. Unequal sizes of samples were intended to illustrate the case when one event within a sample was corrupted and had to be discarded. For each pair of the considered values of sample sizes the virtual experiment was performed one million times. The test whether or not a pair of samples comes from the same population was run using six methods denoted by different colors. False positives obtained by each method are given as a percent of the performed million virtual experiments for each combination of sample pair sizes.

Dependence of the obtained results on the type and standard deviation of the event distribution was weak, and it was negligible compared to the dependence on the sample size and the method of comparison. Performance of the *t*-test method complied with the value declared by its *p* parameter of 5% and 1% regardless of the sample size not only for the two normal distributions of events for which this method is designed, but for the other four considered distributions that fall outside the scope of its application as well. The best overall method with respect to the Type I error was the distribution s.d. method. However, the standard deviation of a biomedical data distribution to which a control sample belongs is usually not available; therefore, in such cases one must rely on the methods that use only sample data. The sample range method is often thought of as poor statistics; however, for sample sizes equal or larger than 5, this method was the best and it ensured Type I error smaller than 0.8%. For sample sizes larger or equal to 9, the error of the sample range method was smaller than 0.005%. The *t*-

test $p=1\%$ method appeared as the method of choice for the samples of size 3 and 4. Sample corruption could be accounted for by taking the smallest sample size within an experiment as the referent.

The same qualitative dependence, regardless of the type as well as of the standard deviation of the data distribution, enabled general ranking of the applied methods. The method with the smallest Type I error was the distribution s.d. method, whereas the largest error of this type was obtained for the sample s.e.m. method. For samples with six or more events the methods listed by the increasing value of the error from the best to the worse were the distribution s.d., sample range, sample s.d., *t*-test $p=1\%$, *t*-test $p=5\%$, and sample s.e.m. method. In biostatistics, usually the acceptable value for the power of a test is 80% [39], which leads to the 20% limit for an error. Note that the sample s.e.m. method exceeds this limit.

3.2. Type II error

Had it been applied to the entire population, an effective exposure or treatment would have changed the distribution of the data of interest. Therefore, in order to detect effective treatments, samples must be compared with a method that ensures low probability of wrongly concluding that there is no difference between the two distributions (false negative). In our virtual experiments each pair of samples was compared by seven methods, for each combination of sample sizes the virtual experiment was repeated one million times, and for each method the Type II error was calculated as the percentage of false negatives. It was assumed that the two data distributions used in an experiment, P_1 and P_2, can have different standard deviations, σ_1 and σ_2, respectively, which takes into account that the studied effect can influence not only the mean of the data distribution, but its standard deviation as well. In reality, it is possible to determine the standard deviation of only one data distribution – the one which is not changed by the studied effect. Therefore, when the distribution s.d. method was used to compare two samples, the standard deviation of only one of the two distributions was used. However, in order to allow for an effect to cause a decrease as well as an increase of the standard deviation, two distribution s.d. methods were considered, each taking one of the two considered data distributions to be the event distribution not exposed to the studied effect. Since not one but two distribution s.d. methods were studied, instead of six methods compared in Section 3.1, seven methods were considered here.

The dependence of the Type II error on sample size, on effect intensity, D, as well as on the type and standard deviations of data distributions from which samples were taken, is given in Fig. 3. The four pairs of event distributions as well as four intensities of studied treatments defined in Fig. 1b were considered.

The definitions of distribution s.d., sample s.d., and sample s.e.m. methods outline the expected qualitative Type II error outcomes and imply that their Type II error associated with the distribution s.d. σ_2 (note that $\sigma_2>\sigma_1$) method is the largest, after which comes the sample s.d. error, and finally the error corresponding to the sample s.e.m. method, being the smallest.

The method with the smallest Type II error was the sample s.e.m. method. Contrary to the Type I error, the *t*-test $p=5\%$ method had smaller Type II error than the *t*-test $p=1\%$ method. For strong effects, all methods except the *t*-test $p=1\%$ method had a very small Type II error. The values of this type of error converged with the sample size increase and enabled stable ranking of methods for larger sample sizes. The sample size that provided the stable method ranking decreased with the increase of D, and ranged from 9 for $D=1$ to 6 for $D=3$.

The sample s.e.m. method which had the largest Type I error turned out to be the best regarding the Type II error. The method characterized with the smallest Type I error was the distribution s.d. method. Unfortunately, the performance of this method regarding the Type II error depended on the way a treatment or exposure affected a population. If a treatment causes an increase of the standard deviation of data distribution, i.e., in our example, if $\sigma_1<\sigma_2$, the distribution s.d. method was the second best. However, if a treatment caused a decrease of the standard deviation, the distribution s.d. method, i.e., the distribution s.d. σ_2 method had a poor performance regarding the Type II error.

Since the results shown in each row in Fig. 3 are qualitatively the same it could be concluded that the dependence of the Type II error on the method used for sample comparison, on D, and on the sample size is much stronger than on the distribution type and standard deviation of the event distributions the samples were drawn from. The general conclusion regarding the Type II error was that the best method was the sample s.e.m. method. Further, since the performance of the distribution s.d. method strongly depends on how a treatment used in an experiment changes the data distribution, it is worth considering the *t*-test $p=5\%$ method instead of the distribution s.d. σ_1 method as the second best method. For $D=1$, in addition to the sample s.e.m. method, whose power was larger than 80% for any considered sample size, the *t*-test $p=5\%$ method was the only other method that had the studied type of error smaller than 20% for all the considered distribution types, though in the limited sample size range. Unfortunately, the *t*-test methods had the most abrupt increases of the error with the sample size decrease, which caused the error corresponding to these two methods to exceed the 20% limit in all the considered cases. The cutoff occurred at larger values of sample size for larger distribution overlapping, i.e., for smaller D, and at larger sample sizes for the *t*-test $p=1\%$ than for the *t*-test $p=5\%$ method. The influence of sample corruption, i.e., the cases with $n_2=n_1-1$, indicated that the smallest sample size used in an experiment should be used as the referent sample size.

3.3. Average error

Although both Type I and Type II errors are important, the levels of their importance may differ and can be tailored to ones needs with the weighting factors. We assumed that the two error types are equally important and we used their average to determine the overall ranking of the methods. Note that the probability of false conclusion, $P(\varepsilon)$, is equal to the average error under the assumption that the probabilities of false positive and false negative outcomes are equal, $P(\mathrm{d})=P(\mathrm{nd})=0.5$. Namely,

$$P(\varepsilon)=\frac{P(\varepsilon|\mathrm{nd})\cdot P(\mathrm{nd})+P(\varepsilon|\mathrm{d})\cdot P(\mathrm{d})}{P(\mathrm{nd}|\varepsilon)+P(\mathrm{d}|\varepsilon)}=\frac{\varepsilon_{\mathrm{I}}+\varepsilon_{\mathrm{II}}}{2},$$

since $P(\mathrm{nd}|\varepsilon)+P(\mathrm{d}|\varepsilon)=1$.

As was the case with the Type II error, the pairs of data distributions depicted in Fig. 1b were considered and the obtained average errors are given in Fig. 4. The Type I error used in averaging was the one obtained for the unaffected data distribution. Therefore, the Type I error corresponding to the distribution P_1 was used for all the methods except for the distribution s.d. σ_2 method for which the Type I error corresponding to the distribution P_2 was used. As was the case with the Type I and Type II errors, their average depended very weakly on the type and standard deviation of the distribution. The exceptions were the distribution s.d. methods, which, for the average error, followed the trend established for the Type II error. The average error decreased with the increase of the distance between the populations, D, as well as with the increase of sample size.

For D values larger than 1, the distribution s.d. σ_1 method was the best and the sample s.d. method was the second best method for all the considered distributions. For $D=1$, if the samples were

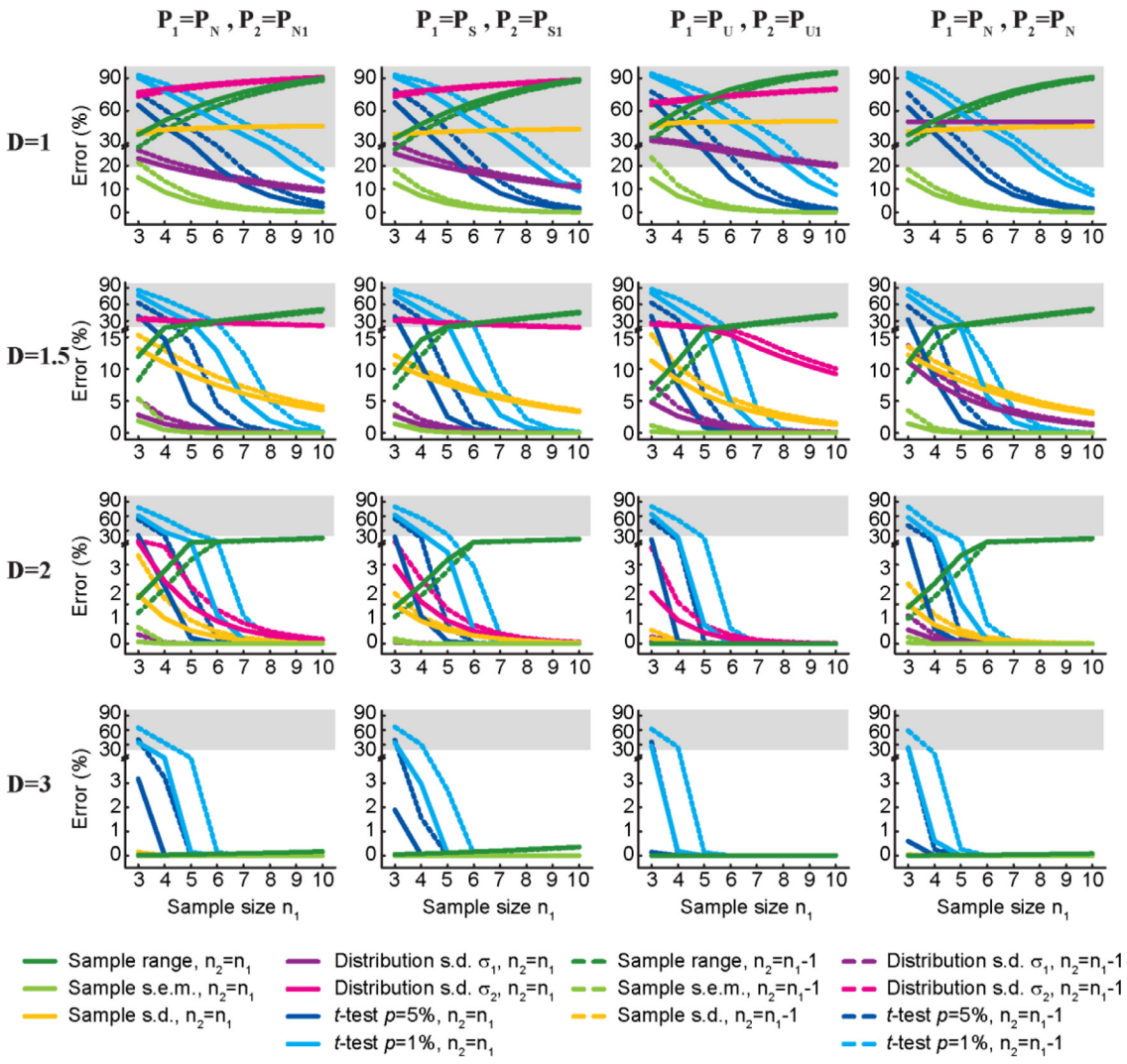

Fig. 3. Performance of methods given as probability of false negative. The placement of graphs corresponds to the placement of the distribution pairs in Fig. 1b used as sample sources. The same set of sixteen combinations of sample sizes n_1 and n_2 as well as the same labeling were used as in Fig. 2. The error values above the acceptable value of 20% are shaded. The influence of the distributions and standard deviation of data is negligible compared to the influence of the intensity of applied effect, method of comparison, and sample size.

taken from the normal or skewed distributions (the first row in the first and second column of graphs in Figs. 1b and 4), the best and the second best methods were the distribution s.d. σ_1 method and the *t*-test $p=5\%$ method, respectively. For the best method, the sample size cutoffs were at size 4 and 5 for the normal and skewed distribution, respectively, whereas for the second best method the sample size limit was at 6 for both distributions. Note that the referent sample size is the smaller one within the compared pair of samples. For the uniform distributions and normal distributions with equal standard deviations, represented respectively in the third and fourth columns of graphs in Fig. 1b, and the distribution s.d. σ_1 method had the probability of wrongly missing a difference larger than 20% if $D=1$, as can be seen from the corresponding graphs in Fig. 4. Therefore, the best and the only available method became the *t*-test $p=5\%$ method. For the uniform distributions as well as for the normal distributions with equal standard deviations, the sample size limit was 6. If the Type II error for weak effects was not to be larger than the corresponding Type I error of approximately 5%, the sample size had to be larger than 8, as can be seen from the graph in the first column and first row in Fig. 3.

If only non-overlapping distributions were considered, i.e., $D=3$, which is likely the case for the experiments that report differences between samples of sizes smaller than 6, the ranking of methods from the best to the worst was the distribution s.d. σ_2, distribution s.d. σ_1, sample range, sample s.d., *t*-test $p=1\%$, *t*-test $p=5\%$, and sample s.e.m. method. Note that in this case, the best readily available method, i.e., the method relying on sample data, is the sample range method. From Fig. 4 it could be seen that the difference between the overall performances of the distribution s.d. σ_1 and distribution s.d. σ_2 method decreased with the increase of D and that they became equal for $D=3$. For the case of normal distributions with equal standard deviations (fourth column of graphs in Figs. 1b and 4), i.e., $\sigma_1=\sigma_2$, the two methods became one method that took the role the distribution s.d. σ_1 method had for all other considered distributions and that was the best overall method for D larger than 1.

It can be summarized that the best overall method with respect to the average error was the distribution s.d. σ_1 method. For $D=1$ the second best was the *t*-test $p=5\%$ method. For all other values of D the second best was the sample s.d. method since it had no restrictions on the minimal sample size imposed by the 20% limit associated with the Type II error.

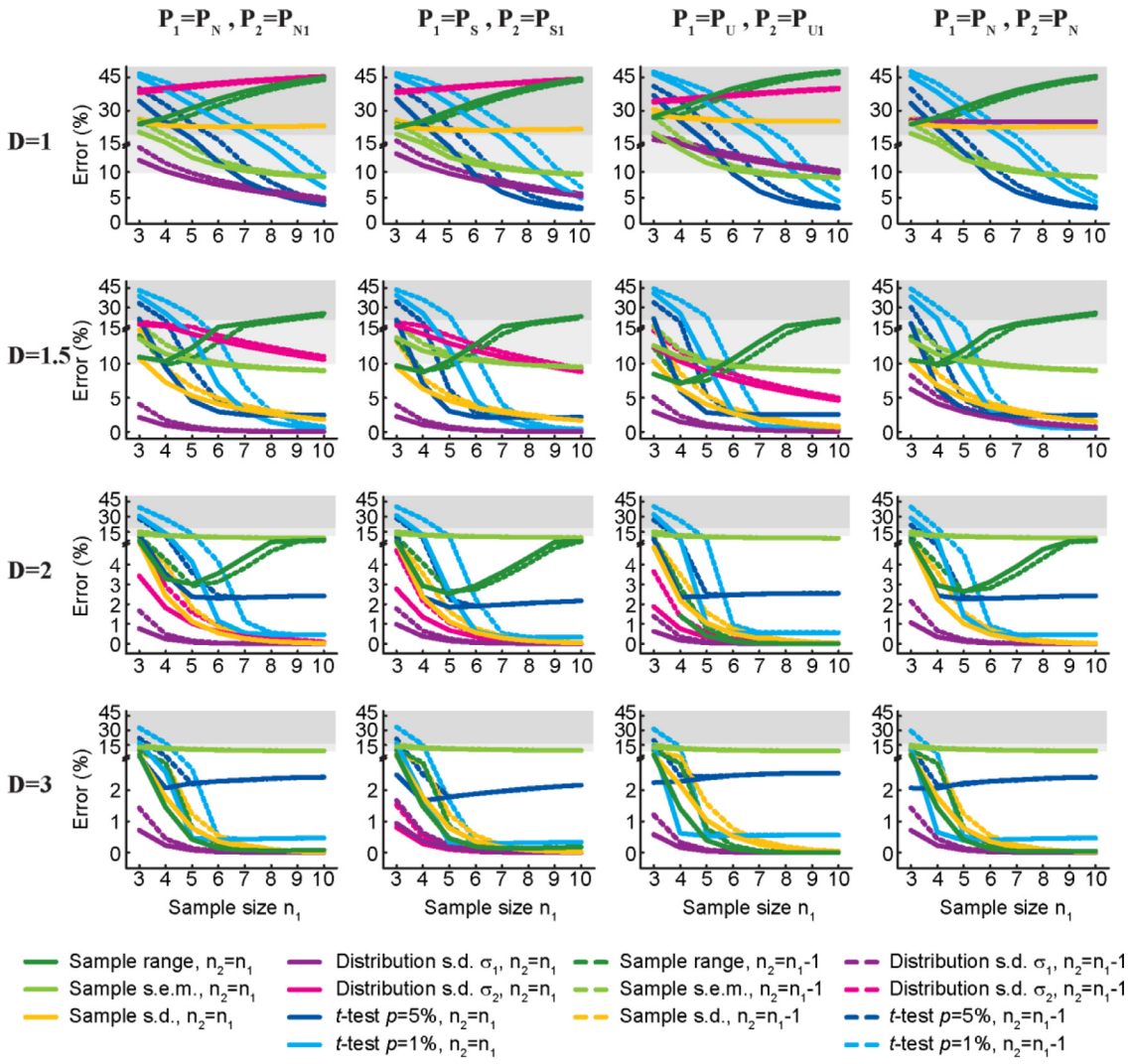

Fig. 4. Performance of methods with respect to average error. The figure format is the same as the format of Fig. 3. In addition to the 20%, the 10% error limit is depicted with the lighter shade of gray since averaging places the actual acceptable average error bond between these two values.

3.4. Choosing sample size and method

Our results indicated that, for each of the considered methods, there were conditions under which a particular method had the best performance. The generally applicable sample size and method should be independent on the experimental conditions, i.e., on the studied effect as well as on the data distribution of a parameter the effect is acting upon. However, the populations from which the groups of collected data come, distributions of data within these populations as well as the extent of their overlapping are determined by the effect that is being studied in an experiment; therefore, they are not known in advance and they cannot be determined from the collected data due to its very small size. On the other hand, the sample sizes and the method used for statistical analysis are fully controllable. Consequently, it is the sample size and method of comparison that must be carefully chosen in order to obtain the most from the gathered data in terms of information quantity as well as accuracy.

Since the generally applicable sample size and method of comparison must comprise the worst considered cases, it was the maximal error that was used to determine them. As the referent sample size, n, the smaller of the compared samples was used, namely $n = \min(n_1, n_2)$. Consequently, the maximal Type I and Type II errors became

$$\varepsilon_{\mathrm{I}}(n, D, m) = \max(\varepsilon_{\mathrm{I}}(n_1 = n, n_2 = n, D, m), \varepsilon_{\mathrm{I}}(n_1 = n + 1, n_2 = n, D, m))$$

$$\varepsilon_{\mathrm{II}}(n, D, m) = \max(\varepsilon_{\mathrm{II}}(n_1 = n, n_2 = n, D, m), \varepsilon_{\mathrm{II}}(n_1 = n + 1, n_2 = n, D, m)),$$

i.e., the worse of the cases having equal smaller sample size within the compared sample. For each of the four considered pairs of data distributions, maximal error was defined as

$$\varepsilon_{\mathrm{P}_1,\mathrm{P}_2}(n, D, m) = \max(\varepsilon_{\mathrm{I}}(n, \mathrm{P}_1, m), \varepsilon_{\mathrm{I}}(n, \mathrm{P}_2, m), \varepsilon_{\mathrm{II}}(n, \mathrm{P}_1, \mathrm{P}_2, D, m),),$$

where ε_{I} and $\varepsilon_{\mathrm{II}}$ are the probabilities of wrong positive and wrong negative outcomes, n is the referent size of the compared samples, P_1 and P_2 are the data distributions that samples were taken from, D defines the studied effect intensity, and m is a sample comparison method. For the maximal error of the distribution s.d. σ method, the larger of the errors corresponding to the distribution s.d. σ_1 and the distribution s.d. σ_2 method was used, i.e.,

$$\varepsilon_{\mathrm{P}_1,\mathrm{P}_2}(n, D, \text{popul. s.d.}\,\sigma) = \max(\varepsilon_{\mathrm{P}_1,\mathrm{P}_2}(n, D, \text{popul. s.d.}\,\sigma_1), \varepsilon_{\mathrm{P}_1,\mathrm{P}_2}(n, D, \text{popul. s.d.}\,\sigma_2)).$$

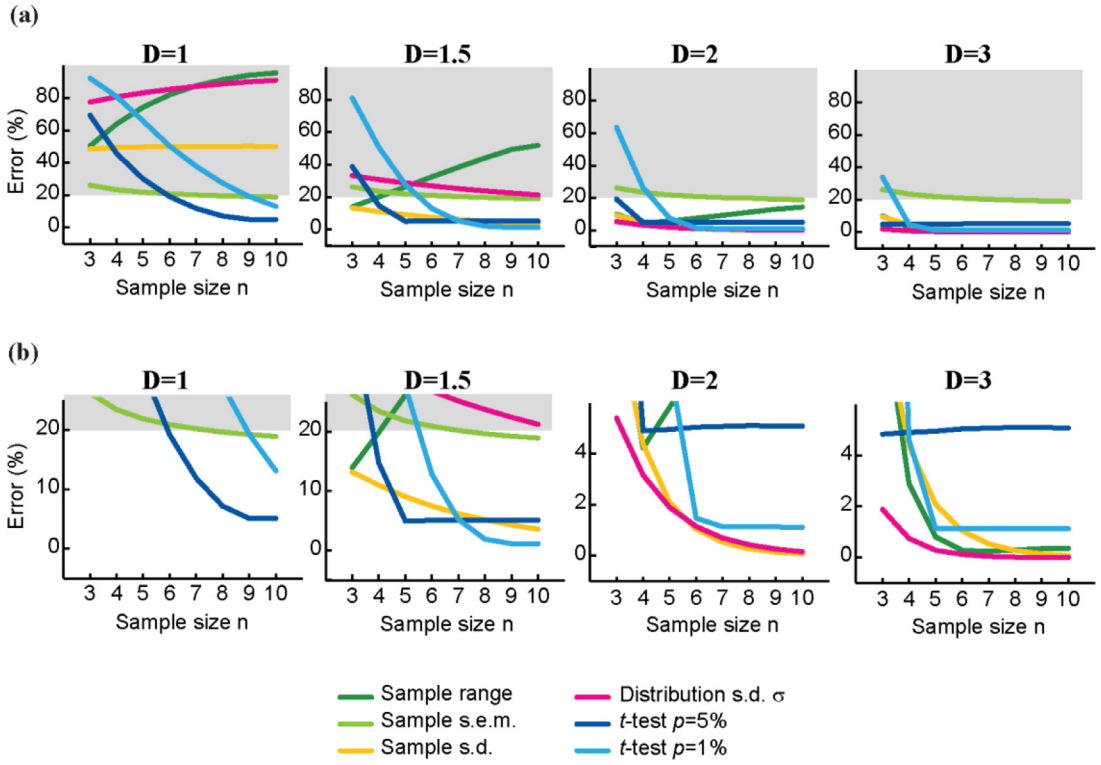

Fig. 5. Maximal error. The graphs in panel (b) emphasize lower part of the corresponding graphs in panel (a). For each size of the smaller sample within a pair the maximal error is taken to be the largest of the probabilities to wrongly miss or detect a difference among all errors that correspond to four considered pairs of probabilities. The error values above the acceptable value of 20% are shaded. The sample size and method of comparison should provide minimal value of the maximal error.

Further, the worst of the four considered pairs was selected, i.e.,

$$\varepsilon(n, D, m) = \max(\varepsilon_{P_N,P_N}(n, D, m), \varepsilon_{P_N,P_{N1}}(n, D, m), \varepsilon_{P_S,P_{S1}}(n, D, m), \varepsilon_{P_U,P_{U1}}(n, D, m))$$

The obtained maximal errors are shown in Fig. 5. Since strength of the effect studied in an experiment is normally unknown, general applicability regardless of the effect strength can be granted only if the worst of the considered cases is considered. The worst considered case with respect to the effect strength is the weak effect case $D=1$; therefore, the maximal error independent on D was

$$\varepsilon(n, m) = \max(\varepsilon(n, D, m)) = \varepsilon(n, D = 1, m).$$

In general, larger sample size provides better accuracy leading to a tradeoff when choosing optimal sample size and method of comparison. As seen from the graphs corresponding to the weak effects, i.e., to $D=1$ in Fig. 5, in our case minimal value of $\varepsilon(n, m)$ was achieved with the *t*-test 5% method and two sample sizes, namely

$$\min(\varepsilon(n, m)) = \varepsilon(9, t-\text{test } 5\%) = \varepsilon(10, t-\text{test } 5\%).$$

Consequently, the smaller of the two sample sizes is chosen and the generally applicable sample size and method of comparison were found to be $n=9$ and the *t*-test 5% method.

The minimal power of a test in biomedical statistics is set to 80%. Therefore, the methods with the maximal error larger than 20% were discarded since they did not comply with this requirement. The sample size was constrained as well, since we considered only $n \leq 10$. Consequently, the maximal error, $\varepsilon(n, m)$, and search for its minimum can be viewed as an optimization function and optimization procedure, respectively.

4. Discussion

The generally applicable, optimal sample size and method for qualitative comparison of very small samples were found to be $n=9$ and the *t*-test 5% method. Under the common assumption in biostatistics that the considered effect does not change the standard deviation of normal distribution of studied events, which corresponds to the example $P_1 = P_2 = P_N$, the sample size ensuring weak effects detection with an error smaller than 5% was found to be 8. This sample size is equal to the smallest acceptable sample size recommended in USA. Note that the sample of size 9 is obtained here as the optimal regardless of the experimental data distribution. Having the 20% error limit in mind, Fig. 5 also revealed that weak effects could not be detected with sample sizes smaller than 6, which is the smallest acceptable sample size recommended in EU. For $D=1$, the probabilities of the *t*-test 5% method to wrongly detect a difference, which is constant, and to miss a difference, which decreases with the sample size increase, intersect at $n=9$. Consequently, the maximal error for $D=1$ is equal to the probability of the *t*-test 5% method to register a false positive for $n \geq 9$ and a false negative for $n < 9$. If weak effects were to be detected with the probability of false negative equal to or smaller than the probability of false positive, the sample size had to be 9 or larger. If for some reason the sample size could not be chosen, the comparison methods with the smallest maximal error for the sample size ranges 3–5 and 6–10 were the sample s.e.m. method and the *t*-test $p=5\%$ method, respectively, in the most general case that includes weak effects.

We found that the frequent use of a *t*-test with smaller *p* values in biomedical research causes a dramatic increase of the probability of false negative, whereas a larger *p* value increases the probability of false positive only to the value declared by the chosen *p*. The detection of weak effects with the *t*-test $p=5\%$ came at the

expense of a larger average error if a treatment or exposure happened to be not so weak or ineffective. In other words, if one is interested only in the cases that correspond to $D \geq 2$, the method of choice should be the sample s.d. method, or the sample range method for very strong effects, i.e., for $D = 3$, regardless of the sample size.

For example, if a significant difference between samples of the size 4 is reported using the t-test $p = 1\%$ method, the studied effect must have been strong or very strong since we obtained that the likeliness of the false negative corresponding to the chosen method and sample size was on the average 78.79%, 48.32%, 20.18%, and 2.06% for weak, moderate, strong and very strong effects, respectively. If the data had been analyzed with the sample s.d. method, the same result would have been obtained with the smaller probability of the false negative of 0.86% for strong or 0.0025% for very strong effects. The comparison of the average errors for strong and very strong effects corresponding to the sample s.d. method of 2.31% and 1.88%, and to the t-test $p = 1\%$ method of 10.47% and 1.41%, respectively, favors sample s.d. method, as well. For commonly used smaller values of t-test's parameter p, i.e., $p < 0.01$, average error values will be larger; therefore, the argumentation in favor of sample s.d. method will be stronger.

If experiments had been performed with samples of the size 9, the probability of wrongly concluding that a treatment was effective and ineffective, including weak effects, would have been 4.76% and smaller than 2.70%, respectively, using the t-test $p = 5\%$ method. However, if weak effects had been excluded, the chances for erroneous conclusions regarding effective and ineffective treatments would have been 4.76% and 0.01% for the t-test $p = 5\%$ method, and 0.09% and 3.37% for the sample s.d. method, respectively. Exclusion of moderate effects favored sample s.d. method even more, since in that case the average errors corresponding to the t-test $p = 5\%$, t-test $p = 1\%$, and sample s.d. method were 2.37%, 0.45%, and smaller than 0.07%.

In all the considered cases with $D > 1.5$ or if only the Type I error is of importance, which, judging by the number of reports that use sample sizes smaller than 6, seem to be the cases biomedical research community is often interested in, it was actually the distribution s.d. method that was the best method regardless of the sample size. However, the standard deviation of the unaffected data distribution, σ, on which this method is based, is usually not readily available. Therefore, if general opinion is that biomedical research should be restricted to these cases, it seems worthwhile to take upon Gosset's suggestion [37] and look into the possibility of finding out the standard deviation of the data distribution from which the unaffected sample, i.e., the control group, is drawn. It is very rare that a large biomedical population can be used for experimenting. However, the same biomedical parameter is often investigated in a number of experiments during a single study, as well as in different studies conducted by the same or different research teams. Regardless of their source, the data corresponding to the unaffected samples could be merged into an event distribution, and event distributions of different commonly used parameters could be grouped in a publicly available data base.

The presented study does not include cases with treated and control samples originating from different types of data distributions. However, such cases are not expected to cause significant changes in the obtained results because it was shown that the data distribution type is the least influential of the considered parameters. On the other hand, the consideration of larger distribution overlapping, i.e., smaller D, as well as the search for conditions and methods that will enable overall accuracy better than 95% will be much more significant. The extension of the study in these directions must include sample sizes larger than 10.

5. Conclusion

If a strength of an effect studied in an experiment is not known, the sample size 9 and the t-test method with its p parameter set to 5% were obtained as the generally applicable sample size and method for qualitative comparison of very small samples. The obtained sample size and method of comparison insure the accuracy of reporting that samples are different as well as not-different to be larger than 95% regardless of the strength and nature of the effect applied in our virtual experiments. The increase of the sample size from 5 to 9 decreased the error of missing a weak effect from 30.11 to 4.25%. In other words, doubling the sample size led to seven time better accuracy of the conclusion. For comparison of small biomedical samples, a cost-effectiveness analysis becomes a tradeoff between the cost, sample size, achieved accuracy, experimenting ethics, and ethical aspects of the implementation of the obtained results to humans. Having this in mind, the analysis of the accuracy gained by the sample size increase indicated that the obtained small sample size, 9, was cost-effective, as well. A rough estimate showed that the use of sample sizes smaller than 6, which exclude the detection of weak effects expected to be the most present in nature, is not uncommon in biomedical research. For such sample sizes, the optimal method of comparison was obtained to be the sample s.d. method. However, we strongly suggest that the sample sizes smaller than 9 should not be used in a typical biomedical research, and that if such sizes are used in a published research they must be well argued and justified by the experimental conditions and/or results of interest.

Acknowledgment

This work was supported by the Serbian Ministry of Education, Science and Technological Development under grants III-45003 and III-41019.

Author disclosure statement

No competing financial interests exist.

References

[1] C. Adcock, Sample size determination: a review, Statistician 46 (1997) 261–283.
[2] A.L. Hand, J.D. Stamey, D.M. Young, Bayesian sample-size determination for two independent Poisson rates, Comput. Methods Prog. Biomed 104 (2011) 271–277.
[3] M. Rotondi, A. Donner, Sample size estimation in cluster randomized trials: an evidence-based perspective, Comput. Stat. Data An. 56 (2012) 1174–1187.
[4] S. Zhang, J. Cao, C. Ahn, A GEE approach to determine sample size for pre- and post-intervention experiments with dropout, Comput. Stat. Data An. 69 (2014) 114–121.
[5] C. Ahn, J.E. Overall, S. Tonidandel, Sample size and power calculations in repeated measurement analysis, Comput. Methods Prog. Biomed. 64 (2001) 121–124.
[6] F. Gao, A.K. Manatunga, S. Chen, MSurvPow: a FORTRAN program to calculate the sample size and power for cluster-randomized clinical trials with survival outcomes, Comput. Methods Prog. Biomed. 78 (2005) 61–67.
[7] T. Yamada, N. Kinukawa, T. Nakamura, Y. Nose, Simulation program for power and sample size determination in logistic analysis of single nucleotide polymorphisms when the response variable is subject to misclassification, Comput. Methods Prog. Biomed. 96 (2009) 42–48.
[8] M. Meyners, Equivalence tests – a review, Food Qual. Prefer. 26 (2012) 231–245.
[9] G. Shieh, A comparative appraisal of two equivalence tests for multiple standardized effects, Comput. Methods Prog. Biomed. 126 (2016) 110–117.
[10] G.B. Byrnes, A Markov model for sample size calculation and inference in vaccine cost-effectiveness studies, Stat. Med. 21 (2002) 3249–3260.
[11] S.-J. Sarker, A. Whitehead, K. Iftekhar, A C++ program to calculate sample sizes for cost-effectiveness trials in a Bayesian framework, Comput. Methods Prog. Biomed. 110 (2013) 471–489.
[12] P. Musonda, M.N. Hocine, H.J. Whitaker, C.P. Farrington, Self-controlled case series analyses: small-sample performance, Comput. Stat. Data An. 52 (2008) 1942–1957.
[13] M. Macaš, L. Lhotská, E. Bakstein, D. Novák, J. Wild, T. Sieger, P. Vostatek, R. Jech, Wrapper feature selection for small sample size data driven by complete error estimates, Comput. Methods Prog. Biomed. 108 (2012) 138–150.

[14] S. Liu, E.A. Maharaj, A hypothesis test using bias-adjusted AR estimators for classifying time series in small samples, Comput. Stat. Data An. 60 (2013) 32–49.
[15] J.D. Wright, J.P. Hughes, Y. Ostchega, S.S. Yoon, T. Nwankwo, Mean systolic and diastolic blood pressure in adults aged 18 and over in the United States, 2001–2008, National Center for Health Statistics, Hyattsville, MD, 2011.
[16] J. Escobedo, X. Velasco, F. Pellegrini, M. Copetti, Bimodal blood glucose distribution in a Mexican Indian population. Should diagnostic cut-off values be revised in specific populations? J. Diabet. Res. Clin. Metabol. (2013). http://www.hoajonline.com/journals/pdf/2050-0866-2-19.pdf, doi:10.7243/2050-0866-2-19.
[17] Y. Yang, J. Fan, S. May, Bimodality of plasma glucose distributions in whites: a bootstrap approach to testing mixture models, J. Data Sci. 8 (2010) 483–493.
[18] A.S. Penman, W.D. Johnson, The changing shape of the body mass index distribution curve in the population: implications for public health policy to reduce the prevalence of adult obesity, Prevent. Chron. Dis. 3 (3) (2006) 1–4.
[19] Cancer Research UK, 2017. All cancers excluding non-melanoma skin cancer (C00-97 Excl. C44): 2010-2012 http://www.cancerresearchuk.org/sites/default/files/cstream-node/cases_crude_all_0.pdf.
[20] R.A. Romero, T.B. Sutton, Sensitivity of *Mycosphaerella fijiensis*, causal agent of black Sigatoka of banana, to propiconazole, Phytopathology 87 (1997) 96–100.
[21] E. Limpert, W.A. Stahel, M. Abbt, Log-normal distributions across the sciences: Keys and clues, BioScience 51 (2001) 341–352.
[22] A. Hart, Mann–Whitney test is not just a test of medians: differences in spread can be important, Br. Med. J. 323 (2001) 391–393.
[23] J.A. Sterne, G.D. Smith, Sifting the evidence: what's wrong with significance tests? Br. Med. J. 322 (2001) 226–231.
[24] P. Nagele, Misuse of standard error of the mean (SEM) when reporting variability of a sample. A critical evaluation of four anaesthesia journals, Br. Med. J. 90 (2003) 514–516.
[25] D.L. Vaux, Error message, Nature 428 (2004) 799.
[26] S.C. Landis, S.G. Amara, K. Asadullah, et al., A call for transparent reporting to optimize the predictive value of preclinical research, Nature 490 (2012) 187–191.
[27] G. Cumming, F. Fidler, D.L. Vaux, Error bars in experimental biology, J. Cell Biol. 177 (2007) 7–11.
[28] D.L. Vaux, Know when your numbers are significant, Nature 492 (2012) 180–181.
[29] J.B. Carlin, L.W. Doyle, Statistics for clinicians. 8: non-parametric methods for continuous or ordered data, J. Paediatr. Child Health 39 (2003) 309–311.
[30] N. Altman, M.I. Krzywinski, Points of significance: clustering, Nat. Methods 14 (2017) 545–546.
[31] K.L. Sainani, The value of scatter plots, PM R 8 (2016) 1213–1217.
[32] T.J. Santner, V. Pradhan, P. Senchaudhuri, C.R. Mehta, A. Tamhane, Small sample comparison of confidence intervals for the difference of two independent binomial proportions, Comput. Stat. Data An. 51 (2007) 5791–5799.
[33] P. Delicado, M.N. Goria, A small sample comparison of maximum likelihood, moments and L-moments methods for the asymmetric exponential power distribution, Comput. Stat. Data An. 52 (2008) 1661–1673.
[34] S.A. Julious, M.J. Campbell, D.G. Altman, Estimating sample sizes for continuous, binary, and ordinal outcomes in paired comparisons: practical hints, J. Biopharm. Stat. 9 (1999) 241–251.
[35] R. Wang, S.W. Lagakos, R.J. Gray, Testing and interval estimation for two-sample survival comparisons with small sample sizes and unequal censoring, Biostatistics 11 (2010) 676–692.
[36] M. Biswas, A.K. Ghosh, A nonparametric two-sample test applicable to high dimensional data, J. Multivar. Anal. 123 (2014) 160–171.
[37] Student, the probable error of a mean, Biometrika 6 (1908) 1–25.
[38] C. Di Giorgio, A. Krempff, H. Guiraud, P. Binder, C. Tiret, G. Dumenil, Atmospheric pollution by airborne microorganisms in the city of Marseilles, Atmos. Environ. 30 (1996) 155–160.
[39] E.J. Hanrahan, G. Madupu, Appleton & Lange's Review of Epidemiology & Biostatistics For USMLE, Appleton & Lange, Norwalk, CT, 1994.

Design of a Combined Function Magnet With Individually Adjustable Functions

Andjelija Ž. Ilić, *Member, IEEE*, Saša T. Ćirković, Milan M. Ilić, *Member, IEEE*, and Jasna L. Ristić-Djurović

***Abstract*— Design of combined function magnets for accelerators is often limited to minor modifications of the existing components, maintaining the high quality of the main harmonic field component, but restricting the range of operation. We investigate the possibility to achieve a wide range of both steering magnetic flux density and focusing field gradients, by utilizing two individually powered magnet parts. A general design methodology is presented, enabling fully customized design and optimization of magnets for different applications. The design procedure is illustrated via a detailed design of a magnet proposed for application in the stripping extraction system of a multipurpose cyclotron.**

***Index Terms*— Accelerator magnets, analytical modeling, combined function magnets (CFMs), design optimization, finite-element analysis, ion beam focusing, ion beam steering.**

I. Introduction

SPACE and cost reduction in the design of system components is one of the current topics in accelerator physics and related technologies. Combined function magnets (CFMs) present an attractive solution to achieve the desired compact design. Most often, the CFMs are used in beam lines, storage rings, synchrotrons, and linear accelerators [1]–[7]. A reduction in an otherwise very large number of magnets, required in these structures, is facilitated by combining of dipole, quadrupole, and/or sextupole fields in a fewer number of components. In many cases, the CFM design relies on the standard quadrupole or sextupole design, with the addition of extra coils, resulting in the combined function. This seems to be the most straightforward solution from the standpoint of maintaining the high field quality, while avoiding a cumbersome custom CFM design, as well as possible fabrication errors. If independent powering of the additional coils is enabled, a combined function is established; however, additional field components remain supplemental and adjustable within a limited range. Without independent powering, the ratios of the harmonic field components are fixed by design. When CFMs are incorporated into compact structures, such as medical gantries or medical accelerators [8], [9], it is reasonable to undertake a custom design and optimization of magnets. After fabrication and assembly, further analyses are usually conducted to assess the performance and to ensure fulfillment of the design goals [10], [11].

We investigate a general design methodology and parameter optimization for the customized CFM design with the individually adjustable bending and focusing functions. Namely, the ferromagnetic structure and the pole profile shapes are sought, that allow the CFM operation in various regimes, depending on the powering of the coils. The feasibility of the proposed concept has been confirmed in our previous study [12]. Two independently powered slanted dipoles comprised the CFM, whose design specifications were set having in mind its utilization in the extraction system of a multipurpose cyclotron. The increased design complexity for the extraction system comes as a price for the cost-efficient acceleration of a number of ion beams for various applications, obtained by changing the operating mode of the machine. Stripping extraction systems are a good solution for the extraction of more than one beam into a single transport line [13]–[15]. If both the negative and positive ion beams are accelerated, beam paths, as well as transverse emittances, will vary significantly after the stripping extraction, depending on the sign of ion charge during acceleration [16]–[19]. Directions of ion beams accelerated as positive will not differ very much among themselves; however, focusing of the beams in the horizontal direction will be required as soon as they leave the cyclotron. For the ion beams accelerated as negative, focusing after extraction is usually not required, due to the change of sign during stripping. However, directions after the extraction will be significantly different from those of ion beams accelerated as positive. Therefore, adjustable strong horizontal focusing, combined with weak horizontal bending, is needed for the ion beams accelerated as positive, whereas strong horizontal bending in the opposite direction is required for beams accelerated as negative. As explained in [12], a single device per cyclotron is required, ion beams will pass through the CFM only once, off-centered from the device axis, and the minimization of higher multipole harmonics is not critical to the extracted beam quality.

The design optimization that is the subject of this paper is quite general and applicable to diverse slanted dipole CFM designs. We employ it in the detailed development of the

Manuscript received December 7, 2016; revised February 5, 2017 and March 15, 2017; accepted March 15, 2017. Date of publication March 20, 2017; date of current version May 16, 2017. This work was supported by the Serbian Ministry of Education, Science, and Technological Development under Grant III-45003.

A. Ž. Ilić, S. T. Ćirković, and J. L. Ristić-Djurović are with the Institute of Physics, University of Belgrade, 11080 Zemun-Belgrade, Serbia (e-mail: andjelijailic@ieee.org; sasa.cirkovic@ipb.ac.rs; jasna@stanfordalumni.org).

M. M. Ilić is with the School of Electrical Engineering, University of Belgrade, 11120 Belgrade, Serbia, and also with the Department of Electrical and Computer Engineering, Colorado State University, Fort Collins, CO 80523-1373 USA (e-mail: milanilic@etf.rs).

Color versions of one or more of the figures in this paper are available online at http://ieeexplore.ieee.org.

Digital Object Identifier 10.1109/TNS.2017.2684745

CFM for the stripping extraction in a multipurpose cyclotron, building upon the results of our previous study, which was to check on the validity of the proposed concept rather than to achieve the final device configuration. While the superconducting CFM design relies mostly on optimizing the coil winding configuration [8], [20], modeling of the ferromagnetic core electromagnets, as well as ferromagnetic dominated superconducting magnets (superferric magnets), focuses on achieving the most suitable pole profile configuration [2], [21]. However, unless a large degree of angular (polar) symmetry is assumed, it is preferable to perform both the linear and the nonlinear analysis. Although extensive numerical calculations are indispensable in the accurate modeling of ferromagnetic cores, mapping of the complete design space in that way would be unpractical. On the other hand, analytical modeling of current sheets can provide a good first approximation of the field due to the coils, permanent magnets, or highly saturated ferromagnetic parts. Therefore, we suggest the following methodology. In the first step, an individual slanted dipole is modeled analytically, mapping the relevant magnetic field parameters for that case. The purpose of analytical modeling is to estimate the relative changes in magnetic field parameters of interest with variation of dipole geometrical parameters. With the use of obtained data, the ranges of input parameters for accurate but time consuming numerical calculations can be narrowed. A more realistic analytical model for the slanted dipole is assumed in this paper, in comparison to [12], and the optimization is extended to the six-parameter design space. Additionally, a pool of the best solutions is selected instead of a single set of parameters, to ensure that no good solutions are omitted. Some of the parameters are then fixed, and the rest of the analysis is performed using the finite-element software tools. Special attention is directed to the linearity of the magnetic flux density within the beam area. In particular, poor linearity in the single dipole case prevents obtaining the field of satisfactory quality for different combinations of coil currents. Excellent linearity of the single dipole magnetic flux density, obtained analytically, will be somewhat deteriorated in practice due to the nonlinear behavior of magnetic materials. Sum of the dipole fields additionally includes the coupling effects; even so, satisfactory field quality can be expected if the initial requirements were stringent enough. Pole profiling is performed last, followed by the analysis of operating modes that can be attained. Iterative pole profiling can be done if further improvements in any of the design criteria are required. An outline of the necessary steps in the optimization process is next illustrated through the design of the CFM for the stripping extraction system.

II. Analytical Problem Modeling

Analytical modeling of a single slanted off-centered dipole, relying on the two-parameter ideal dipoles model, as well as the four-parameter current stripes model, has been performed in [12]. Despite the fact that the first model is point-based, whereas the second model is infinitely long in parallel to the CFM axis, general conclusions regarding the pole positioning and the slant angle optimization were similar. The positioning of the poles with respect to the CFM axis is defined using the

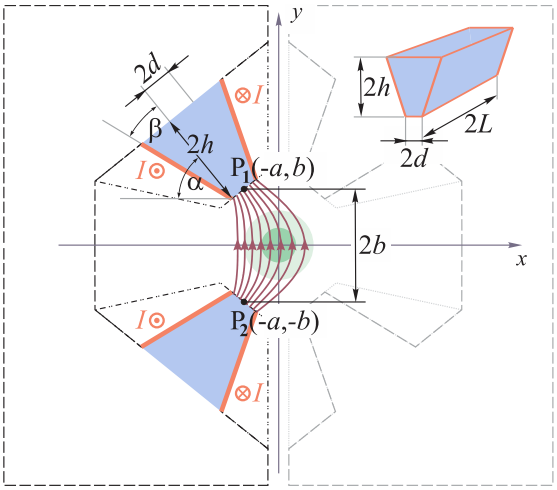

Fig. 1. Generalized slanted dipole CFM design. Only half of the CFM and its magnetic flux lines are shown. Independent powering of the two identical halves allows the CFM operation in various regimes. Linearity of the achieved fields within the beam area, depicted by the green circle about the origin, should be as good as possible. Geometrical parameters that can be varied in the design optimization are denoted in the figure. These are: the normalized half-distance between the poles of a dipole, b/a, slant angle, α, wedge angle, β, normalized half-width of the poles, d/a, normalized half-height of the poles, h/a, and normalized half-length of the poles, L/a. The small top right figure shows a side view of a pole tip, with denoted dimensions.

aspect ratio, b/a, of the rectangle whose sides equal the vertical and the horizontal distance of the pole midline from the CFM axis, as shown in Fig. 1. The slant angle is denoted by α. The four-parameter model additionally considered the pole width and height. However, in order to realistically model the actual pole geometry, we must also account for the finite length of the structure, as well as the widening of the poles toward the yoke. Widening of the poles toward the yoke improves the magnetic flux leading capabilities of the entire dipole, whereas the narrower pole tips result in the desired good field linearity in the beam area. With this proper positioning of the ferromagnetic–vacuum boundary surface, and assuming the uniform magnetization over the volume of a single pole, effect of the ferromagnetic material on the magnetic flux density can be modeled using the equivalent magnetization currents

$$\mathbf{J}_{\mathrm{mS}} = \mathbf{M} \times \mathbf{n}. \tag{1}$$

In (1), $\mathbf{M}$ denotes the magnetization vector, $\mathbf{J}_{\mathrm{mS}}$ the surface current density vector due to the equivalent magnetization currents, and $\mathbf{n}$ the surface normal, i.e., the unit vector perpendicular to the boundary surface, directed from the ferromagnetic outwards. The assumption of uniform magnetization is appropriate for modeling of permanent magnets or highly saturated ferromagnetic cores, whereas for a smaller magnetomotive force this model gives a first approximation of the magnetic flux density due to the ferromagnetic material. Magnetic flux density components resulting from the current coils in a vacuum are typically several times smaller than the total magnetic flux density components due to the coils and magnetic cores. Therefore, to keep the analytical model simple, we assume close adherence of the current coils to the core boundary surfaces. Four current sheets per pole are

modeled—two rectangular current sheets perpendicular to the xOy plane as shown in Fig. 1, as well as two trapezoidal current sheets parallel to the xOy plane at a distance $z = \pm L$ from the xOy plane.

Denoting the coil current per unit width of the current sheet by J_{ccS}, the total model current, I, results from integration over the current sheet width of the total surface current density $\mathbf{J}_0 = \mathbf{J}_{\mathrm{ccS}} + \mathbf{J}_{\mathrm{mS}}$. For the rectangular and trapezoidal sheets, $J_0^R = |\mathbf{J}_0^R| = I\cos\beta/(2h)$ and $J_0^T = |\mathbf{J}_0^T| = I/(2h)$, respectively. Each of the four current sheets can be regarded as a collection of finite straight thin wires, such as the one shown in Fig. 2, carrying the current $\mathrm{d}I$ and producing the magnetic flux density component $\mathrm{d}B$ [22], [23]

$$dB = \frac{\mu_0 dI}{4\pi R}(\sin\theta_2 - \sin\theta_1). \tag{2}$$

The shortest (perpendicular) distance of the considered field point F to the thin finite wire axis is denoted by R. Angles θ_1 and θ_2 are measured between the direction of R and the lines connecting the field point F to the two wire ends, with θ_1 corresponding to the point of current entrance into the wire and θ_2 corresponding to the point of current exit from the wire. Free space permeability is denoted by μ_0. Vector $\mathrm{d}\mathbf{B}$ is perpendicular to the plane defined by the wire and the field point F, and related to $\mathrm{d}I$ by the right-hand rule. Closed-form analytical expressions for the magnetic flux density of the rectangular current sheets [23] are obtained by integrating (2)

$$B_{xS} = \frac{\mu_0 J_0^R}{4\pi} \times \begin{cases} \displaystyle\sum_{tq=0,1} (-1)^{tq} \ln\left(\frac{\sqrt{L^2+u_S^2}-L}{\sqrt{L^2+u_S^2}+L}\right) & x_S = 0 \\ \displaystyle\sum_{tq=0,1} 2(-1)^{tq} \ln\left(\frac{|x_S|\cdot\left(-1+\sqrt{1+(x_S^2+u_S^2)/L^2}\right)}{\sqrt{x_S^2+u_S^2}}\right) & x_S \neq 0 \end{cases}$$

$$B_{yS} = \frac{\mu_0 J_0^R}{4\pi} \times \begin{cases} 0, & x_S = 0 \\ \displaystyle\sum_{tq=0,1} 2(-1)^{(tq+1)} \arcsin\left(\frac{u_S\cdot \mathrm{sgn}(x_S)\cdot L}{\sqrt{L^2+x_S^2}\sqrt{x_S^2+u_S^2}}\right) & x_S \neq 0 \end{cases}$$

$$u_S = y_S + 2h(1-tq)/\cos\beta. \tag{3}$$

Local coordinate axes, x_S and y_S, for the rectangular sheet of the upper pole closer to the global x-axis (shown in Fig. 1), are rotated by $(3\pi/2+\beta-\alpha)$ with respect to the x- and y-axes. Local coordinates, x_S and y_S, of the upper pole sheet closer to the y-axis, are rotated by $(3\pi/2-\beta-\alpha)$ with respect to the x- and y-axes. Local y_S-axis belongs to the plane of the sheet, whereas x_S-axis is perpendicular to y_S, as well as a sheet edge closest to the beam area. Sign of the B_{x_S} component for the rectangular sheet closer to the y-axis is opposite than that shown in (3).

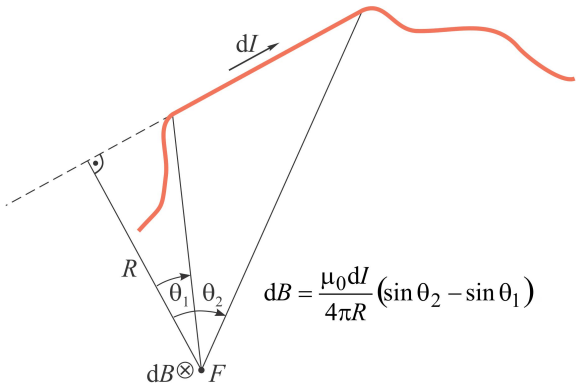

Fig. 2. Magnetic flux density for a finite straight thin wire. Current sheets corresponding to the vacuum–ferromagnetic material boundary surfaces can be regarded as collections of finite straight wires.

Field points of interest for analytical modeling all belong to the x-axis. Therefore, local coordinates are calculated using

$$\begin{aligned} x_S &= (x+a+d\sin\alpha-(b-d\cos\alpha)/\tan(\alpha-\beta))\cdot\sin(\alpha-\beta) \\ y_S &= (x+a+d\sin\alpha-(b-d\cos\alpha)/\tan(\alpha-\beta))\cdot\cos(\alpha-\beta) \\ &\quad +(b-d\cos\alpha)/\sin(\alpha-\beta)) \end{aligned} \tag{4}$$

for the rectangular sheet closer to the x-axis, and using

$$\begin{aligned} x_S &= (x+a-d\sin\alpha-(b+d\cos\alpha)/\tan(\alpha+\beta))\cdot\sin(\alpha+\beta) \\ y_S &= (x+a-d\sin\alpha-(b+d\cos\alpha)/\tan(\alpha+\beta))\cdot\cos(\alpha+\beta) \\ &\quad +(b+d\cos\alpha)/\sin(\alpha+\beta)) \end{aligned} \tag{5}$$

for the rectangular sheet closer to the y-axis. Due to symmetry, the lower pole contributions are exactly the same as those of the upper pole. Vertical magnetic flux density component due to the rectangular sheets equals

$$B_y = \mp 2B_{x_S}\cos(\alpha\mp\beta) \mp 2B_{y_S}\sin(\alpha\mp\beta). \tag{6}$$

Upper signs correspond to the sheet closer to the x-axis and lower (plus) signs to the sheet closer to the y-axis.

Contributions to the magnetic flux density B_y, of all four trapezoidal current sheets located at a distance $z = \pm L$ from the xOy plane, are identical. These are obtained by numerical integration of (2), taking care of different distances R and angles θ_1, θ_2, in every integration step, as well as different $\mathrm{d}\mathbf{B}$ directions. With B_y determined everywhere along the x-axis, relevant magnetic field parameters for analytical optimization can be calculated.

The horizontal distance of the pole midline from the CFM axis, a, is used as the scaling factor in the geometrical description of a slanted dipole. Six parameters are used for the description: normalized half-distance between the poles of a dipole, b/a, slant angle, α, wedge angle, β, normalized half-width of the poles, d/a, normalized half-height of the poles, h/a, and normalized half-length of the poles, L/a, as shown in Fig. 1. Size of the beam area, represented by the

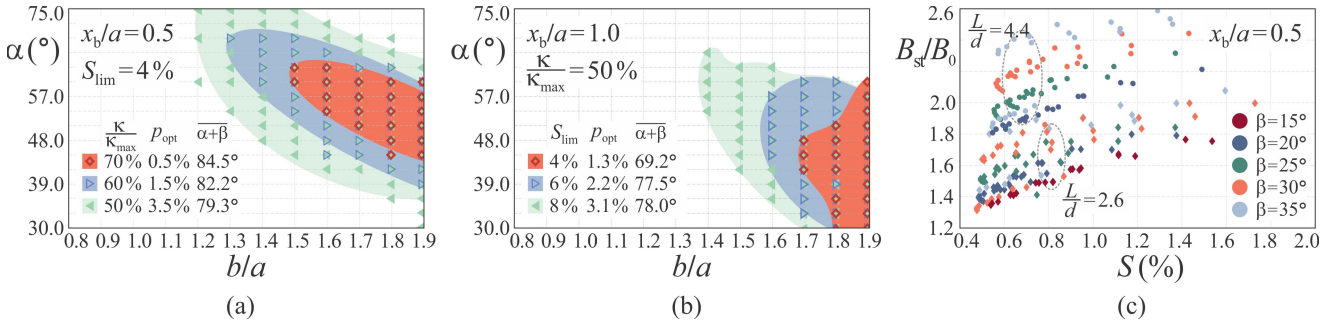

Fig. 3. Summary of the analytical optimization results. (a) Considered beam area, $2x_b$, is set equal to the horizontal distance between a pole and the CFM axis, a, whereas the linearity coefficient S is required to be smaller or equal to 0.040. Sets of model parameters are depicted as areas in the space defined by the pole positioning parameter, b/a, and the slant angle, α. Regions of the best field quality in terms of the bending and focusing coefficients embedded in the parameters $\kappa/\kappa_{\max}$ and p_{opt}, as well as the corresponding magnet geometry parameter combined of the slant and wedge angles, $\overline{\alpha+\beta}$, are shown in different colors (shades of gray). (b) If the extended beam area ($x_b/a = 1$) is considered and the beam quality parameter, $\kappa = |B_{\text{st}}/B_0| \cdot |aG/B_0|$, is limited to the half of the maximum obtainable, the S_{lim} constraint is more stringent. The regions corresponding to $S \leq 0.040$, $S \leq 0.060$, and $S \leq 0.080$ in the extended beam area, which provide $S \leq 0.012$, $S \leq 0.018$, and $S \leq 0.025$ in the main beam area, respectively, are shown in different colors (shades of gray). (c) Best solutions conforming to the $\kappa/\kappa_{\max} \geq 60\%$ requirement, under the restriction $S \leq 0.040$, are shown as data points indicating the achieved combinations of the linearity and bending coefficients for the two pole aspect ratios, L/d, depicted as circles and diamonds. The results are arranged with the wedge angle β as a parameter. Increased β results in improved steering capabilities of the device.

normalized beam area radius, x_b/a, and depicted by the green circle in Fig. 1, is taken as an additional parameter. Adopting variable ratio x_b/a broadens the possibilities to optimize the position of the poles, as a is not fixed by the given beam area size. Although L/a can be considered a design parameter for short magnets, the CFM in our example is intended to steer and focus the beam over a longer distance of about 40 cm. Pole aspect ratio, $L/d = (L/a)/(d/a)$, is therefore used as a parameter for the design space mapping. Its value is kept fixed in every optimization run, while b/a, α, β, d/a, h/a, and x_b/a are varied. Different pole aspect ratios are investigated to account for the corresponding different widths of the pole tips.

The most important parameters in assessing the quality of the magnetic field are the steering and focusing capabilities, as well as linearity of the magnetic flux density within the beam area, hence enabling wide range of operating currents for the two dipoles comprising the CFM. All parameters are calculated in the midplane between the upper and the lower part of the slanted dipole. Steering magnetic flux density is defined as

$$B_{\text{st}} \equiv B_y(x = 0) \tag{7}$$

and the focusing gradient, G, is defined as the x-component of the magnetic flux density gradient along the x-axis, where both of the horizontal magnetic field components vanish

$$G \equiv \left.\frac{\partial B_y}{\partial x}\right|_{x=0}. \tag{8}$$

Both B_{st} and G are calculated at the origin. The linearity coefficient of B_y is defined as the averaged discrepancy between the actual magnetic flux density and its linear approximation as $Gx + B_{\text{st}}$ along the line segment $x \in [-x_b, x_b]$

$$S = \frac{2\pi}{x_b \mu_0 J_0} \int_{-x_b}^{x_b} |B_y - Gx - B_{\text{st}}| dx. \tag{9}$$

Please note the normalization of S by B_0, $B_0 = \mu_0 J_0/(4\pi)$. Due to the assumption of uniform magnetization, analytical model serves only to estimate the impact of varying geometrical parameters to the overall field quality. Thus, it helps reduce the range of parameters for further investigation. Bending and focusing coefficients are scaled to B_0 as well, and expressed as B_{st}/B_0 and aG/B_0, respectively.

The limiting linearity coefficient, S_{lim}, is defined and results exceeding this limit are rejected. The optimization criterion is taken to be $\kappa_{\max} = \max\ (|B_{\text{st}}/B_0| \cdot |aG/B_0|)$, as in [12]. Instead of adopting a single set of parameters corresponding to $\kappa_{\max}$, a pool of the solutions is selected, such that $\kappa = |B_{\text{st}}/B_0| \cdot |aG/B_0|$ does not fall below a certain percentage of $\kappa_{\max}$. The best solutions pool usually does not exceed a few percent of the initial design parameter combinations; this percentage is denoted by p_{opt}. For example, if $S \leq 4\%$ for $x_b/a = 0.5$ is required, sets of parameters resulting in κ larger than $0.7 \cdot \kappa_{\max}$ comprise 0.5% of the initial design parameter combinations. Using the described procedure, regions of good field quality to be further considered in the CFM design are obtained. Separate pool of results is determined for every x_b/a value, since S increases for a larger x_b/a and, consequently, κ as a function of S_{lim} decreases. Smaller x_b/a corresponds to the placement of poles farther away from the beam area. Large x_b/a leads to a smaller magnet size, which is desired, while it can present an obstacle to attaining the required values of the magnetic field parameters. Thus we adopt moderate $x_b/a = 0.5$ to represent the main beam area, with linearity coefficient also checked in the extended beam area defined by $x_b/a = 1.0$. We set $S_{\text{lim}} = 4\%$, as the linearity coefficient in the main beam area should not exceed 5% in the final design. Field linearity is even improved after the numerical design, as presented below. Therefore, a further tradeoff is possible between the field linearity and magnet size. The summary of the optimization results is shown in Fig. 3. Fig. 3(a) shows the regions of the best magnetic field in terms of the bending and focusing coefficients. Fig. 3(b) investigates the effects of setting more stringent requirement of $S \leq 4\%$, $S \leq 6\%$, and $S \leq 8\%$, for the extended beam area, resulting in $S \leq 1.2\%$, $S \leq 1.8\%$, and $S \leq 2.5\%$, in the main beam area,

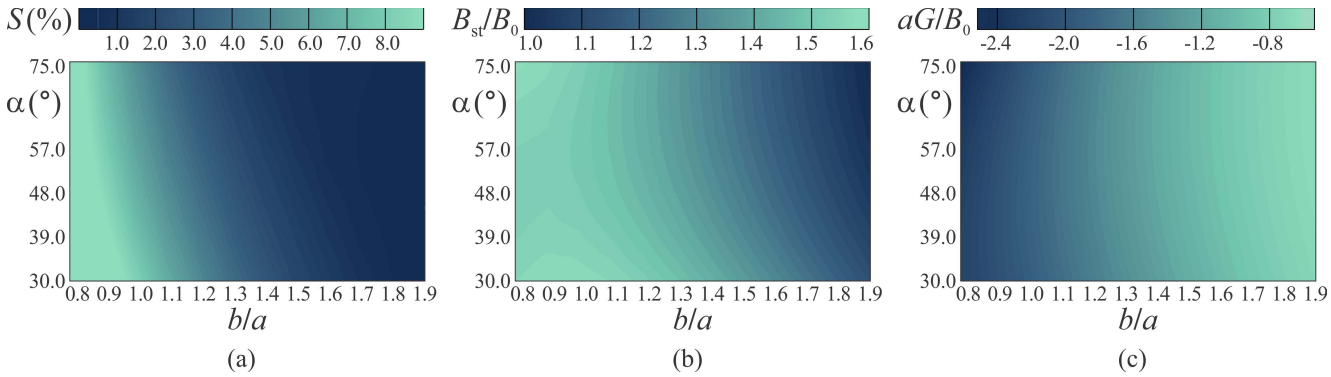

Fig. 4. Influence of pole distance, b/a, and slant angle, α, on slanted dipole properties. The remaining design parameters are fixed to: $\beta = 15°$, $d/a = 0.45$, $h/a = 1.5$, $x_b/a = 0.5$, and $L/d = 4.4$. (a) Field linearity coefficient, S. (b) Normalized steering magnetic flux density, B_{st}/B_0. (c) Focusing coefficient, aG/B_0. Parameter optimization requires a tradeoff between linearity and bending / focusing capabilities of the device.

respectively. Ranges of the two parameters that describe the pole positioning, b/a and α, are narrower than the ones in [12], as $b/a > 2$ produces weaker bending and focusing, while the linearity coefficient worsens for too small b/a. Similarly, previous results show a slant angle variation from 30° to 75° to be a good optimization range for most purposes. The six-parameter data is represented against b/a and α, where multiple solutions with same b/a and α may be overlapping. When checking on pole position and angle α selected in [12], $b/a = 1.65$ and $\alpha = 51°$, these values fall into the region of excellent κ product, $\kappa/\kappa_{\max} \approx 0.7$, with the linearity better than 4% within the main beam area. In the extended beam area, $S \leq 6\%$ is achievable. Fig. 3(c) shows best solutions corresponding to the $\kappa = 0.6 \cdot \kappa_{\max}$ region in Fig. 3(a), rearranged with the wedge angle β as a parameter, indicating the achieved combinations of the linearity and bending coefficients. Wedge angle, β, is varied from zero up to the limiting value defined by either $\alpha - \beta = 0$ or $\alpha + \beta = 90°$. Average sum of angles $\alpha + \beta$ is very close to the maximal allowed value of 90° for the regions of best solutions in Fig. 3. As can be seen from Fig. 3(c), increased β enables stronger steering, while not necessarily impairing linearity.

Fig. 4 shows the effect of varying pole position and slant angle on the linearity, bending and focusing coefficients, with other parameters fixed. There is a tradeoff between linearity on one side and bending and focusing capabilities on the other. In this model, as opposed to [12], the surface current density, J_0, is kept constant rather than the total current, I. Thus, the material magnetization can be assumed to be almost uniform for different values of h/a. Increase of h/a produces only a slight increase of bending and focusing coefficients, along with a slight decrease in linearity. Effect of the pole half-width, d/a, is pronounced, with worse linearity and stronger bending and focusing in the case of wider poles. For $h/a = 1.5$, $d/a = 0.45$, $\beta = 15°$, $x_b/a = 0.5$, and $L/d = 4.4$, the obtained values of the field linearity, bending and focusing coefficients are 0.73%, 1.19, and −0.89, respectively.

III. Numerical Parameter Optimization

Unlike the analytical optimization utilizing the closed-form expressions or 1-D numerical integration, large number of parameters for the numerical optimization would result in the unreasonably long design times. Based on the results of analytical modeling, positioning of the poles is defined by $b/a = 1.65$ and $\alpha = 51°$, and relatively large pole half-height, $h/a = 1.45$. At this point, size of the CFM has to be determined, and we adopt the scaling parameter $a = 100$ mm, which is commensurate with twice the radius of the main beam area. This results in the total pole height of $2h = 290$ mm, whereas the planned CFM length is $2L = 400$ mm. Pole width has been shown to significantly impact the field quality, hence the comparison of the two values is performed: $2d = 90$ mm and $2d = 156$ mm. Parameter d corresponds to the width of the pole face that is initially flat and will be shaped subsequently. Wedge angle, β, has been varied between zero and 30°, as an increase of the bending and focusing coefficients is expected with the initial pole widening. Too large β could lead to deteriorated linearity, without much further gain in bending and focusing coefficients, due to the coupling with the other slanted dipole. By means of numerical calculations, field parameters and spatial distribution are accurately determined. Calculations were performed utilizing the first-order node-based elements for 3-D modeling in the Mermaid finite-element suite for magnetostatics [24]. Although a notably high magnetic flux saturation density material is considered in the analyzed model, i.e., a measured *BH* curve of the Steel 1010 [25], other standard magnetic materials, with lower saturation densities, can be utilized just as well, with no influence on the proposed design and derived conclusions. First, normalized magnetic field parameters are used for analytical modeling. Second, maximal magnetomotive force assumed in the final design, *NI*, represents 78% of the one corresponding to the saturation of the Steel 1010. Please note that other high quality steels can produce slightly different results, e.g., Steel 1008 yields less than only 1% difference in magnetic flux density in the beam area, from the results reported here, with up to 6% higher magnetic flux density inside the ferromagnetic material. Examples of other *BH* curves showing high *B*-field saturations, i.e., magnetic flux density over 2 T, can be found in [26]. Energy error in all computational simulations was kept below 0.035%. Effects of the pole width and wedge angle to the magnetic flux density, illustrated in Figs. 5 and 6, are taken

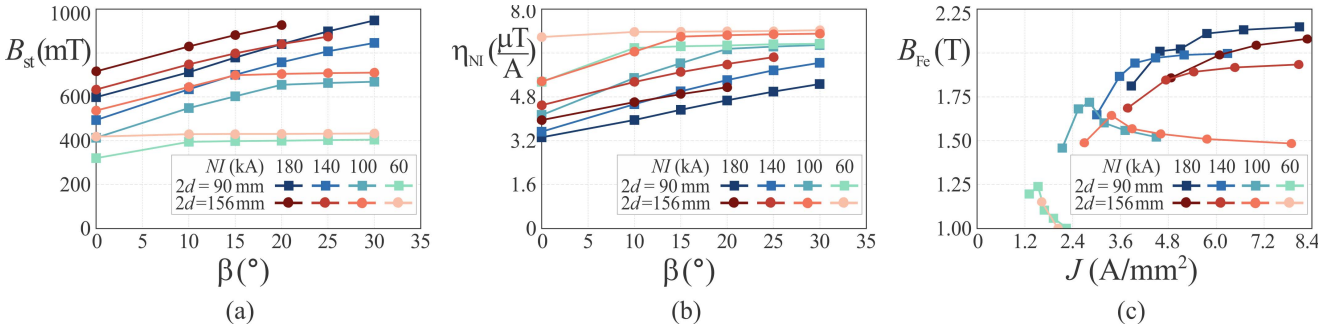

Fig. 5. Influence of the wedge angle, β, on the steering magnetic flux density and magnet efficiency, defined as $\eta_{NI} \equiv B_{st}/NI$, for two pole widths. To account for the coupling between the two slanted off-centered dipoles comprising the CFM, magnetomotive forces in the two dipoles were set as equal ($NI_1 = NI_2 = NI$). (a) Larger angles β result in the increased B_{st}, except where limited by the coupling. (b) Efficiency in utilization of magnetomotive force, calculated as the obtained B_{st} per unit current, is higher for smaller NI and larger β. (c) Current coil cross section is reduced with the widening of ferromagnetic wedge, as reflected in the increase of coil current density, J, with the increase in β. Magnetic flux density inside the ferromagnetic material, B_{Fe}, is checked. As we assumed, the CFM is less sensitive to the coupling of its dipoles for larger currents NI, where the material is in saturation.

into account when defining these parameters. Shaping of the pole tips is explained with the aid of Fig. 7.

As the magnetic flux density is dominated by the ferromagnetic material contribution, and the limitations on current density exclude the realization of a very thin coil current sheet as supposed in the analytical model, the current coils in the numerical model fill the entire cross section between the angle $\alpha+\beta$ and the 90°. This is denoted in Fig. 1 by the outer wedges outlined by the dashed lines, and also in Fig. 8 as the current coils of the optimized CFM. Current coil cross section is thus reduced with the increase in wedge angle, β. Consequently, the coil current density, J, is increased as well as the magnetic flux density in the beam area, due to the wider pole shape. For the water-cooled coils, the commonly used rule of thumb value for maximal coil current density of 10 A/mm^2 leads to J_{max} in the range 7.4–8.4 A/mm^2 when taking into account that water-cooling passages and insulation can comprise up to 25% of the actual cross section of the coils. When the two halves of the CFM are powered by magnetomotive forces of similar intensities, coupling by the material magnetization may hinder the effectiveness of further increase in angle β.

Obtainable steering magnetic flux density, B_{st}, for different parameter settings is shown in Fig. 5(a). Comparison of different models is facilitated if we look at the coil current required to produce a desired B_{st}, as a measure of efficiency in utilization of magnetomotive force

$$\eta_{NI} \equiv \frac{B_{st}}{NI}. \tag{10}$$

Fig. 5(b) demonstrates that the utilization of weaker currents is generally more efficient; however, for very low currents we observe no gain in an increase of the wedge angle. (For a larger pole half-width, d, the limiting occurs at smaller angles β; yet, the produced field is stronger for a large d and the η_{NI} is therefore higher.) For moderate currents, the CFM is less sensitive to the coupling of its dipoles. For example, for the magnetomotive force of $NI = 140$ kA and $2d = 90$ mm, the increase of β from zero to 10°, 15°, and 20°, results in an increase of B_{st} by a factor of 1.29, 1.42, and 1.54, respectively. In this case, ferromagnetic material is in saturation, as shown in Fig. 5(c) by the magnetic flux density, B_{Fe}, at the point

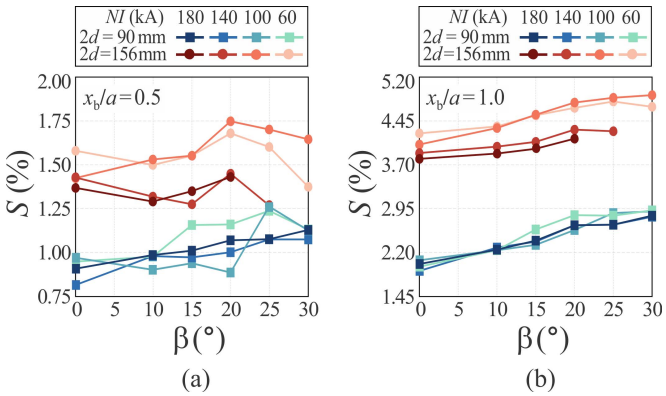

Fig. 6. Influence of wedge angle, β, on the linearity coefficient, S, for two pole widths. The effect, on the linearity coefficient, of varying pole width, d, is much more pronounced than an increase in S with the increase in β. (a) Field linearity in the main beam area is significantly better (S is lower) for the narrower poles. (b) Field linearity in the extended beam area.

$(x_f, y_f) = (-135 \text{ mm}, 165 \text{ mm})$. Data is represented as a function of coil current density, J, which remains below the critical value of $J_{max} = 8.4$ A/mm^2 for all the analyzed cases. Additionally, only the four right-most data points in Fig. 5(c) correspond to $J > 7$ A/mm^2. Some of the calculation results were left out due to large J, which is the reason, for example, why the dark red curve, corresponding to $2d = 156$ mm and $NI = 180$ kA, shows only four data points instead of six.

Variation of the linearity coefficient, S, with the angle β and the pole width, d, is shown in Fig. 6. For the numerical model, linearity coefficient is normalized to B_{st} instead of B_0

$$S = \frac{1}{2x_b B_{st}} \int_{-x_b}^{x_b} |B_y - Gx - B_{st}| dx. \tag{11}$$

The effect of varying pole width, d, is much more pronounced than an increase in S due to the increase in β. Therefore, the pole width is adjusted first, based on the linearity requirements and simulated data for various d and β. In our case, the smaller d ($2d = 90$ mm) is adequate, as it keeps the linearity coefficient for the main beam area about 1% and produces moderately high magnetic flux density. The latter can be further improved through the pole tips shaping. The wedge angle is chosen as $\beta = 20°$, to avoid B_{st} limiting observed

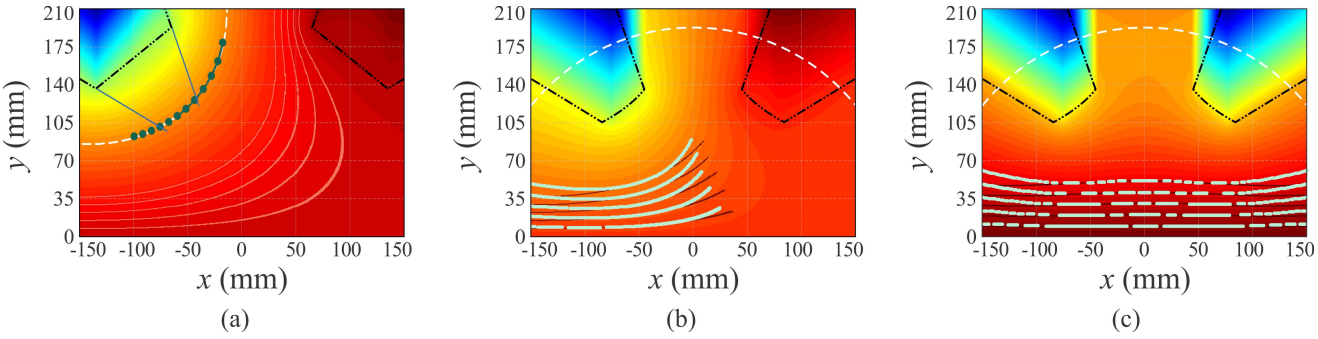

Fig. 7. Shaping of the pole tips aimed at preserving the obtained good linearity coefficient of the magnetic flux density in the beam area. (a) Magnetostatic equipotential lines corresponding to the magnetic flux density component due to the ferromagnetic cores, which are outlined by the black dashed-dotted-dotted lines. We extend the ferromagnetic cores so that the pole tip (green dots) conforms to the shape of an equipotential line (white dashed line). The resulting increase in bending and focusing capabilities is obtained with minimal disruption to the shape of equipotential lines close to the x-axis and thus to the linearity coefficient. (b) Equipotential lines after the pole tips correction for the magnetomotive force of the dipole on the right equal to zero. New (light green) equipotential lines do not deviate a lot from the initial ones (dark red). (c) Comparison of equipotential lines after the correction (solid light green) with the initial ones (dark red) for the magnetomotive forces of the two dipoles set equal. Actual pole tips after the correction are denoted by the black dashed-dotted-dotted lines. There are no free currents inside the circles denoted by the white dashed lines.

for $NI_1 = NI_2 = 100$ kA at larger β. The corresponding coil cross section area equals 312.2 cm^2. With the wedge shape completely defined, the next step is the design of pole tips.

Placement of the pole surfaces closer to the beam area increases the magnetic flux density and thus the steering and focusing capabilities of the CFM. Care should be taken at this point to avoid the unwanted increase of the linearity coefficient. We use the simple approach of shaping pole surfaces to conform to the already attained magnetic equipotential lines due to the ferromagnetic material. Magnetic scalar potential is defined for the source-free domains, where $\nabla \times \mathbf{H} = \nabla \times (\mathbf{B}/\mu_0 - \mathbf{M}) = 0$ and $\nabla \cdot \mathbf{H} = -\nabla \cdot \mathbf{M}$. In the initial design, the region bounded by the white dashed lines in Fig. 7(b) and (c) is vacuum. We subtract the magnetic flux density for the current coils in vacuum from the one due to the coils and ferromagnetic cores, thus extracting the influence of the ferromagnetic. Component $\mathbf{B}_m$, due to the magnetization $\mathbf{M}$, can be represented as a scalar function gradient, $\mathbf{B}_m = -\mu_0 \nabla \phi_m$. Horizontal components of B_m vanish along the x-axis due to symmetry. For the reference point R at infinity and the field point F, the magnetic scalar potential, ϕ_m, is obtained by the numerical integration

$$\phi_m = \int_F^R \mu_0^{-1} \mathbf{B}_m \cdot dl = - \int_{\substack{y=0 \\ x=x_F}}^{y_F} \mu_0^{-1} B_y \cdot dy. \qquad (12)$$

Analysis for several magnetomotive forces of the left dipole (NI_1), namely, 60, 80, 100, 120, and 140 kA, and $NI_2 = 0$, results in the same shapes of the equipotential lines which differ only in the associated values of the potential. An arbitrary line can be used to fit the pole surface profile. We extend the ferromagnetic wedge toward the beam area and adapt the pole surface to the part of the chosen equipotential line between the wedge surfaces, as shown in Fig. 7(a). Comparison of the newly obtained equipotential lines (light green) with the initial dark red ones reveals some deviation for a limiting case of $NI_2 = 0$, i.e., when a single coil is on, but taking into account both ferromagnetic cores. There is almost no change in the line shapes for similar magnetomotive

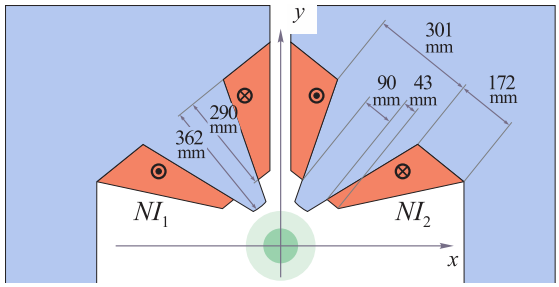

Fig. 8. Finally obtained CFM comprising the two slanted off-centered dipoles (upper half). Optimized values of geometrical parameters are: $a = 100$ mm, $b = 165$ mm, $d = 45$ mm, $h = 145$ mm, $L = 200$ mm, $\alpha = 51°$, and $\beta = 20°$. Width of the coil cross section increases from $w_1 = 43$ mm, close to the pole tips, to $w_2 = 172$ mm. The cross section area is 312.2 cm^2. Wide range of operating conditions is achieved using different magnetomotive forces NI_1 *and* NI_2.

forces NI_1 and NI_2. Relevant field quality parameters before and after the correction, for the two cases, are compared in Tables I and II. We notice a slight linearity improvement, as both the linearity coefficient and the maximal relative error inside the beam area, denoted as *M.R.E.*, are expressed as a percentage of the steering magnetic flux density. For $NI_2 = 0$, an increase of B_{st} in comparison to the initial wedge model ranges from 31% at 0.20 T (60 kA) to 8% at 0.30 T (140 kA), along with an increase of focusing gradient, G, of about 50%. When a strong dipolar field component is desired, magnetomotive forces NI_1 and NI_2 are taken almost equal, resulting in a strong positive coupling between the two dipoles. Such coupling is beneficial as it helps attain the higher magnetic flux density. Compared to the initial model, B_{st} is increased by 50% at 0.40 T and by 25% at 0.75 T.

If necessary, the linearity can be further improved by the additional pole shaping. If acceptable from the standpoint of coil current density and the required magnetic field parameters, further reduction of the magnet size can be done in an iterative procedure aimed at preserving the attained linearity and the shape of the magnetic field lines. Finally, pole shaping with the intent to optimize the magnetic field quality by reducing

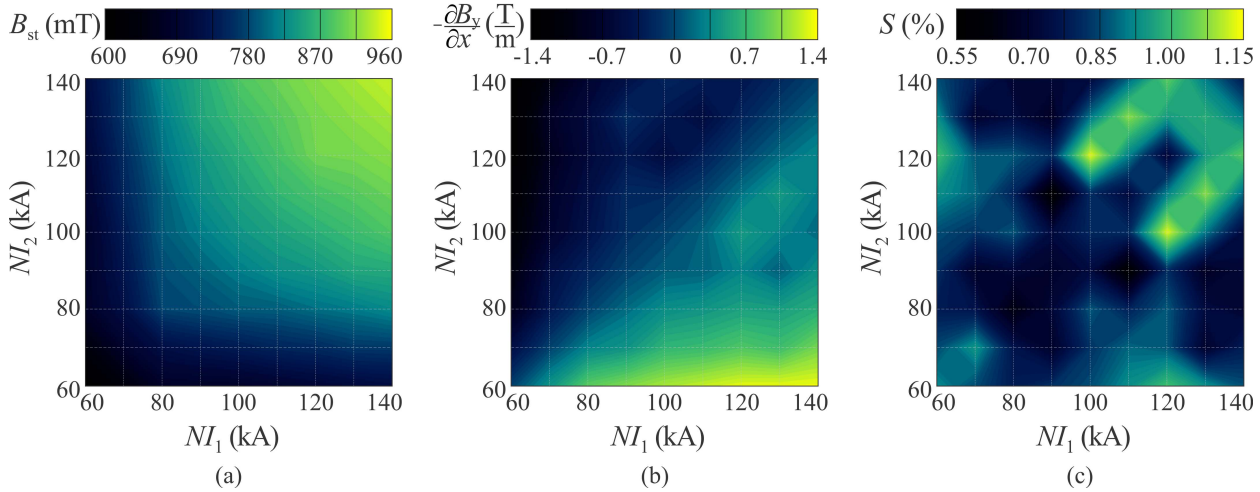

Fig. 9. Available combinations of steering magnetic flux density and focusing field gradient for the magnetomotive forces, NI_1 and NI_2, of the same signs and moderate magnitudes between 60 kA and 140 kA. (a) Steering magnetic flux density from 0.6 T up to almost 1 T is achieved with the chosen wedge geometry and pole surface placement. (b) Focusing gradient, $G = \partial By/\partial x|_{x=0}$, of up to ± 1.4 T/m can be attained in combination with the strong steering ($B_{st} > 0.6$ T). (c) Linearity coefficient, S, for the above shown ranges of magnetomotive forces is excellent, below 1% for a large part of this region of CFM operation.

TABLE I
OBTAINED FIELD CHARACTERISTICS FOR THE LEFT DIPOLE CURRENT ONLY

NI_1 (kA)	B_{st} (mT)	G (T/m)	S (%)	*M.R.E.* (%)
Initial wedge model for magnetic poles				
60.0	198.26	–2.02	3.77	10.92
80.0	240.60	–1.97	1.47	6.49
100.0	267.28	–2.23	1.39	4.72
120.0	284.08	–2.31	1.69	6.91
140.0	299.96	–2.52	1.48	4.62
Magnetic poles with shaped pole tips				
60.0	259.99	–3.02	0.90	2.63
80.0	284.07	–3.32	1.44	3.14
100.0	298.08	–3.51	1.36	3.61
120.0	313.07	–3.74	0.89	4.00
140.0	324.92	–3.94	1.20	5.50

TABLE II
OBTAINED FIELD CHARACTERISTICS FOR EQUAL DIPOLE CURRENTS

NI (kA)	B_{st} (mT)	S (%)	*M.R.E.* (%)
Initial wedge model for magnetic poles			
60.0	400.61	1.13	2.38
80.0	529.15	1.22	2.90
100.0	654.66	1.02	2.28
120.0	700.71	1.82	3.38
140.0	752.20	1.77	3.50
Magnetic poles with shaped pole tips			
60.0	600.66	0.93	1.76
80.0	780.48	0.63	1.54
100.0	837.55	0.81	1.73
120.0	905.76	0.72	1.75
140.0	942.68	0.79	1.81

the higher multipole harmonics could be performed. Such additional pole shaping should utilize the methods similar to those described in [7] and [26].

IV. SELECTION OF THE OPERATING CONDITIONS

The upper half of finally obtained CFM is shown in Fig. 8. In order to define the available range of operating conditions for the final design, we performed the mapping of the field parameters of interest, B_{st}, G, and S, as well as of the magnetic flux density vector throughout the beam area. Both magnetomotive forces, NI_1 and NI_2, are allowed to take values from the [−140 kA, 140 kA] interval. Sets of operating diagrams that correspond to different magnetomotive force ranges are used to locate the pairs (NI_1, NI_2) that produce the desired steering and focusing of the beam. For example, the dependence of the magnetic flux density, focusing gradient and linearity coefficient on the (NI_1, NI_2) pair is presented by the diagrams in Fig. 9, for the strong steering ($B_{st} > 0.6$ T) achieved using the coil currents in the [60 kA, 140 kA] range. When using a single coil current, larger focusing gradients of up to 4 T/m are available, compared to maximal 1.4 T/m for the combinations illustrated in Fig. 9. Even stronger focusing is available by the magnetomotive forces of the opposite signs, albeit combined with very weak steering.

The two limiting field requirements from [18] are easily achieved, with an excellent magnetic field quality in the main beam area. For the beam of protons which are accelerated as H^- ions, $B_{st} = 0.70$ T is required and no focusing is needed. Magnetomotive forces should be set as $NI_1 = NI_2 = 70.91$ kA, resulting in the linearity coefficient $S = 0.95\%$ for the main beam area and $S = 0.99\%$ for the [−100 mm, 100 mm] interval. Maximal relative error of B_{st} is 1.88% and 2% for the two beam areas, respectively. The reported required coil current density, $J = 2.27$ A/mm^2, being rather low, provides a vast space of tolerance for manufacturing of the required ampere-turns. Namely, depending on the actual size and shape of the conductor, as well as the actual space taken up by the

water-cooling passages, it might be necessary to use higher current density to compensate for fewer ampere-turns. Ion beam accelerated as H_2^+ requires $B_y = -1.00\ \mathrm{T/m} \cdot x - 0.15\ \mathrm{T}$ in the main beam area. It is achieved using $NI_1 = -8.55$ kA and $NI_2 = -9.75$ kA, with $S = 0.59\%$ and maximal error of 1.66% in the main beam area. Maximal deviation from the requirements at the edges of the extended beam area equals 18.56%, increasing the overall linearity coefficient to 4.59%.

V. Conclusion

The design procedure for CFMs is outlined. It can serve: 1) to determine the limits to the regions of parameters resulting in the desired beam steering and focusing along with the acceptable magnetic field linearity; 2) to assess the ranges of the desired functions that can be jointly achieved; and 3) to optimize magnet parameters according to specifications. It is illustrated by performing the detailed design of the previously proposed CFM for the stripping extraction system of a multipurpose cyclotron. With the careful exploration of the design space, we fulfilled the field linearity requirement, simultaneously achieving somewhat stronger steering and focusing capability of the device than with the previously considered simple model of the proposed device. The limiting reference fields from [18] are achieved in the two cases with a very comparable quality. The gain of the newly proposed design strategy is best illustrated by the reduction of the device length, from $2L = 800$ mm to $2L = 400$ mm, as well as by the significantly lower required magnetomotive forces and current densities. Magnetic flux density of 0.7 T is obtained for the equal coil currents of 70.91 kA, i.e., the current density of 2.27 A/mm^2, in the two dipoles. The newly obtained results demonstrate that the stronger steering and focusing could be achieved if required, by increasing magnetomotive forces, device length, or by additional pole surface adjustments if necessary.

References

[1] H. Hahn and R. C. Fernow, "Superconducting combined function magnets," *IEEE Trans. Nucl. Sci.*, vol. 30, no. 4, pp. 3402–3404, Aug. 1983.

[2] R. C. Gupta and G. H. Morgan, "A design for a high field combined function superferric magnet," *IEEE Trans. Nucl. Sci.*, vol. 32, no. 5, pp. 3687–3688, Oct. 1985.

[3] G. H. Biallas, N. Belcher, D. Douglas, T. Hiatt, and K. Jordan, "Combined Panofsky quadrupole & corrector dipole," in *Proc. 25th Particle Accel. Conf.*, Albuquerque, NM, USA, Jun. 2007, pp. 602–604.

[4] A. Madur *et al.*, "Harmonic sextupoles for the advanced light source low emittance upgrade," *Nucl. Instrum. Methods Phys. Res. A, Accel. Spectrom. Detect. Assoc. Equip.*, vol. 649, no. 1, pp. 39–41, Sep. 2011.

[5] M. Werner, V. Vrankovic, and D. C. George, "Design and measurement of the SLS booster combined function magnets," *IEEE Trans. Appl. Supercond.*, vol. 10, no. 1, pp. 248–251, Mar. 2000.

[6] S. P. Møller *et al.*, "Status of the injection system for the Australian synchrotron project," in *Proc. 21st Particle Accel. Conf.*, Knoxville, TN, USA, May 2005, pp. 3271–3273.

[7] G. Sinha and G. Singh, "Design and characterization of combined function multipole magnet for accelerators," *Rev. Sci. Instrum.*, vol. 79, no. 12, p. 123302, Dec. 2008.

[8] D. S. Robin *et al.*, "Superconducting toroidal combined-function magnet for a compact ion beam cancer therapy gantry," *Nucl. Instrum. Methods Phys. Res. A, Accel. Spectrom. Detect. Assoc. Equip.*, vol. 659, no. 1, pp. 484–493, Dec. 2011.

[9] A. Morita *et al.*, "Design and measurement of a combined function magnet intended for a cancer therapy accelerator," *Phys. Rev. ST-Accel. Beams*, vol. 4, no. 12, p. 122401, Dec. 2001.

[10] M. Yoon, J. Corbett, M. Cornacchia, J. Tanabe, and A. Terebilo, "Analysis of a storage ring combined-function magnet: Trajectory calculation and alignment procedure," *Nucl. Instrum. Methods Phys. Res. A, Accel. Spectrom. Detect. Assoc. Equip.*, vol. 523, nos. 1–2, pp. 9–18, May 2004.

[11] M. Seidl, "Identification and correction of antisymmetric field components in combined function magnets," *Phys. Rev. ST-Accel. Beams*, vol. 5, no. 6, p. 062402, Jun. 2002.

[12] J. L. Ristić-Djurović, S. Ćirković, and A. Ž. Ilić, "Magnet with uncoupled combined functions," *IEEE Trans. Nucl. Sci.*, vol. 60, no. 6, pp. 4618–4626, Dec. 2013.

[13] S.-Z. An *et al.*, "Stripping extraction calculation and simulation for CYCIAE-100," *Chin. Phys. C (HEP & NP)*, vol. 33, no. 2, pp. 42–46, Jun. 2009.

[14] D. Vandeplassche *et al.*, "Extraction simulations for the IBA C70 cyclotron," in *Proc. 18th Int. Conf. Cyclotrons Appl.*, Giardini Naxos, Italy, 2007, pp. 63–65.

[15] D. Solivajs *et al.*, "A study of charge-exchange beam extraction from the multi-purpose isochronous cyclotron DC-72," *J. Elect. Eng.*, vol. 55, nos. 7–8, pp. 201–206, 2004.

[16] J. L. Ristić-Djurović and N. Nešković, "Analytical prediction of ion stripping extraction from isochronous cyclotrons," *IEEE Trans. Nucl. Sci.*, vol. 59, no. 2, pp. 268–271, Apr. 2012.

[17] J. L. Ristić-Djurović and N. Nešković, "Influence of cyclotron magnet gap size on stripping extraction," *IEEE Trans. Nucl. Sci.*, vol. 58, no. 3, pp. 1188–1195, Jun. 2011.

[18] J. L. Ristić-Djurović and S. Ćirković, "Unidirectional stripping extraction from a cyclotron which accelerates light as well as heavy ions," *Phys. Rev. ST-Accel. Beams*, vol. 6, no. 3, p. 033501, Mar. 2003.

[19] J. L. Ristić-Djurović, "Stripping extraction of positive ions from a cyclotron," *Phys. Rev. ST-Accel. Beams*, vol. 4, no. 12, p. 123501, Dec. 2001.

[20] P. R. Sarma, "Ideal coil shape for combined function superconducting magnets," *J. Phys. D, Appl. Phys.*, vol. 40, no. 10, pp. 3056–3059, 2007.

[21] P. R. Sarma, S. K. Pattanayak, and R. K. Bhandari, "New method of designing pole profile in combined function magnets of high field quality," *Rev. Sci. Instrum.*, vol. 70, no. 6, pp. 2655–2660, Jun. 1999.

[22] B. M. Notaroš, *Electromagnetics*. Upper Saddle River, NJ, USA: Prentice-Hall, 2010.

[23] A. Ž. Ilić *et al.*, "Analytical description of two-dimensional magnetic arrays suitable for biomedical applications," *IEEE Trans. Magn.*, vol. 49, no. 12, pp. 5656–5663, Dec. 2013.

[24] *Mermaid 2-D and 3-D User's Guide*, SIM, Novosibirsk, Russia, 1994.

[25] J. K. Cobb and R. A. Early, "The new SLAC permeameter," Tech. Rep. SLAC-TN-89-04, Dec. 1989; Available:. [Online]. Available: http://www.slac.stanford.edu/cgi-wrap/getdoc/slac-tn-89-004.pdf

[26] *Steel 1008 BH Curve*. [Online]. Available: http://fieldp.com/Myblog/2010/saturation-curves-for-common-soft-magnetic-materials/

[27] S. Ćirković, J. L. Ristić-Djurović, A. S. Vorozhtsov, A. Ž. Ilić, and N. Nešković, "Method for fine magnet shaping in cyclotrons," *IEEE Trans. Nucl. Sci.*, vol. 56, no. 5, pp. 2821–2827, Oct. 2009.

Environ Sci Pollut Res (2016) 23:1584–1597
DOI 10.1007/s11356-015-5109-z

RESEARCH ARTICLE

Homogeneous static magnetic field of different orientation induces biological changes in subacutely exposed mice

Ivan D. Milovanovich[1] · Saša Ćirković[2] · Silvio R. De Luka[1] · Drago M. Djordjevich[1] · Andjelija Ž. Ilić[2] · Tamara Popović[3] · Aleksandra Arsić[3] · Danilo D. Obradović[4] · Dejan Oprić[4] · Jasna L. Ristić-Djurović[2] · Alexander M. Trbovich[1]

Received: 26 January 2015 / Accepted: 21 July 2015 / Published online: 17 September 2015

Abstract It has been shown that static magnetic field (SMF) of moderate intensity produces considerable impact on biological systems. SMF can be homogeneous or inhomogeneous. In many studies, inhomogeneous SMF was employed. Aware that inhomogeneous SMF could result in experimental variability, we investigated the influence of a vertical homogeneous SMF of different orientation. Male Swiss-Webster 9- to 10-week-old mice were subacutely exposed to upward- and downward-oriented SMF of 128 mT generated by a cyclotron for 1 h/day during a 5-day period. We found that SMF affected various organs and that these effects were, to some degree, dependent on SMF orientation. Both upward- and downward-oriented SMF caused a reduction in the amount of total white blood cells (WBC) and lymphocytes in serum, a decrease of granulocytes in the spleen, kidney inflammation, and an increase in the amount of high-density lipoprotein (HDL). In addition, upward-oriented SMF caused brain edema and increased spleen cellularity. In contrast, downward-oriented SMF induced liver inflammation and a decrease in the amount of serum granulocytes. These effects might represent a specific redistribution of pro-inflammatory cells in blood and among various organs. It appears that homogeneous SMF of 128 mT affected specific organs in the body, rather than simultaneously and equally influencing the entire body system.

Keywords Homogeneous static magnetic field of different orientation · Liver · Brain · Kidney · Spleen · Serum

Responsible editor: Philippe Garrigues

Ivan D. Milovanovich and Saša Ćirković contributed equally to this work.

✉ Alexander M. Trbovich
aleksandar.trbovic@mfub.bg.ac.rs;
alexander.m.trbovich@gmail.com

[1] Department of Pathological Physiology, School of Medicine, University of Belgrade, Dr Subotića 9, 11000 Belgrade, Serbia

[2] Institute of Physics, University of Belgrade, Pregrevica 118, 11080 Zemun-Belgrade, Serbia

[3] Institute for Medical Research University of Belgrade, Laboratory for Nutrition and Metabolism, Tadeuša Košćuška 1, 11000 Belgrade, Serbia

[4] Department of Pathology, School of Medicine, University of Belgrade, Dr Subotića 9, 11000 Belgrade, Serbia

Introduction

Two types of magnetic fields are widely present in the human environment—an alternating and a static magnetic field (SMF). Biological effects of alternating magnetic field have been extensively investigated since alternating electromagnetic fields are widely used in electrical power systems as well as in information and telecommunications technologies. In contrast, there is scarce data on SMF activity impact on human health (Heinrich et al. 2011). The main sources of SMF that is stronger than a geomagnetic field are found in various medical devices. SMF, which is difficult to shield and easily penetrates biological tissues, may be classified as weak (<1 mT), moderate (1 mT to 1 T), strong (1 to 5 T), and ultrastrong (>5 T). Unlike SMF of weak and, to some degree, SMF of strong intensity, SMF of moderate intensity has considerable effects on biological systems (Rosen 2003, Dini and Abbro 2005). These effects are mediated by interaction with moving charges (ions, proteins, etc.) and magnetic materials found in tissues as a consequence of several physical mechanisms (Schenck 2005, Saunders 2005). Homogeneous as well as inhomogeneous SMF was employed in many studies that report its

significant effects (Abdelmelek et al. 2006, Elferchichi et al. 2007, Hashish et al. 2008, Amara et al. 2009, Elferchichi et al. 2010, Lahbib et al. 2010, László et al. 2007, Vergallo et al. 2013, Csillag et al. 2014, Kiss et al. 2015). Although it can be argued that spatial dependence introduced by field inhomogeneity is more likely to mimic realistic exposures to environmental fields, homogeneous magnetic fields offer an advantage for in vivo experiments with moving animals in that they ensure identical exposure conditions at every point of the experimental volume. Exposure dosage is equal at every point of animal body, regardless of animal position during the course of experiment. We therefore decided to employ a homogeneous SMF.

A significant influence of inhomogeneous SMF of moderate intensities with checkerboard configuration, i.e., of spatially alternating SMF with a period of 2 cm in both directions was reported (László et al. 2007, Vergallo et al. 2013, Csillag et al. 2014, Kiss et al. 2015). Thorough description, analysis, and optimization of the field (László et al. 2007) that was later used in a number of biomedical experiments (for example, in Vergallo et al. 2013, Csillag et al. 2014, Kiss et al. 2015) established justifiable cause-and-effect relationship between the applied field and the obtained results. Averaging of a spatially alternating field over the entire surfaces parallel to the magnetic checkerboard would result in zero magnetic flux density vector and mean field gradient. Therefore, the mean intensity of the applied SMF and strong local field gradients were the cause of the observed effects and the overall beneficial influence of SMF. Homogeneity of the cyclotron SMF that is used in our study is much better than that of the exposure systems commonly used in biomedical experiments. Consequently, any possible biological effect of field gradients is excluded and all observed results are due to the applied field intensity in the chosen direction. We exploited the possibilities of the cyclotron magnet to check if the field orientation as well as the field intensity applied throughout the experimental volume is of importance, the motivation for the former being the accounts of significance of field orientation in the inhomogeneous (Djordjevich et al. 2012) as well as in the homogeneous (Todorović et al. 2015) SMF. With the intention to single out the influence of the field orientation, we used downward as well as upward-oriented vertical, highly homogeneous SMF of moderate intensity. The intensity of the SMF was adjusted to 128 mT motivated by the existence of research data on the effects of the horizontal homogeneous SMF of the same intensity (Chater et al. 2006, Elferchichi et al. 2007, Amara et al. 2009, Lahbib et al. 2010, Elferchichi et al. 2010, Ghodbane et al. 2014), allowing for the comparison of the results.

The thorough study reported by Colbert et al. (2009) revealed that magnetic fields are often poorly described, lacking critical data on magnet characteristics, measured field strength, and estimated distance of the magnet from the target tissue. As a result, inferences drawn from such reports cannot be precisely associated with the applied SMFs. To the contrary if, as suggested by Colbert et al. (2009), all ten SMF dosage and treatment parameters deemed necessary for the full description of the applied SMF were systematically reported, as for example, in our study and in László et al. (2007), replication of experiments by other investigators as well as comparison with the results of exposures to different magnetic fields is enabled.

Biological response to moderate SMF is wide-ranging, involving different types of cells in various tissues and organs. For example, it has been shown in in vitro system that exposure to SMF caused a significant initial decline in ROS production by human peripheral blood neutrophils that was reversible after longer incubation time (Poniedzialek et al. 2013). Moreover, it has been demonstrated that SMF exposure had beneficial effects in a murine model of allergic inflammation via mobilization of cellular ROS-eliminating mechanism (Csillag et al. 2014). It has been also shown that SMF of moderate intensity induces hematological changes in exposed mice that resemble hypoxia-like status (Elferchichi et al. 2010). In addition, the hypoxia-like status is associated with a sympathetic hyperactivity that could be attributed to stress reaction of exposed animals (Abdelmelek et al. 2006). Using an in vivo experimental model of mouse ear edema, it has been suggested that the place of SMF action may be in the lower spinal region (Kiss et al. 2015). In vivo experiments also demonstrated antinociceptive effects of SMF in invertebrate (László and Hernádi 2012), mice (László et al. 2007, László and Gyires 2009) and humans (László et al. 2012). In vitro analysis of the effects of SMF on human macrophages and lymphocytes provided a possible explanation for the effect observed in vivo (Vergallo et al. 2013). Namely, it was shown that SMF exposure (of 200 mT average intensity) suppresses inflammation by reducing release of pro-inflammatory cytokines IL-6, IL-8, and TNF-α from macrophages and by enhancing release of anti-inflammatory cytokine IL-10 from lymphocytes (Vergallo et al. 2013). SMF of 128 mT can also induce tissue changes in various organs such as the liver, kidney, and brain of exposed animals (Amara et al. 2007, Amara et al. 2009), as well as in cell culture (Sahebjamei et al. 2007). These changes were attributed to oxidative stress. Another possibility is that the tissue changes induced by SMF were caused by the redistribution of inflammatory cells (Djordjevich et al. 2012). We were specifically interested to assess whether changes in hematological parameters could be directly related to changes observed in various organs from the same animals. Since changes in the blood may be specific to the hematological system and may not cause or reflect changes in the organs, we investigated whether changes in the blood corresponded to changes in selected organs, which had previously been studied by others in SMF of 128 mT. In our case, the spleen and kidney were selected for the experiment since they are involved in regulation of blood content.

On the other hand, the liver and brain were studied as target organs for possible redistribution of blood cells and consequent oxidative damage. In addition, we chose the liver as an example of a target body organ because of its central role in lipid metabolism, which we studied in-depth.

Phospholipids are a class of lipids in which a phosphate group replaces one of the fatty acids. They are a major structural component of all cell membranes where they are involved in forming lipid bilayers. Phospholipids are amphipathic molecules containing a hydrophilic phosphate group and a hydrophobic fatty acid tail. The four phospholipids that predominate in the plasma membrane of mammalian cells are phosphatidylcholine, phosphatidylethanolamine, phosphatidylserine, and sphingomyelin. Besides a structural role, phospholipids also have a metabolic role. They act as sources of intracellular signals in response to extracellular signals which interact with receptors on the outer layer of the plasma membrane. Phospholipid fatty acids of the cell membrane are precursors of lipid mediators, with eicosanoids (prostaglandins, thromboxanes, leukotrienes) being one of the most important. They, also, play a role in signal transduction and gene transcription pathways (Kremmyda et al. 2011). The liver plays an important role in the synthesis and metabolism of phospholipids. The structure of hepatocyte membrane phospholipids is dependent on nutritional intake and affects liver metabolic functions (Oguzhan et al. 2006). The fatty acid profile of liver phospholipids and triglycerides is known to be influenced by many factors, including dietary intake, age, gender, and endogenous metabolism (Oguzhan et al. 2006). However, magnetic field influence on the total fatty acids in an organism has been scarcely reported (Lahbib et al. 2010, Elferchichi et al. 2010). In the present study, we monitored the liver as a key representative organ of possible SMF influence on phospholipids.

We investigated the effects of homogeneous SMF on subacutely exposed animals by primary studying the hematological system and the liver, but we also monitored the brain, kidney, and spleen. Since literature analysis showed limited data regarding the interaction of differently oriented moderate SMF on biological systems, the present study was designed to investigate the effects of subacute exposure to differently oriented 128 mT SMF on mice.

Materials and methods

Animals

Male Swiss-Webster mice, weighing on average 23±3 g, 9–10 weeks old, obtained from the Military Medical Academy Animal Research Facility (Belgrade, Serbia) were used. Mice were housed at four or five animals per cage and offered regular mouse feed and drinking water ad libitum. All experimental protocols involving animals were reviewed and approved by the University of Belgrade, Faculty of Medicine Experimental Animals Ethics Committee. Furthermore, all experiments were conducted in accordance with procedures described in the National Institutes of Health Guide for Care and Use of Laboratory Animals (Washington, DC, USA), as well as in accordance with the US-NIH guidelines for conducting magnetic field experiments on animals.

Magnetic field

Customarily, experiments performed in accelerator facilities utilize ion beams. However, the VINCY Cyclotron located at the Vinča Institute of Nuclear Sciences is still under construction. Its ferromagnetic structure is fully assembled and operative but still accessible, allowing employment of a strong static magnetic field as an experimental tool.

The VINCY Cyclotron is a sector-focused isochronous multipurpose machine (Nešković et al. 2003). Special attention was devoted to an extremely precise design of sectors on pole tips of the electromagnet to enable acceleration of the widest possible range of ion beams (Ćirković et al. 2009). Power consumption is minimal in the most frequent operating mode, while an appropriate choice of electrical currents of main coils and ten pairs of trim coils results in different isochronous magnetic fields that could be used for various modes of operation (Ćirković et al. 2008). The produced magnetic field between the two poles is highly homogeneous in the sector regions and in the valley regions; however, it abruptly changes in the vicinity of sector edges and the gradient of the magnetic field in that narrow area is strong. The main coil current can be set up to 1000 A, whereas the maximum mean magnetic field may reach 2 T. The electromagnet pole diameter measures 2 m, and it has four sectors per pole whose azimuthal width is 42°.

Magnetic flux density of 128 mT, desired for our experiment, was produced by setting the main coil current to 36.5 A, without necessity to use trim coils for further field adjustment. Field intensity is larger between the sectors and smaller in the valleys. For our experiment, it was convenient to center cages with experimental animals in the middle of the valley, well away from sector edges to avoid high magnetic field gradients in this region, as shown in Fig. 1. Cages, 19 cm high, 35.5 cm long, and 20.5 cm wide, were placed inside the circle of radius 80 cm (from the center of the cyclotron) to avoid the stray field components at radii larger than 84 cm. The desired magnetic field was achieved with less than 0.68 % variation throughout the above described area; therefore, SMF was considered highly homogeneous throughout the experimental volume. Note that the field produced by solenoids often used for exposure setups is about an order of magnitude less homogenous than the field we used.

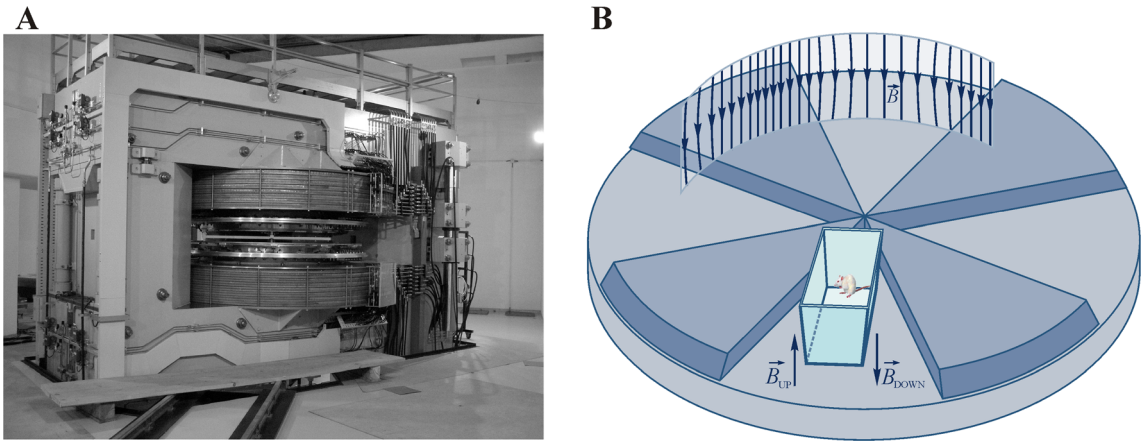

Fig. 1 The VINCY Cyclotron used as an experimental SMF exposure setup. **a** Photograph of the VINCY Cyclotron. **b** The lower pole of cyclotron magnet and position of the cage with animals in the middle of the cyclotron valley (drawn to scale). The produced magnetic field, depicted by the magnetic flux lines in the valley and above the sector, *B*, was vertical. The direction of the field was chosen to be directed upwards or downwards for the two groups of SMF exposed animals, denoted as the up group and down group, and is represented by the vectors B_{UP} and B_{DOWN}, respectively. The variation of the magnetic field intensity was smaller than 0.68 % everywhere in the experimental volume. Magnetic flux density used was 128 mT

The geomagnetic field is directed downward in the northern hemisphere and upward in the southern hemisphere, i.e., in the same and the opposite direction to gravity, respectively. Therefore, experiments in two sets of magnetic field exposures were performed; in the first set, we used the magnetic field oriented in the same direction as gravity (down group), and in the second, the magnetic field oriented upwards (up group). The third group of animals was control (sham exposed).

Experimental design

Mice were randomly divided into three groups (9 mice per group). All three groups were kept under same conditions. The first experimental group was exposed to the upward-oriented 128 mT SMF (up group) for 1 h/day over a 5-day period. The second experimental group was exposed to the downward-oriented 128 mT SMF (down group) for 1 h/day over a 5-day period. The exposure period was always between 8 and 12 a.m. on a consecutive day under standard light exposure and constant temperature. The control group was sham exposed. Following a 5-day period, all mice were sacrificed and the blood, spleen, liver, brain, and kidney were collected for further analyses. These analyses were performed blindly, with material marked just with a code and people conducting the analyses unaware of sample group origin.

Blood and spleen parameters

Blood parameters [red blood cells (RBS), lymphocytes, neutrophils, basophils, eosinophils, platelets (Plt), hemoglobin (Hgb), hematocrit (Hct), mean corpuscular volume (MCV), mean corpuscular hemoglobin (MCH), mean corpuscular hemoglobin concentration (MCHC)] were determined using hematological counter ABX Pentra 80X (Montpellier, France) according to the manufacturer's recommendations. The total number of granulocytes in blood and spleen samples was calculated by summing neutrophils with basophils and eosinophils. Total serum cholesterol, HDL, LDL, triglycerides, C-reactive protein (CRP), and alanine aminotransferase (ALT) were determined using BioSystems photometer type BTS-330 (Barcelona, Spain), according to manufacturer's recommendations.

Spleen cellularity was prepared and analyzed by the previously explained procedure (Djordjevich et al. 2012).

Total lipid extraction from the liver

Obtained liver tissue was first homogenized using a 2:1 chloroform/methanol mixture and washed with a fivefold smaller volume of water or saline. The resulting mixture was separated into two phases. The lower phase was a total pure lipid extract. Liver tissue (1 g) was lyophilized and chloroform/methanol (2:1) and butylhydroxytoluene (BHT) as antioxidant were mixed. When the mixture was allowed to stand, a biphasic system was obtained. After evacuation, water was added. After centrifugation, the upper phase was put away until complete separation of the system was achieved. Further evacuation was done with 2:1 solvent systems: methanol/benzene, acetone/benzene, and ethanol/benzene. Addition and evacuation of chloroform and subsequent addition of hexane rendered the sample ready for thin liquid chromatography (TLC) (Tepšić et al. 2008).

Fatty acid analysis

The phospholipid fraction was isolated from the extracted lipids by one-dimensional (TLC) neutral lipid solvent system of hexane:diethyl ether:acetic acid (87:2:1) using Silica Gel GF plates (C. Merck, Darmstadt, Germany). The phospholipid fraction was scraped into glass tubes, and phospholipid fatty acids (FAs) methyl esters were prepared by transmethylation with sodium hydroxide (2 mol dm–3) in methanol (heated at 85 °C for 1 h) and after that with sulfuric acid (1 mol dm–3) in methanol (heated 85 °C for 2 h). After 30 min, samples of esters were centrifuged, upper phase were put into tubes and evaporated by technical nitrogen. FA methyl ester derivates formed from isolated plasma phospholipids fraction were separated by gas chromatography (GC) using Shimadzu GC 2014 (Kyoto, Japan) equipped with a flame ionization detector and DB-23 fused silica gel capillary column. The flame ionization detector was set at 250 °C, the injection port at 220 °C, and the oven temperature programmed from 130 to 190 °C at the heating rate of 3 °C/min (Folch et al. 1957). Comparing sample peak retention times with authentic standards (Sigma Chemical Company) and/or the (PUFA)-2 standard mixtures (Restec) identified individual FAs methyl esters.

Estimated activities of desaturase system

Several fatty-acid indices, reflecting desaturase and elongase activity, were derived from primary data (Cvetković et al. 2010). The ratios of 20:4/20:3, 20:3/18:2, and 22:6/22:5 were used as a measure of estimated Δ5-desaturase, Δ6-desaturase, and Δ4-desaturase activities, respectively, while 18:1/18:0 and 18:0/16:0 ratios represented estimated Δ9-desaturase and elongase activities.

Histology analysis

Brain, liver, spleen, and kidney tissues were prepared for histological analysis by the procedure explained earlier (Bancroft and Gamble 2001). In short, tissues were fixated in formalin (10 % formaldehyde-water solution) for 24 h and than embedded in paraffin. Generated 5-μm sections were mounted on slides and stained with hematoxylin (Bio-Optica, Milan, Italy) and eosin (MP Biomedicals LLC, Illkirch Cedex, France). Analysis of stained sections was conducted by two independent pathologists that used a light microscope Olympus BX41 (Tokyo, Japan) and made micrographs with Sony Exwave HAD digital camera, model SSC-DC50AP (Tokyo, Japan). Immunohistochemical (IHC) analysis was conducted with the CD3 (polyclonal rabbit anti-human CD3; Dako Denmark A/S; Glosturp, Denmark), CD15 (monoclonal mouse anti-human CD15 clone carb-3; Dako North America Inc., Camarillo, CA, USA), and CD20 (monoclonal mouse anti-human CD20cy clone L26; Dako Denmark A/S; Glosturp, Denmark) antibodies. After exposing tissue to primary antibodies for 1 h, slides were rinsed with water and then the secondary antibody was applied for 15 min. Detection was conducted by employing a horse radish peroxidase kit (UltraVision Large Volume Detection System Anti-Polyvalent, HRP (Ready-To-Use); Thermo Fisher Scientific, (Chestershire, UK). CD3 is a marker for T lymphocytes (Felgar et al. 1997), CD20 is a marker for B lymphocytes (Pinkus and Said 1988), and CD15 is a marker for granulocyte lineage (Barry et al. 2002).

Statistical analysis

Statistical analysis of obtained data was performed using software SPSS for Windows, version 16.0 (SPSS, Chicago, IL, USA). Differences among groups were evaluated by one-way ANOVA, followed by Fischer's LSD test. Distribution of non-parametric data was analyzed by chi-square test. The level of significance was set at $p<0.05$.

Results

Histological characteristics

Tissue morphology of the liver, spleen, kidney, and brain is presented in Fig. 2. The liver in the down group showed significant inflammation. Liver infiltrate localization was periportal and predominantly made of granulocytes and lymphocytes. Edematous hepatocytes were also present. The spleen did not show any pathological changes among groups, though congestive hyperemia was visible in all three groups, which is a usual finding following sacrifice. The kidney showed increased inflammation (nonspecific pyelonephritis) in exposed animals, but not in sham animals. Brain edema characterized by edematous neurons was present in the up group, but not in the down and sham groups.

Histological analysis

Tissue characteristics of mice exposed to SMF of different orientations are presented in Table 1. The liver in the down group showed significant inflammatory characteristics when compared to up and sham groups ($p<0.05$). The spleen did not show any pathological changes among groups ($p>0.05$). The kidney showed increased inflammation in exposed animals (up and down group) when compared to control animals ($p<0.05$). Brain tissue expressed significant edematous neurons in the up group when compared to the down and sham groups ($p<0.05$).

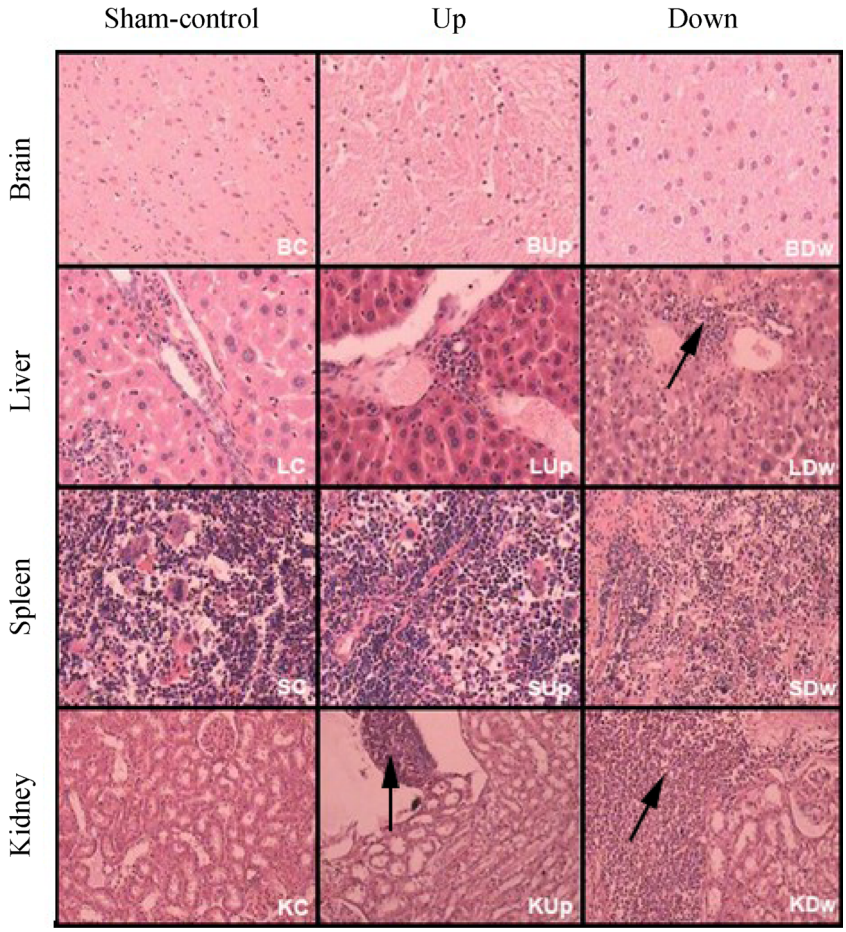

Fig. 2 Histological characteristics of the brain, liver, spleen, and kidney in mice exposed (up group, down group) or unexposed (sham-control) to SMF of different orientations. *BC* brain tissue in unexposed mice (brain control), *BUp* brain tissue in mice exposed to up-oriented SMF, *BDw* brain tissue in mice exposed to down-oriented SMF. *LC* liver tissue in unexposed mice (liver control), *LUp* liver tissue in mice exposed to up-oriented SMF, *LDw* liver tissue in mice exposed to down-oriented SMF. *SC* splenic tissue in unexposed mice (spleen control), *SUp* splenic tissue in mice exposed to up-oriented SMF, *SDw* splenic tissue in mice exposed to down-oriented SMF. *KC* kidney tissue in unexposed mice (kidney control), *KUp* kidney tissue in mice exposed to up-oriented SMF, *KDw* kidney tissue in mice exposed to down-oriented SMF. *Arrow* shows inflammatory cells

Immunohistochemical analysis

Immunohistochemical (IHC) analysis of cell infiltrates in renal tissue is presented in Fig. 3. Initial determination of cell infiltrates in all affected organs was done by light microscopy. A confirmation of correct histological reading was conducted in a renal tissue by IHC analysis. In panel A, inflammatory cells are visible. In panel B, CD15 positive granulocytes are marked. In panel C, the CD3 positive T lymphocytes are shown. In panel D, the CD20 positive B lymphocytes are presented.

Table 1 Results of histological analysis of mice exposed (up group, down group) or unexposed (sham-control) to SMF of different orientation

	Histology	Sham-control	Up group	Down group
Liver	Normal [*n*(%)]	9 (100)	8 (88.9)	4 (44.4)
	Inflammation [*n*(%)]	0 (0)	1 (11.1)	5 (55.6)
Spleen	Normal [*n*(%)]	9 (100)	9 (100)	9 (100)
	Inflammation [*n*(%)]	0 (0)	0 (0)	0 (0)
Kidney	Normal [*n*(%)]	8 (88.9)	5 (55.6)	3 (33.3)
	Inflammation [*n*(%)]	1 (11.1)	4 (44.4)	6 (66.7)
Brain	Normal [*n*(%)]	8 (88.9)	1 (11.1)	9 (100)
	Edema [*n*(%)]	1 (11.1)	8 (88.9)	0 (0)

Blood parameters

Blood parameters in control mice and mice exposed to differently oriented SMF are shown in Table 2. Exposure of mice to differently oriented SMF did not alter the platelet count or Hgb, Hct, MCV, MCH, MCHC values among groups ($p>0.05$). However, SMF of a different orientation influenced the serum lipids. There was a significant increase in serum values of HDL in exposed animals (up and down group) when compared to unexposed ones (61.50±5.13 and 56.21±2.38 vs. 41.77±5.13; $p<0.01$ and $p<0.05$, respectively). Total serum cholesterol, LDL, and triglycerides did not change significantly among groups, but there was a trend of total cholesterol increase and LDL decrease in exposed groups (up and down group) ($p>0.05$). C-reactive protein also did not change under the influence of differently oriented SMF (0.59±0.09 and 0.64±0.12 vs. 0.78±0.32; $p>0.05$), but we observed a significant increase of ALT in down group when compared to sham group (63.50±8.17 vs. 42.33±3.87; $p<0.05$). In general, besides statistically significant results, the trend of increased values vs. sham group was more pronounced in the down group and the trend of decreased values vs. sham group was more pronounced in the up group.

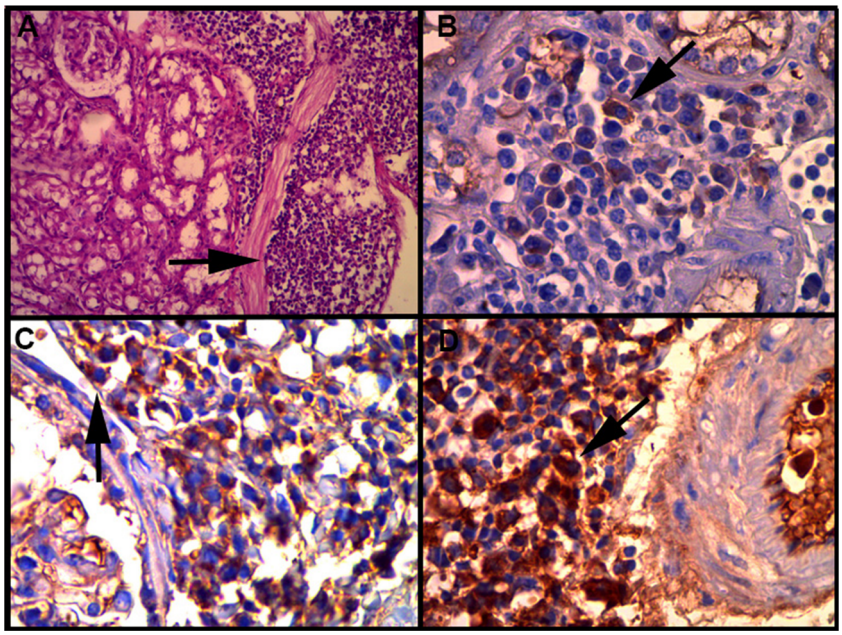

Fig. 3 Immunohistochemical (IHC) analysis of cell infiltrates in renal tissue. **a** Renal tissue, magnification ×10, hematoxylin-eosin staining. *Arrow* shows inflammatory cells. **b** Renal tissue, magnification ×40, monoclonal mouse anti-human CD15 (granulocyte marker). *Arrow* shows CD15 positive granulocyte. **c** Renal tissue, magnification ×40, polyclonal rabbit anti-human CD3 (T lymphocyte marker). *Arrow* shows CD3 positive T lymphocyte. **d** Renal tissue, magnification ×40, monoclonal mouse anti-human CD20 (B lymphocyte marker). *Arrow* shows CD3 positive B lymphocyte

Blood cellularity

Blood cellularity in mice exposed (up, down) or unexposed to SMF of different orientation is shown in Fig. 4. Total serum white blood cells (WBC) count was found to be significantly lower in exposed (up and down group) when compared to unexposed animals (3.49±0.50 and 3.31±0.30 vs. 6.61±0.70; $p<0.01$) (panel A). This decrease in exposed groups was mainly due to a reduction in serum lymphocytes (2.74±0.36 and 2.97±0.27 vs. 5.47±0.61; $p<0.01$) (panel D) and to a decrease in serum granulocytes, especially in down group (0.26±0.03 vs. 0.87±0.10; $p<0.01$ compared to sham group and 0.26±0.03 vs. 0.66±0.14; $p<0.05$ compared to up group) (panel C). While decrease in total WBC and serum lymphocytes were about the same in up and down groups, it is worth noting that statistically significant decrease in serum granulocytes occurred exclusively in the down group. This decrease in serum granulocytes was statistically significant not only versus the sham group but also versus the up group. SMF of a different orientation did not alter RBC count among groups ($p>0.05$) (panel B).

Table 2 Blood parameters in mice exposed (up group, down group) or unexposed (sham-control) to SMF of different orientations

Blood parameter	Sham-control	Up group	Down group
Plt (10^9/L)	1311.86±59.99	1140.60±80.24	1266.25±41.49
Hgb (g/L)	125.42±5.39	130.00±3.52	132.00±6.50
Hct (L/L)	0.41±0.02	0.42±0.09	0.43±0.02
MCV (fl)	48.29±1.30	48.62±0.65	48.71±0.94
MCH (pg)	15.00±0.49	15.12±0.23	15.29±0.36
MCHC (g/L)	308.14±4.97	309.75±3.53	309.86±1.84
Total cholesterol (mg/dL)	76.17±3.97	78.73±6.79	89.48±5.71
HDL (mg/dL)	41.77±5.13	56.21±2.38*	61.50±6.19**
LDL (mg/dL)	25.81±6.61	10.74±6.31	16.16±7.26
Triglycerides (mg/dL)	52.94±3.53	48.88±4.37	59.13±5.35
ALT (IU/L)	42.33±3.87	51.29±7.94	63.50±8.17*
CRP (mg/dL)	0.78±0.32	0.59±0.09	0.64±0.12

Data are presented as mean±SEM

Plt platelets, *Hgb* hemoglobin, *Hct* hematocrit, *MCV* mean corpuscular volume, *MCH* mean corpuscular hemoglobin, *MCHC* mean corpuscular hemoglobin concentration, *HDL* high-density lipoprotein, *LDL* low-density lipoprotein, *ALT* alanine-aminotransferase, *CRP* C-reactive protein

*$p<0.05$ compared to control; **$p<0.01$ compared to control

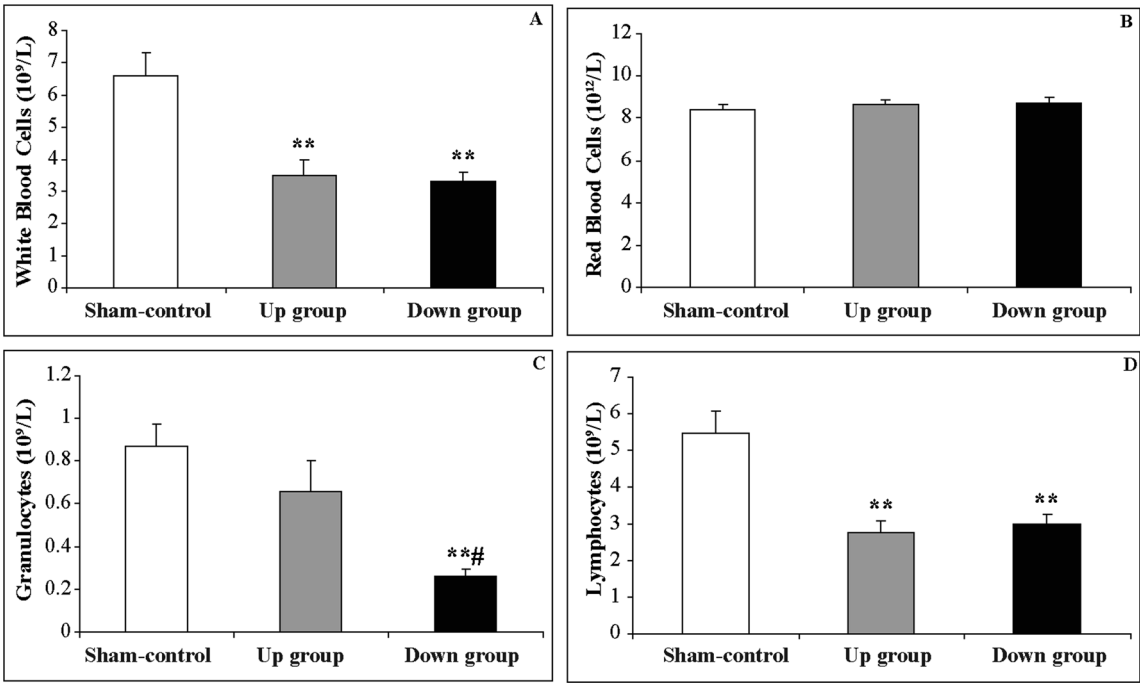

Fig. 4 Blood cellularity in mice exposed (up group, down group) or unexposed (sham-control) to SMF of a different orientation. Data are presented as mean±SEM. **a** Total serum white blood cells in mice exposed (up group, down group) or unexposed (sham-control) to SMF of a different orientation; **b** serum red blood cells in mice exposed (up group, down group) or unexposed (sham-control) to SMF of a different orientation; **c** total serum granulocytes in mice exposed (up group, down group) or unexposed (sham-control) to SMF of a different orientation; **d** serum lymphocytes in mice exposed (up group, down group) or unexposed (sham-control) to SMF of a different orientation; $^{**}p<0.01$ compared to control; $\#p<0.05$ compared to up group

Spleen cellular parameters

Spleen cellular parameters in mice exposed to SMF of a different orientation are presented in Fig. 5. Total spleen cellularity in mice exposed to upward-oriented SMF was significantly higher when compared to those exposed to downward-oriented SMF (1.08±0.05 vs. 0.69±0.03; $p<0.01$) and to control mice (1.08±0.05 vs. 0.73±0.05; $p<0.01$) (panel A). However, there was no difference in spleen red blood cell count among groups (30.54±3.26 vs. 34.51±1.4 vs. 34.71±1.05; $p>0.05$, respectively) (panel B). Spleen granulocytes in the up group were significantly lower when compared to the sham group (2.2±0.28 vs. 8.26±1.30; $p<0.01$) and spleen granulocytes in the down group were also significantly lower when compared to the sham group (1.64±0.19 vs. 8.26±1.30; $p<0.01$) (panel C). In contrast, spleen lymphocytes did not alter among groups under the influence of SMF of different orientation ($p>0.05$) (panel D).

Liver phospholipid profile

Liver phospholipid profile in mice exposed to SMF of a different orientation is presented in Table 3. There was no difference in total saturated fatty acids (SFA). However, in mice exposed to downward-oriented SMF, there was a significant increase in content of palmitic acid (16:0) when compared to control mice (24.54±0.19 vs. 22.90±0.70; $p<0.01$). There was also an increase of palmitic acid in the upward-oriented group when compared to sham group, but this increase was on the border of significance (24.01±0.13 vs. 22.90±0.70; $p=0.05$). Stearic acid (18:0) content showed tendency of decrease in exposed groups, but without statistical significance ($p>0.05$). There was no difference in monounsaturated fatty acids (MUFA) in general. However, content of palmitoleic acid (16:1n-7) showed a significant, twofold increase in exposed animals (up and down group) when compared to sham group (0.82±0.06 and 0.84±0.07 vs. 0.40±0.04; $p<0.01$). On the other hand, oleic acid (18:1n-9) did not show alterations among the groups ($p>0.05$). The amount of vaccenic acid (18:1n-7) significantly increased in the down group, but not in the up group, when compared to sham group (2.49±0.14 vs. 1.97±0.17) and also in the down group when compared to the up group (2.49±0.14 vs. 1.96±0.18). Not only that polyunsaturated fatty acids (PUFA) did not alter, but neither did the sum of omega-3 fatty acids (n-3), the sum of omega-6 fatty acids (n-6), or the ratio of omega-6 to omega-3 (n-6/n-3). However, dihomo-γ-linolenic acid (20:3n-6) was reduced in the exposed groups (up and down) when compared to sham group (1.06±0.08 and 1.12±0.02 vs. 1.40±0.11; $p<0.01$). In addition, α-linolenic acid (18:3n-3) was reduced in the down group when compared to both sham group (0.40±0.04 vs. 0.62±0.07; $p<0.05$) and the up group (0.40±0.04 vs. 0.67±

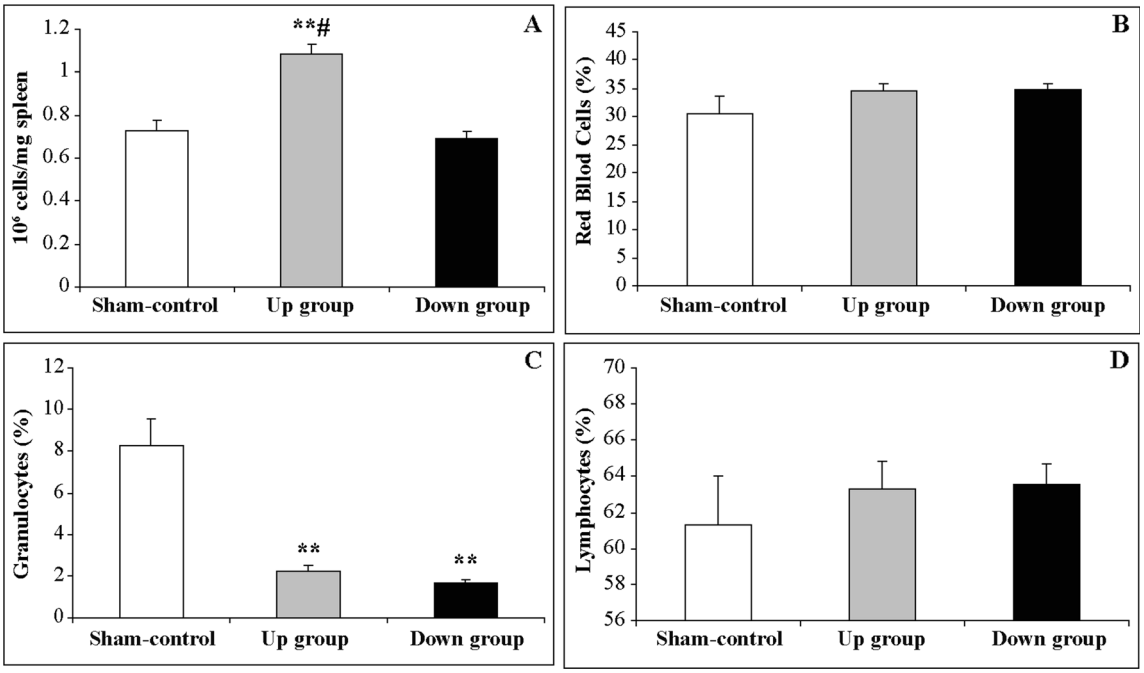

Fig. 5 Spleen cellularity in mice exposed (up group, down group) or unexposed (sham-control) to SMF of a different orientation. Data are presented as mean±SEM. **a** Total spleen cellularity in mice exposed (up group, down group) or unexposed (sham-control) to SMF of different orientation; **b** spleen red blood cells in mice exposed (up group, down group) or unexposed (sham-control) to SMF of a different orientation; **c** spleen granulocytes in mice exposed (up group, down group) or unexposed (sham-control) to SMF of different orientation; **d** spleen lymphocytes in mice exposed (up group, down group) or unexposed (sham-control) to SMF of different orientation; $**p<0.01$ compared to control; $\#p<0.01$ compared to down group

0.08; $p<0.01$). At the same time, α-linolenic acid from the up group did not change when compared to sham group ($p>0.05$). Overall, in both up and down groups, there was a statistically significant change in content of palmitoleic (16:1n-7) and dihomo-γ-linolenic acid (20:3n-6) that occurred in the same direction. Namely, both the amount of palmitoleic acid and the dihomo-γ-linolenic acid decreased when compared to sham group. However, in three situations, a change in the amount of fatty acids was observed exclusively in the down group. Namely, palmitic (16:0) and vaccenic (18-1n7) acids increased and α-linolenic acid (18:3n-3) decreased in the down group when compared to sham group.

Desaturase and elongase activities

Desaturase and elongase activities in the liver in mice exposed to SMF of a different orientation are presented in Table 4. Delta 9 (Δ9) desaturase activity did not change in groups of exposed or unexposed animals ($p>0.05$). Elongase activity decreased in the liver of exposed animals (up and down groups) when compared to sham group (0.73±0.03 and 0.70±0.01 vs. 0.81±0.03; $p<0.05$ and $p<0.01$, respectively). Delta 6 (Δ6) desaturase and elongase also showed significant decrease in livers of exposed animals (up and down groups) when compared to control animals (0.07±0.01 and 0.07± 0.003 vs. 0.09±0.01; $p<0.05$). Delta 5 (Δ5) desaturase showed significant increase in the up group compared to sham group (13.52±0.88 vs. 10.64±1.02; $p<0.05$) but did not differ when compared to the down group (13.52±0.88 vs. 12.27± 0.32; $p>0.05$).

Animal weight

There was no significant difference in animal weight or food intake among the groups at the beginning and at the end of the experiment (data not shown).

Discussion

In this study, we investigated the influence of a homogeneous, differently oriented static magnetic field (SMF) of 128 mT on hematological parameters, tissue characteristics, and lipid content in subacutely exposed mice. Aiming to single out the influence of field orientation, we used downward- as well as upward-oriented vertical homogeneous SMF (Fig. 1). SMF affected various organs and these effects were, to some degree, dependent on the SMF orientation. Since the field gradients were negligible, any possible biological effect of varying field gradients was excluded and all the observed effects were appropriated to the applied field intensity in the chosen direction.

Table 3 Fatty acid profiles of liver phospholipids in mice exposed (up group, down group) or unexposed (sham-control) to SMF of different orientation

Fatty acids (%)	Sham-control	Up group	Down group
SFA	41.42±0.97	41.60±0.72	41.79±0.26
16:0	22.90±0.70	24.01±0.13	24.54±0.19**
18:0	18.51±0.64	17.60±0.68	17.25±0.25
MUFA	10.26±0.98	11.21±0.71	10.90±0.60
16:1 n-7	0.40±0.04	0.82±0.06**	0.84±0.07**
18:1 n-9	7.89±0.83	8.43±0.82	7.58±0.51
18:1 n-7	1.97±0.17	1.96±0.18	2.49±0.14*[a]
PUFA	48.33±0.61	47.19±0.88	47.31±0.48
n-6	31.88±0.32	31.14±0.60	30.80±0.49
18:2 n-6	15.97±0.16	15.94±0.63	15.74±0.43
20:3 n-6	1.40±0.11	1.06±0.80**	1.12±0.02*
20:4 n-6	14.30±0.39	13.91±0.53	13.72±0.11
22:4 n-6	0.21±0.01	0.23±0.01	0.22±0.01
n-3	16.44±0.74	16.05±1.11	16.50±0.81
18:3 n-3	0.62±0.07	0.67±0.08	0.40±0.04**[a]
20:5 n-3	0.52±0.15	0.56±0.16	0.72±0.16
22:5 n-3	0.70±0.08	0.75±0.06	0.82±0.04
22:6 n-3	14.61±0.66	14.07±1.18	14.56±0.78
n-6/n-3	1.96±0.10	2.01±0.17	1.91±0.12
MUFA/SFA	0.25±0.07	0.27±0.05	0.26±0.04
PUFA/SFA	1.17±0.09	1.14±0.09	1.13±0.03

Values are presented as means±SEM

SFA saturated fatty acids, *MUFA* monounsaturated fatty acids, *PUFA* polyunsaturated fatty acids

*$p<0.05$ compared to control; **$p<0.01$ compared to control

[a] $p<0.05$ compared to Up group

Both upward- and downward-oriented magnetic field caused a decrease in the amount of total WBC and lymphocytes in serum, a decrease of granulocytes in the spleen, kidney inflammation, and an increase in the amount of HDL. In addition, upward-oriented SMF caused brain edema and increased spleen cellularity. In contrast, downward-oriented SMF induced liver inflammation and a decrease in the amount of serum granulocytes. It appears that SMF of 128 mT affected specific organs in the body, rather than simultaneously and equally influencing the entire body system.

We initially found inflammation in the liver after exposure to the down-oriented SMF of 128 mT (Fig. 2; Table 1). These histological findings were confirmed by an increase of serum ALT in the down group only (Table 2). Enzyme ALT is found in the highest concentration in the liver, and it is typically used to detect liver injury. Moreover, we have been the first to discover specific changes in fatty acid profile following SMF exposure. We observed exclusively in the down group an increase in pro-inflammatory palmitic fatty acid (16:0) (Soto-Vaca et al. 2013, Wu et al. 2014) and a decrease in anti-inflammatory α-linolenic fatty acid (18:3 n-3) (Ren et al. 2007, Erdinest et al. 2012) (Table 3). It has been shown that palmitic acid increases the level of pro-inflammatory TNF-alpha and IL-6 (Staiger et al. 2004, Zhou et al. 2013). An increase in palmitic fatty acid that we observed could be a consequence of a reduced activity of the enzyme elongase 18:0/16:0 that converts palmitic fatty acid into stearic fatty acid (18:0) (Table 4). In the case of α-linolenic acid, which is an essential fatty acid, we can speculate that employed SMF affected its metabolism in the liver. SMF of 128 mT may directly affect activity of enzymes by inducing their conformational changes. Alternatively, SMF may act through the rearrangement of membrane phospholipids, leading to a flux of ions (Rosen 1993) that alters enzyme functions. Observing that 128 mT SMF affected differently the two enzymes that contain the same metal, magnesium (enzyme Δ6 desaturase and elongase 20:3n-6/18:2n-6 and enzyme Δ5 desaturase 20:4n-6/20:3n-6), while at the same time, enzyme Δ9 desaturase 18:1n-9/18:0 that contains a different metal, iron, was not affected (Table 4), we conclude that SMF influence was probably at the membrane level, rather than at the level of enzymes' conformational change. This explanation is based on the important role of the liver in synthesis and degradation of phospholipids that are a major component of cell membranes (Rigotti et al. 1994). Alteration of membrane fatty acids changes membrane fluidity and ion flux and, consequently, the function of various enzymes (McGarry 2002). The ratio of unsaturated to saturated fatty acids influences membrane fluidity in bacteria (Mihoub et al. 2012) and in mammals (Perona et al. 2007). Moderate intensity SMF

Table 4 Estimated activities of desaturases and elongases in the liver in mice exposed (up group, down group) or unexposed (sham-control) to SMF of different orientations

Enzyme	Sham-control	Up group	Down group
Δ9 desaturase 18:1n-9/18:0	0.43±0.14	0.49±0.15	0.44±0.10
elongase18:0/16:0	0.81±0.03	0.73±0.03*	0.70±0.01**
Δ6 desaturase and elongase 20:3n-6/18:2n-6	0.09±0.01	0.07±0.01*	0.07±0.003*
Δ5 desaturase 20:4n-6/20:3n-6	10.64±1.02	13.53±0.88*	12.28±0.32

Values are presented as means±SEM

Significantly different from control: *$p<0.05$ compared to control; **$p<0.01$ compared to control

influences cell membrane ratio of unsaturated versus saturated fatty acids in bacteria, representing an adaptive reaction (Mihoub et al. 2012). However, in our study, although some fatty acids increased and some decreased, the total ratio of MUFA/SFA and PUFA/SFA of liver phospholipids did not change (Table 3), probably because of different intensity and duration of SMF exposure.

Various studies have shown an increase in free radical production and degradation of lipid bilayers in liver cells in SMF exposed animals (Watanabe et al. 1997, Amara et al. 2007, Hashish et al. 2008). This disruption of lipid membranes causes cellular edema and loss of functional integrity, which leads to histological changes and decreased liver function. In our experiments, we observed a tendency of a decrease in direct cholesterol transport via LDL and significant increase in reverse cholesterol transport via HDL (Table 2). An explanation for these findings could be that cholesterol synthesis, uptake, and degradation in liver decreased under SMF influence. As a consequence, there was a tendency of serum total cholesterol increase in exposed animals, mainly due to HDL increase. HDL is a major serum lipoprotein in rodents and its fluctuation affects total serum cholesterol to a significant extent (Lizenko et al. 2008). In previously conducted experiments, increased serum total cholesterol was accompanied by an increase in serum triglycerides (Lahbib et al. 2010), which we did not observe. The increase in serum triglycerides observed in their experiment could be due to different duration of applied SMF.

In the kidney, as in the liver, an inflammatory infiltrate was present in SMF exposed animals, causing nonspecific pyelonephritis (Fig. 2). The extent of this infiltrate was more pronounced in the down group. Other studies showed that besides the liver, SMF of 128 mT can also cause decreased activity of anti-oxidative enzymes in the kidney that leads to increased lipid peroxidation and oxidative stress (Amara et al. 2007, Ghodbane et al. 2011). We reported here morphological changes in the kidney as reflected by infiltration of various inflammatory cells (Fig. 3). Furthermore, we showed that morphological changes, observed in the kidney and liver of exposed animals, were more profound in the down group (Table 1). The specificity of our findings in the liver and kidney was confirmed by histological analysis of spleen, where no inflammation was observed (Fig. 2, Table 1).

In contrast to the liver and kidney, the brain showed edematous changes in upward exposed animals (Table 1, Fig. 2). Various animal studies showed that SMF causes increased blood-brain permeability (Saunders 2005). SMF can also induce changes in Na/K pump redistribution especially in the cytoplasm of affected neurons (Nikolić et al. 2013). Increased permeability of the blood-brain barrier and functional changes in Na/K pump can cause neuron swelling. It was shown that 128 mT SMF induces hypoxia-like status in exposed rats (Elferchichi et al. 2007). When hypoxia develops, one of the first organs that are affected is the brain, with intraneuronal edema that we observed in the up group (Fig. 2).

Spleen cellularity is bound to the amount of RBC and WBC in serum. WBC consists of granulocytes and lymphocytes. Lymphocytes make the majority of WBC in mice (Green 1966). Analysis of the spleen has revealed a significant increase in spleen total cellularity (RBC and WBC together) in the up group (Fig. 5, panel A). This is a consequence of a fact that even a small increase in percentage of lymphocytes could cause a large increase in total spleen cellularity. We also observed a significant decrease in spleen granulocyte count in exposed animals (up and down) (Fig. 5, panel C) with concomitant decrease in serum granulocytes found mainly in the down group (Fig. 4, panel C). Previous research also showed a decrease in splenic granulocytes under the influence of SMF that was explained by increased phagocytosis and oxidative stress followed by death of granulocytes (Elferchichi et al. 2007). In our case, serum WBC and lymphocytes were also decreased in both exposed groups (Fig. 4, panel A and panel D). The total serum WBC reduction was probably a consequence of lymphocyte redistribution among the serum and various tissues. Namely, a decrease in serum lymphocytes in both groups of exposed animals (Fig. 4, panel D) was followed by an increase in lymphocyte content in the liver and kidney (Fig. 2 and Fig. 3).

Red blood cell count did not statistically change in the blood or in the spleen between exposed and unexposed animals. Additionally, there were no changes in hemoglobin content or in MCV, MCH, and MCHC values among groups (Table 2). This is in accordance with findings that rats exposed to a magnetic field of extremely low frequency for 50 and 100 days did not show alteration in RBC count (Cakir et al. 2009). Additionally, a previous study also showed that SMF of moderate intensity do not influence plasma red blood cell count (Elferchichi et al. 2007). We concluded that various intensities of magnetic fields and different exposure times do not influence RBC count in the blood and spleen of experimental animals. This is probably due to diamagnetic property of RBC and fast recovery of RBC after exposure to SMF (Schenck 2005).

Previous research showed that SMF influences the biological system by causing pro-inflammatory changes and an increase in production of reactive oxygen species (Sahebjamei et al. 2007, Hashish et al. 2008, Zhao et al. 2011, Todorović et al. 2015). Namely, these studies stated that SMF increased phagocytosis and death of granulocytes, associated with production of free radicals. Our experiments showed a redistribution of granulocytes and lymphocytes that was dependent upon SMF orientation. In addition, previous studies (Bras et al. 1998, Chionna et al. 2003) demonstrated cytoskeleton reorganization and modulation of orientation of lymphocytes following exposure to moderate static magnetic field. They hypothesized that some sublethal damage persists in the cells, even

when the cell morphology still seems to be normal, since it is known that SMF interferes with DNA repair processes (Ghodbane et al. 2013). Our observed inflammatory changes in the liver and kidney of exposed animals may not be connected to the previously observed oxidative stress (Amara et al. 2007). It has been suggested that SMF increases the level of acetylcholine by enhancing its release and by decreasing its degradation (Xu et al. 2011). Increased level of acetylcholine induces blood vessel dilatation and permeability that leads to granulocyte and lymphocyte infiltration of the surrounding tissue. However, another study showed that inhomogeneous SMF could inhibit the release of pro-inflammatory cytokines IL-6, IL-8, and TNF-α from leukocytes (Vergallo et al. 2013). The inhibition of release of pro-inflammatory cytokines from granulocytes and lymphocytes could be the factor explaining the absence of CRP increase in our experiment despite inflammatory changes in the observed tissue (Pepys and Hirschfield 2003). Here, presented results have been obtained in a very controlled environment with the outbred strain, which renders them even more significant.

Conclusion

We investigated the influence of downward- and upward-oriented homogeneous SMF of 128 mT on subacutely exposed mice. Our results suggested that SMF of moderate intensity produced pro-inflammatory effects that depended on its orientation. We discovered that upward-oriented SMF caused changes in the serum, spleen, kidney, and brain, while downward-oriented SMF influenced the serum, kidney, and liver. Observed changes varied from brain edema and alterations in blood total WBC count and spleen granulocyte count to inflammation of the liver and kidney. Mechanisms that led to inflammation of affected organs were direct infiltration of inflammatory cells, whereas, in the case of liver, we also found an increase of pro-inflammatory palmitic fatty acid and a decrease in anti-inflammatory α-linolenic fatty acid. Further studies are needed to fully understand these processes.

Acknowledgment This study was supported by the grant numbers III-41013, III-41019, III41030, III-45003, and III-45006 from the Ministry of Education, Science and Technological Development, Government of Serbia. The experiment was performed at the Vinča Institute of Nuclear Sciences, Laboratory of Physics (010) to whose staff we thank for enabling access to the Cyclotron, as well as for their assistance and support.

Conflict of interest The authors declare that they have no competing interests.

Role of funding source No funding body had any involvement in the preparation or content of this article or in the decision to submit it for publication.

References

Abdelmelek H, Molnar S, Servais S, Cottet-Emard JM, Pequignot JM, Favier R, Sakly M (2006) Skeletal muscle HSP72 and norepinephrine response to static magnetic field in rat. J Neural Transm 113: 821–827

Amara S, Abdelmelek H, Garrel C, Guiraud P, Douki T, Ravanat J, Favier A, Sakly M, Ben Rhouma K (2007) Zinc supplementation ameliorates static magnetic field-induced oxidative stress in rat tissues. Environ Toxicol Pharmacol 23:193–197

Amara S, Douki T, Garel C, Fevier A, Sakly M, Ben Rhouma K, Abdelmelek H (2009) Effects of static magnetic field exposure on antioxidative enzymes activity and DNA in rat brain. Gen Physiol Biophys 28:260–265

Bancroft JD, Gamble M (2001) Theory and practice of histological techniques. 5th ed. Churchill Livingstone, Edinburgh

Barry SM, Condez A, Johnson MA, Janossy G (2002) Determination of bronchoalveolar lavage leukocyte populations by flow cytometry in patients investigated for respiratory disease. Cytometry 50(6): 291–297

Bras W, Diakun GP, DíazJF MG, Kramer H, Bordas J, Medrano FJ (1998) The susceptibility of pure tubulin to high magnetic fields: a magnetic birefringence and X-ray fiber diffraction study. Biophys J 74:1509–1521

Cakir DU, Yokus B, Akdag MZ, Sert C, Mete N (2009) Alterations of hematological variations in rats exposed to extremely low frequency magnetic fields (50 Hz). Arch Med Res 40:352–356

Chater S, Abdelmelek H, Douki T, Garrel C, Favier A, Sakly M, Ben Rhouma K (2006) Exposure to static magnetic field of pregnant rats induces hepatic GSH elevation but not oxidative DNA damage in liver and kidney. Arch Med Res 37:941–946

Chionna A, Dwikat M, Panzarini E, Tenuzzo B, Carlà EC, Verri T, Pagliara P, Abbro L, Dini L (2003) Cell shape and plasma membrane alterations after static magnetic fields exposure. Eur J Histochem 47(4):299–308

Colbert AP, Wahbeh H, Harling N, Connelly E, Schiffke HC, Forsten C, Gregory WL, Markov MS, Souder JJ, Elmer P, King V (2009) Static magnetic field therapy: a critical review of treatment parameters. Evid-Based Complement Alternat Med 6:133–139

Csillag A, Kumar BV, Szabó K, Szilasi M, Papp Z, Szilasi ME, Pázmándi K, Boldogh I, Rajnavölgyi É, Bácsi A, László JF (2014) Exposure to inhomogeneous static magnetic field beneficially affects allergic inflammation in a murine model. J R Soc Interface 11:20140097

Cvetković Z, Vučić V, Cvetković B, Petrović M, Ristić-Medić D, Tepšić J, Glibetić M (2010) Abnormal fatty acid distribution of the serum phospholipids of patients with non-Hodgkin lymphoma. Ann Hematol 89:775–782

Ćirković S, Ristić-Djurović JL, Ilić AŽ, Vujović V, Nešković N (2008) Comparative analysis of methods for isochronous magnetic field calculation. IEEE Trans Nucl Sci 55(6):3531–3538

Ćirković S, Ristić-Djurović JL, Vorozhtsov AS, Ilić AŽ, Nešković N (2009) Method for fine magnet shaping in cyclotrons. IEEE Trans Nucl Sci 56(5):2821–2827

Dini L, Abbro L (2005) Bioeffects of moderate-intensity static magnetic fields. Micron 36:195–217

Djordjevich DM, De Luka SR, Milovanovich ID, Janković S, Stefanović S, Vesković-Moračanin S, Ćirković S, Ilić AŽ, Ristić-Djurović JL, Trbovich AM (2012) Hematological parameters' changes in mice subchronically exposed to static magnetic fields of different orientations. Ecotoxicol Environ Saf 81:98–105

Elferchichi M, Abdelmelek H, Sakly M (2007) Effects of sub-acute exposure to static magnetic field on iron status and hematopoiesis in rats. Turk J Hematol 24:64–68

Elferchichi M, Mercier J, Coisy-Quivy M, Metz L, Lajoix A, Rene Gross R, Belguith H, Abdelmelek H, Sakly M, Lambert K (2010) Effects

of exposure to a 128-mT static magnetic field on glucose and lipid metabolism in serum and skeletal muscle of rats. Arch Med Res 41: 309–314

Erdinest N, Shmueli O, Grossman Y, Ovadia H, Solomon A (2012) Anti-inflammatory effects of alpha linolenic acid on human corneal epithelial cells. Invest Ophtalmol Vis Sci 53(8):4396–406

Felgar RE, Macon WR, Kinney MC, Roberts S, Pasha T, Salhany KE (1997) TIA-1 expression in lymphoid neoplasms. Identification of subsets with cytotoxic T lymphocyte or natural killer cell differentiation. Am J Pathol 150:1893–1900

Folch J, Lees M, Sloane Stanley GH (1957) A simple method for the isolation and purification of total lipids from animal tissues. J Biol Chem 226(1):497–509

Ghodbane S, Amara S, Garrel C, Arnaud J, Ducros V, Favier A, Sakly M, Abdelmelek H (2011) Selenium supplementation ameliorates static magnetic field-induced disorders in antioxidant status in rat tissues. Environ Toxicol Pharmacol 31:100–106

Ghodbane S, Lahbib A, Sakly M, Abdelmelek H (2013) Bioeffects of static magnetic fields: oxidative stress, genotoxic effects and cancer studies. Biomed Res Int 2013:602987. doi:10.1155/2013/602987

Ghodbane S, Amara S, Lahbib A, Louchami K, Sener A, Sakly M, Abdelmelek H (2014) Vitamin E prevents glucose metabolism alterations induced by static magnetic field in rats. Environ Sci Poll Res 21(22):12731–12738

Green EL (1966) Biology of the laboratory mouse. Dover publications, New York

Hashish AH, El-Missiry MA, Abdelkader HI, Abou-Saleh RH (2008) Assessment of biological changes of continuous whole body exposure to static magnetic field and extremely low frequency electromagnetic fields in mice. Ecotoxicol Environ Saf 71:895–902

Heinrich A, Szostek A, Nees F, Meyer P, Semmler W, Flor H (2011) Effects of static magnetic fields on cognition, vital signs, and sensory perception: a meta analysis. J Magn Reson Imaging 34(4):758–763

Kiss B, László JF, Szalai A, Pórszász R (2015) Analysis of the effect of locally applied inhomogeneous static magnetic field-exposure on mouse ear edema—a double blind study. PLoS ONE 10(2), e0118089

Kremmyda L-S, Tvrzicka E, Stankova B, Zak A (2011) Fatty acids as biocompounds: their role in human metabolism, health and disease—a review. Part 2: fatty acid physiological roles and applications in human health and disease. Biomed Pap Med Fac Univ Palacky Olomouc Czech Repub 155(3):195–218

Lahbib A, Elferchichi M, Ghodbane S, Belguith H, Chater S, Sakly M, Abdelmelek H (2010) Time-dependent effects of exposure to static magnetic field on glucose and lipid metabolism in rat. Gen Physiol Biophys 29:390–395

László J, Reiczigel J, Székely L, Gasparics A, Bogár I, Bors L, Rácz B, Gyires K (2007) Optimization of static magnetic field parameters improves analgesic effect in mice. Bioelectromagnetics 28:615–627. doi:10.1002/bem.20341

László J, Gyires K (2009) 3 T homogeneous static magnetic field of a clinical MR significantly inhibits pain in mice. Life Sci 84:12–17

László JF, Hernádi L (2012) Whole body static magnetic field exposure increases thermal nociceptive threshold in the snail, Helix pomatia. Acta Biol Hung 63(4):441–452

László JF, Farkas P, Reiczigel J, Vágó P (2012) Effect of local exposure to inhomogeneous static magnetic field on stomatological pain sensation—a double-blind, randomized, placebo-controlled study. Int J Radiat Biol 88(5):430–438

Lizenko MV, Regerand TI, Bakhirev AM, Lizenko EI (2008) Comparative biochemical analysis of lipids of blood serum-lipoproteins of human and some animal species. J Evol Biochem Physiol 44(5):581–590

McGarry JD (2002) Lipid metabolism I. In: Devlin TM (ed) Texbook of biochemistry with clinical correlations, 5th edn. Wiley-Liss, New York, pp 693–726

Mihoub M, El May A, Aloui A, Chatti A, Landoulsi A (2012) Effects of static magnetic fields on growth and membrane lipid composition of Salmonella typhimurium wild-type and dam mutant strains. Int J Food Microbiol 157:259–266

Nešković N, Ristić-Djurović J, Vorojtsov SB, Beličev P, Ivanenko IA, Ćirković S, Vorozhtsov AS, Bojović B, Dobrosavljević A, Vujović V, Čomor JJ, Pajović SB (2003) Status report of the VINCY Cyclotron, Nukleonika vol. 48 suppl. 2 (2003),—Special Issue—Proc. of the XXXIII European Cyclotron Progress Meeting, Warsaw and Krakow, Poland, September, 17–21, 2002, S135-S139

Nikolić L, Bataveljić D, Andjus PR, Nedeljković M, Todorović D, Janać B (2013) Changes in the expression and current of the Na+/K+ pump in the snail nervous system after exposure to a static magnetic field. J Exp Biol 216(18):3531–3541

Oguzhan B, Sancho V, Acitores A, Villanueva-Peñacarrillo M-L, Portois L, Chardigny J-M, Sener A, Carpentier YA, Malaisse WJ (2006) Alteration of adipocyte metabolism in ω3 fatty acid-depleted rats. Horm Metab Res 38(12):789–798

Pepys MB, Hirschfield GM (2003) C-reactive protein: a critical update. J Clin Invest 111:1805–1812

Perona JS, Vögler O, Sánchez-Domínquez JM, Montero E, Escribá PV, Ruiz-Gutierrez V (2007) Consumption of virgin olive oil influences membrane lipid composition and regulates intracellular signaling in elderly adults with type 2 diabetes mellitus. J Gerontol A Biol Sci Med Sci 62(3):256–263

Pinkus GS, Said JW (1988) Hodgkin's disease, lymphocyte predominance type, nodular-further evidence for a B cell derivation. L & H variants of Reed-Sternberg cells express L26, a pan B cell marker. Am J Pathol 133:211–217

Poniedzialek B, Rzymski P, Karczewski J, Jaroszyk F, Wiktorowicz K (2013) Reactive oxygen species (ROS) production in human peripheral blood neutrophils exposed in vitro to static magnetic field. Electromagn Biol Med 32(4):560–568

Ren J, Han EJ, Chung SH (2007) In vivo and in vitro anti-inflammatory activities of alpha-linolenic acid isolated from Actinidia polygama fruits. Arch Pharm Res 30(6):708–714

Rigotti A, Marzolo MP, Nervi F (1994) Lipid transport from the hepatocyte into the bile. Curr Top Memb 40:579–615

Rosen AD (1993) A proposed mechanism for the action of strong static magnetic fields on biomembranes. Int J Neurosci 73:115–119

Rosen AD (2003) Mechanism of action of moderate-intensity static magnetic fields on biological systems. Cell Biochem Biophys 39(2): 163–173

Sahebjamei H, Abdolmaleki P, Ghanati F (2007) Effects of magnetic field on the antioxidant enzyme activities of suspension-cultured tobacco cells. Bioelectromagnetics 28:42–47

Saunders R (2005) Static magnetic fields: animal studies. Prog Biophys Mol Biol 87:225–239

Schenck JF (2005) Physical interactions of static magnetic fields with living tissues. Prog Biophys Mol Biol 87:185–204

Soto-Vaca A, Losso JN, McDonough K, Finley JW (2013) Differential effect of 14 free fatty acids in the expression of inflammation markers on human arterial coronary cells. J Agric Food Chem 61(42):10074–10079

Staiger H, Staiger K, Stefan N, Wahl HG, Machicao F, Kellerer M, Häring HU (2004) Palmitate-induced interleukin-6 expression in human coronary artery endothelial cells. Diabetes 53:3209–3216

Tepšić V, Pavlović M, Ristić-Medić D, Ristić V, Lekić N, Tepšić J, Debeljak-Martačić J, Milićević M, Glibetić M (2008) Influence of dietary fats on serum phospholipid fatty acid composition and its relation to obesity in animals. Acta Vet 58:33–41

Todorović D, Perić-Mataruga V, Mirčić D, Ristić-Djurović J, Prolić Z, Petković B, Savić T (2015) Estimation of changes in fitness components and antioxidant defense of Drosophila subobscura (Insecta, Diptera) after exposure to 2.4 T strong magnetic field. Environ Sci Pollut Res 22:5305–5314. doi:10.1007/s11356-014-3910-8

Vergallo C, Dini L, Szamosvölgyi Z, Tenuzzo BA, Carata E, Panzarini E, László JF (2013) In vitro analysis of the anti-inflammatory effect of inhomogeneous static magnetic field-exposure on human macrophages and lymphocytes. PLoS ONE 8(8), e72374

Watanabe Y, Nakagawa M, Miyakoshi Y (1997) Enhancement of lipid peroxidation in the liver of mice exposed to magnetic field. Industrial Health 35:285–230

Wu D, Liu J, Pang X, Wang S, Zhao J, Zhang X, Feng L (2014) Palmitic acid exerts pro-inflammatory effects on vascular smooth muscle cells by inducing the expression of C-reactive protein, inducible nitric oxide synthase and tumor necrosis factor-α. Int J Mol Med 34(6):1706–12

Xu S, Okano H, Tomita N, Ikada Y (2011) Recovery effects of a 180 mT static magnetic field on bone mineral density of osteoporotic lumbar vertebrae in ovariectomized rats. eCAM 2011:ID620984:1–8

Zhao G, Chen S, Wang L, Zhao Y, Wang J, Wang X, Zhang WW, Wu R, Wu L, Wu Y, Xu A (2011) Cellular ATP content was decreased by a homogeneous 8.5 T static magnetic field exposure: role of reactive oxygen species. Bioelectromagnetics 32:94–101

Zhou BR, Zhang JA, Zhang Q, Permatasari F, Xu Y, Wu D, Yin ZQ, Luo D (2013) Palmitic acid induces production of proinflammatory cytokines interleukin-6, interleukin-1β, and tumor necrosis factor-α via a Nf-κB-dependent mechanism in HaCaT keratinocytes. Mediators Inflamm 2013:530429. doi:10.1155/2013/530429

IEEE TRANSACTIONS ON

NUCLEAR SCIENCE

A PUBLICATION OF THE IEEE NUCLEAR AND PLASMA SCIENCES SOCIETY

NUCLEAR & PLASMA SCIENCES SOCIETY

DECEMBER 2013 VOLUME 60 NUMBER 6 IETNAE (ISSN 0018-9499)

PART II OF TWO PARTS

SYMPOSIUM ON RADIATION MEASUREMENTS AND APPLICATIONS (SORMA WEST 2012)
OAKLAND, CA, USA, MAY 14–17, 2012

18TH REAL TIME CONFERENCE (RT2012)
BERKELEY, CA, USA, JUNE 11-15, 2012

19TH INTERNATIONAL WORKSHOP ON ROOM-TEMPERATURE SEMICONDUCTOR DETECTORS (RTSD)
ANAHEIM, CA, USA, OCTOBER 27–NOVEMBER 3, 2012

(Contents Continued on Page 4581)

IEEE

(Contents Continued from Front Cover)

REGULAR PAPERS

ACCELERATOR TECHNOLOGY

DIGITAL SIGNAL PROCESSING

DOSIMETRY

GAS DETECTORS

RADIATION EFFECTS

RADIATION IMAGING

RADIATION INSTRUMENTATION

READOUT ELECTRONICS

Magnet with Uncoupled Combined Functions

Jasna L. Ristić-Djurović, Saša Ćirković, and Andjelija Ž. Ilić, *Member, IEEE*

***Abstract*—Efficient extraction by ion stripping of a number of ion beams from a multipurpose cyclotron through the same transport line could be achieved with a combined function magnet. Characteristics of a combined magnet used for this purpose are significantly different from those of commonly used combined function magnets. For example, bending and focusing functions must be independently adjustable, beam paths are not centered to the device's axis, only one device is needed per cyclotron, and requirements regarding maximal achievable quadrupole and dipole fields as well as field linearity are not as demanding as for combined function magnets used for other applications. Using two analytical models as well as a simple numerical model, it is shown that two independently powered slanted dipoles, off-centered and arranged symmetrically with respect to the beam area, could efficiently serve as a combined function magnet in the stripping extraction system of a multipurpose cyclotron.**

***Index Terms*—Accelerators, combined function magnets, cyclotrons, stripping extraction.**

I. Introduction

A MULTIPURPOSE cyclotron provides a number of ion beams for different applications for the cost of a single machine. However, diversity of operating modes a machine delivers increases the difficulties encountered during its design and construction. Extraction of more than one beam from a multipurpose cyclotron into a single transport line is often achieved with the stripping extraction system [1]–[4]. In a cyclotron which accelerates negative as well as positive ion beams beam paths and transverse emittances after stripping extraction significantly depend on the sign of ion charge during acceleration [5]–[8]. Directions of ion beams accelerated as positive do not differ very much; however, these beams need to be focused in the horizontal direction as soon as they leave the cyclotron. Directions after extraction of ion beams accelerated as negative, although close to each other, significantly differ from those of ion beams which are accelerated as positive. After extraction ion beams accelerated as negative usually do not need to be focused because they change their sign, i.e., they become positive, during stripping and are therefore not defocused by the pole-edge field. Consequently, to efficiently prepare all the extracted beams for further transport through the same transport line a device providing adjustable strong horizontal focusing combined with weak horizontal bending for beams accelerated as positive as well as strong horizontal bending in the opposite direction for beams accelerated as negative is needed. Due to the limited available space in the extraction region, these functions should preferably be delivered by a single device–the combined function magnet.

Combined function magnets are commonly used in storage rings, synchrotrons, beam lines, linear accelerators, as well as in cancer therapy devices, see for example [9]–[16] and references therein. General practical and theoretical approaches to designing a combined function magnets for these purposes are given in [17]–[19], whereas some important questions that need to be considered for their effective operation are addressed in [20]–[22].

Requirements for the combined function magnet suitable for the stripping extraction system of a multipurpose cyclotron significantly differ from those of the magnets used for the mentioned purposes. If it is a part of a cyclotron extraction system, the combined function magnet needs only dipole and quadrupole components of the magnetic field; however, these components must be independently adjustable. For this type of application, not only that the beam paths through the magnet are not centered to the device's axis, but are in fact widely horizontally distributed over the aperture in the first half of the magnet's length [7]. The tolerable levels of field components other than the bending and focusing components as well as of the fringe field are fairly high. Consequently, the linearity of the achieved field in the beam area as well as the sharp fringe field decrease does not have to be met as rigorously as is the case with other types of applications. In [7], for example, the focusing magnetic field gradients are determined using the step size of 0.05 T/m which is 5% of the strongest gradient needed. In addition, the sizes of the beams which require strong focusing are two times smaller than the considered beam area. On the other hand, the beams which require strong bending travel through the entire horizontal range of the considered beam area and the bending fields needed for different ion beams were calculated in [7] with five significant digits. However, these beams do not require focusing and their horizontal size is more than five times smaller than the considered beam area. Therefore, the linearity offset close to the beam area borders as high as 5% will not cause significant defocusing problems. If necessary, bending offsets in the beam area can be accounted for by using achieved shape of the field instead of the assumed linear dependence in the calculation of the bending field required for a particular beam. Finally, only a single combined function magnet is needed in the stripping extraction system of a multipurpose cyclotron.

The most common way to provide focusing is with a quadrupole structure of a magnet, whereas for independent adjustability of focusing and bending functions two uncoupled

Manuscript received July 10, 2013; revised August 23, 2013; accepted November 06, 2013. Date of publication December 03, 2013; date of current version December 11, 2013. This work was supported by the Serbian Ministry of Education, Science and Technological Development under Grant III45003 .

The authors are with the Innovation Center, School of Electrical Engineering, University of Belgrade, 11120 Belgrade, Serbia (e-mail: jasna@stanfordalumni.org; sasa.cirkovic@ic.etf.bg.ac.rs; andjelijailic@ ieee.org).

Color versions of one or more of the figures in this paper are available online at http://ieeexplore.ieee.org.

Digital Object Identifier 10.1109/TNS.2013.2290309

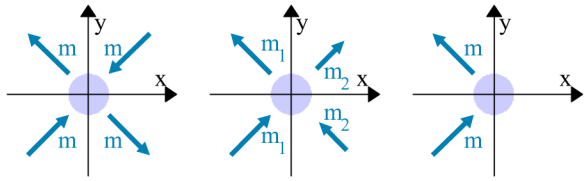

Fig. 1. Concept evolution. In each of the three sketches the ion beam area is indicated by a shaded circle, whereas the poles are represented by their magnetic moment vectors. The leftmost sketch corresponds to a typical quadrupole. If its poles are independently powered in pairs, as shown in the middle sketch, values of the two magnetic moments, m_1 and m_2, serve to adjust bending as well as focusing of an ion beam. This concept will work if the two slanted as well as off-centered poles shown in the rightmost sketch provide linear field in the beam area.

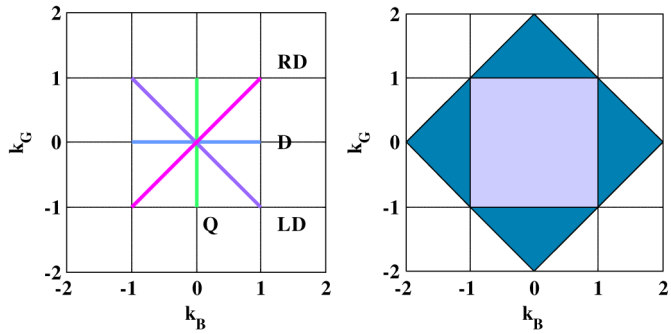

Fig. 2. Available sets of bending and focusing factors. The bending and focusing factors, k_{B} and k_{G}, scale the fields of a considered device to their maximums, i.e., $B_y = k_{\mathrm{G}} \cdot G_{\max} \cdot x + k_{\mathrm{B}} \cdot B_{\max}$. The line segments in the left graph represent a typical quadrupole, Q, dipole, D, and two slanted dipoles displaced to the left and to the right of the beam line, LD and RD. When independently powered slanted dipoles LD and RD are combined into a single device, their bending and focusing factors, $k_{\mathrm{BL}} = -k_{\mathrm{GL}} = k_1$ and $k_{\mathrm{BR}} = k_{\mathrm{GR}} = k_2$, determine bending and focusing factors of the new device as $k_{\mathrm{B}} = k_1 + k_2$ and $k_{\mathrm{G}} = k_2 - k_1$. Consequently, the two line segments representing each slanted dipole as a single device in the left graph expand into the area shown in the right graph. The original ranges of bending and focusing factors, $[-1, 1]$, are uncoupled and are shown as lighter inner square. In addition, four sets of factors depicted as the darker triangles are now available.

input parameters must be available. Both of these requirements are met if a quadrupole is composed of two independently powered slanted dipoles, see Fig. 1. Initially, we assume that each of the dipoles can affect the other one only by the effective change in the field levels, rather than by the major qualitative field changes such as the field linearity. The magnetic moments of a slanted dipole's poles are not parallel, instead they are both inclined with respect to the y-axis by the same angle but in the opposite directions. In a typical quadrupole all four poles are azimuthally equidistant, whereas above described slant angle of a pole can have an arbitrary value. In addition, unlike a typical dipole whose target area is around its axis, the slanted dipole outlined in the right sketch in Fig. 1 is off-centered with respect to the beam area, i.e., the coordinate system origin. If a quadrupole composed of a slanted off-centered dipole and its independently powered mirror image is to be used as a combined function magnet, each of the slanted dipoles has to produce approximately linear field in the beam area in the vertical direction, i.e., $B_y = G \cdot x + B_{\mathrm{st}}$. Linear field of the slanted dipole ensures that when two such fields are added in the proposed combined function magnet, the resulting sum is linear as well, regardless of the excitation current intensities which cause the two components.

Asymmetric excitation of a quadrupole by shunting part of the current from one pair of the coils is described in [23]. Our generalization of the problem to slanted dipoles is aimed at providing the dependence between the slanted dipole geometry and the achieved field quality. Note that the asymmetrically excited quadrupole is a special case of the combined function magnet composed of two slanted dipoles.

Operation of five devices with respect to bending and focusing is illustrated in Fig. 2. The left graph is devoted to a typical quadrupole, Q, a typical dipole, D, a slanted dipole shifted to the left of the beam area, LD, and its mirror image, i.e., a slanted dipole displaced to the right of the beam area, RD. The fifth device, the combined magnet composed of the two slanted dipoles is represented in the right graph. To enable comparison of the devices, bending and focusing factors, k_{B} and k_{G}, which define bending and focusing properties of a device, are expressed with respect to the device's maximal steering field and focusing gradient, $B_{\max}$ and $G_{\max}$, respectively. Therefore, a particular operating mode of a device is defined by k_{B} and k_{G}, which can, in general, take any value between -1 and 1. For a typical quadrupole $k_{\mathrm{B}} = 0$, whereas for a typical dipole $k_{\mathrm{G}} = 0$. If a slanted off-centered dipole is displaced to the right of the coordinate system origin its bending and focusing factors are equal, $k_{\mathrm{G}} = k_{\mathrm{B}}$, whereas for its mirror image, denoted as shifted to the left of the beam area, $k_{\mathrm{G}} = -k_{\mathrm{B}}$. When the two independently powered slanted off-centered dipoles are composed into a combined function magnet the operating area expands from the two line segments shown in the left graph into the square depicted in the right graph in Fig. 2. For ion beams accelerated as negative, operating conditions of the device will be chosen from the most-right dark triangle, i.e., from the area where $k_{\mathrm{B}} > 1$ and $k_{\mathrm{G}} \approx 0$. After extraction, ion beams accelerated as positive need strong focusing as well as weak bending and both bending and focusing factors should be negative. Consequently, the operating mode of the combined function magnet is most likely to be chosen from the left half of the lower dark triangle, i.e., from the area defined by $k_{\mathrm{B}} < 0$ and $k_{\mathrm{G}} < -1$.

A single value of $k_{\mathrm{B}} \in (-2, 2)$ or $k_{\mathrm{G}} \in (-2, 2)$ in the combined function magnet can be achieved by multiple combinations of the field scaling factors of the left and right slanted dipole, k_1 and k_2, see Fig. 3. Even though k_{B} as well as k_{G} is not governed by a single parameter k_1 or k_2, the mapping of sets of pairs $(k_{\mathrm{B}}, k_{\mathrm{G}}) \leftrightarrow (k_1, k_2)$ is of one-to-one type. Consequently, the values of k_{B} and k_{G} can be adjusted independently.

The problem comes down to ensuring that a single slanted off-centered dipole can provide approximately linear magnetic field in the beam area. The concept is validated by modeling the slanted off-centered dipole with two analytical models as well as with one numerical model.

II. Analytical Models

A. Ideal Dipoles

In the first approximation of a slanted off-centered dipole each of its poles is modeled with an ideal dipole, as shown in Fig. 4. The diameter of the beam area as well as the horizontal pole offset from the coordinate system origin is fixed and taken

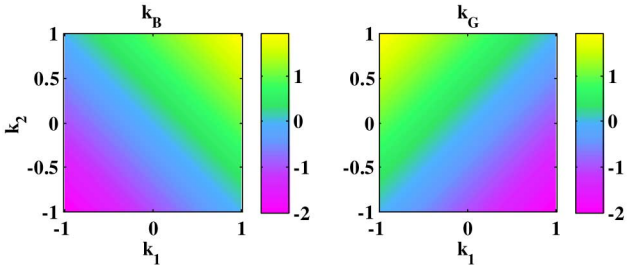

Fig. 3. Input/output mapping. The bending and focusing factors of the combined function magnet are uncoupled because the mapping $(k_{\mathrm{B}}, k_{\mathrm{G}}) \leftrightarrow (k_1, k_2)$ is a one-to-one mapping.

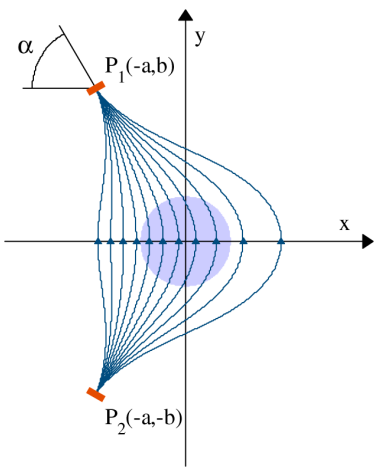

Fig. 4. Ideal dipoles model. Each pole of the slanted off-centered dipole is modeled by an ideal dipole inclined with respect to the horizontal axis by a slant-angle, α. The distance between the ideal dipoles is $2b$ and they are both shifted to the left of the beam axis by a. The diameter of the considered beam area is taken to be a, as well; therefore, this parameter is further used as the scaling factor for distances.

to be a. Consequently, a is used as the scaling factor, whereas the spatial parameters expected to shape the resulting magnetic field are α and b/a.

Magnetic field of an ideal dipole positioned at the origin of the coordinate system and aimed along the z-axis is defined in [24] as

$$B_x = \frac{\mu_0 m}{4\pi} \cdot \frac{3xz}{R^5}$$
$$B_y = \frac{\mu_0 m}{4\pi} \cdot \frac{3yz}{R^5}$$
$$B_z = \frac{\mu_0 m}{4\pi} \cdot \left[\frac{3z^2}{R^5} - \frac{1}{R^3}\right], \qquad (1)$$

where $R = \sqrt{x^2+y^2+z^2}$, $\mu_0 = 4\pi \cdot 10^{-7}$ H/m and m is ideal dipole magnetic moment. After appropriate coordinate transformation for each of the two poles of the slanted off-centered dipole and summation, these formulas lead to the vertical magnetic field component along the horizontal axis, i.e., for $y = 0$:

$$B_y(x) = B_0 \cdot \left[\left(1+\frac{x}{a}\right)^2 + \frac{b^2}{a^2}\right]^{-5/2} \cdot \left[3\frac{b}{a}\left(1+\frac{x}{a}\right)\cos\alpha + \left(2\frac{b^2}{a^2} - \left(1+\frac{x}{a}\right)^2\right)\sin\alpha\right], \qquad (2)$$

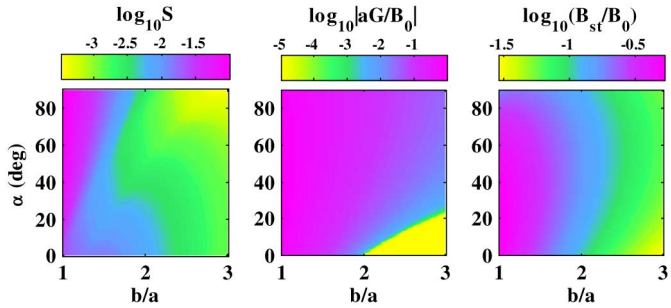

Fig. 5. Influence of slant-angle, α, and pole distance, b/a, on device properties. The dependence of the field linearity coefficient, S, as well as of normalized focusing and bending capabilities, aG/B_0 and B_{st}/B_0, on α and b/a is shown in the right, middle and left graph, respectively. In general, small values of S and large values of aG/B_0 and B_{st}/B_0 are desired; however, the values of α and b/a which correspond to any desired optimization criterion can be determined from the depicted data.

where $B_0 = \mu_0 m/(2\pi a^3)$, whereas α, a and b are defined in Fig. 4. The values of B_y and of its derivative at $x = 0$ are used to define steering and focusing capabilities of the device, B_{st} and G as

$$B_{\mathrm{st}} \equiv B_y(0) = B_0 \cdot \left(1+\frac{b^2}{a^2}\right)^{-5/2} \cdot \left[3\frac{b}{a}\cos\alpha + \left(2\frac{b^2}{a^2}-1\right)\sin\alpha\right]$$
$$G \equiv \left.\frac{\partial B_y}{\partial x}\right|_{x=0} = B_0\frac{3}{a} \cdot \left(1+\frac{b^2}{a^2}\right)^{-7/2} \cdot \left[\frac{b}{a}\left(\frac{b^2}{a^2}-4\right)\cos\alpha + \left(1-4\frac{b^2}{a^2}\right)\sin\alpha\right]. \qquad (3)$$

These are used to linearly approximate B_y along the line segment $x \in [-a/2, a/2]$ as $Gx + B_{\mathrm{st}}$, as well as to further quantitatively express linearity coefficient of B_y as

$$S = \frac{1}{aB_0}\int_{-a/2}^{a/2} |B_y - Gx - B_{\mathrm{st}}|dx. \qquad (4)$$

The influence of the slant angle, α, and vertical pole distance expressed as b/a, on the linearity, focusing and bending coefficients of the resulting field is given in Fig. 5. To broaden the applicability of the results, bending and focusing coefficients are scaled to B_0 and are defined as B_{st}/B_0 and aG/B_0, respectively.

Since the discrepancy between the achieved field and its linear approximation does not have to be very small if the combined function magnet is used as a part of the cyclotron stripping extraction system, the geometry of the ideal dipole model is optimized using the optimization criterion $\max(|B_{\mathrm{st}}/B_0| \cdot |aG/B_0|)$ and the restriction $S \leq 0.004$. The corresponding optimized geometry of the ideal dipoles model has $\alpha = 60°$ and $b/a = 1.7$. The normalized horizontal and vertical components of the magnetic field obtained with this geometry in the beam area are given in Fig. 6. The values of the focusing and bending parameters as well as field linearity

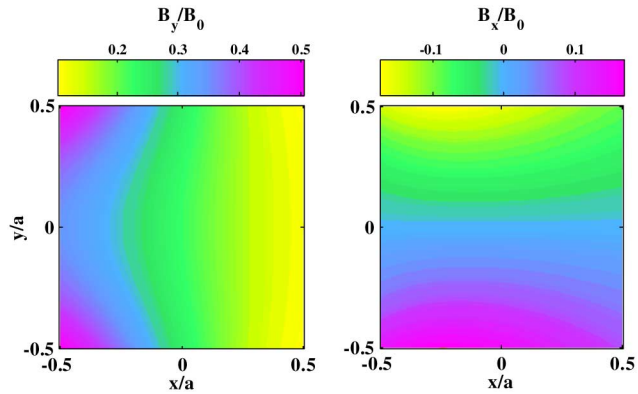

Fig. 6. Normalized magnetic field components. For the ideal dipoles model with $\alpha = 60°$ and $b/a = 1.7$, the magnetic field in the beam area follows the desired pattern along x-axis as well as along y-axis. Namely, B_y is approximately linear and $B_x \cong 0$ for $y = 0$, whereas for $x = 0$ it is the other way around, i.e., $B_y \cong const.$ and B_x is approximately linear. However, the contour lines noticeably deviate from straight lines away from the axes.

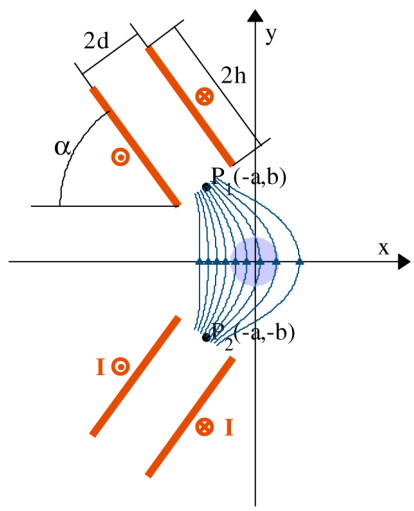

Fig. 7. Current stripes model. Infinite current stripes are expected to be a better model of a lengthy device. In addition to the slant angle, α, and pole distance expressed as b/a, which were used to define an ideal dipoles model, two new parameters, the stripe distance and width, expressed as d/a and h/a, respectively, must be considered as well. Following the principle established for the ideal dipoles model, all the distances, including the additional parameters are normalized to the beam area diameter i.e. the horizontal offset of the poles, a.

coefficient, as defined by (3) and (4) are $aG/B_0 = -0.26$, $B_{\rm st}/B_0 = 0.22$, and $S = 0.0039$.

Despite promising results regarding the shape of the field the ideal dipoles model must be taken with caution because it does not take into account considerable length of a combined function magnet suitable for cyclotron extraction system, which is of the order of 0.5 m [7].

B. Infinitely Long Current Stripes

With the aim to obtain a more realistic model of a lengthy slanted off-centered dipole its poles are represented each with two infinitely long current stripes, Fig. 7. There are four parameters whose influence on the field must be considered: the slant angle, α, normalized half-distance between the poles, b/a, normalized half-width of the poles, d/a, and normalized half-width of the current stripes, h/a.

Magnetic field of the current stripes model is examined using the same parameters that were used in the case of the ideal dipoles model, i.e., the scaled bending and focusing parameters, $B_{\rm st}/B_0$ and aG/B_0, as well as the linearity coefficient, S. An infinitely long current stripe is treated as a collection of infinitely long wires; therefore, its magnetic field is calculated by integrating magnetic fields of infinite wires over the stripe width. Using the expression given in [24] for the strength of the magnetic field at a distance r from an infinitely long wire with current $\mathrm{d}I$,

$$\mathrm{d}B = \frac{\mu_0 \mathrm{d}I}{2\pi r}, \tag{5}$$

the magnetic field of an infinitely long current stripe defined by $y \in [-h, h]$ and its uniformly distributed total current, I, is calculated to be

$$\begin{aligned} B_x &= \frac{\mu_0 I}{8\pi h} \ln \frac{x^2 + (y-h)^2}{x^2 + (y+h)^2} \\ B_y &= \frac{\mu_0 I}{8\pi h} \left(\arctan \frac{y+h}{x} - \arctan \frac{y-h}{x} \right). \end{aligned} \tag{6}$$

Using formulas (6) for the magnetic field of a single infinitely long current stripe, characterized by its width, $2h$, and uniformly distributed total current, I, after appropriate coordinate transformation for different stripes within the model and summation, the vertical magnetic field component of the slanted off-centered dipole along the horizontal axis, i.e., for $y = 0$, is calculated to be

$$\begin{aligned} B_y(x)/B_0 = \frac{a}{h} \sum_{i=1,2} \sum_{j=3,4} \{(-1)^{i+j-1} \\ \cdot [\cos\alpha \ln(x_i^2 + x_j^2) + 2 \sin\alpha \arctan(x_j/x_i)]\} \end{aligned} \tag{7}$$

where

$$\begin{aligned} x_1 &= (x/a + 1)\sin\alpha - b/a \cos\alpha + d/a \\ x_2 &= (x/a + 1)\sin\alpha - b/a \cos\alpha - d/a \\ x_3 &= (x/a + 1)\cos\alpha + b/a \sin\alpha \\ x_4 &= (x/a + 1)\cos\alpha + b/a \sin\alpha + 2h/a, \end{aligned} \tag{8}$$

$B_0 = \mu_0 I/(4\pi a)$, $\mu_0 = 4\pi \cdot 10^{-7}$ H/m, and I is stripe current, whereas α, a, b, d, and h are defined in Fig. 7. Since $B_{\rm st}/\mathrm{B}_0 = B_y(0)/B_0$, the formula for the scaled bending parameter, $B_{\rm st}/\mathrm{B}_0$, is identical to (7); however, the values for x_1, x_2, x_3, and x_4 are now

$$\begin{aligned} x_1 &= \sin\alpha - b/a \cos\alpha + d/a \\ x_2 &= \sin\alpha - b/a \cos\alpha - d/a \\ x_3 &= \cos\alpha + b/a \sin\alpha \\ x_4 &= \cos\alpha + b/a \sin\alpha + 2h/a. \end{aligned} \tag{9}$$

These values, defined by (9), should be used to calculate scaled focusing parameter, aG/B_0, as well:

$$\begin{aligned} aGB_0 \equiv \frac{a}{B_0} \left.\frac{\partial B_y}{\partial x}\right|_{x=0} = \frac{2a}{h} \sum_{i=1,2} \sum_{j=3,4} \{(-1)^{i+j-1} \\ \cdot [x_i \sin(2\alpha) + x_j \cos(2\alpha)]/(x_i^2 + x_j^2)\}. \end{aligned} \tag{10}$$

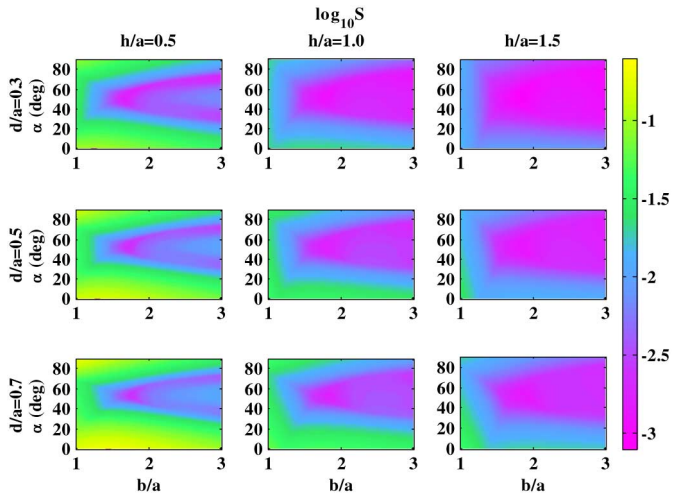

Fig. 8. Field linearity coefficient. Each of the nine graphs gives the dependence of S on α and b/a for a particular pair of values of d/a and h/a. The first, second and third row of graphs corresponds to d/a value of 0.3, 0.5, and 0.7, respectively. Each graph in the first, second and third column represents a set of current stripes models with the value of h/a equal to 0.5, 1.0, and 1.5, respectively. The areas corresponding to the desirable low values of S are larger for smaller d/a and larger h/a.

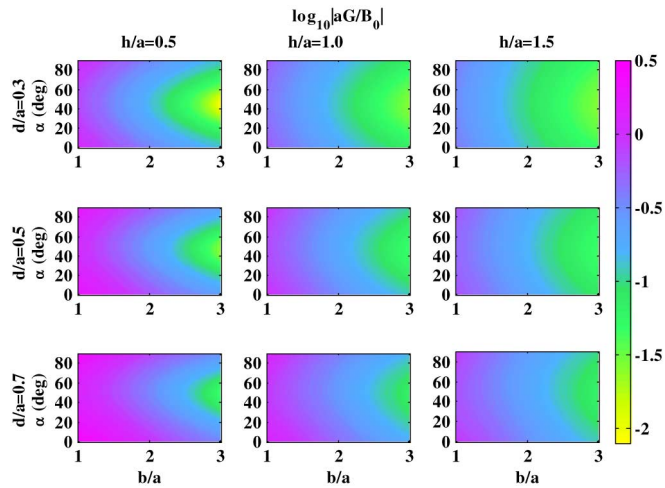

Fig. 9. Beam focusing coefficient. The format of the figure is the same as for Fig. 8. The areas corresponding to the desirable large values of aG/B_0 are larger for larger d/a and smaller h/a. The models with smaller values of b/a provide stronger focusing.

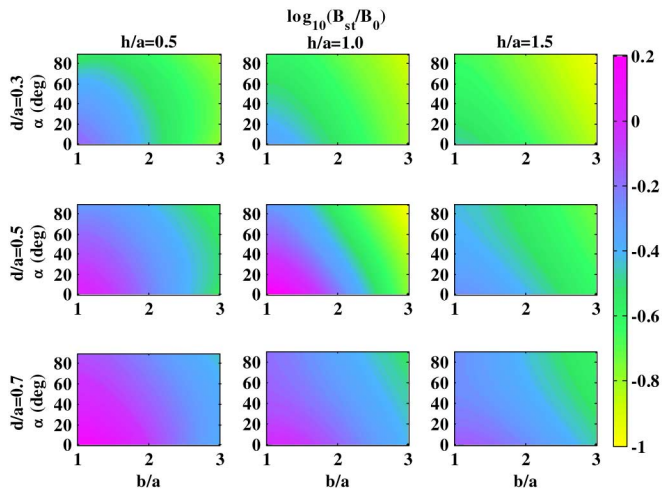

Fig. 10. Beam bending coefficient. The format of the figure is the same as for Fig. 8. The areas corresponding to the desirable large values of $B_{\rm st}/B_0$ are larger for larger d/a and smaller h/a. The models with smaller values of α and b/a provide stronger steering.

Further, B_y calculated with (7) and (8), G determined by (10) and (9), as well as $B_{\rm st}$ defined with (7) and (9) are used in (4) to obtain S, the linearity coefficient of B_y along the line segment $x \in [-a/2, a/2]$, which corresponds to the current stripes model.

In the ideal dipoles model each of the three considered characteristics of the magnetic field depends on the two parameters, α and b/a; therefore, the dependence is illustrated with a single contour plot per magnetic field characteristics, see Fig. 5. In the current stripes model there are four parameters whose influence has to be investigated, α, b/a, d/a, and h/a. Consequently, the dependence of the linearity coefficient, S, focusing parameter, aG/B_0, and bending parameter, $B_{\rm st}/B_0$, on these four parameters is each depicted with the nine contour plots in Figs. 8, 9, and 10, respectively.

Comparison of the results shown in Figs. 8, 9, and 10 reveals that the process of defining the four model parameters, α, b/a, d/a, and h/a, must be a trade-off between small values of the linearity coefficient and large values of the focusing and bending coefficients. The optimization criterion and restrictions should be chosen in accordance with the desired field linearity as well as with the focusing and bending strengths needed in a particular design of the device. For the sake of consistency, the optimization criterion, $\max(|B_{\rm st}/B_0| \cdot |aG/B_0|)$, and the restriction, $S \leq 0.004$, used here as an example are the same as those used for the ideal dipoles model. The obtained optimized geometry of the current stripes model has $\alpha = 51°$, $b/a = 1.65$, $d/a = 0.7$, and $h/a = 0.5$. The scaled horizontal and vertical components of the magnetic field obtained with this geometry in the beam area are given in Fig. 11. The values of the corresponding focusing, bending and field linearity coefficients are $aG/B_0 = -0.62$, $B_{\rm st}/B_0 = 0.81$, and $S = 0.004$.

Table I lists the considered optimized example in the first row and compares it with the models resulting from three other optimization conditions. The two models with $\alpha = 45°$ and $b/a = 1$ are the limiting examples of an independently powered quadrupole. The model in the second row represents a typical quadrupole with the minimal linearity coefficient, whereas the one in the third row is characterized by the maximal bending coefficient. Comparison of these two models with other models of a typical quadrupole revealed that the two limiting models are such with respect to all three considered coefficients. Namely, the model with the minimal linearity coefficient also has the minimal values of the focusing and bending coefficients, whereas the one with the maximal bending coefficient is characterized with the maximal linearity and focusing coefficients, as well. The typical quadrupole model with the most linear field, i.e., the smallest S, is inferior to our optimized model in all respects. The typical quadrupole model with the maximal values of the coefficients does provide 2.2 times stronger focusing as well as 1.2 stronger bending than our optimized model; however, it is 13 times less linear. In addition, there

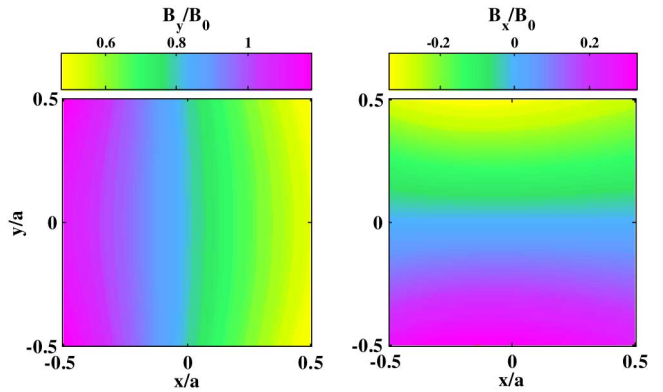

Fig. 11. Normalized magnetic field components. The scaled vertical (left graph) and horizontal (right graph) magnetic field components correspond to the current stripes model with $\alpha = 51°$, $b/a = 1.65$, $d/a = 0.7$, and $h/a = 0.5$. The contour lines do not deviate very much from the desired vertical and horizontal straight lines pattern for B_y and B_x, respectively. The deviation from the desired pattern is more pronounced at larger distances from the axes.

TABLE I
COMPARISON OF FOUR MODEL GEOMETRIES

$\alpha(°)$	b/a	d/a	h/a	S	aG/B_0	B_{st}/B_0
51	1.65	0.7	0.5	0.004	-0.62	0.81
45	1	0.3	1.5	0.014	-0.34	0.27
45	1	0.7	0.5	0.053	-1.36	1.00
30	1.15	0.7	0.5	0.050	-1.40	1.10

are examples of other models which provide stronger focusing as well as bending even with slightly better linearity than the independently powered typical quadrupole, as can be seen from the third and fourth row of Table I.

The field linearity, focusing as well as bending coefficients predicted by the infinite current stripes model satisfy the requirements set for the combined function magnet used in the extraction system of a multipurpose cyclotron. Validity of this analytical model as well as of the concept of slanted off-centered dipoles is further tested by a numerical model.

III. NUMERICAL MODEL

The numerical model whose geometry is given in Fig. 12 is constructed and its magnetic field is calculated with MERMAID–a 3-D software package based on the first order finite elements method [25]. A 3-D mesh of the model is constructed from a non-uniform 2-D triangular mesh in $z = const.$ planes and a non-uniform 1-D grid in the z-direction.

Having in mind comparison of the analytical and numerical models, the geometry of the numerical model is chosen to resemble as closely as possible the geometry of the infinite current stripes model. In order to also relate the numerical model to the existing example given in [7], it was assumed that $a = 10$ cm and that the coils are powered by $NI = 100$ kA. The resulting magnetic flux density at the mid-length of the device is given in Fig. 13. The obtained values of the steering field and focusing field gradient at the coordinate system origin are $B_{st} = 0.36$ T and $G = 2.3$ T/m.

The fields obtained with the numerical model and two analytical models are compared in Fig. 14. Unlike in Figs. 6 and

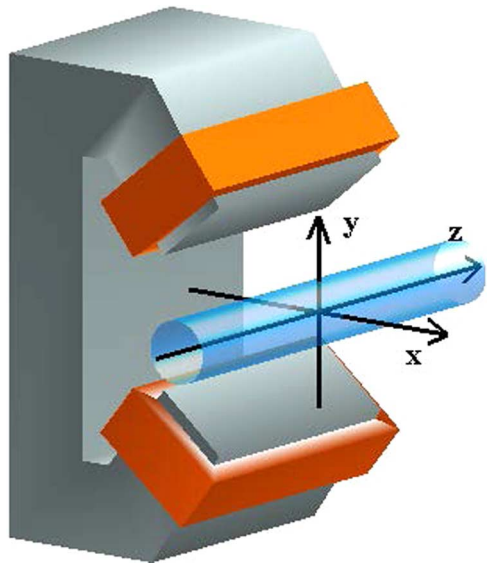

Fig. 12. Numerical model. The placement and width of the inner layers of the coils, i.e., next to the iron, in the $z = 0$ plane are identical to those of the infinite current stripes in the optimized current stripes model, namely, $\alpha = 51°$, $b/a = 1.65$, $d/a = 0.7$, and $h/a = 0.5$. The coil thickness and length in the z-direction is taken to be $w/a = 0.3$ and $L/a = 4$, respectively. The magnetic properties of the iron are defined with one of the $B - H$ curves embedded in the numerical modeling software.

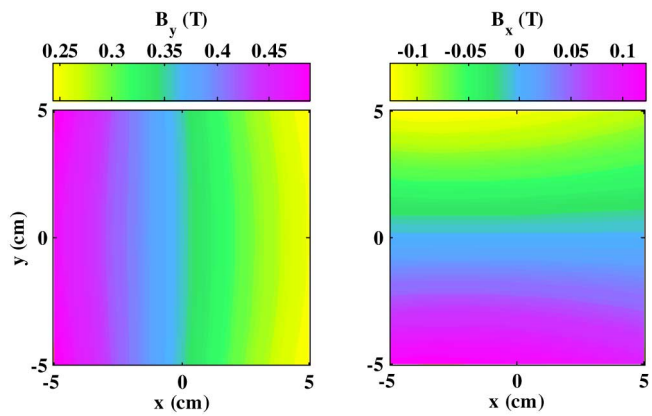

Fig. 13. Magnetic field components. The vertical and horizontal magnetic flux density components in the mid-plane, i.e., for $z = 0$, of the numerical model are given in the left and right graph, respectively. The longitudinal field component, B_z, is negligible. The contour lines do not deviate very much from the desired vertical straight lines for B_y and horizontal lines for B_x.

11, where B_0 is used for field normalization, the fields are here normalized to B_{st} in order to enable quantitative as well as qualitative comparison of the models.

The slanted dipole off-centered to the left of the beam area depicted in Fig. 12 is combined with its mirror image, referred to earlier as the slanted dipole displaced to the right of the beam line. Both dipoles are assumed to have the same maximal values of steering and focusing components of their fields, $B_{max} = 0.36$ T and $G_{max} = 2.3$ T/m, obtained from Fig. 13; however, the dipoles are independently powered to broaden the range of the resulting field according to Fig. 2. As stated earlier, the two input parameters, k_1 and k_2, are not independently responsible one for the focusing and the other for the bending function of the combined magnet. Fortunately, the needed excitation levels of

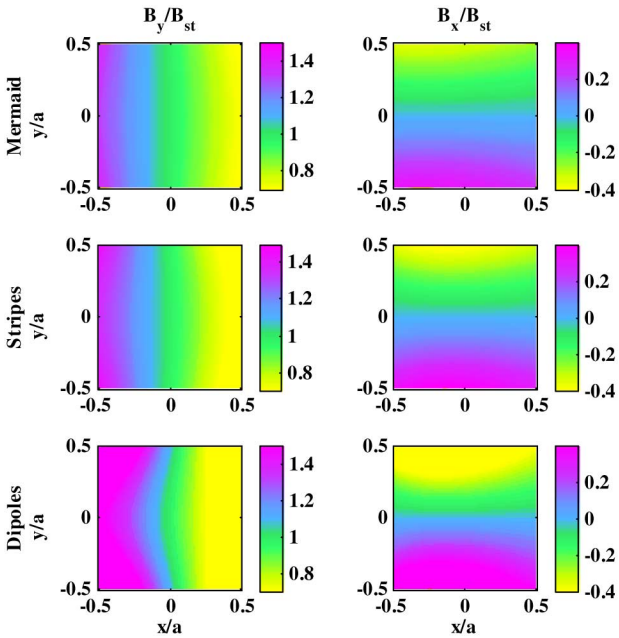

Fig. 14. Model comparison. The vertical, B_y (left column of graphs), and horizontal, B_x (right column of graphs), magnetic field components in the plane $z = 0$, of the numerical, current stripes, and ideal dipoles model are depicted in the first, second, and third row of graphs, respectively. To enable comparison, the field components are scaled to the steering field of the corresponding model. Note the good qualitative as well as quantitative agreement between the numerical model and the analytical model with infinite current stripes.

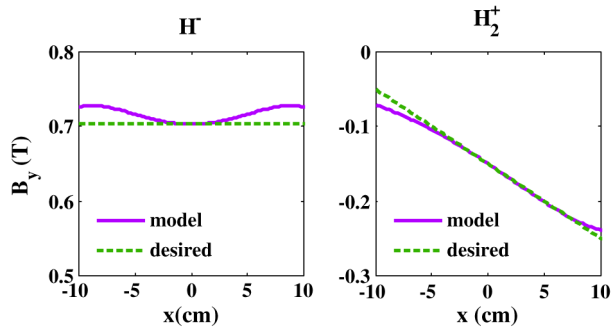

Fig. 15. Comparison of achieved and desired fields. To illustrate the applicability of the proposed design of the combined function magnet its fields are compared with the two limiting fields needed by the stripping extraction system described in [7]. The maximal relative errors of the achieved fields in the beam area, i.e. between -5 cm and 5 cm, are 1.87% for the H^- ions and 3.00% for the beam accelerated as H_2^+ ions, whereas for the two times larger interval, $x \in [-10\text{ cm},\ 10\text{ cm}]$, the maximal relative errors are 3.24% and 13.84%, respectively.

the two slanted dipoles are easily determined from the desired focusing and bending coefficients as $k_1 = (k_\mathrm{B} - k_\mathrm{G})/2$ and $k_2 = (k_\mathrm{B} + k_\mathrm{G})/2$.

To illustrate applicability of the described device in the stripping extraction system of multipurpose cyclotrons the limiting requirements for the combined function magnet from [7] are considered. For the beam of protons which are accelerated to the energy of 55 MeV as H^- ions the field needed in the combined function magnet is $B_y = 0.70$ T. Consequently, $k_\mathrm{B} = k_1 + k_2 = 1.97$ and $k_\mathrm{G} = k_2 - k_1 = 0$, which correspond to the scaling factors of the left and right off-centered dipoles $k_1 = 0.98$ and $k_2 = 0.98$, see Fig. 2 caption. For the ion beam accelerated as H_2^+ ions to 44 MeV, which are extracted as 22 MeV protons, the field in the combined magnet needs to be $B_y = -1$ T/m $\cdot\, x - 0.15$ T. Therefore, $k_\mathrm{B} = -0.42$, $k_\mathrm{G} = -0.43$, $k_1 = 0.01$, and $k_2 = -0.43$. The needed fields and those achieved in the numerical model of the proposed combined function magnet are shown in Fig. 15.

The purpose of the presented numerical model is to validate the analytical model and the principle of device's operation as well as to illustrate their applicability. In an engineering design of a particular device this numerical model can serve only as a first step in the design process. The good agreement between the numerical model and the analytical current stripes model ensures that Figs. 8, 9, and 10 can be used to determine the first estimate of the geometry of a device with the desired focusing and bending characteristics. Even though a simplified numerical model similar to the one presented here provides validation of the desired performance of a device, during the engineering design further steps towards a more realistic model as well as better field quality are due. For example, field linearity could be improved by changing the pole profile from the simple flat surface to the shape determined analytically using the method similar to the one described in [17] or numerically using the approach analogous to the one shown in [26]. Unlike the numerical model discussed here, in designing a particular device numerical modeling will focus on fulfilling engineering requirements rather than on resembling the analytical model. For example, the coil thickness as well as magnetomotive force would be adjusted in accordance with the resulting current density rather than with the similarity to the analytical model.

To illustrate a more realistic numerical modeling we use the same limiting requirements represented by the fields $B_y = 0.70$ T and $B_y = -1$ T/m $\cdot\, x - 0.15$ T, as for the simplified numerical model. The currents needed to achieve the field of 0.35 T or the gradient of 0.5 T/m with the slanted dipole modeled by the analytical, optimized infinite current stripes model are 432 kA and 80 kA, respectively. Consequently, the critical, the larger value of the two, $\mathrm{I}_\mathrm{max} = 432$ kA, is used further for rough estimates of the realistic numerical model parameters. Unlike the analytical, the numerical model takes into account iron core, which enlarges the field due to magnetization. In addition, iron pole shape, which can follow any of the equipotential surfaces, enables field enhancement resulting from the decrease of the distance between the dipole poles. At the same time, since the two slanted dipoles in our example of the combined magnet are closer to each other than are the two poles within a dipole, the coupling between the two dipoles is expected to cause the field decrease as well as the field gradient increase. Namely, the iron cores of both slanted dipoles affect the resulting field even if only one of the dipoles is powered. The analytical infinite stripes model can be used to roughly estimate this effect as $C_C = B(a,b)/B(-a,b) = 9.84\%$, where $B(-a,b)$ and $B(a,b)$ are, respectively, the field produced by the one slanted dipole at its pole tip and at the mirror image of its pole tip, i.e., at the point where the pole of the mirror dipole within the combined magnet would be. In order to take this effect into account the realistic numerical

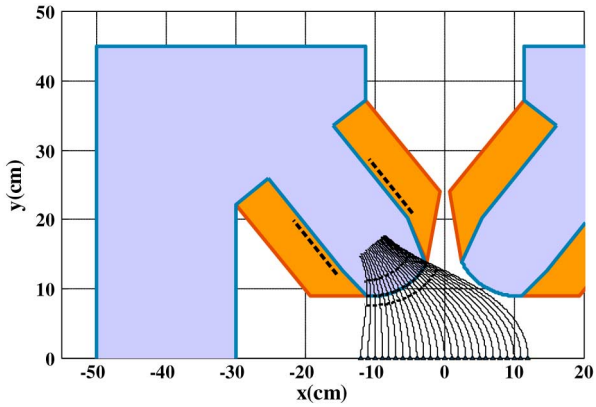

Fig. 16. Realistic numerical model. The infinite current stripes of the analytical model are indicated by the dashed straight line segments. The magnetic field lines corresponding to the analytical model are used to calculate three equipotential surfaces depicted with dashed black curves, the middle of which is used as a pole profile for the realistic numerical model. The coil width is taken to be $w = 6$ cm. The coil's outer height is extended to 17 cm compared to 10 cm wide current stripes, whereas on the inside the coils match the pole length. The iron core is 80 cm long along the z-axis.

model must include both slanted dipoles, unlike the simplified numerical model discussed previously. In a realistic numerical model the desired fields have to be achieved with a reasonable value of the induction current, i.e. the coil current density should not exceed $J_{\max} = 10$ A/mm^2. The mentioned estimates can be related to the coil's cross-section, S_{coil}, and field enhancement provided by the iron cores, C_{Fe}, as $S_{\text{coil}} \cdot C_{\text{Fe}} = (1 + C_c) \cdot I_{\max}/J_{\max} = 474.5$ cm^2. For example, if the iron core provides field enhancement factor equal to 4, the cross-section of the coils needs to be approximately 120 cm^2. The outline of a numerical model based on these estimates is shown in Fig. 16. Since the estimates are based on the analytical model the obtained outline of the numerical model should be treated as the second step in the design process. When designing a particular combined function magnet gap size, dipole coupling, as well as induction current density have to be carefully considered and further numerical model adjustments must follow.

IV. Conclusion

The proposed design of a combined function magnet offers simple and cost-effective way to improve extraction from multipurpose cyclotrons. Using two analytical models and one numerical model, it is shown that two independently powered, slanted, as well as off-centered dipoles form a combined function magnet suitable for use in the stripping extraction system of a multipurpose cyclotron. Bending and focusing functions of the magnet are uncoupled and each of them can be independently chosen to have any value between the two values which correspond to the limiting excitations of a single slanted off-centered dipole. In addition, each function of the combined magnet can have a value as high as double its limiting value corresponding to the slanted dipole. These additional values of one of the coefficients, bending or focusing, are achieved at the expense of the corresponding available range of the other coefficient. Although the bending as well as the focusing coefficient of the combined magnet is not governed by a single input parameter, the needed excitation coefficients of the two slanted dipoles are easily calculated using two linear expressions.

Applicability of the proposed combined function magnet is illustrated using the limiting fields of an example stripping extraction system and acceptable discrepancy between the desired and achieved fields is obtained. Nevertheless, the considered very simplified numerical model with its straight edges leaves numerous possibilities for field improvements. For example, the pole shape could be refined using a method similar to the one described in [17]. The shape and size of the numerical model is chosen to match the optimized analytical current stripes model. Therefore, optimization of the numerical model similar to the optimizations of the two analytical models performed using the data in Fig. 5 and Figs. 8, 9, and 10, is likely to improve the obtained field as well.

On the other hand, due to not so tight field accuracy requirements it seems worthwhile not only to optimize the geometry of the combined magnet, but to explore the possibility of obtaining a combined function magnet using the geometry of a typical quadrupole, as well. In [27] and [28] it was shown that a simple cost-effective change of the powering scheme of an existing device can lead to qualitatively different device. Similarly, extending the asymmetric excitation of a typical quadrupole, suggested in [23], to fully independent powering of its two-by-two poles can produce a combined function magnet suitable for ion beam extraction from a multipurpose cyclotron.

References

[1] S. Z. An, F. P. Guan, H. D. Guan, S. M. Wei, H. J. Yao, Y. J. Bi, J. Q. Zhong, X. L. Jia, T. J. Zhang, Y. L. Lü, G. F. Song, B. Ji, and T. Ge, "Stripping extraction calculation and simulation for CYCIAE-100," *Chinese Phys. C (HEP & NP)*, vol. 33, no. 2, pp. 42–46, Jun. 2009.

[2] D. Vandeplassche, W. Beeckman, W. Kleeven, S. Zaremba, J. L. Delvaux, L. Medeiros-Romao, J. C. Amélia, Y. Jongen, and J. Fermé, "Extraction simulations for the IBA C70 cyclotron," in *Proc. 18th Int. Conf. Cyclotrons Their Applications*, Giardini Naxos, Italy, Oct. 1-5, 2007, pp. 63–65.

[3] D. Solivajs, O. N. Borisov, A. Gall, G. G. Gulbekian, J. Keníž, J. Kliman, S. Králik, and M. Pavlovič, "A study of charge-exchange beam extraction from the multi-purpose isochronous cyclotron DC-72," *J. Elect. Engrg.*, vol. 55, no. 7–8, pp. 201–206, 2004.

[4] D. H. An, J. S. Chai, H. S. Chang, B. H. Hong, S. Hong, I. S. Jung, J. Kang, Y. Kim, M. Y. Lee, C. S. Park, J. Y. Suk, and T. K. Yang, "The stripping extraction system in the KIRAMS-13 cyclotron," in *Proc. 3rd Asian Particle Accelerator Conf.*, Gyeongju, Korea, Mar. 22-26, 2004, pp. 111–112.

[5] J. L. Ristić-Djurović and N. Nešković, "Analytical prediction of ion stripping extraction from isochronous cyclotrons," *IEEE Trans. Nucl. Sci.*, vol. 59, no. 2, pp. 268–271, Apr. 2012.

[6] J. L. Ristić-Djurović and N. Nešković, "Influence of cyclotron magnet gap size on stripping extraction," *IEEE Trans. Nucl. Sci.*, vol. 58, no. 3, pp. 1188–1195, Jun. 2011.

[7] J. L. Ristić-Djurović and S. Ćirković, "Unidirectional stripping extraction from a cyclotron which accelerates light as well as heavy ions," *Phys. Rev. Special Topics—Accel. Beams*, vol. 6, p. 033501, Mar. 2003.

[8] J. L. Ristić-Djurović, "Stripping extraction of positive ions from a cyclotron," *Phys. Rev. Special Topics—Accel. Beams*, vol. 4, p. 123501, Dec. 2001.

[9] V. V. Kashikhin, Y. I. Alexahin, N. V. Mokhov, and A. V. Zlobin, "High-field combined-function magnets for a 1.5 × 1.5 TeV muon collider storage ring," in *Proc. 3rd Int. Particle Accelerator Conf.*, New Orleans, LA, USA, May 20-25, 2012, pp. 3587–3589.

[10] S. C. Leemann, J. Ahlbäck, Å. Andersson, M. Eriksson, M. Johansson, L. -J. Lindgren, M. Sjöström, and E. Wallén, "Status of the MAX IV storage rings," in *Proc. 1st Int. Particle Accelerator Conf.*, Kyoto, Japan, May 23-28, 2010, pp. 2618–2620.

[11] A. Madur, D. Arbelaez, S. Marks, S. Prestemon, D. Robin, R. Schlueter, C. Steier, and W. Wan, "Harmonic sextupoles for the Advanced Light Source low emittance upgrade," *Nucl. Instrum. Meth. A*, vol. 649, pp. 39–41, 2011.

[12] S. P. Møller, H. Bach, F. Bødker, T. G. Christiansen, A. Elkjær, S. Friis-Nielsen, N. Hauge, J. Kristensen, L. Kruse, and B. R. Nielsen, "Status of the injection system for the Australian synchrotron project," in *Proc. 21st Particle Accelerator Conf.*, Knoxville, TN, USA, May 16-20, 2005, pp. 3271–3273.

[13] T. Nakamoto, N. Higashi, T. Ogitsu, A. Terashima, Y. Ajima, M. Anerella, R. Gupta, H. Hattori, T. Ichihara, Y. Iwamoto, N. Kimura, Y. Makida, T. Obana, K. Tanaka, P. Wanderer, and A. Yamamoto, "Design of superconducting combined function magnets for the 50 GeV proton beam line for the J-PARC neutrino experiment," *IEEE Trans. Appl. Supercond.*, vol. 14, no. 2, pp. 616–619, Jun. 2004.

[14] C. M. Spencer, C. Adolphsen, M. Berndt, D. R. Jensen, R. Rogers, J. C. Sheppard, S. St. Lorant, T. B. Weber, J. Weisend, II, H. Brueck, and F. Toral, "Measuring the magnetic center behavior and field quality of an ILC superconducting combined quadrupole-dipole prototype," *IEEE Trans. Appl. Supercond.*, vol. 20, no. 3, pp. 1964–1968, Jun. 2010.

[15] D. S. Robin, D. Arbelaez, S. Caspi, C. Sun, A. Sessler, W. Wan, and M. Yoon, "Superconducting toroidal combined-function magnet for a compact ion beam cancer therapy gantry," *Nucl. Instrum. Meth. A*, vol. 659, pp. 484–493, 2011.

[16] A. Morita, Y. Iwashita, A. Noda, T. Shirai, H. Tongu, M. Umezawa, K. Hiramoto, and M. Tadokoro, "Design and measurement of a combined function magnet intended for a cancer therapy accelerator," *Phys. Rev. Special Topics—Accel. Beams*, vol. 4, p. 122401, Dec. 2001.

[17] G. Sinha and G. Singh, "Design and characterization of combined function multipole magnet for accelerators," *Rev. Sci. Instrum.*, vol. 79, p. 123302, Dec. 2008.

[18] P. R. Sarma, "Ideal coil shape for combined function superconducting magnets," *J. Phys. D: Appl. Phys.*, vol. 40, pp. 3056–3059, 2007.

[19] P. R. Sarma, S. K. Pattanayak, and R. K. Bhandari, "New method of designing pole profile in combined function magnets of high field quality," *Rev. Sci. Instrum.*, vol. 70, no. 6, pp. 2655–2660, Jun. 1999.

[20] S. Koscielniak, "Analysis of orbits in combined function magnets," in *Proc. 23rd Particle Accelerator Conf.*, Vancouver, Canada, May 4-8, 2009, pp. 5038–5040.

[21] M. Yoon, J. Corbett, M. Cornacchia, J. Tanabe, and A. Terebilo, "Analysis of a storage ring combined-function magnet: Trajectory calculation and alignment procedure," *Nucl. Instrum. Meth. A*, vol. 523, pp. 9–18, 2004.

[22] M. Seidl, "Identification and correction of antisymmetric field components in combined function magnets," *Phys. Rev. Special Topics—Accel. Beams*, vol. 5, p. 062402, Jun. 2002.

[23] V. N. Litvinenko, Y. Wu, B. Burnham, J. M. J. Madey, and S. H. Park, "Performance of achromatic lattice with combined function sextupoles at Duke storage ring," in *Proc. 16th Particle Accelerator Conf.*, Dallas, Texas, USA, May 1-5, 1995, pp. 796–798.

[24] R. P. Feynman, R. B. Leighton, and M. Sands, *The Feynman Lectures on Physics*. Menlo Park, CA: Addison-Wesley, 1977, vol. 2, ch. 13, 6th printing.

[25] *Mermaid 2-D and 3-D User's Guide*. Novosibirsk, Russia: SIM, 1994.

[26] S. Ćirković, J. L. Ristić-Djurović, A. S. Vorozhtsov, A. Ž. Ilić, and N. Nešković, "Method for fine magnet shaping in cyclotrons," *IEEE Trans. Nucl. Sci.*, vol. 56, no. 5, pp. 2821–2827, Oct. 2009.

[27] J. L. Ristić-Djurović, S. Ćirković, and A. Ž. Ilić, "Optimization of equally charged quadrupole parameters," *IEEE Trans. Nucl. Sci.*, vol. 60, no. 3, pp. 2161–2169, Jun. 2013.

[28] J. L. Ristić-Djurović, S. Ćirković, and A. Ž. Ilić, "Ion beam acceleration with radio frequency powered rainbow lens," *IEEE Trans. Nucl. Sci.*, vol. 60, no. 2, pp. 1272–1279, Apr. 2013.

Importance of Accurate Static Equilibrium Orbit Calculation in Cyclotron Design

Andjelija Ž. Ilić, *Member, IEEE*, Jasna L. Ristić-Djurović, and Saša Ćirković

***Abstract*—Knowledge of the static equilibrium orbit properties is crucial for cyclotron design and development. With the increase of computational speed, numerical orbit calculations are more and more often employed as a part of other methods. Direct numerical integration of the canonical equations of motion is used most often for orbit calculations. We propose an original method for the calculation of static equilibrium orbit properties by direct trajectory tracking in the real, configuration space, and compare it with the method most commonly used.**

***Index Terms*—Cyclotrons, magnetic fields, optimization methods, particle beam dynamics, static equilibrium orbit properties.**

I. Introduction

STATIC EQUILIBRIUM ORBIT (SEO) calculations are an indispensable tool in the design and development of modern cyclotrons [1]–[7]. Since the cyclotron magnetic field has the double role in the process of acceleration, of guiding the ion beam bunch toward the field regions corresponding to the energies of ions and focusing the trajectories of ions, much of the accelerated orbit behavior can be deduced from the analysis of the field itself. Analytical expressions of different levels of complexity and accuracy [8], [9], developed over time, are nowadays almost completely abandoned in favor of numerical techniques. Numerical calculation of orbits for a large number of ion energy values gives a measure of quality of the designed magnetic field through its level of isochronism as well as the focusing properties. Computer codes for the simulation of ion beam acceleration using the well-known ray tracing method also rely on the SEO calculations. Namely, the transition matrix parameters used to transform the non-central trajectories about the central ray are determined from SEO analysis [10], [11].

Computational speed improvements over the last decades led us, as well as other authors, to employ the orbital frequency criterion as an error assessment tool in the iterative process of isochronous magnetic field calculation [12], [13], and iterative cyclotron magnet shimming [14]–[16]. We have also employed the SEO calculation as a subroutine, used in the centering of trajectories, in the program module devoted to the optimization of accelerated equilibrium orbits (AEO) [17]. Precise SEO positioning played important role in determining of the focusing limit of a cyclotron using the beam dynamics simulation [18]. Whereas accurate calculation is important in the field analysis, it becomes an imperative when the SEO determination routines are used in the optimization process.

The SEO determination technique most commonly found in literature is based on direct numerical integration of the canonical equations of motion and is described in [1]. Static equilibrium orbit is defined as the closed orbit possessing the same N-fold symmetry as the guiding magnetic field, where N corresponds to the number of cyclotron magnetic sectors. It is unique for every considered particle energy. In numerical SEO analysis, there may be more than one appropriate closed orbit, concordant with numerical criteria, in the vicinity of the actual SEO. Highly accurate two-parameter optimization, used in [1] to locate the optimal closed orbit, is based on the well-known Newton iterative method. One of the major benefits of such iteration scheme is its rapid convergence when the error has been sufficiently reduced. On the other hand, the selected orbit is always the one closest to the initial guess, taken approximately for the first considered energy point and later extrapolated from the already obtained results.

During the design of the self-written software packages for ion beam dynamics VINDY and VINDY-A [17]–[20], we developed original algorithms for SEO determination. Same as the rest of the program modules written over time, the SEO calculation routines use the direct trajectory tracking in the real, configuration space, rather than solving the canonical equations of motion. Here we propose and describe the SEO determination method of a remarkable accuracy, used for different optimization purposes as described in [13], [14], and [17]. Two-parameter optimization of the SEO, used by our method, searches over the range of parameters in the vicinity of the optimal SEO in order to position it more precisely.

All of the presented examples use the layout and magnetic field maps given in [21]–[24]. The calculated isochronized magnetic field map corresponding to the H^- ion is used as an input in the evaluation of method performance. This particular field map is chosen due to the availability of data on the corresponding static equilibrium orbits calculated by CYCLOPS code described in [1]. Therefore, the method we propose is compared with the method most commonly used in literature. The accuracy of the method in dealing with the more realistic measured isochronized magnetic field is examined as well.

Manuscript received July 12, 2013; revised September 11, 2013; accepted September 27, 2013. Date of publication November 05, 2013; date of current version December 11, 2013. This work was supported in part by the Ministry of Education, Science and Technological Development of Serbia through the project III-45003.

The authors are with the Innovation Center, School of Electrical Engineering, University of Belgrade, 11120 Belgrade, Serbia (e-mail: andjelijailic@ieee.org; jasna@stanfordalumni.org; kosjera@beotel.net).

Color versions of one or more of the figures in this paper are available online at http://ieeexplore.ieee.org.

Digital Object Identifier 10.1109/TNS.2013.2284194

II. Method Description

Two distinct numerical techniques need to be combined to provide the SEO analysis tool. The first one is the numerical integration of the trajectory of an ion, i.e., trajectory tracking. The other one is the optimization method used to determine the SEO. The insufficient accuracy of numerical integration directly translates into inaccurate orbit positioning regardless of optimization method used. This can be avoided easily, by setting stringent accuracy requirements. Optimization itself becomes a limiting factor for the SEO positioning in that case. The complete method description is built by treating its various parts in the following subsections.

A. Numerical Integration

The charged particle motion inside a cyclotron is described by general equations of particle motion in an electromagnetic field of electric field strength $\mathbf{E}$ and magnetic induction $\mathbf{B}$:

$$\frac{\mathrm{d}\mathbf{r}(t)}{\mathrm{d}t} = \frac{1}{m_0}\sqrt{1-\left(\frac{v(t)}{c}\right)^2}\,\mathbf{p}(t) \tag{1}$$

and

$$\frac{\mathrm{d}\mathbf{p}(t)}{\mathrm{d}t} = \frac{q}{m_0}\left(m_0\,\mathbf{E}(t,\mathbf{r}) + \sqrt{1-\left(\frac{v(t)}{c}\right)^2}\,\mathbf{p}(t)\times\mathbf{B}(\mathbf{r})\right). \tag{2}$$

The position of the particle is $\mathbf{r}$, its momentum is $\mathbf{p}$, and v is the velocity intensity. The rest-mass of the particle is m_0, q is the electric charge, and c is the speed of light. Equations (1) and (2) are solved using the adaptive time step Runge-Kutta method of the fourth order. The time step is chosen to comply with the two accuracy requirements: the maximal allowed local error of position calculation is x_{err}, while the local error of the momentum calculation must not exceed p_{err}, given as a fraction of the initial momentum. In the SEO analysis, the parameter p_{err} is recalculated for each considered energy. The two accuracy requirements are not fully independent from each other. High accuracy of position calculation inherently sets bounds on the momentum calculation error. As opposed to that, the local momentum error bound p_{err} alone is not limiting enough in the regions where the electric field is close to zero, which is the case with SEO analysis. In such cases it controls the momentum direction, as well as the constancy of the momentum intensity, important since the Runge-Kutta method is not symplectic. Combined, the two requirements result in an excellent control of the size of the time step.

B. Two-Parameter Optimization Requirements

The positioning of the SEO, for any given test ion energy T, comprises the optimization of exactly two parameters: the initial radial position and the initial momentum direction in the median plane of a cyclotron, where the SEO is located. Any initial azimuthal position is acceptable in the search for a closed orbit; therefore, a point at the midline of a sector or at the midline of a valley is often taken for simplicity. Due to the N-fold symmetry of orbits, radial coordinate as well as momentum direction angle of an ideal SEO should have identical values at the cross-sections with all radial semi-axes, obtained by the rotation of positive x-axis by $360°/N$. This requirement is virtually the same as the one imposed in [1]. If checked after a full turn, it defines the compliance with the perfectly closed orbit. The ideal closed orbit also has to be centered in the x- and y-direction in case of even N, or one of the two directions if N is odd. In the realistic magnetic fields, which are not perfectly symmetric, combinations of different requirements yield different results. It can be useful to define a number of control parameters, comprising ion position and momentum direction angle at various points along the path of integration. Weighting coefficients are used to choose among the predefined parameters of a flexible optimization criterion.

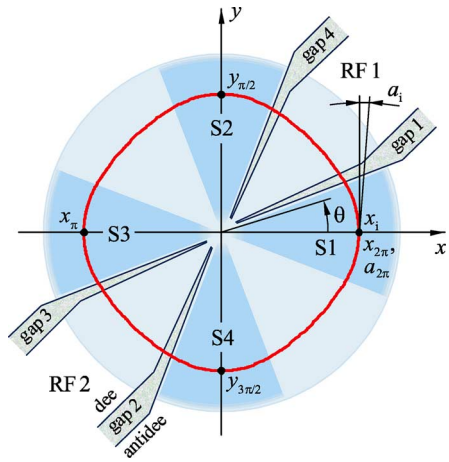

Fig. 1. The layout of a cyclotron and the coordinate system used. The control points along the integration path as well as the direction angles of the initial and final momentum vectors, used by our optimization criterion, are denoted on an example static equilibrium orbit.

C. Optimization Criterion

For $N = 4$, as in our examples, it is convenient to take the cross-sections of the tracked orbits with the coordinate axes as the control points along the path of integration. Therefore, we employ the following optimization criterion:

$$\begin{aligned} f_{\mathrm{oc}}(x_{\mathrm{i}}, a_{\mathrm{i}}) = {} & w_1\cdot(x_{\mathrm{i}}+x_\pi)^2 + w_2\cdot(y_{\pi/2}+y_{3\pi/2})^2 \\ & + w_3\cdot(y_{\pi/2}+x_\pi)^2 + w_4\cdot(x_{\mathrm{i}}-x_{2\pi})^2 + w_5 \\ & \cdot(\sin(a_{\mathrm{i}})-\sin(a_{2\pi}))^2, \end{aligned} \tag{3}$$

where x_{i} and a_{i} represent the considered initial radial position and initial momentum direction angle, respectively. Angle a_{i} is measured clockwise from the positive y-axis in the xy-plane. The coordinate system as well as the direction of increase of the azimuthal coordinate θ is defined in Fig. 1. Azimuth $\theta = 0$ coincides with the first sector midline. Test ion coordinates $y_{\pi/2}, x_\pi, y_{3\pi/2}, x_{2\pi}$ and $a_{2\pi}$, used as the control parameters, are obtained from the full-turn of the test ion trajectory tracking starting from $(x_{\mathrm{i}}, a_{\mathrm{i}})$. The sin (a_{i}) and sin $(a_{2\pi})$ in (3) correspond to the normalized momentum x-components, $P_{\mathrm{x,\,i}}$ and $P_{\mathrm{x},2\pi}$. Optimization criterion is defined in a separate procedure, allowing simple addition of different criteria customized for various cases. As stated in the Subsection B, if N is odd orbit

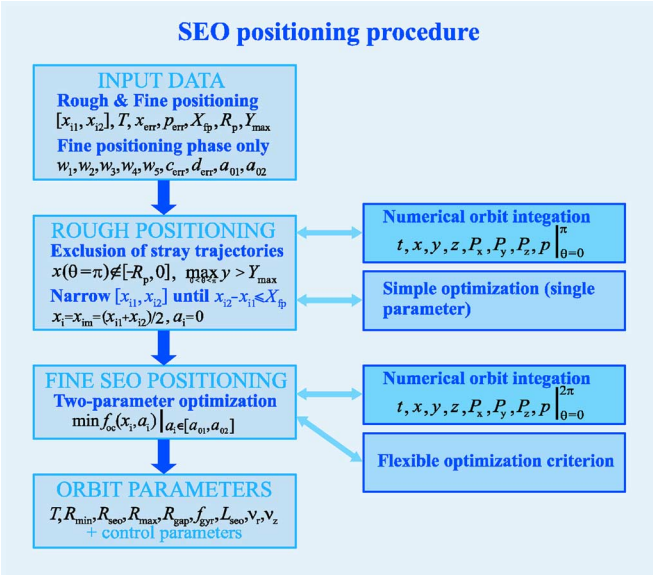

Fig. 2. The schematic representation of the optimization algorithm used to determine the static equilibrium orbits. Flexible optimization criterion results in a remarkable accuracy, while the division into the rough and the fine positioning phase makes the method efficient.

is centered in one of the two directions, here it is the y-direction. Inclusion of radial semi-axes is desired. In the case of spiral sectors, it is advisable to include both position and momentum direction angle at several points along the path of integration as the control parameters. Weighting coefficients w_1, w_2, w_3, w_4, and w_5 are specified in the input file. Although each of them can be an arbitrary real number, we investigated the effect to the finally obtained SEO of setting each of the weighting coefficients either equal to zero or equal to one. The obtained binary arrays $(w_1, w_2, w_3, w_4, w_5)$ correspond to different optimization criteria.

D. Rough SEO Positioning

In order to make the whole procedure as much user-friendly as possible, arbitrarily broad range of input radii $[x_{i1}, x_{i2}]$ can be specified. First, we exclude the trajectories that either exit the cyclotron pole region or never cross the y-axis. Then, the single parameter, x_i, optimization is used to further narrow the $[x_{i1}, x_{i2}]$ interval, until it reaches a given X_{fp} limit. The two just described parts of the SEO positioning comprise the rough positioning phase. The precise two-parameter optimization is reffered to as the fine positioning phase of an algorithm schematically represented in Fig. 2. Exclusion of stray trajectories is performed as long as at least one of the three conditions is met: the final radial position x_f, after the half-turn ($\theta = 0$ to $\theta = \pi$) of the test ion trajectory tracking with initial radius x_{i1} and initial angle $a_i = 0$, exceeds the cyclotron pole radius, R_p; nonnegative x_f is obtained after the half-turn starting from x_{i2} and $a_i = 0$; y-coordinate anywhere along the orbit exceeds $Y_{max} = 1.5 \cdot R_p$, ($R_p = 1$ m here). Iterative adjustment of the lower and upper limit radii, x_{i1} and x_{i2}, by a relatively large Δx_i, ($\Delta x_i = 10$ cm here), has computational cost negligible in comparison to the fine positioning phase. Further interval $[x_{i1}, x_{i2}]$ narrowing also proceeds fast: starting from $x_{im} = (x_{i1} + x_{i2})/2$ and $a_i = 0$, we track the half-turn of the trajectory. Based on positive or negative $x_{im} + x_f$, or $x_{im} + x_f = 0$, we replace $x_{i2} = x_{im}$, $x_{i1} = x_{im}$, or $x_{i1} = (x_{i1} + x_{im})/2$, $x_{i2} = (x_{i2} + x_{im})/2$, respectively. The process is repeated until the $x_{i2} - x_{i1} \leq X_{fp}$ condition is reached. For the odd number of sectors, negative radial coordinate at the last cross-section of half-turn particle trajectory with one of the coordinate semi-axes has to be used instead of x_f. In order for the method to be applicable to cyclotrons with spiral sectors, analytical estimate of the initial momentum direction angle, $\alpha(x_i)$, would be necessary. Instead of $a_i = 0$, the initial angle $a_i = \alpha(x_i)$ is to be used throughout the rough positioning phase. However, detailed analysis of spiral sectors is beyond the scope of this paper. The described procedure alone would be sufficient for the SEO positioning, if the input magnetic field were ideally symmetric and its change with radius ideally smooth. In reality, this can not be fully achieved and the procedure moves on to the two-parameter adjustment.

E. Fine SEO Positioning

In the fine SEO positioning phase, each of the values x_{i1}, x_{i2}, and x_{im} is kept fixed, while the optimal a_i that minimizes the quality criterion f_{oc} for each of them is searched for. Thus, we obtain a_{i1}, a_{i2}, and a_{im}, as well as f_{oc1}, f_{oc2}, and f_{ocm}. Upon that, the pair of initial parameters (x_i, a_i) characterized by the larger f_{oc1}, or f_{oc2}, is being replaced by (x_{im}, a_{im}), and the corresponding f_{oc} value by f_{ocm}. Optimal a_i for the fixed value of x_i is searched for as long as the interval of the remaining momentum angles is larger than some predefined allowed direction error d_{err}. Similarly, new pairs (x_i, a_i) are found until the search interval becomes smaller than c_{err}, the allowed SEO positioning error.

F. Choice of Weighting Coefficients

Binary arrays of weighting coefficients, $(w_1, w_2, w_3, w_4, w_5)$, correspond to different optimization criteria, several of them compared in Table I, for the symmetric calculated magnetic field map and the realistic measured magnetic field map for the same H^- ion. We assess the orbit shape quality through the compliance of all radial position coordinates at the crossing points with coordinate axes, as well as the compliance of initial and final momentum direction angle, shown in Table I. Formally, the same norm as the one given in (3) can be used, with all weighting coefficients set to 1.0. A larger number of control points along the path of integration can be used if desired. As opposed to what we might expect, the requirement that the orbit is x-centered and y-centered produces better overall orbit shape than the requirement on closeness in terms of equality of initial and final (x, a). That can be seen by the inspection of the first and second column of Table I. As shown in the next two columns, y-centeredness requirement inclusion gives excellent orbit for the calculated field map and significantly improves the orbit obtained with the measured field map. It is enough, in that case, to only control the initial and final momentum, since omitting the fourth term in (3) results in no changes. The last two columns investigate the effect of the requirement that the radial coordinates at the midlines of the second and third sector

TABLE I
VARIATION OF SEO CONTROL PARAMETERS FOR DIFFERENT CHOICES OF INPUT WEIGHTING COEFFICIENTS

(w_1,w_2,w_3,w_4,w_5)	(1, 1, 0, 0, 0)	(0, 0, 0, 1, 1)	(0, 1, 0, 1, 1)	(0, 1, 0, 0, 1)	(1, 0, 1, 0, 0)	(0, 1, 1, 0, 0)
Calculated isochronized magnetic field						
x_i (mm)	769.4690	769.4711	769.4690	769.4690	769.4825	769.4736
x_π (mm)	769.4690	769.4769	769.4690	769.4690	769.4659	769.4745
$x_{2\pi}$ (mm)	769.4690	769.4515	769.4690	769.4690	769.4616	769.4538
$y_{\pi/2}$ (mm)	769.4690	769.4284	769.4690	769.4690	769.4270	769.4281
$y_{3\pi/2}$ (mm)	769.4690	769.5076	769.4690	769.4690	769.5118	769.5085
a_i (°)	0.002662	0.000000	0.002662	0.002662	0.000000	0.000000
$a_{2\pi}$ (°)	0.002662	0.000253	0.002662	0.002662	0.000101	0.000175
Measured isochronized magnetic field						
x_i (mm)	769.5574	769.5519	769.5525	769.5525	769.6300	769.5557
x_π (mm)	769.5574	769.5625	769.5625	769.5625	769.5416	769.5593
$x_{2\pi}$ (mm)	769.5562	769.5519	769.5513	769.5512	769.5142	769.5544
$y_{\pi/2}$ (mm)	769.5595	769.5613	769.5590	769.5588	769.5302	769.5593
$y_{3\pi/2}$ (mm)	769.5595	769.5564	769.5587	769.5588	769.7887	769.5593
a_i (°)	0.014286	0.014362	0.014212	0.014202	0.000000	0.014256
$a_{2\pi}$ (°)	0.014118	0.014362	0.014211	0.014202	0.000697	0.014148

be equal, combined with the x-centeredness or y-centeredness of the orbit. The obtained results are inferior to the previously obtained ones even for the symmetric field map. We may notice from the presented data the difference in the maximal radial coordinates of an orbit in x- and y-direction for the measured field. Therefore, the usage of the third term in (3) is not practical. We set $w_1 = w_2 = 1.0, w_3 = w_4 = w_5 = 0.0$, and use the requirement on x-centeredness and y-centeredness of the orbit throughout the rest of this paper.

G. Determination of Orbit Parameters

Once the initial parameters $(x_{\rm im}, a_{\rm im})$ minimizing the quality criterion $f_{\rm oc}$ are found, the full turn of the test ion trajectory tracking is performed to gather most of the orbit data and a few more turns are tracked with the trajectory off-centered by $\Delta r_0 = 0.1$ mm radially or $\Delta z_0 = 0.1$ mm axially. Additional turns serve to calculate the frequencies of betatron oscillations from the time intervals between each two passes of radial and axial perturbance functions, Δr and Δz, through zero. The gyration frequency, just calculated as the inverse of time needed to perform a single turn starting from $(x_{\rm im}, a_{\rm im})$, is multiplied by twice the averaged zero-crossing intervals and the reciprocal of the product equals betatron tune. The output data comprises the ion test energy, T, minimal, mean, maximal radii of the SEO, $R_{\rm min}, R_{\rm seo}, R_{\rm max}$, radial coordinate while traversing the accelerating gap, $R_{\rm gap}$, gyration frequency, $f_{\rm gyr}$, orbit circumference, i.e., the single turn trajectory length, $L_{\rm seo}$, radial and axial betatron tunes, $\nu_{\rm r}$ and $\nu_{\rm z}$, as well as the control parameters listed in Table II.

TABLE II
COMPARISON OF CHARACTERISTIC CONTROL PARAMETERS ALONG THE ORBIT FOR THE TWO METHODS, FOR THREE ENERGIES

	VINDY-A	CYCLOPS
	***T* = 10 MeV**	
x_i (mm)	353.83458206	353.81400000
x_π (mm)	-353.83458196	-353.85438956
$x_{2\pi}$ (mm)	353.83458254	353.81568188
$y_{\pi/2}$ (mm)	353.83458187	353.84420425
$y_{3\pi/2}$ (mm)	-353.83458184	-353.82336024
a_i (°)	0.0158096126	0.0145456797
$a_{2\pi}$ (°)	0.0158096541	0.0140864955
$R_{\rm seo}$ (mm)	343.615504	343.466858
f_g (MHz)	20.035898	20.035924
	***T* = 30 MeV**	
x_i (mm)	604.32695793	604.32900000
x_π (mm)	-604.32695849	-604.32497597
$x_{2\pi}$ (mm)	604.32695828	604.32882352
$y_{\pi/2}$ (mm)	604.32695795	604.32660361
$y_{3\pi/2}$ (mm)	-604.32695777	-604.32765372
a_i (°)	0.0041450369	0.0041598455
$a_{2\pi}$ (°)	0.0041451272	0.0042163061
$R_{\rm seo}$ (mm)	585.802025	585.205190
f_g (MHz)	20.038663	20.038660
	***T* = 50 MeV**	
x_i (mm)	769.46900599	769.46910000
x_π (mm)	-769.46900616	-769.46913179
$x_{2\pi}$ (mm)	769.46900547	769.46867637
$y_{\pi/2}$ (mm)	769.46900614	769.46813324
$y_{3\pi/2}$ (mm)	-769.46900619	-769.46984645
a_i (°)	0.0026619722	0.0027189712
$a_{2\pi}$ (°)	0.0026619340	0.0027150101
$R_{\rm seo}$ (mm)	744.240292	743.715520
f_g (MHz)	20.040972	20.040973

III. RESULTS AND THEIR UTILIZATION

The obtained gyration frequency and betatron oscillation frequencies (tunes) for the calculated H^- ion magnetic field map are shown in Figs. 3 and 4, respectively. The results of our calculations are compared to the results previously obtained using the code CYCLOPS [22], [25]. Calculation accuracy in [25] was set to $\varepsilon = 5 \cdot 10^{-5}$, and the accuracy requirements controlling the numerical integration in our method were set to $x_{\rm err} = 100$ nm, $p_{\rm err} = 0.1$ ppm. The accuracy requirements on the SEO positioning were set to $c_{\rm err} = 10^{-5}$ nm, $d_{\rm err} = 10^{-6}$ rad. Static equilibrium orbit data is calculated for test ion energies from 0.2 MeV to 68.0 MeV, with the data step 0.2 MeV. The agreement of the two sets of results is excellent; in Fig. 4 we had to use rather thick line to represent the CYCLOPS data, since the two sets of data completely overlap. The general shape of the two gyration frequency curves in Fig. 3 is identical as well; however, there is somewhat larger amount of small oscillations

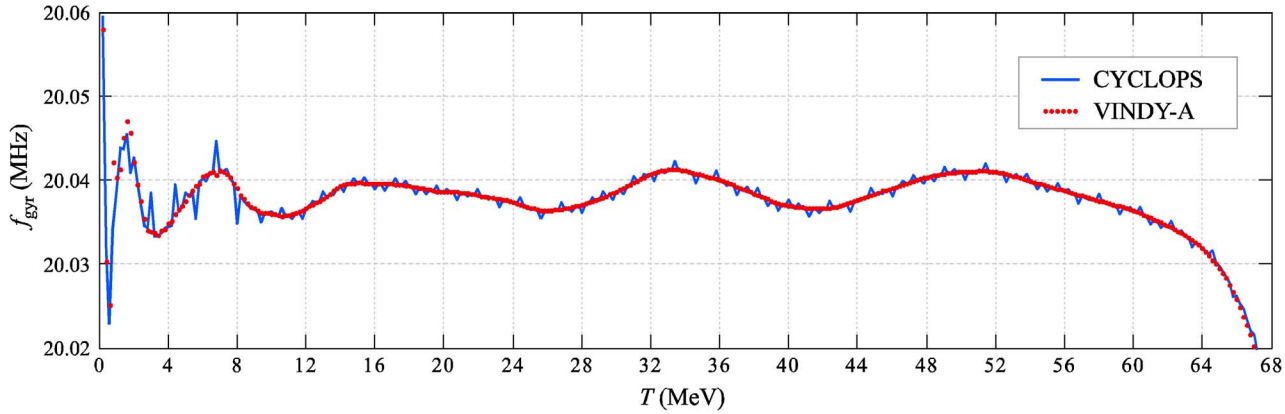

Fig. 3. Orbital gyration frequencies for the calculated H^- ion magnetic field map. Comparison of newly obtained results (VINDY-A) with those obtained using the CYCLOPS code [25] gives excellent agreement, except for the small oscillations in the CYCLOPS result. Such oscillations are due to slight variations in the obtained initial parameters (x_i, a_i) in the vicinity of the optimal closed orbit, where a number of orbits meet the numerical accuracy requirements (see Table I). The calculation accuracy of $\varepsilon = 5 \cdot 10^{-5}$ in [25] might be insufficient if the data is to be used as input of other procedures.

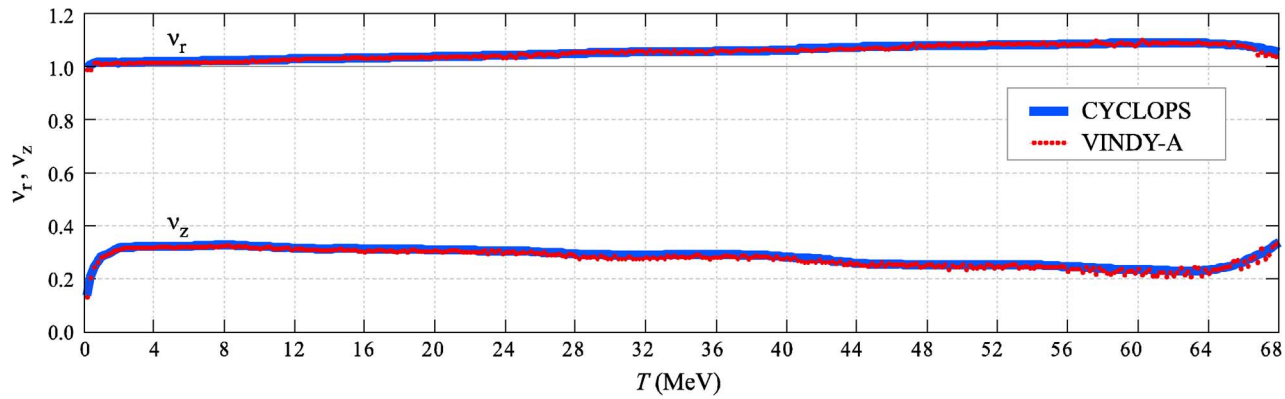

Fig. 4. Radial and axial betatron oscillation frequencies (tunes), ν_r and ν_z, for the calculated H^- ion magnetic field map. Betatron tunes are found by determining the zero-crossing periods, a method commonly used in signal processing. The two sets of results overlap in almost all points, therefore the CYCLOPS data is represented by a very thick line and our data as smaller dots.

in the CYCLOPS data. There is more than one orbit concordant with the numerical algorithm accuracy requirements in the vicinity of the orbit adopted as SEO, and such small oscillations can be attributed to finding a pair of initial parameters (x_i, a_i) slightly astray from the optimal. This problem could be removed in part, or even completely, by addopting better computation accuracy. The consistency in the gyration frequency calculation shown by our method is probably due to the fact that x- and y-centeredness combined in an optimization criterion actually produce better overall orbit shape, than the usual requirement on orbit closeness, as illustrated in Table I. The comparison of characteristic control parameters along the orbit is given in Table II, for initial parameters (x_i, a_i) determined by the two methods, for three energies. Fig. 5 compares the realistic measured with the calculated isochronous magnetic field map. In the following, examples of the recent utilization of described procedures as subroutines in other methods are given.

A. Isochronous Field Calculation Using Gyration Frequencies

The constancy of the ion gyration frequency checked by the use of numerical methods is the ultimate quality measure for an isochronous magnetic field. A step further is to employ the gyration frequency adjustment in the process of isochronous field calculation. In the method suggested in [13], we choose to adjust the magnetic field source rather than the field itself in order to guarantee the magnet capability to produce the calculated field. Cyclotron magnet responds to the joint effect of the main and the trim coils as an effective main coil current inducing the desired magnetic field at a given radius, termed in [13] the effective induction current. The measured response of the magnet was available for the twenty values of the main coil current, at the measurement grid points in the median plane defined by $R_m = 0, 1, 2, \ldots, 100$ cm, $\theta = 0, 1, 2, \ldots, 359°$. Alternatively, simulated magnetic fields for a number of main coil currents can be used. The gyration frequency dependence on the mean orbit radius is obtained from the SEO simulation in each of the field maps at a number of energy points. It is used to obtain the set of values corresponding to the mean orbit radii R_m. The effective induction current producing the desired gyration frequency is found for each radius separately, using the cubic spline interpolation. The azimuthal variation of the magnetic field corresponding to the considered effective current is determined in the same way. Azimuthal variations at different radii are merged into the isochronized field and the corresponding gyration frequency distribution over the radii is obtained. If the

TABLE III
COMPARISON OF MEAN ORBIT RADIUS, $R_{\rm seo}$, AND THE NORMALIZED ORBIT CIRCUMFERENCE, $L_{\rm seo}/(2\pi)$

T (MeV)	$R_{\rm seo}$ (mm)	$L_{\rm seo}/(2\pi)$ (mm)	ΔR (mm)	$\Delta R/R_{\rm seo}$ (%)
10.0	343.616	344.745	1.130	0.329
20.0	481.963	483.672	1.709	0.355
30.0	585.802	587.803	2.001	0.342
40.0	671.529	673.622	2.093	0.312
50.0	744.240	747.308	3.068	0.412
60.0	808.868	812.731	3.863	0.477

desired isochronism level is not yet achieved, the solution is refined iteratively, although only few (even one) iterations result in a remarkable accuracy. As shown by comparison of methods given in [13], deviation of the realistic from the calculated magnetic field, due to the finite number of trim coils, is the least for the suggested method. Our method, as well as the CYCLOPS, calculates the mean orbit radius, $R_{\rm seo}$, by the standard definition of the mean value of a physical variable. It should be noted that another parameter often used in the cyclotron community, the average radius based on the arc length, $L_{\rm seo}/(2\pi)$, is always larger than $R_{\rm seo}$ by an amount depending on the angle between the arc tangent and the circle tangent in each integration step, $\xi(\theta)$.

$$R_{\rm seo} = \frac{1}{2\pi}\int_0^{2\pi} r(\theta)\mathrm{d}\theta < \frac{1}{2\pi}\int_0^{2\pi}\frac{r(\theta)}{\cos\xi(\theta)}\mathrm{d}\theta = \frac{1}{2\pi}\int_0^{2\pi}\mathrm{d}l = \frac{L_{\rm seo}}{2\pi}. \quad (4)$$

As shown in Table III, the discrepancy between the two in our case is less than 0.5%; however, for orbits with the more pronounced scalloping it can be much larger.

B. Fine Magnet Shaping by Azimuthal and Axial Shimming

The method for fine magnet shaping described in [14] uses the three-dimensional computer modeling of the magnet in combination with static equilibrium orbit calculations to relate the particular magnetic sector shape and the corresponding radial dependence of the ion gyration frequency. The gyration frequency is treated as a function of the sector shape and the equation linking the two is solved numerically by the regula falsi method. The pre-calculated magnetic field criterion and the empirical weight factors for the shape estimate are avoided by relying directly on the gyration frequency adjustment. The method is applicable to all radially dependent types of sector shimming, namely the azimuthal, axial-polar and axial-median shimming. It works equally well with straight as well as with spiral sectors and can be used to determine the pole thickness in the cyclotrons with azimuthally non-varying magnetic fields. Two initial limiting sector shapes are required, the two corresponding gyration frequency dependencies on the mean equilibrium orbit radius, $R_{\rm seo}$, defined by (4), and the desired gyration frequency. The method is characterized by the excellent accuracy and fast convergence.

C. Accelerated Equilibrium Orbit (AEO) Centering

Accelerated equilibrium orbit centering based on the hard edge gap approximation customarily uses approximate analytical formulas to relate the relative increase in radius with the relative energy gain while traversing the accelerating gap. The very efficient orbit centering method is proposed in [17], relying on tabulated orbit parameters from the SEO analysis. Orbit centering starts from the middle of the valley on the SEO corresponding to the test ion energy. The amount of energy gained at each accelerating gap is numerically integrated. We use the cubic spline interpolation and the tabulated dependence of gap radial coordinate, $R_{\rm gap}$, on the test ion energy to obtain the five values of $R_{\rm gap}$. Differences in $R_{\rm gap}$ after and before each gap correspond to the orbit center movement. The barycenter of an outlined parallelogram-like contour corresponds to the shift of the initial ion coordinates required for the single turn centering. Although the procedure can be used iteratively, for medium to large energy values a single step of this single turn centering is adequate.

D. Betatron Tunes Calculation Using the AEO

Determination of the zero crossing periods, a method commonly used in signal processing and applied here to calculate the betatron tunes from the SEO analysis, is readily adapted to the AEO analysis. The test ion travelling along the optimized or presumed AEO is tracked simultaneously with the two other ions, one off-centered radially and the other elevated from the median plane. The radial and axial perturbations of the trajectories of the two ions with respect to the one following the AEO are considered almost sinusoidal signals whose frequency is to be found. For each time interval between the two zero-crossings, the averaged test ion energy during that interval is found, and the corresponding gyration frequency interpolated from the SEO analysis data using the cubic spline method. Betatron tunes obtained using the AEO are shown in part (b) of Fig. 5 by the solid red (dark gray) line. Consistent with the result obtained by the SEO analysis, the newly calculated tunes are found along the orbit that is not perfectly centered at all radii and that accounts for realistic energy gains during the acceleration.

E. Focusing Limit of a Cyclotron

The maximal obtainable energy of ions accelerated in a cyclotron is determined either by the bending capabilities or by the focusing capabilities of the machine, depending on the bending and focusing constants and ion specific charge. The focusing limit represents the ion energy at which the axial defocusing caused by the radial field growth overpowers focusing introduced by azimuthally varying fields. It is most often determined using the axial beam instability criterion based on the approximate analytical expressions for betatron tunes. In [18], critical SEO for axial instability is determined as the one whose maximal orbit radius corresponds to the maximum of radial magnetic field gradient in the considered limiting magnetic field. This is the orbit characterized by the maximal degree of axial beam defocusing, out of all orbits in the vicinity of extraction radius. Beam dynamics simulations along the critical SEO are employed to assess the extent of the beam defocusing as the maximal half-envelope achieved along the several simulated turns on the SEO. The focusing limit is taken to be the ion

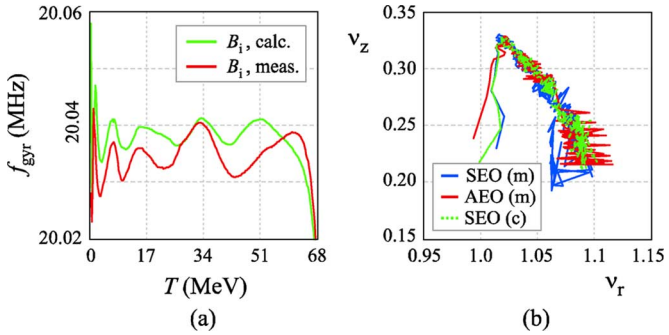

Fig. 5. Comparison of orbit properties for the measured and calculated H^- ion magnetic field map. Measured magnetic field map is obtained with the set of main and trim coil currents providing the field closest to the desired calculated field. (a) There is a significant gyration frequency difference between the two field maps. (b) The betatron oscillation frequencies seem to be much less affected by the field differences. The two cases, denoted as SEO (m) for the measured and SEO (c) for the calculated field map, are best discerned from the ν_z versus ν_r plot. The betatron tunes calculated from the radial and axial perturbations of accelerated equilibrium orbit in the measured magnetic field map, denoted as AEO (m), are shown as well. Large oscillations of the ν_r tune calculated using the AEO can be contributed to additional radial perturbation due to the imperfect orbit centering.

extraction energy corresponding to the maximal half-envelope reaching 135% of the initial vertical beam size. It is shown that the obtained focusing limit can be more than 9% smaller than that obtained from the approximate expressions. Focusing limit obtained by means of beam dynamics simulations is not only more accurate; it is actually achievable in reality, unlike the one from the approximate expressions that corresponds to the infinitely large beam size.

IV. Conclusion

During the creation of our self-written software packages for ion beam dynamics, highly accurate original method for the calculation of static equilibrium orbits was developed. It has been used in many other program modules we developed, but the method itself was not previously described. It is proposed here and compared in terms of accuracy with the method prevalent in existing literature, showing excellent agreement. In its many applications as a subroutine, it has proven to be robust and fast as well. The flexible quality criterion utilizing several weighting coefficients is used in the optimization process. A comparison given in Section II, using different combinations of weighting coefficients, corresponds to investigating several different optimization criteria. Except for the usual analysis of already obtained magnetic field maps, several examples of recent utilization of the proposed method within other methods are outlined. Remarkable consistency in finding the initial parameters (x_i, a_i) of each SEO is identified as the major factor contributing to the high accuracy and fast convergence of all outlined methods.

References

[1] M. M. Gordon, "Computation of closed orbits and basic focusing properties for sector focused cyclotrons and the design of "CYCLOPS"," *Part. Accel.*, vol. 16, pp. 39–62, 1984.

[2] A. Goswami, P. Sing Babu, and V. S. Pandit, "Behavior of space charge dominated beam in a high-current compact cyclotron," *Nucl. Instrum. Methods Phys. Res. A*, vol. 562, no. 1, pp. 34–40, Jun. 2006.

[3] T. Zhang, H. Yao, J. Yang, J. Zhong, and S. An, "The beam dynamics study for the CYCIAE-100 cyclotron," *Nucl. Instrum. Methods Phys. Res. A*, vol. 676, pp. 90–95, June 2012.

[4] B. Wang *et al.*, "Computer design of a compact cyclotron," *Phys. Part. Nucl. Lett.*, vol. 9, no. 3, pp. 288–298, May 2012.

[5] J. X. Zhang, T. A. Antaya, and R. E. Block, "Beam dynamics of a compact SC isochronous cyclotron—Preliminary study of central region," in *Proc. 2nd Int. Particle Accel. Conf.*, San Sebastian, Spain, 2011, pp. 643–645.

[6] J. Kang *et al.*, "Design study on magnet and RF systems of a 5 MeV H^- cyclotron," in *Proc. 17th Int. Conf. Cyclotrons and Their Applications*, Tokyo, Japan, 2005, pp. 378–380.

[7] M. K. Craddock and Y.-N. Rao, "Cyclotron and FFAG studies using cyclotron codes," in *Proc. 19th Int. Conf. Cyclotrons and Their Applications*, Lanzhou, China, 2011, pp. 395–397.

[8] H. L. Hagedoorn and N. F. Verster, "Orbits in an AVF cyclotron," *Nucl. Instrum. Methods*, vol. 18–19, pp. 201–228, 1962.

[9] M. M. Gordon and D.-O. Jeon, "Improved formulas for calculating cyclotron orbit properties," *Nucl. Instrum. Methods Phys. Res. A*, vol. 301, no. 2, pp. 182–190, Mar. 1991.

[10] C. J. Kost and G. H. Mackenzie, "COMA—A linear motion code for cyclotrons," *IEEE Trans. Nucl. Sci.*, vol. 22, no. 3, pp. 1922–1925, Jun. 1975.

[11] B. M. Bardin, J. H. Hettmer, W. P. Jones, and C. J. Kost, "Orbit dynamics of the Indiana University cyclotron," *IEEE Trans. Nucl. Sci.*, vol. 18, no. 3, pp. 311–314, Jun. 1971.

[12] B. Qin *et al.*, "A pythonic integrated solution for virtual prototyping of cyclotrons," *Nucl. Instrum. Methods Phys. Res. B*, vol. 261, no. 1–2, pp. 56–59, Aug. 2007.

[13] S. Ćirković, J. L. Ristić-Djurović, A. Ž. Ilić, V. Vujović, and N. Nešković, "Comparative analysis of methods for isochronous magnetic-field calculation," *IEEE Trans. Nucl. Sci.*, vol. 55, no. 6, pp. 3531–3538, Dec. 2008.

[14] S. Ćirković, J. L. Ristić-Djurović, A. S. Vorozhtsov, A. Ž. Ilić, and N. Nešković, "Method for fine magnet shaping in cyclotrons," *IEEE Trans. Nucl. Sci.*, vol. 56, no. 5, pp. 2821–2827, Oct. 2009.

[15] B. Qin *et al.*, "Precise isochronous field shimming using correlation matrix for compact cyclotrons," *Nucl. Instrum. Methods Phys. Res. A*, vol. 691, pp. 129–134, Nov. 2012.

[16] P. Sing Babu, A. Goswami, P. R. Sarma, and V. S. Pandit, "Optimization of sector geometry of a compact cyclotron by random search and matrix methods," *Nucl. Instrum. Methods Phys. Res. A*, vol. 624, no. 3, pp. 560–566, Dec. 2010.

[17] A. Ž. Ilić, J. L. Ristić-Djurović, S. Ćirković, A. Dobrosavljević, and N. Nešković, "Optimal acceleration in isochronous straight sector cyclotrons," *IEEE Trans. Nucl. Sci.*, vol. 56, no. 3, pp. 1498–1506, Jun. 2009.

[18] S. T. Ćirković, J. L. Ristić-Djurović, A. Ilić, N. Nešković, A. S. Vorozhtsov, and S. B. Vorozhtsov, "Focusing limit of a cyclotron: Axial betatron instability against beam dynamics approach," *Nucl. Technol. Radiat. Protect.*, vol. 21, no. 2, pp. 40–46, Dec. 2006.

[19] J. L. Ristić-Djurović, N. Nešković, and S. Ćirković, "Compound particle tracking algorithm: Application to the foil stripping extraction system design," in *Proc. 6th Int. Computational Accelerator Phys. Conf.*, 2000 [Online]. Available: http://www.icap2000.de/frames/index.htm

[20] A. Ž. Ilić, J. L. Ristić-Djurović, and S. T. Ćirković, "Preliminary results of ion trajectory tracking in the acceleration region of the VINCY cyclotron," *Nucl. Technol. Radiat. Protect.*, vol. 21, no. 1, pp. 29–33, Jun. 2006.

[21] N. Nešković *et al.*, "Status report of the VINCY cyclotron," *Int. J. Nucl. Res. NUKLEONIKA*, vol. 48, no. suppl. 2, pp. s135–s139, 2003.

[22] A. Ž. Ilić, "Optimal acceleration of particles in multipurpose isochronous cyclotrons," Ph.D. dissertation, School of Elect. Eng., Univ. of Belgrade, Belgrade, Serbia, Oct. 2010, (in Serbian).

[23] S. T. Ćirković, "Determining of the operating magnetic field and operating diagram of a multipurpose cyclotron," Ph.D. dissertation, School of Elect. Eng., Univ. of Belgrade, Belgrade, Serbia, Jun. 2009, (in Serbian).

[24] S. T. Ćirković, "Measurement and calculation of the isochronous magnetic fields of the VINCY cyclotron," M.Sc. thesis, School of Elect. Eng., Univ. of Belgrade, Belgrade, Serbia, Jul. 2000, (in Serbian).

[25] S. B. Vorozhtsov, A. S. Vorozhtsov, and P. Beličev, Isochronous Field and Equilibrium Orbit Dynamical Properties of the VINCY Cyclotron Belgrade, Serbia, Internal Rep., Jul. 2005.

IEEE TRANSACTIONS ON

NUCLEAR SCIENCE

A PUBLICATION OF THE IEEE NUCLEAR AND PLASMA SCIENCES SOCIETY

NUCLEAR & PLASMA SCIENCES SOCIETY

JUNE 2013 VOLUME 60 NUMBER 3 IETNAE (ISSN 0018-9499)

PART III OF THREE PARTS

SYMPOSIUM ON RADIATION MEASUREMENTS AND APPLICATIONS (SORMA WEST 2012)
OAKLAND, CA, USA, MAY 14–17, 2012

REGULAR PAPERS

ACCELERATOR TECHNOLOGY

ANALOG AND DIGITAL CIRCUITS

(Contents Continued on Page 2145)

IEEE

(Contents Continued from Front Cover)

(Contents Continued on Page 2146)

(Contents Continued from Page 2145)

READOUT ELECTRONICS

SCINTILLATION DETECTORS

SOLID STATE DETECTORS

TRIGGERS AND FRONT END SYSTEMS

Optimization of Equally Charged Quadrupole Parameters

Jasna L. Ristić-Djurović, Saša Ćirković, and Andjelija Ž. Ilić, *Member, IEEE*

***Abstract*—A quadrupole with equally charged electrodes could be used to focus as well as to accelerate ion beams. The equality of electrode charges causes the driving electric field of this device to be qualitatively different from that of other devices with a similar structure composed of four rod-like electrodes. For the same reason, the area of strong field influence on the beam is shifted towards the entrance and exit of the device. Consequently, it is expected that the device's performance depends on the shapes of its entrance and exit regions. The device parameters whose influence is studied are aperture radius, gap size, and rod length. Performance of the device is quantified with accelerating and focusing potentials, which are obtained as integrals of axial and radial electric fields. These variables are further used to choose optimal values of the device parameters for desired operation of the device.**

***Index Terms*—Electrostatic focusing, field description, linear accelerators, performance estimates, quadrupoles.**

I. Introduction

THE operation of an electrostatic quadrupole whose poles are all positively charged is first studied in [1] and [2], using the helical shape of the electrodes. Here, an equally charged quadrupole (ECQ) is taken to have straight rod-like electrodes, which are parallel to the device's axis and are equidistantly distributed around it. If the voltage used to power the electrodes is electrostatic, the ECQ device can operate as a lens [3], [4]. If the driving electric force alternates in time with appropriately chosen radio frequency (RF), the ECQ device could produce significant ion beam acceleration, as shown by the ion beam dynamics simulations in [5] and [6].

The ECQ device is analyzed in [6] with the intent to increase available ion beam energy of the existing low energy ion beam facility by applying electrode voltages equal in sign rather than alternating in sign to the existing device with the quadrupole-like structure. The obtained results indicated that the described low-cost changes of electrode polarity and use of grounded cylindrical shield may lead to further application span broadening of the considered ion beam facility as well as of other similar facilities if the ECQ device parameters are adequately adjusted. Note that, as in [4] and [6], the rod radius and the distance between the rods are chosen to be equal to the values corresponding to the existing device, here as well. Consequently, the ratio between the rod radius and the radius of the aperture amongst the rods has the value of 8/9.

Even though the geometry of an ECQ device is similar to a number of other devices or device components, for example those described in [7]–[15], the equality of electrode voltages in an ECQ device produces qualitatively different electric fields. To illustrate the difference, electric fields within the ECQ and quadrupole lenses with the same geometry are compared in Figs. 1 and 2.

The axial and radial components of the field are chosen for comparison because they could serve as an estimate of accelerating and focusing capability of a device. In the simplest analytical model the ECQ lens as well as the quadrupole lens is approximated with four uniformly charged finite wires. The devices are situated in the cylindrical coordinate system whose origin is in the middle of the lens and whose z-axis is coinciding with the device's axis. The positions of the wires are

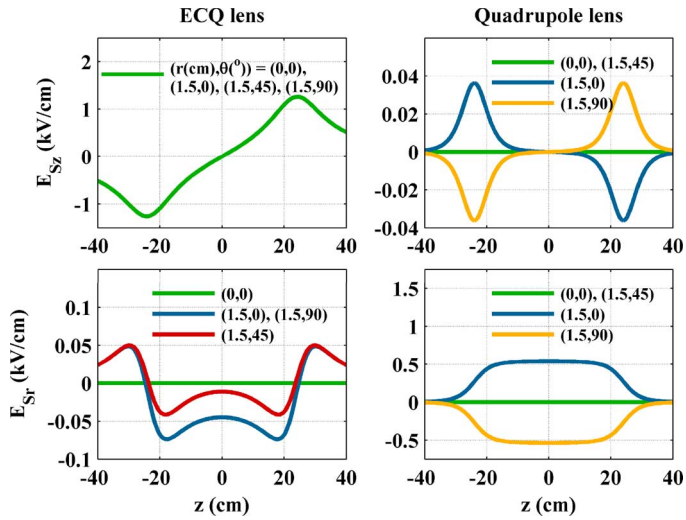

Fig. 1. Comparison of electric fields corresponding to simple analytical models of ECQ and quadrupole lens. The axial and radial electric field components, E_{Sz} and E_{Sr}, are given along the lines parallel to the z-axis, which are defined by their radial and azimuthal coordinates, r and θ. Four rod-like electrodes are approximated with four uniformly charged finite wires. The wires are positioned along the edges of imaginary quadratic prism. The wire length and the sides of quadratic prism bases are taken to be $L_w = 48$ cm and $d_w = 12$ cm, respectively. For the ECQ lens specific charges of the wires are all equal, $Q'_{w1} = Q'_{w2} = Q'_{w3} = Q'_{w4} = 0.36\ \mu$C/m, whereas for the quadrupole lens $Q'_{qw1} = Q'_{qw3} = -0.36\ \mu$C/m and $Q'_{qw2} = Q'_{qw4} = 0.36\ \mu$C/m.

Manuscript received December 15, 2012; revised February 16, 2013; accepted March 16, 2013. Date of publication April 30, 2013; date of current version June 12, 2013. This work was supported by the Ministry of Education, Science and Technological Development of Serbia through the project "Physics and Chemistry with Ion Beams," no. III45006 and was performed while the authors were at the Vinča Institute of Nuclear Sciences, University of Belgrade 11001 Belgrade, Serbia.

The authors were with the Vinča Institute of Nuclear Sciences, University of Belgrade 11001 Belgrade, Serbia. They are now with the Innovation Center, School of Electrical Engineering, University of Belgrade 11120 Belgrade, Serbia (e-mail: jasna@stanfordalumni.org; kosjera@vinca.rs; andjelijailic@ieee.org).

Color versions of one or more of the figures in this paper are available online at http://ieeexplore.ieee.org.

Digital Object Identifier 10.1109/TNS.2013.2253618

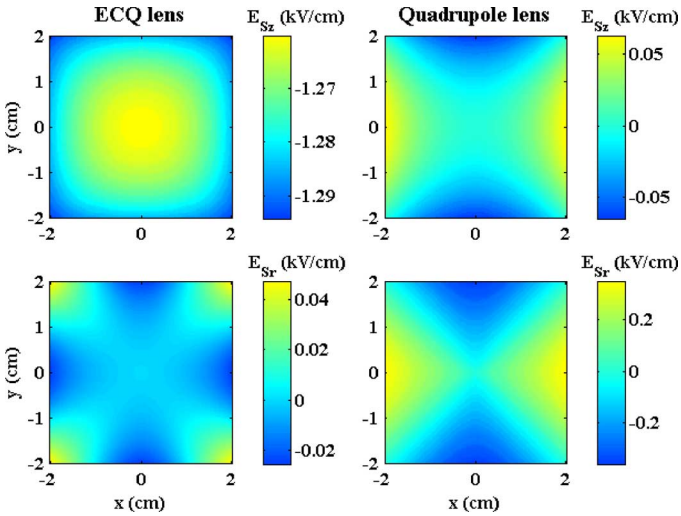

Fig. 2. Electric fields in transverse plane. The axial and radial electric field components, $E_{\mathrm{S}z}$ and $E_{\mathrm{S}r}$, are given in the plane $z = -24$ cm. The simple analytical finite wires models used to represent the ECQ and the quadrupole lens are the same as those in Fig. 1. The depicted shape of the fields justifies the use of the line segments in the half-planes $\theta = 0^\circ$ and $\theta = 45^\circ$ for data analysis.

defined with radial and azimuthal coordinates given as pairs $(r_{\mathrm{w}i}, \theta_{\mathrm{w}i}) = (d_{\mathrm{w}}/\sqrt{2}, 0^\circ), (d_{\mathrm{w}}/\sqrt{2}, 90^\circ), (d_{\mathrm{w}}/\sqrt{2}, 180^\circ)$, and $(d_{\mathrm{w}}/\sqrt{2}, 270^\circ)$ for $i = 1, 2, 3$, and 4, respectively, where d_{w} is the distance between the two neighboring wires. The axial and radial electric fields within the simplest (subscript S) analytical models $E_{\mathrm{S}z}$ and $E_{\mathrm{S}r}$ are calculated using analytical formulas for finite wires

$$E_{\mathrm{S}z}(r,\theta,z) = \frac{Q'}{4\pi\varepsilon_0}\sum_{i=1}^{4}(-1)^{i\cdot C_q}\cdot\left(\frac{1}{r_{2i}}-\frac{1}{r_{1i}}\right)$$

$$E_{\mathrm{S}r}(r,\theta,z) = \frac{Q'}{4\pi\varepsilon_0}\sum_{i=1}^{4}(-1)^{i\cdot C_q} \cdot\left(\frac{r-r_{\mathrm{w}i}\cos(\theta-\theta_{\mathrm{w}i})}{r_{2i}\,(p_2+r_{2i})}-\frac{r-r_{\mathrm{w}i}\cos(\theta-\theta_{\mathrm{w}i})}{r_{1i}\,(p_1+r_{1i})}\right) \quad (1)$$

where

$$r_{1i} = \sqrt{r^2 + r_{\mathrm{w}i}^2 - 2rr_{\mathrm{w}i}\cos(\theta-\theta_{\mathrm{w}i}) + p_1^2},$$
$$r_{2i} = \sqrt{r^2 + r_{\mathrm{w}i}^2 - 2rr_{\mathrm{w}i}\cos(\theta-\theta_{\mathrm{w}i}) + p_2^2},$$
$$p_1 = z + \frac{L_{\mathrm{w}}}{2},$$
$$p_2 = z - \frac{L_{\mathrm{w}}}{2},$$

Q' is charge density, and constant C_q adjusts the sign of the charge, i.e., $C_q = 1$ for the quadrupole lens, whereas for the ECQ lens, $C_q = 0$. Note that finite wires are an approximation of somewhat shorter rods. For example, for $d_{\mathrm{w}} = 12$ cm, and the rod radius of 4 cm, good agreement between the simplest analytical field corresponding to $L_{\mathrm{w}} = 48$-cm-long finite wires and numerically modeled field of $L_r = 40$-cm-long rods is obtained in [6].

The azimuthal positions of lines along which the calculated fields are given in Fig. 1 are chosen to correspond to the limiting fields in one of the devices or both of them. The field components along the lines in $\theta = 0^\circ$ and $\theta = 90^\circ$ planes have limiting values for the quadrupole lens, whereas, for the ECQ device, the limiting radial fields are in $\theta = 0^\circ$ and $\theta = 45^\circ$ planes. This is consistent with twofold and fourfold symmetry of the quadrupole and ECQ device, respectively. The radial component of the field, i.e., the focusing capability, in the ECQ lens is an order of magnitude smaller than in the quadrupole lens. However, the limiting radial fields have the same sign and shape for the ECQ lens compared to the opposite effects, i.e., focusing and defocusing, in the two mutually perpendicular transverse directions of the quadrupole lens. On the other hand, the axial component of the field, i.e., the accelerating capability of the ECQ device is practically equal along all considered line segments and is more than an order of magnitude larger than that of the standard quadrupole device. In the quadrupole device, the radial as well as axial field components fall to zero much faster with distance from the device's entrance and exit than is the case for the ECQ device.

The axial and radial electric fields shown in Fig. 2 are calculated in the transverse plane containing wire tips, using simple analytical models of the ECQ and quadrupole lenses. In the vicinity of the z-axis, the contour plots corresponding to the ECQ lens reveal similarities with the contour plots of the einzel lens fields. The further away the transverse plane is from the wire tips and coordinate system origin, the broader is the area around the z-axis where the contour lines of the ECQ lens fields resemble circles.

The simplest estimates of the ECQ device fields shown in Figs. 1 and 2 indicate that, despite of its quadrupole structure, operation of this device is more similar to the einzel lens if it is used for focusing and to the drift tube Sloan–Lawrence accelerator if it is used for acceleration.

The simplest analytical estimate given with (1) predicts very slow fringe field decay for an ECQ device. In order to gain control of the field shape in the entrance as well as exit region, a grounded cylindrical shield around four rod-like electrodes is introduced. It is to be expected that parameters that define the geometry of the entrance and exit, e.g., the size of the apertures on the grounded cylinder and the distance between the apertures and electrode ends, will play an important role in shaping the field as well as in the device's performance. Consequently, additional effort is due in order to describe the field in the entrance and exit region of the device.

II. Finite Wires Model

In the finite wires model of an ECQ device, the rod-like electrodes are modeled with finite wires, as in the simplest analytical model. In addition, the grounded cylindrical shield is modeled with two grounded conducting planes. It is assumed that the grounded cylinder has an infinite outer radius, i.e., that the cylinder bases are extended into planes. The influence of these two conducting surfaces is calculated by first adding the fields of the two images of four finite wires (see Fig. 3) and then by subtracting the fields resulting from the missing parts of the planes due to apertures. Therefore, the axial and radial components of approximated field are obtained as $E_z = E_{\mathrm{S}z} + E_{\mathrm{I}1z} + E_{\mathrm{I}2z} - E_{\mathrm{A}1z} - E_{\mathrm{A}2z}$ and $E_r = E_{\mathrm{S}r} + E_{\mathrm{I}1r} + E_{\mathrm{I}2r} -$

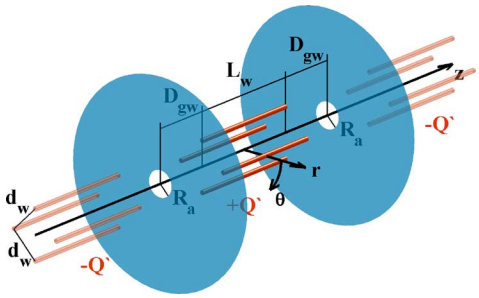

Fig. 3. Finite wires model of ECQ device. In addition to four $L_{\rm w}$ = 48-cm-long wires uniformly charged with charge density $+Q'$, and each two adjacent positioned $d_{\rm w}$ = 12 cm apart, two infinite grounded planes are introduced. The planes have apertures with radius $R_{\rm a}$ and are placed at the distance $D_{g\rm w}$ from each end of the wires. The influence of the two planes is modeled using the method of images.

$E_{\rm A1}r - E_{\rm A2}r$, where $E_{\rm S}z$ and $E_{\rm S}r$ are components of the simplest (subscript S) analytical electric field defined with (1). The fields corresponding to the two images (subscripts $i1$ and $i2$) are $E_{{\rm I}1z}(r,\theta,z) = -E_{{\rm S}z}(r,\theta,z-z_{\rm I1})$, $E_{{\rm I}1r}(r,\theta,z) = -E_{{\rm S}r}(r,\theta,z-z_{\rm I1})$, $E_{{\rm I}2z}(r,\theta,z) = -E_{{\rm S}z}(r,\theta,z-z_{\rm I2})$, and $E_{{\rm I}2r}(r,\theta,z) = -E_{{\rm S}r}(r,\theta,z-z_{\rm I2})$, where $z_{\rm I1} = -L_{\rm w} - 2D_{g\rm w}$ and $z_{\rm I2} = L_{\rm w} + 2D_{g\rm w}$ are axial shifts of the two images with respect to the original. The axial and radial field components corresponding to the apertures (subscript A), i.e., to the missing parts of grounded planes, are numerically integrated as

$$
\begin{aligned}
&E_{{\rm A}iz}(r,\theta,z)\\
&\quad=\int_{\rho=0}^{R_{\rm a}}\int_{\varphi=0}^{2\pi}\frac{E_{{\rm S}z}(\rho,\varphi,z_{{\rm A}i})}{4\pi\, d_i^2}\,\frac{\vec{d_i}\cdot\vec{z}}{d_i z}\;\rho\;d\varphi\;d\rho\\
&\quad=\int_{\rho=0}^{R_{\rm a}}\int_{\varphi=0}^{2\pi}\frac{E_{{\rm S}z}(\rho,\varphi,z_{{\rm A}i})\;(z-z_{{\rm A}i})\;\rho\;d\varphi\;d\rho}{4\pi\left(r^2+\rho^2-2r\rho\cos(\varphi-\theta)+(z-z_{{\rm A}i})^2\right)^{3/2}}\\
&E_{{\rm A}ir}(r,\theta,z)\\
&\quad=\int_{\rho=0}^{R_{\rm a}}\int_{\varphi=0}^{2\pi}\frac{E_{{\rm S}z}(\rho,\varphi,z_{{\rm A}i})}{4\pi\, d_i^2}\,\frac{\vec{d_i}\cdot\vec{r}}{d_i r}\;\rho\;d\varphi\;d\rho\\
&\quad=\int_{\rho=0}^{R_{\rm a}}\int_{\varphi=0}^{2\pi}\frac{E_{{\rm S}z}(\rho,\varphi,z_{{\rm A}i})\,(r-\rho\cos(\varphi-\theta))\;\rho\;d\varphi\;d\rho}{4\pi\left(r^2+\rho^2-2r\rho\cos(\varphi-\theta)+(z-z_{{\rm A}i})^2\right)^{3/2}}
\end{aligned}
\tag{2}
$$

where $z_{{\rm A}i} = (-1)^i\,(L_{\rm w}/2 + D_{g\rm w})$ and $i = 1, 2$, for the entrance and exit aperture (subscripts A1 and A2), respectively.

After completion of all the calculations, the field within the finite wires model depends on the spatial coordinates r, θ, and z, as well as on $R_{\rm a}$, $D_{g\rm w}$, and $L_{\rm w}$. The parameters of the finite wires model $D_{g\rm w}$ and $L_{\rm w}$ are related to the rod length L_r and distance between apertures and rods, D_g, in the real device through the equation $L_{\rm w} + 2\,D_{g\rm w} = L_r + 2\,D_g$, i.e., the distance between the grounded planes in Fig. 3 is equal to the length of the real device's grounded cylinder. Consequently, $z_{{\rm I}i} = (-1)^i\,(L_r + 2\,D_g) = 2z_{{\rm A}i}$, for $i = 1, 2$. In order to enable comparison, the results are sorted using the same set of parameters, namely, L_r and D_g, in this section for the finite wires model as well as in the following sections for data corresponding to the cylindrical rods model.

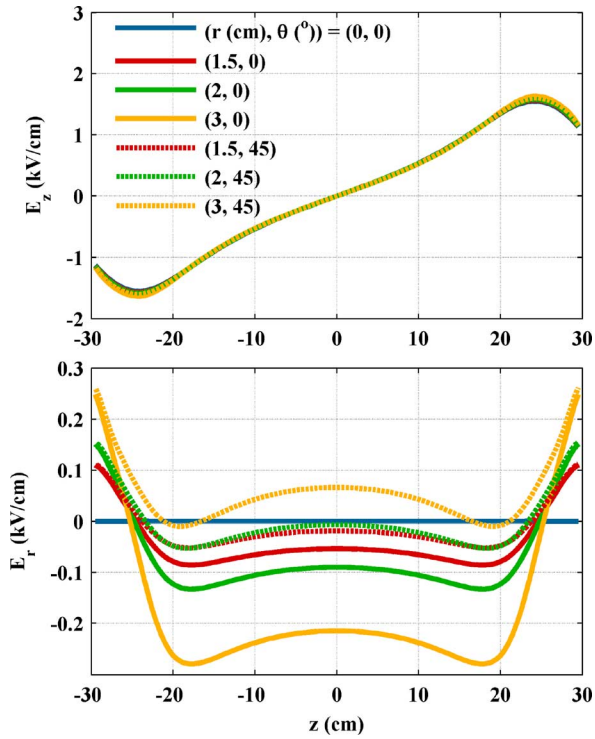

Fig. 4. Electric field of finite wires model. The aperture radius and gap size of the model are taken to be $R_{\rm a}$ = 4.5 cm and D_g = 10 cm. The axial and radial electric field components E_z and E_r are given along seven line segments. The line segments stretch between the two grounded planes, $z \in [-30$ cm, 30 cm], they are parallel to the z-axis and are determined by their radial and azimuthal coordinates, (r_i, θ_i), equal to (0 cm, 0°), (1.5 cm, 0°), (1.5 cm, 45°), (2 cm, 0°), (2 cm, 45°), (3 cm, 0°), and (3 cm, 45°), for i = 1, 2, 3, 4, 5, 6, and 7.

If the fields of the finite wires model and the cylindrical rods model, which will be described later, are to be comparable, special attention must be paid to adjusting the voltages in the two models. For all examples of the cylindrical rods model, the voltage of the electrodes is set to 20 kV. Consequently, the charge density in each sample finite wires model is calculated from the equations $V(R_{\rm a}, 0, L_r/2 + D_g) = 0$ kV and $V(d_{\rm w}/\sqrt{2} - R_r,\ 0,\ L_r/2) = 20$ kV, where $V(r,\theta,z)$ is electrostatic potential derived from the electric field of the finite wires model and R_r = 4 cm is radius of the electrodes in the cylindrical rods model.

Rather than being uniformly distributed, the charge is piling up at wire tips. Therefore, the shape of the fields around z = 0 cm predicted by the finite wires model is not expected to be accurate. Consequently, the influence of L_r on the approximated fields is not investigated; instead, it was taken that L_r = 40 cm, and $L_{\rm w}$ = 48 cm.

The dependence of the field on the spatial parameters r, θ, and z within the volume around the device's axis for sample values of aperture radius $R_{\rm a}$ and gap size D_g is illustrated in Fig. 4. The axial field component practically does not depend on the radial as well as on the azimuthal position. The limiting radial field components, which correspond to $\theta = 0°$ and $\theta = 45°$, form wider range at larger radii.

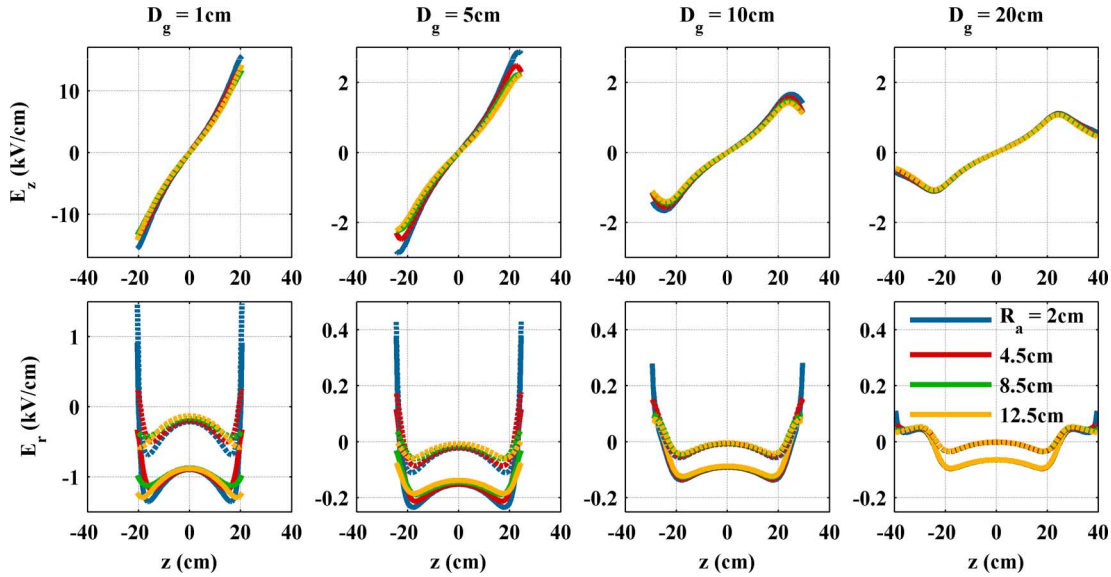

Fig. 5. Dependence of fields in finite wires model on $R_{\rm a}$ and D_g. The field components are given between the grounded planes along line segments parallel to the z-axis at $r = 1.5$ cm. The data corresponding to azimuthal line segment positions $\theta = 0°$ and $\theta = 45°$ are depicted with solid and dashed lines, respectively. The axial and radial components of the field E_z and E_r are given in the first and second row of graphs, respectively. Each column of graphs corresponds to the gap value, D_g, indicated in its title. In each graph, different line colors are dedicated to different values of $R_{\rm a}$.

The dependence of the field components on the aperture radius as well as on the size of the gap between the rods and the grounded cylinder's bases is given in Fig. 5. The approximated field depends much more strongly on the gap size D_g than on the aperture radius $R_{\rm a}$. Further, the field change is much steeper for smaller values of D_g. Although small, the influence of $R_{\rm a}$ is larger for smaller values of D_g and $R_{\rm a}$. The graphs in the first column, for $D_g = 1$ cm, have larger scales compared to the scales of the corresponding graphs in the remaining three columns. Note that the value of $D_{g\rm w}$ corresponding to $D_g = 1$ cm is negative, i.e., $D_{g\rm w} = -3$ cm; therefore, the finite wires and their images overlap and the resulting field is equal to the one corresponding to $L_{\rm w} = 36$ cm and $D_g = 3$ cm.

Analysis of the finite wires model has shown that performance of the ECQ device can be modified by adjusting the geometry of its entrance and exit regions. However, due to unrealistic assumption of uniform charge distribution along wires, a better numerical model of the device must be used in order to prove the hypothesis as well as to obtain quantitative device performance predictions.

III. Cylindrical Rods Model

In order to obtain highly accurate electric fields usable for device performance predictions, the geometry of the ECQ device is numerically modeled, and its fields are calculated with the commercially available software package WIPL-D [16]. The electromagnetic solver incorporated in this package models arbitrarily shaped structures with wires and plates as basic building blocks. Electrically large bilinear generalized quadrilaterals are used for modeling metallic plates, lossy or lossless dielectrics as well as magnetic surfaces. The surface integral equations are solved with the method of moments and surface sources as unknowns. For the ECQ device, the boundary conditions come down to the requirement that the electric field components tangential to the metallic surfaces of the rods and of the grounded cylinder are equal to zero.

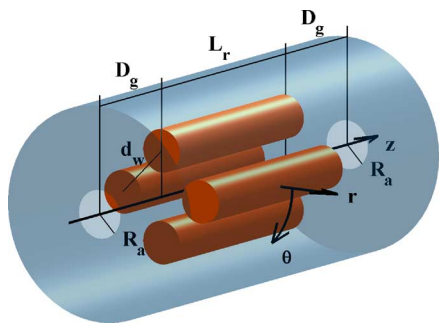

Fig. 6. Numerically modeled structure of ECQ device. Four cylindrical rods with base radius $R_r = 4$ cm replace the wires used in the finite wires model. The distance between axes of each two neighboring rods is equal to the distance between the wires in the finite wires model, $d_{\rm w} = 12$ cm, i.e., the rods are positioned at $(r_{r1}, \theta_{r1}) = (6\sqrt{2}\ \text{cm}, 0°)$, $(r_{r2}, \theta_{r2}) = (6\sqrt{2}\ \text{cm}, 90°)$, $(r_{r3}, \theta_{r3}) = (6\sqrt{2}\ \text{cm}, 180°)$, and $(r_{r4}, \theta_{r4}) = (6\sqrt{2}\ \text{cm}, 270°)$. The rods are housed in a grounded cylinder with base radius of 20 cm. The values of aperture radius $R_{\rm a}$ gap between rods and grounded cylinder base D_g, as well as rod length L_r, vary and are different for different examples of the model.

The device is modeled with four cylindrical rods used as electrodes and a surrounding grounded cylinder with entrance and exit apertures (Fig. 6). The electrostatic potential of the rods is taken to be 20 kV.

The dependences of axial E_z and radial E_r components of calculated field on spatial coordinates r, θ, and z in a sample cylindrical rods model are given in Fig. 7. These results can be compared with those corresponding to the finite wires model shown in Fig. 4, because the values of model parameters $R_{\rm a}$, D_g, and L_r are taken to be the same in both cases. The qualitative behavior of the fields corresponding to the two models agrees well. As is the case for the finite wires model, for the cylindrical model, as well, the axial field component is practically dependent only on z, whereas the radial field component

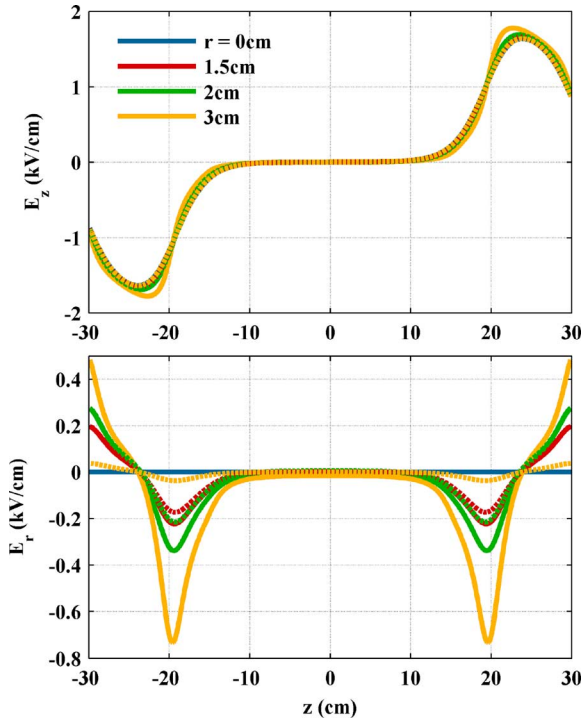

Fig. 7. Electric field of cylindrical rods model. The figure format is identical to the one of Fig. 4. The aperture radius, gap size, and rod length of the model are, as well, taken to be equal to those of finite wires model in Fig. 4, i.e., $R_{\rm a} = 4.5$ cm, $D_g = 10$ cm, and $L_r = 40$ cm. Data given along line segments with different radial positions are depicted by different colors. The azimuthal line segments positions $\theta = 0^\circ$ and $\theta = 45^\circ$ are indicated by solid and dashed lines, respectively.

is more azimuthally dependent at larger radii. The shapes of the fields in the entrance and exit regions of the device are similar for both models. However, outside the entrance and exit regions, the discrepancy between the fields corresponding to the two models is large. This is a consequence of the assumption taken in the finite wires model that charge is uniformly distributed along the wires. Inside the cylindrical rods model, away from the rods ends, the field is negligible; therefore, it seems that the field does not depend on the rods length.

The dependence of fields in the cylindrical rods model on $R_{\rm a}$ and D_g is illustrated in Figs. 8 and 9 for $L_r = 40$ cm and $L_r = 20$ cm, respectively. From both of these figures, the conclusions regarding the influences of the parameters $R_{\rm a}$ and D_g on the field are similar to the ones drawn for the finite wires model from Fig. 5. Namely, the dependence of field components on the gap size D_g is stronger than on the aperture radius $R_{\rm a}$. The data in Figs. 5 and 8 cannot be quantitatively compared despite the equality of all three device parameters in the corresponding graphs because of different radial positions of line segments used, i.e., $r = 1.5$ cm for the finite wires model, whereas for the cylindrical rods model, $r = 2$ cm. For the finite wires model the line segments with radial position $r = 1.5$ cm are chosen in order to stay clear from the apertures for all model examples with $R_{\rm a} = 2$ cm. The finite wires model is an approximate model and, as such, it does not describe reality well around edges. Examples of the cylindrical rods model are designed in WIPL-D; therefore, field calculations around edges are performed with high accuracy. However, unlike the finite wires model where the model parameters $R_{\rm a}$, D_g, and L_r are easily changed by adjusting the appropriate values in an input file, changing the model parameters values, as well as field calculation, for the cylindrical rods model is more time consuming. To speed up the process, the fields in the cylindrical rods models are calculated only along the selected line segments, rather than in the entire model volume. The line segments with larger value of r are chosen because obtained data are intended to be used primarily for device performance prediction, and focusing properties are more pronounced at larger r. The anomalies that occur close to the apertures in the example models with $R_{\rm a} = 2$ cm and that are the most noticeable in E_z curves corresponding to $D_g = 5$ cm and $D_g = 10$ cm models in both Figs. 8 and 9 reflect the edge position $r = R_{\rm a} = 2$ cm.

A comparison of the results shown in Figs. 8 and 9 reveals that the rod length does not influence the shape of the fields in the important entrance and exit regions. Closer inspection shows that the graphs in Fig. 8, which correspond to $L_r = 40$ cm, can be obtained by cutting the corresponding graphs in Fig. 9, which correspond to $L_r = 20$ cm, at $z = 0$ cm and inserting straight lines equal to zero from $z = -10$ cm to $z = 10$ cm. Although L_r cannot directly influence ECQ device performance, it may serve to adjust synchronization between an ion beam and a quasi-static RF voltage. However, it should be noted that the zero field region in the models with $L_r = 20$ cm is very short. Therefore, this value of L_r is very close to the lower limit after which the entrance and exit regions of the device overlap and are likely to no longer have entrance and exit region fields equal to those corresponding to larger values of L_r.

The electric fields obtained for a number of sample cylindrical rods models illustrated in Figs. 8 and 9 confirm the conclusion drawn from the study performed with the finite wires model. Namely, the model parameters D_g and, to much lesser extent $R_{\rm a}$, can influence the electric field of an ECQ device and, consequently, its performance. Further, electric field shape is more sensitive on D_g as well as $R_{\rm a}$ for smaller values of D_g. Influence of $R_{\rm a}$ increases with its decrease, as well.

To justify the approach of analyzing electric fields along the chosen line segments as well as to illustrate similarities with the einzel lens and the drift tube accelerator, axial and radial electric fields of an ECQ device are given in four transverse planes in Fig. 10. The shown results confirm that the device acts upon an ion beam primarily around the rod tips as well as inside the gaps between the grounded cylinder and the rod tips. Note that the ratio between the rod radius R_r and the rod aperture radius, $R_{\rm ra} = d_{\rm w}/\sqrt{2} - R_r$, is equal to 8/9 for all the considered examples. For larger values of this ratio, the fields along the $\theta = 45^\circ$ line will be less different from the ones along the $\theta = 0^\circ$ direction, and, consequently, the corresponding dashed curves will be closer to the solid curves in Figs. 7–9. Fig. 10 also verifies that focusing capabilities of the ECQ device depend more on $R_{\rm ra}$ than on R_r, as well as that the radial and azimuthal dependence of accelerating abilities of the device are negligible compared to their axial dependence. Therefore, in order to apply the obtained results to other devices, for small D_g and focusing estimates, the rod aperture radius $R_{\rm ra}$ should be used as the

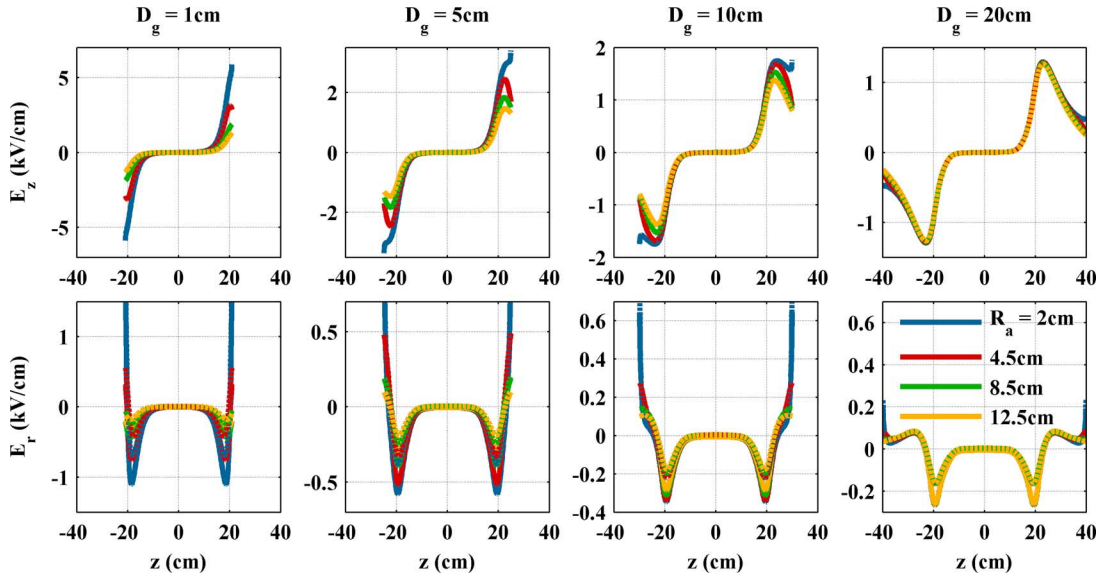

Fig. 8. Dependence of fields in cylindrical rods model on $R_{\rm a}$ and D_g for $L_r = 40$ cm. The format of the figure is equal to the one of Fig. 5. Here, the rod length is taken to be $L_r = 40$ cm, as well; however, the line segments along which the field components are given are parallel to the z-axis at $r = 2$ cm. The data corresponding to the azimuthal line segment positions $\theta = 0^\circ$ and $\theta = 45^\circ$ are depicted with solid and dashed lines, respectively.

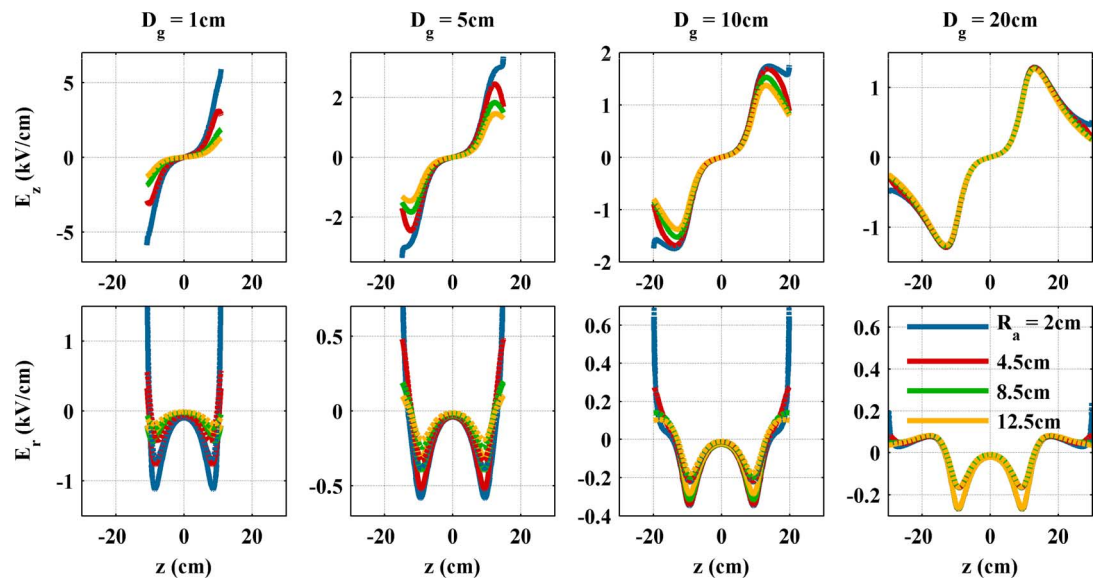

Fig. 9. Dependence of fields in cylindrical rods model on $R_{\rm a}$ and D_g for $L_r = 20$ cm. The format of the figure is equal to the one of Fig. 8. The results shown in Figs. 8 and 9 correspond to two examples of the cylindrical rods model which differ only in the value of L_r.

scaling factor, whereas, for large D_g and acceleration estimates, $d_{\rm w}$ is a better choice for the scaling factor.

As mentioned earlier, axial E_z and radial E_r electric fields can be used as indicators of accelerating and focusing capabilities of a device. Due to the high computational accuracy of WIPL-D used to calculate the fields in a number of sample cylindrical rod models, these fields can be further used to quantitatively estimate ECQ device performance for different values of model parameters D_g and $R_{\rm a}$.

IV. Device Performance

Accurate performance of a device is usually obtained with ion beam dynamics simulations. However, interaction between a device and an ion beam depends not only on the device parameters but on the ion beam parameters as well, e.g., ion energy, charge, and mass. If the device performance is to be evaluated independently, the forces acting on a beam within the fully extended beam path volume must be evaluated. Focusing/defocusing as well as accelerating/decelerating effects accumulate along the path of a test ion through a device. Consequently, integrals of radial and axial components of electric field could be used to evaluate device performance.

Instead of integration over the complete, fully extended beam path volume, we integrate over the line segments corresponding to the limiting fields. For the ECQ device, limiting electric fields occur in the $\theta = 0^\circ$ and $\theta = 45^\circ$ planes due to the fourfold symmetry of the device. Therefore, we establish parameters $f_{\rm A}$

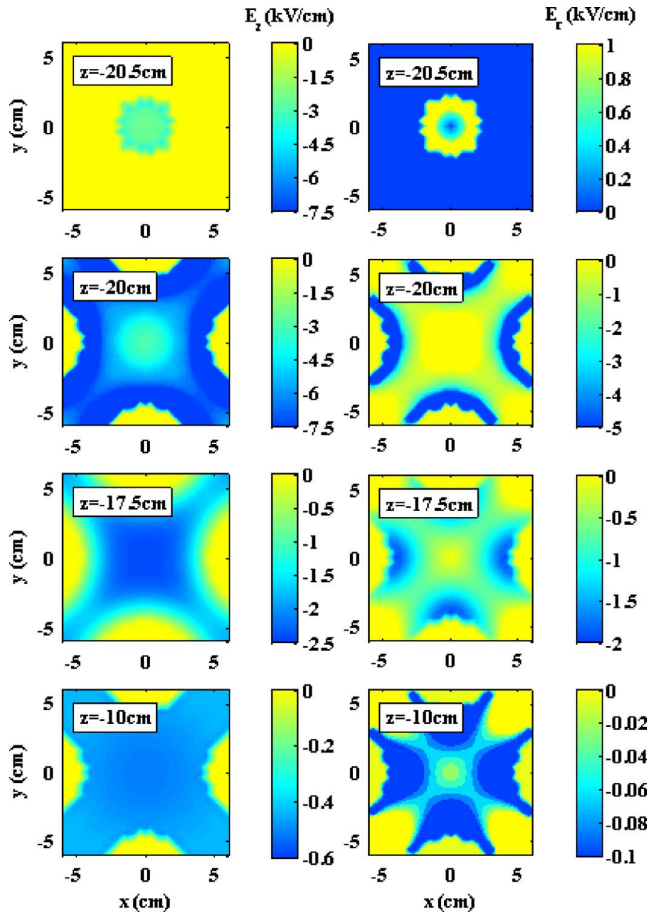

Fig. 10. Axial and radial electric fields in sample transverse planes. The parameters of the cylindrical rods model are $D_g = 0.5$ cm, $R_a = 2$ cm, and $L_r = 40$ cm. Consequently, the transverse planes chosen for the field sampling, $z = -20.5$ cm, -20 cm, -17.5 cm, and -10 cm, correspond to the axial positions of the grounded cylinder entrance aperture, electrode tips, maximal focusing plane, and quarter-length of the device, respectively. The fields at $z = -10$ cm are an order of magnitude smaller than those within the entrance region of the device, i.e., at the remaining three axial positions.

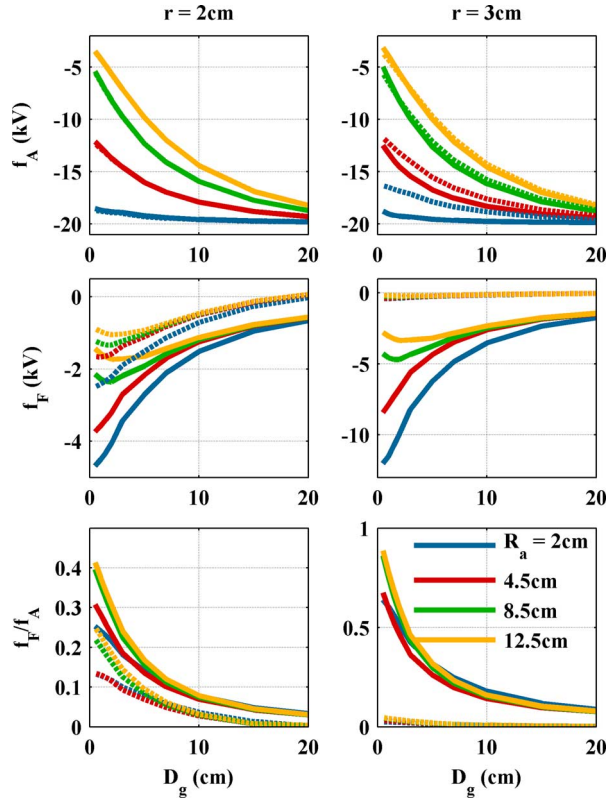

Fig. 11. ECQ device performance. The dependence of the ECQ device's accelerating f_A and focusing f_F potentials, as well as of their ratio f_F/f_A, on the gap size, D_g and aperture radius R_a is shown. The accelerating and focusing potentials are calculated using (3). The data corresponding to the two values of line segment radius, $r = 2$ cm and 3 cm are given in the first and second column of graphs, respectively. The limiting values occurring in the $\theta = 0°$ plane are given as solid lines, whereas those in the $\theta = 45°$ plane are depicted as dashed lines. Different values of R_a are marked with different line colors. The results are obtained for sample models with $L_r = 20$ cm; however, the figure is identical for $L_r = 40$ cm, as can be seen from Fig. 12.

and f_F as measures of ECQ device accelerating and focusing capabilities:

$$f_A(D_g, R_a, r, \theta) = \int_{z=-L_r/2-D_g}^{z=0} E_z(z)\, dz = (-1) \cdot \int_{z=0}^{z=L_r/2+D_g} E_z(z)\, dz$$

$$f_F(D_g, R_a, r, \theta) = \int_{z=-L_r/2-D_g}^{z=0} E_r(z)\, dz = \int_{z=0}^{z=L_r/2+D_g} E_r(z)\, dz \quad (3)$$

where r and θ are coordinates of the line segment along which the integrals are computed. Because of their units, we refer to f_A and f_F as accelerating and focusing potential, respectively. These parameters are used to quantitatively express performance of the ECQ device in Fig. 11. To achieve smoother dependencies on D_g, a number of sample models in addition to those represented by corresponding data in Figs. 8 and 9 are created.

Even though the performance parameters shown in Fig. 11 are calculated for sample models with $L_r = 20$ cm, the results are practically equal to those for $L_r = 40$ cm, as can be seen from Fig. 12. This confirms the conclusion drawn earlier that the ECQ device acts upon a beam in the vicinity of device's entrance and exit, whereas the region in between is the drift space. Note that this independence of Fig. 11 on L_r is valid for $L_r \geq 20$ cm, because entrance and exit region fields overlap around $z = 0$ for lower values of L_r.

The accelerating potential does not depend significantly on r or on θ. Since f_A changes its sign at $z = 0$ cm, a beam is decelerated in the entrance region and accelerated in the exit region. The focusing potential is negative along both $\theta = 0°$ and 45° line segments for $r = 2$ cm. For $r = 3$ cm and $\theta = 0°$, the absolute value of the focusing potential is larger than for $r = 2$ cm. Consequently, for $\theta = 0°$, focusing is stronger for larger distances from the devices axis, as it should be for a focusing device. For $r = 3$ cm and $\theta = 45°$, the focusing potential is approximately equal to zero, i.e., a beam is neither being focused nor defocused. Excellent focusing properties are somewhat shaded by the fact that the ratio f_F/f_A is smaller than 1, which means that more power is spent on acceleration/deceleration than on focusing. On the other hand, this indicates

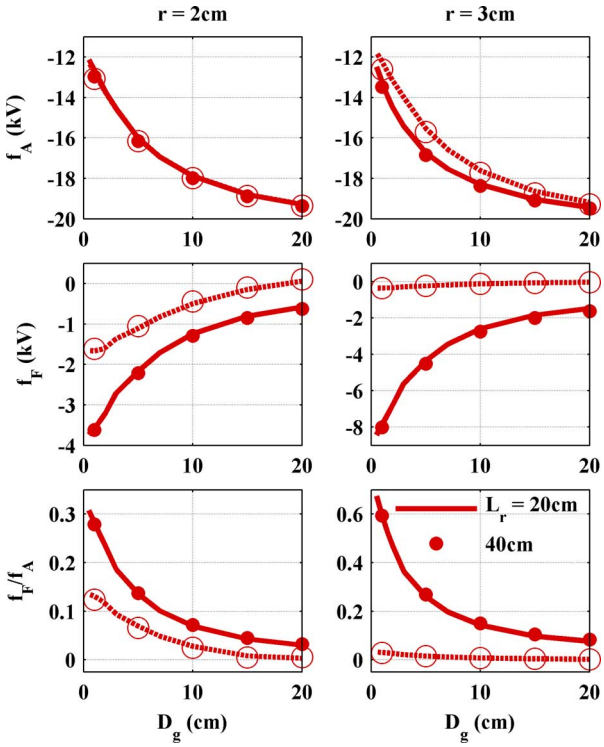

Fig. 12. Dependence of focusing and accelerating potentials on L_r. The figure format is identical to the one of Fig. 11. The solid line and filled symbols represent data in the $\theta = 0°$ plane, whereas dashed line and open symbols correspond to the $\theta = 45°$ plane. For clarity, only data corresponding to $R_a = 4.5$ cm is shown; the agreement between the results corresponding to the two different values of L_r is excellent for other values of R_a, as well.

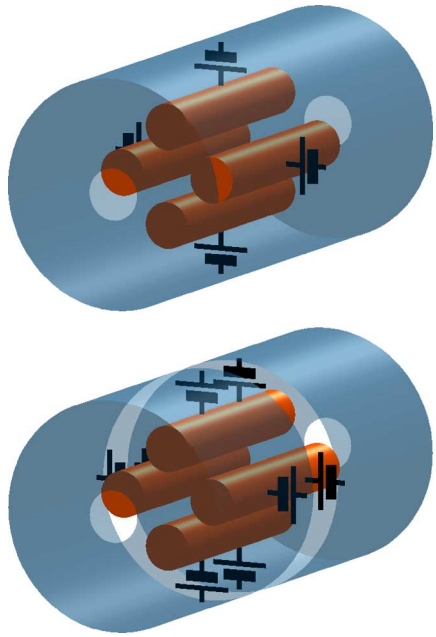

Fig. 13. Geometries of ECQ device. The upper figure gives the geometry of the ECQ lens and RF ECQ accelerator. Four dc power supplies correspond to the ECQ lens. For the RF ECQ accelerator, these are replaced with four ac power supplies. The lower figure depicts the dc ECQ accelerator. The missing stripe in the grounded cylinder and four additional properly connected dc power supplies enable the desired change of axial field orientation in the entrance region.

that the device could work more efficiently as an accelerator if its voltage is reversed for $z < 0$. These conclusions prove that the initial estimates arisen from Fig. 1 are correct.

If the device is to serve as an accelerator, E_z must change its sign for $z < 0$. This can be achieved either by applying RF voltage, as illustrated in [6], or by altering the device's geometry, as shown in Fig. 13. In the former case, the field is quasi-static; therefore, at any given moment, E_z still has different signs for $z < 0$ and for $z > 0$. The test ion ideally synchronized with the applied RF field only perceives E_z as positive throughout the device. Regardless of whether the change of E_z's sign for $z < 0$ is real or fictitious, it is accompanied by the E_r's change of sign in the same region. As a result, an ion beam will be defocused in the entrance region and focused in the exit region of the device. Due to a favorable value of f_F/f_A, more energy is spent on acceleration than on defocusing.

The dependencies in Fig. 11 can be used to adjust the device parameters to achieve desired performance. If the device is to be used as an ECQ lens, D_g should be chosen to be as small as possible. The value for R_a is a tradeoff between stronger focusing achieved with smaller values of R_a and larger f_F/f_A obtained with larger R_a.

In the ECQ accelerator, D_g should be as large as possible, although gain in performance decays with the increase in D_g. Smaller values of R_a provide somewhat stronger acceleration, whereas for larger R_a, defocusing in the entrance region is slightly weaker. If entering defocusing is to be overcome by exit focusing, medium values of D_g as well as R_a should be chosen.

Note that R_r/R_{ra} is equal to 8/9 for all the considered examples, which is smaller than the typical value of 8/7. Larger values of this ratio will cause dashed curves in Figs. 11 and 12 to be closer to those depicted by solid lines. The strongest interaction between the ECQ device and a beam occurs in the vicinity and within the gaps between the rod tips and the bases of the surrounding cylinder. Consequently, R_{ra} and d_w should be considered as scaling parameters when using data in Figs. 11 and 12 for performance estimates of other devices with a similar structure. For acceleration estimates and large D_g, a good choice is d_w, whereas R_{ra} is more suitable for focusing estimates and small D_g.

V. Conclusion

The ECQ device acts upon an ion beam within its entrance and exit regions, i.e., in the regions between the apertures and electrodes. If the electrode length is above the limiting value, the acting entrance and exit regions are separated by the drift space spreading out on both sides of the middle of device length. Therefore, the device parameters influencing its performance are the aperture radius and the aperture-electrode gap size. If it is above the lower limit, the electrode length does not influence device performance; however, it plays a role in synchronization with a beam if device operates in RF mode. The parameter whose value should be chosen with most care is the gap size. The aperture radius is used for fine adjustments of the device performance. If the device is to serve as a lens, the gap size should be small, whereas efficient acceleration is achieved

with large gap sizes. The roles of the entrance and exit regions may be adjusted to be different by choosing different values of the corresponding gap sizes and aperture radii. For example, the combination of large entrance and small exit gap size provides neutralization of entrance defocusing, although less efficient acceleration. In the ECQ device, the percentage of driving power used for focusing is always smaller than the one spent on deceleration/acceleration. Nevertheless, the ECQ lens may be appealing for weak focusing because its focusing potential along a fixed radial position oscillates between the strongest focusing at the azimuthal positions of electrodes and either weaker focusing or no action at the azimuths corresponding to the midline between electrodes.

References

[1] L. Xiu, L. Dong, S. Ohnuma, and C. D. Meitzler, "A new design of helical electrostatic quadrupole and its quasi-octupole mode of operation," in *Proc. 3rd Eur. Particle Accelerator Conf.*, Berlin, Germany, Mar. 24–28, 1992, pp. 1533–1535.

[2] L. Xiu, S. Ohnuma, K. Wang, C. D. Meitzler, and Y. Xu, "Test of the transport properties of a helical electrostatic quadrupole and quasi-octupole," in *Proc. 15th Particle Accelerator Conf.*, Washington, DC, USA, May 17–20, 1993, pp. 3148 –3150.

[3] N. Nešković, I. Telečki, B. Bojović, and S. Petrović, "A square electrostatic rainbow lens: Catastrophic ion beam focusing," *Nucl. Instrum. Methods A*, vol. 635, no. 1, pp. 1–7, Apr. 2011.

[4] I. Telečki, S. Petrović, P. Beličev, B. Rađenović, R. Balvanović, B. Bojović, and N. Nešković, "Focusing properties of a square electrostatic rainbow lens," *Nucl. Instrum. Methods A*, vol. 694, pp. 224–233, 2012.

[5] J. L. Ristić-Djurović and A. Ž. Ilić, "Role and significance of uniform distribution in a study of ensemble of particles," *IEEE Trans. Nucl. Sci.*, vol. 60, no. 1, pp. 236–245, Feb. 2013.

[6] J. L. Ristić-Djurović, S. Čirkovič, and A. Ž. Ilić, "Ion beam acceleration with radio frequency powered rainbow lens," *IEEE Trans. Nucl. Sci.*, vol. 60, no. 2, pt. 2, pp. 1272–1279, 2013.

[7] D. A. Swenson, "Status of the RFD linac structure development," in *Proc. 20th Int. LINAC Conf.*, Monterey, CA, USA, Aug. 21–25, 2000, pp. 935–937.

[8] C. P. Welsch, M. Grieser, J. Ullrich, A. Wolf, and C. Gläβner, "An electrostatic quadrupole doublet with an integrated steerer," in *Proc. 9th Eur. Particle Accelerator Conf.*, Lucerne, Switzerland, Jul. 5–9, 2004, pp. 1234–1236.

[9] F. M. Bieniosek, C. M. Celata, E. Henestroza, J. W. Kwan, L. Prost, P. A. Seidl, A. Friedman, D. P. Grote, S. M. Lund, and I. Haber, "2-MV electrostatic quadrupole injector for heavy-ion fusion," in *Phys. Rev. Special Topics—Accel. Beams*, Jan. 2005, vol. 8, p. 010101.

[10] C. P. Welsch, M. Grieser, J. Ullrich, and A. Wolf, "An ultra-low-energy storage ring at FLAIR," *Nucl. Instrum. Methods A*, vol. 546, pp. 405–417, 2005.

[11] A. J. Kreiner, J. W. Kwan, A. A. Burlón, H. Di Paolo, E. Henestroza, D. M. Minsky, A. A. Vlada, M. E. Debray, and H. Somacal, "A tandem-electrostatic-quadrupole for accelerator-based BNCT," *Nucl. Instrum. Methods B*, vol. 261, pp. 751–754, 2007.

[12] A. J. Kreiner, H. Di Paolo, A. A. Burlon, J. M. Kesque, A. A. Valda, M. E. Debray, Y. Giboudot, P. Levinas, M. Fraiman, V. Romeo, H. R. Somacal, and D. M. Minsky, "Accelerator-based boron neutron capture therapy and the development of a dedicated tandem-electrostatic-quadrupole," in *Proc. 7th Latin Amer. Symp. Nucl. Phys. Appl.*, Cusco, Peru, Jun. 11–16, 2007, pp. 17–24.

[13] G. A. Westenskow, D. Grote, F. Bieniosek, and J. W. Kwan, "A multi-beamlet injector for heavy ion fusion reactor: Experiments and modeling," in *Proc. 22nd Particle Accelerator Conf.*, Albuquerque, NM, USA, Jun. 25–29, 2007, pp. 3777–3781.

[14] D. A. Swenson, "CW proton LINAC for the BNCT application," in *Proc. 24th Linear Accelerator Conf.*, Victoria, BC, Canada, Sep.–Oct. 29–3, 2008, pp. 220–222.

[15] M. J. King, G. T. Miller, J. Reijonen, Q. Ji, N. Andresen, F. Gicquel, T. Kalvas, K.-N. Leung, and J. W. Kwan, "Initial evaluation of a pulsed white spectrum neutron generator for explosive detection," *IEEE Trans. Nucl. Sci.*, vol. 56, no. 3, pt. 2, pp. 1283–1287, 2009.

[16] "WIPL-D Microwave," Software and User's Manual. Belgrade, Serbia, WIPL-D d.o.o, 2005.

IEEE TRANSACTIONS ON

NUCLEAR SCIENCE

A PUBLICATION OF THE IEEE NUCLEAR AND PLASMA SCIENCES SOCIETY

NUCLEAR & PLASMA SCIENCES SOCIETY

APRIL 2013 VOLUME 60 NUMBER 2 IETNAE (ISSN 0018-9499)

PART II OF TWO PARTS

(Contents Continued on Page 1253)

IEEE

(Contents Continued from Front Cover)

(Contents Continued on Page 1254)

(Contents Continued from Page 1253)

SOLID STATE DETECTORS

Ion Beam Acceleration With Radio Frequency Powered Rainbow Lens

Jasna L. Ristić-Djurović, Saša Ćirković, and Andjelija Ž. Ilić, *Member, IEEE*

***Abstract*—The electrostatic quadrupole lens, quadrupole accelerator and square rainbow lens as well as radio frequency quadrupole accelerator all have similar structure with four rod-like electrodes. Unlike the last one, which is powered by the alternating voltage, the first three are electrostatic devices. Each two adjacent electrodes of a common electrostatic lens have equal magnitude and opposite signs of their electric potentials, whereas, electric potentials of rainbow lens's electrodes are all equal in magnitude as well as in sign. If powered by the appropriate radio frequency instead of a DC voltage, the rainbow lens transforms into an ion beam accelerator which could cost-effectively broaden the available energy range of low energy ion beam facilities.**

***Index Terms*—Electrostatic quadrupoles, ion beam dynamics, linear accelerators.**

I. Introduction

THE electrostatic quadrupole accelerator has been introduced in [1]–[3]. More recently electrostatic accelerating gaps and focusing electrostatic quadrupole lenses are combined, for example, in [4], [5]. Another electrostatic device similar to the electrostatic quadrupole lens, the electrostatic square rainbow lens is shown to have focusing properties as well [6], [7]. Unlike the electrostatic quadrupole lens whose four electrodes are powered by static electric voltages equal in intensity but alternating in sign with respect to the azimuthal position of the electrodes [8]–[10], the electrode voltages of electrostatic rainbow lens are all equal in sign. Contrary to these electrostatic devices, four electrodes in a radio frequency quadrupole accelerator are powered by radio frequency (RF) voltage, see, for example, [11]–[13] and references therein. The RF voltage, four rods and focusing quadrupole field resulting from independent operation at different electric potential of two pieces each supporting two electrodes are combined in the RF-Focused Interdigital (RFI) and RF-Focused Drift tube (RFD) linac structures [14], [15]. With the aim to broaden the application scope of the low energy FAMA facility [16], in what follows we show that a rainbow lens can be transformed into an accelerator by relatively small, low cost changes.

The accelerating axial electric field created by slanting the electrodes of electrostatic rainbow lens with respect to its axis

Manuscript received October 25, 2012; revised November 24, 2012; accepted November 25, 2012. Date of publication February 11, 2013; date of current version April 10, 2013. This work was supported in part by the Ministry of Education and Science of Serbia through the project "Physics and Chemistry with Ion Beams," no. III45006.

The authors are with the Vinča Institute of Nuclear Sciences, Laboratory of Physics (010), University of Belgrade, 11001 Belgrade, Serbia (e-mail: jasna@stanfordalumni.org; kosjera@vinca.rs; andjelijailic@ieee.org).

Color versions of one or more of the figures in this paper are available online at http://ieeexplore.ieee.org.

Digital Object Identifier 10.1109/TNS.2012.2230452

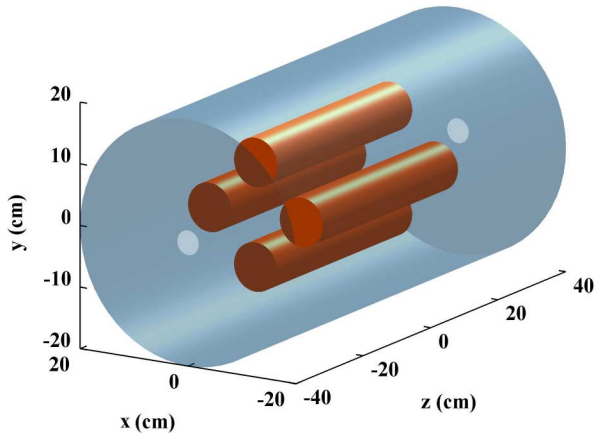

Fig. 1. Electric quadrupole accelerator. Four $L_{\mathrm{r}} = 40$ cm long cylindrical rods with base radius $R_{\mathrm{r}} = 4$ cm are positioned between $z = -20$ cm and $z = 20$ cm at $(x_{\mathrm{r}1}, y_{\mathrm{r}1}) = (6\sqrt{2}\ \mathrm{cm}, 0\ \mathrm{cm}), (x_{\mathrm{r}2}, y_{\mathrm{r}2}) = (0\ \mathrm{cm}, 6\sqrt{2}\ \mathrm{cm}), (x_{\mathrm{r}3}, y_{\mathrm{r}3}) = (-6\sqrt{2}\ \mathrm{cm}, 0\ \mathrm{cm})$, and $(x_{\mathrm{r}4}, y_{\mathrm{r}4}) = (0\ \mathrm{cm}, -6\sqrt{2}\ \mathrm{cm})$. The rods are housed in a grounded cylinder with base radius, $R_{\mathrm{g}} = 20$ cm, aperture radius, $R_{\mathrm{a}} = 2$ cm, and length, $L_{\mathrm{g}} = 80$ cm.

[17] turned out to be insufficiently effective [18]. Consequently, for noticeable acceleration the acceleration method had to be changed. Namely, if its DC voltage source is replaced with the medium to high RF power supply, the rainbow lens becomes a quasi electrostatic instead of an electrostatic device and can efficiently accelerate ion beams.

If the four rods housed in a grounded cylinder are all powered by the same properly adjusted RF voltage an ion beam would be accelerated through the entrance as well as exit accelerating gap between the rods and the base of grounded cylinder, see Fig. 1. To validate the principle as well as to illustrate its efficiency, interaction between a test proton beam and the described device is used. In the first approximation the electric field of the device is replaced by the analytical electric field of uniformly charged finite wires. Once the principle is proven to work it is further tested with the realistic electromagnetic field obtained by modeling the device with the commercially available software package WIPL-D [19]. Test ion trajectories within the proton beam are simulated using the self-made software package VINDY [20].

II. Analytical Estimate

In order to test the idea an analytical model of the device is composed. Four parallel, equally charged finite wires are positioned along the edges of imaginary quadratic prism which coincide with the axes of the rods shown in Fig. 1. The distance between two adjacent wires, $d_{\mathrm{w}} = 12$ cm, is equal to the distance between the axes of neighboring rods; however, in order

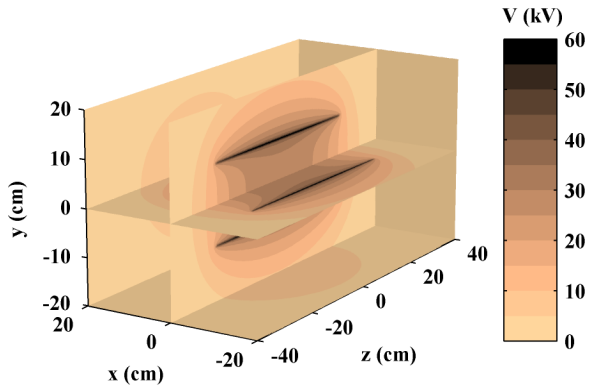

Fig. 2. Electric potential of four uniformly charged finite wires. The wires are each charged with the uniform charge density $Q' = 0.36\ \mu$C/m. The resulting potential of the electrostatic field is shown in the $x = 0, y = 0, z = 40$ cm, $x = 20$ cm, and $y = -20$ cm planes.

to better match the electric potential of the rods, the length of the wires is extended to $L_{\rm w} = 48$ cm compared to the length of the rods, $L = 40$ cm. Electric field is calculated using analytical formulas for uniformly charged finite wires

$$E_x(x,y,z) = \frac{Q'}{4\pi\varepsilon_0}\sum_{i=1}^{4}\left(\frac{(x-x_{{\rm w}i})}{r_{2i}(p_2+r_{2i})} - \frac{(x-x_{{\rm w}i})}{r_{1i}(p_1+r_{1i})}\right)$$
$$E_y(x,y,z) = \frac{Q'}{4\pi\varepsilon_0}\sum_{i=1}^{4}\left(\frac{(y-y_{{\rm w}i})}{r_{2i}(p_2+r_{2i})} - \frac{(y-y_{{\rm w}i})}{r_{1i}(p_1+r_{1i})}\right)$$
$$E_z(x,y,z) = \frac{Q'}{4\pi\varepsilon_0}\sum_{i=1}^{4}\left(\frac{1}{r_{2i}} - \frac{1}{r_{1i}}\right), \qquad (1)$$

where $p_1 = z + L_{\rm w}/2, r_{1i} = \sqrt{(x-x_{{\rm w}i})^2 + (y-y_{{\rm w}i})^2 + p_1^2}, p_2 = z - L_{\rm w}/2, r_{2i} = \sqrt{(x-x_{{\rm w}i})^2 + (y-y_{{\rm w}i})^2 + p_2^2}, Q'$ is charge density and pairs $(x_{{\rm w}i}, y_{{\rm w}i})$ are wire coordinates equal to $(d_{\rm w}/\sqrt{2}, 0), (0, d_{\rm w}/\sqrt{2}), (-d_{\rm w}/\sqrt{2}, 0)$, and $(0, -d_{\rm w}/\sqrt{2})$ for $i = 1, 2, 3$, and 4, respectively. The wires stretch between $z = -24$ cm and $z = 24$ cm. Being a vector, electric field is not easy to visualize; therefore, it is the electric potential corresponding to the calculated electric field that is given in five sample planes in Fig. 2. Better matching between the electrostatic potentials of the four wires and of the four rods is achieved if the wire length is extended at each end by $R_{\rm r} = 4$ cm because the equipotential ellipsoid of a wire, which contains the circumference of the rod's base, is than not only longer but is thinner as well and therefore closer to the rod's cylinder. Adjusted length of the wires together with the charge density of $Q' = 0.36\ \mu$C/m provide that the analytical field of finite wires and the field corresponding to the real device given in Fig. 1, have the same values of electrostatic potential of 0 kV at $x = 0$ cm, $y = 0$ cm, $z = L_{\rm r} = 40$ cm, and 20 kV at $x = d_{\rm w}/\sqrt{2} - R_r = 6.5$ cm, $y = 0$ cm, $z = L_{\rm r}/2 = 20$ cm. Note that, unlike in [6], the point of zero potential is chosen to be within the beam path volume; therefore, the agreement between the ion beam simulations in the approximated and in the realistic field is expected to be reasonably good.

A beam of protons traveling along the z-axis from $z = -40$ cm to $z = 40$ cm is first decelerated until it reaches $z = 0$ cm and then accelerated for the rest of the path. A proton could be accelerated throughout its path if the electric potential of the wires is time varying and changing its sign when the proton reaches $z = 0$ cm. If the charge, uniform along wire's length, is alternating in time with radio frequency $f_{\rm RF}$, i.e.,

$$Q'(t) = Q'_0 \sin(2\pi f_{\rm RF} t - \phi_{\rm RF}), \qquad (2)$$

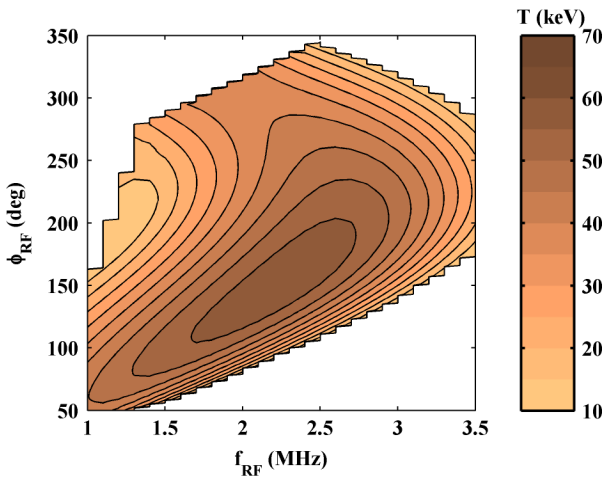

Fig. 3. Output energy dependence on frequency and phase of power supply. The initial proton energy of 10 keV is increased to $T = 58.5$ keV with $f_{\rm RF} = 2.3$ MHz and $\phi_{\rm RF} = 156.0°$.

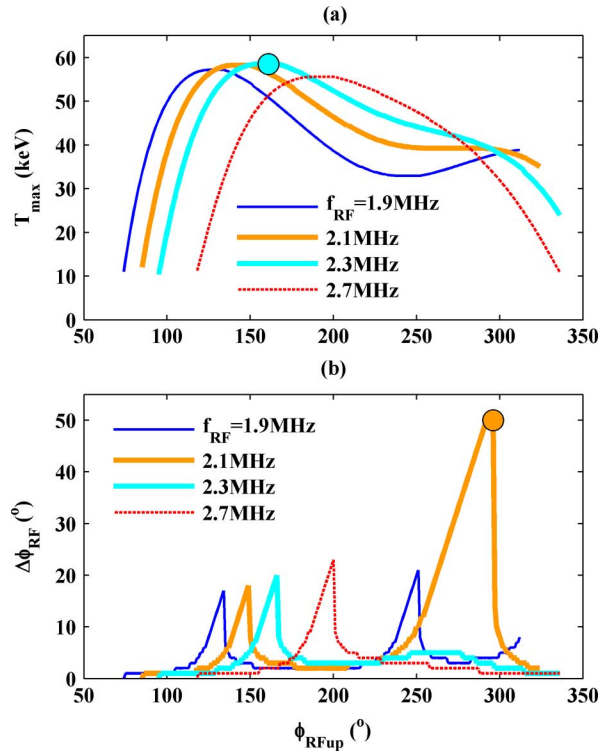

Fig. 4. Optimal acceleration conditions. Maximal proton energy within a beam bunch, $T_{\rm max}$, and phase width of a beam bunch, $\Delta\phi_{\rm RF} = \phi_{\rm RFup} - \phi_{\rm RFlow}$, are shown in graphs (a) and (b), respectively. Each point corresponds to a beam bunch traveling along the z-axis whose energy spread after acceleration is 1 %. The optimal accelerations corresponding to the global maxima $\max(T_{\rm max})$ and $\max(\Delta\phi_{\rm RF})$ are marked with circles in graphs (a) and (b), respectively.

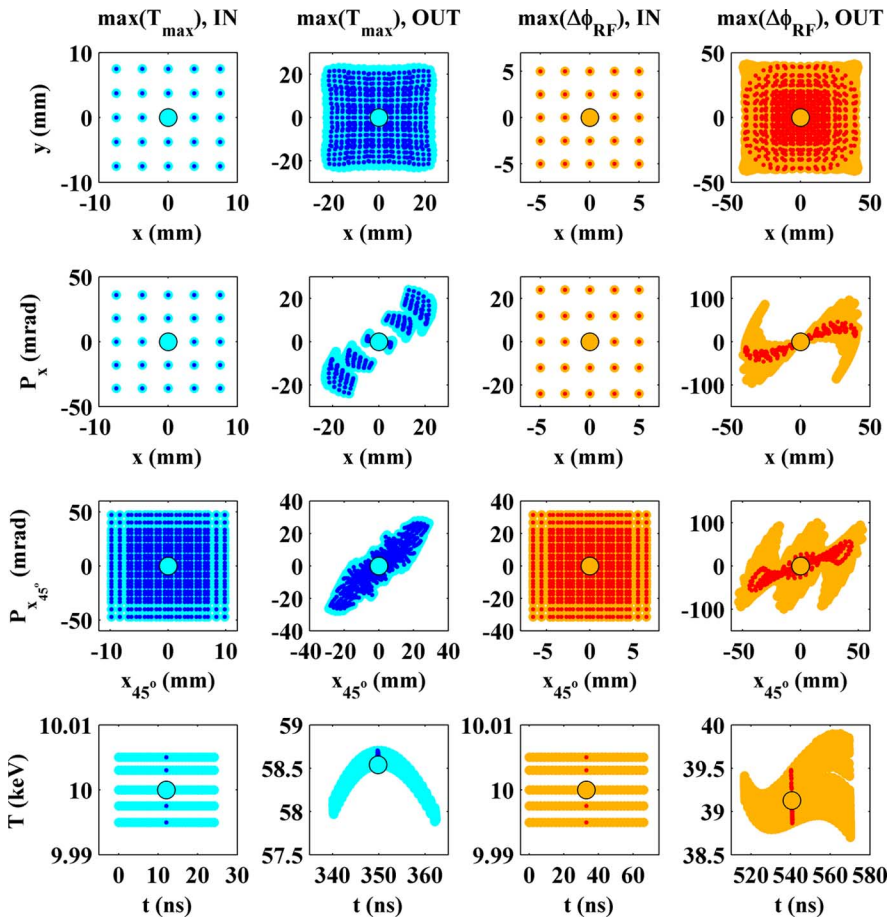

Fig. 5. Optimal accelerations. The graphs in the first and second column correspond to the optimal acceleration with respect to the maximal achieved ion energy within a bunch, $\max(T_{\max})$, and, consequently, to the conditions given in the first row of Table I. The optimal acceleration depicted by the graphs in the third and fourth column correspond to the maximal phase width criterion, $\max(\Delta\phi_{\mathrm{RF}})$, and to the second row of Table I. The first and third columns of graphs show the initial proton bunches at the device entrance $z = -40$ cm, whereas the output bunches at $z = 40$ cm are given in the second and fourth columns. In each graph, the total of 96 875 simulated test particles is shown. The graphs in the first row give transverse, i.e., $x - y$, images of the simulated beam. Due to the fourfold symmetry, the transverse emittances along mutually perpendicular axes, e.g., along x- and y-axis, are identical. Therefore, in order to fully represent the beam its transverse emittances are given along the two axes which are 45° apart. Consequently, the second and third row of graphs is devoted to the $x - P_x$ and $x_{45^\circ} - P_{x_{45^\circ}}$ emittances of the beam, respectively. The images of the beam bunch in the longitudinal phase space, $t - T$, are given in the fourth row of graphs. The central ion within the bunch is depicted by a circle on all graphs. The test ions within the bunch which are in phase with the accelerating voltage are depicted by dark dots. Angular as well as spatial spreads of the beam caused by the normalized momentum are much larger than those induced by the spatial coordinate. The output energy depends mostly on the timing between the test ion and the accelerating RF voltage. The least influential parameter is the initial ion energy.

the electric field defined with (1) will resume the same time dependence. Note that for our example $Q_0' = 0.36$ μC/m. Given the size of the device, the time dependent electric field can be treated as quasi static as long as the condition $f_{\mathrm{RF}} \ll (2\pi L_{\mathrm{g}}\sqrt{\varepsilon\mu})^{-1} \cong 60$ MHz is satisfied.

The energy a proton gains during its interaction with the field defined with (1) and (2) depends on the synchronization between the two, i.e., it depends on the field's frequency and phase, f_{RF}, ϕ_{RF}, as well as on the initial energy of a proton, T_0. The dependence of the output proton energy, T, on f_{RF} and ϕ_{RF} is given in Fig. 3 for the initial proton energy of $T_0 = 10$ keV. The data is obtained by simulating proton trajectories along z-axis for different values of f_{RF} and ϕ_{RF}.

In order to determine optimal conditions for acceleration of a beam bunch rather than a single proton, the data in Fig. 3 is further analyzed. Acceleration of a beam bunch whose energy spread after acceleration is 1 % is investigated using four criteria: maximal output energy of a single proton within a bunch, $T_{\max}$, phase width of a bunch, $\Delta\phi_{\mathrm{RF}}$, averaged energy, T_{av}, and total energy of a bunch, T_{tot}. Since the chosen energy spread of 1 % is rather small, the shapes of the curves defining the dependence of the maximal proton energy within a bunch and the averaged energy are very similar and the values of f_{RF} and ϕ_{RF} corresponding to the maxima of these curves are practically equal. The same is true for the second and fourth criteria, i.e., for the bunch width and total energy. Therefore, only two out of four dependencies are shown in Fig. 4. The values corresponding to the optimal acceleration with respect to all four criteria are given in Table I. Note that the maxima of curves $\Delta\phi_{\mathrm{RF}}(\phi_{\mathrm{RFup}})$ in graph (b) in Fig. 4 correspond to the intervals with local minimum, local maximum or inflection point of curves $T_{\max}(\phi_{\mathrm{RFup}})$ in graph (a). In particular, the global maximum in graph (b) corresponds to the phase interval which contains inflection point of the corresponding curve, $f_{\mathrm{RF}} = 2.1$ MHz, in graph (a).

Using the data from the first two rows of Table I as initial conditions for ion beam dynamics simulations, the two optimal accelerations marked with circles in Fig. 4 are further investi-

TABLE I
OPTIMAL ACCELERATION CONDITIONS IN ANALYTICAL ELECTRIC FIELD CORRESPONDING TO FINITE WIRES

criterion	f_{RF} (MHz)	ϕ_{low} (°)	ϕ_{up} (°)	T_{max} (keV)	$\Delta\phi_{RF}$ (°)	T_{av} (keV)	T_{tot} (MeV)
max(T_{max})	2.3	146	166	**58.5**	20	58.3	1.2
max($\Delta\phi_{RF}$)	2.1	244	294	39.1	**50**	38.9	2.0
max(T_{av})	2.3	146	161	58.5	15	**58.4**	0.9
max(T_{tot})	2.1	243	293	39.2	50	38.9	**2.0**

gated and the results are shown in Fig. 5. A proton bunch is represented with the spatial coordinates x and $x_{45°}$, normalized momentums, P_x and $P_{x45°}$, energy, T, and time, t. Because of the fourfold symmetry of the device and axial beam symmetry $x-P_x$ and $y-P_y$ graphs are identical. Therefore, for data presentation purposes $y-P_y$ graphs are replaced with $x_{45°}-P_{x45°}$ graphs, where $x_{45°}$ is the axis rotated clockwise 45° with respect to the x-axis in the $x-y$ plane.

The limits of initial test ion phase space coordinates are chosen in accordance with the proton beam obtained with the p-VINIS ion source [21]. The ion source provides a beam whose spatial as well as angular distribution is Gaussian with $2\sigma = 2.5$ mm and $2\sigma = 12$ mrad, respectively. The energy spread within the ion source plasma is smaller than 1 eV. However, input variables should be distributed over sufficiently wider intervals if the simulated input-output mapping is to be used to interpolate the output corresponding to any desired distribution of input variables, as described in [22]. Therefore, in our optimal acceleration study, the initial spatial as well as angular beam spread is taken to be 6σ for the optimal acceleration with $\max(T_{\max})$, and 4σ for the $\max(\Delta\phi_{\mathrm{RF}})$ example. In both cases it was taken that the initial energy spread is 10 eV. Further, all input parameters are taken to be equally spaced as well as uniformly distributed. Consequently, ion beam simulations are performed once and the output corresponding to any desired distribution of input variables is obtained much faster by the method described in [22]. Note that the spatial beam spreads in Fig. 5 exceed grounded cylinder aperture of $R_a = 2$ cm at $z = -40$ cm as well as at $z = 40$ cm; therefore, the depicted results could be used to determine the acceptance of the device, as well.

As can be seen from the last row of graphs in Fig. 5, the analytical quasi static electric field of four finite wires can efficiently accelerate a proton beam. The maximal ion energy achieved in the examples of proton beam acceleration with finite wires shown in [22] and [23] is 37 % larger because the wires were 8 cm shorter and the applied charge density was almost two times larger.

III. NUMERICAL MODEL

Encouraging results shown in Fig. 5 must be validated by a more realistic approximation of electromagnetic field. The structure shown in Fig. 1 is modeled using the commercially available software package WIPL-D [19]. The three-dimensional electromagnetic solver incorporated in this package models arbitrarily shaped structures with wires and plates as basic building blocks. Because it is a frequency domain solver based on the higher order method of moments it is well-suited for closed region problems and the method of choice for open

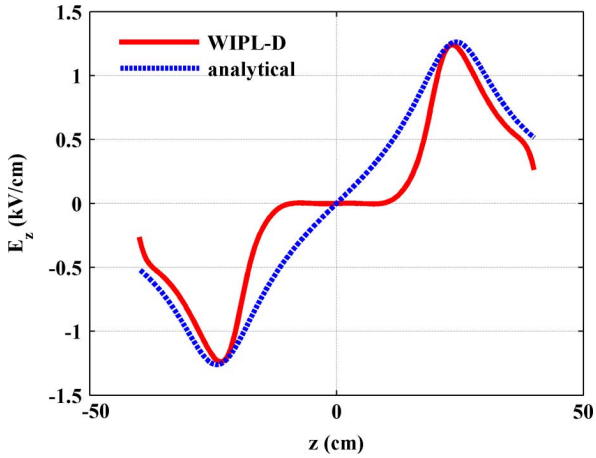

Fig. 6. Comparison between realistic and analytical electric field. Due to the difference between the numerically modeled and approximate analytical electric field along the axis of the device maximal achievable energy of a test proton is expected to be lower than the value predicted for the analytically computed field. Note that, along the z-axis, the total electric field has only axial component, i.e., $E = E_z$ if $x = y = 0$ cm.

regions modeling. Metallic plates, lossy or lossless dielectric as well as magnetic surfaces are modeled with electrically large bilinear generalized quadrilaterals, which provide very good flexibility and geometrical accuracy. The higher order numerical engine ensures that highly accurate results are achieved efficiently.

If proton beam accelerations in the analytically approximated and numerically modeled field are to be compared the appropriate parameters corresponding to the two cases have to be adjusted. In order to preserve field symmetry, power lines are attached to the four electrodes and the grounded cylinder in the middle of the device. To match the approximated field electrostatic potential of 20 kV at $x = d_w/\sqrt{2} - R_r = 6.5$ cm, $y = 0$ cm, $z = L_r/2 = 20$ cm, the amplitude of the voltage applied to the rod electrodes is taken to be 20 kV as well.

The shape of the real electric field is reasonably well approximated in the previous section with the field corresponding to uniformly charged finite wires because the length of wires is extended and the points with zero and driving electrostatic potential are chosen carefully. However, for the analytical finite wires approximation it was assumed that charge distribution along the wires is uniform; therefore, the largest discrepancy between the realistic and approximated field is caused by the charge pile up at the edges of the device, see Fig. 6. Note that the fields are given at their peaks, i.e., the value of sine in (2) as well as in the appropriate expression for total field obtained with WIPL-D are taken to be 1.

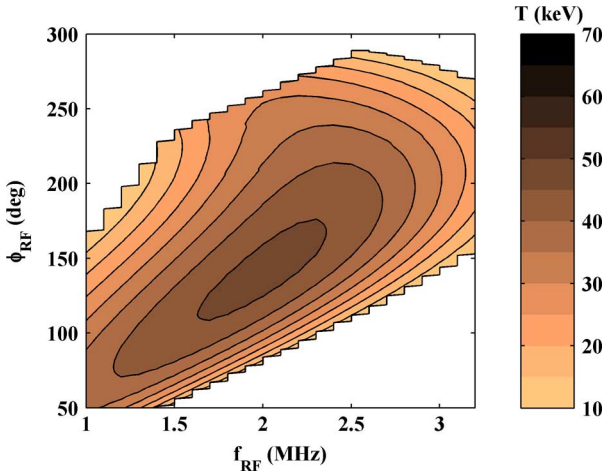

Fig. 7. Output energy dependence on frequency and phase of power supply for numerically modeled field. The initial proton energy of 10 keV is increased to $T = 46.6$ keV with $f_{\mathrm{RF}} = 2.0$ MHz and $\phi_{\mathrm{RF}} = 140.0°$. As expected, the maximal achieved energy is 20 % smaller compared to the value predicted by the simulation in analytically approximated field, see Fig. 3.

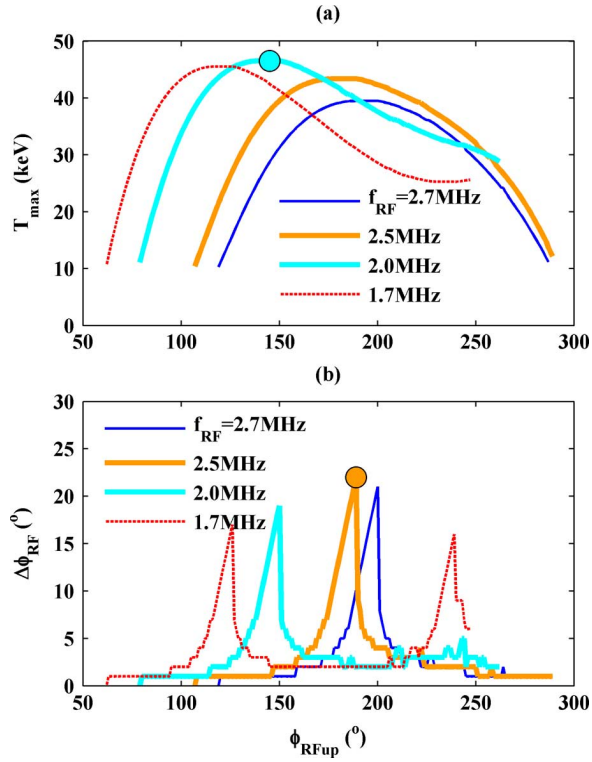

Fig. 8. Optimal acceleration conditions in numerically modeled field. The figure format is identical to the one of Fig. 4. Each point corresponds to a beam bunch traveling along the z-axis whose energy spread after acceleration is 1 %. The optimal accelerations corresponding to the global maximums $\max(T_{\max})$ and $\max(\Delta\phi_{\mathrm{RF}})$ are depicted with circles in graphs (a) and (b), and fully defined in the first and second row in Table II, respectively.

The device dimensions and the considered frequencies provide that the corresponding electromagnetic field is quasi static; therefore, the influences on ion beam dynamics of the real and imaginary magnetic as well as imaginary electric parts of the modeled electromagnetic field are negligible. Regardless, all components of the realistic electromagnetic field obtained with numerical modeling are used in ion beam dynamics simulations. The ion beam dynamics simulations performed with the analytical field shown in Figs. 3 and 4 and Table I are repeated using the numerically modeled electromagnetic field and the results are given in Figs. 7 and 8 and Table II, respectively.

In the analytically calculated field, optimal accelerations with respect to the $\max(T_{\max})$ and $\max(\Delta\phi_{\mathrm{RF}})$ conditions correspond to the phase intervals which contain local maximum and inflection point of the matching $T_{\mathrm{RF}}(\phi_{\mathrm{RFup}})$ curve, respectively, see Fig. 4. However, in the modeled field both considered optimal accelerations correspond to the local maxima of the matching $T_{\mathrm{RF}}(\phi_{\mathrm{RFup}})$ curve. Consequently, beam bunch dynamics of the two optimal accelerations in the modeled field are more alike than is the case for the analytically approximated field, see Figs. 5 and 9. For the same reason, the beam bunch dynamics simulations shown in Fig. 9 are performed using equally wide intervals of spatial as well as angular coordinates of 6σ for the both considered cases of optimal acceleration, i.e., the simulation intervals for the $\max(\Delta\phi_{\mathrm{RF}})$ case are extended from 4σ to 6σ.

Wide ranges of input as well as output variables in Figs. 5 and 9 are chosen to illustrate the acceptances of the studied devices, i.e., of the finite wires and of the rods housed in the grounded cylinder, respectively. In order to depict a realistic optimal acceleration, the method described in [22] and n-dimensional linear interpolation are applied to the input-output mapping shown in first and second column of Fig. 9, to obtain the output which corresponds to realistically distributed initial parameters of a proton bunch. The result is given in Fig. 10. The initial distribution of the bunch is chosen in accordance with the output of the p-VINIS ion source [21]. After the interaction with the device, the proton beam bunch is defocused and is twice as wide in the transverse direction as before the interaction. While time distribution does not change significantly, energy distribution seems to evolve from the random uniform into a log-normal distribution.

IV. Device Properties

When used as an electrostatic piece of equipment the rainbow lens is intended to be a focusing device. However, as a side effect, in the vicinity of lens's entrance a beam is decelerated and farther along its path close to the exit it is accelerated, see Fig. 11. The focusing strength, i.e., the radial component of electric field is limited by the beam energy, which has to be large enough to overcome entering deceleration. The ratio between the driving, focusing and the side effect, accelerating/decelerating force is unfavorable because $|E_{\mathrm{r}}| < |E_{\mathrm{z}}|$.

If the device is used as quasi static the sign of the sine multiplier is negative roughly for $z < 0$; consequently, a beam is accelerated through the entering as well as exit gap. The side effect is distributed first as undesired defocusing through the first half and then favorable focusing later along the second half of beam path through the device. The net side effect is unfortunately undesired defocusing due to larger beam energy and consequently shorter path along the radial direction for $\mathrm{z} > 0$. The ratio $|E_{\mathrm{z}}/E_{\mathrm{r}}| > 1$ indicates that the device is more efficient as an accelerator than as a lens. Note that these relations depend on the size of accelerating gaps, $(L_g - L_r)/2$, rod length, L_{r}, as

TABLE II
OPTIMAL ACCELERATION CONDITIONS IN NUMERICALLY MODELED ELECTROMAGNETIC FIELD CORRESPONDING TO ROD ELECTRODES

criterion	f_{RF} (MHz)	ϕ_{low} (°)	ϕ_{up} (°)	T_{max} (keV)	$\Delta\phi_{RF}$ (°)	T_{av} (keV)	T_{tot} (MeV)
max(T_{max})	2.0	131	150	**46.6**	19	46.4	0.9
max($\Delta\phi_{RF}$)	2.5	167	189	43.4	**22**	43.2	1.0
max(T_{av})	2.0	131	145	46.5	14	**46.4**	0.7
max(T_{tot})	2.4	160	182	44.7	22	44.5	**1.0**

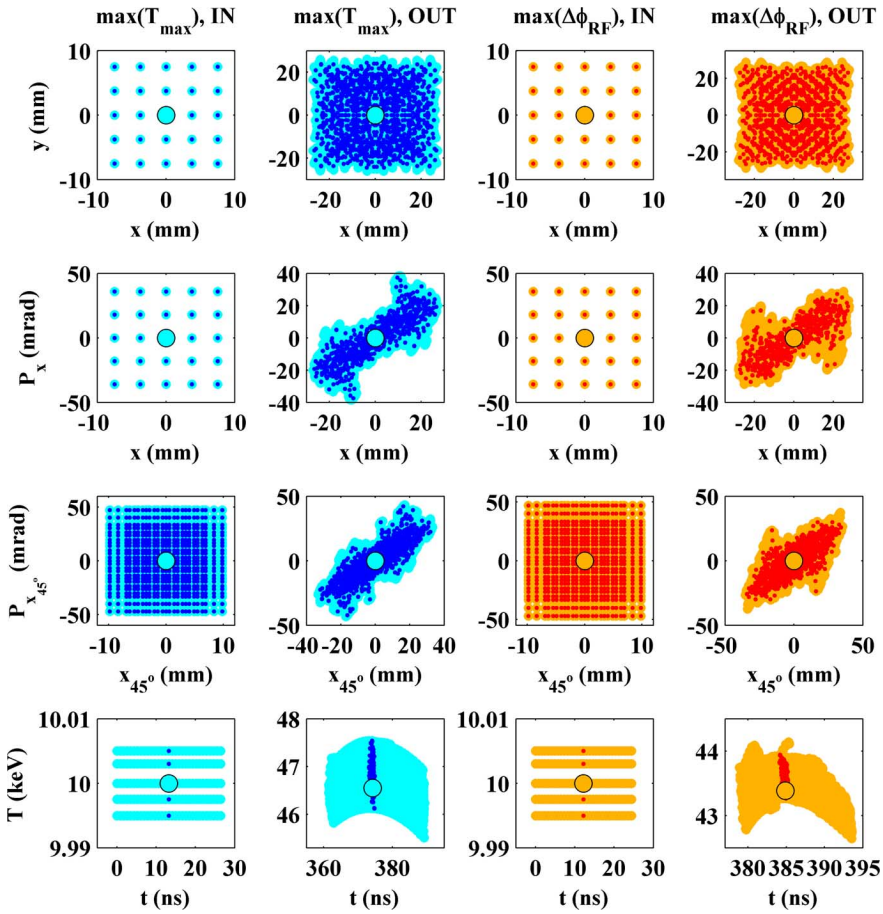

Fig. 9. Optimal accelerations in numerically modeled field. The figure format and the number of simulated test ions are equal to those in Fig. 5. The optimal RF frequency values are $f_{\mathrm{RF}} = 2.0$ MHz and 2.5 MHz for $\max(T_{\max})$ and $\max(\Delta\phi_{\mathrm{RF}})$ criterion, as given in the first and second row of Table II, respectively. One of these two non-random uniform input-output mappings, the one corresponding to $\max(T_{\max})$, is used to obtain the optimal acceleration of realistically distributed beam bunch shown in Fig. 10.

well as aperture radius, R_{a}, see Fig. 1. The values used in our study are chosen in accordance with the existing device; however, in order to achieve maximal efficiency of either focusing or accelerating task, a thorough study of these dependencies should be performed.

As can be seen from Fig. 11, acceleration occurs primarily within the gaps between the electrode tips and the grounded cylinder bases. Consequently, acceleration achieved with the rainbow accelerator is of the drift tube type, as is the case for the RF focused drift tube (RFD) and RF focused interdigital (RFI) linac structures, see [14], [15] and references therein. However, the electrodes in these devices are divided in two pairs and each pair operates at different electric potential. Consequently, the resulting quadrupole-like field produces opposite effects along the two mutually perpendicular transverse axes which contain electrode centers, in our example these are x- and y-axis, and no effect along the axes rotated for 45°, i.e., along x_{45°- and y_{45°-axis. On the other hand, equal polarity of the rainbow accelerator electrodes provides equal effect along the x- and y-axis, as well as less intense but still the same type of effect along the x_{45°- and y_{45°-axis.

In order to fully describe the device, its capabilities to accelerate various ion beams to different energies should be investigated and relationships between the desired beam characteristics and device parameters should be defined. As the first step in this direction, for protons with initial energy of 10 keV, we give Table III which relates the final energy of accelerated proton, $T_{\max}$, with the required RF voltage parameters: amplitude, V_0, frequency, f_{RF}, and phase limits, ϕ_{low} and ϕ_{up}.

Illustration of the rainbow effect, detailed technical parameters of the rainbow accelerator as well as more thorough discussion about its capabilities will be given in [24].

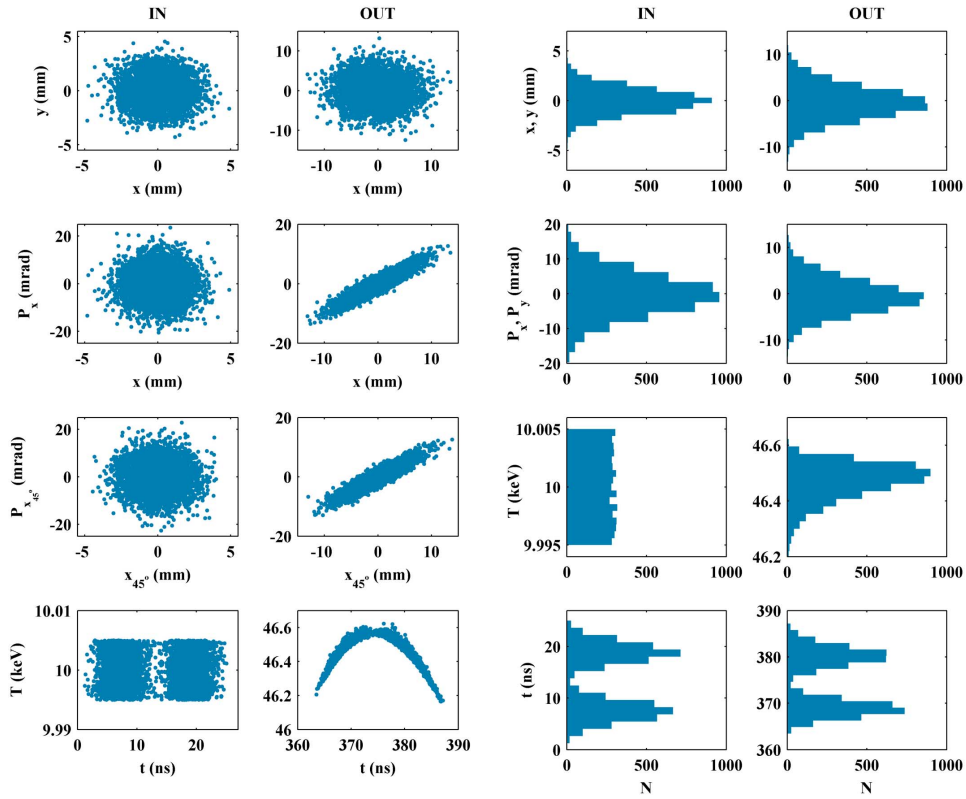

Fig. 10. Optimal acceleration of realistically distributed proton bunch. Only optimal acceleration with respect to $\max(T_{\max})$ criterion is considered. The initial and final phase space coordinates of 5000 test particles shown in the first and second column of graphs follow the form accepted in Figs. 5 and 9. The initial spatial coordinates, x and y, as well as normalized momentums, P_x and P_y, follow Gaussian distribution, initial test ion energy, T, is taken to have random uniform distribution, whereas time of arrival at $z = -40$ cm plane, t, has a distribution typical for the output of a device known as the beam buncher. The initial distributions are defined by the histograms in third column. After the interaction with the device the output parameters are distributed according to the histograms in fourth column.

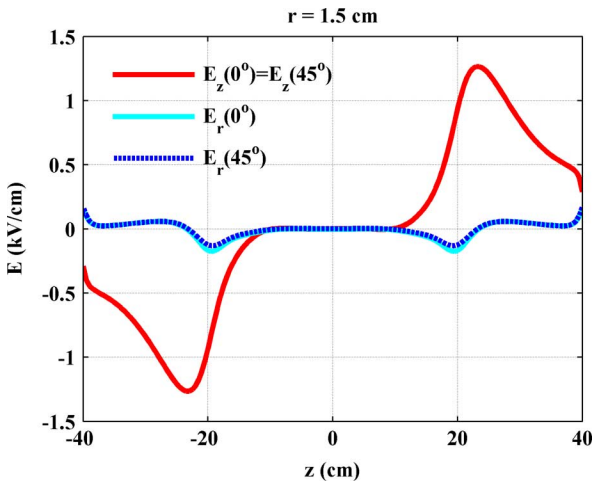

Fig. 11. Peak axial and radial components of electric field. The peak values of axial and radial electric field components, E_z and E_r, are given along two straight segments parallel to the z-axis at the distance $r = 1.5$ cm. The field components $E_z(0^\circ)$ and $E_r(0^\circ)$ correspond to $x = 1.5$ cm and $y = 0$ cm, whereas $E_z(45^\circ)$ and $E_r(45^\circ)$ are given along the line defined with $x_{45^\circ} = 1.5$ cm and $y_{45^\circ} = 0$ cm.

V. Conclusion

By changing its power supply from DC to RF voltage the electrostatic rainbow lens can be transformed into an ion beam accelerator. It is efficient and inexpensive way to broaden available beam energy span of the existing low energy ion beam facilities. Despite of physical as well as functional similarities between the RF rainbow accelerator, electrostatic quadrupole accelerator, and RF quadrupole accelerator, the acceleration achieved with the RF rainbow accelerator is in its nature the most similar to the one of the drift tube Sloan-Lawrence accelerator. Due to the equal polarity of the electrodes the resulting effects are identical along the transverse x- and y-axis and are of the same type but lesser intensity along the x_{45°- and y_{45°-axis. The RFD as well as RFI linac structures apply the same drift tube type acceleration; however, the quadrupole-like field in these devices produce opposite effects along the x- and y-axis and no effect along the x_{45°- and y_{45°-axis. It seems worthwhile to further investigate the dependence of the RF rainbow accelerator operation on the size of its aperture radius, accelerating gap and electrode length, as well as to accordingly perform consequent optimization of its operation.

TABLE III
Optimal Acceleration Conditions for $\max(T_{\max})$ Criterion

V_0 (kV)	f_{RF} (MHz)	ϕ_{low} (°)	ϕ_{up} (°)	T_{max} (keV)
20	2.0	131	150	46.6
40	2.5	138	157	82.6
60	2.9	142	161	118.4
80	3.3	148	169	154.0
100	3.6	151	172	189.6

ACKNOWLEDGMENT

The authors thank N. Nešković for numerous fruitful discussions.

REFERENCES

[1] E. A. Abramyan, "Transformer type accelerators for intense electron beams," *IEEE Trans. Nucl. Sci.*, vol. 18, pp. 447–455, 1971.

[2] D. A. Goldberg *et al.*, "A multi-aperture electrostatic quadrupole (MESQ) accelerator for neutral beam injection," *Bull. Am. Phys. Soc.*, vol. 27, p. 1142, 1982.

[3] O. A. Anderson, L. Soroka, C. H. Kim, R. P. Wells, C. A. Matuk, P. Purgalis, J. W. Kwan, M. C. Vella, W. S. Cooper, and W. B. Kunkel, "Applications of the constant-current variable-voltage dc accelerator," *Nucl. Instrum. Meth. B*, vol. 40–41, pt. 2, pp. 877–880, 1989.

[4] F. M. Bieniosek, C. M. Celata, E. Henestroza, J. W. Kwan, L. Prost, P. A. Seidl, A. Friedman, D. P. Grote, S. M. Lund, and I. Haber, "2-MV electrostatic quadrupole injector for heavy-ion fusion," *Phys. Rev. Special Topics-Accel. Beams*, vol. 8, p. 010101, Jan. 2005.

[5] A. J. Kreiner, J. W. Kwan, A. A. Burlón, H. Di Paolo, E. Henestroza, D. M. Minsky, A. A. Vlada, M. E. Debray, and H. Somacal, "A tandem-electrostatic-quadrupole for accelerator-based BNCT," *Nucl. Instrum. Meth. B*, vol. 261, pp. 751–754, 2007.

[6] N. Nešković, I. Telečki, B. Bojović, and S. Petrović, "A square electrostatic rainbow lens: Catastrophic ion beam focusing," *Nucl. Instrum. Meth. A*, vol. 635, no. 1, pp. 1–7, Apr. 2011.

[7] I. Telečki, S. Petrović, P. Beličev, B. Rađenović, R. Balvanović, B. Bojović, and N. Nešković, "Focusing properties of a square electrostatic rainbow lens," *Nucl. Instrum. Meth. A*, vol. 694, pp. 224–233, 2012.

[8] J. J. Livingood, *Principles of Cyclic Particle Accelerators*. New York: Van Nostrand, 1961, pp. 311–313.

[9] E. Close and W. B. Herrmannsfeldt, "Numerical simulation of the transport of intense beams of heavy ions in an electrostatic quadrupole system," *IEEE Trans. Nucl. Sci.*, vol. 28, no. 3, pp. 2425–2427, 1981.

[10] M. Reiser, "Comparison of Gabor lens, gas focusing, and electrostatic quadrupole focusing for low-energy ion beams," in *Proc. 1989 IEEE Particle Accelerator Conf. Accelerator Science Technol.*, 1989, pp. 1744–1747.

[11] J. W. Staples, RFQ's—An Introduction CA, Sept. 1990, LBL-29472, Lawrence Berkeley Lab., Univ. California Berkeley.

[12] M. Weiss, "Introduction to RF linear accelerators," *CAS School: Fifth General Accelerator Physics Course*, pp. 913–953, 1994, CERN-94-01.

[13] R. Gaur and P. Shrivastava, "Beam dynamics and electromagnetic design studies of 3 MeV RFQ for SNS programme," *J. Electromagn. Anal. Appl.*, vol. 2, pp. 519–528, 2010.

[14] D. A. Swenson, "CW proton linac for the BNCT application," in *Proc. 24th Linear Accelerator Conf.*, Victoria, BC, Canada, Sept. 29–Oct. 3 2008, pp. 220–222.

[15] D. A. Swenson, "Status of the RFD linac structure development," in *Proc. 20th Int. Linac Conf.*, Monterey, CA, Aug. 21–25, 2000, pp. 935–937.

[16] A. Dobrosavljević, P. Beličev, V. Jocić, N. Nešković, I. Trajić, V. Vujović, and L. J. Vukosavljević, "Facility for modification and analysis of materials with ion beams (FAMA)," in *Proc 19th Int. Conf. Cyclotrons Their Applications*, Lanzhou, China, Sep. 6–10, 2010, pp. 108–110.

[17] N. Nešković, Vinča Institute for Nuclear Sciences. Belgrade, Serbia, Jan. 2011, private communication.

[18] J. L. Ristić-Djurović, "Acceleration with four uniformly charged finite wires," unpublished.

[19] Software and User's Manual WIPL-D Microwave. Belgrade, Serbia, 2005, WIPL-D d.o.o.

[20] J. Ristić-Djurović, N. Nešković, and S. Ćirković, "Compound particle tracking algorithm: Application to the foil stripping extraction system design," in *Proc. 6th Int. Computational Accelerator Physics Conf.*, Darmstadt, Germany, Sep. 11–14, 2000 [Online]. Available: http://www.icap2000.de/frames/index.htm, Available:

[21] P. Belićev, B. Bojović, M. Rajčević, and N. Y. Kazarinov, "Injection transport line of the VINCY Cyclotron," in *Proc. 17th Int. Conf. Cyclotrons Their Appl.*, Tokyo, Japan, Oct. 18–22, 2004, pp. 489–491.

[22] J. L. Ristić-Djurović and A. Ž. Ilić, "Role and significance of uniform distribution in a study of ensemble of particles," *IEEE Trans. Nucl. Sci.*, DOI: 10.1109/TNS.2012.2225153, to be published.

[23] J. L. Ristić-Djurović, A. Ilić, and S. Ćirković, Finite Wire Accelerator INN Vinča, Dec. 2011, Internal report.

[24] N. Nešković, J. L. Ristić-Djurović, S. Petrović, P. Belićev, B. Rađenović, S. Ćirković, A. Ž. Ilić, and A. Dobrosavljević, in preparation.

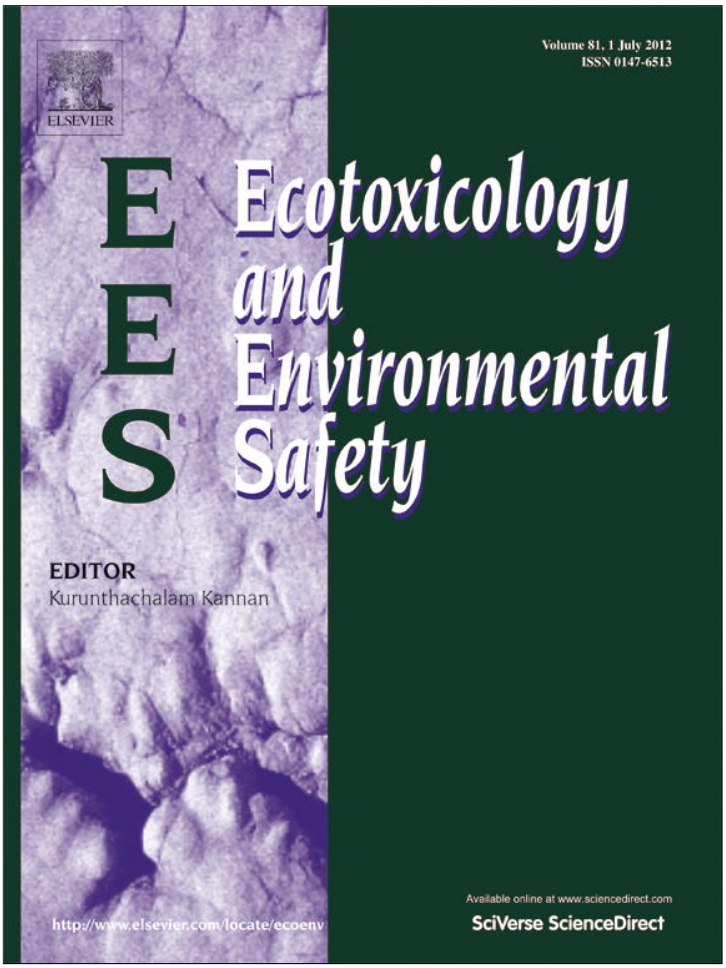

Ecotoxicology and Environmental Safety 81 (2012) 98–105

Contents lists available at SciVerse ScienceDirect

Ecotoxicology and Environmental Safety

journal homepage: www.elsevier.com/locate/ecoenv

Hematological parameters' changes in mice subchronically exposed to static magnetic fields of different orientations

Drago M. Djordjevich [a,1,2], Silvio R. De Luka [a,1,2], Ivan D. Milovanovich [a,2], Saša Janković [b,3], Srdjan Stefanović [b,3], Slavica Vesković-Moračanin [b,3], Saša Ćirković [c,4], Andjelija Ž. Ilić [c,4], Jasna L. Ristić-Djurović [c,4], Alexander M. Trbovich [a,2,*]

[a] Department of Pathological Physiology, School of Medicine, University of Belgrade, Dr Subotića 9, 11000 Belgrade, Serbia
[b] Institute of Meat Hygiene and Technology, Kaćanskog 13, 11000 Belgrade, Serbia
[c] Laboratory of Physics (010), Vinča Institute of Nuclear Sciences, University of Belgrade, P.O. Box 522, 11001 Belgrade, Serbia

ARTICLE INFO

Article history:
Received 28 February 2012
Received in revised form
27 April 2012
Accepted 28 April 2012
Available online 23 May 2012

Keywords:
Static magnetic field
Hematology
Iron

ABSTRACT

Static magnetic fields (SMFs) are time independent fields whose intensity can be spatially dependent. This study investigates influence of subchronic continuous exposure to upward and downward directed SMF on hematological parameters and spleen cellularity in mice. The experiment is performed on the Northern hemisphere; consequently, the vertical component of geomagnetic field is directed downward. Male, Swiss-Webster, 6 weeks old mice were exposed to the vertically declining SMF. Mice were divided in three groups and continuously exposed or not exposed for 28 days to the SMF characterized by the averaged field of 16 mT and averaged field gradient of 10 mT/cm. Differently oriented SMF did not alter hemoglobin and hematocrit content among the groups. However, the groups exposed to the upward and downward fields had statistically significant higher levels of serum transferrin compared to the control. Moreover, spleen cellularity in animals in the downward group was significantly higher compared to the upward and control group. In addition, spleen lymphocytes in both of the exposed groups were significantly higher than in the control group. In contrast, spleen granulocytes in the exposed groups were significantly lower than in the control group. Significant decrease was also observed in brain and liver iron content with concomitant increase of iron in serum and spleen in exposed animals. Subchronic continuous exposure to 16 mT SMF caused lymphocyte and granulocyte redistribution between spleen and blood. This distribution is typical for stress induced hematological changes. These results suggest that observed changes were not due to an unspecific stress response, but that they were rather caused by specific adaptation to subchronic SMF exposure.

1. Introduction

Beneficial and adverse effects of magnetic fields on human body have been assessed for long time. The frequency of exposure to magnetic fields has increased with rapid advances in science and technology, such as magnetic resonance imaging (MRI) diagnosis, nuclear magnetic resonance (NMR) spectroscopy and passenger transport systems that are based on magnetic levitation (World Health Organization, 2006a). Therefore, it has become necessary to systematically elucidate the influence of magnetic fields on the body.

Static magnetic fields (SMFs) are time independent fields whose intensity could be spatially dependent. In our experiment, the magnetic field does not change in time; therefore it is static. However, it has different values in space so it is spatially dependent. There are four SMF parameters relevant for the interaction with a biological system: target tissue(s), magnet characteristics, magnet support device, and dosing regimen (Colbert et al., 2009). SMFs are difficult to shield and can freely penetrate biological tissues (Hashish et al., 2008). However, not only the field intensity, but also the gradient of the field has important role in biological effects of SMF (McLean et al., 1995; Markov, 2007a). SMF can interact directly with moving charges (ions, proteins, etc.) and magnetic materials found in tissues through several physical mechanisms (World Health Organization, 2006a).

* Corresponding author. Fax: +381 11 2685 340.
E-mail addresses: aleksandar.trbovic@mfub.bg.ac.rs, alexander.m.trbovich@gmail.com (A.M. Trbovich).
URLS: http://www.mfub.bg.ac.rs (D.M. Djordjevich), http://www.mfub.bg.ac.rs (S.R. De Luka), http://www.mfub.bg.ac.rs (I.D. Milovanovich), http://www.inmesbgd.com (S. Janković), http://www.inmesbgd.com (S. Stefanović), http://www.inmesbgd.com (S. Vesković-Moračanin), http://www.vinca.rs (S. Ćirković), http://www.vinca.rs (A.Ž. Ilić), http://www.vinca.rs (J.L. Ristić-Djurović), http://www.mfub.bg.ac.rs (A.M. Trbovich).
[1] Equally contributed and, thus, share first authorship.
[2] Fax: +381 11 2685 340.
[3] Fax: +381 11 2651 825.
[4] Fax: +381 11 2447 963.

0147-6513/$ - see front matter © 2012 Elsevier Inc. All rights reserved.
http://dx.doi.org/10.1016/j.ecoenv.2012.04.025

Small artificial sources of SMFs are common, ranging from specialized (audio speakers components, battery-operated motors, microwave ovens) to trivial (refrigerator magnets) (Stuchly, 1986; Kowalczuk et al., 1991; World Health Organization 2006a; Hashish et al., 2008). These small magnets can produce fields of up to few mT within a centimeter or so of their magnetic poles that further decrease with square distance reaching levels of few μT (World Health Organization, 2006b; Hashish et al., 2008). A number of studies of in vitro biological response to applied magnetic field suggest the existence of biological "windows" (Markov et al., 1975; Ukolova et al., 1975; Bawin and Adey, 1976; Azanza and del Moral, 1994; Engstrom et al., 2002; Markov, 2007a, 2007b, 2011; Dini and Panzarini, 2010). These windows represent combinations of amplitude, frequency of exposure and exposure duration within which the optimal response is observed, and once outside this range, the response is found to be significantly smaller. This demonstrates the principle that more does not necessarily mean better (Markov 2007a). For SMFs, several windows have been reported, such as 0.5–2 mT, 15–20 mT and 45–50 mT (Markov et al., 1975; Zukov and Lazarovich, 1989; Markov, 2005, 2007a, 2011).

A large numbers of SMF studies have been performed on cells and cellular components, genetic material, reproduction and development, physiological and behavioral responses (World Health Organization, 2006a; Health Protection Agency, 2008). When taken as a whole, they do not suggest any acute detrimental effects on major development, behavioral or physiological parameters for short-term exposures (Schenck, 2000; Löscher, 2003; Hashish et al., 2008). However, some detrimental effects have been noticed in in vitro experiments with hippocampal slides. Namely, electromagnetic field of 2–3 mT caused small transient depression of excitatory postsynaptic potentials followed by a long-lasting amplification of the potentials, while electromagnetic field of 8–10 mT depressed excitatory postsynaptic potential (Trabulsi et al., 1996). This effect was attributed to the activity of intracellular calcium channels that were affected by SMF leading to fluctuations in the intracellular Ca^{2+} concentration (Wieraszko, 2000). Taken together, long-term experiments still need to be conducted to assess effects of subchronic and chronic exposure to SMF. There are several scientific articles concerning the biological effects of the 15–20 mT SMF in vitro (Markov, 2005; World Health Organization, 2006a; Tavasoli et al., 2009) or in vivo (World Health Organization, 2006a; Health Protection Agency, 2008). However, biological effects of 15 mT SMF on hematological samples were only investigated in in vitro experiments (Tavasoli et al., 2009; Elblbesy, 2010). Thus far, SMF studies showed that both extremely low frequency magnetic field and SMF alter hematological parameters in rats and mice (Schenck, 2000; Hashish et al., 2008). Spleen total lymphocyte count, as well as spleen T and B lymphocyte count are also affected by SMF in mice (Hashish et al., 2008).

On the basis of these results and the fact that the upward and downward directed magnetic fields have different effects on biological systems (Krylov and Tarakanova, 1960; Ružič et al., 1993; Yano et al., 2001; Eccles, 2005; World Health Organization, 2006a; Health Protection Agency, 2008), we decided to investigate influence of subchronic continuous exposure to 16 mT SMF oriented upwards as well as downwards on hematological parameters and spleen cellularity in mice. However, the magnetic field we used decreases vertically and ranges from 29.7 mT to 5.8 mT throughout the mice body. Consequently, different parts of animal bodies were exposed to different field intensity. The averaged value of the magnetic field throughout the experimental volume potentially occupied by the mice is 16 mT. To our knowledge, nobody else had previously compared separate biological effects of the upward and downward oriented SMF on hematological characteristics in experimental animals.

2. Materials and methods

2.1. Animals

Male Swiss-Webster mice, 6 weeks old, obtained from the Military Medical Academy Animal Research Facility (Belgrade, Serbia) were used. Mice were housed at four or five animals per cage and offered regular mouse feed and drinking water ad libitum.

All experimental protocols involving animals were reviewed and approved by the University of Belgrade School of Medicine Experimental Animals Ethics Committee. Furthermore, all experiments were conducted concordant to procedures described in the National Institutes of Health Guide for Care and Use of Laboratory Animals (Washington, DC, USA).

2.2. Magnetic field

As a source of spatially dependent SMF MADU stripes (The Mihailo Pupin Institute, Belgrade, Serbia; patent number YU 48907/02, Republic of Serbia Intellectual Property Office, Belgrade, Serbia; patent number WO 99/60581, World Intellectual Property Organization, Brussels, Belgium, EU) were used. The MADU stripes are designed to provide easy-to-carry magnetic field, whose aim is to penetrate into the body, rather than to affect just the body surface, when deployed to humans or animals. The type L MADU stripe (Fig. 1Panel A) as well as the experimental setup (Fig. 1Panel B) is depicted in Fig. 1. Due to the five rows of embedded permanent magnetic rods the width of the type L MADU stripe is comparable to its length; therefore, it is rather a sheet than a stripe. If the magnetic axes of the embedded rods alternate in direction throughout the sheet, the resulting magnetic field is predominantly horizontal, parallel to the sheet's surface and the volume of its influence is relatively thin layer above the sheet's surface. If the magnetic axes of the rods are all oriented in the same direction the resulting magnetic field is predominantly vertical, orthogonal to the sheet's surface and it spreads further away from the sheet. It has been shown that if the magnetic axes of the rods have the same direction, either upwards or downwards, the depth of the resulting magnetic field penetration through a tissue is in general 4–8 times larger than is the case if the upward and downward directions of the magnetic axes alternate throughout the sheet (Markov, 2007a). Consequently, the former can be used to study its influence on the body, whereas the latter is more likely to affect just the skin of an animal or a human. Since the experiment is performed on the Northern hemisphere, the vertical component of geomagnetic field is directed downwards and SMF of MADU stripes has the same or opposite direction to this field. The downward direction of vertical component of geomagnetic field is consistent with the geomagnetic reversal. Namely, the south pole of the Earth's magnetic field attracts the north pole of the compass magnet; therefore, the south geomagnetic pole is located in the northern Arctic region in the vicinity of the north geographic pole (Campbell, 2001). The field intensity of MADU stripes is measured using Digital Teslameter DTM-151 (Group 3 Technology, Auckland, New Zealand), whose resolution is 0.005 mT for the range of up to 0.3 T. The precision of the reading for the same range is 0.01%. The 3D simulation of the magnetic field of the MADU sheet is performed using Mermaid software (SIM, Novosibirsk, Russia). The obtained computer model gives the relative values of the magnetic field, i.e., these values must be multiplied by a multiplicative constant in order for the model to match the reality. The multiplicative constant is determined by the magnetic field calibration procedure, which uses magnetic field values measured at several chosen points. In our case, the field is measured in the four horizontal planes instead of just at several points. Consequently, not only that the multiplicative constant is determined, but the validity of the computer model is also confirmed. The values of the obtained magnetic field are shown in Fig. 2 for the four planes parallel at four different distances to the XY-plane, $Z=0.5$ cm, 1 cm, 2 cm, and 4 cm. The XY-plane at $Z=0$ contains tops of the embedded magnetic rods. Origin 7.0 software (OriginLab, Northampton, MA, USA) was used for graphing the 3D calculations generated with Mermaid software. As explained earlier, the magnetic field calculated with the 3D Mermaid model is calibrated using the measured data.

Although static, the magnetic field we use in the experiment is spatially dependent. The farther away from the surface of the magnet, the smaller is the magnetic field. Spatial dependence of variables is described by the variable's gradient, i.e. its change per distance. The gradient is obtained by subtracting the values of the variables at two adjacent points and then dividing the difference by the distance between the two points. In our case not only the magnetic field but the gradient of the magnetic field has different values at different points of the experimental volume, i.e. the cage and mice body. To fully describe the field we used, we give the values of the field at different points in space (Fig. 2). In order to summarize the information given in the figure we provide two numbers. The averaged magnetic field is obtained by summing the values of the magnetic field at different points in the experimental volume and dividing the sum by the number of points. The averaging of the gradient of the magnetic field is performed in the same manner, i.e., all the values are summed and then divided by the number of points. The maximal value of magnetic field is 60 mT and it occurs immediately above the magnets, i.e. at $Z=0$ mm. In order to classify the experiment according to the common magnetic field window classification

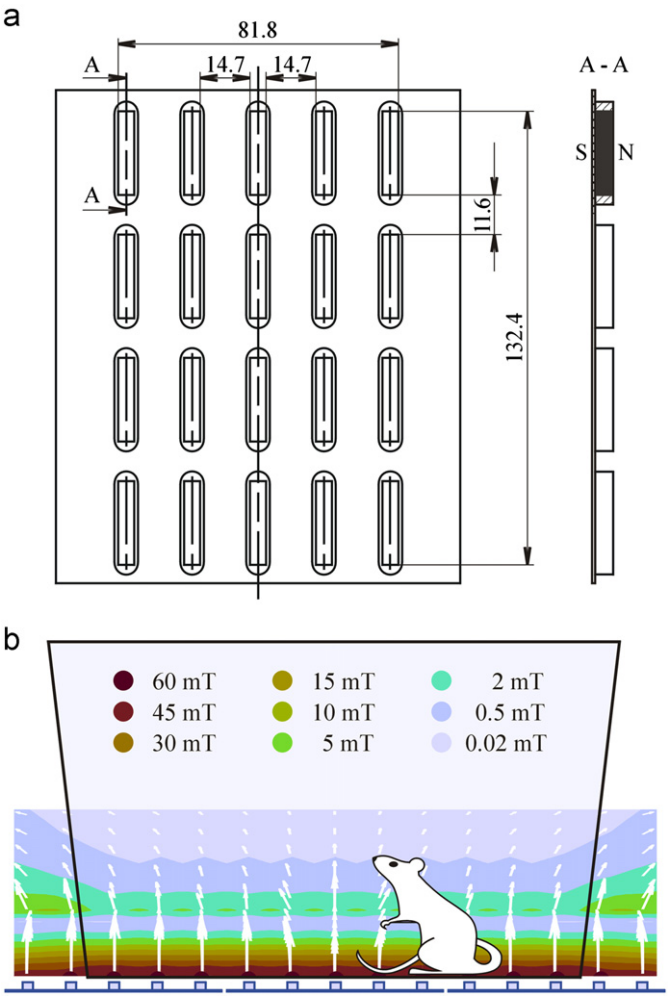

Fig. 1. Graphic presentation of MADU stripe (Panel A) and experimental setup (Panel B). Panel A The type L MADU stripe contains twenty ceramic ferromagnetic rods made of barium ferrite ($BaFe_{12}O_{19}$) embedded in a plastic sheet. The size of each rod is 4.8 mm × 24.4 mm × 4.8 mm. Magnetic rods are equidistantly distributed along *X* as well as along *Y*-axes, the distance between them being 14.7 mm and 11.6 mm, respectively. The magnetic axes of the rods are vertical and equally directed; the example shown corresponds to the upward directed magnetic field. Panel B Experimental setup. The vertical cross-section through the middle of the experimental setup is shown. The plastic cage with 4 or 5 animals is placed over MADU stripes. The magnetic field of MADU stripes is distributed throughout the experimental volume. The intensity of the magnetic field is indicated by different shades (colors). Also shown are magnetic lines of force. (For interpretation of the references to color in this figure legend, the reader is referred to the web version of this article.)

scheme (Markov et al., 1975; Zukov and Lazarovich, 1989; Markov, 2005, 2007a, 2011) the averaged values of the applied magnetic field and magnetic field gradient are used. The MADU stripes were placed directly beneath the two animal Plexiglas cages that were separated out by 10 cm. The animals were freely moving inside the cages; consequently, it seems reasonable to perform magnetic field averaging over the volume potentially occupied by the mice bodies. Since the height of a mice was 2 cm, we assumed that they were predominantly exposed to the part of SMF limited by the horizontal planes at $Z=0.5$ cm and $Z=2$ cm. The averaged magnetic field and magnetic field gradient in the defined volume are calculated to be 15.63 mT and 9.8 mT/cm, respectively. Therefore, it can be concluded that the mice were exposed to the part of spatially dependant SMF of the MADU stripes characterized by the average magnetic field of 16 mT and average magnetic field gradient of 10 mT/cm.

2.3. Experimental design

Mice were randomly divided into three groups (9 per group). All three groups were kept under same conditions. The first experimental group was exposed to the upward oriented SMF (Up group). The second experimental group was exposed to the downward oriented SMF (Down group). The permanent magnets embedded in the MADU stripes cannot be removed or turned off. Therefore, instead of using sham exposed animals we use a control group exposed to the ambient magnetic field. The ambient field is measured and the obtained value is 40 μT, which is only 0.25% of the field to which Up and Down groups are exposed. Note that the magnetic field above MADU stripes is measured; therefore, it is the sum of the field produced by MADU magnets and the ambient magnetic field.

Exposure to SMF was conducted using three MADU stripes of different orientation that were placed under the plastic animal cage continuously for 28 days. Food consumption was measured daily and body mass weekly. Following the exposure period of 28 days, all mice were sacrificed and blood and spleen were collected for further analyses that were blindly performed.

2.4. Blood and spleen parameters

Blood parameters [erythrocytes, lymphocytes, monocytes, neutrophils, basophils, eosinophils, hemoglobin, hematocrit, MCV (mean corpuscular volume), MCH (mean corpuscular hemoglobin), MCHC (mean corpuscular hemoglobin concentration)] were determined using Hematological counter ABX Pentra 80X (Montpellier, France) according to manufacturer's recommendations. The total number of granulocytes in blood sample was calculated by summing neutrophils with basophils, and eosinophils.

Serum transferrin was analyzed using BioSystems photometer type BTS-330 (Barcelona, Spain) according to manufacturer's recommendations. Transferrin saturation was calculated from iron (Fe) and total iron binding capacity (TIBC) as serum Fe/TIBC × 100.

Spleen was excised, connective and fat tissue were removed, and then spleen was weighted. A weighted part of the tissue was minced in 1 ml of saline and dispersed through 0.1 mm cell sieve (KDL, Anping, China) until only the remaining connective (white) tissue was visible. This cell suspension was additionally resuspended by pulling and pushing it 10 times through 0.45 μm needle placed on top of 5 ml syringe (Nipro, Zaventem, Belgium). Total cellular count was determined using counting chamber (Fein-Optik, Jena, Germany) and expressed as a number of nucleated cells per microliter of soluble homogenized tissue. A separate part of spleen tissue was macerated, dispersed through 0.1 mm cell sieve and smeared for hematological analysis. Spleen smears stained with May Grünwald–Giemsa (Carlo Erba, Rodano, Italy) were used to count erythrocytes, lymphocytes and granulocytes in ten visual fields by scoring 100 cells per one visual field of counting chamber and were expressed as a percentage of total number of counted cells (Vranic et al., 2000).

Iron was determined in serum, brain, liver and spleen tissue. Total serum iron was determined using BioSystems photometer type BTS-330 (Barcelona, Spain) according to manufacturer's recommendations. Transferrin-bound ferric ions in the serum samples were released by guadinium and reduced to ferrous by means of hydroxylamine. Ferrous ions reacted with ferrozine, forming a colored complex that was measured by spectrophotometer.

Brain, liver, and spleen tissue samples were prepared by microwave digestion (ETHOS TC, Milestone S.r.l., Sorisole, Italy) according to manufacturer's recommendations. Tissue of interest (0.5 g) was treated with 8 ml of nitric acid (HNO_3) and 2 ml of hydrogen peroxide (30% H_2O_2); temperature program was as follows: 5 min from room temperature to 180 °C then 10 min hold at 180 °C. After cooling, samples were transferred with deionisated water in 50 ml volumetric flask. Analyses were carried out on atomic absorption spectrometer "SpectrAA 220" (Varian, Palo Alto, California, USA) according to Varian Atomic Absorption Spectrometers (AAS) Analytical Methods. Analytical quality control was achieved by analyzing certified reference material BCR-186 (Community Bureau of Reference—BCR, Brussels, Belgium), which is lyophilized pig kidney used for determining trace elements (Institute for Reference Materials and Measurements, Geel, Belgium). Replicate analyses were undertaken within the range of certified values. Iron values were expressed as μg of Fe per mg of dried analyzed tissue.

2.5. Statistical analysis

Statistical analysis was performed using software SPSS for Windows, version 10.0 (SPSS, Chicago, IL, USA). Difference between groups was evaluated by one-way ANOVA, followed by Fischer's LSD test. The level of significance was set at $p < 0.05$.

3. Results

3.1. Blood parameters

Blood parameters in control mice and mice exposed to differently oriented SMF are shown in Table 1. There was a trend in blood lymphocytes reduction and blood granulocytes increase in mice exposed to SMF. However, the exposure of mice to the differently oriented SMF did not alter erythrocytes and leukocytes count (lymphocytes, monocytes, neutrophils, basophils, granulocytes;

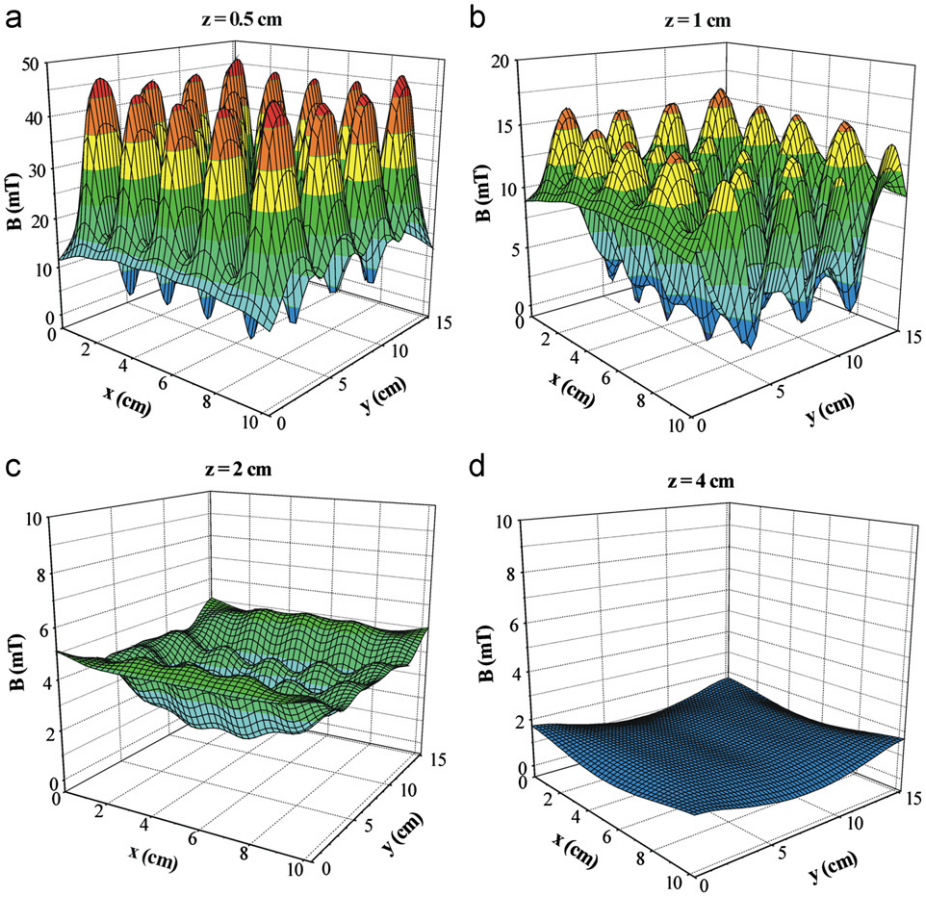

Fig. 2. Magnetic field of type L MADU stripe. Panels A, B, C, and D represent the magnetic field in the horizontal plane at $Z=0.5$ cm, 1 cm, 2 cm, and 4 cm, respectively. Panel A—The magnetic field in the horizontal plane at $Z=0.5$ cm; Panel B—The magnetic field in the horizontal plane at $Z=1$ cm; Panel C—The magnetic field in the horizontal plane at $Z=2$ cm; Panel D—The magnetic field in the horizontal plane at $Z=4$ cm.

Table 1
Blood parameters in mice exposed (Up group, Down group) or not exposed (Control group) to SMF of different orientation for 28 days.

Blood parameter	Up group	Down group	Control group
Erythrocytes ($\times 10^{12}$/L)	7.63 ± 0.39	6.93 ± 0.46	6.99 ± 0.55
Lymphocytes ($\times 10^{9}$/L)	2.03 ± 0.37	1.63 ± 0.20	4.19 ± 2.65
Monocytes ($\times 10^{9}$/L)	0.11 ± 0.04	0.12 ± 0.05	0.20 ± 0.14
Neutrophils ($\times 10^{9}$/L)	0.31 ± 0.06	0.29 ± 0.07	0.21 ± 0.04
Basophils ($\times 10^{9}$/L)	0.03 ± 0.01	0.04 ± 0.02	0.02 ± 0.01
Granulocytes ($\times 10^{9}$/L)	0.35 ± 0.07	0.33 ± 0.076	0.22 ± 0.056
Hemoglobin (g/L)	114.88 ± 4.89	101.38 ± 6.92	106.10 ± 7.54
Hematocrit (L/L)	0.38 ± 0.02	0.34 ± 0.02	0.35 ± 0.03
MCV (fL)	50.25 ± 1.28	48.67 ± 0.78	50.20 ± 1.21
MCH (pg)	15.13 ± 0.35	15.00 ± 0.29	15.40 ± 0.27
MCHC (g/L)	302.00 ± 2.96	306.33 ± 2.03	303.90 ± 2.31
Transferrin (mg/dL)	47.96 ± 2.78**,***	37.99 ± 2.58*	26.10 ± 3.83

Data are expressed as mean $\pm$ SEM.

* $p < 0.05$ compared to control group.
** $p < 0.01$ compared to control group.
*** $p < 0.05$ compared to the down group.

$p > 0.05$). In addition, differently oriented SMF did not alter hemoglobin and hematocrit content, nor MCV, MCH or MCHC values among the groups ($p > 0.05$).

The up and down groups had statistically significant higher levels of serum transferrin compared to the control group (47.96 ± 2.78 and 37.99 ± 2.58 vs. 26.1 ± 3.83; $p < 0.01$ and $p < 0.05$, respectively). Additionally, animals exposed to the upward oriented SMF had higher levels of serum transferrin than those exposed to the downward field (47.96 ± 2.78 vs. 37.99 ± 2.58; $p < 0.05$). Taken together, both SMF exposed groups demonstrated statistically significant decrease in transferrin saturation, when compared to control animals, with more pronounced reduction in the down group (Fig. 3).

3.2. Spleen cellularity

Spleen cellular parameters in mice exposed to SMF of different orientation are shown in Fig. 4. Spleen cellularity in animals

exposed to the downward oriented SMF was significantly higher compared to those exposed to the upward oriented field (0.80 ± 0.02 vs. 0.60 ± 0.04; $p < 0.01$), and to control (0.80 ± 0.02 vs. 0.34 ± 0.02; $p < 0.01$). In addition, spleen cellularity in animals exposed to the upward oriented SMF (Fig. 4A) was significantly higher when compared to the control group (0.60 ± 0.04 vs. 0.34 ± 0.02; $p < 0.01$). However, there was no difference in spleen erythrocyte count (Fig. 4B) among the groups (20.49 ± 3.64 vs. 17.43 ± 1.76 vs. 20.12 ± 1.75; $p > 0.05$).

Spleen lymphocytes in the up group (Fig. 4C) were significantly higher than in the control group (75.90 ± 3.46 vs. 68.20 ± 1.38; $p < 0.05$) and spleen lymphocytes in the down group were also significantly higher when compared to control group (79.04 ± 1.71 vs. 68.20 ± 1.38; $p < 0.01$). In contrast, spleen granulocytes in the up (3.58 ± 0.72) and the down (3.52 ± 0.29) groups (Fig. 4D) were significantly lower than in the control group (11.66 ± 0.83; $p < 0.01$).

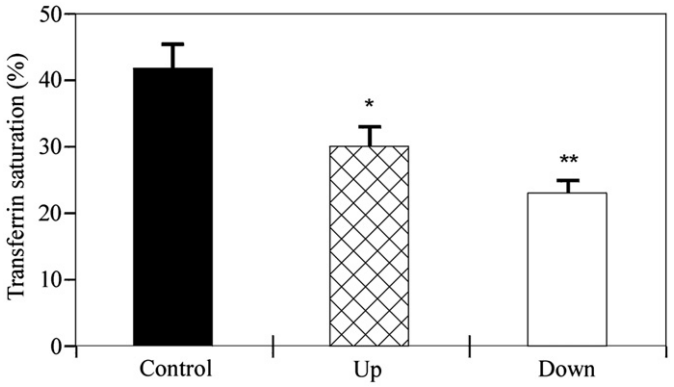

Fig. 3. Plasma transferrin saturation values in mice exposed (up, down) or not exposed (control) to SMF of different orientation for 28 days. Data are expressed as mean ± SEM; $^{*}p < 0.05$ compared to control group; $^{**}p < 0.01$ compared to control group.

3.3. Serum and tissue iron content

Tissue and serum iron values in mice exposed to SMF of different orientation are shown in Fig. 5.

Brain showed significant decrease in iron content in the down group (15.75 ± 0.43) when compared to the up (18.92 ± 0.32) and the control group (19.92 ± 0.80; $p < 0.01$) (Fig. 5A).

Liver showed significant decrease in iron content in the up (261.73 ± 15.61) as well as in the down group (252.03 ± 10.96) when compared to the control group (310.30 ± 15.84; $p < 0.05$ and $p < 0.01$, respectively) (Fig. 5B).

Spleen showed significant increase in iron content in the up group (Fig. 5C) when compared to the control group (513.06 ± 35.79 vs. 394.85 ± 18.35; $p < 0.05$).

Serum showed significant increase in iron content in the up group (4.30 ± 1.40) compared to the down (2.22 ± 0.45) and the control group (2.83 ± 1.22; $p < 0.01$ and $p < 0.05$, respectively) (Fig. 5D).

3.4. Animal food intake and body mass

There was no difference in food intake between exposed and control animals. In addition, there was no difference in body mass between exposed and unexposed animals. (Data not shown)

4. Discussion

The applied static magnetic field was not uniform, but was vertically declining. In addition to vertical decrease the field variation in horizontal planes is intense and has local maxima and minima. The spatially averaged magnetic field of 16 mT is used as the closest approximation for the experiment classification by the magnetic field windows criteria.

Our investigation showed an increase in total spleen cellularity in mice exposed to 16 mT SMF of either orientation. In addition, total spleen cellularity was higher in the downward oriented SMF than in the upward oriented SMF or in the case of unexposed animals. The spleen lymphocyte count showed a statistically significant increase in SMF exposed animals, with a pronounced

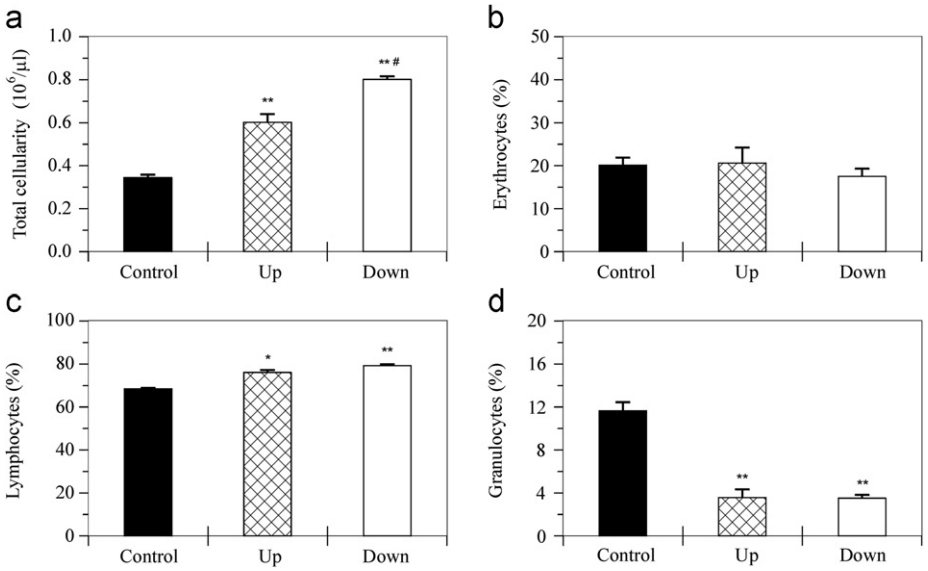

Fig. 4. Spleen cellular parameters in mice exposed to SMF of different orientation. Panel A—Total spleen cellularity in mice exposed (up, down) or not exposed (control) to SMF of different orientation for 28 days; Panel B—Spleen erythrocytes in mice exposed (up, down) or not exposed (control) to SMF of different orientation for 28 days; Panel C—Spleen lymphocytes in mice exposed (up, down) or not exposed (control) to SMF of different orientation for 28 days; Panel D—Spleen granulocytes in mice exposed (up, down) or not exposed (control) to SMF of different orientation for 28 days; Data are expressed as mean ± SEM; $^{*}p < 0.05$ compared to control group; $^{**}p < 0.01$ compared to control group; $^{\#}p < 0.01$ compared to the up group.

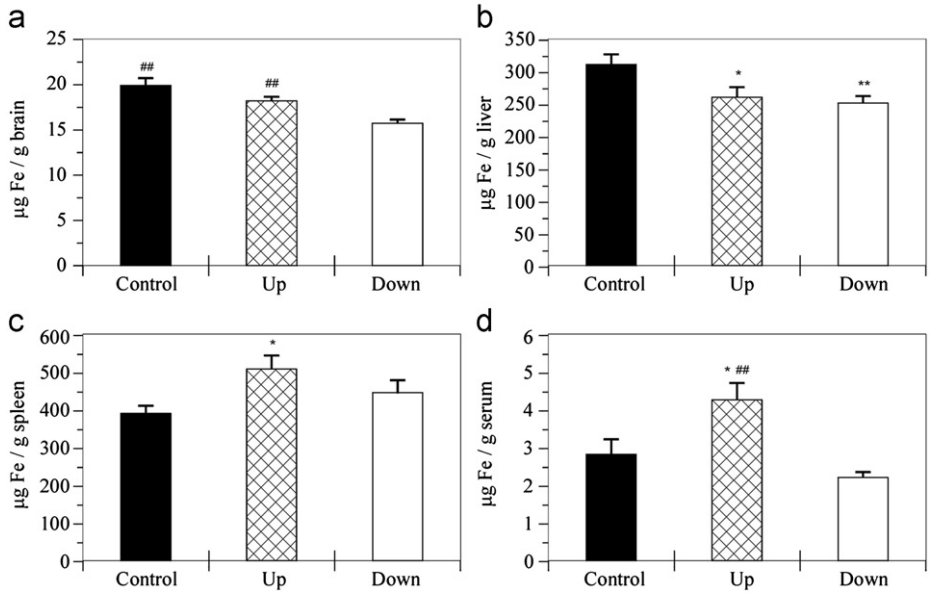

Fig. 5. Tissue and serum iron values in mice exposed to SMF of different orientation. Panel A—Brain iron values in mice exposed (up, down) or not exposed (control) to SMF of different orientation for 28 days; Panel B—Liver iron values in mice exposed (up, down) or not exposed (control) to SMF of different orientation for 28 days; Panel C—Spleen iron values in mice exposed (up, down) or not exposed (control) to SMF of different orientation for 28 days; Panel D—Serum iron values in mice exposed (up, down) or not exposed (control) to SMF of different orientation for 28 days; Data are expressed as mean ± SEM; $^{*}p < 0.05$ compared to control group; $^{**}p < 0.01$ compared to control group; $^{\#\#}p < 0.01$ compared to the down group.

increase in the down group. We assumed that the increase in total spleen cellularity was due to the rise of lymphocyte count in exposed animals. This is additionally supported by the fact that majority of leukocytes in mice are lymphocytes (Green, 1966) and even a small increase in percent of lymphocytes could cause a large increase in total spleen cellularity. There was a simultaneous tendency of blood lymphocyte count decrease in SMF exposed animals. This result is in contrast to findings of decreased splenic lymphocytes in mice exposed to 2.9 μT SMF (Hashish et al., 2008). The exposure time in that study (30 days) was similar to exposure period in our experiment, but the intensity of SMF in our experiment was around 5000 time higher, namely 16 mT. The difference in SMF intensities, strain of experimental animals (Swiss-Webster in our experiment and Swiss BALB/c in theirs) and type of used magnets (our magnetic stripes versus their classical magnetic disks) could account for the difference in splenic lymphocyte count. However, blood lymphocyte count showed similar patterns in both studies. We assumed that due to subchronic exposure and concurrent adaptation, the spleen, which is a main lymphopoietic organ in mice (Green, 1966), increased lymphocytes production and their preservation in the organ without statistically significantly decreasing blood lymphocytes.

Previous research showed that SMF influences biological system in a way that causes proinflammatory changes, as well as an increase in production of reactive oxygen species (Sahebjamei et al., 2007; Hashish et al., 2008; Zhao et al., 2011). We found a statistically significant decrease in spleen granulocyte count and a tendency of blood granulocyte count to increase in SMF exposed animals. These findings are comparable to those from other studies, which demonstrate granulocyte count increase in blood of SMF exposed mice (Hashish et al., 2008). Explanation behind the observed changes in our study could be that phagocytosis and death of granulocytes, which are associated with production of free radicals, are increased in splenic tissue of animals exposed to either SMF orientation.

Red blood cells count did not change in blood or in spleen between exposed and unexposed group. This is in accordance with findings that mice exposed to SMF for 30 days and rats exposed to extreme low frequency magnetic field for 50 and 100 days did not show alteration in red blood cell count (Hashish et al., 2008; Cakir et al., 2009). We concluded that various intensities of SMF and different exposure time do not influence red blood cells count in blood and spleen of experimental animals. This is probably due to fast recovery of the red blood cells after their exposure to the SMF.

Iron is an absolute requirement for most forms of life because of its unusual flexibility to serve both as an electron donor and an acceptor. It can be potentially toxic since free iron in the cell can catalyze conversion of hydrogen peroxide to free radicals. To prevent this scenario, all life forms that use iron bind that iron to proteins. This allows cells to benefit from iron while limiting its ability to harm. Majority of iron is located in hemoglobin molecules of red blood cells (RBCs), and the rest is stored in a form of ferritin in liver, spleen, and bone marrow. The liver's stores of ferritin are the primary physiologic source of reserve iron in the body. Macrophages also store iron as part of process of breaking down and processing hemoglobin. Once RBCs are degraded, macrophages recycle iron by putting it onto transferrin molecules that carry iron through the blood. In addition, macrophages require iron for their own antibacterial activity (Alford et al., 1991).

Main iron storage organs in mice are liver, heart and brain (Hahn et al., 2009). In our experiment, liver demonstrated a marked decrease of iron content in the up and in the down groups when compared to control animals. Besides liver, we have also determined the amount of iron in spleen and brain. While dynamics of iron in liver of animals in the exposed groups was the same, there was a difference in dynamics of iron in brain and spleen from the animals exposed to the upward or the downward directed field when compared to control. Namely, in the animals exposed to the upward magnetic field, the amount of iron did not change in the brain; it dropped in the liver and increased in spleen. On the other hand, in the animals exposed to the downward magnetic field, the amount of iron decreased both in the brain and liver while remaining unchanged in the spleen. Results from the animals exposed to the upward field may suggest

relocation of iron from storage in liver to spleen for possible lymphopoiesis. However, the effects of downward magnetic field on iron are harder to explain. Iron in brain is tightly regulated and its elimination is undesired. While too much iron can cause oxidative stress, too little iron can result in energy insufficiency. It was unclear where brain and liver iron relocates in animals exposed to the downward magnetic field. We considered macrophages to be a possible destination of this process. To test this hypothesis, we measured serum iron and transferrin in all animal groups.

Transferrins are iron-binding blood plasma proteins that control the level of free iron in biological fluids (Crichton and Charloteaux-Wauters, 1987). The affinity of transferrin for iron is very high, but progressively decreases with pH going down below neutrality. Liver is a key source of the transferrin production but other places such as brain also produce transferrin. The main role of transferrin is in transport of iron from absorption center in duodenum or from RBCs recycling centers in reticuloendothelial macrophages to tissues. Transferrin is not only crucial for erythropoiesis and cell division (Macedo and de Sousa, 2008), but also plays a role in innate immunity. Transferrin is responsible for iron withholding that impedes bacterial survival. Consequently, the level of transferrin decreases in inflammation (Ritchie et al., 1999). However, in mice the level of transferrin increases in inflammation during acute phase response (Barnum-Huckins et al., 1997).

In our experiments, we have noticed different serum iron dynamics in animals exposed to the magnetic field while there was no difference in pattern of transferrin production or transferrin saturation between exposed groups. In the up group serum iron and production of transferrin increased, while transferrin saturation decreased when compared to control. In the down group serum iron did not change, transferrin saturation decreased and transferrin production increased compared to control. In both groups decreases in transferrin saturation could be explained by possible decrease of pH or by increases in transferrin production. The transferrin production in the case of the up group should have been larger than the surplus of iron. Serum iron in the up group could have increased due to transport from liver to spleen. Serum iron in the down group did not change. There is a possibility that iron in the down group ended up in the macrophages and this could be the reason that no changes in serum or spleen iron were detected there.

It has been recently shown that short-term exposure to SMF (128 mT/1 h/5 days) produced statistically significant decrease in serum iron (Elferchichi et al., 2007). The same experimental design demonstrated that SMF (128 mT/1 h/5 days) induced sympathetic hyperactivity in rats (Abdelmelek et al., 2006). This result has been explained through the high turnover of norepinephrine in the noradrenergic system that could negatively influence the peristaltic activity implicated in the assimilation of divalent elements such as iron (Abdelmelek et al., 2006). This could be true for acute exposure; however, after 28 days of exposure to SMF the level of serum iron increased in our experiment, most probably as a result of redistribution from other compartments rich in iron such as liver. The rise of spleen content showed the main end point of iron relocation. It is well established that through the Fenton reaction, ferro ion (Fe^{2+}) transforms the weak oxidant hydrogen peroxide into hydroxyl radical ($HO^{\bullet -}$), one of the most reactive species in nature (Arredondo and Nunez, 2005). Iron is important for immune response in several ways. Macrophages exhibit reduced bactericidal activity and neutrophils have reduced activity of the iron-containing enzyme myeloperoxidase when there is a lack of iron. Iron deficiency also results in decreased T-lymphocyte numbers and in decreased T-lymphocyte blastogenesis and mitogenesis (Kuvibidila et al., 1999). Therefore, our results are in line with the supposition that increased iron level in the spleen could contribute to the proinflammatory response. This result goes along with the increase in the serum granulocytes and decreased lymphocytes, the findings that previously have been shown to contribute to the increase in immune response and oxidative stress (Hashish et al., 2008).

Alongside proinflammatory effect, our results lead us to assume that 16 mT SMF induced chronic stress. Static magnetic field exposure induces a common stress response in cell cultures, in spite of the differences related to exposure time and to the cell types (Dini and Abbro, 2005). In our study, the level of serum transferrin also changed under the influence of SMF. Namely, mice exposed to the upward oriented SMF had higher values of serum transferrin than mice exposed to the downward oriented SMF or unexposed animals. Mice exposed to the downward oriented SMF also had higher levels of transferrin when compared to unexposed animals. A similar finding was observed in study of mice exposed to 128 mT SMF and it was explained as an increase in iron metabolism induced by SMF (Elferchichi et al., 2007). In addition, transferrin in mice has a role in unspecific acute phase response to inflammation as its positive indicator (Barnum-Huckins et al., 1997). Since exposure period in our study was 28 days, increased transferrin level in treated animals is more likely specific adaptive reaction to subchronically induced SMF stress rather than an unspecific stress reaction. Transferrin saturation was reduced in both SMF groups when compared to control. However, the rise of serum transferrin was so immense (almost doubled in the up group), that it might surpass the need for saturation. Also, iron level in the spleen increased, and it may not be achieved with reduced transferrin saturation, so the saturation may be decreased, but not to extent to disturb iron distribution.

Our results have demonstrated that continuous exposure to 16 mT SMF has no effect on body mass and food intake. Various researchers had similar findings using SMF of different field intensity or different exposure times on rats and mice (Margonato et al., 1995; Robertson et al., 1996; High et al., 2000). The overall data on food consumption and body mass confirm that SMF cause adaptation to stress in subchronically exposed animals.

The validity and significance of our results is additionally substantiated by the fact that we worked with an outbred, genetically diverse strain of mice, since statistical significance is achieved more easily when using a genetically identical inbred strain of mice.

5. Conclusions

Our study is the first, to our knowledge, in vivo experiment that has simultaneously used separate upward and downward oriented magnetic fields. We employed spatially dependent SMF with the average intensity of 16 mT to investigate hematological parameters in our model. Obtained results showed significant increase in total spleen cellularity in SMF exposed animals, especially in animals exposed to the downward directed magnetic field. Moreover, subchronic continuous exposure to the spatially dependent SMF whose average intensity of 16 mT was found to cause lymphocyte and granulocyte redistribution between spleen and blood, in a way that is typical for stress induced hematological changes. Serum transferrin levels, body mass and food intake confirm that these changes are not due to an unspecific stress response, but rather that they are caused by specific adaptation to subchronic SMF exposure.

Conflict of interest

The authors have no conflict of interest regarding the material and information presented in the article.

Role of funding source

No funding body had any involvement in the preparation or content of this article or in the decision to submit it for publication.

Acknowledgment

This study was supported by the grants No III-41013 and No III-41019 from the Ministry of Education and Science, Government of Serbia

References

Abdelmelek, H., Molnar, A., Servais, S., Cottet-Emard, J.M., Pequignot, J.M., Favier, R., Sakly, M., 2006. Skeletal muscle HSP72 and norepinephrine response to static magnetic field in rat. J. Neural. Transm. 113, 821–827.

Alford, C.E., King Jr., T.E, Campbell, P.A., 1991. Role of transferrin, transferrin receptors, and iron in macrophage listericidal activity. J. Exp. Med. 174 (2), 459–466.

Arredondo, M., Nunez, M.T., 2005. Iron and copper metabolism. Mol. Asp. Med. 26, 313–327.

Azanza, M.J., del Moral, A., 1994. Cell membrane biochemistry and neurobiological approach to biomagnetism. Prog. Neurobiol. 44, 517–601.

Bawin, S.M., Adey, W.R., 1976. Sensitivity of calcium binding in cerebral tissue to weak environmental electric fields oscillating at low frequency. Proc. Natl. Acad. Sci. USA 73, 1999–2003.

Barnum-Huckins, K.M., Martinez, A.O., Rivera, E.V., Adrian Jr., E.K, Herbert, D.C., Weaker, F.J., Walter, C.A., Adrian, G.S, 1997. A comparison of the suppression of human transferrin synthesis by lead and lypopolysaccharide. Toxicology 118, 11–22.

Cakir, D.U., Yokus, B., Akdag, M.Z., Sert, C., Mete, N., 2009. Alterations of hematological variations in rats exposed to extremely low frequency magnetic fields (50 Hz). Arch. Med. Res. 40, 352–356.

Campbell, W.H., 2001. Nature's magnetism, Earth Magnetism: A Guided Tour Through Magnetic Fields. Harcourt/Academic Press, San Diego, pp. 1–23 (Chapter 1).

Colbert, A.P., Souder, J., Markov, M., 2009. Static magnetic field therapy: methodological challenges to conducting clinical trials. Environmentalist 29, 177–185.

Crichton, R.R., Charloteaux-Wauters, M., 1987. Iron transport and storage. Eur. J. Biochem. 164 (3), 485–506.

Dini, L., Abbro, L., 2005. Bioeffects of moderate-intensity static magnetic fields on cell cultures. Micron 36, 195–217.

Dini, L., Panzarini, E., 2010. The influence of a 6 mT static magnetic field on apoptotic cell phagocytosis depends on monocyte/macrophage differentiation. Exp. Biol. Med. 235, 1432–1441.

Eccles, N.K., 2005. A critical review of randomized controlled trials of static magnets for pain relief. J. Altern. Complement. Med. 11 (3), 495–509.

Elblbesy, M.A., 2010. Effect of static magnetic field on erythrocytes characterizations. J. Biomed. Sci. Eng. 3, 300–303.

Elferchichi, M., Abdelmelek, H., Sakly, M., 2007. Effects of sub-acute exposure to static magnetic field on iron status and hematopoiesis in rats. Turk. J. Hematol. 24, 64–68.

Engstrom, S., Markov, M.S., McLean, M.J., Holcomb, R.R., Markov, J.M., 2002. Effects of non-uniform static magnetic fields on the rate of myosin phosphorylation. Bioelectromagnetics 23, 475–479.

Green, E.L., 1966. Biology of the laboratory mouse. Dover publications, New York.

Hahn, P., Song, Y., Ying, G.S., He, X., Beard, J., Dunaief, J.L., 2009. Age-dependent and gender-specific changes in mouse tissue iron by strain. Exp. Gerontol. 44, 594–600.

Hashish, A.H., El-Missiry, M.A., Abdelkader, H.I., Abou-Saleh, R.H., 2008. Assessment of biological changes of continuous whole body exposure to static magnetic field and extremely low frequency electromagnetic fields in mice. Ecotoxicol. Environ. Saf. 71, 895–902.

Health Protection Agency, 2008. Static Magnetic Fields. Report of the independent Advisory Group on Non-ionising Radiation. RCE-6. Documents of the Health Protection Agency. Radiation, Chemical and Environmental Hazards. Chilton, U.K.

High, W.B., Sikora, J., Ugurbil, K., Garwood, M., 2000. Subchronic in vivo effects of a high static magnetic field (9.4T) in rats. J. Magn. Reson. Imaging 12, 122–139.

Kowalczuk, C.I., Sienkiewicz, Z.J., Saunders, R.D., 1991. Biological Effects of Exposure to Non-ionizing Electromagnetic Fields and Radiation. I. Static Electric and Magnetic Fields (NRPB-R238). National Radiation Protection Board, Chilton, U.K.

Krylov, A.V., Tarakanova, G.A., 1960. Magnetotropism of plants and its nature. Plant. Physiol. 7, 156–160.

Kuvibidila, S.R., Kitchens, D., Baliga, B.S., 1999. In vivo and in vitro iron deficiency reduces protein kinase C activity and translocation in murine splenic and purified T cells. J. Cell. Biochem. 74, 468–478.

Löscher, W., 2003. Potential risks of magnetic fields: experimental studies on teratogenicity and carcinogenicity of static and extremely low frequency magnetic fields. In: McLean, M.J., Engström, S., Holcomb, R.R. (Eds.), Magnetotherapy: Potential Therapeutic Benefits and Adverse Effects. The Floating Gallery, New York, pp. 41–56.

Macedo, M.F., de Sousa, M., 2008. Transferrin and the transferrin receptor: of magic bullets and other concerns. Inflamm. Allergy—Drug Targets 7 (1), 41–52.

Margonato, V., Nicolini, P., Conti, R., Zecca, L., Veicsteinas, A., Cerretelli, P., 1995. Biologic effects of prolonged exposure to ELF electromagnetic fields in rats: II. 50 Hz magnetic fields. Bioelectromagnetics 16, 343–355.

Markov, M.S., Todorov, S.I., Ratcheva, M.R., 1975. Biomagnetic effects of the constant magnetic field action on water and physiological activity. In: Jensen, K., Vassileva, Y. (Eds.), Physical Bases of Biological Information Transfer. Plenum Press, New York, pp. 441–445.

Markov, M.S., 2005. "Biological windows": a tribute to W. Ross Adey. Environmentalist 25, 67–74.

Markov, M.S., 2007a. Therapeutic application of static magnetic fields. Environmentalist 27, 457–463.

Markov, M.S., 2007b. Magnetic field therapy: a review. Electromagn. Biol. Med. 26, 1–23.

Markov, M.S., 2011. How living systems recognize applied electromagnetic fields. Environmentalist 31 (2), 89–96.

McLean, M.J., Holcomb, R.R., Wamil, A.W., Pickett, J.D., Cavopol, A.V., 1995. Blockade of sensory neuron action potentials by a static magnetic field in the 10 mT range. Bioelectromagnetics 16, 20–32.

Ritchie, R.F., Palomaki, G.E., Neveux, L.M., Navolotskaia, O., Ledue, T.B., Craig, W.Y., 1999. Reference distributions for the negative acute-phase serum proteins, albumin, transferrin and transthyretin: a practical, simple and clinically relevant approach in a large cohort. J. Clin. Lab. Anal. 13 (6), 273–279.

Robertson, I.G., Wilson, W.R., Dawson, B.V., Zwi, L.J., Green, A.W., Boys, J.T., 1996. Evaluation of potential health effects of 10 kHz magnetic fields: a short-term mouse toxicology study. Bioelectromagnetics 17, 111–122.

Ružič, R., Jerman, I., Jeglic, A., Fefer, D., 1993. Various effects of pulsed and static magnetic fields on the development of Castanea sativa Mill in tissue culture. Electro-Magnetobiol 12, 165–177.

Sahebjamei, H., Abdolmaleki, P., Ghanati, F., 2007. Effects of magnetic field on the antioxidant enzyme activities of suspension-cultured tobacco cells. Bioelectromagnetics 28, 42–47.

Schenck, J.F., 2000. Safety of strong magnetic fields. J. Magn. Reson. Imaging 12, 2–19.

Stuchly, M.A., 1986. Human exposure to static and time-varying magnetic fields. Health Phys 51, 215–225.

Tavasoli, Z., Abdolmaleki, P., Mowla, S.J., Ghanati, F., Sarvestani, A.S., 2009. Investigation of the effects of static magnetic field on apoptosis in bone marrow stem cells of rat. Environmentalist 29 (2), 220–224.

Trabulsi, R., Pawlowski, B., Wieraszko, A., 1996. The influence of steady magnetic fields on the mouse hippocampal evoked potentials in vitro. Brain. Res. 728 (1), 135–139.

Ukolova, M.A., Kvakina, E.B., Garkavi, L.H., 1975. Stages of Magnetic Field Action. Problems of Action of Magnetic Fields on Biological Systems, vol. 1. Nauka, Moscow, pp. 57–71.

Vranic, V., Savovski, K., Dedovic, N., Dimitrijevic, B., 2000. Hematological toxicity associated with tiazofurin-influence on erythropoiesis. Toxicol. Lett. 114, 81–90.

Wieraszko, A., 2000. Dantrolene modulates the influence of steady magnetic fields on hippocampal evoked potentials in vitro. Bioelectromagnetics 21 (3), 175–182.

World Health Organization, 2006a. Static Fields (Environmental Health Criteria: 232). Geneva, Switzerland.

World Health Organization, 2006b. Electromagnetic Fields and Public Health: Static Electric and Magnetic Fields. WHO Fact Sheet #299, Geneva, Switzerland.

Yano, A., Hidaka, E., Fujiwara, K., Iimoto, M., 2001. Induction of primary root curvature in radish seedlings in a static magnetic field. Bioelectromagnetics 22 (3), 194–199.

Zhao, G., Chen, S., Wang, L., Zhao, Y., Wang, J., Wang, X., Zhang, W.W., Wu, R., Wu, L., Wu, Y., Xu, A., 2011. Cellular ATP content was decreased by a homogeneous 8.5 T static magnetic field exposure: role of reactive oxygen species. Bioelectromagnetics 32, 94–101.

Zukov, B.N., Lazarovich, V.G., 1989. Magnetotherapy in Angiology. Zdorovie, Kiev, p. 111.

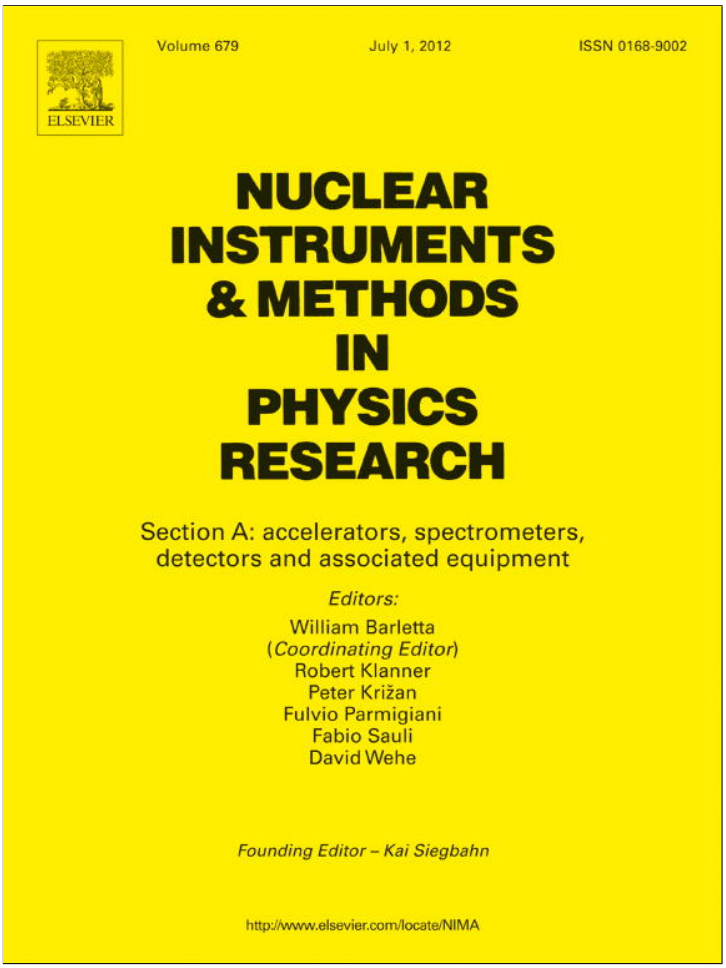

Nuclear Instruments and Methods in Physics Research A 679 (2012) 54–60

Contents lists available at SciVerse ScienceDirect

Nuclear Instruments and Methods in Physics Research A

journal homepage: www.elsevier.com/locate/nima

Minimization of the measurement errors induced by the cyclotron magnetic field measurement system

Saša Ćirković*, Andjelija Ž. Ilić, Aleksandar Dobrosavljević, Roman Balvanović, Jasna L. Ristić-Djurović

Laboratory of Physics 010, Vinča Institute of Nuclear Sciences, University of Belgrade, PO Box 522, 11001 Belgrade, Serbia

ARTICLE INFO

Article history:
Received 15 December 2011
Received in revised form
27 February 2012
Accepted 4 March 2012
Available online 23 March 2012

Keywords:
Cyclotrons
Ion beams
Magnetic field measurement
Systematic error
Data analysis

ABSTRACT

Systematic errors caused by the deficiencies of the measurement equipment are occurring relatively often in the engineering practice. The magnetic field measurement system of the VINCY Cyclotron has been designed well; however, due to the practical limitations in the machining process fabrication errors are imminent. We present our experiences with the produced measurement system and the techniques used for the detection and correction of errors. A change in the measuring protocol is suggested in order to overcome otherwise unavoidable errors caused by measuring system machining imperfections.

1. Introduction

Magnetic field plays crucial role in the operation of an isochronous cyclotron. During the acceleration, beam ions are guided, focused, and synchronized with the accelerating radio-frequency voltage under the influence of the isochronous magnetic field. A lot of patience and care is taken to obtain the desired magnetic field as accurately as possible. Among other procedures, the precise magnetic field measurements must be conducted during the process of the magnetic field design and realization.

Magnetic field measurements represent an integral part of the iterative magnet shimming campaign. In the design of a multipurpose cyclotron, measurements are performed for the nominal as well as for a number of important non-nominal operating modes of the cyclotron. The obtained detailed maps of the magnetic fields additionally form a permanent database for the cyclotron control system and serve in the development of the future experimental programs as well.

VINCY Cyclotron is a compact multipurpose isochronous cyclotron for the acceleration of both light and heavy ions [1]. Three groups of magnetic field measurements are performed, the first one resulting in twenty magnetic field maps for different main coil currents, the second group summing up to a total of hundred magnetic field maps for different combinations of the main and trim coils currents, and the third one comprised of the isochronized magnetic field maps corresponding to the four test ions of the VINCY Cyclotron. Acquirement of a large quantity of required data took a lot of time and manpower in spite of the automatized measurement procedures.

The magnetic field measurement system of the VINCY Cyclotron is custom built in accordance with the relevant cyclotron geometrical parameters as well as the basic accuracy and flexibility requirements [2]. Fabrication of the system parts is conducted within the specifications in all aspects except for the measurement arm, which in lack of long enough titanium rods was created from the two pieces welded together. It was only perceived as a problem during the measurement system exploitation, but it turned out to be of a little consequence. In spite of that, the usual machining process tolerances led to the small but consequential errors in the Hall probe positioning. The origin, effects, and detection of these errors are described. Their possible correction is investigated, but proven to be only partial with the planned approach to the system operation. It is shown that the complete avoidance of the noticed errors is possible with the modified measurement procedure, i.e., system utilization.

2. Cyclotron magnetic field measurement systems

Mostly contributing to the nonlinearities of the materials used, the cyclotron magnetic field design represents a cumbersome task. Starting with the approximate analytical estimates, followed by the accurate numerical magnetic field modeling, characterization of

* Corresponding author. Tel.: +381 11 2454965; fax: +381 11 2447963.
E-mail addresses: kosjera@vinca.rs (S. Ćirković), andjelijailic@ieee.org (A.Ž. Ilić), alexd@vinca.rs (A. Dobrosavljević), broman@vinca.rs (R. Balvanović), jasna@stanfordalumni.org (J.L. Ristić-Djurović).

0168-9002/$ - see front matter © 2012 Elsevier B.V. All rights reserved.
http://dx.doi.org/10.1016/j.nima.2012.03.018

materials and measurements on the reduced model of the cyclotron magnet, it is finalized through the iterative magnet shimming campaign. Availability of the sophisticated software tools for detailed three-dimensional modeling of magnet systems allows for the simulated magnetic field maps usage in the analysis and optimization of the magnet design, once the magnetic properties of the materials are well known. An excellent example of a measurement system for determination of material magnetic properties, primarily B-H curves, can be found in [3]. Most commonly used methods and instruments for magnetic measurements are described in [4].

As pointed out in [5], magnetic field mapping machines for cyclotron magnets belong to the special purpose equipment and are custom built to match the cyclotron being designed. An interesting example of such system realized with the flip-coil arrays mounted on a rotating beam is the magnetic field survey system for the TRIUMF Cyclotron magnet [6]. The choice of the flip coils was motivated by the troublesome control of temperature dependent output of the Hall probes of the time. The rotating beam was made out of aluminum and deflected naturally under its own weight; it was prebowed upwards to account for that problem. The Hall probe positioner, designed for the PSI Cyclotron a decade later, already utilized Hall probes with the much lower temperature coefficients, allowing the system operation without special thermostatic facilities [7]. It utilized two 110° circular segments and a radial bar moving in azimuthal direction on the segments, carrying two Hall probes mounted on the carriage which was moving in radial direction on the bar. Azimuthal positioning was performed by means of the two nonmagnetic stainless steel tapes with precisely drilled position holes and controlled by the two photo cells. Namely, a coincidence network connected with the photo cells assured that the virtual line, going through the centers of both Hall probes, always showed to the coordinate center.

Many of the recent measurement system designs use the method similar to that in [6], with the long measurement arm, fixed in the machine center, rotating azimuthally and carrying the Hall probe that can perform radial movement [8,9]. An example of especially robust and reliable magnetic field mapping system is described in [10]. Azimuthal accuracy in this system is obtained by mechanical indexation, i.e., the outer ring carries cogged segments with one cog for every 0.5°. Similar principle is used for radial positioning, i.e., to avoid any problems that can be related to the use of the synthetic belt for radial movement, the rack rail moved by a gear wheel and the shuttle fastened to it are used. A completely different approach to the magnetic field mapping is presented in [11], where the magnetic field mapping in the Cartesian coordinate system is performed and the measured data subsequently converted into the field data in the polar coordinates, required for further analysis. The presented measurement system is fast and very accurate, due to the high precision mechanical *x*-*y* stage with the two Hall probes, ensuring remarkably accurate alignment with the coordinate system of the machine. The in-depth analysis of the results obtained by measurements is a major part of the iterative magnetic field forming process [8–11]. It employs harmonic analysis, as well as the beam dynamics calculations.

3. Magnetic field measurement system of the VINCY Cyclotron

The realized magnetic field measurement system and its operation are illustrated in Fig. 1. Measurements are performed by the miniature ($14\times5\times2\ \mathrm{mm}^3$) Hall probe MPT-141, whose small sensitive area of $1\times0.5\ \mathrm{mm}^2$ enables high precision. A temperature sensor is included in the probe, allowing for the corrections of all temperature dependent effects. Measured values are sent to the control unit using the DTM-141 Teslameter; the combined relative accuracy of the probe and the Teslameter is 0.01% [12].

The MPT-141 Hall probe is mounted on a movable cart and kept in place in its center by means of the small gap at its axis. The cart travels along the measurement arm made of titanium to be light and firm, and to ensure minimal side effects in the presence of a strong magnetic field. The arm is supported at the center of the magnet by the vertical shaft and at two points at the circumference of the supporting ring by the supporting wheels. It is located in the median plane of the VINCY Cyclotron.

Azimuthal positioning of the measurement arm, and thus the Hall probe, is performed by the OMRON servo motor with an optical incremental encoder of 8000 pulses/rev. It is supervised by another 15-bit optical absolute encoder. The theoretical precision of azimuthal positioning is 1.7″ while the accuracy of the absolute encoder readout is 40″. Radial Hall probe positioning is performed by the OMRON servo motor as well, acting upon the toothed belt gear made of Kevlar that advances the movable cart. Servo motor is equipped with an 8000 pulses/rev optical incremental encoder, but the reduction gear with zero clearance and gear reduction ratio 1:29 is used. The resulting theoretical precision of radial positioning is 0.6 μm.

In the fully automatized standard measurement procedure, the measurement arm rotates in the azimuthal direction from $\theta=0°$ to $\theta=180°$. The Hall probe, carried by the movable cart, travels along the measurement arm and scans the magnetic field from one to the other side of the pole (from $R=+100$ cm to $R=-100$ cm). When the probe reaches the final position, the measurement arm moves in the azimuthal direction for one step and measurements are repeated. In this manner the whole circular surface in the median plane is covered and the complete magnetic field map obtained. The usual azimuthal step is 1° and the usual radial step 10 mm.

4. Systematic measurement error

Magnet shimming procedures are always iterative, proceeding from the coarse magnetic structure to the finer and finer one. At the beginning of the second phase of the VINCY Cyclotron magnetic field measurements the existence of relatively strong first harmonic component, equaling 3 mT, in the central region of the machine has been noticed [13]. The usual cause of deficiencies in the machining and construction of the ferromagnetic structure was suspected at first; however, additional examination as well as the most precise placement of the magnetic sectors resulted in no improvement at all. Such a result indicated that there is a systematic error brought in by the measurement equipment. We shall describe the techniques used for the detection and correction of errors on the example of magnetic field mapping for the main coil current of 256.5 A and the trim coils currents set to zero. The lower the main coil current, the larger the magnetic field flutter, so that the measurement errors are easier to perceive. The choice made above is especially convenient because it is the lowest of the four main coil currents corresponding to the four test ions of the VINCY Cyclotron. The main coil current of 256.5 A corresponds to the H^- test ion.

We presumed that there might be a problem with the Hall probe positioning. The control measurements, performed for the two different initial azimuthal positions of the Hall probe, confirmed the measurement grid off-centering. Completely different results obtained for the magnetic field first harmonic in the two cases, as shown in Fig. 2, can not be associated with a single considered ferromagnetic structure.

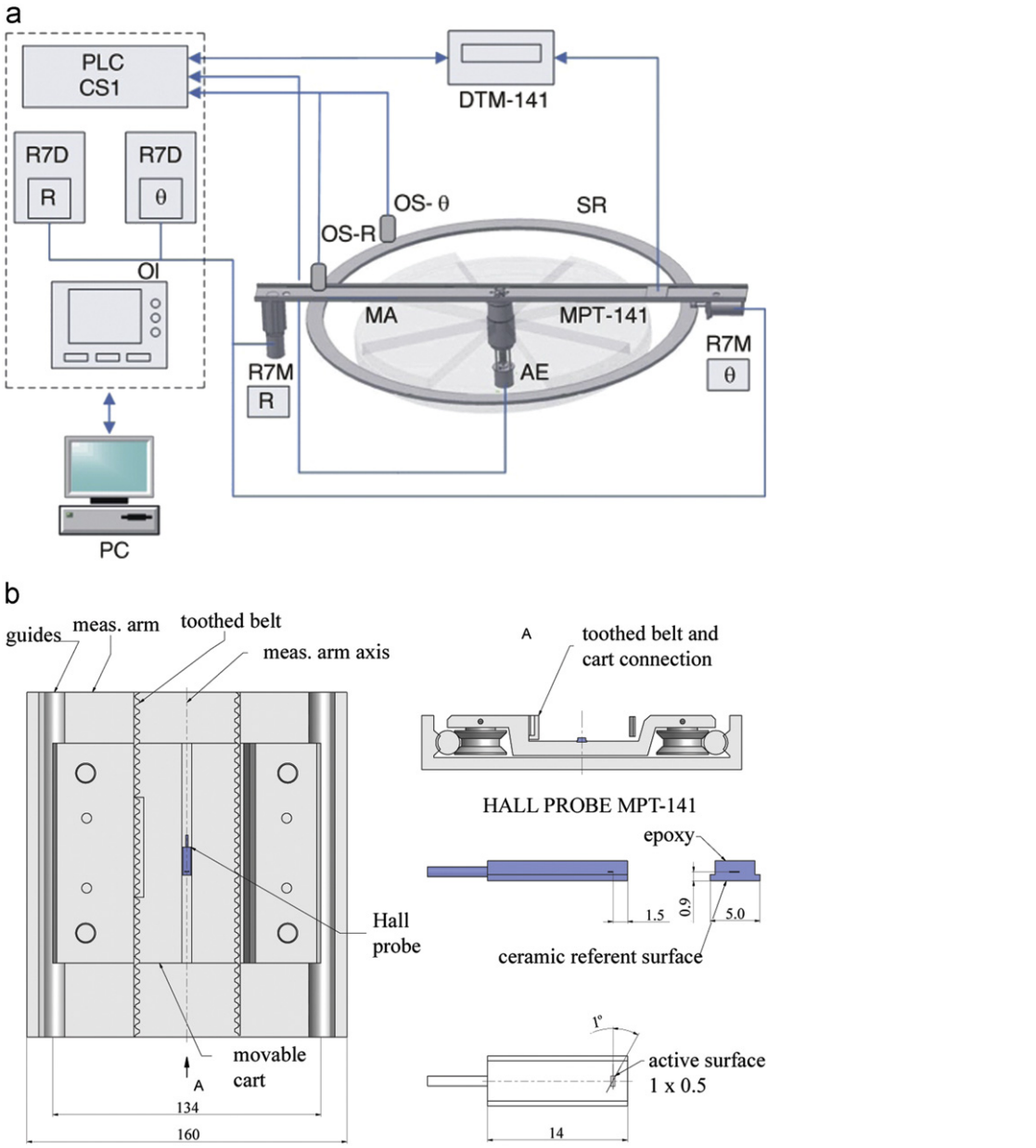

Fig. 1. Magnetic field measurement system of the VINCY Cyclotron (a) and the detailed view of the movable cart carrying the Hall probe (b). The measurement system is comprised of the mechanical subsystem, control unit and measurement instrumentation. (a) Mechanical subsystem elements are: MA – measurement arm, SR – supporting ring, R7M – OMRON servo motors for radial (R) and azimuthal (θ) positioning, AE – absolute encoder. Control unit includes OS-R and OS-θ -optical switches for radial (R) and azimuthal (θ) origin point, respectively, DTM-141 – Digital Hall-Effect Teslameter, PLC CS1 – OMRON servo drivers, OI – operator interface panel, and PC – personal computer with programs and archive of magnetic field maps. Miniature Hall probe MPT-141 acts as the measurement instrumentation. (b) Movable cart carrying the MPT-141 Hall probe. The Hall probe is kept in place in the center of the movable cart by means of the gap located at the cart axis. The cart travels along the measurement arm as guided by the toothed belt gear made of Kevlar. The accuracy of the probe positioning depends on the precision of the cart positioning with respect to the measurement arm as well as the measurement arm positioning with respect to the coordinate system of the VINCY Cyclotron.

The complete check up of all the components of the magnetic field measurement system was performed. The produced measurement arm did not comply with the project specifications. In lack of a long enough single titanium rod, it was created from the two pieces welded together and thus not perfectly straight. Although the manufacturer gave a satisfactory initial estimate of the measurement arm straightness, based on the laser interferometer system measurements, it turned out incorrect. Repeated measurements, using the precise DEA Epsilon 2304 coordinate measuring machine, revealed a misalignment of the two welded pieces by $0^\circ 1' 56''$. It is positioned at $R=750$ mm according to the standard measurement coordinate system. Due to the relatively long legs of an angle, misalignment resulted in a deviation from the straight line of 0.561 mm at $R=1000$ mm, which is out of the ± 0.1 mm tolerance range. Fortunately, with the large enough (0.2–0.3 mm) clearance between the guides and the wheels and the sufficient tension of the belt, the toothed belt dictates the straight and centered trajectory to the movable cart. Angular displacement of the cart trajectory is thereby reduced approximately four times with respect to the misalignment of the two welded pieces. Even with the highest azimuthal magnetic field gradient equaling 330 mT/°, the resulting error due to the misalignment angle would be about 2.5 mT. Influence of the measurement arm deformity itself to the errors is therefore insignificant in comparison to the observed error magnitudes, which can be as high as 220 mT [13].

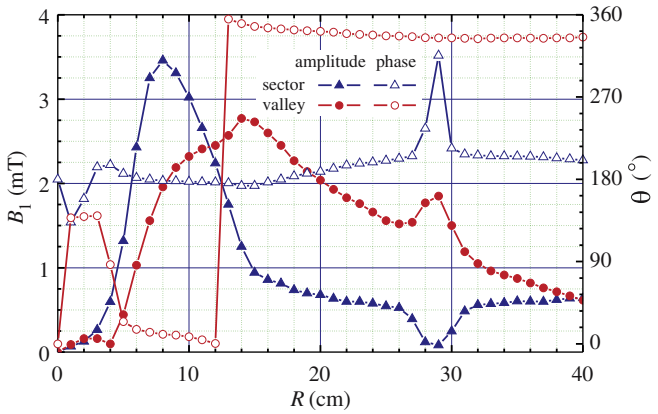

Fig. 2. Systematic error of the magnetic field measurement system. The control measurements are performed for the two different initial azimuthal positions of the Hall probe. The first one coincides with the usual initial azimuthal position, i.e., the midline of the first magnetic sector S1. The amplitude and phase of the first harmonic of the magnetic field in this case are depicted by the blue triangles. Another initial azimuthal position is moved clockwise by 45° with respect to the first one to fall at the midline of the fourth valley. The red circles represent the results for this case. Were the imperfections of the ferromagnetic structure of the VINCY Cyclotron the cause for the existence of the first harmonic component, the obtained first harmonic amplitudes ought to be the same, whereas the phases should be of the same shape only shifted by 45°. However, that is not the case, leading to the conclusion that the measurement system introduces the errors. (For interpretation of the references to colour in this figure legend, the reader is referred to the web version of this article.)

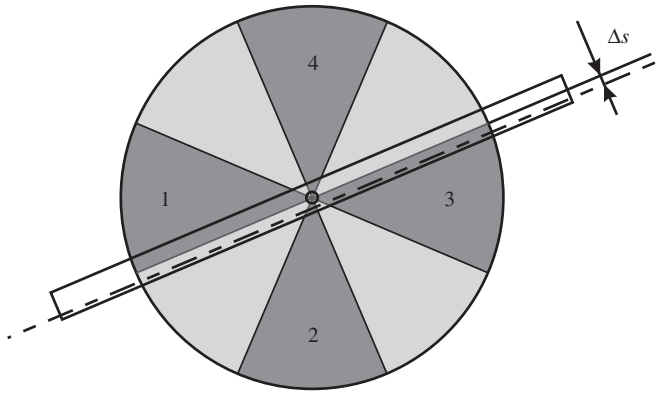

Fig. 3. The Hall probe offset with respect to the symmetry axis of the measurement arm. Measurement arm shaft is fixed in the center of the VINCY Cyclotron and the trajectory dictated by the guides and the toothed belt is straight and centered. Therefore, the arm itself is not the major cause for the measurement grid off-centering. However, the Hall probe travels together with the movable cart along the axis shifted by a small amount Δs with respect to the measurement arm symmetry axis. As a result, the actual measurements are taken at different azimuthal positions than intended. The azimuthal magnetic field gradient in the vicinity of the magnetic sector edges can be as high as 330 mT/°. One of the measured magnetic field values corresponding to the two diametrically opposite azimuths is therefore larger than it should be and the other one is lower. The difference in measured values reaches 220 mT, producing the false asymmetry of the measured magnetic field and the large amounts of unwanted harmonics.

However, the very same clearance between the guides and the wheels, taken to ensure the motion with minimum friction important for radial positioning, as well as the trajectory straightness in case of the minor realization flaws, allows for the movable cart to slightly drift away from the arm symmetry axis. The active measuring surface of the Hall probe can be somewhat off-centered as well, i.e., the probe manufacturer declares the active surface placement tolerance of ± 0.2 mm. In addition to that, the measurement arm deformity may have played the role in the wear out of the wheels and guides by friction while the cart is moving in the vicinity of $R=750$ mm where the deformity occurs. The combination of these effects resulted in the Hall probe offset by a small amount Δs with respect to the measurement arm symmetry axis, occurring during the automatic probe positioning.

The magnetic field of an isochronous cyclotron changes very smoothly with both the radius and azimuth, except in the region around the magnetic sector edges. Very high azimuthal magnetic field gradients in that region provide strong focusing necessary for the isochronous acceleration. As explained in Fig. 3, even a small offset in the azimuthal Hall probe positioning in this region produces the significant amount of unwanted harmonics. The measurement errors corresponding to the two halves of the measurement arm are positively correlated introducing the false asymmetry in the results.

To further examine this assumption, we have introduced the auxiliary "manual" measurement, i.e., the measurement with the manually adjusted azimuthal positioning of the Hall probe. The radial position is kept fixed at $R=8$ cm, where the highest amount of unwanted harmonics was observed, while the measurement arm is rotating through the $[0°, 360°]$ range with the $1°$ step. The azimuthal positioning is achieved by the manual motion of the arm, with the precision of $40''$ given by the absolute encoder readout. Since the probe centering with respect to the arm symmetry axis is identical for all the azimuthal positions, any centering offset that might occur would result in the negatively correlated measurement errors corresponding to the each set of

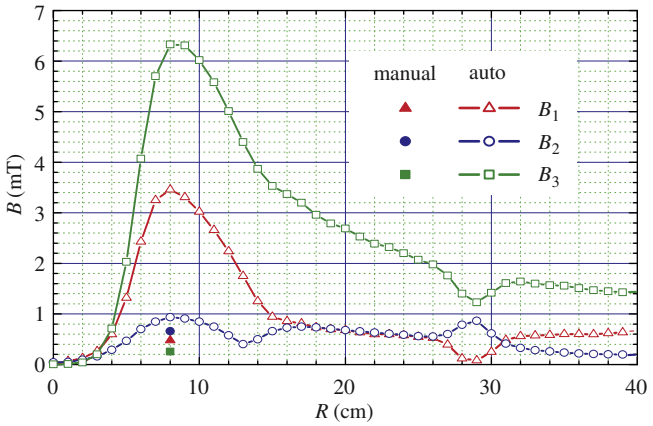

Fig. 4. The amplitudes of the first three measured magnetic field harmonics compared with the control values. Standard measurement procedure errors resulted in the highest amount of unwanted harmonics at the radius $R=8$ cm. The realistic estimates are therefore obtained for this radial position performing the time consuming but very accurate manual adjustment of the Hall probe azimuthal position. The amplitudes of the first and third harmonic are 7.25 and 24.73 times smaller, respectively, when the manual azimuth adjustment is performed. The drop in the second harmonic amplitude equals 29.7%. The obtained results confirm the assumption of the Hall probe offset being the major reason for the off-centering of the measurement grid.

diametrically opposite azimuths. The maximal difference of the measured magnetic field values is therefore the one corresponding to the optical absolute encoder reading precision. For the highest azimuthal magnetic field gradient equaling 330 mT/°, it does not exceed 7.3 mT, a value negligible in comparison with the 220 mT difference obtained during the standard automatic measurement. Manual Hall probe position adjustment therefore provides the realistic control values of the magnetic field differences and field harmonics.

Fig. 4 compares the amplitudes of the first three magnetic field harmonics with the control values for the radius $R=8$ cm, where

the highest amount of unwanted harmonics is discovered. The control values confirm that the actual harmonics amplitudes are considerably smaller than the apparent ones. Therefore, the measurement grid off-centering is predominantly caused by the Hall probe offset Δs. The direct deduction of the actual probe offset at the time of measurement from the collected data, presented in Fig. 4, is not possible. First, the active measuring surface of the Hall probe becomes additionally offset from the center of the probe if there is any tilt with respect to the radial direction. Second, with the standard measurement procedure there is a positive correlation of errors for the diametrically opposite azimuths, which amplifies the effect. It is possible, however, to make a reasonable estimate of the joint effect of these factors, from the assessment of magnetic field gradients and errors shown in Fig. 4. Were all the other effects negligible, offset corresponding to the results in Fig. 4 would be 1 mm; therefore, we may define the estimate, effective Hall probe offset, as $\Delta s_e = 1$ mm.

5. Measurement error correction

The solution of the observed problem was attempted by the Hall probe alignment with respect to the measurement arm. Before the automatic measurement procedure is initiated, the Hall probe and the movable cart are positioned using the vernier caliper and the adjustment of the cart wheels. The probe is fixed and the measurement further performed using the standard procedure. The effect of the Hall probe alignment to the reduction of measurement errors is shown in Fig. 5. The maximal difference ΔB of the measured data obtained for the diametrically opposite azimuthal positions, θ and $\theta+180^\circ$, is on average reduced four times with respect to the standard measurement without the probe alignment. However, at a new level of about 5 mT, it is still unacceptably high. The corresponding effective Hall probe offset equals $\Delta s_e = 0.15$ mm. During the lengthy radial motion along the measurement arm the movable cart, initially aligned with the arm symmetry axis, drifts slightly away. Additionally, perfect alignment is impossible and therefore the positive correlation of offset pertaining to the two diametrically opposite points can produce errors. The realistic control measurements prove that the difference of the magnetic field amplitudes for the opposite azimuths should in the worst case be limited to the [−2 mT, 2 mT] interval.

To further lessen the measurement error and bring it to an acceptable level, we decided to modify the automatic measurements and use only one half of the measurement arm. In that manner, the measured data corresponding to the two opposite azimuthal positions is negatively correlated. As demonstrated in Fig. 6, we finally obtain a good agreement with the control manually measured data. With the modified automatic measurement, the asymmetry of the magnetic field at $R=8$ cm is almost completely lost i.e., ΔB is confined to the [−2 mT, 2 mT] interval. The agreement of the modified automatic measurements with the control manual measurements is easier to discern in the presence of actual magnetic structure imperfections. Therefore, we illustrate the precision of the modified procedure in Fig. 7, comparing it with the control manual measurements at two other radii. An excellent agreement of the results for the two cases is observed, while the standard measurement with the Hall probe alignment gives inadequate results. The amplitudes and phases of the low order magnetic field harmonics with the modified automatic measurement are shown in Fig. 8. The decrease in the level of the low order harmonics is substantial compared to the data in Fig. 4 corresponding to the standard measurement procedure. The low order harmonics are brought to a level concurrent with the manually determined control values shown in Fig. 4 for $R=8$ cm. The harmonic components peak out for radii larger than $R=92$ cm, presenting no problems for extraction since the radius of extraction equals $R_{ex}=84$ cm.

The quality of the realized isochronized magnetic fields as well as the accuracy of measurement procedures can be further assessed from the beam dynamics parameters, such as the betatron oscillation frequencies, gyration frequency fluctuations from its ideal constant value and the corresponding phase excursion of an accelerated particle. The betatron oscillation frequencies can be calculated directly from the magnetic field properties, i.e., the magnetic field harmonic analysis, as well as from the beam dynamics simulations. We use both of these methods and compare

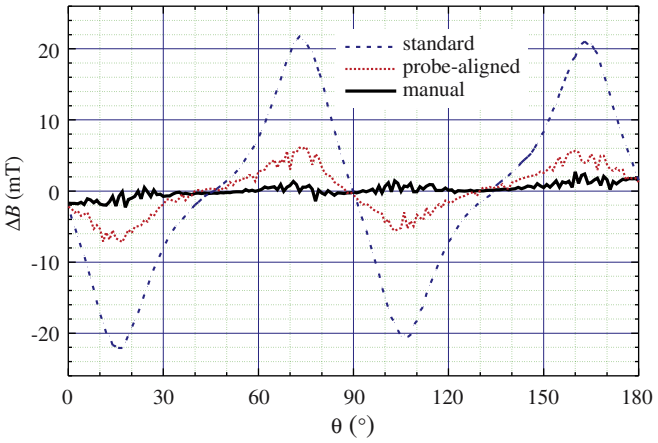

Fig. 5. The alignment of the Hall probe with respect to the measurement arm. The difference ΔB of the magnetic field measured in two diametrically opposite points, at azimuths θ and $\theta+180^\circ$, is shown for the measurement arm azimuthal position θ ranging from 0° to 180° and the Hall probe radial position $R=8$ cm. The results of the standard automatic measurement, standard probe-aligned automatic measurement and the measurement with the manual adjustment of the Hall probe position are compared. The systematic error of the standard measurement procedure is significantly reduced by the Hall probe alignment. However, it is still unacceptably high.

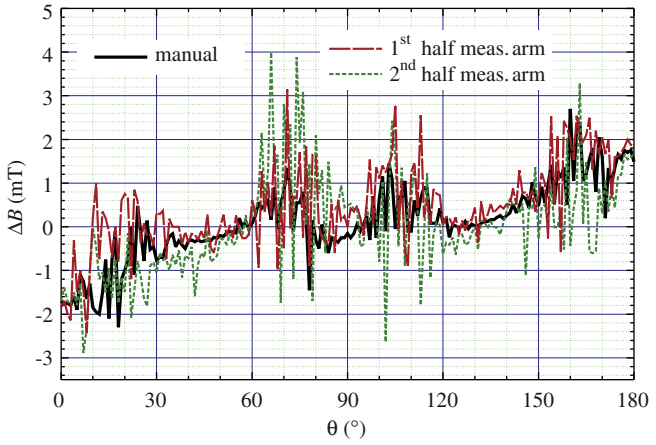

Fig. 6. The modified automatic measurement procedure. We suspected that the total amount of the Hall probe radial movement as well as the correlation of the azimuthal positioning errors for the two halves of the measurement arm play significant role in the buildup of the measurement errors. Therefore, a different approach in the magnetic field measurement is considered and as a result, the systematic measurement errors are finally brought to an acceptable level. The results of the modified measurements, with one and with the other half of the measurement arm, are compared with the manually performed measurement and the agreement of the results is excellent.

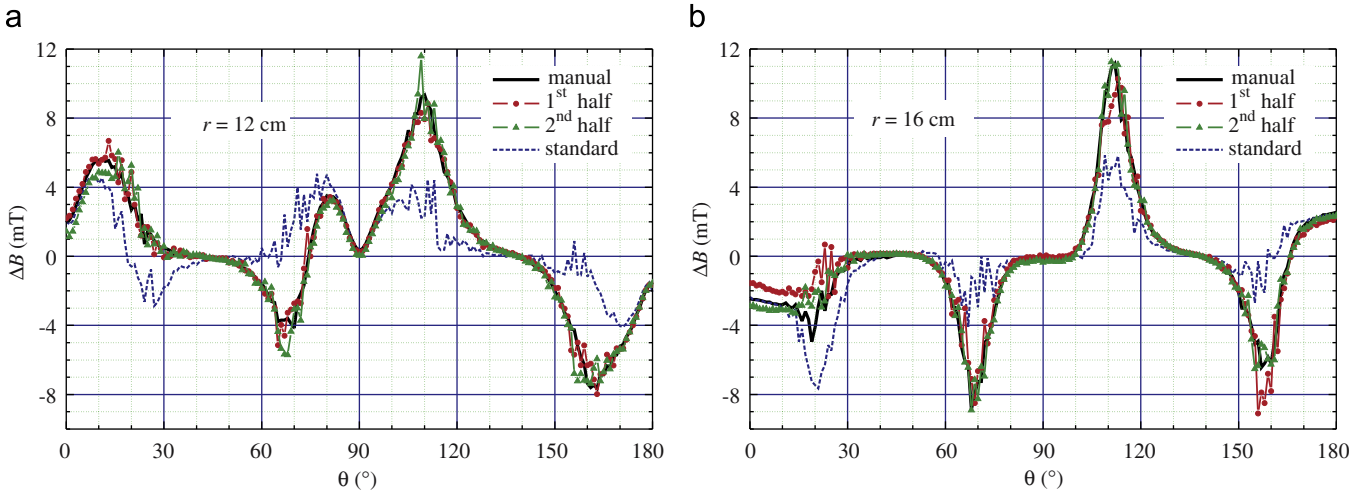

Fig. 7. The difference ΔB of the magnetic field values at diametrically opposite azimuthal points as a measure of the ferromagnetic structure imperfections. Utilizing the modified automatic measurement procedure the difference ΔB at $R=8$ cm is confined to the $[-2$ mT, 2 mT$]$ interval. The remaining differences in the field values at azimuths θ and $\theta+180^\circ$ indicate the actual errors due to the magnetic structure imperfections. Such differences are shown for the measurement arm azimuthal position θ ranging from 0° to 180° and the radial positions $R=12$ cm (left) and $R=16$ cm (right). An excellent agreement of the two independent measurements using the modified automatic procedure with the control manually performed measurements at these radii is observed, while the standard measurement even with the Hall probe alignment (dashed blue line) gives an erroneous result. (For interpretation of the references to colour in this figure legend, the reader is referred to the web version of this article.)

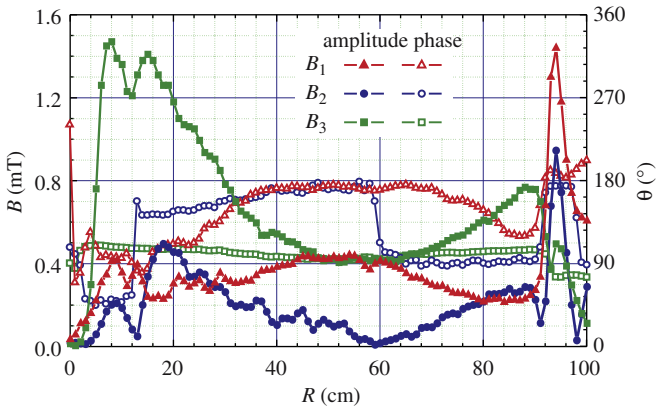

Fig. 8. The amplitudes and phases of the first three measured magnetic field harmonics after the correction of measurement errors. With the modified automatic measurement procedure, the amplitude of the first magnetic field harmonic, as well as the second one, is brought below the level of 0.5 mT. The third magnetic field harmonic shows peaks at the radii $R=8$ cm and $R=16$ cm, reaching the values of 1.5 mT and 1.4 mT, respectively. In the most part of the accelerating region, for radii larger than $R=30$ cm, it lies below 0.8 mT. The radius of extraction is $R_{ex}=84$ cm, therefore the peaks of the harmonic components for radii larger than $R=92$ cm are of no influence. The presented results are greatly improved in comparison to the ones shown in Fig. 4, corresponding to the standard measurement procedure.

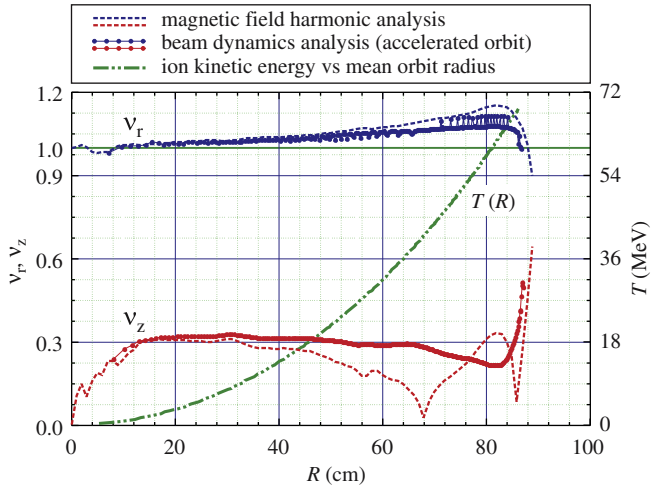

Fig. 9. Radial and axial betatron oscillation frequencies corresponding to the measured isochronized magnetic field map of the H^- test ion, after the measurement error correction. Two methods for the calculation of betatron oscillation frequencies are used, the magnetic field harmonic analysis and the beam dynamics analysis. The latter is performed along the accelerated orbit, resulting in actual betatron oscillation frequencies during the acceleration along the chosen orbit. The results agree well with each other and verify the absence of harmful resonant behavior during the acceleration. The ion kinetic energy dependence on the mean orbit radius is shown in green dash-dot-dot line in order to allow the interpretation of the results in terms of energy. (For interpretation of the references to colour in this figure legend, the reader is referred to the web version of this article.)

the obtained results in Fig. 9 for the measured isochronized magnetic field map of the H^- test ion. The beam dynamics simulations are performed using the self-written software package VINDY-A [14]. The results verify the absence of harmful resonant behavior along the chosen accelerated orbit, and thus the well designed isochronized magnetic field. The ion kinetic energy dependence on the mean orbit radius, shown in green dash-dot-dot line, allows for the interpretation of the results in terms of energy.

The obtained level of isochronism is depicted in Fig. 10. The nominal gyration frequency used for the H^- test ion magnetic field design was $f_g^{nom}=20.037$ MHz, while the obtained mean gyration frequency equals $\overline{f_g}=20.035$ MHz. The relative error of the gyration frequency is shown by the dashed blue line in Fig. 10; it is rather small indicating the well-isochronized magnetic field. As a result of the gyration frequency fluctuations, the phase slip of a particle occurs during the acceleration. The radiofrequency system phase, ϕ_{RF}, has been monitored at the same azimuth ($\theta=45^\circ$) for different particle kinetic energy, i.e., corresponding to the different mean orbit radii along the accelerated orbit. Phase excursion of a particle during the acceleration, $\Delta\phi$, is obtained as the difference between the monitored radiofrequency system phase and its nominal value for the considered azimuth, $\phi_{RF}^{nom}(45^\circ)=90^\circ$. Phase excursion falls into the range of $\pm 5^\circ$, which can be considered an excellent result.

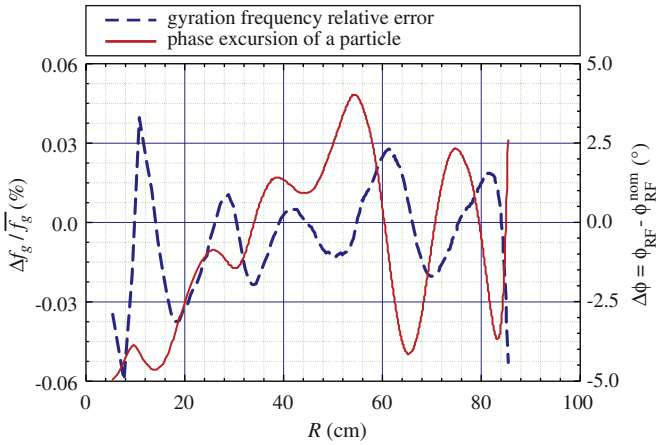

Fig. 10. The deviation from the isochronous acceleration as a result of the measured magnetic field imperfections for the H^- test ion. The magnetic field imperfections translate into the gyration frequency fluctuations i.e., the deviation from the isochronous motion, and further to the phase slip of an accelerated particle. The gyration frequency fluctuations are depicted through the relative error of the gyration frequency f_g, as represented by the dashed blue line. The solid red line shows the resultant phase excursion of a particle, $\Delta\phi$, versus mean orbit radius. The corresponding ion kinetic energy dependence on the mean orbit radius is shown in Fig. 9 (green dash–dot–dot line). The small level of the gyration frequency fluctuations, as well as the remarkably constrained phase excursion less than $\pm 5^\circ$, testify to the high quality of the measured isochronized magnetic field of the H^- test ion. (For interpretation of the references to colour in this figure legend, the reader is referred to the web version of this article.)

6. Conclusion

During the design and construction of the ferromagnetic structure of the multipurpose VINCY Cyclotron, we encountered several serious problems with the generally well devised magnetic field measurement system. One of them was the persisting systematic error stemming from the inability to realize the low friction precise radial movement along with the very rigid requirements on azimuthal precision due to the abrupt azimuthal changes of field amplitudes. We described the two procedures used to check for the amount of errors due to the measurement system and to localize the errors. The severity of the measurement system systematic error can be gauged by a small convenient change in the measurements, such as starting with the different initial position of the probe. The actual errors due to the magnetic structure imperfections can be estimated if the more time consuming but accurate manual measurements are performed in the regions of largest total measurement errors.

The solution of the problem was firstly attempted without the modifications of the original measurement procedure. The Hall probe azimuthal positioning is checked and aligned with the measurement arm prior to every new instance of field mapping. Although the measurement precision improved significantly, the described practice still remained insufficient in coping with the influence of the high azimuthal field gradients to the error buildup, as well as the problems in keeping the probe well aligned during the lengthy radial motion. The modified automatic measurement procedure is adopted that only uses one half of the measurement arm and thereby avoids the positive correlation of the measurement errors. The precision of the modified measurement procedure is illustrated through the comparison with the control manual measurements, magnetic field harmonic analysis and using the beam dynamics simulations.

The main objective of describing our experiences and the problems encountered in the magnetic field measurements was to put them to use to the others dealing with the similar issues, where the precise measurements are of key interest to the final design and the custom built measurement systems are often subject to the rather small but highly consequential realization flaws.

Acknowledgement

This work was supported by Ministry of Education and Science of Serbia through project Physics and Chemistry with Ion Beams, no. III 45006.

References

[1] N. Nešković, J. Ristić-Đurović, S.B. Vorozhtsov, P. Beličev, I.A. Ivanenko, S. Ćirković, A.S. Vorozhtsov, B. Bojović, A. Dobrosavljević, V. Vujović, J.J. Čomor, S.B. Pajović, Status Report on the VINCY Cyclotron, Nukleonika 48 (2) (2003) S135–S139. [Proc. XXXIII European Cyclotron Progress Meeting, Poland, 2002].
[2] A. Dobrosavljević, S. Ćirković, Đ. Košutić, Lj. Vukosavljević, D. Vranić, Automatic system for mapping of the VINCY Cyclotron magnetic field, Nuclear Technology and Radiation Protection, XXI (1) (2006) 13–20.
[3] V.M. Amoskov, V. Belyakov, T. Belyakova, S. Dmitriev, O.G. Filatov, A. Firsov, I. Franko, B. Gikal, G. Gulbekyan, O. Ilyasov, I. Ivanenko, V. Kostyrev, V. Kukhtin, V. Kutchinsky, E. Lamzin, M. Larionov, B. Maximov, A. Semchenkov, O. Semchenkova, S. Sytchevsky, Computerized system for magnetic measurements over extended field range, Preprint JINR P13-2004-153, Dubna, (2004).
[4] K.N. Henrichsen, Classification of magnetic measurement methods, In: S. Turner (Ed.), Proceedings of the CERN Accelerator School on Magnetic Measurement and Alignment, 16–20 March, 1992, Montreux, Switzerland, pp. 70–83, CERN 92-05, Geneva, 1992.
[5] A. Harvey, Mechanical equipment for magnet measurement and alignment. In: S. Turner (Ed.), Proceedings of the CERN Accelerator School on Magnetic Measurement and Alignment, 16–20 March, Montreux, Switzerland, 1992, pp. 228–239, CERN 92-05, Geneva, 1992.
[6] E.G. Auld, D.L. Livesey, A.J. Otter, N. Rehlinger, The magnetic field survey system for the TRIUMF Cyclotron magnet, in: Proceedings of the 4th International Conference on Magnet Technology, 19–22 September, Upton, New York, 1972, pp. 767–772.
[7] B. Berkes, O. Brombach, O. Szavits, Fast field mapping device for cyclotron magnets, IEEE Transactions on Magnetics, MAG, 17 (5) (1981), pp. 2121–2124.
[8] M. Fan, X. Zhang, T. Zhang, C. Liang, Q. Tao, Z. Chao, C. Chu, T. Li, Y. Hu, Y. Chen, H. Zhang, H. Jia, C. Jiao, J. Liu, W. Zhang, C. Zhou, J. Jiao, Y. Hou, Measurement and adjustment of CIAE medical cyclotron magnet, in: Proceedings of the IEEE Particle Accelerator Conference, vol. 4, 17–20 May, Washington, D.C., 1993, pp. 2841–2843.
[9] G. Yu., A.F. Alenitsky, S.A. Chesnov, L.M. Kostromin, E.V. Onischenko, Samsonov, N.L. Zaplatin, Modeling and forming the magnetic field of the heavy ion cyclotron, Problems of Atomic Science and Technology, series, Nuclear Physics Investigations 43 (2) (2004) 78–80.
[10] Y. Paradis, D. Vandeplassche, W. Beeckman, J.-.L. Delvaux, W. Kleeven, L. Medeiros-Romao, S. Zaremba, J.C. Amélia, F. Salicis, The magnetic field mapping system for the IBA C70 Cyclotron, in: Proceedings of the 18th International Conference on Cyclotrons and their Applications, 1–5 October, 2007, Giardini-Naxos, Sicily, Italy, 2007, pp. 78–80.
[11] K.H. Park, Y.G. Jung, D.E. Kim, B.K. Kang, M. Yoon, J.S. Chai, Y.S. Kim, Field mapping system for cyclotron magnet, Nuclear Instruments and Methods in Physics Research Section A 545 (3) (2005) 533–541.
[12] Group3, DTM-151 DIGITAL TESLAMETER with Serial Communications, User's Manual.
[13] N. Grujić, S. Ćirković, D. Košutić, L. Vukosavljević, R. Balvanović, Results of the second phase of measurements of the VINCY Cyclotron, Internal Report, July 2007.
[14] Andjelija Ž. Ilić, Jasna L. Ristić-Djurović, Saša T. Ćirković, Preliminary results of ion trajectory tracking in the acceleration region of the VINCY Cyclotron, Nuclear Technology and Radiation Protection XXI (1) (2006) 29–33.

IEEE TRANSACTIONS ON

NUCLEAR SCIENCE

A PUBLICATION OF THE IEEE NUCLEAR AND PLASMA SCIENCES SOCIETY

APRIL 2012 VOLUME 59 NUMBER 2 IETNAE (ISSN 0018-9499)

(Contents Continued on Page 249)

IEEE

(Contents Continued from Front Cover)

(Contents Continued on Page 250)

(Contents Continued from Page 249)

RADIATION DAMAGE EFFECTS

RADIATION EFFECTS

RADIATION IMAGING

SCINTILLATION DETECTORS

Enhancement of Ion Beam Acceleration Efficiency in Isochronous Cyclotrons

Andjelija Ž. Ilić, *Member, IEEE*, Jasna L. Ristić-Djurović, Saša Ćirković, and Nebojša Nešković

***Abstract*—A novel method for efficient analysis of ion beam acceleration in an isochronous cyclotron is proposed. Numerical simulation is used to perform multiple beam dynamics analyses on the conveniently chosen subsets of data; consequently, the total quantity of studied data is significantly reduced. The obtained results provide direct insight into beam behavior and quality of acceleration. Therefore, the analysis is not only efficient, but detailed and systematic as well. It is used to assess the impact of the accelerated orbit optimization to the enhancement of acceleration efficiency when study is extended from a single test ion to the complete ion beam consideration.**

***Index Terms*—Acceleration efficiency, cyclotrons, multipurpose, optimal acceleration, particle beam acceptances, particle beam dynamics.**

I. Introduction

ISOCHRONOUS or AVF cyclotrons ("azimuthally varying field" cyclotrons) are currently following one of the two development routes. The manufacturers of commercial cyclotrons, facing market competition, are focused on the constant improvement of the small single purpose machines in terms of performances and price [1]–[3]. At the same time, advanced research centers and radioactive ion beam facilities throughout the world are being equipped by the ever larger and more powerful multipurpose isochronous cyclotrons [4]–[11]. Intended for acceleration of various ion beams in different operation regimes, multipurpose cyclotrons often serve for both research and commercial applications. They are used either separately or as elements in a chain of accelerating structures which deliver high energy ion beams.

The method to achieve optimal acceleration of a test ion in isochronized azimuthally varying magnetic fields, with all the imperfections due to machining, construction and field profile realization constraints, has been suggested in our previous work [12]. Although generally applicable, it is expected to be especially useful in the design of multipurpose machines, requiring the simultaneous optimization of more than one operation mode.

The obtained range of optimal accelerating conditions from [12] corresponds to single test ion acceleration. It is very narrow in comparison with the typical beam emittances and can be matched only by a very small fraction of beam ions. However, with the appropriate choice of the referent test ion, the whole beam acceleration is expected to be optimized as well. Detailed beam tracking is required to assess the impact optimization has on the whole beam acceleration.

We propose to apply an accelerated orbit optimization for a referent test ion to the whole ion beam acceleration, so that the statistical center of a beam bunch coincides with the optimal accelerating conditions. In that case, the average variation of the phase space coordinates from their optimal values would be the least. The acceleration efficiency throughout the beam acceptance region is evaluated in order to quantify the overall impact of such optimization. Analysis efficiency results from the in-depth examination of beam dynamics on the conveniently chosen subsets of the initial six-dimensional phase space coordinates. Namely, numerical simulations offer the benefit of separate analysis on different subsets of data and only subsequent to this the joint interpretation of the results. The measurement systems observe all six phase space dimensions at once, and probably because of that, the beam tracking analyses as well are customarily conducted in the six-dimensional phase space as a whole. The computational power available nowadays allows for comprehensive and accurate beam dynamics simulations. Previous analysis of optimal accelerating conditions in very high intensity beams, employing millions of particles, can be found in [13]–[15]. Our primary goal was to perform accurate and systematic acceleration efficiency study when using a small personal computer. To obtain the accurate results, the coordinate coupling is constantly kept in mind and the data subsets are chosen accordingly. The total quantity of data is thereby significantly reduced, keeping the benefit of providing direct insight into the quality of the acceleration process. Beam acceptance, its distribution with respect to the acceleration efficiency, and the coupling of phase space coordinates are analyzed.

As an illustration of the method, and to yield general insight into the behavior of the beam as a whole, detailed beam tracking is performed for the input parameters corresponding to the VINCY Cyclotron [13] and the 65 MeV H^- test ion. The measured magnetic field used is the same as in [12]; it provides the best obtainable isochronism in the considered magnetic structure with the available ranges of main and trim coil currents [17], [18]. The first harmonic mode of the cyclotron operation corresponds to the H^- test ion acceleration. The accelerating region layout and the main characteristics of the VINCY Cyclotron are given in Fig. 1 and Table I, respectively.

The computer simulations are performed using the ion beam tracking module of the self written VINDY-A software package

Manuscript received November 01, 2011; revised December 13, 2011; accepted December 13, 2011. Date of publication February 07, 2012; date of current version April 13, 2012. This work was supported by the Serbian Ministry of Education and Science through the project "Physics and Chemistry with Ion Beams" (III45006).

The authors are with the Vinča Institute of Nuclear Sciences, Laboratory of Physics (010), 11001 Belgrade, Serbia (e-mail: andjelijailic@ieee.org).

Color versions of one or more of the figures in this paper are available online at http://ieeexplore.ieee.org.

Digital Object Identifier 10.1109/TNS.2011.2180737

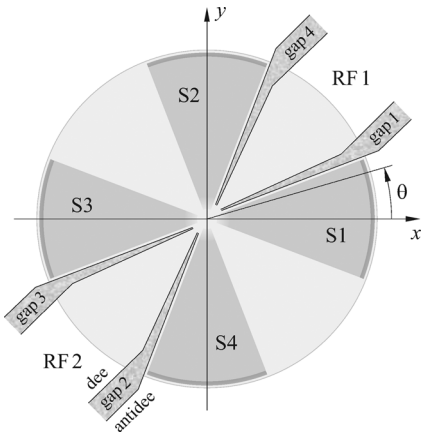

Fig. 1. The layout of the VINCY Cyclotron's accelerating region. Four straight sectors of the multipurpose compact isochronous Cyclotron VINCY are denoted as S1, S2, S3 and S4. Two radiofrequency resonators, denoted as RF1 and RF2, are located in the first and third valley of the VINCY Cyclotron. The average angular distance between the midlines of the accelerating gaps of each resonator equals 41°, allowing the acceleration in the first, second, third and fourth harmonic mode. The beam rotates clockwise, whereas the azimuthal angle θ is measured contraclockwise, as denoted.

TABLE I
MAIN CHARACTERISTICS OF THE VINCY CYCLOTRON

Type	compact isochronous, multipurpose
Ion specific charges	0.15 – 1.00
Number of sectors	4
Sector azimuthal width	42°
Spiral angle	0
Pole diameter	2 m
Maximal magnetic induction in the machine center	1.97 T
Hill gap	36 mm
Valley gap	190 mm
Bending constant	135 MeV
Focusing constant	69 MeV
Number of dees	2
Average angular width of the dee	34°
Aver. angular width of the antidee	48°
RF frequency range	17 MHz – 31 MHz
Harmonic modes	1, 2, 3, 4
Peak RF voltage	100 kV
Injection	spiral inflector
Ion sources	External
Extraction	stripping foil

[12], [19]. The fourth order Runge-Kutta method, with the adaptive time step algorithm, is employed. The calculation accuracy is kept within 1×10^{-5} when the backward tracking and then forward tracking through the complete accelerating region is performed. The beam acceptance analysis implies much wider range of the initial phase space coordinates than is the one corresponding to a typical ion beam bunch in a cyclotron. The particle-particle solver for space-charge effects is thus turned off and ion transmission and the corresponding acceleration efficiency assessed for each of the considered beam ions independently of the others.

II. Optimal Acceleration of a Test Ion

In [12], the ion acceleration is optimized by the adjustment of the radiofrequency (RF) electrode parameters and the accelerating orbit centering. The synchronization between the ion and the accelerating voltage depends on the achievable isochronism of the magnetic field and is addressed by the RF parameters adjustment. Orbit centering reduces the differences between the mean energy increments per gap for different gaps, which in ideal case should be equal. As a first step, the averaged discrepancy between the RF frequency and the gyration frequency is minimized, to account for the gyration frequency fluctuations. Next, the accelerating orbit is centered using the hard edge gap approximation with the numerical integration of the gap energy gains. The static equilibrium orbit (SEO) is taken as the initial guess at the large radii. A single iteration of this single turn centering is sufficient, contributing to the efficiency of the method. The optimal RF phase curve is then calculated, taking into account that a part of the RF phase fluctuations is induced by the insufficient isochronism and thus unavoidable. To separate it from the fluctuations due to improper trajectory centering or poor synchronization with the accelerating voltage, we assume the ideal acceleration during which the test ion moves along the SEOs and jumps from one SEO to another at the midlines of the accelerating gaps. With such an approximation, the impact of the unavoidable level of fluctuations is minimized by reducing the averaged RF phase deviation from nominal value for a considered azimuth. The optimized orbit obtained using these three steps is not unique; instead the method results in a number of accelerated orbits providing excellent quality of acceleration.

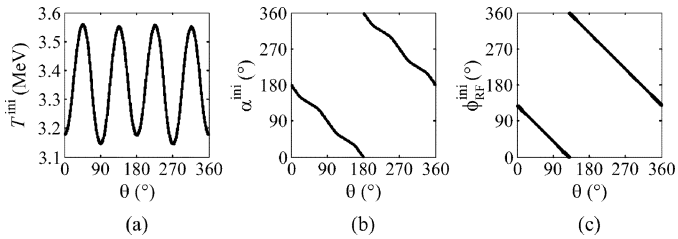

Fig. 2. The complete sets of initial conditions yielding the optimal acceleration of the H^- test ion in the VINCY Cyclotron. (a) The optimal initial energy, $T^{\rm ini}$. (b) The optimal initial momentum vector direction angle, $\alpha^{\rm ini}$, measured clockwise with respect to the positive y-axis. (c) The optimal initial RF phase, $\phi^{\rm ini}_{\rm RF}$. For the considered radius $R_{\rm a}$ and an arbitrary azimuth θ, the phase space coordinates in the median plane of a cyclotron resulting in optimal acceleration are obtained by interpolation from the sets' elements. What appears to be a thick curve in each part of the figure is actually a strip; instead of a single value a range of acceptable values for each initial parameter is obtained for every azimuthal position. The method for defining the complete continuous sets of input parameters shown above is explained in [12].

III. Initial Conditions

The optimization procedure has been shown to be highly accurate and very efficient, and it is also fully automatized. For a given test ion, the corresponding magnetic field and harmonic mode of the cyclotron operation, the complete sets of optimal accelerating conditions at the beginning of the accelerating region are defined. The radius $R_{\rm a}$ denotes the beginning of the accelerating region. It is chosen so that the ion beam dynamics at larger radii is not affected by the possible electrode configuration changes in the central region. Fig. 2 shows optimal initial conditions for the 65 MeV H^- test ion, for $R_{\rm a} = 200\,{\rm mm}$. The phase space coordinates for an arbitrary azimuth θ are obtainable by interpolation from the sets' elements, which cover the

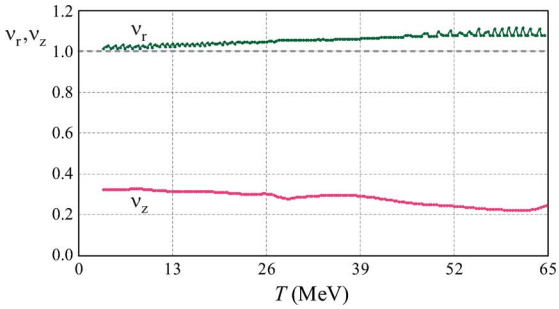

Fig. 3. Betatron tunes vs. energy in tracking along the chosen accelerated orbit. The variation of betatron oscillation frequencies during the acceleration confirms that the initial conditions for acceleration are properly chosen. The coupling between the radial and vertical oscillation modes $\nu_r = 5 \cdot \nu_z$ is quickly traversed at about 44 MeV. There are no dangerous resonant conditions.

range from zero to 360°. Here we take $\theta = 15°$, as this azimuth does not coincide with any distinctive initial azimuth, such as the edge or the midline of the magnetic sector, the midline of the valley, the accelerating gap, etc. The chosen accelerated orbit is therefore representing the majority of the optimized accelerated orbits corresponding to the initial coordinates shown in Fig. 2. Betatron tunes during the acceleration along the chosen orbit are calculated and the results shown in Fig. 3 verify that no severe problems due to the coupling resonances are to be expected.

IV. Accelerating Region Acceptances

The six-dimensional phase space volume of the ion beam emittance or the accelerating structure acceptance can not be visualized in a simple and comprehensible manner. The ion beam emittance, i.e., the phase space region occupied by the beam bunch, is usually represented by the two-dimensional distributions of particles obtained as the emittance projections to the radial, axial and longitudinal phase plane. It is not convenient to use the same approach for the representation of the structure acceptance, i.e., the range of permissible phase space coordinates resulting in the ion transmission through the structure. To keep the information on the coordinate coupling, we use the six-dimensional phase space volume cross sections resembling the "slices of the volume", instead.

The phase space coordinates are denoted as Δr, p_r , Δz, p_z , $\Delta\phi$, and ΔT, corresponding to the ion position vector and ion momentum vector angle components in the radial and axial direction, relative to the central ion, to the ion phase relative to the central ion phase, and to the kinetic energy relative to the central ion kinetic energy, respectively. The ion phase, $\Delta\phi$, is measured in the direction of motion. The beam acceptance cross sections with the radial, Δr-p_r, axial, Δz-p_z, and longitudinal, $\Delta\phi$-ΔT, phase plane, with the other four phase space coordinates coinciding with the corresponding central ion ones, are called the decoupled radial, axial and longitudinal acceptances. They are shown in Fig. 4. The corresponding Twiss parameters as well as the acceptance statistics are given in Table II.

Almost perfect centeredness of all the particles belonging to the decoupled acceptances about the origins of the three phase space planes in Fig. 4 verifies that the chosen accelerated orbit of a referent, central particle is indeed the optimal one. The acceleration efficiency of an ion is measured by its averaged energy gain per accelerating gap, $\overline{\Delta T_{\rm gap}}$, as in [12]. It is calculated for every point belonging to the decoupled acceptances and the resulting accelerating region acceptance distribution with respect to the acceleration efficiency is shown in Fig. 5.

TABLE II
Twiss Parameters and Beam Acceptance Statistics for the Decoupled Accelerating Region Acceptances

Twiss Parameters *				
	α (1)	β (u_x/u_{p_x})	γ (u_{p_x}/u_x)	ε ($\pi \cdot u_x \cdot u_{p_x}$)
RADIAL	0.35	0.24	4.71	$3.19 \cdot 10^3$
AXIAL	-0.12	0.60	1.70	123.35
LONGITUDINAL	-0.26	$6.56 \cdot 10^{-3}$	$0.16 \cdot 10^3$	$5.11 \cdot 10^3$
Beam Acceptance Statistics *				
	$\overline{\Delta x}$ (u_x)	$\overline{p_x}$ (u_{p_x})	$\sigma_{\Delta x}$ (u_x)	σ_{p_x} (u_{p_x})
RADIAL	0.00	2.86	24.44	108.52
AXIAL	0.00	0.00	7.61	12.84
LONGITUDINAL	-1.01	141.35	5.11	806.92

* The longitudinal units u_x and u_{p_x} are given in degrees and keV; the corresponding radial and axial units are mm and mrad, respectively. In the radial, axial and longitudinal direction the pair $(\Delta x, p_x)$ corresponds to the coordinate pair $(\Delta r, p_r)$, $(\Delta z, p_z)$ and $(\Delta\phi, \Delta T)$, respectively.

The axial particle motion in an isochronous cyclotron is usually decoupled from both the radial and longitudinal motion, as shall be proven explicitly in the following sections. The axial acceptance area shown in Figs. 4 and 5, obtained for the optimal values of other four phase space coordinates, is the largest and beam ions outside of this area shall under no conditions reach the radius of extraction. It is limited by the small vertical distance between the sectors of the cyclotron magnet. The radial and longitudinal acceptance, on the other hand, are determined by the insufficient focusing or lost synchronization. As a result, the axial acceptance is small, while the acceleration efficiency is excellent for all the ions.

The acceleration efficiency is very good for about half of the transmitted beam ions in the radial and in the longitudinal phase plane. It is excellent ($\overline{\Delta T_{\rm gap}} \geq 22.2$ keV) for about 10% of the input phase space coordinates in the center of the acceptance area for both phase space planes. Having in mind the usual beam emittances of the considered test ion in the VINCY Cyclotron [20]–[22], the following may be concluded. The axial emittance at the beginning of the accelerating region fits in the Δz and p_z coordinate ranges of ± 6 mm and ± 10 mrad, respectively; thus, it is much smaller than the corresponding beam acceptance. Even with the decrease in the acceptance area due to the deviations of other phase space parameters, the axial ion beam dynamics should still represent no problem at all. The radial ion beam emittance, with Δr and p_r within ± 10 mm and ± 20 mrad, respectively, allows for an excellent matching unless impeded by the inflector system or the central region design restrictions. The same holds true for the usual energy range at this point, ± 0.25 MeV; however, the input ion beam phase deviation with respect to the phase of an accelerating RF voltage is much wider than the $\pm 5.5°$ phase interval seen to result in the best acceleration efficiency according to Fig. 5. It fits in the range of $\pm 25°$. Due to the suboptimal accelerating conditions a part of

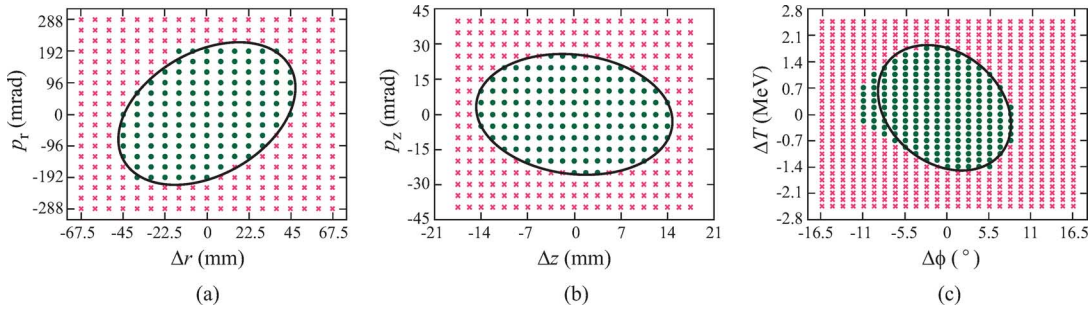

Fig. 4. Beam acceptance cross sections with the radial (a), axial (b) and longitudinal (c) phase plane, corresponding to the 65 MeV H^- ion beam motion in the accelerating region of the VINCY Cyclotron. The phase space coordinates belonging to the decoupled accelerating region acceptances are shown as green dots, whereas the other input guesses for the beam trajectory tracking simulation appear as red crosses. The origin of the six-dimensional phase space corresponds to the optimal initial conditions for acceleration shown in Fig. 2. The phase ellipses shown are determined so, as to best encompass the simulation results. Note that the accelerating region axial acceptance is about 25 times smaller than the radial acceptance.

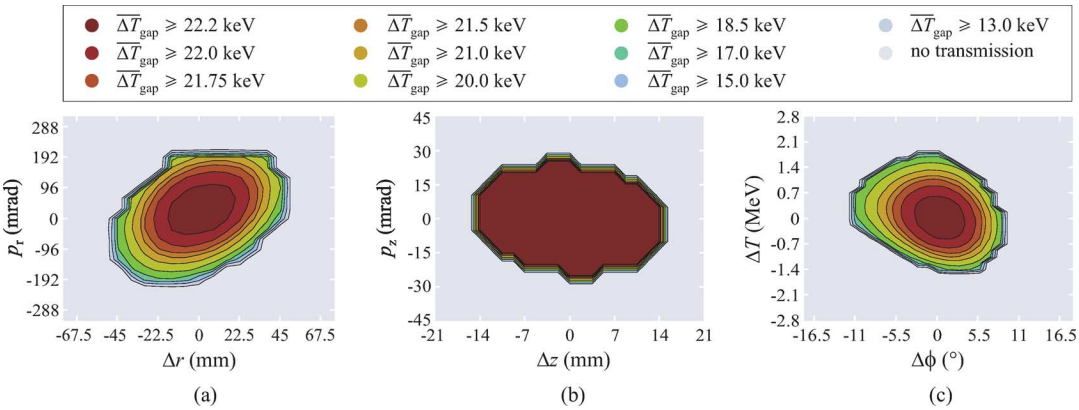

Fig. 5. The accelerating region acceptance distribution with respect to the acceleration efficiency for the 65 MeV H^- ion beam. The acceleration efficiency, measured by the averaged energy gain per accelerating gap, $\overline{\Delta T_{gap}}$, is excellent for about 10% of input phase space coordinates in the center of the acceptance area in the radial phase plane (a) and in the longitudinal phase plane (c). However, all of the input phase space coordinates in the axial phase plane, belonging to the acceptance area, are characterized by excellent acceleration efficiency (b). The latter is due to the small vertical distance between the sectors of the cyclotron magnet preventing the transmission of beam ions, as opposed to the insufficient focusing and synchronization responsible for stopping of beam ions in the other two cases. For the same reason, the accelerating region axial acceptance is significantly smaller than the radial acceptance.

the beam ions might lose synchronization with the accelerating voltage and leave the beam bunch.

V. Coupling of the Phase Space Coordinates

In order to completely describe the six-dimensional beam acceptance ellipsoid we need to analyze the two-dimensional phase space volume cross sections corresponding to different nonzero combinations of other four phase space coordinates. The range of input guesses shown in Figs. 4 and 5 for the beam trajectory tracking is wide enough for the investigation of coordinate coupling. Randomly chosen initial phase space coordinates, as well as a reasonable number of equidistant ones, require an extremely lengthy simulation to provide enough data for the desired analysis. Moreover, a huge quantity of data resulting from such analysis is unnecessary. The radial acceptance is of a particular interest to the adjustment of initial conditions for acceleration. The radial emittance of an incoming ion beam bunch needs to be matched with the radial acceptance at a considered point. The initial range of input ion beam phase deviations can be reduced by introducing the ion beam buncher and ion beam chopper in the vertical channel guiding the ion beam to the spiral inflector. The initial energy range mostly depends on the characteristics of the ion source employed. Because of the axial symmetry, the optimal initial conditions will always be in the median plane of a cyclotron. Therefore, the influence of other phase space coordinates to the radial acceptance and the acceleration efficiency in the radial phase plane has been investigated. For each of the parameters, equidistant initial guesses are taken, i.e., the distribution of test ions at start is uniform. The total number of initial guesses for the beam trajectory tracking is thus greatly reduced without any loss of relevant information.

Fig. 6 shows the influence of ion energy, its phase with respect to the RF voltage, axial position and axial momentum to the radial accelerating region acceptance. For a change in ion energy in the vicinity of optimal initial conditions from Fig. 2 the corresponding shift of the phase space ellipse is almost linear. In the first approximation, it is given by:

$$\Delta r^{\mathrm{cen}} = 28.6 \cdot \Delta T, \quad p_{\mathrm{r}}^{\mathrm{cen}} = 2.86 + 16.0 \cdot \Delta T, \qquad (1)$$

with the coordinates of the phase space ellipse center, Δr^{cen} and $p_{\mathrm{r}}^{\mathrm{cen}}$, given in mm and mrad, and ion energy deviation ΔT in MeV. Parameters Δr^{cen} and $p_{\mathrm{r}}^{\mathrm{cen}}$ are obtained as the statistical mean values of the coordinates within the acceptance area.

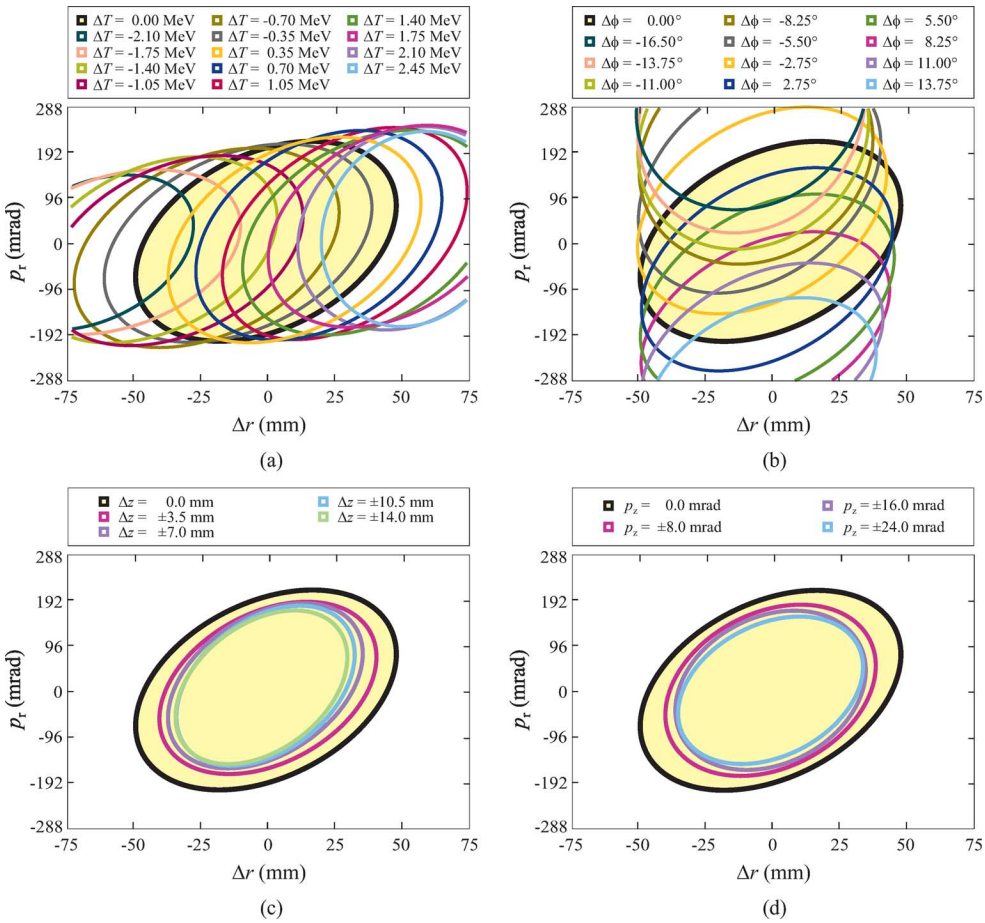

Fig. 6. The coupling of the accelerating region radial acceptance with other four phase space coordinates. The deviations from the optimal values of ion energy (a) or its phase with respect to the accelerating radiofrequency voltage (b), denoted by ΔT and $\Delta\phi$, lead to the almost linear shifts of the phase space ellipse defining the radial acceptance. The change of the phase space ellipse position is accompanied by very small variations in the ellipse shape and orientation, as well as the decrease in size of the acceptance area. The deviations from the optimal values of axial position (c) or axial momentum (d) of an ion, Δz and p_z , respectively, do not cause any significant changes of the phase space ellipse position, shape, or orientation, but the decrease in size of the acceptance area is pronounced. Therefore, the radial motion of an ion is not influenced by its axial motion, whereas the decrease of six-dimensional acceptance is the direct consequence of the accelerating region axial acceptance.

TABLE III
THE RADIAL ACCEPTANCE TWISS PARAMETERS DEPENDENCE ON ION ENERGY

ΔT (MeV)	α (1)	β ($\frac{\text{mm}}{\text{mrad}}$)	γ ($\frac{\text{mrad}}{\text{mm}}$)	ε (π·mm·mrad)
-1.05	0.3142	0.3930	2.7958	2.7563
-0.70	0.3232	0.3396	3.2521	3.1592
-0.35	0.3177	0.2770	3.9743	3.2134
0.00	0.3491	0.2384	4.7057	3.1876
0.35	0.3599	0.2513	4.4949	3.1607
0.70	0.3672	0.2887	3.9305	3.1585
1.05	0.3693	0.3353	3.3896	3.1351

The acceptance ellipse size, shape and slope change slightly as illustrated by the data in Table III.

Similarly, the ion phase deviation, $\Delta\phi$, with respect to the accelerating RF voltage leads to the almost linear shift of the phase space ellipse defining the radial acceptance:

$$\Delta r^{\text{cen}} \approx 0\,, \quad p_{\text{r}}^{\text{cen}} = 2.86 - 20.6 \cdot \Delta\phi, \qquad (2)$$

TABLE IV
THE RADIAL ACCEPTANCE TWISS PARAMETERS DEPENDENCE ON ION PHASE DEVIATION

$\Delta\phi$ (°)	α (1)	β ($\frac{\text{mm}}{\text{mrad}}$)	γ ($\frac{\text{mrad}}{\text{mm}}$)	ε (π·mm·mrad)
-5.50	0.0539	0.1550	6.4706	3.1066
-2.75	0.2554	0.2030	5.2479	3.1831
0.00	0.3491	0.2384	4.7057	3.1876
2.75	0.3853	0.2181	5.2657	3.0111
5.50	0.2947	0.1689	6.4355	2.9686

with Δr^{cen} and $p_{\text{r}}^{\text{cen}}$ in mm and mrad, and $\Delta\phi$ in degrees. The comparison of Twiss parameters α, β, γ and ε, for several values of phase deviation is given in Table IV.

The analysis of the accelerating region radial acceptance coupling with the axial position and axial momentum gives qualitatively different results. There are no significant changes of the phase space ellipse position, shape, or orientation, but the decrease in size of the acceptance area as a consequence of the decreased axial acceptance is pronounced. The corresponding Twiss parameters for different values of Δz and p_z are given in Tables V and VI, respectively.

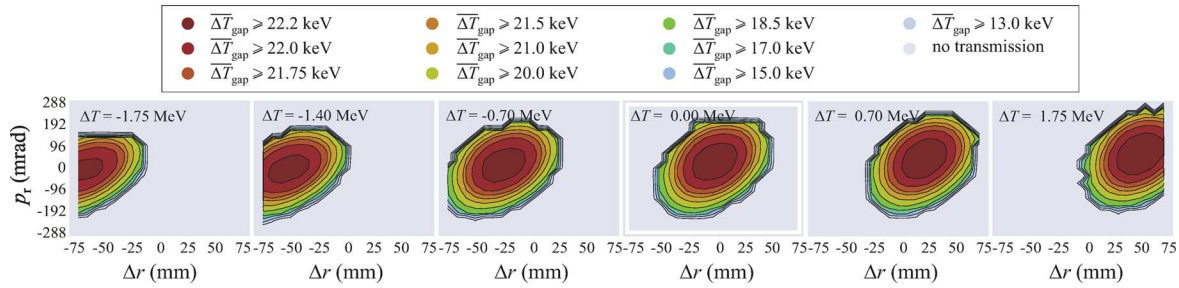

Fig. 7. The ion energy influence on the acceleration efficiency distribution over the radial acceptance. With an increase in ion energy, $\Delta T > 0$, there is no reduction in size of the acceptance area characterized by the largest acceleration efficiency. The set of coordinate pairs in the radial phase plane, $(\Delta r, p_r)$, which corresponds to the most efficient acceleration varies in accordance with the phase space ellipse shifts. The decrease in ion energy, $\Delta T < 0$, leads to the significant reduction in size of the most efficiently accelerated part of the acceptance, as well as to the decrease of overall radial acceptance. Therefore, ion energy lower than the optimal one cannot be accounted for merely by the convenient choice of radial phase space coordinates.

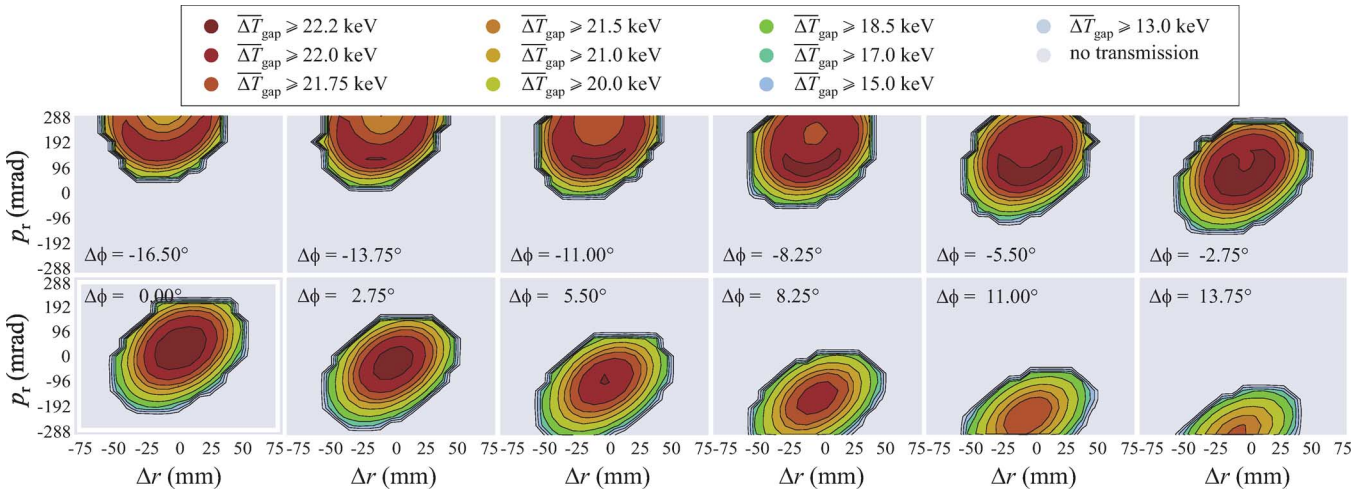

Fig. 8. The ion phase deviation influence on the acceleration efficiency distribution over the radial acceptance. Positive values of the ion phase offset, $\Delta\phi$, correspond to the ions leading in comparison with $\Delta\phi = 0$, whereas for $\Delta\phi < 0$ ions are lagging. Regardless of the sign of $\Delta\phi$, a decline of acceleration efficiency is considerable, rapid, and much more pronounced than the corresponding decrease of radial acceptance. The findings confirm that ion phase offset has the major influence on acceleration efficiency in cyclotrons.

TABLE V
THE RADIAL ACCEPTANCE TWISS PARAMETERS DEPENDENCE ON AXIAL POSITION

Δz (mm)	α (1)	β ($\frac{mm}{mrad}$)	γ ($\frac{mrad}{mm}$)	ε (π·mm·mrad)
0.0	0.3491	0.2384	4.7057	3.1876
±3.5	0.3574	0.2386	4.7264	2.1926
±7.0	0.4139	0.2314	5.0609	2.0036
±10.5	0.3343	0.2142	5.1901	1.8718
±14.0	0.3599	0.2311	4.8880	1.7219

TABLE VI
THE RADIAL ACCEPTANCE TWISS PARAMETERS DEPENDENCE ON AXIAL MOMENTUM

p_z (mrad)	α (1)	β ($\frac{mm}{mrad}$)	γ ($\frac{mrad}{mm}$)	ε (π·mm·mrad)
0.0	0.3491	0.2384	4.7057	3.1876
±8.0	0.3170	0.2339	4.7057	2.1442
±16.0	0.3093	0.2107	5.1997	1.8983
±24.0	0.3611	0.2364	4.7817	1.7281

VI. INFLUENCE OF THE COUPLED INPUT PARAMETERS ON THE ACCELERATION EFFICIENCY

The key question when assessing the quality of acceleration is how much the changes in the coupled input parameters influence the acceleration efficiency. Fig. 7 shows that the increase in ion energy with respect to the optimal value results solely in the acceptance shift according to (1). However, the decrease in energy causes the reduction in size of the radial phase space area with the best acceleration efficiency. Fig. 8 demonstrates that the ion phase deviation, $\Delta\phi$, leads to the very pronounced deterioration in the acceleration efficiency, regardless of the sign of $\Delta\phi$. The overall decrease in the acceleration efficiency is larger than 10% for $\Delta\phi = \pm 5.5°$. As shown in Fig. 9, the axial parameters have no impact on the acceleration efficiency in the radial phase space plane.

The presented analysis presumes a uniform distribution of particles in each of the six dimensions of a phase space. It is convenient since the distribution of ions within a beam bunch differs from case to case. Knowledge of the ion distribution for a particular case, along with the system acceptance for the uniform distribution, enables optimization of the beam parameters. It may happen that the central particle is not the one best suited

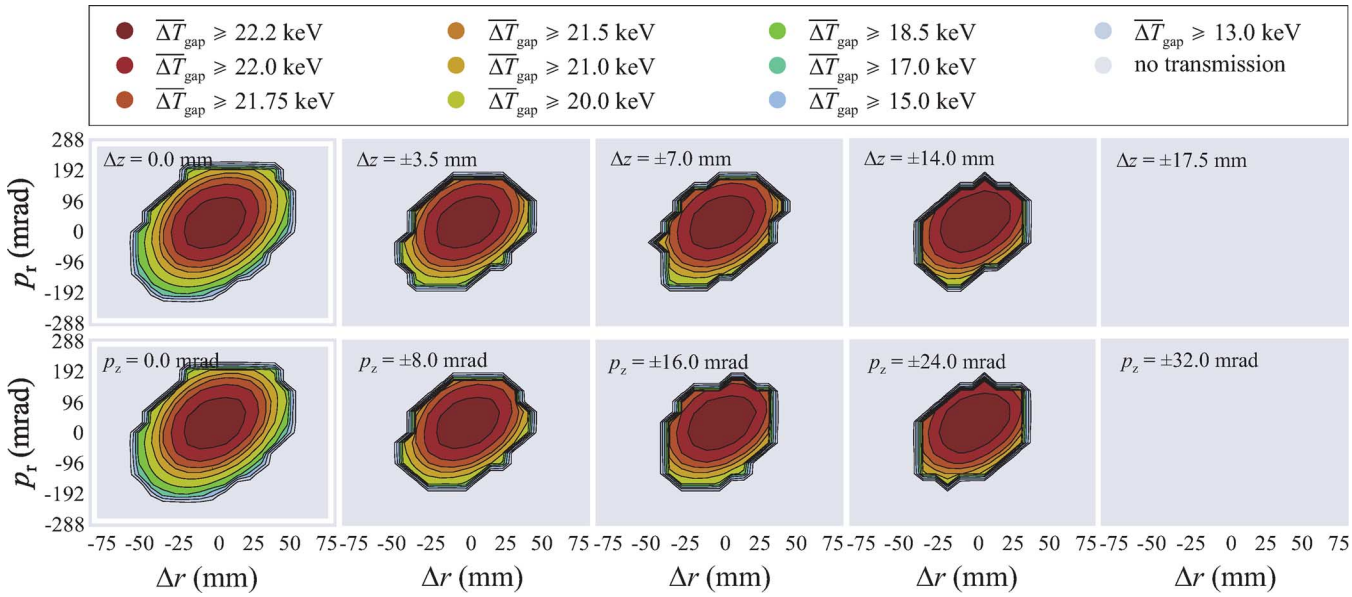

Fig. 9. The influence of the axial phase plane coordinates on the acceleration efficiency distribution over the radial acceptance. Acceleration efficiency within the radial acceptance, is influenced by neither the axial position, Δz, (top), nor by the axial momentum, p_z, (bottom). The area in the center of radial acceptance, corresponding to the excellent acceleration efficiency, is conserved with changes of both Δz and p_z , as long as the acceleration to the extraction energy is achievable. Beam ions characterized by lower values of acceleration efficiency are lost first, with the increase in magnitude of Δz or p_z .

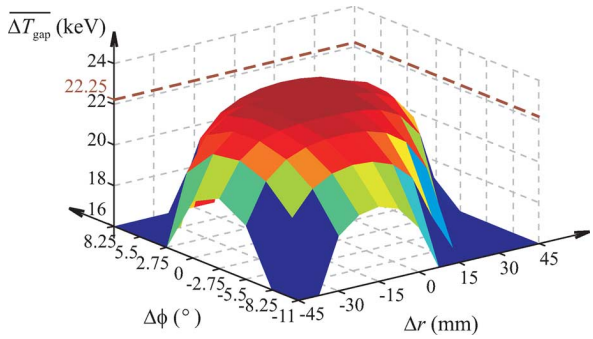

Fig. 10. The influence of the RF phase offset and orbit decentering on the acceleration efficiency. The acceleration efficiency for the 65 MeV H^- test ion is the highest and almost constant for $-20\ \text{mm} < \Delta r < 20\ \text{mm}$ and $-4° < \Delta\phi < 4°$. With further offset in the particle – RF voltage synchronization or larger orbit decentering, the acceleration efficiency rapidly decreases. While the radial dimension of the ion beam is usually much smaller than the acceptable range of Δr, the phase width of the accelerated test beam bunch is typically wider than its optimal range. This is why the RF phase offset is most often the critical parameter linked to the deterioration of acceleration efficiency.

for the accelerated orbit matching, i.e., that some other particle should be the referent one.

VII. Influence of the RF Phase Offset and Orbit Decentering on the Acceleration Efficiency

The obtained data can be further exploited to analyze the influence of the RF phase offset and orbit decentering on the acceleration efficiency. The upper limit of orbit decentering may be estimated as the initial radial deviation, Δr, for the ion trajectories characterized by the initial radial momentum $p_r = 0$. The RF phase offset is estimated by the initial beam ion phase deviation, $\Delta\phi$. The results shown in Fig. 10 emphasize once again the critical impact of input range of phase deviations to the acceleration efficiency in an isochronous cyclotron. The radial dimension of the ion beam is usually much smaller than the acceptable beam decentering. A proper choice of initial conditions for acceleration can reduce the first problem and fully account for the second one.

VIII. Coupling of All Six Phase Space Coordinates

Finally, for the sake of completeness and to confirm the above conclusions, the accelerating region acceptances have been analyzed using the randomly chosen input phase space coordinates for beam tracking. The range of input guesses is the same as in previous analysis, i.e., as in Figs. 4 and 5. Beam tracking analysis has been performed on a total of 20 000 ions, a number chosen to be comparable with the sum of 18 410 ions used in all the previous calculations together.

The six-dimensional beam acceptance projections to the radial, axial and longitudinal phase planes are shown in Fig. 11. The coupling between the motions in different directions can be analyzed, finding the particular ranges of input phase space coordinates shown in parts (a) and (c) in different symbols. As seen before, changes in only ΔT or only $\Delta\phi$ in the vicinity of optimal initial conditions, lead to almost linear shifts of the radial phase space ellipse given by (1) and (2). Due to such coupling of coordinates, projections of the six-dimensional acceptance are spread throughout the radial and the longitudinal phase planes. An excellent agreement of the axial acceptance projection and the decoupled axial acceptance verifies that the axial motion is decoupled from the other two. The equal distribution of the large dots in Fig. 11, whether they are surrounded by the green squares or not, testifies that the radial or longitudinal motion are not affected by the axial phase space coordinates either.

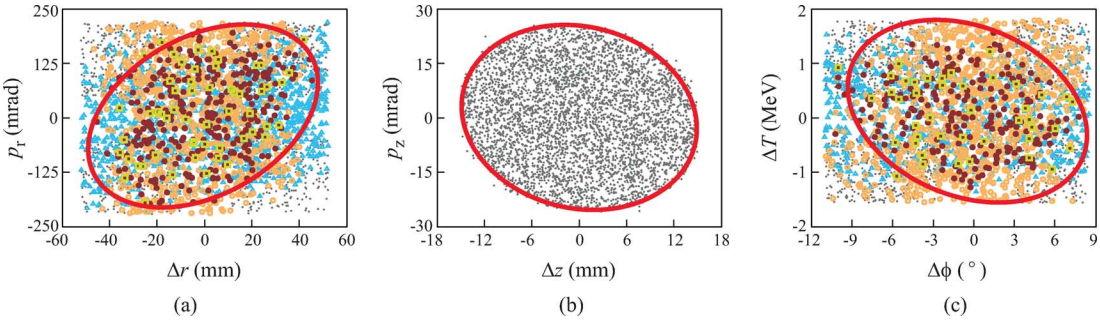

Fig. 11. Coupling between the radial (a), axial (b) and longitudinal (c) motion in the accelerating region of the VINCY Cyclotron. The agreement between the axial projection of the six-dimensional acceptance represented by dots and the decoupled axial acceptance ellipse from Fig. 4 is excellent (b), verifying that the axial motion is decoupled from the motion in radial and longitudinal directions. The other two motions are mutually coupled. The conditions $\Delta r \in \delta_{\mathrm{r}}$, $p_{\mathrm{r}} \in \delta_{\mathrm{P_r}}$, $\Delta z \in \delta_{\mathrm{z}}$, $p_{\mathrm{z}} \in \delta_{\mathrm{P_z}}$, $\Delta\phi \in \delta_{\phi}$, and $\Delta T \in \delta_{\mathrm{T}}$, are approximated by $-10\,\mathrm{mm} < \Delta r < 10\,\mathrm{mm}$, $-50\,\mathrm{mrad} < p_{\mathrm{r}} < 50\,\mathrm{mrad}$, $-5\,\mathrm{mm} < \Delta z < 5\,\mathrm{mm}$, $-8\,\mathrm{mrad} < p_{\mathrm{z}} < 8\,\mathrm{mrad}$, $-2.75 < \Delta\phi < 2.75°$, and $-350\,\mathrm{keV} < \Delta T < 350\,\mathrm{keV}$, respectively. Blue triangles and orange circles correspond to $\Delta\phi \in \delta_{\phi}$ and $\Delta T \in \delta_{\mathrm{T}}$ in part (a), and to $\Delta r \in \delta_{\mathrm{r}}$ and $p_{\mathrm{r}} \in \delta_{\mathrm{P_r}}$ in part (c). In part (a) they depict the radial phase ellipse movements defined by (1) and (2). Fulfillment of both conditions, shown by the large dark violet dots, defines the corresponding decoupled acceptances and completely agrees with the solid line ellipses copied from Fig. 4. Additionally, the ions complying with $\Delta z \in \delta_{\mathrm{z}}$ and $p_{\mathrm{z}} \in \delta_{\mathrm{P_z}}$ as well are represented by the green squares. Their equal distribution throughout the corresponding phase space ellipses validates the assumption that the axial phase plane coordinates exhibit no influence to radial and longitudinal motion.

The axial phase plane is therefore fully decoupled from the other two planes.

IX. Conclusion

The novel method for detailed, systematic and efficient beam tracking analysis has been described. Its main benefit lies in the capability to obtain a lot of relevant results with a very limited quantity of input data. Separate analyses on the conveniently chosen subsets, i.e., subspaces, of input phase space coordinates were used. Care is taken to interpret the results correctly by accounting for the coordinate coupling. All the results in Sections III–V were obtained from beam tracking analyses on a total of 18 410 ions. However, they give much better insight into the improvement of the quality of acceleration than the results of Section VI, obtained with the total of 20 000 randomly chosen initial phase space coordinates.

It is confirmed that the ion beam motion in the axial phase plane is fully decoupled from both the radial and longitudinal motions. Further, it is shown that all of the beam ions within the axial acceptance have excellent acceleration efficiency. Axial input beam parameters do have impact on the beam ion transmission for those ions whose radial or longitudinal initial phase coordinates are non-optimal.

The acceleration efficiency for the 65 MeV $\mathrm{H^-}$ test ion is excellent ($\overline{\Delta T}_{\mathrm{gap}} \geq 22.2\,\mathrm{keV}$) for about 10% of the input phase space coordinates in the center of the decoupled acceptance area for both radial and longitudinal phase space planes. Therefore, although the range of optimal accelerating conditions for the referent particle, shown in Fig. 2, is relatively narrow, the regions of the phase space planes characterized by the excellent acceleration efficiency are very wide. For five out of six phase space coordinates the six-dimensional ion beam acceptance is wide enough to completely optimize the acceleration process. Only the RF phase range of accelerated beam is wider than the phase interval seen to result in the best acceleration efficiency.

The coupling of the phase space coordinates has been investigated from the point of view of the influence on the radial acceptance and the acceleration efficiency in the radial phase plane of the other four phase space coordinates. It is of a particular interest to know the effects of coupling on the radial acceptance in order to adjust the radial emittance of an incoming ion beam bunch. It has been shown that changes in ion energy or ion phase deviation in the vicinity of optimal initial conditions lead to almost linear shifts of the radial phase space ellipse. The radial phase space area corresponding to the excellent acceleration efficiency is significantly reduced for the ion energy smaller than the optimal. The ion phase deviation leads to the very pronounced overall deterioration in the acceleration efficiency, whether an ion is leading or lagging. For the phase deviation of $\pm 5.5°$, the overall decrease in the acceleration efficiency is larger than 10%.

The presented detailed analysis confirms that the method proposed in [12] is of a great importance for improvement of the quality of acceleration in an isochronous cyclotron. The accelerating region acceptance distribution with respect to the acceleration efficiency allows for optimal acceleration of the most of beam ions.

References

[1] Y. Jongen *et al.*, "High-intensity cyclotrons for radioisotope production and accelerator driven systems," *Nucl. Phys. A*, vol. 701, pp. 100c–103c, Apr. 2002.

[2] R. R. Johnson *et al.*, "Advances in intense beams, beam delivery, targetry, and radiochemistry at advanced cyclotron systems," *Nucl. Instrum. Methods Phys. Res. B*, vol. 261, no. 1–2, pp. 803–808, Aug. 2007.

[3] A. M. J. Paans, "Compact cyclotrons for the production of tracers and radiopharmaceuticals," *Int. J. Nucl. Res. NUKLEONIKA*, vol. 48, no. Suppl. 2, pp. s169–s172, 2003.

[4] M. Duval, M. P. Bourgarel, and F. Ripouteau, "New compact cyclotron design for SPIRAL," *IEEE Trans. Magn.*, vol. 32, no. 4, pp. 2194–2196, Jul. 1996.

[5] R. E. Tribble *et al.*, "A facility upgrade at Texas A&M University for accelerated radioactive beams," *Euro. Phys. J.–ST*, vol. 150, no. 1, pp. 255–258, Nov. 2007.

[6] R. C. York *et al.*, "Proposed upgrade of the NSCL," in *Proc. IEEE Particle Accelerator Conf.*, 1995, vol. 1, pp. 345–347.

[7] S. Kurashima *et al.*, "Developments at JAEA AVF cyclotron facility for heavy-ion microbeam," in *Proc. 18th Int. Conf. Cyclotrons and Their Applications*, Catania, Italy, 2008, pp. 131–133.

[8] B. N. Gikal *et al.*, "DUBNA Cyclotrons – status and plans," in *Proc. 17th Int. Conf. Cyclotrons and Their Applications*, Tokyo, Japan, 2005, pp. 100–104.

[9] S. Brandenburg, "The superconducting cyclotron AGOR: Accelerator for light and heavy ions," in *1987 Proc. IEEE Particle Accelerator Conf.*, Washington, DC, 1987, pp. 376–378.
[10] D. Rifuggiato, L. Calabretta, and G. Cuttone, "Ten years of operation with the LNS superconducting cyclotron," in *Proc. 17th Int. Conf. Cyclotrons and Their Applications*, Tokyo, Japan, 2005, pp. 118–120.
[11] M. Fukuda *et al.*, "Design studies of the K900 JAERI superconducting AVF cyclotron for the research in biotechnology and materials science," in *Proc. 16th Int. Conf. Cyclotrons and Their Applications*, New York, 2001, pp. 189–191.
[12] A. Ž. Ilić, J. L. Ristić-Djurović, S. Ćirković, A. Dobrosavljević, and N. Nešković, "Optimal acceleration in isochronous straight sector cyclotrons," *IEEE Trans. Nucl. Sci.*, vol. 56, no. 3, pp. 1498–1506, Jun. 2009.
[13] A. Adelmann *et al.*, "The object oriented parallel accelerator library (OPAL), design, implementation and application," in *Proc. Int. Computational Accelerator Physics Conf.*, San Francisco, CA, 2009, pp. 107–110.
[14] Y. J. Bi *et al.*, "Challenges in simulating MW beams in cyclotrons," in *Proc. 46th ICFA Advanced Beam Dynamics Workshop*, Morschach, Switzerland, 2010, pp. 295–299.
[15] Y. J. Bi *et al.*, "Towards quantitative simulations of high power proton cyclotrons," *Phys. Rev. ST, Accel. Beams*, vol. 14, no. 5, pp. 054402-1–9, May 2011.
[16] N. Nešković *et al.*, "Status report of the VINCY Cyclotron," *Int. J. Nucl. Res. NUKLEONIKA*, vol. 48 (Suppl. 2), pp. s135–s139, 2003.
[17] S. Ćirković, J. L. Ristić-Djurović, A. Ž. Ilić, V. Vujović, and N. Nešković, "Comparative analysis of methods for isochronous magnetic field calculation," *IEEE Trans. Nucl. Sci.*, vol. 55, no. 6, pp. 3531–3538, Dec. 2008.
[18] N. Grujić, S. Ćirković, D. Košutić, L. Vukosavljević, and R. Balvanović, "Results of the second phase of measurements of the VINCY Cyclotron," Internal Rep., Jul. 2007.
[19] A. Ž. Ilić, J. L. Ristić-Djurović, and S. T. Ćirković, "Preliminary results of ion trajectory tracking in the acceleration region of the VINCY Cyclotron," *Nucl. Technol. Radiat. Protect.*, vol. 21, no. 1, pp. 29–33, Jun. 2006.
[20] P. Beličev *et al.*, "Ion beam dynamics in the central region of the VINCY Cyclotron," in *Proc. 34th Euro. Cyclotron Progress Meeting*, Belgrade, Serbia, Oct. 6–8, 2005.
[21] P. Beličev *et al.*, "VINCY Cyclotron H^- ion beam dynamics: A new spiral inflector and the midplane acceleration," Internal Rep., Feb. 2006.
[22] E. E. Perepelkin *et al.*, "Ion beam dynamics in the VINCY Cyclotron," in *Proc. 35th Euro. Cyclotron Progress Meeting*, Nice, France, Nov. 2–5, 2006.

Biomagnetic Priming—Possible Strategy to Revitalize Old Mustard Seeds

Jelena Jovičić-Petrović,[1] Vera Karličić,[1]* Ivana Petrović,[1] Saša Ćirković,[2] Jasna L. Ristić-Djurović,[2] and Vera Raičević[1]

[1]*Faculty of Agriculture, University of Belgrade, Belgrade, Serbia*
[2]*Institute of Physics, University of Belgrade, Belgrade, Serbia*

Different priming methods were developed to improve seed germination and the early growth of seedlings. This study aimed to examine the combined effect of bacterial inoculation and static magnetic field on white mustard (*Sinapis alba* L.) germination. A plant growth-promoting bacterial strain *Bacillus amyloliquefaciens* D5 ARV was used for biopriming. The static magnetic field of 90 mT was applied for 5 and 15 min. Analyses of abscisic acid, chlorophyll, anthocyanins, flavonoids content, nitrogen balance index, and bacterial indole-3-acetic acid were used to explain observed effects. Bacterial inoculation improved seed germination, whereas exposure to 90 mT for 15 min suppressed germination. Such an unfavorable effect was neutralized when the treatment with the static magnetic field was combined with bacterial inoculation. The highest germination percentage was a result of synergistic action of *B. amyloliquefaciens* D5 ARV and 15 min long exposure to 90 mT, which induced an increase of 53.20% in the number of germinated seeds. The static magnetic field induced the increase of bacterial indole-3-acetic acid production threefold times. Biomagnetic priming caused a metabolic shift from primary to secondary metabolism in the white mustard seedlings. An adequate combination of biological priming and static magnetic field treatment can be successfully used in old seed revitalization and germination improvements. © 2021 Bioelectromagnetics Society

Keywords: ***Bacillus amyloliquefaciens*; biopriming; static magnetic field; germination; white mustard**

INTRODUCTION

White mustard (*Sinapis alba* L.) is a spring annual oilseed crop grown mainly in Europe. Its broad utilization (food and pharmaceutical industry, textile, biogas, and soap production) indicates a significant economic value. However, crop yields are highly dependent on seed germination and rapid emergence, which are crucial steps for plants' establishment [Tribouillois et al., 2016]. Despite the longevity of dry seeds, their storage for prolonged periods of time leads to the aging process, the decline in quality, and viability loss at varying rates [De Vitis et al., 2020]. These result in germination failure, which can also be caused by seed dormancy. There is little data about the connection between seed viability lost after dry storage and seed dormancy, but according to Nguyen [2014], these conditions are linked with similar mechanisms and represent main targets to increase crop productivity. Seed deterioration causes large economic losses for growers, seed producers, and represents a significant challenge for seed banks and agrobiodiversity preservation. Certain seed properties that change over time are the main factors affecting germination; however, environmental conditions, moisture, temperature, and oxygen content are associated with seed germination as well [De Vitis et al., 2020; Min et al., 2019]. White mustard is characterized as an outcrossing species with high self-incompatibility, as well as a crop with low possibilities for in vitro cultures, which is why breeding and biotechnological manipulation is limited as a tool to improve seed traits [Klóska et al., 2012]. As customers are to be provided with high-quality and long-living seeds, different priming methods are proposed to improve the potential of seed germination. Seed germination decrease during prolonged storage can be partially restored by seed priming treatments. Numerous priming

Grant sponsor: Ministry of Education, Science and Technological Development, The Republic of Serbia, contract number: 451-03-68/2020-14/200116, grant number: 45003.

Conflicts of interest: None.

*Correspondence to: Vera Karličić, Faculty of Agriculture, Nemanjina 6, 11080 Belgrade, Serbia. E-mail: vera.karlicic@agrif.bg.ac.rs

Received for review 31 July 2020; Accepted 21 January 2021

DOI:10.1002/bem.22328
Published online 00 Month 2021 in Wiley Online Library (wileyonlinelibrary.com).

methods are based on the use of chemical and physical agents [Zheng et al., 2016; Forti et al., 2020]. However, seed treatment with beneficial microorganisms represents a useful eco-friendly alternative [Forti et al., 2020].

Bacterial seed inoculation is a promising technique directed toward achieving resistance to different abiotic [Kasim et al., 2013] and biotic stresses [Singh et al., 2020]. Bacterial strains selected for such a procedure, commonly referred to as plant growth-promoting bacteria (PGPB), demonstrate a set of properties that enable successful seed colonization, as well as the plant growth-promoting (PGP) effect at the early stage of plant growth.

Among other applications, PGPB are most commonly used for seeds' inoculation [Mahmood et al., 2016]. Consequently, in addition to the plant growth being supported from the germination stage and seedling establishment, its resistance to abiotic and biotic stresses is achieved as well [Jiménez-Arias et al., 2017; Ren et al., 2019; Singh et al., 2020]. As the inoculation practice implies seed soaking in bacterial suspension followed by redrying, these techniques can be classified as biopriming [Mahmood et al., 2016].

Recently, a number of studies have shown that seed exposure to a static magnetic field (SMF) is beneficial to various crops and medicinal plants, such as maize, soybean, sweet pepper, and wheat [Ahamed et al., 2013; Ćirković et al., 2017; Kataria et al., 2017; Michalak et al., 2019]. It was discovered that SMF can improve germination of not only standard but also of non-standard seeds as well and that it continues its influence on the initial plant growth stage [Afsal et al., 2016]. Although the beneficial effect of magnetic field on plants has been detected numerous times, the biochemical and physiological mechanisms of the magnetic field effect on seed stimulation are not yet completely understood.

It is confirmed that SMF can affect bacterial growth patterns, biofilm formation, antibiotic susceptibility, enzyme activity, etc. [Ren et al., 2017; Raouia et al., 2020]. Consequently, if SMF is applied to PGPB, the effects on bacterial PGP traits, seeds, and plant-microbe interaction can be expected. The aim of our work is to determine the individual and simultaneous effects of seed priming with PGPB and SMF on white mustard germination, emergence, and early growth. To the best of our knowledge, the interaction between bacterial inoculation and SMF, and their influence on seed germination have not yet been studied. The analysis of the SMF effect on bacterial indole-3-acetic acid (IAA), as well as seed abscisic acid (ABA) assay, contributed to our attempt to clarify the observed effect on germination and early stage of plant growth.

MATERIALS AND METHODS

Bacterial Strain

The bacterial strain used in the research is *Bacillus amyloliquefaciens* D5 ARV (NCBI GenBank Accession No KT265087; Bethesda, MD). The strain was isolated from coal-mine overburden waste (Mining Basin Kolubara, Lazarevac, Serbia), and obtained from the collection of Department for Environmental Microbiology, Faculty of Agriculture, Belgrade, Serbia. The strain is siderophore and is an IAA producer, capable of both surface and endophytic colonization [Karličić, 2017].

Plant Material

White mustard (*Sinapis alba* L.) seeds were used for the experiments two years after the expiration date defined by the producer (Institute "Josif Pančić," Belgrade, Serbia). Seeds were kept in their original package at room temperature (20–30 °C), and their germination rate was determined to be 47% at the beginning of the experiment. The remaining, non-germinated seeds (53%) were subjected to a viability test with 1% 3,5- triphenyltetrazolium chloride. Red-stained embryos were noticed at 86% of non-germinated seeds and considered as viable.

Production of IAA

The determination of IAA production was done colorimetrically using the method described by Patten and Glick [2002]. The bacterial strain was grown in the minimal media supplemented with 100 mg/ml of l-tryptophan (Sigma-Aldrich, Taufkirchen, Germany). After 48 h, the absorbance of the 530 nm line was measured (T70 UV/VIS Spectrometer; PG Instruments, Lutterworth, UK). The concentration of IAA was determined by comparison with the standard curve of IAA (Sigma-Aldrich) in a 1–100 μg/ml range. In order to examine the effect of SMF on IAA production, the strain was exposed to SMF of 90 mT for 5, 15 min, and 24 h, and then incubated in minimal media supplemented with l-tryptophan.

SMF

The experimental setup used for exposure to SMF was assembled using permanent magnets of size $100 \times 150 \times 25$ mm (ferrite block magnet B150-100-25FA; GAUS Group, Požarevac, Serbia). The magnets were secured in pairs in aluminum frames, and the samples were exposed to the magnetic field in the gap between two frames. The distance between the frames and, consequently, the intensity of the magnetic field, was adjusted with the sliders; see Figure 1. The gap between

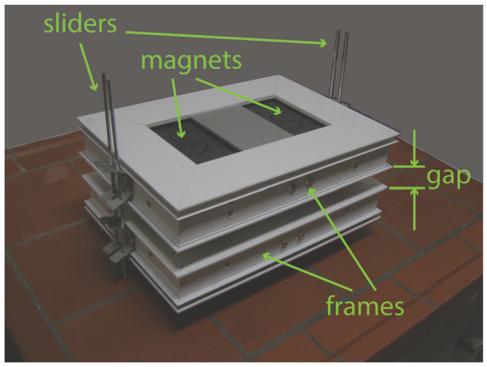

Fig. 1. Experimental setup used for sample exposure to the static magnetic field. The setup contains four permanent magnet blocks secured in two aluminum frames. Each frame holds two magnets with distance adjusted with the sliders. Note that the vertical gap between the magnets is larger than the depicted gap between the frames.

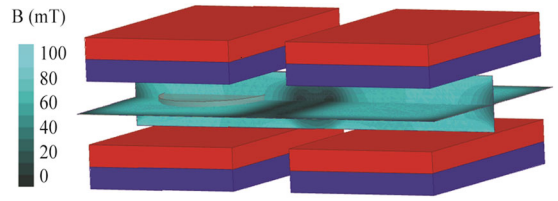

Fig. 2. Numerical simulation of the magnetic field. Aluminum does not change magnetic field,and aluminum frames of the experimental setup depicted in Figure 1 were not taken into account in the computer modeling. The gap between the magnets in the numerical model here is 38 mm, whereas the corresponding gap between the aluminum frames in the real experimental setup was 19 mm. The properties of the ferromagnetic material used in the computer model were adjusted so that the values of the magnetic field obtained by numerical simulation in the computer model match the nine measured values in the real experimental setup. Consequently, the numerically obtained contour plots of field intensity that are given in the horizontal and vertical planes through the middle of the experimental volume represent field intensities in the real experimental setup. The cylindrical volume occupied with the seeds is indicated as the light gray cylinder. The field intensity in the center of the gap was 90 mT.

the lower and upper pair of magnets was 38 mm, which provided a field intensity of 90 mT in the center of the gap. The seeds were placed in Petri dishes so the experimental volume was a cylinder with a diameter of 70 mm and height of 10 mm. The field intensity was measured in the nine points uniformly distributed in the mid-plane of the gap using DTM-151 Teslameter (Group3 Technology, Auckland, New Zealand). The obtained values were used for the numerical modeling (Mermaid 3D; SIM, Novosibirsk, Russia) and calibration of the model of the experimental setup. The parameters of the ferromagnetic material that was used in computer modeling of the four permanent magnets were adjusted so that the computer-simulated values of the magnetic field match the measured values in the nine check-points. Consequently, the overall magnetic field distribution obtained numerically can be taken to represent the magnetic field in reality. The numerical model and magnetic field intensity in the experimental volume are given in Figure 2. The field variation inside the experimental volume was found to be $\pm$6.61%.

The geomagnetic field intensity in Belgrade, i.e., at the geographic location of the experiment, is 48 μT. However, the intensity of the ambient magnetic field in the lab area where the experiment was conducted was measured and was found to vary between 70 and 100 μT. The samples were exposed to the magnetic field for 5 and 15 min.

Seed Treatment

The total amount of seeds was surface sterilized with 3% H_2O_2 for 20 min, immediately washed five times with sterile, distilled water to eliminate all traces of sterilant, and left to dry in aseptic conditions. Dry and surface-sterilized seeds were divided into portions intended for different treatments in seed germination test, ABA analyses, and glasshouse trial.

The seeds portion predetermined for inoculation was bioprimed with a suspension consisting of overnight *B. amyloliquefaciens* D5 ARV culture. The liquid culture used to obtain bacterial suspension was prepared by cultivation in Nutrient Broth medium (Institute of Virology, Vaccines and Sera "Torlak," Belgrade, Serbia) for 24 h at 30 °C. Afterwards, the fresh culture was centrifuged at 6000*g* for 15 min, the supernatant was discharged, and the residue was rinsed twice in sterile water. The bacterial pellet was resuspended in water and the suspension density was adjusted to 10^8 CFU/ml (absorbance of 1 at 600 nm; T70 UV/VIS Spectrometer). Seeds were inoculated by immersion into the bacterial suspension for 1 h at room temperature using a rotary shaker set at 100 rpm (KS 260 basic; IKA, Staufen, Germany) followed by drying in aseptic conditions.

The portions predetermined for treatments without inoculation (control and SMF treatment) were prepared in the same way, but using sterile water instead of the bacterial suspension.

Seed Germination

The germination test was performed in Petri dishes with a filter paper soaked with 5 mL of sterile water. The experiment was carried out in three replicates per treatment, using 30 seeds per Petri dish. The SMF effect

on germination of inoculated and uninoculated seeds was tested by placing the Petri dishes with seeds in SMF for 5 and 15 min. Control Petri dishes contained uninoculated seeds that were not exposed to SMF. Seeds were incubated in darkness, at 25 °C for 1 week.

The seed germination test was performed in the following treatments.

Control: uninoculated seeds, without exposure to SMF; D5 ARV: seeds inoculated with *B. amyloliquefaciens* D5 ARV, without exposure to SMF; SMF_5: uninoculated seeds, exposed to SMF for 5 min; SMF_{15}: uninoculated seeds, exposed to SMF for 15 min; SMF_5—D5 ARV: seeds inoculated with *B. amyloliquefaciens* D5 ARV, exposed to SMF for 5 min; SMF_{15}—D5 ARV: seeds inoculated with *B. amyloliquefaciens* D5 ARV, exposed to SMF for 15 min. Seeds with radicles of 2 mm or longer were counted, and the percentage of germinated seeds was determined.

This trial was preceded by a test that evaluates the effect of the sterilization technique on germination. Comparison of germination percentage of unsterilized and seed sterilized with 3% H_2O_2 showed no statistically significant differences at $P = 0.05$.

ABA Analysis

ABA analysis was performed by ELISA immunoassay [Asch, 2000]. Prior to ABA analysis, the seeds were treated as described in Seed Germination section. Thereafter, 0.5 g of seed powder was mixed with water and PVP (polyvinylpyrrolidone) for 24 h at 4°C in a thermomixer (ThermoMixer Comfort; Eppendorf, Hamburg, Germany). After centrifugation for 15 min at 4 °C and 13,200 rpm (Sigma 2-16K, Newtown, UK), the supernatant was used to make dilutions. A plate coated with ABA conjugate was washed with sodium phosphate buffer. Afterwards, 100 µl of the specific sample and 100 µl of primary antibody-MAC (Sigma-Aldrich) were added to the wells. Following 3 h of plate incubation at 4 °C, 200 µl of secondary antibody (Sigma-Aldrich) was added. The color reaction appeared as a result of secondary antibody bonding with the substrate (*p*-nitro-phenyl phosphate). The absorbance was measured at 405 nm by a spectrophotometer (Tecan; Sunrise, Männedorf, Switzerland). Commercial ABA (Sigma-Aldrich) was used to prepare the standard curve.

Glasshouse Trial

White mustard seeds were treated in the same manner as described in Seed Germination section and sown on the commercially available substrate Florabalt Seed 2 (Floragard Vertriebs, Oldenburg, Germany), a product intended to accelerate plant emergence. The experiment was conducted in three replicates, with 30 seeds per container in each replicate. After one week, the number of emerged plants, as well as their fresh and dry mass was determined. Additionally, total chlorophyll content (µg/cm^2), nitrogen balance index (NBI), the index of flavonoids, and anthocyanins in leaves were measured by a non-destructive method (Dualex Force-A device, Orsay Cedex, France). NBI is calculated as chlorophyll:flavonoids ratio and was used as an indicator of nitrogen deficiency and changes in nitrogen and carbon metabolism [Cerović et al., 2012].

Statistical Analysis

The statistical analyses were performed using the analyses of variance by Statistica software (StatSoft, Tulsa, OK). Mean values of data were compared by the Tukey test at a significance level of $P = 0.05$.

RESULTS

Effect of Biomagnetic Priming on White Mustard Germination and Emergence

Results of the germination test showed that biopriming without SMF treatment increased the percentage of germinated seeds. The increase of 40.43% (relative difference) in the number of germinated seeds (Fig. 3) indicates the potential of *B. amyloliquefaciens* D5 ARV strain for use in the biopriming of white mustard seeds. The response to SMF was found to be dependent on the treatment duration. While SMF_5 increased germination percentage, SMF_{15} led to lower seed germination compared with the control. However, the negative effect of longer exposure to SMF was neutralized if combined with the bacterial inoculation. Germination percentages were significantly higher for the SMF_5—D5 ARV and SMF_{15}—D5 ARV treatment (44.68% and 53.20%, respectively) compared with control. Such interaction of biopriming and SMF treatment appeared to give even better results than bacterial inoculation itself. The results point to the beneficial effects of synergistic interaction between the bacterial inoculation and SMF_{15} in achieving a better germination percentage. The combined application of SMF_5 and biopriming improved the effect achieved by SMF_5, but those results showed lower germination than *B. amyloliquefaciens* D5 ARV inoculation.

The emergence of white mustard plants in the glasshouse trial confirmed the effects noticed in the germination experiment (Fig. 4). The highest emergence percentage was observed in D5 ARV and SMF_{15}—D5 ARV treatments (an increase of 8.96% and 11.94%, respectively). Even though the SMF treatments significantly lowered the level of emergence, their combination with *B. amyloliquefaciens* D5 ARV inoculation alleviated

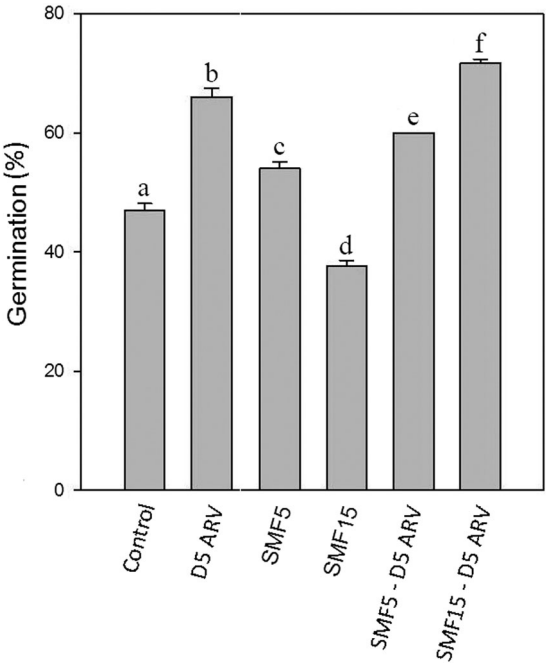

Fig. 3. Germination percentage of white mustard seed inoculated with *Bacillus amyloliquefaciens* D5, and/or treated by a static magnetic field of 90 mT for 5 and 15 min. Mean values with the same letter are not significantly different according to the Tukey test ($P = 0.05$).

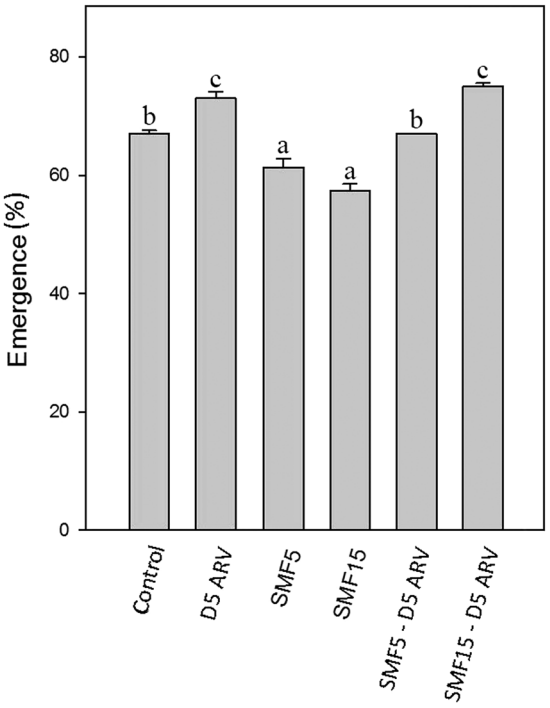

Fig. 4. The emergence percentage in glasshouse trial. White mustard seeds were inoculated with *Bacillus amyloliquefaciens* D5, and/or treated by the static magnetic field of 90 mT for 5 and 15 min. Mean values with the same letter are not significantly different according to the Tukey test ($P = 0.05$).

the negative effect on seed emergence. Moreover, SMF_{15} combination with *B. amyloliquefaciens* D5 ARV inoculation caused the highest emergence percentage.

Production of Bacterial IAA in SMF

The SMF as abiotic stress influenced the amount of IAA produced by *B. amyloliquefaciens* D5 ARV (Table 1). *B. amyloliquefaciens* D5 ARV produced more than three times higher concentrations of IAA when exposed to SMF of 90 mT for 15 min. Also, the results show that the exposure prolonged to 24 h did not cause changes in IAA amount, compared with the control. It seems that longer exposure leads to some kind of adaptation to abiotic stress. On the other hand, exposure to SMF of 90 mT for 5 min resulted in lower concentrations of IAA produced by *B. amyloliquefaciens* D5 ARV.

ABA Content in Primed Seeds

The highest concentrations of ABA were found in the control conditions. Inoculation and SMF treatment led to a decrease in ABA concentration. The treatments with SMF had the least intense effect on ABA content, while inoculation with *B. amyloliquefaciens* D5 ARV contributed significantly more to ABA reduction (a decrease of 53%). The addition of SMF treatment changed the effect of inoculation with *B. amyloliquefaciens* D5 ARV on ABA content. Treatments SMF_5—D5 ARV and SMF_{15}—D5 ARV lowered ABA concentrations for 17% and 49%, respectively. The SMF treatment of uninoculated seeds was the least effective and resulted in the ABA content reduction of approximately 17%, regardless of the exposure duration; see Table 2.

Early Growth Parameters of White Mustard

Content of chlorophyll, flavonoids, and anthocyanins in leaves. The treatments with only SMF did not induce significant changes of chlorophyll content in leaves, whereas inoculation with both SMF_{15} and *B. amyloliquefaciens* D5 ARV induced an increase of chlorophyll content by 28.20% on average. A similar effect on chlorophyll accumulation is present in the treatment D5 ARV (an increase by 30.58%; Fig. 5A).

Slightly elevated anthocyanin content was noted in the plants after exposure to a combination of SMF and inoculation (Fig. 5B). The amount of flavonoids was significantly increased in the sample corresponding to the D5 ARV and SMF_{15}—D5 ARV treatments, by 67.65% and 100%, respectively (Fig. 5C). In all of the analyzed

TABLE 1. Production of Indole-3-Acetic Acid (IAA) by *Bacillus amyloliquefaciens* D5 ARV in Static Magnetic Field (90 mT Exposed for 5 min, 15 min, and 24 h)

Treatment	Control	SMF_5	SMF_{15}	SMF_{24h}
IAA (μg/ml)	2.9 ± 0.3^b	2.1 ± 0.1^a	10.4 ± 0.5^c	2.9 ± 0.2^b

Mean values with the same letter are not significantly different according to the Tukey test ($P = 0.05$).

treatments, the chlorophyll/flavonoids ratio (NBI) decreased compared with the control, but the degree of its decline was statistically significant in the case of inoculation with *B. amyloliquefaciens* D5 ARV and SMF_{15}—D5 ARV treatment. The obtained values range from 36.65% of the decrease for SMF_{15}—D5 ARV to 6.70% of the decrease for SMF_5—D5 ARV (Fig 5D). At the same time, there was a significant increase in the content of flavonoids for the treatments D5 ARV and SMF_{15}—D5 ARV (55% and 87%, respectively).

Fresh and dry biomass. Fresh biomass of plants showed a decrease when seeds were inoculated with D5 ARV bacteria or exposed to SMF_{15} in combination with D5 ARV. Those treatments caused the same degree of changes in fresh biomass (a decrease of around 14.30%). There was no statistically significant difference between other treatments and the control (Fig. 6A).

The effect of biopriming caused an increase in dry biomass by 18.51%. The most significant changes occurred when the inoculation with *B. amyloliquefaciens* D5 ARV strain was combined with 15 min exposure to SMF, in which case an increase of 24.44% was detected (Fig. 6B).

DISCUSSION

Worldwide, different methods are being studied to improve seed germination, and biopriming as well as SMF treatment have been proposed as successful tools [Michalak et al., 2019; Forti et al., 2020]. In this study, we investigated the possibility of using *B. amyloliquefaciens* D5 ARV and SMF in priming of old white mustard seed. Karličić et al. [2017] had shown that *B. amyloliquefaciens* D5 ARV used in the current research has the potential for application in sustainable cultivation of plants, aimed to alleviate environmental stress. On the other hand, beneficial effects of SMF on plant growth are well-documented and Ćirković et al. [2017] showed that application of SMF increased germination speed of wheat. Our study combines these two methods and obtained results indicate that biomagnetic priming has favorable effects.

TABLE 2. ABA Content in Seeds after Bacterial Inoculation and/or Static Magnetic Field Treatment

Treatment	ABA content (ng/g fresh weight)	Treatment	ABA content (ng/g fresh weight)
Control	1348.2 ± 97.81^d	D5 ARV	638.5 ± 20.99^a
SMF_5	1114.5 ± 86.97^c	SMF_5—D5 ARV	1116.5 ± 87.63^c
SMF_{15}	1116.23 ± 63.08^c	SMF_{15}—D5 ARV	691.0 ± 39.87^b

Mean values with the same letter are not significantly different according to the Tukey test ($P = 0.05$).

The highest germination percentage of white mustard was achieved as a result of the synergistic action of *B. amyloliquefaciens* D5 ARV and SMF of 90 mT that was applied for 15 min. This method provided a 53.20% increase in the number of germinated seeds. In seed production, such improvement can be decisive in assorting produced seeds as sowing seeds, so the significant economic losses can be avoided.

The positive effect of magnetic field on seed germination of *Satureja bachtiarica*, *Urtica dioica*, and other plants was reviewed in Nyakane et al. [2019]. Feizi et al. [2020] reported positive effects of SMF of 50 mT on germination rate, radicle length, and shoot dry mass of *S. alba*. SMF treatment prior to germination affects the following development phases, growth, and photosynthetic efficiency [Shine et al., 2011]. Our results indicate that the SMF effect on plant germination is highly dependent on the duration of seed exposure; a treatment extension for 10 min caused the opposite effect on seed germination. Also, SMF effects on growth and metabolism of microorganisms are reported. In our study, *B. amyloliquefaciens* D5 ARV exposure to SMF for 15 min resulted in a significant increase of IAA production. SMF increased growth rate of *B. subtilis*, *Pseudomonas stutzeri*, *Cupriavidus metallidurans*, and *Rhodococcus equi* [Al-Khaza'leh and Al-fawwaz, 2015; Mansouri et al., 2019], and production of metabolites (IAA, ACC, and siderophore) and enzyme activities [Haritwal et al., 2015]. However, SMF treatment can affect not only plants and microbes, but also the overall plant-microbe interaction, which is the main focus of the presented research. The individual effects on plants and microbes are interrelated and can alleviate and modulate each other. The result of that interaction determines the final effect of SMF treatment on plant growth and that is one of the main points of our study.

Also, the results of this study indicate that the effect of SMF on bacteria is time-dependent. This was confirmed by the IAA analysis, which showed that

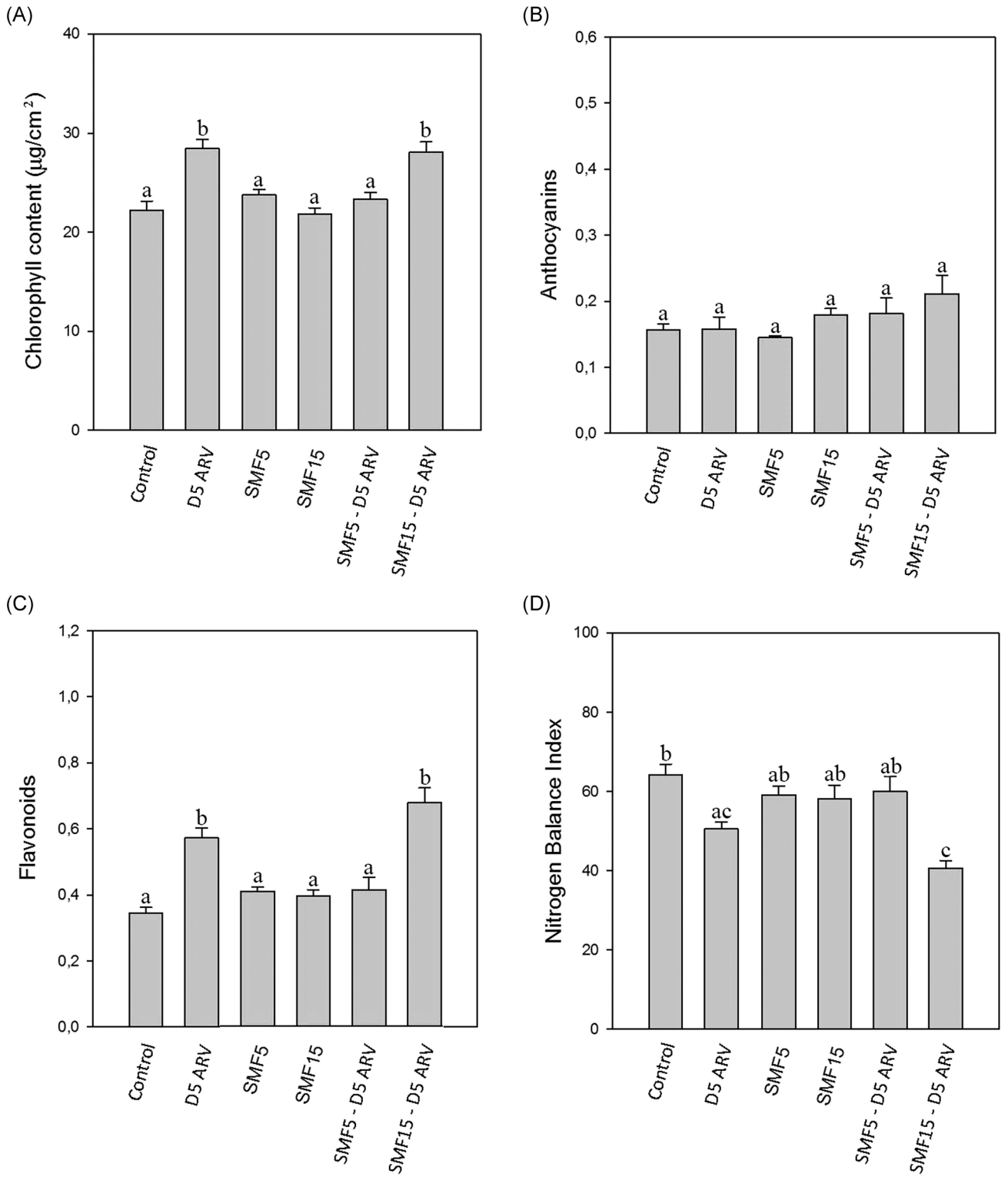

Fig. 5. The content of chlorophyll (**A**),anthocyanins (**B**), flavonoids (**C**), and nitrogen balance index (**D**) in the leaves of white mustard inoculated with *Bacillus amyloliquefaciens* D5, and/or treated by the static magnetic field of 90 mT for 5 and 15 min. Mean values with the same letter are not significantly different according to the Tukey test ($P = 0.05$).

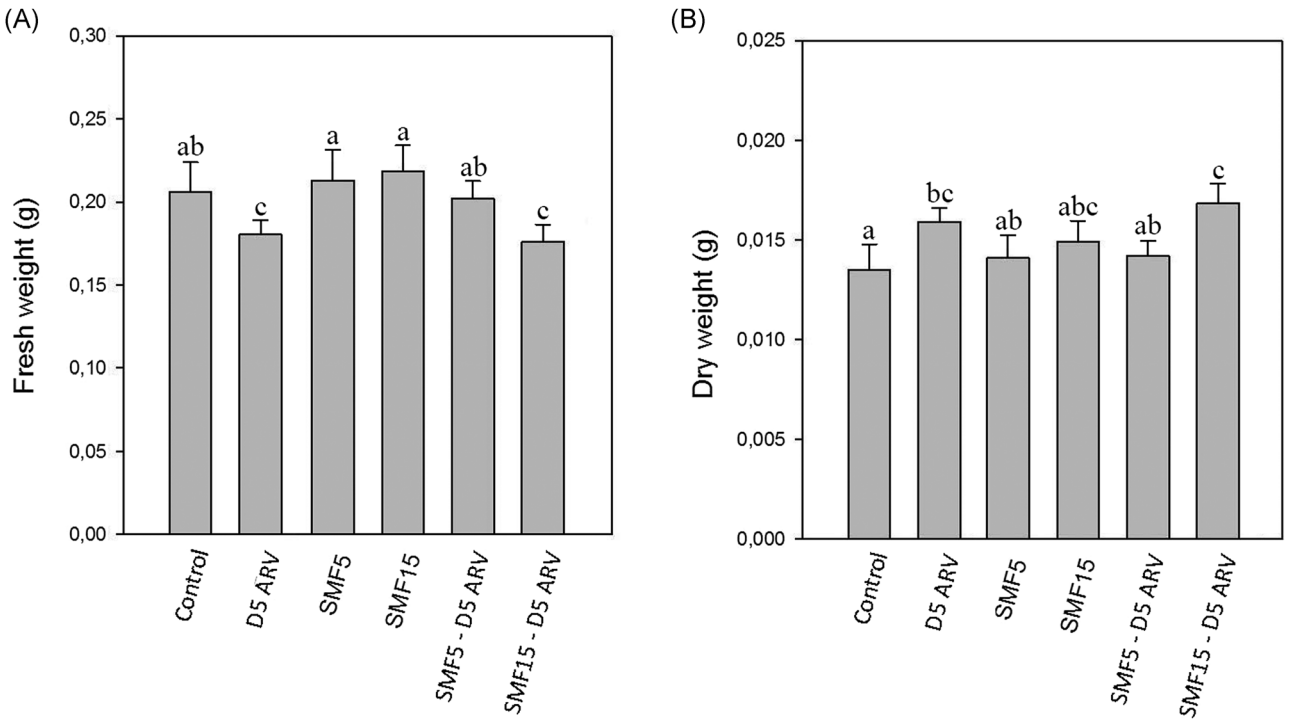

Fig. 6. Fresh (**A**) and dry mass (**B**) of white mustard seedlings grown in glasshouse trial after seed treatment with *Bacillus amyloliquefaciens* D5, and the static magnetic field of 90 mT for 5 and 15 min. Mean values with the same letter are not significantly different according to the Tukey test ($P = 0.05$).

SMF expresses different effects on IAA production depending on the SMF treatment duration. Production of phytohormones, such as IAA, is one of the major traits of PGPB, determining their effect on plant growth, and acting as a signaling molecule that modulates the communication between plants and microorganisms [Duca et al., 2014]. The large number of bacteria interacting with plant roots is shown to produce IAA, which affects root growth, formation of lateral roots, and root growth initiation [Emami et al., 2019]. In addition, it is shown that IAA represents an integral part of a plant's response to diverse unfavorable stress conditions, and the amount of endogenous IAA changes as a response to different abiotic factors [Sharma et al., 2015]. It is shown that the IAA amount in plants is dependent on oxidative degradation of IAA which occurs under abiotic stress [Kovtun et al., 2000], and bacterial IAA as an exogenous auxin can alleviate those unfavorable effects. IAA's role in the alleviation of seed dormancy caused by salt stress is reported by Egamberdieva [2009]. Relying on the previous studies, we can assume that significant change in IAA production by *B. amyloliquefaciens* D5 ARV is one of the reasons for its increased beneficial effect on white mustard germination after SMF treatment.

On the other hand, when exposed to abiotic stress, plants exhibit effective cellular responses and initiate stress-specific complex pathways [Gull et al., 2019]. The responses include changes in the synthesis of compounds such as ABA, jasmonic acid, salicylic acid, and ethylene [Verma et al., 2016; Gull et al., 2019], as well as phenolic acids and flavonoids [Singh et al., 2014]. The ABA-dependent pathways are predominant in response to abiotic stress. As reviewed in Arc et al. [2013], ABA content is directly related to germination inhibition and prolongation of the dormancy period. ABA is known as "stress hormone," which induces synthesis of the reserve, and "stress proteins" in seeds, and contributes to seed resistance to drying [Vishwakarma et al., 2017]. Observing germination results, it is obvious that reduced concentration of ABA leads to increased seed germination in the SMF_5 treatment. However, longer exposure of the seed to SMF leads to lower germination percentage, despite the decrease in ABA. The negative effect of longer exposure to SMF is neutralized by bacterial inoculation. Seed inoculation with *B. amyloliquefaciens* D5 ARV showed positive effects on germination (a relative increase of 40.43% in the number of germinated seeds) by itself, as well as when it is combined with SMF (SMF_{15}—D5 ARV

provided a relative increase of 53.20% in germinated seeds). At the same time, those were the treatments with the lowest ABA content (Table 2).

ABA-IAA interaction is crucial for the seed germination process. Liu et al. [2013] showed that the effect of auxins and ABA on seed dormancy is interdependent—ABA synthesis is modified by auxins in *Arabidopsis thaliana*. It is obvious that the combination of D5 ARV treatment and SMF_{15} did not inhibit germination; on the contrary, it had a stimulative effect. At the same time, IAA levels were the highest when *B. amyloliquefaciens* D5 ARV was exposed to SMF for 15 min. This indicates that an increase in germination is a consequence of IAA accumulation induced by SMF_{15}—D5 ARV treatment. Other authors also recorded the positive effect of IAA on seed germination. IAA priming increased the germination rate, index, and speed in cotton [Zhao et al., 2020]. IAA also increases germination in *Arabidopsis thaliana*, but at the same time downregulates the transcription of negative seed regulator *ABI3* [Hussain et al., 2020].

The emergence of white mustard plants tested in a commercial substrate shows a similar mode of behavior as was the case in the germination trial. Although the emergence percentages were higher than germination, the observed effects of the applied treatments were less intense for emergence than for germination. It was noticed that white mustard germination was higher in the commercial substrate, compared with germination tests in Petri dishes. Such a result is unusual, but El-Keblawy et al. [2018] reported a similar observation. In their experiment, *Aristida adscensionis* attained a significant difference in the final germination percentage between potted soils (44.91%) and Petri dishes (9.20%). Those differences can be explained by a better water-air regime in the substrate. This is supported by the difference in results of germination tests performed on soaked paper (which is a commonly used practice in laboratories), and some other substrates with better water distribution, such as agar-agar [Valencia-Díaz and Montaña, 2003]. In the case of the present study, an additional factor maybe the composition of the chosen substrate, primarily designed to improve germination and support early growth stages.

The fresh biomass decrease and dry biomass increase indicate that the effect of D5 ARV and simultaneous effect of *B. amyloliquefaciens* D5 ARV and SMF_{15} on plants is based on the metabolic changes, namely, in these treatments the accumulation of plant metabolites is stimulated, which increases dry mass. The reason for such a change is in carbon redistribution between primary and secondary metabolism, and these results are consistent with the data obtained by the NBI measurements. NBI is used as an indicator of changes in carbon and nitrogen status, even more reliable than the analyses of nitrogen content in leaves [Cartelat et al., 2005]. This parameter is very precise, with a root-mean-square error below 2 mg of nitrogen per g of dry mass [Cerović et al., 2015], and it can even be used for fine-tuning of fertilization, as shown by Agati et al. [2015]. If the availability of nitrogen is low, plants allocate the residue of carbon to polyphenols' synthesis [Massad et al., 2012]. Our results showed that the treatments with the highest degree of fresh mass decrease and dry mass increase (D5 ARV and SMF_{15}—D5 ARV) also had the highest accumulation of flavonoids and chlorophyll. Still, chlorophyll accumulation was not high enough to maintain high NBI, which decreased in those treatments due to high flavonoid accumulation. A similar trend is noticed in treatments SMF_5, SMF_{15}, and SMF_5—D5 ARV, where NBI also decreased slightly in comparison with control. NBI decrease is caused by the redirection of metabolism from primary to secondary [Meyer et al., 2006]. Primary metabolites are essential for plant growth; however, stress factors can cause an increased synthesis of secondary metabolism. As secondary metabolites are important for stress defense, plants need to distribute energy between growth and defence processes in the most efficient manner [Lavinsky et al., 2015], which is in accordance with carbon: nitrogen nutrient balance hypothesis [Massad et al., 2012]. Still, as NBI can be used as an indicator of changes in metabolic fluxes, future research should include confirmation by their more precise measurements, such as mass spectroscopy or isotopic labeling.

Besides flavonoids, our results show an increase in the synthesis of anthocyanins which is not statistically significant but detected in plants subjected to treatments D5 ARV, SMF_{15}, SMF_5—D5 ARV, and SMF_{15}—D5 ARV. These compounds contribute to the oxidative stress response as they have an important role in the removal of reactive oxygen species (ROS) [Finni et al., 2011]. This is in correspondence with literature data which interpret priming as a weak stress factor that leads to "stress memory" in plants, better preparing them for abiotic and biotic stress in their environment [Wang et al., 2017]. Biopriming fits into the previous definition by causing the redistribution between primary and secondary metabolism, and switches on different defense mechanisms in the plant [Conrath et al., 2006]. Still, our results showed that positive effects are not present just in the case of secondary metabolites, but also chlorophyll (treatment D5 ARV and SMF_{15}—D5 ARV). That indicates that these treatments lead to a general rise of metabolism, concurring with literature data showing that biopriming can lead to higher nutrient uptake [Prasad et al., 2016] and higher crop productivity by increasing chlorophyll content [Mahmood and Kataoka, 2018]. As shown in Figure 5, the highest increase of flavonoids and anthocyanins is

noticed in SMF_{15}—D5 ARV treatment, which is also the treatment with the highest IAA production. Literature data support these findings—exogenous application of IAA induces an increase of antioxidant defence and increases nitrogen metabolism [Gong et al., 2019]. Shine et al. [2011] point out increased ROS production (superoxide and hydroxide radicals) in germinated soybean seeds, after SMF treatment with 150 and 200 mT during 1 h. There are not many ROS in dry seeds; however, during seed hydration in the initial stages of germination, metabolic activation leads to ROS accumulation. ROS accumulation can be related to faster germination and increased respiration, but its role in biomagnetic priming should be further evaluated. In addition, future research could include some other components of the antioxidant defence system. Flavonoids are part of the non-enzymatic defense system, including also glutathione, vitamin C, tocopherols, and carotenoids [Foyer et al., 1994]. Determination of the changes in these components could contribute to a further explanation of the observed effect. Additional explanations could relate to changes in the activity of antioxidant enzymes (superoxide dismutase, catalase, peroxidase) and particularly to the enzymes of the ascorbate-glutathione cycle (glutathione reductase, dehydroascorbate reductase, and ascorbate peroxidase).

The presented results indicate that plant response to the SMF and bacterial inoculation is a result of complex metabolic and biochemical changes. The observed effects are a consequence of different regulatory mechanisms, and some of them are controlled by ABA-dependent signaling pathways.

CONCLUSION

This study represents the first-time report on the co-effect of two different seed treatments, SMF treatment and biopriming. The obtained results indicate that biomagnetic priming can be used to improve old seed germination. A significantly higher germination improvement was achieved by combining the application of PGPB and SMF compared with applying only PGPB. The duration of seed exposure to SMF appeared to be a specific factor affecting white mustard germination and emergence. The highest germination and emergence percentage was achieved by the synergistic action of *B. amyloliquefaciens* D5 ARV and SMF of 90 mT that was applied for 15 min (the number of germinated seeds was increased by 53.20%, and the number of emerged seedlings was increased by 11.94%). The studied bacterial strain showed different responses depending on the SMF treatment duration. SMF induced more than three times higher production of IAA by *B. amyloliquefaciens* D5 ARV. Considering the importance of IAA for plant-microbial interactions, such an effect can represent one of the main modes of biomagnetic priming action.

Application of biomagnetic priming causes a metabolic shift from primary to secondary metabolism in white mustard seedlings. Metabolic changes are evident in the increased accumulation of anthocyanins and flavonoids, which are important components of the antioxidant non-enzymatic system.

A number of published studies show that specific SMF treatments have a stimulative effect on germination. Finding the most optimal SMF treatment should take into account the SMF effects on rhizospheric bacteria, as well as the overall plant-microbe interaction.

REFERENCES

Afsal I, Ur Rehman H, Naveed M, Basra SMA. 2016. Recent advances in seed enhancements. In: Susana A, Balestrazzi A, editors, *New Challenges in Seed Biology—Basic and Translational Research Driving Seed Technology*. London: Intech Open Science. pp 47–74.

Agati G, Foschi L, Grossi N, Volterrani M. 2015. In field non-invasive sensing of the nitrogen status in hybrid bermudagrass (*Cynodon dactylon* × *C. transvaalensis* Burtt Davy) by a fluorescence-based method. Europ J Agron 63:89–96.

Ahamed MEM, Elzaawely AA, Bayoumi YA. 2013. Effect of magnetic field on seed germination, growth and yield of sweet pepper (*Capsicum annuum* L.). Asian J Crop Sci 5:286–294.

Arc E, Sechet J, Corbineau F, Rajjou L, Marion-Poll A. 2013. ABA crosstalk with ethylene and nitric oxide in seed dormancy and germination. Front Plant Sci 4:63.

Asch F. 2000. *Laboratory Manual on Determination of Abscisic Acid by Indirect Enzyme Linked Immuno Sorbent Assay (ELISA)*. Taastrup, Denmark: The Royal Veterinary and Agricultural University. pp 1–21.

Al-Khaza'leh KA, Al-fawwaz AT. 2015. The effect of static magnetic field on *E. coli*, *S. aureus* and *B. subtilis* viability. J Nat Sci Res 5:153–157.

Cartelat A, Cerovic ZG, Goulas Y, Meyer S, Lelarge C, Prioul JL, Barbottin A, Jeuffroy MH, Gate P, Agati G, Moya I. 2005. Optically assessed contents of leaf polyphenolics and chlorophyll as indicators of nitrogen deficiency in wheat (*Triticum aestivum* L.). Field Crops Res 91:35–49.

Cerović ZG, Ghozlen NB, Milhade C, Obert M, Debuisson S, Moigne ML. 2015. Nondestructive diagnostic test for nitrogen nutrition of grapevine (*Vitis vinifera* L.) based on dualex leaf-clip measurements in the field. J Agric Food Chem 63:3669–3680.

Cerović ZG, Masdoumier G, Ghozlen NB, Latouche G. 2012. A new optical leaf-clip meter for simultaneous non-destructive assessment of leaf chlorophyll and epidermal flavonoids. Physiol Plant 146:251–260.

Ćirković S, Bačić J, Paunović N, Popović TB, Trbovich AM, Romčević N, Ristić-Djurović JL. 2017. Influence of 340 mT static magnetic field on germination potential and mid-infrared spectrum of wheat. Bioelectromagnetics 38:533–540.

Conrath U, Beckers GJM, Flors V, García-Agustín P, Jakab G, Mauch F, Newman AM, Pieterse CMJ, Poinssot B, Pozo

MJ, Pugin A, Schaffrath U, Ton J, Wendehenne D, Zimmerli L, Mauch-Mani B. 2006. Priming: Getting ready for battle. Mol Plant Microbe Interact 19:1062–1071.

De Vitis M, Hay FR, Dickie JB, Trivedi C, Choi J, Fiegener R. 2020. Seed storage: Maintaining seed viability and vigor for restoration use. Restor Ecol 28:S249–S255.

Duca D, Lorv J, Patten CL, Rose D, Glick BG. 2014. Indole-3-acetic acid in plant—Microbe interactions. Antonie Van Leeuwenhoek 106:85–125.

Egamberdieva D. 2009. Alleviation of salt stress by plant growth regulators and IAA producing bacteria in wheat. Acta Physiol Plant 31:861–864.

Emami S, Alikhani HA, Pourbabaei AA, Etesami H, Sarmadian F, Motessharezadeh B. 2019. Assessment of the potential of indole-3-acetic acid producing bacteria to manage chemical fertilizers application. Int J Environ Res 13:603–611.

El-Keblawy A, Gariola S, Elsheikh EAE, Hussain MI, Abhilash PC. 2018. Variability in seed germination behavior of six grasses under laboratory and natural field conditions: implications for restoration of degraded lands in subtropical arid deserts. Trop Ecol 59:715–726.

Feizi H, Salari A, Kaveh H, Firuzi Y. 2020. Investigation of static magnetic field durability treatment on seed and seedling features of mustard (*Sinapis alba* L.). Z Arznei- Gewurzpfla 24:75–79.

Finni A, Brunetti C, Di Ferdinando M, Ferrini F, Tattini M. 2011. Stress-induced flavonoid biosynthesis and the antioxidant machinery of plants. Plant Sign Behav 6:709–711.

Forti C, Shankar A, Singh A, Balestrazzi A, Prasad V, Macovei A. 2020. Hydropriming and biopriming improve *Medicago truncatula* seed germination and upregulate DNA repair and antioxidant genes. Genes 11:1–15.

Gull A, Lone AA, Wani NUI. 2019). Biotic and Abiotic Stresses in Plants. In: de Oliveira AB, editor, *Abiotic and Biotic Stress in Plants*. London: Intech Open Science. pp 1–7.

Foyer CH, Lelandais M, Kunert KJ. 1994. Photooxidative stress in plants. Physiol Plant 92:696–717.

Gong Q, Li Z, Wang L, Dai T, Kang Q, Niu D. 2019. Exogenous of indole-3-acetic acid application alleviates copper toxicity in Spinach seedlings by enhancing antioxidant systems and nitrogen metabolism. Toxics 8:1.

Haritwal A, Chaudhary M, Mohan D, Modi G. 2015. Study of magnetic field treatment on rhizosphere. Int J Eng Res Technol 4:73–77.

Hussain S, Kim SH, Bahk S, Ali A, Nguyen XC, Yun DJ, Chung WS. 2020. The auxin signaling repressor IAA promotes seed germination through down-regulation of *ABI3* transcription in *Arabidopsis*. Front Plant Sci 11:11.

Jiménez-Arias D, Carrillo-Perdomo E, García-Machado FJG, Luis Jorge JC, Borges AA. 2017. Priming crops to cope with stress: Advances in seed-priming approach. In: Gorawala P, Mandhatri S, editors, *Agricultural Research Updates*. New York, NY: Nova Science Publishers. pp 15–46.

Karličić V. 2017. *Plant Growth Promoting Bacteria as a Potential in Devastated Soils Ecoremediation (Doctoral dissertation)*. Belgrade: University of Belgrade. pp 1–188.

Karličić V, Radić D, Jovičić-Petrović J, Lalević B, Morina F, Golubović Ćurguz V, Raičević V. 2017. The possibility of using overburden waste for London plane (*Platanus* x *acerifolia*) growth: The role of plant growth promoting microbial consortia. IFOREST—Biogeosci Forestry 10:692–699.

Kasim WA, Osman ME, Omar MN, Abd El-Daim IA, Begai S, Meijer J. 2013. Control of drought stress in wheat using plant growth-promoting bacteria. J Plant Growth Regul 32:122–130.

Kataria S, Baghel L, Guruprasad KN. 2017. Pre-treatment of seeds with static magnetic field improves germination and early growth characteristics under salt stress in maize and soybean. Biocatal Agric Biotechnol 10:83–90.

Klóska L, Cegielska-Taras T, Piętka T. 2012. Regeneration capacity of selected genotypes of white mustard (*Sinapis alba* L.). In Vitro Cell Dev Biol 48:180–188.

Kovtun Y, Chiu WL, Tena G, Sheen J. 2000. Functional analysis of oxidative stress-activated mitogen-activated protein kinase cascade in plants. Proc Natl Acad Sci USA 97:2940–2945.

Lavinsky AO, Magalhães PC, Ávila RG, Diniz MM, de Souza TC. 2015. Partitioning between primary and secondary metabolism of carbon allocated to roots in four maize genotypes under water deficit and its effects on productivity. Crop J 3:379–386.

Liu X, Zhang H, Zhao Y, Feng Z, Li Q, Yang HQ, Luan S, Li J, He ZH. 2013. Auxin controls seed dormancy through stimulation of abscisic acid signaling by inducing ARF-mediated ABI3 activation in *Arabidopsis*. PNAS 110:15485–15490.

Mahmood A, Kataoka R. 2018. Potential of biopriming in enhancing crop productivity and stress tolerance. In: Rakshit A, Singh HB, editors, *Advances in Seed Priming*. Singapore: Springer Nature. pp 127–145.

Mahmood A, Turgay OC, Farooq M, Hayat R. 2016. Seed biopriming with plant growth promoting rhizobacteria: A review. FEMS Microbiol Ecol 92:fiw112.

Mansouri A, Abbes C, Mouhoub RB, Hassine SB, Landoulsi A. 2019. Enhancement of mixture pollutant biodegradation efficiency using a bacterial consortium under static magnetic field. PLOS One 14:e0208431.

Massad TJ, Dyer LA, Vega CG. 2012. Costs of defense and a test of the carbon-nutrient balance and growth-differentiation balance hypotheses for two co-occurring classes of plant defense. PLOS One 7:e47554.

Meyer S, Cerović ZG, Goulas Y, Montpied P, Demotes-Mainard S, Bidel LPR, Moya I, Dreyer E. 2006. Relationships between optically assessed polyphenols and chlorophyll contents, and leaf mass per area ratio in woody plants: a signature of the carbon-nitrogen balance within leaves? Plant Cell Environ 29:1338–1348.

Michalak I, Lewandowska S, Niemczyk K, Detyna J, Bujak H, Arik P, Bartniczak A. 2019. Germination of soybean seeds exposed to the static/alternating magnetic field and algal extract. Eng Life Sci 19:986–999.

Min JE, Hong JY, Kwon SW, Park JH. 2019. Integrated metabolomics signature for assessing the longevity of *Panax ginseng* seeds. J Sci Food Agric 99:6089–6096.

Nguyen TP. 2014. *Seed Dormancy and Seed Longevity From Genetic Variation to Gene Identification (Doctoral dissertation)*. Utrecht, Netherlands: Utrecht University. pp 1–140.

Nyakane NE, Markus ED, Sedibe MM. 2019. The effects of magnetic fields on plants growth: A comprehensive review. Int J Food Eng 5:79–87.

Patten CL, Glick BR. 2002. Role of *Pseudomonas putida* indoleacetic acid in development of the host plant root system. Appl Environ Microbiol 68:3795–3801.

Prasad R, Kamble S, Sripathy UR, Udaya KV, Bhaskar K, Singh DP. 2016. Seed bio-priming for biotic and abiotic stress management. In: Singh DP, Singh HB, Prabha R, editors, *Microbial Inoculants in Sustainable Agricultural Productivity*, 1:New Delhi: Springer. pp 211–228.

Raouia H, Hamida B, Khadidja A, Ahmed L, Abdelwaheb C. 2020. Effect of static magnetic field (200 mT) on biofilm formation in *Pseudomonas aeruginosa*. Arch Microbiol 202:77–83.

Ren X-M, Guo S-J, Tian W, Chen Y, Han H, Chen E, Li B-L, Li Y-Y, Chen Z-J. 2019. Effects of plant growth-promoting bacteria (PGPB) inoculation on the growth, antioxidant activity, Cu uptake, and bacterial community structure of rape (*Brassica napus* L.) grown in Cu-contaminated agricultural soil. Front Microbiol 10:1455.

Ren Z, Leng X, Liu Q. 2017. Effect of a static magnetic field on the microscopic characteristics of highly efficient oil-removing bacteria. Water Sci Technol 77:296–303.

Sharma E, Sharma R, Borah P, Jain M, Khurana JP. 2015. Emerging roles of auxin in abiotic stress responses. In: Pandey GK, editor, *Elucidation of Abiotic Stress Signaling in Plants*, 1:New York, NY: Springer. pp 299–328.

Shine MB, Guruprasad KN, Anjali A. 2011. Enhancement of germination, growth and photosynthesis in soybean by pre-treatment of seeds with magnetic field. Bioelectromagnetics 32:474–484.

Singh DP, Prabha R, Meena KK, Sharma L, Sharma AK. 2014. Induced accumulation of polyphenolics and flavonoids in cyanobacteria under salt stress protects organisms through enhanced antioxidant activity. Am J Plant Sci 5:726–735.

Singh S, Singh UB, Malviya D, Paul S, Sahu PK, Trivedi M, Paul D, Saxena AK. 2020. Seed biopriming with microbial inoculant triggers local and systemic defense responses against *Rhizoctonia solani* causing banded leaf and sheath blight in maize (*Zea mays* L.). Int J Environ Res Public Health 17:1396.

Tribouillois H, Dürr C, Demilly D, Wagner MH, Justes E. 2016. Determination of germination response to temperature and water potential for a wide range of cover crop species and related functional groups. PLoS One 11:e0161185.

Valencia-Díaz S, Montaña C. 2003. Effects of seed age, germination substrate, gibberelic acid, light, and temperature on seed germination in *Flourensia cernua* (*Asteraceae*), a Chihuahuan desert shrub. Southwest Nat 48:1–13.

Verma V, Ravindran P, Kumar PP. 2016. Plant hormone-mediated regulation of stress responses. BMC Plant Biol 16:86.

Vishwakarma K, Upadhyay N, Kumar N, Yadav G, Singh J, Mishra RK, Kumar V, Verma R, Upadhyay RG, Pandey M, Sharma S. 2017. Abscisic acid signaling and abiotic stress tolerance in plants: A review on current knowledge and future prospects. Front Plant Sci 8:161.

Wang X, Liu F, Jiang D. 2017. Priming: A promising strategy for crop production in response to future climate. J Integr Agric 16:2709–2716.

Zhao T, Deng X, Xiao Q, Han Y, Zhu S, Chen J. 2020. IAA priming improves the germination and seedling growth in cotton (*Gossypium hirsutum* L.) via regulating the endogenous phytohormones and enhancing the sucrose metabolism. Ind Crop Prod 155:112788.

Zheng M, Tao Y, Hussain S, Jiang Q, Peng S, Huang J, Cui K, Nie L. 2016. Seed priming in dry direct-seeded rice: Consequences for emergence, seedling growth and associated metabolic events under drought stress. Plant Growth Regul 78:167–178.

Influence of 340 mT Static Magnetic Field on Germination Potential and Mid-Infrared Spectrum of Wheat

Saša Ćirković,[1] Jasmina Bačić,[2] Novica Paunović,[1] Tamara B. Popović,[3] Alexander M. Trbovich,[4] Nebojša Romčević,[1] and Jasna L. Ristić-Djurović[1]*

[1]*Institute of Physics, University of Belgrade, Belgrade, Serbia*
[2]*Agricultural Extension Service Institute Tamiš, Pančevo, Serbia*
[3]*Institute for Medical Research, University of Belgrade, Belgrade, Serbia*
[4]*School of Medicine, University of Belgrade, Belgrade, Serbia*

In a number of studies, a static magnetic field was observed to positively influence the growing process of various plants; however, the effect has not yet been related to possible structural changes. We investigate if the static magnetic field that improves germination of wheat also alters wheat's near-infrared spectrum. Two groups of seeds were exposed to 340 mT for 16 h cumulatively. The first group was exposed 8 days for 2 h per day, while the second group was exposed 4 h per day for 4 consecutive days. One half of each of the exposed seed groups as well as of the unexposed control groups was sown, and the other half was used for mid-infrared spectra measurements. The sown seeds were monitored for 3 weeks after sowing. Germination of the groups exposed to the magnetic field was faster compared to corresponding non-exposed groups that were grown under the same conditions. The magnetic field exposure caused the enhancement of one O─H peak at 3,369 cm^{-1} and two C═O peaks at 1,662 cm^{-1} and 1,740 cm^{-1} in the mid-infrared spectrum. The effect was more pronounced for the 4 day, 4 h/day exposure. Bioelectromagnetics. 38:533–540, 2017. © 2017 Wiley Periodicals, Inc.

Keywords: strong static magnetic field; wheat; infrared peaks intensity change; growing enhancement; hydroxyl and carbonyl groups

INTRODUCTION

Rapid technological advances in the last few decades have established electromagnetic radiation as inevitably surrounding the entire planet. Numerous studies related to the influence of electromagnetic radiation on humans and life in general have been conducted. In particular, a static magnetic field of various intensities and homogeneities has been shown to affect humans, animals, insects, and bacteria, as well as plants. For example, it was shown that 5 min exposure to a static magnetic field of 0–192 mT peak-to-peak magnetic induction and 19 T/m lateral gradient could potentially help stomatologists as a drug-free, fast, and easy-to-use alternative method of local anesthesia [László et al., 2012]. An inhomogeneous static magnetic field of 31.7–232.0 mT was shown to have a cytoprotective effect on low-cisPt-concentration-treated SH-SY5Y cells, suggesting that exposure to various sources of static magnetic field in cancer patients under a cisPt regimen should be strictly controlled [Vergallo et al., 2014]. Milovanovich et al. [2016] reported that an upward and downward-oriented homogeneous static magnetic field of 128 mT affected spleen, brain, kidney, and liver in mice after 1 h/day exposure during a 5 day period. The subacute exposure to the homogeneous static magnetic field of 128 mT for 1 h per day in 15 consecutive days induced a pseudoanemia status with an increase in MCT4 and Glut4 proteins in glycolytic muscle of rats [Elferchichi et al., 2016]. A strong, homogeneous static magnetic field of 2.4 T was reported to be a potential stressor influencing fitness components and antioxidant defense

Grant sponsor: Ministry of Education, Science and Technological Development, Government of Serbia; grant number: III-45003.

Conflict of interest: None.

*Correspondence to: Jasna L. Ristić-Djurović, Institute of Physics, University of Belgrade, Pregrevica 118, 11080 Belgrade, Serbia. E-mail: jasna@stanfordalumni.org

Received for review 22 November 2016; Accepted 18 April 2017

DOI: 10.1002/bem.22057
Published online 12 July 2017 in Wiley Online Library (wileyonlinelibrary.com).

in *Drosophila* flies after 2 h of exposure [Todorović et al., 2015]. The investigation of secondary structures of protein in *Escherichia coli* (*E. coli*) and *Staphylococcus aureus* (*S. aureus*) exposed to an ultra-strong static magnetic field of 10 T for 5–60 min revealed little impact on *S. aureus*, but strong impact on *E. coli* [She et al., 2009].

There are also numerous studies that address the influence of magnetic fields on plants. The removal of local geomagnetic field for the whole growth period under laboratory conditions was shown to negatively affect the reproductive growth of *Arabidopsis*, which further affected the yield and harvest index [Xu et al., 2013]. On the contrary, Pietruszewski and Martinez [2015] reviewed studies that applied various magnetic fields and achieved improved quality of sowing material. For example, exposure of irrigation water for 6 s or of snow pea (*Pisum sativum* L var. macrocarpon) and Kabuli chickpea (*Cicer arietinum* L) seeds for 10 s to an inhomogeneous static magnetic field with peak magnetic field intensity of 136 mT led to a significant increase in the emergence rate index, shoot dry weight, and contents of N, K, Ca, Mg, S, Na, Zn, Fe, and Mn in both seedling varieties [Grewal and Maheshwari, 2011]. Jan et al. [2015] conducted a standard 7-day test in a reduced and enhanced geomagnetic environment of 4 and 100 μT as well as in a strong static magnetic field environment of 150 mT. The results showed that the 4 μT field significantly stimulated growth rate, and the 150 mT field seemed to have the potential to increase initial Chl *a* fluorescence and energy dissipation in *Lemna minor* plants. Shine et al. [2011] reported a beneficial effect of pre-sowing magnetic treatment for improving germination parameters and biomass accumulation in soybean. Several magnetic field strengths ranging from 0 to 300 mT in 50 mT steps as well as exposure times of 30, 60, and 90 min were shown to improve germination-related parameters like water uptake, speed of germination, seedling length, fresh weight, dry weight, and vigor indices of soybean seeds under laboratory conditions. In 1-month-old treated plants, leaf area and leaf fresh weight showed more than twofold enhancement, polyphasic chlorophyll *a* fluorescence transients gave a higher fluorescence yield, and total soluble protein map of leaves showed increased intensities in two bands. Pre-sowing exposures of spring wheat seeds to two values of a magnetic dose, a parameter defined to be proportional to exposure time and square of the magnetic induction, were observed to cause dose-dependent increase in germination and yield [Pietruszewski and Kania, 2010]. Vashisth and Nagarajan [2008] exposed seeds of chickpea (*Cicer arietinum* L.) to static magnetic fields with strengths of 0–250 mT in steps of 50 mT for 1–4 h and obtained significantly enhanced laboratory germination, speed of germination, seedling length, and seedling dry weight. In soil, seeds exposed to the three most efficient treatments produced significant increase in seedling dry weights, root length, root surface area, and root volume of 1-month-old plants. These three magnetic fields also improved coat membrane integrity as it reduced seed leachate electrical conductivity.

Infrared spectroscopy is commonly used to identify and study non-organic as well as organic chemicals. The peaks in an infrared spectrum correspond to various types of oscillations within a molecule and are mapped into functional groups and chemical bonds. A number of studies applied this technique to analyze wheat. For example, near infrared spectroscopy was used for wheat quality testing [Delwiche et al., 2011], and for predicting its quality characteristics and functionality [Dowell et al., 2006]. Mid-infrared spectroscopy was used by Amir et al. [2013] to identify wheat varieties, by Morales-Ortega et al. [2013] to characterize water-extractable arabinoxylans from spring wheat flour, and by Guo et al. [2015] to detect fluorescent brighteners in wheat flour. On the other hand, the influence of a magnetic field on the infrared spectrum of a material was not addressed as often. She et al. [2009] studied the effect of an ultra-strong static magnetic field on the 1,600–1,700 cm^{-1} range of FTIR spectrum of protein in bacteria, and Kolotovska et al. [2006] investigated the influence of a strong magnetic field on molecular alignment in thin vanadyl phthalocyanine films grown by organic molecular beam deposition.

Our objective was to examine if static magnetic fields that caused enhanced wheat germination also changed the mid-infrared spectrum of the exposed wheat. The importance of this hypothesis lies in its truthful outcome, which may enable possible application of infrared spectroscopy in detecting and studying structural changes in seeds caused by static magnetic fields and in analyzing possible mechanisms of action between these fields and organic materials.

The magnetic fields in our study were chosen to be strong, that is of the order of hundreds of mT, since such fields had been observed to cause increased germination of various plants [Vashisth and Nagarajan, 2008; Grewal and Maheshwari, 2011; Shine et al., 2011] as well as to affect other species [László et al., 2012; Vergallo et al., 2014; Elferchichi et al., 2016; Milovanovich et al., 2016]. The experiences of other researchers were also used to determine the exposure time schedule. The exposure times were taken to be of the order of 1 h/day [Vashisth and Nagarajan, 2008;

Todorović et al., 2015; Elferchichi et al., 2016; Milovanovich et al., 2016] for several consecutive days [Jan et al., 2015; Elferchichi et al., 2016; Milovanovich et al., 2016]. In the referenced studies, the effects of the magnetic field were shown to be exposure-dependent; however, a firm correlation between the effect intensity and applied exposure characteristics was not reported. With the aim to reduce the number of variable parameters of the exposure, we opted for two exposure schedules with equal cumulative exposure times, that is equal exposure doses [Pietruszewski and Kania, 2010]. Consequently, in our study the seeds were exposed to a 340 mT static magnetic field, 2 and 4 h/day for 8 and 4 days, respectively.

MATERIALS AND METHODS

Wheat

A wheat seed (*Triticum aestivum* L.) used in the experiment was of a certified variety (Pobeda, Institute of Field and Vegetable Crops, Novi Sad, Serbia), which is characterized by a very good winter-hardiness, good resistance to lodging, and powdery mildew. Its test weight is 80–87 kg/hl, protein content 12–15%, and wet gluten content around 32%. The seeds selected for the experiment were similar in size, color, and shape.

Wheat Germination

The experiment was conducted in two subsequent parts, each of which involved exposed and control groups of seeds. The two exposed groups were subject to two different magnetic field influences whereas the control groups were sham-exposed. Each of the four groups had 100 seeds that were planted 25 per pot. Plastic pots of 16 cm in diameter were filled with 2,300 ml of 3:1 mixture of sterilized soil and sand. The seeds were sown in laboratory conditions. Two groups of seeds, each contained in four pots, were housed in a growth chamber, and were monitored for 3 weeks. One of the groups was the control group, that was sham exposed, and the other group was exposed to the magnetic field; however, the researcher handling the germination was not aware of which one was which. In both parts of the experiment, the exposed and control groups were subject to the same growing conditions; however, the settings were different for the two parts. During the first part of the experiment the day/night cycle conditions in the growth chamber were programmed to temperatures of 16/12 °C, relative humidity of 70%/70%, and time interval cycles of 12/12 h. In the second part of the experiment, the second set of eight pots, four of which contained non-exposed and four with exposed seeds, were subject to a temperature of 22 °C and relative humidity of 70% that were kept constant for the entire course of the experiment. During each part of the experiment the germination rate was observed for 3 weeks after sowing.

Data and Statistics

The germination percentage was calculated as

$$G = 100 \cdot \frac{n_g}{N_s},$$

where n_g is number of germinated seeds and N_s is number of sown seeds that were in our experiment equal to 25 per pot. Note that in our case the total number of seeds was 100 for all seed groups, which makes the germination percentage equal to the total number of germinated seeds. The values of the mean and standard error of the mean were calculated as

$$\overline{G} = \frac{\sum_{i=1}^{N_p} G_i}{N_p},$$

$$\mathrm{SEM_G} = \frac{s_G}{\sqrt{N_p}} = \sqrt{\frac{\sum_{i=1}^{N_p} \left(G_i - \overline{G}\right)^2}{(N_p - 1)N_p}},$$

where G_i is germination percentage in the ith pot, $N_p = 4$ is the number of pots, and s_G is standard deviation of the germination percentage.

The germination time was calculated as

$$t_g = \frac{\sum n_t \cdot t}{\sum n_t},$$

where n_t is number of seeds that germinated at day t after sowing, and the standard error of the mean was obtained as

$$\mathrm{SEM_t} = \frac{s_t}{\sqrt{N_g}} = \sqrt{\frac{\sum_{i=1}^{N_g} \left(t_i - t_g\right)^2}{(N_g - 1)N_g}},$$

where s_t is the standard deviation of germination time and N_g is the total number of germinated seeds.

Data statistics were calculated in Matlab. The groups were compared using the germination time and built-in function ttest2 for Student's t-test method that

uses Satterthwaite's approximation for effective degrees of freedom. The function performs an unpaired two sample *t*-test with pooled or unpooled variance estimate. The test checks the hypothesis that two independent samples come from distributions with equal means. Data are assumed to come from normal distributions with unknown but equal variances. The null hypothesis is "the means are equal" and positive result of the test indicates that the null hypothesis can be rejected. The *P*-value is the probability of observing the given result, or one more extreme, by chance if the null hypothesis is true, that is small values of P cast doubt on the validity of the null hypothesis.

A change of peak intensity caused by an exposure to the magnetic field was calculated as well. If the intensity of a peak, I, between the wavenumbers ν_1 and ν_2 is taken to be the surface under the absorbance curve, namely

$$I(\nu_1, \nu_2) = \int_{\nu_1}^{\nu_2} A \mathrm{d}\nu,$$

where A is absorbance, then the relative peak intensity increase caused by exposure becomes

$$\Delta I(\nu_1, \nu_2) = \frac{I_{\text{exposed}}(\nu_1, \nu_2) - I_{\text{control}}(\nu_1, \nu_2)}{I_{\text{control}}(\nu_1, \nu_2)}.$$

Magnetic Field

The samples were exposed to the static magnetic field produced with a custom-made electromagnet depicted in Figure 1. The operating parameters were set to produce 340 mT in the center of the 2-cm gap between the poles, as measured with a digital teslameter (DTM-151, Group3 Technology, Auckland, New Zealand) with a resolution of 0.002 mT. Four plastic vials containing 25 seeds each were held within the magnet gap by a wooden holder. Exposed seeds were placed in the experimental volume of $1 \times 1 \times 6\,\text{cm}^3$ around the center of the gap, as indicated in Figure 1. Outer surfaces of the electromagnet's coils were water cooled. Temperature measurements away from the magnet and in the magnet's gap during the 4 h of magnet operation showed that coil heating did not produce a temperature increase in the experimental volume.

The numerical simulation of the magnet confirmed that the magnetic field variation within the experimental volume was between 339.5 and 340 mT, which is less than 0.15%. The seeds in the first part of the experiment were exposed 2 h per day for 8 consecutive days, and exposure corresponding to the second part of the experiment was 4 h per day for 4 consecutive days. Control groups were sham-exposed. All exposures were performed in duplicate in order to provide seeds for sowing as well as for infrared spectrum measurements.

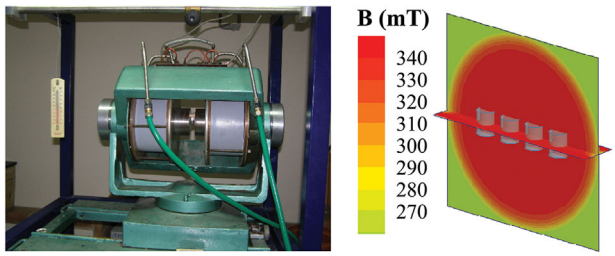

Fig. 1. Electromagnet and magnetic field within its gap. Pole diameter was 10 cm and gap between poles was adjusted to 2 cm. Magnetic field in the center was chosen to be 340 mT, which is about one half of 675 mT being the maximal magnetic induction that corresponds to chosen gap size. Tap water running through green hoses was used to cool outer surfaces of coils in order to eliminate possible temperature increase in experimental volume. Numerically simulated magnetic field is given in the $2 \times 10\,\text{cm}^2$ and $10 \times 10\,\text{cm}^2$ regions in horizontal and vertical planes through the gap center, respectively, along with placement of seeds during exposure in four plastic vials. Field within the experimental volume can be considered to be homogeneous.

Infrared Spectroscopy

Infrared reflectivity measurements were performed at room temperature with a Fourier-transform IR spectrometer (DA-8, ABB Bomem, Québec City, Canada). KBr beamsplitter and liquid-nitrogen-cooled Hg-Cd-Te (MCT) detector were used to cover the wavenumber range between 600 and 4,000 cm^{-1}. The spectra were recorded with a resolution of 2 cm^{-1} and with a very large number (500) of interferometer scans added for each spectrum in order to obtain high quality spectra. The spectra were measured in vacuum (0.2 mbar) in order to eliminate the presence of rotational-vibrational modes of CO_2 and water vapor present in air. The samples were prepared for IR spectrum measurements by grounding the wheat seeds, mixing the obtained flour with KBr powder, and by pressing the mixture into tablets always using the same pressure of $2\,\text{t/cm}^2$. Preprocessing of the spectra was performed in three steps. The spectra were smoothed using a Savitzky-Golay polynomial smoothing filter, which was followed by baseline subtraction and SNV normalization.

Exposures of seeds within the electromagnet, germination, and infrared spectra measurements were handled in two different institutions by three different

researchers who were not aware of the conditions the seed groups had previously been under; therefore, the study was double-blind.

RESULTS

Wheat germination results are given in Figures 2 and 3. Average germination times of the control and exposed groups in the first part of the experiment were t_g (control I) = 10.20 days and t_g (exposed I) = 9.02 days. In the second part of the experiment, we obtained values t_g (control II) = 7.02 days and t_g (exposed II) = 6.31 days. Consequently, in the first part of the experiment exposure to the magnetic field caused 11.5% decrease in the average germination time, whereas in the second part of the experiment, the magnetic field caused germination time to drop by 10.1%. Different growing conditions produced faster germination of the control group in the second part than in the first part of the experiment by 31.1%.

The mid-infrared absorbance spectra of the exposed as well as of the unexposed, that is sham exposed, grounded seeds are shown in Figure 4. Both of the considered exposures to the magnetic field caused broadening of the peak at 3,369 cm^{-1} and increased intensity of the peaks at 1,662 and 1,740 cm^{-1}, as well as decrease of all other peaks. The peak at 3,369 cm^{-1} corresponds to the O—H stretch, whereas the peaks at 1,662 and 1,740 cm^{-1} are associated with C=O stretches [Coates, 2000; Morales-Ortega et al., 2013]. To enhance visibility of the effects, differences between the absorbances, ΔA, are given in Figure 5.

The absorbance increases between $\nu_1 = 1{,}610\ cm^{-1}$ and $\nu_2 = 1{,}770\ cm^{-1}$ (C=O stretches) were calculated to be $\Delta I_{2h8d} = 5.4\%$ and $\Delta I_{4h4d} = 8.2\%$, whereas in the wavenumber range between $\nu_1 = 3{,}040\ cm^{-1}$ and $\nu_2 = 3{,}945\ cm^{-1}$ (O—H stretch) they were $\Delta I_{2h8d} = 11.4\%$ and $\Delta I_{4h4d} = 14.7\%$.

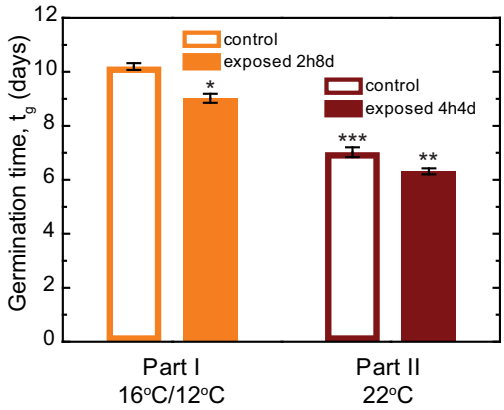

Fig. 3. Comparison of average germination times. Germination times are given as mean ± SEM. Exposed group differs compared to control group with $P < 0.001$ (*) and $P < 0.01$ (**) in the first and second part of the experiment, respectively. Difference between control groups in the first and second part of the experiment was obtained with $P < 0.001$ (***).

DISCUSSION

Results given in Figures 2 and 3 indicate that seed exposure to the magnetic field caused faster germination in both parts of the experiment, that is, regardless of the exposure schedule and of the conditions that were applied later in the growth chamber. However, due to germination dependence on the growing conditions as well as on the magnetic field exposure, the difference in growth conditions in the two parts of the experiment prevented the quantitative comparison of the achieved germination

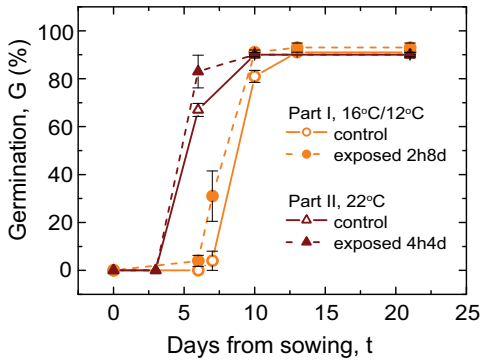

Fig. 2. Dynamics of germination. Exposures to magnetic field caused faster germination. Constant growth temperature of 22 °C caused faster germination than temperatures of 16/12 °C during 12 h-day/12 h-night cycle. Data points and error bars are presented as mean ± SEM of data corresponding to appropriate four pots.

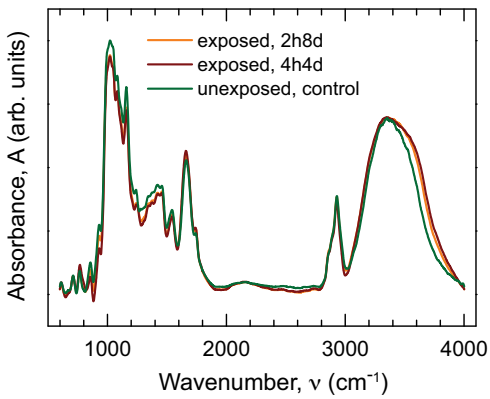

Fig. 4. Mid-infrared spectra. Exposures to magnetic field caused enhancement of oxygen peaks at 3,369 cm^{-1} (O—H stretch), 1,662 cm^{-1} (C=O stretch), and 1,740 cm^{-1} (C=O stretch), and decrease of all other peaks.

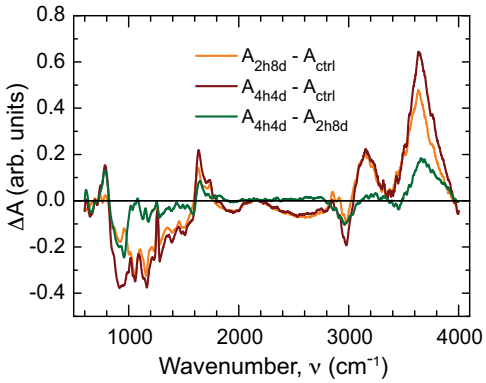

Fig. 5. Change in mid-infrared spectrum induced by magnetic field. Cumulative exposure time was equal to 16 h in both exposure time schedules; however, effects induced by 4 h/day exposure for 4 consecutive days were more pronounced.

potentials and applied exposure parameters. Growth chamber conditions applied in the second part of the experiment were favorable in terms of germination, as can be seen from comparison of the control groups. The germination enhancement of the exposed group in the second part of the experiment was the joint effect of exposure and growth conditions.

The mid-infrared absorbance spectra shown in Figure 4, in general, follow the shape of the wheat spectra given by other authors [Amir et al., 2013; Morales-Ortega et al., 2013; Guo et al., 2015]. The differences between the absorbances, ΔA, given in Figure 5 reveal that exposure to the magnetic field caused changes in the absorbance, and the effects were stronger for the 4 h/day exposure for 4 days than those corresponding to the 2 h/day exposure for 8 days. Since exposure doses were equal for both exposures, it seems that the dominant exposure parameter is the duration of the uninterrupted exposure rather than the cumulative exposure duration.

The wheat absorbance spectra were obtained from physiologically inactive seeds that were not subject to any other difference in treatment except for the magnetic field. Consequently, the magnetic field effect is not combined with growth conditions, as was the case with the germination potential, and quantitative comparisons were possible. Effects of the two magnetic field exposures on the wheat absorbance spectra were quantitatively compared using peak intensity increases, and exposure of 4 h/day during 4 days was more efficient than exposure of 2 h/day for 8 days by approximately 3%. Note that peak intensity was evaluated as the integral of the band instead of only its height because simple band height evaluation is more sensitive to noise, and integration provides better accuracy. In order to minimize the influence of all other factors except the magnetic field, the exposed and sham exposed samples used in the infrared spectral analysis were, except for exposure, otherwise treated in absolutely the same way. Namely, prior to exposure the physiologically inactive seeds for the control and exposed groups were taken from the same batch, whereas after exposure the tablets were prepared, and spectral analysis was conducted immediately following exposure.

Possible mechanisms of action between a magnetic field and biological materials were accessed by several authors [Brocklehurst, 1997; Eveson et al., 2000; Rosen, 2003; Shine et al., 2012; Lahbib et al., 2014]. Brocklehurst [1997] estimated the effects of isotopic substitution on the yield of chemical reactions involving radical pairs with the aim to explore the possible usefulness of magnetic isotope effects, especially to detect processes affected by magnetic fields. A review of the role of static magnetic fields in vitamins and glucose metabolism conducted by Lahbib et al. [2014] concluded that the primary cause of changes in cells after incubation in an external static magnetic field was the disruption of free radical metabolism and the elevation of their concentration leading to oxidative stress. Shine et al. [2012] found the influence of 150 and 200 mT on the production of reactive oxygen species in soybean, and Eveson et al. [2000] reported on the effects of weak magnetic fields on radical recombination reactions in micelles. The mechanism suggested by Rosen [2003] was based on diamagnetic anisotropic properties of membrane phospholipids. He proposed that reorientation of these molecules during moderate static magnetic field exposure would result in deformation of the imbedded ion channels, thereby altering their activation kinetics.

Studies that use infrared spectroscopy in their analysis of materials focus on peaks in an infrared spectrum, because various peaks correspond to chemical bonds of different types. Consequently, any change in a peak indicates a change in the corresponding chemical bond. She et al. [2009] detected a magnetic field effect similar to the one we detected at 1,662 cm^{-1}. They studied the effect of an ultra-strong static magnetic field of 10 T on the secondary structures of protein in bacteria by analyzing the 1,600–1,700 cm^{-1} range of FTIR spectrum that corresponded to the amide I region. They found that magnetic field caused 3.46–9.92% of random coils in the secondary structure of protein in *E. coli* to turn into helices. The conversion of β-sheets from intermolecular into intramolecular indicated that cohesion among molecules decreased and intramolecular hydrogen bonds were enhanced. Kolotovska et al. [2006] used infrared spectroscopy to study the influ-

ence of a strong magnetic field on the molecular alignment in thin vanadyl phthalocyanine films grown by organic molecular beam deposition and reported that integral intensity of the peak of the layer grown in the magnetic field was 14% larger compared to that of the film grown without magnetic field. In our study, the integral peak intensity increase caused by the magnetic field is in the range of 5.4–14.7% and is in agreement with those reported by She et al. [2009] and Kolotovska et al. [2006]. A peak intensity increase is commonly interpreted as a stronger molecule polarity or a larger number of a particular bond. Given that wheat is a complex mixture of organic molecules, the peak intensity is a sum of contributions of all molecules containing the corresponding bond. Knowing a molecular composition of wheat [Koehler and Wieser, 2013], we may conclude that a hydroxyl (OH) group is a part of the chemical structure of octacosanol and proteins, whereas a carbonyl (C═O) group belongs to amino acids in proteins. The observed peak changes in the 340 mT static magnetic field could be a consequence of the nucleophilic interaction of free oxygen electrons, from both hydroxyl and carbonyl groups, with n-3 long unsaturated fatty acid double-bonds. Since our results indicate that a static magnetic field simultaneously caused enhanced germination and changes in the mid-infrared spectrum, it seems worthwhile to investigate if some of the enhanced O─H and C═O bonds are located within the phytohormones or participate in chemical reactions with them.

CONCLUSION

Exposure to a 340 mT static magnetic field for cumulatively 16 h simultaneously caused an increase in wheat seed germination and changes in the mid-infrared spectrum. Therefore, the hypothesis that a static magnetic field that causes enhanced germination can also induce changes in the infrared spectrum of wheat seeds was shown to be true. Since infrared spectra are records of chemical bonds in a material and its structural composition, it can further be concluded that static magnetic fields can cause weak changes in the distribution of chemical bonds in wheat seeds. The peaks at 3,369 cm^{-1} (O─H stretch), 1,662 cm^{-1} (CO stretch), and 1,740 cm^{-1} (C═O stretch) were enhanced, whereas the intensity of all other peaks decreased. Changes in the infrared spectrum were more pronounced when 16 h exposure was divided into 4 h–4 days than when the exposure schedule was 2 h–8 days. Due to the simultaneous effect of the field on wheat germination and infrared spectrum, it seems plausible that the affected bonds are within phytohormons or that they participate in chemical reactions with them. Further studies that use infrared spectroscopy to detect structural changes induced by a static magnetic field may lead to better understanding of the mechanism of action between a static magnetic field and wheat germination. Also, a quantitative correlation between germination enhancement and changes in infrared spectra may enable a faster search for optimal field intensity and exposure time, since it would eliminate the need for complete germination and growth of a large number of seed groups exposed to various exposure schemes.

REFERENCES

Amir RM, Anjum FM, Khan MI, Khan MR, Pasha I, Nadeem M. 2013. Application of Fourier transform infrared (FTIR) spectroscopy for the identification of wheat varieties. J Food Sci Technol 50:1018–1023.

Brocklehurst B. 1997. Magnetic isotope effects in biology: A marker for radical pair reactions and electromagnetic field effects? Int J Radiat Biol 72:587–596.

Coates J. 2000. Interpretation of infrared spectra, a practical approach. In: Meyers RA, editor. Encyclopedia of Analytical Chemistry. Chichester, England: John Wiley & Sons. pp 10815–10837.

Delwiche SR, Graybosch RA, St. Amand P, Bai G. 2011. Starch waxiness in hexaploid wheat (*Triticum aestivum L.*) by NIR reflectance spectroscopy. J Agric Food Chem 59: 4002–4008.

Dowell FE, Maghirang EB, Xie F, Lookhart GL, Pierce RO, Seabourn BW, Bean SR, Wilson JD, Chung OK. 2006. Predicting wheat quality characteristics and functionality using near-infrared spectroscopy. Cereal Chem 83: 529–536.

Elferchichi M, Mercier J, Ammari M, Belguith H, Abdelmelek H, Sakly M, Lambert K. 2016. Subacute static magnetic field exposure in rat induces a pseudoanemia status with increase in MCT4 and Glut4 proteins in glycolytic muscle. Environ Sci Pollut Res 23:1265–1273.

Eveson RW, Timmel CR, Brocklehurst B, Hore PJ, McLauchlan KA. 2000. The effects of weak magnetic fields on radical recombination reactions in micelles. Int J Radiat Biol 76:1509–1522.

Grewal HS, Maheshwari BL. 2011. Magnetic treatment of irrigation water and snow pea and chickpea seeds enhances early growth and nutrient contents of seedlings. Bioelectromagnetics 32:58–65.

Guo X-X, Hu W, Liu Y, Gu D-C, Sun S-Q, Xu C-H, Wang X-C. 2015. Rapid analysis and quantification of fluorescent brighteners in wheat flour by Tri-step infrared spectroscopy and computer vision. J Mol Struct 1099: 393–398.

Jan L, Fefer D, Košmelj K, Gabarščik A, Jerman I. 2015. Geomagnetic and strong static magnetic field effects on growth and chlorophyll a fluorescence in *Lemna minor*. Bioelectromagnetics 36:190–203.

Koehler P, Wieser H. 2013. Chemistry of cereal grains. In: Gobbetti M, Gänzle M, editors. Handbook on Sourdough Biotechnology. New York: Springer Science + Business Media. pp 11–45.

Kolotovska V, Friedrich M, Zahn DRT, Salvan G. 2006. Magnetic field influence on the molecular alignment of vanadyl phthalocyanine thin films. J Cryst Growth 291:166–174.

Lahbib A, Ghodbane S, Sakly M, Abdelmelek H. 2014. Vitamins and glucose metabolism: The role of static magnetic fields. Int J Radiat Biol 90:1240–1245.

László JF, Farkas P, Reiczigel J, Vágó P. 2012. Effect of local exposure to inhomogeneous static magnetic field on stomatological pain sensation—a double-blind, randomized, placebo-controlled study. Int J Radiat Biol 88:430–438.

Milovanovich ID, Ćirković S, De Luka SR, Djordjevich DM, Ilić AŽ, Popović T, Arsić A, Obradović DD, Oprić D, Ristić-Djurović JL, Trbovich AM. 2016. Homogeneous static magnetic field of different orientation induces biological changes in subacutely exposed mice. Environ Sci Pollut Res 23:1584–1597.

Morales-Ortega A, Carvajal-Millan E, López-Franco Y, Rascón-Chu A, Lizardi-Mendoza J, Torres-Chavez P, Campa-Mada A. 2013. Characterization of water extractable arabinoxylans from a spring wheat flour: Rheological properties and microstructure. Molecules 18:8417–8428.

Pietruszewski S, Kania K. 2010. Effect of magnetic field on germination and yield of wheat. Int Agrophys 24:297–302.

Pietruszewski S, Martinez E. 2015. Magnetic field as a method of improving the quality of sowing material: A review. Int Agrophys 29:377–389.

Rosen AD. 2003. Mechanism of action of moderate-intensity static magnetic fields on biological system. Cell Biochem Biophys 39:163–173.

She Z, Hu X, Zhao X, Ren Z, Ding G. 2009. FTIR investigation of the effects of ultra-strong static magnetic field on the secondary structures of protein in bacteria. Infrared Phys Techn 52:138–142.

Shine MB, Guruprasad KN, Anand A. 2011. Enhancement of germination, growth, and photosynthesis in soybean by pretreatment of seeds with magnetic field. Bioelectromagnetics 32:474–484.

Shine MB, Guruprasad KN, Anand A. 2012. Effect of stationary magnetic field strengths of 150 and 200 mT on reactive oxygen species production in soybean. Bioelectromagnetics 33:428–437.

Todorović D, Perić-Mataruga V, Mirčić D, Ristić-Djurović J, Prolić Z, Petković B, Savić T. 2015. Estimation of changes in fitness components and antioxidant defense of Drosophila subobscura (Insecta, Diptera) after exposure to 2. 4 T strong static magnetic field. Environ Sci Pollut Res 22:5305–5314.

Vashisth A, Nagarajan S. 2008. Exposure of seeds to static magnetic field enhances germination and early growth characteristics in chickpea (*Cicer arietinum L.*). Bioelectromagnetics 29:571–578.

Vergallo C, Ahmadi M, Mobasheri H, Dini L. 2014. Impact of inhomogeneous static magnetic field (31.7–232.0 mT) exposure on human neuroblastoma SH-SY5Y cells during cisplatin administration. PLoS ONE 9:e113530.

Xu C, Wei S, Lu Y, Zhang Y, Chen C, Song T. 2013. Removal of the local geomagnetic field affects reproductive growth in *Arabidopsis*. Bioelectromagnetics 34:437–442.

IEEE TRANSACTIONS ON

MAGNETICS

A PUBLICATION OF THE IEEE MAGNETICS SOCIETY

DECEMBER 2013 VOLUME 49 NUMBER 12 IEMGAQ (ISSN 0018-9464)

(Contents Continued on Page 5594)

IEEE

(Contents Continued from Page 5593)

Analytical Description of Two-Dimensional Magnetic Arrays Suitable for Biomedical Applications

Andjelija Ž. Ilić[1], Saša Ćirković[1], Drago M. Djordjevic[2], Silvio R. De Luka[2], Ivan D. Milovanovich[2], Alexander M. Trbovich[2], and Jasna L. Ristić-Djurović[1]

[1]Innovation Center, School of Electrical Engineering, University of Belgrade, Belgrade 11120, Serbia
[2]Department of Pathological Physiology, School of Medicine, University of Belgrade, Belgrade 11000, Serbia

Two-dimensional magnetic arrays are used to generate a magnetic field that pervades a layer of volume above the array's surface, often creating regions of high magnetic flux density gradients. We have recently employed an array with equally oriented magnetic moments of individual elements in several biomedical experiments. We have chosen this type of array because of the slowly decreasing magnetic field it produces, which extends far from the array's surface and permeates the experimental volume. In order to fully define experimental conditions related to the applied magnetic field, we derive exact closed-form expressions for the magnetic flux density. Based on these analytical expressions and exploiting the array periodicity, a method is proposed for the approximate assessment of the main magnetic field parameters of interest—mean magnetic flux density and mean gradient of its component perpendicular to the array's surface. The obtained approximate assessment can further serve as a tool for the design of arrays with the desired mean field parameters. All the results are verified and validated by comparison with the finite element modeling as well as measurements.

***Index Terms*—Analytical modeling, finite element methods, magnetic arrays, magnetic field measurement, permanent magnets.**

I. Introduction

TWO-DIMENSIONAL magnetic arrays are used in a number of applications including optical switching (electromagnetic mirror arrays) and other microactuator systems, microsensors, acoustic transducers, magnetic bearings, unique microscale components self-assembly, synchronous permanent magnet planar motors, and magnetic levitation [1]–[11]. A primary goal in these applications is to create regions of high magnetic flux density gradients. Array configurations using alternating magnetic axes of the neighboring elements, or magnetic axes rotated as suggested by Halbach [12], seem to be utilized more often. In that case, the obtained magnetic fields exert their influence mainly in the narrow region close to the array's surface, with the magnetic flux lines predominantly parallel to the surface and alternating in direction between the adjacent elements. When the array elements all have identically oriented magnetic moments perpendicular to the array's surface, the resultant field extends further from the surface. Field distribution at the surface is wavy, since the magnetic flux lines partially close in between the adjacent elements. The majority of the magnetic flux lines, however, add up together to form a resultant predominantly perpendicular magnetic flux density, always positive after some boundary distance.

The latter type of the magnetic array, with equally oriented magnetic axes, can be used to generate static magnetic fields suitable for biomedical research. Permanent magnets as well as their combinations in a form of small arrays are already used in the field of physical therapy and rehabilitation. Although the underlying mechanisms of action are not fully understood, experimental data suggests beneficial therapeutic effects in treating arthritis, reducing inflammation and wound healing, pain and stress relief and improving microcirculation [13]–[17]. However, according to [18], poor field description is the major flaw in a large number of publications investigating the biomedical effects of field exposure. Recently, we utilized the two-dimensional magnetic arrays with equally oriented magnetic axes in our experiments described in [19], [20]. Magnetic arrays were assembled using the appropriate number of the so-called type L (large) MADU stripes, five-by-four equidistant permanent magnet arrangements used in the field of physical therapy and rehabilitation [21]. These smaller magnetic arrays were readily available to us and we placed them side by side to ensure optimal magnetic field coverage throughout the experimental volume. Three MADU stripes, i.e., the total of fifteen-by-four individual ferromagnetic rods are placed below the small standard animal cages, as shown in Fig. 1. For the large cages, six stripes arranged as an array of twelve-by-ten ferromagnetic rods are needed.

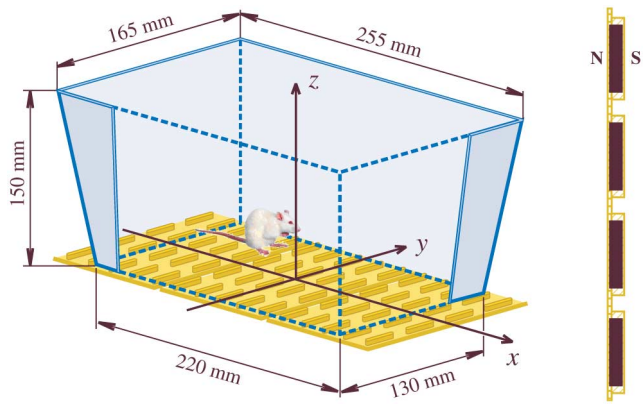

Fig. 1 Two-dimensional magnetic array used in biomedical research and referent coordinate system. The produced slowly decreasing magnetic field extends far from the surface of an array. Vertical cross-section of an array, corresponding to the plane $x = 0$ and halving the magnets along the y-axis, is shown on the right. Small permanent ferromagnetic rods are embedded into an elastic but firm rubber sheet that in no way disrupts the magnetic field.

The Fourier series expansion seems to be the method of choice in the analysis of large magnetic arrays [6], [7], while the smaller, non-periodic arrays are often analyzed using

Manuscript received March 15, 2013; revised July 10, 2013; accepted August 06, 2013. Date of publication August 08, 2013; date of current version November 20, 2013. Corresponding author: A. Ž. Ilić (e-mail: andjelijailic@ieee.org).

Color versions of one or more of the figures in this paper are available online at http://ieeexplore.ieee.org.

Digital Object Identifier 10.1109/TMAG.2013.2277831

the finite-element method (FEM) [1], [11]. Use of equivalent sources, i.e., magnetization currents or surface magnetic charges to represent the material properties, accordingly with the theorem of equivalence [22], [23], results in field integrals that can be solved either analytically or numerically. One choice of equivalent sources may result in expressions that are easier to solve, or only solvable [24]. The flat sided individual magnets lead to analytically solvable integrals. Expressions for the magnetic field of a single cuboid magnet, based on the magnetic charges, were first given in [25]. We derive easy to implement closed-form expressions for the two-dimensional magnetic array, i.e., the magnetic flux density in an arbitrary field point, based on the equivalent magnetization currents and field derivation for a single current sheet. We discuss how to adapt these complete expressions to the case of alternating magnetic axes as well as non-periodic arrays.

For arrays with equally oriented magnetic axes, magnetic flux density, $\mathbf{B}$, after some distance from the array's surface is predominantly perpendicular to the surface, i.e., the vector $\mathbf{B}$ is approximately parallel to the z-axis in Fig. 1 ($B_\mathrm{x}, B_\mathrm{y} << B_\mathrm{z}$). Disregarding the much smaller variations of the vector $\mathbf{B}$ in planes parallel to the array's surface ($\frac{\partial B_\mathrm{z}}{\partial x}, \frac{\partial B_\mathrm{z}}{\partial y} << \frac{\partial B_\mathrm{z}}{\partial z}$), we consider only its pronounced change in the z-axis direction and introduce the "magnetic flux density gradient" as the negative z-component of the gradient of $B_z(x, y, z)$:

$$G_\mathrm{z}(x, y, z) = -\mathrm{grad}_\mathrm{z} B_\mathrm{z}(x, y, z) = -\frac{\partial B_\mathrm{z}(x, y, z)}{\partial z}. \quad (1)$$

The mean magnetic flux density and the mean gradient of its z-component in horizontal planes, as well as their dependence on the z-coordinate, are the main parameters of interest in describing these arrays. We propose a method for the fast preliminary assessment of these two parameters, based on the periodicity of the z-component of magnetic field. Both the detailed field expressions and the fast estimate are verified and validated by comparison with the finite-element calculations as well as the measured data. Further, the magnetic flux density variation throughout the experimental volume, including the stray magnetic field, is studied using the finite-element calculations. Possible optimization strategies, using the approximate analytical expressions as a tool to adjust the mean field parameters in the experimental volume, are briefly discussed. We expect this work to be useful both to researchers and to practitioners in the fields of two-dimensional magnetic array design and biomedical applications.

II. Analytical Model

The development of analytical expressions starts with considering the basic building block of the two-dimensional array, the single ferromagnetic rod. Remanent magnetization is either known in advance or it can be determined using the material characterization by measurements as explained in Section III. For the array we analyzed as an example the value of remanent magnetization was unavailable. Using the magnetic field measurements, we obtained $M_\mathrm{r} = 60.0\ \mathrm{A \cdot m^2/kg}$.

Due to the principal role of the considered stripes to easily conform to parts of the human body, magnetic array is created by embedding $4.8\ \mathrm{mm} \times 24.4\ \mathrm{mm} \times 4.8\ \mathrm{mm}$ sized ferromagnetic rods into an elastic rubber stripe or sheet. The influence of the rubber can be completely neglected in all calculations. For a different substrate, care should be taken of its influence.

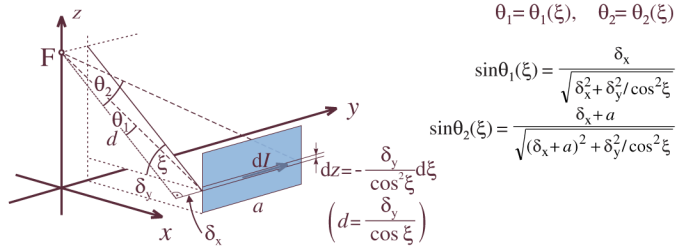

Fig. 2 Magnetic flux density calculation for a single current sheet. Defining the angle ξ as the field point elevation above the horizontal plane that contains the elemental current segment $\mathrm{d}I$, we can express all other parameters as a function of ξ in order to simplify the analytical integration.

Assuming the uniform magnetization over the volume of a ferromagnetic rod, the produced magnetic field is identical to that corresponding to a short solenoid of rectangular cross-section. The surface current density vector, $\mathbf{J}_\mathrm{mS}$, is given by

$$\mathbf{J}_\mathrm{mS} = \mathbf{M} \times \mathbf{n} \quad (2)$$

where the magnetization vector is denoted by $\mathbf{M}$ and $\mathbf{n}$ represents the surface normal, i.e., the unit vector perpendicular to the magnet-air boundary surface, directed from the magnet outwards. We obtain $J_\mathrm{mS} = \rho \cdot M_\mathrm{r} = 294.0 \cdot 10^3$ A/m.

Each of the four sides of rectangular cross-section solenoid is a flat current sheet that can be considered as a collection of very thin wires carrying the elemental currents $\mathrm{d}I$. Magnetic flux density, $\mathbf{B}$, is perpendicular to the plane defined by the straight finite wire and the field point F, shown in Fig. 2, and related to $\mathrm{d}I$ by the right-hand rule. Magnitude is evaluated directly from the Biot-Savart law [22]:

$$B = \frac{\mu_0 \mathrm{d}I}{4\pi d}(\sin\theta_2 - \sin\theta_1)\ . \quad (3)$$

Above, d represents the shortest (perpendicular) distance from the arbitrary considered field point F to the conductor axis and also defines the referent axis for the measurement of angle θ. Angles θ_1 and θ_2 correspond to the point of current entrance into the conductor and its exit, respectively.

Due to cancellation of other field components, vector $\mathbf{B}$ on the single solenoid axis has only the component in the axis direction. Defining the angle ξ as the field point elevation above the plane parallel to the xOy that contains the elemental current segment $\mathrm{d}I$, we can express all other parameters as a function of ξ in order to simplify the integration. Throughout this work the plane $z = 0$ coincides with the top surface of the magnetic array, including the rubber wrap whose thickness on each side is $t = 0.8$ mm. Therefore, $z_1 = z + t + h$ and $z_2 = z + t$ correspond to the field point vertical distance from the bottom and top surface of the ferromagnetic rods whose sides are $a = 24.4$ mm and $b = 4.8$ mm, and height is $h = b$. Angles $\xi_{\mathrm{a}1}$, $\xi_{\mathrm{a}2}$, and $\xi_{\mathrm{b}1}$, $\xi_{\mathrm{b}2}$, match z_1 and z_2. The elemental currents equal $\mathrm{d}I_\mathrm{a} = -J_\mathrm{mS}\frac{b}{2\cos^2\xi_\mathrm{a}}\mathrm{d}\xi_\mathrm{a}$ and $\mathrm{d}I_\mathrm{b} = -J_\mathrm{mS}\frac{a}{2\cos^2\xi_\mathrm{b}}\mathrm{d}\xi_\mathrm{b}$, for the sides a and b, respectively. Integrating $\mathrm{d}B_\mathrm{z} = \mathrm{d}B\cos\xi$ we obtain

$$B_1 = -\frac{\mu_0 J_\mathrm{mS}}{\pi}\left(\int_{\xi_{\mathrm{a}1}}^{\xi_{\mathrm{a}2}} \frac{a\cos\xi_\mathrm{a}\,\mathrm{d}\xi_\mathrm{a}}{\sqrt{a^2\cos^2\xi_\mathrm{a}+b^2}} + \int_{\xi_{\mathrm{b}1}}^{\xi_{\mathrm{b}2}} \frac{b\cos\xi_\mathrm{b}\,\mathrm{d}\xi_\mathrm{b}}{\sqrt{a^2+b^2\cos^2\xi_\mathrm{b}}}\right),$$

$$B_1(z) = \frac{\mu_0 J_\mathrm{mS}}{\pi}\left(\arcsin\left(\frac{2\frac{a}{\sqrt{a^2+b^2}}z}{\sqrt{b^2+4z^2}}\right) + \arcsin\left(\frac{2\frac{b}{\sqrt{a^2+b^2}}z}{\sqrt{a^2+4z^2}}\right)\right)\Bigg|_{z_2}^{z_1}. \quad (4)$$

The magnetic flux density at the array's surface equals $B_1(z = 0) = 103.08$ mT , and at the center of each magnet $B_1(z = -3.2 \text{ mm}) = 189.11$ mT.

Two-dimensional magnetic array is constructed by placing M_a individual ferromagnetic rods in each of the N_a parallel rows in the xOy plane, the magnetic axes all in the z-direction. Magnets are spaced equidistantly with a center-to-center shift $x_\mathrm{d} = 19.5$ mm and $y_\mathrm{d} = 36.0$ mm in the x- and y-direction. Due to the periodicity of the problem, the Fourier series expansion is frequently used in literature. Analytical integration over the heights of all the current sheets involved, as explained above, results in the exact expressions for all three components of the magnetic flux density in an arbitrary considered field point. The obtained expressions are valid for small as well as large arrays, and can be applied to the non-periodic arrays if a set of masking coefficients is properly introduced. However, the array periodicity is exploited to obtain the simple but effective analytical assessment of magnetic field parameters of interest, based on the exact field values at two vertical axes.

With the increase in the number of individual magnets in both dimensions, the magnetic flux density approaches a limiting, final-state distribution of an infinite array, which is periodic with a period of x_d in the x-, and y_d in the y-direction. The magnetic flux density distribution in the central part of a finite array has to be approximately periodic as well, with the hills of the distribution located directly above the magnet centers and the lowest values (valleys) at vertical axes going through the cross-sections of midlines between the rows of magnets. Horizontal vector $\mathbf{B}$ components are small enough in comparison with the z-component to be excluded from the assessment. Therefore, the magnetic flux density on the axes through the points H and V in Fig. 3, denoted $B_\mathrm{H}(z)$ and $B_\mathrm{V}(z)$, represents maxima and minima in horizontal planes. The mean magnetic flux density in a horizontal plane, $\bar{B}_\mathrm{z}(z)$, may in the first approximation be replaced by the arithmetic mean of B_H and B_V. Such an approach will be justified by comparison with measurements and finite-element modeling. In our example, number of array elements is rather small, while the size of individual magnets, their aspect ratio and mutual spacing are considerable. It is, therefore, somewhat of a worst-case scenario for validation of the proposed approach. Vector $\mathbf{B}$ mean value and variation, $\bar{B}_\mathrm{z}(z)$ and $\Delta B_\mathrm{z}(z)$, and its gradient defined by (1), $\bar{G}_\mathrm{z}(z)$ and $\Delta G_\mathrm{z}(z)$, become

$$\begin{aligned}
\overline{B_\mathrm{z}}(z) &= \frac{B_\mathrm{H}(z) + B_\mathrm{V}(z)}{2},\\
\Delta B_\mathrm{z}(z) &= \frac{B_\mathrm{H}(z) - B_\mathrm{V}(z)}{2},\\
\overline{G_\mathrm{z}}(z) &= -\mathrm{grad}_\mathrm{z}\overline{B_\mathrm{z}} = -\frac{1}{2}\left(\frac{\partial B_\mathrm{H}(z)}{\partial z} + \frac{\partial B_\mathrm{V}(z)}{\partial z}\right)\\
&= \frac{G_\mathrm{H}(z) + G_\mathrm{V}(z)}{2},\\
\Delta G_\mathrm{z}(z) &= \frac{G_\mathrm{H}(z) - G_\mathrm{V}(z)}{2},\\
G_\mathrm{H} &= -\frac{\partial B_\mathrm{H}(z)}{\partial z},\ G_\mathrm{V} = -\frac{\partial B_\mathrm{V}(z)}{\partial z}.
\end{aligned} \tag{5}$$

Without loss of generality, we assume the odd number of elements, $M_\mathrm{a} = 2M + 1$, in the x-direction and even, $N_\mathrm{a} = 2N$, in the y-direction. Integrating $\mathrm{d}B_\mathrm{z} = \mathrm{d}B\cos\xi$ over all the current sheets we obtain $B_\mathrm{z}(x, y, z)$. Current sheets parallel to the yOz plane contribute $\mathrm{d}B_\mathrm{x} = \pm\mathrm{d}B\sin\xi$ to vector $\mathbf{B}$, and those parallel to the xOz plane generate y-component, $\mathrm{d}B_\mathrm{y} = \pm\mathrm{d}B\sin\xi$. After representing $\mathrm{d}I = J_\mathrm{mS}\cdot\mathrm{d}z$, $\sin\theta_1$, $\sin\theta_2$, d and $\mathrm{d}z$ as a function of angle ξ, as shown in Fig. 2, two integrals that need to be solved for each current sheet become

$$\begin{aligned}
\int_{\sin\xi_1}^{\sin\xi_2} \frac{\mathrm{d}(\sin\xi)}{\sqrt{P^2 - \sin^2\xi}} &= \arcsin\left(\frac{\sin\xi}{P}\right)\Big|_{\sin\xi_1}^{\sin\xi_2},\\
\int_{\cos\xi_1}^{\cos\xi_2} \frac{\mathrm{d}(\cos\xi)}{\sqrt{\cos^2\xi + R^2}} &= \ln\left(\cos\xi + \sqrt{\cos^2\xi + R^2}\right)\Big|_{\cos\xi_1}^{\cos\xi_2}.
\end{aligned} \tag{6}$$

Therefore, we obtain (7), shown at the bottom of the page. The parameters p and q correspond to the sines of angles θ_0 and ξ, respectively, with θ_0 being the projection of the angle θ to the xOy plane. Upper indices $tp = 0$ and $tp = 1$ correspond to the point of current entrance into the current sheet and its exit, respectively. Upper indices $tq = 0$ and $tq = 1$ denote the bottom surface or the top surface of the ferromagnetic rod, i.e.,

$$\begin{aligned}
B_z(x,y,z) &= \frac{\mu_0 J_\mathrm{mS}}{4\pi}\sum_{i=-M}^{M}\sum_{j=-N}^{N\text{-}1}\sum_{k=1}^{4}\sum_{tp=0}^{1}\sum_{tq=0}^{1}(-1)^{(tp+tq+1)}\arcsin(p_{i,j,k}^{tp}\cdot q_{i,j,k}^{tq}),\\
p_{i,j,k}^{tp} &= \frac{\left(i\cdot x_\mathrm{d} + (-1)^{\left[\frac{k}{2}\right]+tp}\frac{b}{2} - x\right)^{m_2}\cdot\left((j+\frac{1}{2})\cdot y_\mathrm{d} + (-1)^{\left[\frac{k-1}{2}\right]+tp}\frac{a}{2} - y\right)^{m_1}}{\sqrt{\left(i\cdot x_\mathrm{d} + (-1)^{\left[\frac{k}{2}\right]+1+(tp-1)m_2}\frac{b}{2} - x\right)^2 + \left((j+\frac{1}{2})\cdot y_\mathrm{d} + (-1)^{\left[\frac{k-1}{2}\right]+1+(tp-1)m_1}\frac{a}{2} - y\right)^2}},\\
q_{i,j,k}^{tq} &= \frac{\frac{\mathrm{sgn}\left(i\cdot x_\mathrm{d} + (-1)^{m_\mathrm{s}}\frac{b}{2} - x\right)^{m_1}}{\left(-\mathrm{sgn}((j+\frac{1}{2})\cdot y_\mathrm{d} + (-1)^{m_\mathrm{s}}\frac{a}{2} - y)\right)^{m_2}}\cdot(z + t + (1-tq)\cdot h)}{\sqrt{\left(i\cdot x_\mathrm{d} + (-1)^{m_\mathrm{s}}\frac{b}{2} - x\right)^{2m_1}\left((j+\frac{1}{2})\cdot y_\mathrm{d} + (-1)^{m_\mathrm{s}}\frac{a}{2} - y\right)^{2m_2} + (z + t + (1-tq)\cdot h)^2}},\\
m_1 &= \left(1 + (-1)^{k-1}\right)/2,\ m_2 = \left(1 + (-1)^{k}\right)/2,\ m_\mathrm{s} = \left(1 - \mathrm{sgn}\left(k - \frac{5}{2}\right)\right)/2.
\end{aligned} \tag{7}$$

the considered current sheet. Lower indices (i, j) correspond to the i-th element in the j-th row of the magnetic array, while k denotes one of the four current sheets formed by the considered element. For k equal to 1, 2, 3, and 4, current sheet is located at $\Delta x = -b/2$, $\Delta y = -a/2$, $\Delta x = b/2$, and $\Delta y = a/2$, with respect to the center of the considered ferromagnetic rod, respectively. Operator $[\cdot]$ stands for the integer division. As pointed out in [26], expressions describing permanent magnets of rectangular cross-section depend only on the magnet corner positions, which simplifies the calculations. Using (7), $B_{\mathrm{H}}(z) = B_{\mathrm{z}}(0, y_{\mathrm{d}}/2, z)$, $B_{\mathrm{V}}(z) = B_{\mathrm{z}}(x_{\mathrm{d}}/2, 0, z)$, $B_{\mathrm{O}}(z) = B_{\mathrm{z}}(0, 0, z)$, and $B_{\mathrm{P}}(z) = B_{\mathrm{z}}(x_{\mathrm{d}}/2, y_{\mathrm{d}}/2, z)$ are calculated at four characteristic axes through the points H, V, O, and P, denoted in Fig. 3. In our example $M = 7$ and $N = 2$. The magnetic flux density at the top surface of an individual magnet in the central part of a stripe is decreased from $B_1(0)$ to $B_{\mathrm{H}}(0) = 95.80$ mT. At larger z, there is an increase in both $B_{\mathrm{H}}(z)$ and $B_{\mathrm{V}}(z)$ due to the contributions of surrounding rods.

The estimate (5) is based only on the dominant z-component of the magnetic flux density. For the sake of completeness, as well as possible extension of this analytical description to the non-periodic arrays, exact expressions for the horizontal field components are also given in (8), shown at the bottom of the page. Exact description of arrays with alternating magnetic moments of the neighboring elements is obtained easily by multiplying each element of the sums by $(-1)^{i+j}$, or just $(-1)^i$, i.e., $(-1)^j$. For the arrays with rotated magnetic axes, expressions get more complicated. Magnetization currents exist at the top and bottom sides of the magnets as well. Starting from the general expression $\mathbf{J}_{\mathrm{mS}} = J_{\mathrm{x}}^{i,j,k}\mathbf{i}_{\mathrm{x}} + J_{\mathrm{y}}^{i,j,k}\mathbf{i}_{\mathrm{y}} + J_{\mathrm{z}}^{i,j,k}\mathbf{i}_{\mathrm{z}}$, $k \in \{1, 2, 3, 4, 5, 6\}$, where $\mathbf{i}_x$, $\mathbf{i}_y$, and $\mathbf{i}_z$ represent the unit vectors in the x-, y- and z-direction, every term in (7) and (8) is replaced by the three terms, each multiplied by appropriate $J^{i,j,k}$, and the summation over k now includes $k = 5$ and $k = 6$ as well. For the non-periodic arrays a set of masking coefficients $M^{i,j} \in \{0, 1\}$ is introduced, describing the existence of a particular element in an array's matrix.

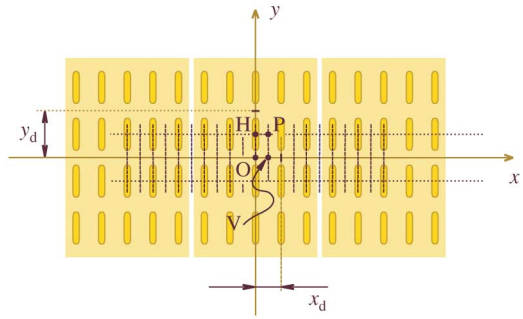

Fig. 3 Characteristic points used in approximate assessment of the mean magnetic field parameters. Mean magnetic flux density in the horizontal planes and its mean gradient given in (5), are approximated using the exact analytically obtained values at the vertical axes going through the points H and V. Magnetic flux density at axes through the points O and P, as well as H and V, is validated by comparisons with the finite-element calculations and measurements performed for nine values of z coordinate. Measurement grid is denoted by the crossings of the dashed lines, along the x-axis and along the two lines parallel to the x-axis.

III. Measurements

Measurements performed on the example two-dimensional array, using Digital Teslameter DTM-151, serve two purposes. Firstly, remanent magnetization is determined from the measured maxima and minima of the vector $\mathbf{B}$ in horizontal planes. Secondly, analytical expressions as well as the finite-element model are validated against the measured data.

As shown in Fig. 3, we used a set of three stripes and a measurement grid, consisting of 21-by-3 points in planes parallel to the xOy plane. Grid step in x- and y-direction equals $x_{\mathrm{d}}/2 = 9.75$ mm and $y_{\mathrm{d}}/2 = 18.0$ mm, which agrees with

$$
\begin{aligned}
B_{\mathrm{x}}(x,y,z) &= \frac{\mu_0 J_{\mathrm{mS}}}{4\pi} \sum_{i=-M}^{M} \sum_{j=-N}^{N-1} \sum_{k=1,3} \sum_{tp=0}^{1} \sum_{tq=0}^{1} \frac{(-1)^{(tp+tq+1)}}{\operatorname{sgn}((j+\frac{1}{2})\cdot y_{\mathrm{d}} + (-1)^{m_{\mathrm{s}}+tp+1}\frac{a}{2} - y)} \\
&\quad \cdot \ln\left(-\left|u_{i,j,k}^{a,tq}\right| + \sqrt{\left(u_{i,j,k}^{a,tq}\right)^2 + \left(r_{i,j,k}^{a,tp}\right)^2} \right), \\
B_{\mathrm{y}}(x,y,z) &= \frac{\mu_0 J_{\mathrm{mS}}}{4\pi} \sum_{i=-M}^{M} \sum_{j=-N}^{N-1} \sum_{k=2,4} \sum_{tp=0}^{1} \sum_{tq=0}^{1} \frac{(-1)^{(tp+tq)}}{\operatorname{sgn}(i\cdot x_{\mathrm{d}} + (-1)^{m_{\mathrm{s}}+tp}\frac{b}{2} - x)} \\
&\quad \cdot \ln\left(-\left|u_{i,j,k}^{b,tq}\right| + \sqrt{\left(u_{i,j,k}^{b,tq}\right)^2 + \left(r_{i,j,k}^{b,tp}\right)^2} \right), \\
r_{i,j,k}^{a,tp} &= \frac{\left(i\cdot x_{\mathrm{d}} + (-1)^{m_{\mathrm{s}}}\frac{b}{2} - x\right)}{\left((j+\frac{1}{2})\cdot y_{\mathrm{d}} + (-1)^{m_{\mathrm{s}}+tp+1}\frac{a}{2} - y\right)}, \qquad r_{i,j,k}^{b,tp} = \frac{\left((j+\frac{1}{2})\cdot y_{\mathrm{d}} + (-1)^{m_{\mathrm{s}}}\frac{a}{2} - y\right)}{(i\cdot x_{\mathrm{d}} + (-1)^{m_{\mathrm{s}}+tp}\frac{b}{2} - x)}, \\
u_{i,j,k}^{a,tq} &= \frac{(i\cdot x_{\mathrm{d}} + (-1)^{m_{\mathrm{s}}}\frac{b}{2} - x)}{\sqrt{\left(i\cdot x_{\mathrm{d}} + (-1)^{m_{\mathrm{s}}}\frac{b}{2} - x\right)^2 + \left(z + t + (1-tq)\cdot h\right)^2}}, \\
u_{i,j,k}^{b,tq} &= \frac{((j+\frac{1}{2})\cdot y_{\mathrm{d}} + (-1)^{m_{\mathrm{s}}}\frac{a}{2} - y)}{\sqrt{\left((j+\frac{1}{2})\cdot y_{\mathrm{d}} + (-1)^{m_{\mathrm{s}}}\frac{a}{2} - y\right)^2 + \left(z + t + (1-tq)\cdot h\right)^2}}, \qquad m_{\mathrm{s}} = \frac{1 - \operatorname{sgn}\left(k - \frac{5}{2}\right)}{2}.
\end{aligned}
\tag{8}
$$

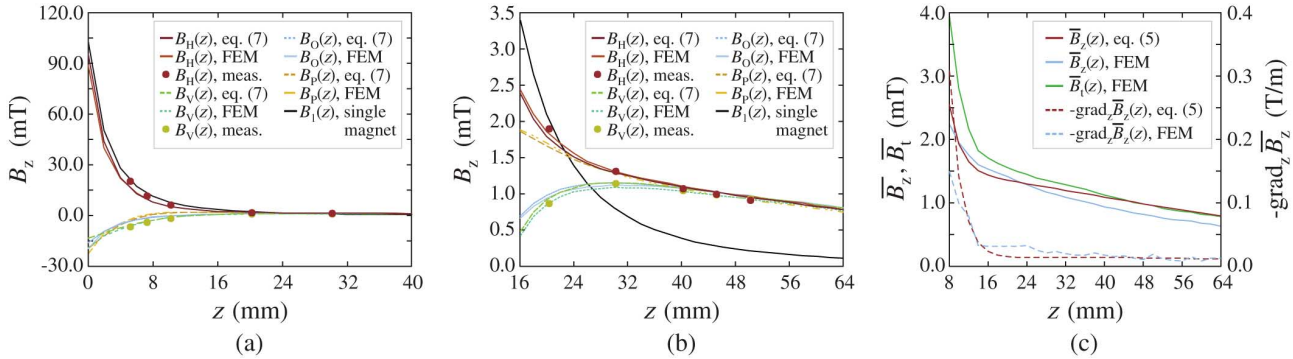

Fig. 4 Agreement of the three sets of results for the magnetic flux density above the array. Due to large magnetic flux density variations with the z coordinate, the same results are shown in parts (a) and (b), but for two different z-ranges. Values of B_z calculated analytically, using (7), and numerically (FEM) agree well and fully correspond to the realistic, measured magnetic flux density data (dots) at eight heights. At larger z, $B_H(z)$ and $B_V(z)$ converge and show slow and almost linear decrease, opposed to rapidly decreasing $B_1(z)$. Analytical estimates, using (5), for $\bar{B}_z(z)$ and its mean gradient defined by (1) are compared to the numerically obtained values in part (c). The difference between the two is mainly a consequence of the finite number of elements comprising the magnetic array. Analytical estimates are good enough to be used for fast parameter assessment or preliminary design. Mean total magnetic flux density, $\bar{B}_t(z)$, where $B_t = \sqrt{B_x^2 + B_y^2 + B_z^2}$, is obtained from finite-element calculations. It is mainly contributed by B_z, and the analytical estimate for $\bar{B}_z(z)$ lies between $\bar{B}_z$ and $\bar{B}_t$.

the hills and valleys of the magnetic flux density distribution. Measurement resolution is 0.005 mT and the reading precision is 0.01%, for the utilized range of up to 0.3 T [27].

Hexagonal barium hexaferrite ($BaFe_{12}O_{19}$), the material out of which the individual magnets are made, is a type of robust ceramics that is generally stable to moisture and resistant to corrosion. One of the most important hard magnetic materials, it is widely used for permanent magnets, magnetic recording media and microwave devices. Its production cost is low, whereas its magnetic properties are very good, e.g., high Curie temperature and high saturation magnetization. These are the material intrinsic properties, unaffected by the microstructure. Theoretical values $T_C = 450°\mathrm{C}$ and $B_r = 480$ mT are reported in [28]. Given the barium hexaferrite density reported in [29], $\rho = 4.9 \cdot 10^3$ kg/m^3, the corresponding saturation magnetization is $M_s = 78.0$ A $\cdot$ m^2/kg. However, other magnetic properties can vary a lot as a function of production process, e.g., sintering time and temperature [29]–[31]. Therefore, a trial value of M_r is used to calculate $B_H(z)$ and $B_V(z)$ according to (7) and the scaling constant for M_r giving the actual field levels is obtained by field measurement in several hill points. Since we collected a large amount of measured data to verify the models, averaged hill and valley magnetic field data for five planes, $z \in \{19.4, 29.4, 39.4, 44.4, 49.4\}$ mm, was used as a reference to find a multiplicative constant that minimizes the mean square difference between the calculated and measured data. However, it is sufficient to measure $B_H(z)$ in three to five points above one of the most central hills, at a distance from the array's surface. Upon the correction, $M_r = 60.0$ A $\cdot$ m^2/kg.

In total, three sets of measurements were performed. Firstly, we measured magnetic field at the array's surface, considering only hills. Values of (55.70 ± 7.22) and (54.34 ± 7.22) mT, given as (mean value $\pm$ standard deviation), are obtained from the repeated measurements for the 'north' and 'south' side of the stripes, respectively. We attribute the differences to the stronger or lighter adhesion to the soft rubber surface or slight tilt of the Hall probe measuring only the perpendicular field component, during the manually conducted measurements. Measured values are somewhat lower than the theoretically predicted 59.62 mT at the height of the active measurement area of the Hall probe, $z = 1.2$ mm.

Second set of measurements followed the measurement grid described above, marked out on a thin glass plate. Data was taken for $z \in \{4.4, 6.5, 9.4, 19.4, 29.4, 39.4, 44.4, 49.4\}$ mm. Estimates for $B_V(z)$ and $B_H(z)$ are obtained by averaging the ten out of 21 values taken along the x- axis, and 22 hill values taken for $y = \pm y_d/2$, respectively. The relative variability of measurements, assessed as the ratio of the standard deviation and the mean value, is twice smaller for the second set of measurements than for the first one.

The third set of measurements was taken following the same procedure as for the second one, with the two and three layers of arrays on top of each other. Its purpose was to verify the analytical expressions for the layered arrays.

IV. Finite Element Modeling

The finite-element calculations can be used to validate the analytical expressions, as well as study the magnetic flux density variation in the experimental volume, including the stray magnetic field. Any software package for magnetostatic analysis and modeling could be used for the two-dimensional magnetic array modeling. We employed the Mermaid FEM suite for magnetostatics [32], [33]. It is a universal tool for the design of permanent and electro-magnets, utilizing first-order scalar elements to solve for the magnetostatic potential. For the best accuracy of the results, the basic two-dimensional triangular mesh is iteratively refined to better conform to the equipotential lines. It is then repeated in the third dimension to form layers of triangular prisms. We used 202 by 208 nodes out of maximal 223 by 223 in this software version, covering a 125.0 mm by 172.4 mm surface, to model a third of an array; the rest of the data is obtained from the symmetry requirements. A total of 61 vertical layers is used, resulting in the total number of nodes equal to 2 562 976. Material properties input, as the remanent magnetic flux density in elements designated as ferromagnetic, $B_r = \mu_0 \cdot M_r = 4\pi \cdot 10^{-7} \cdot M_r$, corresponds to a piece of material very long in the direction of magnetization (compare to 189.11 mT in the centers of our magnets). This is accounted for by considering the actual dimensions of the magnets. Requiring the relative accuracy of the final results of 10^{-4}, the solution is obtained after 2.16 minutes on an Intel Pentium 4 machine at 2.2 GHz.

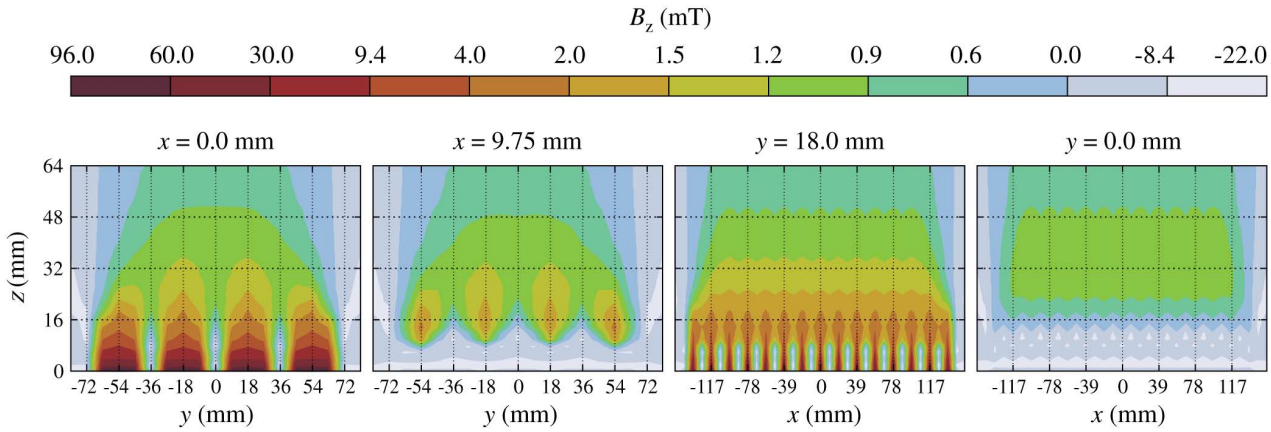

Fig. 5 The magnetic flux density variation in vertical planes obtained using the finite-element calculations. The dominant, B_z component, is shown for the four cross-sections: two parallel to the yOz plane and two parallel to the xOz plane, one of each halving the magnets and the other halving the space between the two rows of magnets. For the cross-sections parallel to the xOz plane the stray magnetic field lies outside the experimental volume, so that the assumptions of the magnetic flux density periodicity are justified. In the cross-sections parallel to the yOz plane that is not the case due to the small number of magnets in y-dimension and large spacing between them. This is the reason for the discrepancies between the approximate analytical estimates and finite-element calculations of $\bar{B}_z(z)$ and $-\mathrm{grad}_z \bar{B}_z(z)$ in Fig. 4.

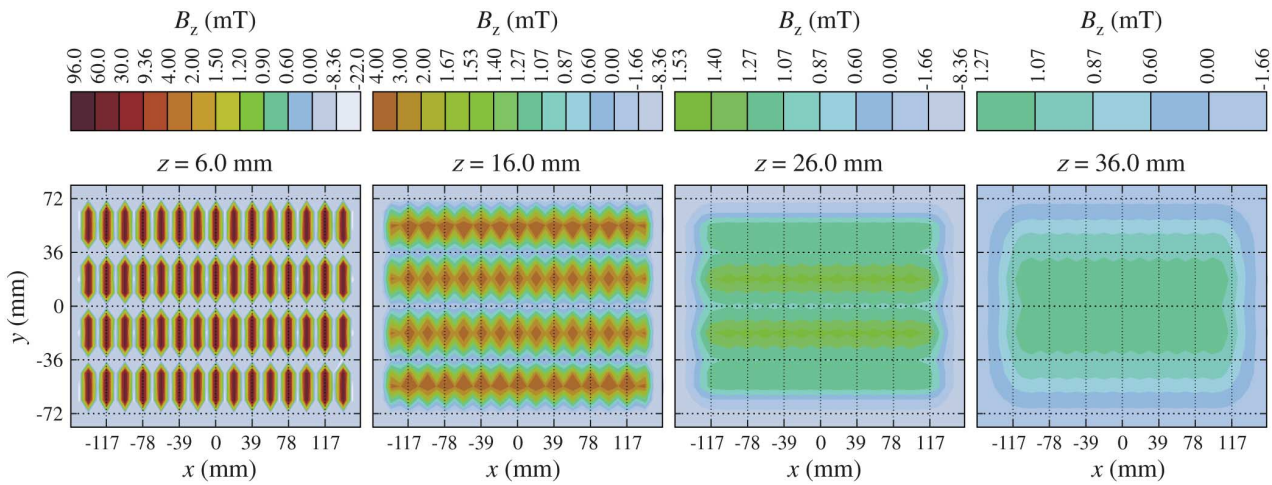

Fig. 6 The magnetic flux density variation in horizontal planes obtained using the finite-element calculations. The magnetic flux density of up to 96 mT is produced right above the ferromagnetic rods, however, flux lines close between the rows of magnets and the variations are large. Above the height of 14 mm flux lines act to increase a resultant field whose distribution in horizontal planes varies much less than with the height above the array. Mean magnetic flux density in the experimental volume is obtained by averaging within the z-ranges of interest.

Obtained results are compared in parts (a) and (b) of Fig. 4 with the analytically calculated data corresponding to the four characteristic axes, through the points H, V, O, and P, denoted in Fig. 3. Both the analytical and the FEM model are validated by comparison with measurements. The agreement of the three sets of results is excellent. The magnetic array field extends much further from the surface and decreases slowly, almost linearly, as opposed to the $B_1(z) \sim z^{-3}$ of a single ferromagnetic rod. Part (c) of Fig. 4 illustrates usefulness of the approximate analytical estimates given by (5) for the fast parameter assessment and preliminary design of magnetic arrays. It compares the analytical estimates with the exact numerically obtained values, which took into account effects caused by the finite number of array elements. Horizontal field components were included in the numerical model. However, the stray fields at the very edges of the stripes were excluded when taking mean values. Numerically obtained z-component mean, $\bar{B}_z(z)$, is somewhat lower than its analytical estimate.

The results are also used to study the magnetic flux density variation throughout the experimental volume, including stray magnetic fields. The two experimental volume cross-sections parallel to the xOz plane, shown in Fig. 5, give evidence of an almost periodic magnetic flux density distribution. For these planes, the regions of the stray field are actually located outside the experimental volume, see Fig. 1. Therefore, the field description suggested by (5) is quite realistic. However, due to the small number of elements (four) in the y-direction and relatively large magnet spacing, the z-component of the vector $\mathbf{B}$ is significantly lower for the two non-central "hills" and "valleys" in the planes parallel to the yOz. The results of analytical calculations and those obtained with FEM are studied using B_z. The FEM data shows that the z-component constitutes more than 96% of the total magnetic flux density in the central hill region and more than 80% everywhere in the hill region. The same amount of 96% is obtained for the "central valley" along the x-axis, by comparing minima of B_z and B_t from $y = -y_d/2$ to $y = y_d/2$ for every considered z. In the other two valleys this quantity decreases with height going as low as 47%. Significant horizontal field components are to be expected when there are three rows of magnets on one side versus only one row on the

TABLE I
MEAN MAGNETIC FIELD PARAMETERS IN THE EXPERIMENTAL VOLUME OBTAINED USING THE FINITE ELEMENT CALCULATIONS

h_1 (mm)	h_2 (mm)	$\overline{B_z}$ (mT)	$\overline{B_t}$ (mT)	$\overline{G_z}$ (T/m)
0.0 *	10.0	15.4394	16.1613	1.8549
0.0 *	20.0	9.1341	9.6192	1.0302
0.0 *	30.0	6.6632	7.0497	0.7165
16.0	46.0	1.1371	1.3127	0.0223
24.0	54.0	0.9719	1.1476	0.0176
32.0	62.0	0.8442	1.0122	0.0141

* for the first three rows $|\bar{B}|$ was used

other and having in mind closure of the flux lines around the edges. The total magnetic flux density, however, does not suffer much of a decline when three valleys are compared: it is exactly the same up to the height of 4 cm and at larger z it does not fall below 80% with respect to the central valley. The total exposure field therefore does not change too much in horizontal planes.

From the FEM data and Fig. 5, it follows that $z = 14$ mm is the limiting height where the magnetic flux lines start to add together to form a resultant positive, slowly decreasing, magnetic flux density ($B_V(14\text{ mm}) = 0.05$ mT). Fig. 6 shows four horizontal cross-sections of the experimental volume, right above the surface of an array, at 16 mm showing small but positive B_V, and the next two at larger z, where the field is predominantly vertical and vertically decreasing. Therefore, it is reasonable to perform parameter averaging in the horizontal planes to get the mean magnetic flux density and its mean gradient defined by (1) as a function of z-coordinate. The actual experimental volume is located between the delimiting planes $z = h_1$ and $z = h_2$, determined by the type of experiment to be conducted. The mean parameters for the experimental magnetic field description are calculated by further averaging between the heights h_1 and h_2. Several cases are presented as an example in Table I.

V. POSSIBLE OPTIMIZATION STRATEGIES

Specific ranges of mean magnetic flux density and its mean gradient as defined by (1) may be required for a certain application. It is worthwhile to briefly discuss two ways of magnetic field modification. Firstly, the slowly decreasing magnetic field of the considered array type allows for the significant field amplification if the heights of equivalent current sheets are increased by stacking the layers of arrays on top of each other. This is illustrated in Fig. 7 and Table II. Whereas a rapid decrease of the single element magnetic flux density prevents effective field increase by stacking magnets, distributed placement of magnets over the surface imposes the linear field decrease with distance and the effect is considerable. It is important that the nonmagnetic support between array elements in no way disrupts the fields produced by other layers. Placement of a large ferromagnetic plate beneath the lowest layer could be used to produce an effect equivalent to doubling the number of layers [22], [23].

The increase in the height of current sheets can be combined with the adjustments of magnet spacings in x- and y-direction to obtain different combinations of mean magnetic flux density, $\bar{B}_z(z)$, and its mean gradient defined by (1), $-\mathrm{grad}_z \bar{B}_z$. Expressions (5) can be used as a design tool for this type of magnetic arrays. As an illustration, in Fig. 8 we present the results of the

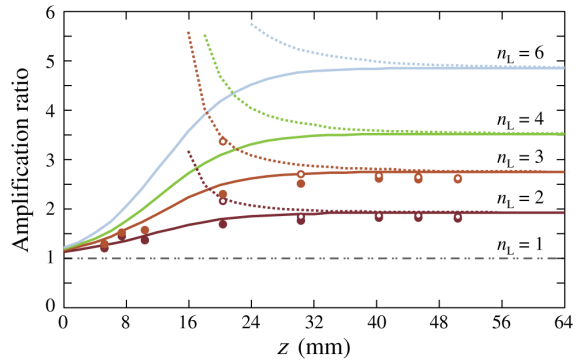

Fig. 7 The magnetic flux density amplification using several layers of arrays on top of each other. The magnetic flux density above the ferromagnetic rods (hills) and in between the rows of magnets (valleys) is obtained analytically, using (7). It is depicted by the solid lines in the case of rods (hills) and by the dashed lines for the valleys. Validity of our assumptions is checked for the number of layers, $n_{L.}$, equal to two and three, and the results measured for eight heights at the hill points and at the valleys are given by the full and unfilled dots, respectively. Due to the slowly decreasing magnetic field, the superposition results in an amplification ratio of almost $n_{L.}$, although every additional layer is shifted by the height of one layer with respect to the others.

TABLE II
MEAN MAGNETIC FIELD PARAMETERS FOR LAYERS OF ARRAYS OBTAINED USING THE ANALYTICAL EXPRESSIONS

h_1 (mm)	h_2 (mm)	$\overline{B_z}$ (mT)	$\overline{B_t}$ (mT)	$\overline{G_z}$ (T/m)
Two layers				
16.0	46.0	2.1932	2.5316	0.0431
24.0	54.0	1.8715	2.2096	0.0350
32.0	62.0	1.6214	1.9442	0.0276
Three layers				
16.0	46.0	3.4402	3.9597	0.0636
24.0	54.0	2.7465	3.2406	0.0518
32.0	62.0	2.3294	2.7931	0.0402

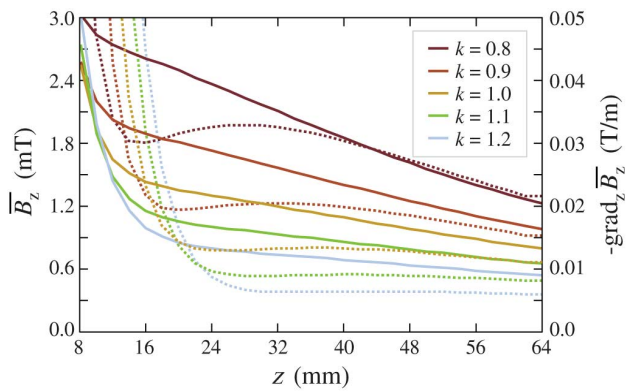

Fig. 8 Possible increase in mean magnetic flux density and its mean gradient given in (5) with the magnet spacing adjustment. The effect to the mean field parameters of the modification in the array element spacing by a factor k is determined using the approximate analytical estimates given in (5). Different combinations of mean magnetic flux density, $\bar{B}_z$, and mean gradient defined by (1), $-\mathrm{grad}_z \bar{B}_z(z)$, are depicted by solid and dashed curves, respectively.

modification in the array element spacing by a factor k, here taken to be the same for x- and y-direction. Were the individual array elements cylindrical instead of brick-shaped, we would obtain the elliptic integrals. If the numerical integration is to be avoided, they can be represented using some of the various expansions, as it was done in [34]. Expressions (7) and (8) become more complicated, but the validity and usefulness of estimates (5) remain unaffected.

VI. Conclusion

We have considered the general case of two-dimensional magnetic arrays with the same orientation of magnetic axes perpendicular to the array's surface. Exact closed-form expressions are derived for the magnetic flux density in an arbitrary field point. An extension to the case of alternating magnetic moments is straightforward, whereas additional terms have to be included for the most general case of an array with different vectors of magnetization from element to element. Exploiting the array periodicity, we propose an approximate assessment of main magnetic field parameters of interest, that can serve as a design tool. Finite-element analysis served for the verification of analytical model, as well as more detailed magnetic field analysis. Both models are validated by comparison with measurements.

Acknowledgment

This work was supported by the Ministry of Education, Science and Technological Development of Serbia through the projects (grants) no. III-45003, III-41013, and III-41019. The authors have no conflict of interest regarding the material and information presented in the article.

References

[1] W. P. Taylor, J. J. Bernstein, J. D. Brazzle, and C. J. Corcoran, "Magnet arrays for use in a 3-D MEMS mirror array for optical switching," *IEEE Trans. Magn.*, vol. 39, no. 5, pp. 3286–3288, Sep. 2003.

[2] T. M. Liakopoulos, W. Zhang, and C. H. Ahn, "Micromachined thick permanent magnet arrays on silicon wafers," *IEEE Trans. Magn.*, vol. 32, pp. 5154–5156, Sep. 1996.

[3] I. Zana and G. Zangari, "Electrodeposited Co–Pt permanent micromagnet arrays on Cu(111)–Si(110) substrates," *IEEE Trans. Magn.*, vol. 38, no. 5, pp. 2544–2546, Sep. 2002.

[4] H. J. Cho and C. H. Ahn, "A bidirectional magnetic microactuator using electroplated permanent magnet arrays," *J. Microelectromech. Syst.*, vol. 11, no. 1, pp. 78–84, Feb. 2002.

[5] S. B. Shetye, J. S. Agashe, and D. P. Arnold, "Investigation of microscale magnetic forces for magnet array self-assembly," *IEEE Trans. Magn.*, vol. 43, no. 6, pp. 2713–2715, Jun. 2007.

[6] D. L. Trumper, W. Kim, and M. E. Williams, "Design and analysis framework for linear permanent-magnet machines," *IEEE Trans. Ind. Applicat.*, vol. 32, no. 2, pp. 371–379, Mar. 1996.

[7] J. Cao, Y. Zhu, J. Wang, W. Yin, and G. Duan, "Analysis and comparison of two-dimensional permanent-magnet arrays for planar motor," *IEEE Trans. Magn.*, vol. 40, no. 6, pp. 3490–3494, Nov. 2004.

[8] J. Cao, Y. Zhu, J. Wang, W. Yin, and G. Duan, "A novel synchronous permanent magnet planar motor and its model for control applications," *IEEE Trans. Magn.*, vol. 41, no. 6, pp. 2156–2163, Jun. 2005.

[9] M. G. Lee and D-G. Gweon, "Optimal design of a double-sided linear motor with a multi-segmented trapezoidal magnet array for a high precision positioning system," *J. Magn. Magn. Mater.*, vol. 281, pp. 336–346, Oct. 2004.

[10] D. Golda and M. L. Culpepper, "Modeling 3D magnetic fields for precision magnetic actuators that use non-periodic magnet arrays," *Precision Eng.*, vol. 32, no. 2, pp. 134–142, Apr. 2008.

[11] G. G. Sotelo, A. C. Ferreira, and R. de Andrade, Jr, "Halbach array superconducting magnetic bearing for a flywheel energy storage system," *IEEE Trans. Appl. Supercond.*, vol. 15, no. 2, pp. 2253–2256, Jun. 2005.

[12] K. Halbach, "Design of permanent multipole magnets with oriented rare earth cobalt material," *Nucl. Instrum. Methods*, vol. 169, no. 1, pp. 1–10, Feb. 1980.

[13] M. I. Weintraub, G. I. Wolfe, and R. A. Barohn *et al.*, "Static magnetic field therapy for symptomatic diabetic neuropathy: A randomized, double-blind, placebo-controlled trial," *Arch. Phys. Med. Rehab.*, vol. 84, no. 5, pp. 736–746, May 2003.

[14] N. A. Segal, Y. Toda, and J. Huston *et al.*, "Two configurations of static magnetic fields for treating rheumatoid arthritis of the knee: A double-blind clinical trial," *Arch. Phys. Med. Rehab.*, vol. 82, no. 10, pp. 1453–1460, Oct. 2001.

[15] C. Vallbona, C. F. Hazlewood, and G. Jurida, "Response of pain to static magnetic fields in postpolio patients: A double-blind pilot study," *Arch. Phys. Med. Rehab.*, vol. 78, no. 11, pp. 1200–1203, Nov. 1997.

[16] H. N. Mayrovitz and E. E. Groseclose, "Effects of a static magnetic field of either polarity on skin microcirculation," *Microvasc. Res.*, vol. 69, no. 1–2, pp. 24–27, Jan. 2005.

[17] Y. Yan, G. Shen, and K. Xie *et al.*, "Wavelet analysis of acute effects of static magnetic field on resting skin blood flow at the nail wall in young men," *Microvasc. Res.*, vol. 82, no. 3, pp. 277–283, Nov. 2011.

[18] A. P. Colbert, H. Wahbeh, and N. Harling *et al.*, "Static magnetic field therapy: A critical review of treatment parameters," *Evidence Based Complem. Altern. Med.*, vol. 6, no. 2, pp. 133–139, Jun. 2009.

[19] D. M. Djordjevich, S. R. De Luka, I. D. Milovanovich, S. Janković, S. Stefanović, S. Vesković-Moračanin, S. Ćirković, A. Ž. Ilić, J. L. Ristić-Djurović, and A. M. Trbovich, "Hematological parameters' changes in mice subchronically exposed to static magnetic fields of different orientations," *Ecotoxicol. Environ. Safety*, vol. 81, pp. 98–105, Jul. 2012.

[20] S. R. De Luka, D. M. Djordjevich, and I. D. Milovanovich *et al.*, "Subchronic exposure to static magnetic field affects zinc and copper content in mice brain and liver," *Cell Biochem. Biophys.*, submitted for publication.

[21] D. Mandic, "Surface magnetized elastic magnetic stripe and application," (WO1999060581) [Online]. Available: http://patentscope.wipo.int/search/en/WO1999060581.

[22] B. M. Notaroš, *Electromagnetics*. Upper Saddle River, NJ, USA: Prentice Hall/Pearson Education, 2010.

[23] C. A. Balanis, *Advanced Engineering Electromagnetics*. Hoboken, NJ, USA: Wiley, 1989.

[24] R. Ravaud and G. Lemarquand, "Comparison of the Coulombian and Amperian current models for calculating the magnetic field produced by radially magnetized arc-shaped permanent magnets," *Progr. Electromagn. Res.*, vol. 95, pp. 309–327, Jul. 2009.

[25] G. Akoun and J. P. Yonnet, "3D analytical calculation of the forces exerted between two cuboidal magnets," *IEEE Trans. Magn.*, vol. MAG-20, no. 5, pp. 1962–1964, Sep. 1984.

[26] F. Bancel, "Magnetic nodes," *J. Phys. D: Appl. Phys.*, vol. 32, no. 17, pp. 2155–2161, Sep. 1999.

[27] *"DTM-151 Digital Teslameter with serial communications,"* Group3, User's Manual.

[28] I. R. Harris and A. J. Williams, "Magnetic materials," in *Materials Science and Engineering*, R. D. Rawlings, Ed. Oxford, U.K.: Eolss Publishers, 2009 [Online]. Available: http://www.eolss.net., in Encyclopedia of Life Support Systems (EOLSS), under the auspices of the UNESCO

[29] P. Shepherd, K. K. Mallick, and R. J. Green, "Magnetic and structural properties of M-type barium hexaferrite prepared by co-precipitation," *J. Magn. Magn. Mater.*, vol. 311, no. 2, pp. 683–692, Apr. 2007.

[30] S. Ram, H. Krishnan, K. N. Rai, and K. A. Narayan, "Magnetic and electrical properties of Bi_2O_3 modified $BaFe_{12}O_{19}$ hexagonal ferrite," *Jpn. J. Appl. Phys.*, vol. 28, no. 4, pp. 604–608, Jan. 1989.

[31] S. R. Janasi, M. Emura, F. J. G. Landgraf, and D. Rodrigues, "The effects of synthesis variables on the magnetic properties of coprecipitated barium ferrite powders," *J. Magn. Magn. Mater.*, vol. 238, no. 2–3, pp. 168–172, Jan. 2002.

[32] MERMAID 2D and 3D User's Guide, SIM, Novosibirsk, Russia, 1994.

[33] N. A. Dubrovin, E. A. Simonov, and S. B. Vorozhtsov, "MERMAID 3D code in ATLAS applications," CERN, Geneva, ATLAS Note ATL-TECH-2001-003, 2001.

[34] J. S. Agashe and D. P. Arnold, "A study of scaling and geometry effects on the forces between cuboidal and cylindrical magnets using analytical force solutions," *J. Phys. D: Appl. Phys.*, vol. 41, no. 10, p. 105001(9), May 2008.

Improvement of magneto-optical quality of high purity $Bi_{12}GeO_{20}$ single crystal induced by femtosecond pulsed laser irradiation

G. S. I. ABUDAGEL[a], S. PETRIČEVIĆ[a], P. MIHAILOVIĆ[a], A. KOVAČEVIĆ[b], J. L. RISTIĆ-DJUROVIĆ[b], M. LEKIĆ[b], M. ROMČEVIĆ[b], S. ĆIRKOVIĆ[b], J. TRAJIĆ[b,*], N. ROMČEVIĆ[b]
[a]*School of Electrical Engineering, University of Belgrade, Bulevar kralja Aleksandra 73, 11000 Belgrade, Serbia*
[b]*Institute of Physics, University of Belgrade, Pregrevica 118, 11080 Belgrade, Serbia*

Femtosecond pulsed laser irradiation can improve optical properties of $Bi_{12}GeO_{20}$ single crystals. We investigate if the effect occurs if the crystals are grown from high purity components. The samples are irradiated by a femtosecond pulsed laser beam of increasing power. The maximal transmittance of 44% occurs at the irradiating laser power of 451 mW. After irradiation, intensity of Raman spectra peaks increase, except for the peak at 203 cm^{-1}, whose intensity decreases. The irradiation also changes the sample colour. Although the Verdet constant does not change, the absorption coefficient decreases significantly, which leads to magneto-optical quality improvement of approximately 70%.

(Received March 3, 2017; accepted August 9, 2017)

Keywords: Bismuth germanium oxide, Laser annealing, Raman spectroscopy, Crystal colour, Magneto-optical quality

1. Introduction

Bismuth germanium oxide ($Bi_{12}GeO_{20}$) from the sillenite group of cubic crystals is commonly abbreviated as BGO or s-BGO. Due to its fitting optical characteristics, such as photoconductivity, photochromism, photorefractivity, piezoelectricity, as well as to electro-optic and magneto-optic effects it supports [1, 2], it has been used in a wide range of optical applications and devices [2–6]. Its cubic cell unit is composed of two formula units, namely of 24 Bi, 40 O and 2 Ge. The Ge atoms positioned in the centre and the vertices of a cube are tetrahedrally coordinated by the oxygen atoms, whereas the Bi atoms are heptacoordinated [7–9]. There are numerous studies that considered properties of doped and un-doped BGO, see for example [10–18], as well as those investigating property changes induced by a wide variety of exposure types such as thermal treatments, particle beams or light treatments [3, 12–16, 19–25].

BGO is a good example of a Faraday rotator crystal possibly applicable in sensor systems. In order to evaluate usability of a crystal for sensing purposes not only its Faraday rotation capability, but its ability to be integrated into a sensing optical system must be considered. In general, in fiber-optic sensing systems optical beams used to sense the measured quantity are guided through the fibers, giving rise to the absorption coefficient as the most important optical property. Crystals with high absorption coefficient are in general less useful for sensor systems because they absorb much of the light and cause low signal-to-noise ratio at the receiving photo diode. If the magnetic field is to be detected, the intensity of light caused by magnetic field modulation is proportional to the Verdet constant, whereas the intensity of light reaching the photodiode as well as the photocurrent is inversely proportional to the crystal absorption. The noise in a fiber optic sensing system is predominantly determined by the noise in the processing electronics and can be expressed as the noise present in the photocurrent. Therefore, the signal-to-noise ratio of the magnetic field sensor is proportional to the Verdet constant and inversely proportional to the absorption coefficient of a crystal. Consequently, due to its proportionality to the signal-to-noise ratio, the magneto-optical quality of a crystal defined as a ratio of the Faraday rotation, which is proportional to the Verdet constant, and the absorption coefficient can be used as a measure of a crystal's applicability in a magnetic field sensing system.

When $Bi_{12}GeO_{20}$ crystals were exposed to pulsed laser beam irradiation, there are examples of laser beam operating in the nanosecond [3], picosecond [23–25], or femtosecond range [26]. In [26] it was determined that femtosecond pulsed laser irradiation of increasing power causes significant changes in the transmittance, transmission spectra, sample colour, Raman spectra, X-ray diffraction pattern, Verdet constant, magneto-optical property, and absorption coefficient of lower quality black $Bi_{12}GeO_{20}$ single crystals. Here we analyze if the same increasing power pattern of femtosecond pulsed laser irradiation has similar effect on the high quality yellow $Bi_{12}GeO_{20}$ single crystals, i.e., on the crystals that were grown from the components whose purity is higher than that of the black crystals, and whose magneto-optical quality is the maximal obtainable by the applied crystal growth technique.

2. Experimental procedure

2.1. Preparation of crystal samples

Single crystals of $Bi_{12}GeO_{20}$ were grown in the air by the Czochralski technique using the MSR 2 crystal puller, Eurotherm temperature controller and the calculated critical crystal diameter, critical rotation rate and pulling rate, as explained in detail in [17, 26]. The system provided small fluctuations in crystal diameter size as well as in melting temperature. The $Bi_{12}GeO_{20}$ seed was oriented in the ⟨111⟩ direction and the charge was a mixture of Bi_2O_3 and GeO_2 in the stoichiometric ratio 6:1. The light yellow crystal samples were obtained using the Bi_2O_3 and GeO_2 purity of 99.999 wt.% and 99.9999 wt.%, respectively. Crystal samples of size 4 mm × 4 mm × 10 mm were cut from the boule and mechanically as well as chemically polished. The technique used to prepare the samples insured maximal sample quality within the limits corresponding to their purity [17].

2.2. Crystal irradiation and characterization

The equipment used to produce the femtosecond pulsed laser beam and establish its wavelength was the Coherent Mira 900F femtosecond laser, Coherent Verdi V-10 pump laser that provided a 532 nm continuous wave pump beam, and Ocean Optics HR2000CG UV-NIR spectrometer. Crystal samples were irradiated along the crystal growth direction (*z*), i.e. along the samples' longest axis. The irradiating laser beam radius provided partial irradiation of the exposed crystal facet. The beam wavelength was 800 nm, whereas its power was increased from 50 mW to 950 mW and was adjusted by a graded filter. The pulses were 90 fs long and had repetition rate of 76 MHz. The samples were irradiated by each beam power for 3 s. The beam power was measured with the Ophir power meter with the thermal and photometric heads. In order to enable comparison of the irradiation effects on the single crystal samples of different purity, i.e., on yellow and black $Bi_{12}GeO_{20}$ samples, the irradiation conditions were intentionally chosen to be identical to those applied to the lower purity black crystals in [26].

The sample colour was calculated from the transmission spectra measured by the Beckman Coulter DU 720 General Purpose UV/VIS spectrometer.

The micro-Raman spectra were recorded at room temperature in the spectral range between 100 and 1100 cm^{-1} with 1 cm^{-1} resolution using the backscattering configuration and the 532 nm line of Verdi G optically pumped semiconductor laser as an excitation source, and the Jobin Yvon T64000 spectrometer, which has nitrogen cooled charge-coupled-device detector.

The Faraday rotation and optical activity were measured by Δ/Σ method at the wavelength of λ = 632.8 nm. After the BGO crystal the orthogonal polarizations of the light beam were separated by the $CaCO_3$ crystal into two parallel beams 3 mm apart. The quadrant photodiode connected into transimpedance stages was used for optoelectronic conversion. This method is described in more details in [26].

3. Results and discussion

The irradiation pattern applied here to the higher purity yellow crystals is identical to the one utilized in [26] to irradiate black crystals grown from the components of lesser purity. Consequently, the obtained results can be compared and the differences can be attributed solely to different sample purity. With the increase of irradiating laser power, the transmittance of irradiated sample undergoes initial growth followed by a decrease, as can be seen in Fig. 1. Comparison with the dependence corresponding to the black crystal given in [26] reveals that the transmittance curves for the black as well as for the yellow crystal has the same shape and that the slopes of the two curves appear to be approximately equal. The curve corresponding to the yellow crystal is shifted to the larger values by approximately 18.8% compared to the curve corresponding to the black crystal. For the yellow crystal, the maximal transmittance of 44.0% occurs at the irradiating laser power of 451 mW, whereas the lower purity black crystal was reported in [26] to have the smaller maximal transmittance value of 25.1% corresponding to 455 mW. It seems that both curves exhibit local irregularities which occur at 197.4–249.7 mW, 552–605 mW and 800–857 mW for the black crystal and at 593–641 mW for the yellow crystal. It is possible that the irregularity in the yellow sample curve for large values of incident power P_0 is not visible because it is outside the considered range of irradiating laser power, or due to insufficient measurement accuracy achieved for yellow crystal data points above 700 mW.

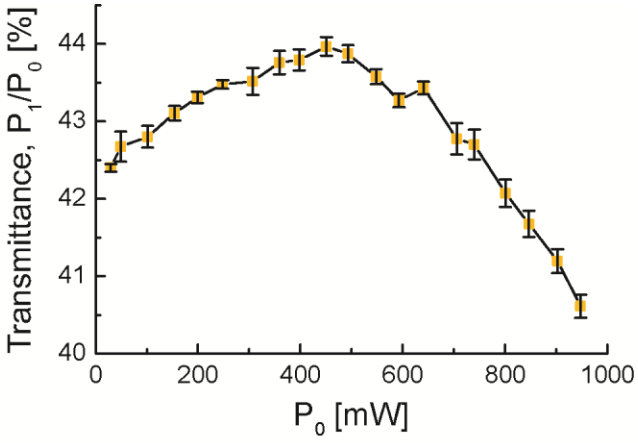

Fig. 1. Change of crystal transmittance with increase of irradiating laser power. For each value of the incident power P_0, a sample is irradiated by the femtosecond laser beam for 3 s. The transmittance is given as P_1/P_0, where P_1 is the transmitted power. The error bars were calculated from the uncertainties of measured values of the incident and transmitted power, ΔP_0 and ΔP_1.

The sample colours before and after irradiation were calculated using the CIE chromaticity coordinates and are given in Fig. 2. Comparison with the results corresponding to the black crystal given in [26] revealed that the change of black crystal colour was more pronounced than that of the yellow crystal presented here.

The Raman spectra of unirradiated and irradiated samples are recorded at room temperature in the spectral range from 150 to 800 cm^{-1} and are shown in Fig. 3. The results obtained for unirradiated crystals are in agreement with those given in [8, 17]. After irradiation the intensity of the *F*(*TO*) peak at 203 cm^{-1} decreased, whereas all other peaks became more pronounced. Despite the difference in purity between the yellow samples studied here and the black crystals considered in [26] the Raman spectra of unirradiated crystals do not differ significantly. As reported in [26], irradiation of the black crystal caused all the peaks of symmetry type *E*, i.e., the peaks at 234, 454, and 619.6 cm^{-1}, to disappear and intensity increase of all other peaks. The change in the same Raman spectrum peaks of $Bi_{12}GeO_{20}$ was reported in [16]; however, the most, medium, and least intense peaks correspond to the annealed, doped, and untreated samples, respectively.

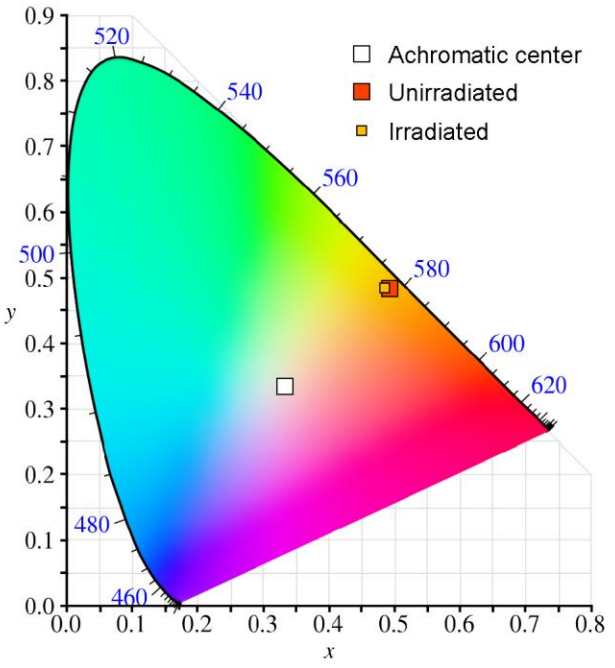

Fig. 2. Colours of irradiated and unirradiated samples in CIE chromaticity diagram.

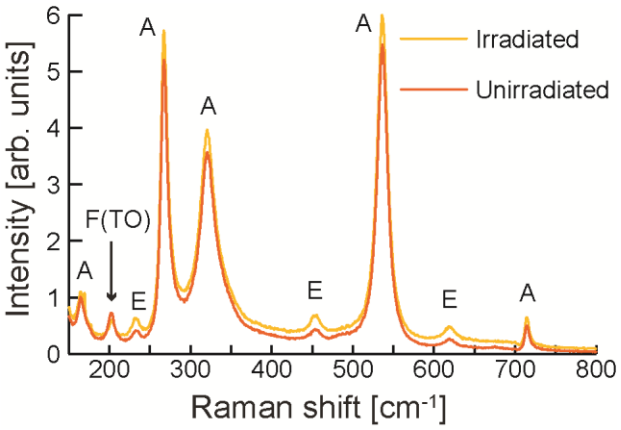

Fig. 3. Raman spectra. Irradiation caused a small upward shift of the crystal spectrum except for the F(TO) type peak at 203 cm^{-1}.

The Verdet constant is calculated from

$$V = \frac{\theta_{0\mathrm{AC}}}{B_0 l} = \frac{1}{2B_0 l}\sin^{-1}\left(\frac{U_1 - U_2}{U_1 + U_2}\right)_{0\mathrm{AC}} \quad (1)$$

where θ_{0AC} is the amplitude of the AC signal, B_0 is the amplitude of the magnetic induction, whereas U_1 and U_2, are the output signal voltages obtained after transimpedance stages from the vertically and horizontally polarized components, respectively. The FFT was used to separate spectral components of U_1 and U_2. The Faraday rotation was determined from the magnitude of the 50 Hz component.

The absorption coefficients were obtained by measuring the difference in beam intensities at the quadrant photodiode [26] with and without BGO crystal in the beam path. The reflection on the BGO crystal was calculated using the normal incidence and BGO refraction index of $n_{\mathrm{BGO}} = 2.55$.

The absorption coefficient, α, was calculated from the beam intensities with and without the crystal present in the beam path, *I(x)* and *I(0)*, and the known crystal length l = 9.8 mm as

$$I(l) = I_0 e^{-\alpha l} \Rightarrow \alpha = -\frac{1}{l}\ln\frac{I(l)}{I_0} \quad (2)$$

The magneto-optical quality is calculated by dividing the Verdet constant by the absorption coefficient. The obtained results are given in Table 1.

Table 1. Magneto-optical properties of irradiated and unirradiated high purity crystal samples.

Property	Unirradiated sample	Irradiated sample
Verdet constant (rad $T^{-1}m^{-1}$)	72	72
Absorption coefficient (cm^{-1})	0.58	0.34
Magneto-optical quality (rad T^{-1})	1.24	2.1

The data given in Table 1 show the effects of femtosecond laser irradiation on the magneto-optical properties of the high purity BGO crystal. The irradiation caused 41.4% decrease in the absorption coefficient and did not influence the Faraday constant. Consequently, the increase in crystal transparency resulted in a significant 70% increase in the magneto-optical quality. As explained earlier, increase in crystal transparency is an important gain from the point of view of a sensor system since the system-level signal-to-noise ratio is directly proportional to the magneto-optical quality of a crystal. Therefore, it is expected that the signal-to-noise ratio of a sensor system would be improved by the same amount as the improvement in the magneto-optical quality induced by the irradiation. Consequently, it can be concluded that the femtosecond pulsed laser irradiation affects the crystal in a positive manner.

4. Conclusions

Femtosecond pulsed laser irradiation of increasing power caused significant changes in optical properties of $Bi_{12}GeO_{20}$ single crystals grown from the components of high purity, as was the case in [26] when the component purity was not so high. The transmittance dependence on the applied irradiation power had the same shape regardless of the purity of the components the crystals were grown from. The curve corresponding to the higher purity crystal, i.e., the yellow crystal, is shifted to the larger values by approximately 18.8%. For the black and yellow crystal, the maximal transmittance of 25.1% and 44.0% occurred at 455 mW and 451 mW, respectively. The Raman spectra peaks became somewhat stronger, except for the *E* type peaks at 234, 454, and 619.6 cm^{-1} in the lower purity black crystal, which disappeared and the yellow crystal peak at 203 cm^{-1} whose intensity decreased. Irradiation also caused slight colour change of the yellow crystal and significant change of the black crystal colour. The Verdet constant did not change; however, the absorption coefficient significantly decreased leading to equally significant increase of the magneto-optical quality of the sample. Consequently, it can be concluded that optical properties of high quality $Bi_{12}GeO_{20}$ single crystals can be improved by irradiation with the femtosecond pulsed laser beam.

Acknowledgements

This work is financially supported by the Serbian Ministry of Education, Science, and Technological Development through the project III45003. We thank Z. Velikić and D. Dramlić for their assistance with transmission spectra measurements and A. Valčić for his help with sample preparation.

References

[1] M. Simon, F. Mersch, C. Kuper, Phys. Status Solidi A. **159**(2), 559 (1997).
[2] V. M. Skorikov, Yu. F. Kargin, A. V. Egorysheva, V. V. Volkov, M. Gospodinov, Inorg. Mater. **41**(1), S24 (2005).
[3] R. A. Ganeev, A. I. Ryasnyansky, B. Palpant, S. Debrus, J. Appl. Phys. **97**, 104303 (2005),
[4] P. Yeh, Introduction to Photorefractive nonlinear optics, first ed., Wiley-Interscience, New York, 1993.
[5] M. J. Weber, J. Lumin. **100**, 35 (2002).
[6] M. Itoh, T. Katagiri, H. Mitani, M. Fujita, Y. Usuki, Phys. Status. Solidi B, **245**(12), 2733 (2008).
[7] S. C. Abrahams, P. B. Jamieson, J. L. Bernstein, J. Chem. Phys. **47**(10), 4034 (1967).
[8] V. I. Burkov, V. S. Gorelik, A. V. Egorysheva, Y. F. Kargin J. Russ. Las. Res. **22**, 243 (2001).
[9] S. F. Radaev, V. I. Simonov, Y. F. Kargin, Eur. J. Solid. State Inorg. Chem. **29**(2), 383 (1992).
[10] N. C. Deliolanis, I. M. Kourmoulis, G. Asimellis, A. G. Apostolidis, E. D. Vanidhis, N. A. Vainos, J. Appl. Phys. **97**(2), 023531 (2005).
[11] C. G. P. Moraes, F. A. A. Jesus, Z. S. Macedo, Adv. Cond. Matter. Phys. **2014**, 968349 (2014), http://dx.doi.org/10.1155/2014/968349.
[12] O. Peña-Rodríguez, J. Olivares, I. Bányász, Opt. Mater. **47**, 328 (2015).
[13] V. M. Skorikov, I. S. Zakharov, V. V. Volkov, E. A. Spirin, Inorg. Mater. **38**(2), 172 (2002).
[14] Z. S. Macedo, C. S. S. Oliveira, A. C. Hernandes, J. Appl. Phys. **102**(3), 034105 (2007).
[15] H. Marquet, J-C. Merle, J-G. Gies, Opt. Mater. **14**, 277 (2000).
[16] P. S. Yu, L. B. Su, H. L. Tang, X. Guo, H. Y. Zhao, Q. H. Yang, J. Xu, Sci. China Tech. Sci. **54**(5), 1287 (2011).
[17] Z. Ž. Lazarević, P. Mihailović, S. Kostić, M. J. Romčević, M. Mitrić, S. Petričević, J. Radunović, M. Petrović-Damjanović, M. Gilić, N. Ž. Romčević, Opt. Mater. **34**, 1849 (2012).
[18] S. Kumaragurubaram, S. Moorthy Babu, C. Subramanian, P. Ramasamy, Indian J. Eng. Mater. Sci. **7**(5-6), 331 (2000).
[19] A. Cremades, J. Piqueras, A. Remón, J.A. García, M. T. Santos, E. Diéguez, J. Appl. Phys. **83**(12), 7948 (1998).
[20] A. Cremades, M. T. Santos, A. Remón, J. A. García, E. Diéguez, J. Piqueras, J. Appl. Phys. **79**(9), 7186 (1996).

[21] I. Stefaniuk, P. Potera, I. Rogalska, D. Wróbel, Current Topics in Biophysics **33**, 231 (2010).
[22] N. Benjelloun, M. Tapiero, J. P. Zielinger, F. Marsaud, J. C. Launay, J. Appl. Phys. **64**(8), 4013 (1988).
[23] R. A. Ganeev, A. I. Ryasnyansky, R. I. Tugushev, M. K. Kodirov, F. R. Akhmedjanov, T. Usmanov, Opt. Quant. Electron. **36**(9), 807 (2004).
[24] M. Sylla, D. Rouède, R. Chevalier, X. Nguyen Phu, G. Rivoire, Opt. Commun. **90**, 391 (1992).
[25] B. Taheri, S. A. Holmstrom, R. C. Powell, J. J. Song, A. M. F. I. Földvári, A. Péter, Opt. Mater. **3**, 251 (1994).
[26] A. Kovačević, J. L. Ristić-Djurović, M. Lekić, B. Hadžić, G. S. I. Abudagel, S. Petričević, P. Mihailović, B. Matović, D. Dramlić, L. M. Brajović, N. Romčević, Mater. Res. Bull. **83**, 284 (2016).

*Corresponding author: jelena@ipb.ac.rs

EXPERIMENTAL ELECTROMAGNET FOR *IN VIVO* EXPOSURE OF SMALL ANIMALS TO ELF ELECTROMAGNETIC FIELDS

Andjelija Ž. Ilić [1], Jasna Lj. Ristić-Djurović [1], Saša Ćirković [1], Milan M. Ilić [2], Alexander M. Trbovich [3]

[1] Innovation Center, School of Electrical Engineering, University of Belgrade, 11120 Belgrade, Serbia
[2] School of Electrical Engineering, University of Belgrade, 11120 Belgrade, Serbia
[3] Department of Pathological Physiology, School of Medicine, University of Belgrade, 11000 Belgrade, Serbia

Abstract. *The ubiquitous presence of electromagnetic (EM) fields in living environment motivates investigation of their influence on biological systems. Existing research data shows a high degree of inconsistency, covers very limited regions of electromagnetic spectrum and in many cases lacks detailed and accurate description of the electromagnetic fields necessary for the replication of experiments. Exposure systems, designed specifically for biomedical research, offer the solution to the above problems. We present experimental electromagnet for in vivo small animal research. It covers both static magnetic field and extra-low frequency (ELF) electromagnetic field range, offering higher EM field intensities than those produced by most other systems.*

Key words: *electromagnetic (EM) fields, static magnetic field (SMF), biological effects, exposure system, in vivo, small animal research*

1. INTRODUCTION

Exposure systems, such as the ones described in [1]–[6], are specialized devices aimed at producing, controlling and monitoring electromagnetic fields for biomedical research. It is a prerequisite for an experiment to be well-designed and for the consistent interpretation of results that the desired fields are accurately adjusted and precisely known. Systems for the *in vitro* research, mostly due to the smaller volume involved, but also because of the relatively static experimental conditions, can be realized with greater precision. Also, most of the systems are intended for a narrow range of EM fields, often for a single frequency and lower field levels. With the notable increase of the variety of small commercial devices being produced and rapid extension of the utilized frequency ranges to the previously unused parts of the electromagnetic spectrum, it becomes increasingly important to systematically investigate the biomedical effects of various EM fields.

We have so far investigated the effects on mice of the two types of static magnetic fields (SMF): inhomogeneous, vertically declining SMF, whose mean magnetic flux density equals 1 mT and its mean gradient equals 0.02 T/m [7], and homogeneous SMF whose magnetic flux density is 128 mT [8]. Results show influence of both considered field types to the circulatory system in mice [9]–[11]. In continuation of our previous work we are interested in further analysis of SMFs of intensity 100 mT and more. Additionally, we plan to extend our research to other EM fields, starting with the extra-low frequency (ELF) range already shown to produce certain biological effects.

In order to employ it in our experiments as well as evaluate the prototype of a product that could be made commercially available, we are currently constructing the exposure system to cover both SMFs and the ELF field range. The most straightforward solution to obtain the required relatively strong field intensities is to use the solenoidal fields, either by placement of experimental animals within a solenoid or by usage of combined solenoidal fields with or without the ferromagnetic core. For the device functioning in the direct-current (DC) regime, DC current generator is to be used. Alternating-current (AC) current source will enable the production of sinusoidal electromagnetic fields. The device will be tested for as wide part of the ELF range, as possible to achieve. Frequency range of 0 Hz to 100 Hz is chosen as an initial requirement.

2. EXPERIMENTAL ELECTROMAGNET REQUIREMENTS AND INITIAL COIL DESIGN

Design requirements for an experimental EM field exposure system can be divided in several subgroups. Among the most important factors are the ones dictated by the user community, including compliance with the usual conditions and practices of a biomedical experiment as well as the ease of utilization. Therefore, experimental electromagnet is devised as a flexible device providing EM fields of different magnitudes, gradients, directions and frequencies. The constituent parts of this device belong to one of the five subgroups: copper wire coils, ferromagnetic (iron) cores, direct and alternating current generators, calibration and measurement equipment and accessory equipment. Accessory equipment has to be specific and very

carefully designed in order to enable flexible and modular use of the device. For example, biomedical experiment regulations and the recommendations for the result interpretation allow comparisons of different parameter influences only if all the data is acquired simultaneously as a result of a single experiment. Two copper wire coils are required if the effects of different static magnetic field directions, such as the same or opposite orientation with respect to the Earth's geomagnetic field, are to be compared. Otherwise, the accessory equipment has to ensure position and power supply adjustment for the two coils, in order to combine their EM fields for increased strength and homogeneity. For the higher EM field magnitudes, ferromagnetic cores have to be used as well. Calibration and measurement equipment includes the ambient EM field measurement panel as well as the equipment for monitoring other physical quantities, such as ambient temperature and temperature inside the experimental volume.

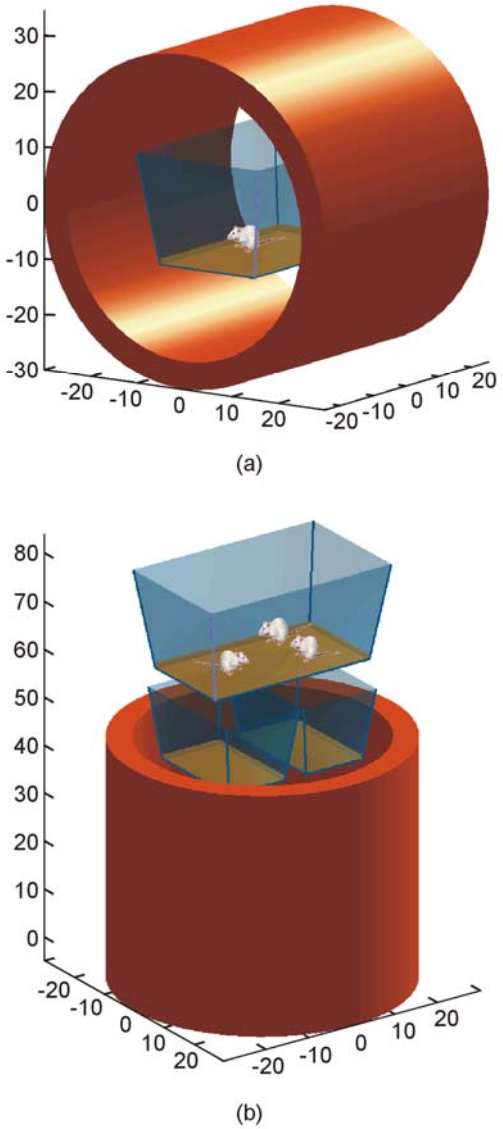

Fig. 1 Copper coils of the experimental electromagnet for *in vivo* exposure to ELF EM fields. To obtain the required relatively strong field intensities above 100 mT, coil size must enable placement of one or several cages inside the solenoid.

2.1. Minimal Size Requirements

For the *in vivo* experiments involving small animals such as mice, care has to be taken of usual routines and rules for their accommodation and treatment. A layer of sawdust is used for padding the cages for mice as this would resemble their natural habitat; animals are fed and watered in the cages. It is most convenient to enable placement of the whole cages occupied by animals within the experimental volume, without disturbing the animals. Not only that it facilitates organization of chronic and sub-chronic experiments; such practice is equally important for the short-term acute exposures to avoid stress as a factor interfering with the actual investigations.

Standard small cages or standard large cages are typically used. Width and length of the small standard cage are 165 mm and 260 mm, respectively, and its height equals 150 mm. Large standard cage is 260 mm wide, 420 mm long, and its height equals 185 mm. This imposes the inner copper coil diameter larger than 500 mm in order to enable its vertical placement as shown in part (b) of Fig. 1. Therefore, the coil stand will support its placement as in Fig. 1 (a), in order to study the influence of horizontally directed fields that penetrate animal's body in all different directions as an animal moves inside the cage, or as shown in Fig. 1 (b) to provide vertical field direction. The cage centered inside the coil results in the higher uniformity of the applied field distribution, whereas to study gradient fields the cage positioning toward the edges or just outside the coil would be appropriate. For the vertical placement of the coil, it can accommodate more than one cage including the combination of large and small cages.

For the preliminary analysis of power requirements and EM field levels that could be produced, we investigate the case where the coil length equals its inner diameter, $l = 2R' = 500$ mm. To keep coil price and weight reasonable, its thickness is initially chosen equal to $R''- R' = 150$ mm. Coil cross-section is shown in part (a) of Fig. 2.

2.2. Limiting Magnetomotive Force

From the user point of view, the need for any specialized power installations can be complicated, expensive and time consuming. Therefore, one of the main requirements for the designed device is to utilize the regular power network. Having in mind maximal wire current density not requiring water-cooling of $J_m = 3$ A/mm², as well as total maximum current of $I_m = 25$ A, we determine the optimal wire diameter of $d = 3$ mm. This choice is illustrated by the data presented in Table 1. Wire diameter d corresponds to the wire cross-section S_w and the number of coils in the given coil cross-section N.

$$N = \frac{S_{coil}}{S_w} = \frac{l(R''-R')}{S_w}. \qquad (1)$$

The total length of the wire used, l_w, and its resistivity, R, with the copper conductivity $\sigma_{Cu} = 58$ MS/m, can be assessed as

$$l_w \approx 2\pi\frac{R'+R''}{2}N, \quad R = \frac{1}{\sigma_{Cu}}\frac{l_w}{S_w}. \qquad (2)$$

Table 1 Magnetomotive force *NI* and coil resistivity *R*

d (mm)	S_w(mm²)	J ($\frac{A}{mm^2}$)	*I* (A)	*N*	*R* (Ω)
1	0.785	3.00	2.36	95493	4280.7
2	3.141	3.00	9.42	23873	267.5
3	7.068	3.00	21.21	10610	52.8
4	12.566	1.99	25.00	5968	16.7
5	19.635	1.27	25.00	3820	6.8

Critical parameter here is the active power that should not exceed 5.5 kW in the monophase regime, under the condition of inductivity compensation for an AC current operation. If the regular power network is to be used, it will be necessary to decrease the current density, resulting in the maximal produced magnetic flux density of 150 mT. This is in agreement with the desired initial design requirements. The following analysis is given for several values of the current density and illustrates field levels that could be produced by the considered coil.

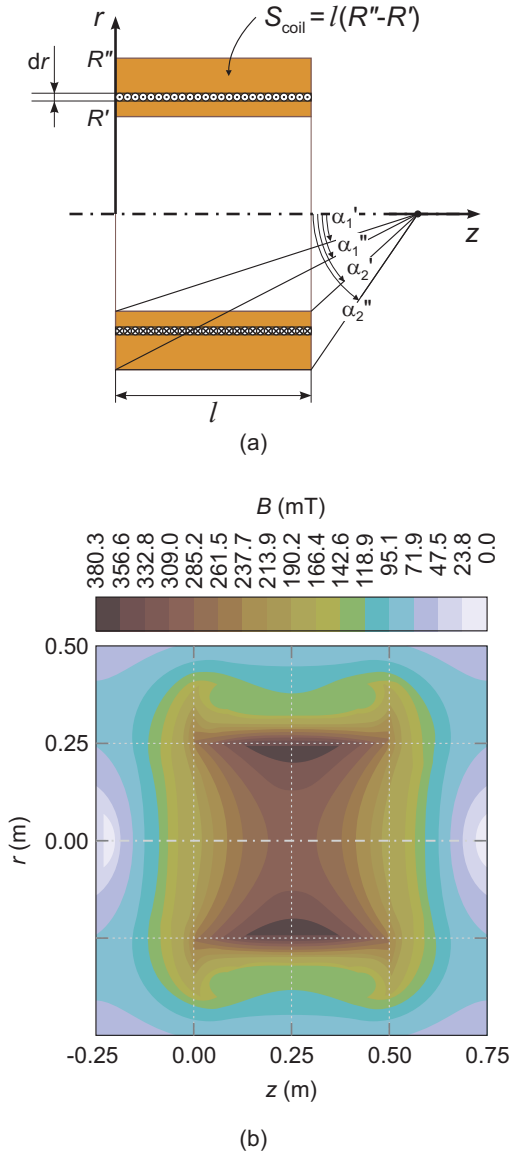

Fig. 2 Copper coil and the produced magnetic flux density. (a) Coil cross-section and the coordinate system used. (b) Calculated three-dimensional magnetic flux density inside and surrounding the coil.

3. Mean Electromagnetic Field Parameters

The described copper coil is modeled using the commercially available Mermaid finite element suite for magnetostatics. Calculated magnetic flux density distribution inside and surrounding the coil, whose cross-section is shown in Fig. 2 (a), is presented in part (b) of Fig. 2. As seen from the figure, nonuniformity of the magnetic flux density distribution is less than 8% in the central part of a solenoid, for $r<125$ mm and $z \in [18, 32]$ mm. Further modeling and optimization of this initial model is due, to additionally improve the field homogeneity in the central part of the device. For the experimenter, it is the mean magnetic flux density over the experimental volume (or the mean maximal magnetic flux density in the experimental volume for the time-varying ELF EM fields) that is of interest. Where applicable, mean *z*-axis gradient of the field, defined as $G_z(z) = -\text{grad}_z B_z(z)$, is another necessary parameter for the field description. Height of the experimental volume most often coincides with the average size of the animal, whereas exposed horizontal range coincides with the size of the cage bottom.

In the case of unavailability of CAE modeling tools such as Mermaid, magnetic flux density and its *z*-axis gradient can be approximately assessed using the analytical expressions for the magnetic flux density along the axis of a thick solenoid, $B_z(z)$.

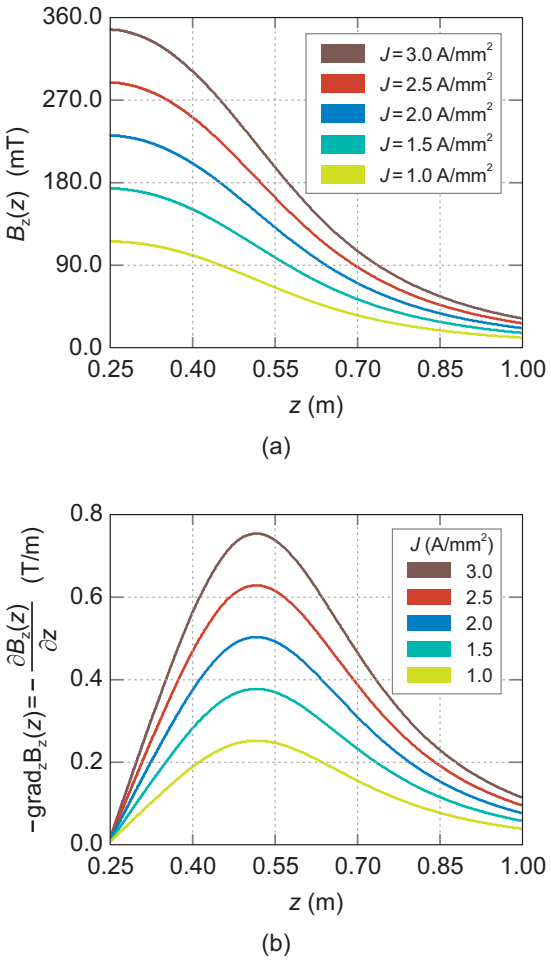

Fig. 3 Magnetic field produced with different coil currents. (a) Magnetic flux density at the solenoid axis. (b) The *z*-axis gradient of the magnetic flux density along the axis.

Integration, from $z = 0$ to $z = l$, of the magnetic flux density on the axis of many constituent circular loops yields an expression for the magnetic flux density along the axis of a thin solenoid:

$$B_z(z) = \frac{\mu_0 NI}{2l}\left(\cos\alpha_1 - \cos\alpha_2\right). \qquad (3)$$

Angles $\alpha 1$ and $\alpha 2$ are denoted in Fig. 2 (a) for the inner layer of copper wire (primed) as well as the outermost layer (double primed). Free space permeability equals $\mu_0 = 4\pi\cdot 10^{-7}$. Further integration, from $r = R'$ to $r = R''$, of the z-axis field components due to layers of wire of thickness dr, magnetomotive force in each layer being equal to $NIdr/(R''-R')$, results in magnetic flux density of a thick solenoid,

$$B_z(z)=\frac{\mu_0 NI}{2l(R''-R')}\left(z\ln\frac{\tan\left(\frac{\pi}{4}+\frac{\alpha_1''}{2}\right)}{\tan\left(\frac{\pi}{4}+\frac{\alpha_1'}{2}\right)} - (z-l)\ln\frac{\tan\left(\frac{\pi}{4}+\frac{\alpha_2''}{2}\right)}{\tan\left(\frac{\pi}{4}+\frac{\alpha_2'}{2}\right)}\right). \qquad (4)$$

Equation (4) has been used to calculate magnetic fields and their gradients for different coil current densities, given in Fig. 3 as an illustration of the electromagnet capabilities. For the vertical coil placement and usual experimental volume height of 35 mm, nonuniformity of the magnetic flux density with height is less than 0.1% and its gradient nonuniformity less than 0.2%. Using the curves such as ones given in Fig. 3, an appropriate combination of field strength and field gradient for exposure of animals can be chosen. Coils will be further optimized for higher field homogeneity in their central regions as well as stronger field gradients toward ends and outside the coils.

4. Conclusions

Novel exposure system for biomedical research, experimental electromagnet for both static magnetic field research and extra-low frequency EM field range, is described. Design guidelines and requirements for such system are defined and explained. These requirements mostly stem from the usual experimental routines and recommendations. Special care has to be taken to ensure flexibility and modularity of the device utilization. Initial electromagnet coil design has been carried on, showing that the desired field strength of 150 mT could be easily achieved using the regular power network available everywhere. Further design to improve field homogeneity and provide stronger field gradients is under way.

Acknowledgement: *This work was supported by the Ministry of Education, Science and Technological Development of Serbia through the project III-45003, and in part by the Public Enterprise "Electric Power Industry of Serbia".*

References

1. M. A. Stuchly, D. W. Lecuyer and J. McLean, " Cancer promotion in a mouse-skin model by a 60-Hz magnetic field: I. Experimental design and exposure system", Bioelectromagnetics, vol. 12, pp. 261-271, October 1991.
2. T. Shigemitsu, K. Takeshita, Y. Shiga and M. Kato, "50-Hz magnetic field exposure system for small animals", Bioelectromagnetics, vol. 14, pp. 107-116, April 1993.
3. A. Paffi, F. Apollonio, G. A. Lovisolo, C. Marino, R. Pinto, M. Repacholi and M. Liberti, "Considerations for developing an RF exposure system: A review for *in vitro* biological experiments", IEEE Trans. Microw. Theory Tech, vol. 58, pp. 2702-2714, October 2010.
4. P. Koester, J. Sakowski, W. Baumann, H.-W. Glock, J. Gimsa, "A new exposure system for the *in vitro* detection of GHz field effects on neuronal networks", Bioelectrochemistry, vol. 70, pp. 104-114, January 2007.
5. L. Visek, P. Togni, J. Vrba and L. Oppl, "Design and comparison of exposure chambers for verification of microwave influence on biological systems", PIERS Online, vol. 3, pp. 1346-1350, August 2007.
6. T. Okuno, "A 100 mT-class ELF magnetic field exposure system for cultured cells", Ind. Health, vol. 34, pp. 113-123, February 1996.
7. A. Ž. Ilić, S. Ćirković, D. M. Djordjevic, S. R. De Luka, I. D. Milovanovich, A. M. Trbovich and J. L. Ristić-Djurović, "Analytical description of two-dimensional magnetic arrays suitable for biomedical applications", IEEE Trans. Magnetics, vol. 49, pp. 5656-5663, December 2013.
8. S. Ćirković, J. L. Ristić-Djurović, A. S. Vorozhtsov, A. Ž. Ilić and N. Nešković, "Method for fine magnet shaping in cyclotrons", IEEE Trans. Nucl. Sci., vol. 56, pp. 2821-2827, October 2009.
9. D. M. Djordjevich, S. R. De Luka, I. D. Milovanovich, S. Janković, S. Stefanović, S. Vesković-Moračanin, S. Ćirković, A. Ž. Ilić, J. L. Ristić-Djurović and A. M. Trbovich, "Hematological parameters' changes in mice subchronically exposed to static magnetic fields of different orientations", Ecotoxic. Environm. Safety, vol. 81, pp. 98-105, July 2012.
10. S. R. De Luka, D. M. Djordjevich, I. D. Milovanovich, S. Janković, S. Stefanović, S. Vesković-Moračanin, S. Ćirković, A. Ž. Ilić, J. L. Ristić-Djurović and A. M. Trbovich, "Subchronic exposure to static magnetic field affects zinc and copper content in mice brain and liver", submitted to Cell Biochem. Biophys.
11. I. D. Milovanovich, D. M. Djordjevich, S. R. De Luka, S. Ćirković, A. Ž. Ilić, J. L. Ristić-Djurović and A. M. Trbovich, "Static magnetic field of different orientations induces various biological changes in exposed mice", unpublished.

Living Molecules: towards Integrative Biophysics of the Cell

ARBRE MOBIEU
BETWEEN ATOM AND CELL

4th ARBRE MOBIEU Plenary Meeting

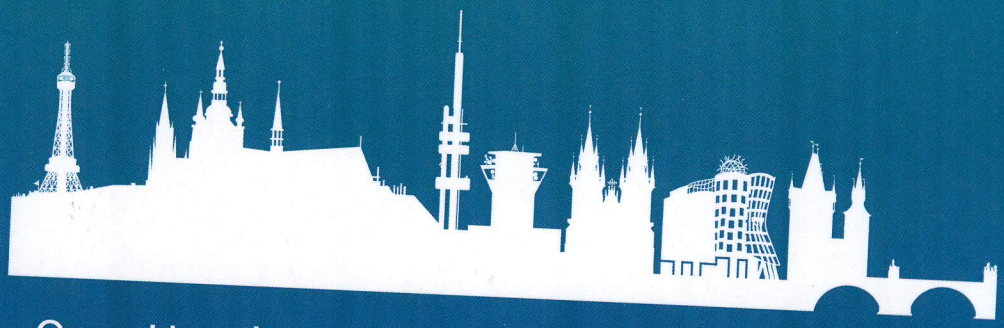

Orea Hotel Pyramida, 24 – 26 February 2020
Prague, Czech Republic

Programme
and
Book of Abstracts

P33
INFLUENCE OF 340MT STATIC MAGNETIC FIELD ON GERMINATION POTENTIAL AND MID-INFRARED SPECTRUM OF WHEAT

Milica Kojadinovic[a], Tamara Popovic[a], Jasmina Debeljak Martacic[a], Jasna Ristic-Đurovic[b], Sasa Cirkovic[b]

[a]Institute for medical research, Centre of research in nutrition and metabolism, University of Belgrade, Dr Subotica 4, Belgrade, Serbia, 11000
[b]Institute of Physics, University of Belgrade, Pregrevica 118, Belgrade, Serbia, 11080
**milica.kojadinovic.imr@gmail.com*

Static magnetic field was observed to positively influence the growing process of various plants; however, the effect has not yet been related to possible structural changes. We investigate if the static magnetic field that improves germination of wheat (Triticum aestivum L) also alters wheat's near-infrared spectrum.
Two groups of seeds were exposed to 340 mT for 16h cumulatively. The first group (I) was exposed 8 days for 2h per day, while the second group (II) was exposed 4h per day for 4 consecutive days. One half of each of the exposed seed groups as well as of the unexposed control groups was sown, and the other half was used for mid-infrared spectra measurements (Fourier-transform IR spectrometer (DA-8, ABB Bomem, Quebec City, Canada). The sown seeds were monitored for 3 weeks after sowing. Germination of the groups exposed to the magnetic field was faster compared to corresponding non-exposed groups that were grown under the same conditions. The magnetic field exposure caused the enhancement of one O—H peak at 3,369cm1 and two C5 5O peaks at 1,662cm1 and 1,740cm1 in the midinfrared spectrum. The effect was more pronounced for the 4 day, 4h/day exposure.
We further examined fatty acids profiles in sown seeds related to see possible effect on lipids. We used GC chromatography method (Shimadzu GC 2014 equipped with a flame ionization detector and DB-23 fused silica gel capillary column). Our result shows no statistical significant changes in two exposed (I and II) groups and unexposed groups in percentage of palmitic, stearic, palmitoleic, oleic and linolenic acids as a composition components of seeds.

Serbian Plant Physiology Society

Institute for Biological Research "Siniša Stanković", University of Belgrade

Faculty of Biology, University of Belgrade

3rd International Conference on Plant Biology

(22nd SPPS Meeting)

9-12 June 2018, Belgrade

Towards pharmacological potential of edible lichen *Evernia prunastri* growing in the mountain region of southern Serbia

PP5-5

Dejan Stojković[1], Gökhan Zengin[2], Marija Smiljković[1], Marina Soković[1]
(dejanbio@yahoo.com)

[1] University of Belgrade, Institute for Biological Research "Siniša Stanković", Bulevar despota Stefana 142, 11000 Belgrade, Serbia.

[2] Selcuk University, Science Faculty, Department of Biology, Campus, 42250, Konya, Turkey

Evernia prunastri (L.) Ach. (*Parmeliaceae*), edible lichen known as oak moss, is traditionally used for making breads by Egyptians. The lichen was tested *in vitro* in this study and linked with *diabetes mellitus* therapy (enzyme inhibition: anti-amylase and anti-glucosidase activities), Alzheimer's and Parkinson's disease treatment (enzyme inhibition: anti-cholinesterase and anti-tyrosinase activities), oxidative stress relief (antioxidant activity: free radical scavenging (DPPH and ABTS), reducing power (CUPRAC and FRAP), metal chelating and phosphomolybdenum assay) and bacterial infections treatment using *in vitro* antibacterial assay. We have determined total phenolic and flavonoid contents in ethyl-acetate (EtOAc) extract of *E. prunastri*. The effects were assessed for investigating biological profiles of *E. prunastri* EtOAc extract and describing the species as functional food. It was shown that *E. prunastri* possessed all biological activities investigated. The extract exhibited inhibitory effects on the activity of enzymes linked to *diabetes mellitus* and those linked to Alzheimer's disease; antioxidant activity and significant antibacterial activity against pathogenic and food contaminant bacterial species. The EtOAc extract of *E. prunastri* only failed in tyrosinase enzyme inhibition. This study showed that edible lichen *E. prunastri* might be classified as functional food with numerous health-beneficial effects in a dose dependent manner.

Keywords: *Evernia prunastri*, phenols, flavonoids, enzymes inhibition, antioxidant activity, antimicrobial activity

This work has been supported by the Serbian Ministry of Education, Science and Technological Development for financial support (Grant No. 173032).

Influence of bio- and magneto-priming on flax seedlings growth

PP5-6

Dušica Ćalić[1], Nina Devrnja[1], Jelena Milojević[1], Maja Milić[1], Snežana Zdravković Korać[1], Vera Karličić[2], Vera Raičević[2], Saša Ćirković[3], Jasna Ristić-Đurović[3]
(calic@ibiss.bg.ac.rs)

[1] University of Belgrade, Institute for Biological Research "Siniša Stanković", Despot Stefan Blvd 142, 11060 Belgrade, Serbia

[2] University of Belgrade, Faculty of Agriculture, Nemanjina 6, 11080 Zemun, Serbia

[3] University of Belgrade, Institute of Physics, Pregrevica 118, 11080 Zemun, Serbia

Flax (*Linum usitatissimum*) is an important food and fiber crop, due to its nutritional and nutraceutical qualities. Flax seeds have been consumed for at least 6,000 years, which makes it one of the world's first cultivated crops. Seed priming with living bacterial inoculum, termed biopriming, involves the application of plant growth-promoting rhizobacteria. The present study was con-

ducted to investigate the effect of growth-promoting rhizobacterium *Bacillus amyloliquefaciens* on the growth of flax seedlings under different strengths of magnetic field. Seedlings were soaked in bacterial suspension and bacteria were allowed to colonize. After ten minutes of soaking, the seedlings were exposed to magnetic field of 60 and 90 mT for 24 h, in dark under laboratory conditions. Untreated seedlings were used as controls. Shoot and root length, number and length of newly formed lateral roots and biomass production were measured after 1, 3, 5, 7 and 10 days. Results indicate that the combinations of magnetic field and plant growth-promoting bacteria gave half- to two-fold better results than bacteria or magnetic field alone. The best result was achieved in seedlings treated with *Bacillus amyloliquefaciens* and 90 mT magnetic field. This work showed a significant impact of bio- and magneto-priming on the improvement of flax seedling growth and biomass productivity.

Keywords: *Bacillus amyloliquefaciens*, *Linum usitatissimum*, static magnetic fields

This work was supported by the Ministry of Education, Science and Technological Development of the Republic of Serbia (Grant Nos. 173015, TR 31080 and III 45003).

Effect of seed magneto-priming on flax (*Linum usitatissimum*) seed germination and subsequent seedling growth

PP5-7

Dušica Ćalić, Dajana Todorović, Branka Petković, Nina Devrnja, Jelena Milojević, Maja Milić, Snežana Zdravković Korać
(calic@ibiss.bg.ac.rs)

University of Belgrade, Institute for Biological Research "Siniša Stanković", Despot Stefan Blvd 142, 11060 Belgrade, Serbia

In the context of seed technology, the use of magneto-priming, as a method for increasing plant production, offers advantages in comparison to conventional treatments with chemical substances. Magneto-priming is a cheap, non-invasive technique, based on the application of magnetic fields (MF) and described as eco-friendly, with proved beneficial effects on seed germination and subsequent plant biomass yield. In this study, seeds of flax (*Linum usitatissimum*), placed on moist filter-paper, were treated with 100 mT MF strength, with exposure time of 0, 24, 48, 72, 96 and 120 h and kept in dark under laboratory conditions. Seeds that were not exposed to magnetic field were used as controls. Efficacy of MF on seed germination and seedlings height, shoot and root length and biomass was evaluated. The MF promoted seed germination rate by 10%-40 %, depending of treatments, compared to control. The growth parameters were better in seedlings exposed to all magnetic treatments, with an increase of up to 60% over the control. MF treatment of 24 h had a 50% better effect than 120 h MF treatment. In addition, the best biomass yield of acclimated plants was achieved after the shortest magnetic exposure treatment. This study suggests a positive effect of stable MF on flax seed germination and subsequent growth of seedlings. Therefore, magnetic field may be useful in organic agriculture in replacing the usage of plant growth regulators.

Keywords: *Linum usitatissimum*, seed germination, static magnetic fields

This work was supported by the Ministry of Education, Science and Technological Development of the Republic of Serbia (Grant Nos. 173015 and 173027).

ABSTRACTS OF TUTORIAL, KEYNOTE, INVITED LECTURES, PROGRESS REPORTS AND CONTRIBUTED PAPERS

of

The Sixth International School and Conference on Photonics PHOTONICA2017

28 August – 1 September 2017
Belgrade Serbia

Editors
Marina Lekić and Aleksandar Krmpot

Technical assistance
Marko Nikolić and Danica Pavlović

Publisher
Institute of Physics Belgrade
Pregrevica 118
11080 Belgrade, Serbia

Printed by
Serbian Academy of Sciences and Arts

Number of copies
300

ISBN 978-86-82441-46-5

Method of preparing biomedical samples for cancer detection by infrared spectroscopy

J. L. Ristić-Djurović[1], S. T. Ćirković[1], N. Paunović[1], J. T. Juloski[2], S. R. De Luka[3], V. M. Ćuk[2], M. Romčević[1], A. M. Trbovich[3] and N. Romčević[1]
[1]*Institute of Physics, University of Belgrade, Belgrade, Serbia*
[2]*University Medical Center "Zvezdara", Clinic for Surgery "Nikola Spasić", Belgrade, Serbia*
[3]*Institute of Pathological Physiology, School of Medicine, University of Belgrade, Belgrade, Serbia*
e-mail:jasna@ipb.ac.rs

Most conventional cancer detection methods are based on the histopathology or tumor markers [1]. In the histopathology, stained tissue samples are visually inspected for various morphological changes under the microscope. Despite the software aids developed for picture analysis the method still remains heavily dependent on subjective, empirical expertise of specialists whose judgments were used to establish threshold levels of variables used in cancer detection. The immunohistochemistry as the most common of cancer marker methods uses the presence or over-expression of certain marker molecules to detect cancerous tissues. The drawback of this method is its limitation to those molecules, i.e., cancer markers it is designed for. In the last two decades, the vibrational spectroscopy applied to tissues emerged as a "molecular pathology" method for cancer detection [2]. The method provides spectral signature of all cellular components present in a sample; therefore, it probes the entire genome, proteome and metabolome of cells and tissues [3]. Consequently, it is sensitive to any changes in the biomolecular compositions and as such offers information that cannot be obtained by any of the conventional methods for cancer detection.

The biomedical samples for spectroscopic analysis are usually prepared by cutting several micrometer thin layers from a formalin-fixed paraffin-embedded tissue or from a frozen tissue [1, 2]. The cuts are then mounted on a suitable substrate, for example zinc selenium, calcium fluoride, barium fluoride. Additionally the samples may undergo deparaffinization or drying. Our samples were prepared in three steps. First, after surgical resection, the tissue specimens were opened, abundantly rinsed with sterile saline solution, dried on a sterile cloth, placed in a liquid nitrogen tank, and transported to the Pathophysiology laboratory of the School of Medicine where all sample tubes were transferred to a –80°C freezer where they were kept until further processing. In the second phase of sample preparation procedure the tissues were chopped at room temperature and homogenized. Homogenates were placed on a microscope slide and then dried in a sterilizator at 60°C for 1 h to remove bulk water. After drying, the samples were scratched from the slide and transferred to eppendorf tubes. In the final sample preparation stage the obtained tissue and dried KBr powder were mixed in the standard as well as in the three times larger ratio and the mixtures were pressed into tablets. Optionally, after 24 h the tablets were grounded and pressed again into tablets. The infrared spectra of the samples obtained using four different preparation procedures were compared. It was shown that larger tissue content as well as additional grounding improves infrared spectra quality.

REFERENCES

[1] M. Diem, A. Mazur, K. Lenau, J. Schubert, B. Bird, M. Miljković C. Krafft, J. Popp, J. Biophotonics 6, 855 (2013).
[2] G. Bellisola, C. Sorio, Am. J. Cancer Res. 2, 1 (2012).
[3] G. Clemens, J. R. Hands, K. M. Dorling, M. J. Baker, Analyst 139, 4411 (2014).

University of Plovdiv "Paisii Hilendarski"
Faculty of Biology, Department of Zoology

INTERNATIONAL CONFERENCE ON ZOOLOGY AND ZOONOSES

PROGRAMME & ABSTRACTS

October 26 – 28, 2016
Hissar, Bulgaria

Plovdiv University Press

P35

Habitat and sex-specific responses of *Drosophila subobscura* exposed to static magnetic field (2.4 T) revealed by analysis of morphological traits

***Tatjana Savić*[1], *Dajana Todorović*[1], *Saša Ćirković*[3], *Sofija Pavković-Lučić*[2], *Branka Petković*[1], *Jelena Trajković*[2]**

[1] University of Belgrade, Institute for Biological Research "Siniša Stanković", 142 Despot Stefan Blvd, Belgrade, Serbia
[2] University of Belgrade, Faculty of Biology, Studentski trg 16, 11000 Belgrade, Serbia
[3] University of Belgrade, Institute of Physics, Pregrevica 118, 11080 Zemun, Serbia

Corresponding author: Tatjana Savić,
e-mail: tanjat@ibiss.bg.ac.rs

ABSTRACT

At the present time, with increased technological development, we are confronted with a growing influence of various forms of magnetic fields that can affect living organisms. Biological effects represent measurable responses to a change in the environment that are not necessarily harmful. Adult phenotype is determined by an individual's genotype and environmental influences, and can be analyzed using measurable morphological traits.

The main goal of this research was to consider how a strong static magnetic field (2.4 T) affects wing size and shape of males and females from two *Drosophila subobscura* populations (collected in beech and oak forest), after placing the first instar larvae near the north (N) and the south (S) pole of the magnet (VINCY Cyclotron magnet) for 2 hours.

Applied static magnetic field (2.4 T) induced habitat – and sex-specific response in *Drosophila subobscura*. Results revealed presence of sexual dimorphism in both wing size and shape, in magnetic field and control groups of two *Drosophila subobscura* populations. Significant differences are found for both wing size and shape only within beech population. Comparing morphological traits between "beech" and "oak" populations, wing shape was significantly different in all treatments for both sexes, while wing size considerably differed only between females exposed to the South Pole.

FOURTH INTERNATIONAL CONFERENCE ON RADIATION AND APPLICATIONS IN VARIOUS FIELDS OF RESEARCH

May 23 - 27, 2016 | Niš | Serbia | rad-conference.org

BOOK OF ABSTRACTS

PUBLISHER: University of Niš, Faculty of Electronic Engineering
P.O.Box 73, 18000 Niš, Serbia
www.elfak.ni.ac.rs

FOR THE PUBLISHER: Prof. Dr. Dragan Mančić

EDITOR: Prof. Dr. Goran Ristić

COVER DESIGN: Vladan Nikolić, PhD

TECHNICAL EDITING: Vladan Nikolić, PhD and Sasa Trenčić, MA

PROOF-READING: Saša Trenčić, MA and Mila Aleksov, MA

PRINTED BY: Sven, Niš

PRINT RUN: 50 copies

The Fourth International Conference on Radiation and Applications in Various Fields of Research (RAD 2016) was financially supported by:

- Central European Initiative (CEI)
- Ministry of Education, Science and Technological Development of the Republic of Serbia

ISBN: 978-86-6125-160-3

EXPOSURE SYSTEM WITH HOMOGENEOUS STATIC AND ELF MAGNETIC FIELDS IN EXPERIMENTAL VOLUME

Slavica Gajić[1], Saša Ćirković[2], Jasna Ristić-Djurović[2], Andjelija Ilić[2], Drago Djordjević[3], Vesna Spasić-Jokić[4]

1 School of Electrical Engineering, University of Banja Luka, Banja Luka, Bosnia and Herzegovina
2 Institute of Physics, University of Belgrade, Belgrade, Serbia
3 School of Medicine, University of Belgrade, Belgrade, Serbia
4 Faculty of Technical Sciences, University of Novi Sad, Novi Sad, Serbia

The omnipresence of electromagnetic fields not only in human environment but all over the Earth raises questions about the positive or negative nature, extent, and threshold levels of influence of this non-ionizing radiation on living organisms. In particular, it has been shown that static, magnetic and extremely low frequency (ELF) electromagnetic fields have significant effects on the skeletal, immune, cardio-vascular, reproductive, as well as the central nervous system. The complexity of electromagnetic fields, i.e., their magnitude, direction, orientation, spatial as well as temporal dependence and gradients, along with requirements related to the specifics of biomedical experiments, e.g., uncertainty of sample positions in *in vivo* experiments, requirements related to experimental volume size and orientation, temperature, light, etc., impose a challenging task to biomedical researchers when describing and specifying their experimental conditions. An exposure system which provides a homogeneous field throughout the experimental volume significantly reduces ambiguities. With the aim to provide the field that will also be scalable and relatively strong within the experimental volume that is large enough for *in vivo* as well as *in vitro* experiments, we considered a solenoid. High homogeneity of the field was achieved with inner modifications of solenoid cross-section. The designed exposure system provides the field with the maximum magnitude of 165 mT and homogeneity of 2 % in the experimental volume with the size of 30 cm x 30 cm x 40 cm.

STATIC MAGNETIC FIELD EFFECTS ON BIOCHEMICAL REACTIONS INVOLVING REACTIVE OXYGEN SPECIES

Silvio R. De Luka[1], Andjelija Ž. Ilić[2], Saša Ćirković[2], Drago M. Djordjević[1], Jasna L. Ristić-Djurović[2], Alexander M. Trbovich[1]

1 School of Medicine, University of Belgrade, Belgrade, Serbia
2 Institute of Physics, University of Belgrade, Belgrade, Serbia

Reactive oxygen species (ROS) are toxic, short-lived, highly reactive by-products of normal physiological and metabolic cellular processes. The excessive production of ROS results in the damage of proteins, lipids, DNA and RNA. Aerobic cells possess antioxidant scavenging mechanisms that are protective against the ROS damage. These relay on the superoxide dismutase (SOD), catalase, glutathione peroxidase (GSHPx), vitamin E and vitamin C. The superoxide anion is converted to the hydrogen peroxide by the action of SOD: cytosolic (Cu/Zn-SOD), mitochondrial (Mn-SOD) or extracellular (Cu-SOD). Alterations in the expression of Cu/Zn-SOD have been implicated as a possible factor in several neurodegenerative disorders (Dröge 2002).

A static magnetic field (SMF) can, among other magnetobiological effects, induce changes in enzyme activity (Amara et al. 2006; Ghodbane et al. 2013). The metabolism of ROS becomes affected, with the reported effects to the lipid peroxidation, tissue damage, etc. whereas the strong and moderately strong SMF can act through the combination of several biophysical mechanisms, it is now accepted that the radical pair mechanism induces changes in the rates and yields of certain biochemical reactions under the influence of weak to moderate SMF (Rodgers 2009). These effects are strongly dependent on the SMF intensity, which could be a reason for the variability of the experimental results obtained by different research groups using various exposure setups.

Free radicals, including the reactive oxygen species, are ubiquitous in biology. Transition metal ions, the compounds of many proteins and enzymes, can act as radical species in biochemical reactions, enabling the modulation by the SMF of the redox cycles of metal-ion containing enzymes. This motivates the investigation not only into the exposure end effects such as the tissue damage, but also into the effects on the molecular level such as the distribution of various metals after exposure to the SMF. The current status of the observed effects to the organism is reviewed by putting into perspective the available data on the SMF induced effects as well as possible health implications.

References

Dröge W. 2002. Free radicals in the physiological control of cell function. Physiol Rev 82: 47-95.

Amara S. et al. 2006. Effects of subchronic exposure to static magnetic field on testicular function in rats. Arch Med Res 37(8):947-952.

Ghodbane S. et al. 2013. Bioeffects of static magnetic fields: oxidative stress, genotoxic effects, and cancer studies. BioMed Research International 2013: 602987.

Rodgers CT. 2009. Magnetic field effects in chemical systems. Pure Appl Chem 81(1): 19-43.

Serbian Genetic Society

Section of Population and Evolutionary Genetics
Section of Medical Genetics

BOOK OF ABSTRACTS

II Symposium of Population and Evolutionary Genetics PEG2012

with Satellite meeting: Population Genetic Studies of Complex Traits in Medicine

Belgrade, Serbia, 09-12 May 2012

III-13 Poster

Biological effects of a strong static magnetic field of 2.1 T in *Drosophila melanogaster* and *Drosophila subobscura*

Tatjana Savić[1], Jasna Ristić – Đurović[2], Branka Janać[1], Dajana Todorović[1], Danica Dimitrijević[1], Saša Ćirković[2], Zlatko Prolić[1]

[1]Institute for Biological Research "Siniša Stanković", University of Belgrade, Belgrade, Serbia
[2] Vinča Institute of Nuclear Sciences, University of Belgrade, Belgrade, Serbia

Organisms are developing and living under the influence of different environmental factors and adapting to possible changes which can be stressful through modulation of their behavioral and physiological responses. One of the omnipresent stressful abiotic factors is magnetic field, which among the complex influence of environmental factors is of particular importance and affects different biological systems.

The effect of a strong static magnetic field on development, viability and sex ratio was studied on laboratory strains of two species, *Drosophila melanogaster* and *Drosophila subobscura* originating from beech and oak forests. First instar larvae of both species were placed separately on the north (N) and south (S) magnetic poles and exposed to the magnetic induction of 2.1 T (VINCY Cyclotron magnet) for 2h.

Apparent biological effects of the N and S magnetic poles were observed in development and viability of both examined species. Results indicate that 2.1 T static magnetic field could be regarded as a potential stressor, influencing different levels of embryonic and post-embryonic development.

e-mail: tanjat@ibbi.ibiss.bg.ac.rs

EVALUATION OF SMF EXPOSURE FIELD LEVELS AND GRADIENTS OBTAINABLE USING THE 2D MAGNETIC ARRAYS*

Andjelija Ž. Ilić **, Saša Ćirković, Jasna L. Ristić-Djurović

Institute of Physics, University of Belgrade, Zemun-Belgrade, Serbia

Abstract. *Two-dimensional magnetic arrays have been proven useful as exposure setups for biomedical experiments with static magnetic fields. Different static magnetic field levels as well as vertical field gradients can be attained from these exposure setups by means of varying the geometrical parameters of an array and the type of magnetic material employed. Evaluation of obtainable field and gradient values has been conducted by varying one by one parameter. Several relevant parameters were chosen to represent the effects of input parameter changes on the magnetic flux density above the array. Calculations were conducted using the exact analytical expression.*

Key words: *Non-ionizing radiation exposures, exposure setups, static magnetic field (SMF), two-dimensional magnetic arrays, parameter adjustment*

DOI: 10.21175/RadJ.2016.02.027

1. INTRODUCTION

Effects of electromagnetic (EM) fields on biological systems can be either beneficial or adversarial. Static magnetic fields (SMF) of low and moderate intensity are shown to have mainly beneficial effects, based on empirical and collected experimental data. Observed therapeutic effects include those related to treating arthritis [1], healing bone fractures [2], and improving microcirculation [3]. Mechanisms of action of SMFs are not yet fully understood.

Experimental magnetic fields are generated using various arrangements of current coils or permanent magnets. Certain types of two-dimensional (2D) magnetic arrays have been successfully employed as exposure setups for SMF generation as well [4], [5]. The type of the array described in [4], with the magnetic axes of individual magnets equally oriented and perpendicular to the array's surface, produces the slowly decreasing magnetic field. In the considered case, individual magnets were distributed across a flat surface periodically at equal distances x_d and y_d in two orthogonal directions. The dominant field component is perpendicular to the surface of the array and an order of magnitude larger than other magnetic field components, provided that individual magnets are not too sparsely placed across the surface. Magnetic flux density variation in planes parallel to the array's surface is significantly smaller than the field decrease with distance from the surface. This allows for the definition of the field gradient perpendicular to the array's surface. This exposure setup therefore produces inhomogeneous magnetic field whose magnetic flux density as well as gradient vary predominantly in the direction perpendicular to the array's surface, with very slight variations in planes parallel to the surface. This configuration enables studying the effects of both magnetic flux density and its gradient.

Different SMF field levels as well as field gradients can be attained by means of varying the geometrical parameters of an array and the type of magnetic material employed. We investigate the effects to the magnetic flux density and its gradient of varying several parameters, with the aim to define the range of SMF exposure field levels and gradients available for conducting experiments.

2. TWO-DIMENSIONAL MAGNETIC ARRAYS WITH EQUALLY ORIENTED MAGNETIC MOMENTS OF ARRAY ELEMENTS

In the investigation of obtainable exposure field levels and gradients we assume an array of N-by-N identical square cross-section magnets, equally spaced on a flat horizontal surface and kept in place by a non-magnetic substrate. We assume equal and vertical orientation of magnetic moments of all magnets. Were the magnets mounted on a ferromagnetic plate instead, similar analysis would apply, with the height of the magnets doubled due to the image theorem.

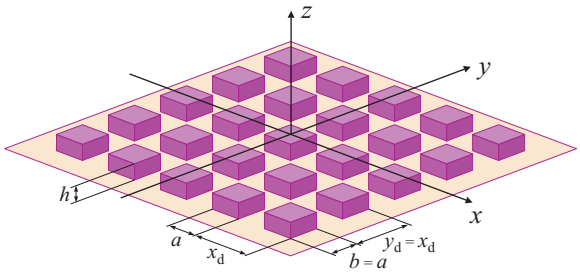

Figure 1. Two-dimensional magnetic array

* The paper was presented at the Third International Conference on Radiation and Applications in Various Fields of Research (RAD 2015), Budva, Montenegro, 2015.

**andjelijailic@ieee.org

Vertical axis is denoted as the z-axis and the whole array is assumed to be symmetrical with respect to the x- and y-direction, as shown in Fig. 1. Rows of magnets are parallel to the x-axis, with the magnet centers spaced by x_d. Distance between the adjacent rows is $y_d = x_d$. Magnetic flux density distribution at the array's surface varies periodically from negative to positive B_z, since the magnetic flux lines partially close between the adjacent elements. With the increase in height, z, above the array's surface the majority of the magnetic flux lines add up together to form a resultant magnetic flux density B_z. Above a low-limit height for conducting experiments, $z = z_0$, magnetic flux density is positive everywhere except for the stray field above the array edges. With the further increase in height, magnetic flux density variation in horizontal planes decreases. We define parameter $z_{1\%}$, as the height above the array above which field variation in the horizontal planes is less than 1%, and $\overline{B}_{z,\,1\%}$ as the corresponding mean magnetic flux density. Magnetic field vertical gradient decreases with height as well, with magnetic field decrease almost linear at larger heights.

Basic properties of several magnetic materials most commonly used for permanent magnets [6], [7] are listed in Table 1. Material remanent magnetization, B_r, and Curie temperature, T_C, as well as the maximum energy product, $(BH)_m$, must all be accounted for when choosing the right magnets for a particular application. Improved energy product is accompanied by the increased cost of permanent magnets, ranging from about 5 USD per kg for ferrites ($BaFe_{12}O_{19}$), to about 50 USD/kg for Alnico, and to about 120 USD/kg for samarium-cobalt and neodymium magnets [8]. High quality neodymium magnets are more expensive, up to about 200 USD/kg. Remanent magnetic flux density corresponds to bulk material, i.e., to a piece of material very long in the direction of magnetization. It is related to the magnetization per unit density, M_r, by the equation $B_r = \mu_0 \cdot \rho \cdot M_r$, where ρ represents the material density. Considering equivalent surface currents resulting from magnetization and real magnet dimensions, actual magnetic flux density is obtained analytically. For the magnetization in the z-direction, four vertical sides of each magnet can be replaced by the current sheets carrying the surface current density $J_{ms} = \rho \cdot M_r$.

Vertical component of the magnetic flux density, $B_z(x,y,z)$, is calculated as the sum of the contributions of all vertical sides of all the magnets comprising the array. For a single square cross-section magnet of side length a and height h magnetic flux density is given by:

$$B_{z1}(x_1,y_1,z)=\frac{\mu_0 J_{ms}}{4\pi}\sum_{k=1}^{4}\sum_{tp=0}^{1}\sum_{tq=0}^{1}(-1)^{(tp+tq+1)}\arcsin\left(p_k^{tp}\cdot q_k^{tq}\right),$$

$$p_k^{tp}=\frac{((-1)^{\left[\frac{k}{2}\right]+tp}\frac{a}{2}-x_1)^{m_2}\cdot((-1)^{\left[\frac{k-1}{2}\right]+tp}\frac{a}{2}-y_1)^{m_1}}{\sqrt{((-1)^{\left[\frac{k}{2}\right]+1+(tp-1)m_2}\frac{a}{2}-x_1)^2+((-1)^{\left[\frac{k-1}{2}\right]+1+(tp-1)m_1}\frac{a}{2}-y_1)^2}},$$

$$q_k^{tq}=\frac{\frac{\mathrm{sgn}((-1)^{m_s}\frac{a}{2}-x_1)^{m_1}}{(-\mathrm{sgn}((-1)^{m_s}\frac{a}{2}-y_1))^{m_2}}\cdot(z+(1-tq)\cdot h)}{\sqrt{((-1)^{m_s}\frac{a}{2}-x_1)^{2m_1}((-1)^{m_s}\frac{a}{2}-y_1)^{2m_2}+(z+(1-tq)\cdot h)^2}},$$

$$m_1=(1+(-1)^{k-1})/2,\ m_2=(1+(-1)^{k})/2,\ m_s=(1-\mathrm{sgn}(k-\tfrac{5}{2}))/2.$$

In the above, x_1 and y_1 are the distances, measured in the direction of x-axis and y-axis, from the magnet center to the field point. Magnet side is denoted by k, numbers 1, 2, 3 and 4 corresponding to the negative x-axis, negative y-axis, positive x-axis and positive y-axis with respect to the magnet center. Square brackets stand for the integer division. Point of current entrance into the current sheet corresponds to $tp = 0$, and the point of current exit to $tp = 1$. Indices $tq = 0$ and $tq = 1$ denote the bottom surface or the top surface of the magnet. Derivation of the above equation, as well as the expressions for x-component and y-component of the magnetic flux density, are given in [4]. It has been shown in [4] that the B_z field component is dominant. Therefore, this evaluation considers only the dominant field component.

Table 1. Basic properties of typical commercial magnetic materials

Material	B_r (T)	$(BH)_m$ (kJ/m³)	T_C (°C)	M_r (Am²/kg)	J_{ms} (A/m)
$BaFe_{12}O_{19}$	0.40	34	450	65.0	318.3
Alnico	1.25	43	860	142.1	994.7
$SmCo_5$	0.88	150	720	85.4	700.3
Sm_2Co_{17}	1.08	220	820	102.3	859.4
$Nd_2Fe_{14}B$	1.28	300	400	135.8	1018.6

3. Results and Discussion

The surface current density, J_{ms}, enters the magnetic flux density equation as the multiplicative factor to scale the expression depending exclusively on the geometrical parameters of an array. Therefore, for a fixed given geometry of an array, difference in the achieved field levels for different magnetic materials corresponds to the ratio of remanent magnetization of materials. This is illustrated by the example shown in Fig. 2, where moderately sized magnets (a = 8 mm, h = 5 mm) were arranged with the gap between every two magnets equal to the magnet length a ($k_d = 1$). Please note that the parameter k_d is introduced as the ratio of the gap size to the magnet size. Corresponding center-to-center magnet spacing equals $x_d = (k_d+1)\cdot a$. Number of individual magnets in a row is taken equal to N = 15 in this as well as in the all other examples.

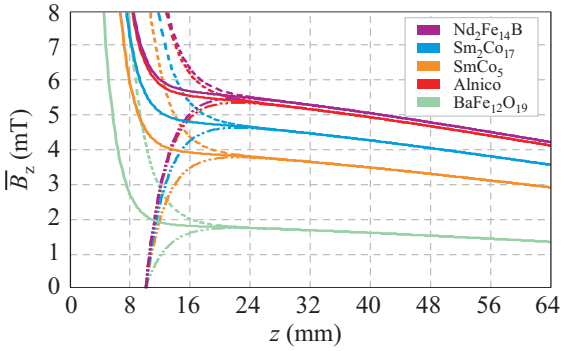

Figure 2. Magnetic flux density along the magnet axis, along the magnet gap axis, and mean magnetic flux density in

horizontal planes above the array, for magnetic materials listed in Table 1 (a = 8 mm, h = 5 mm, x_d = 16 mm)

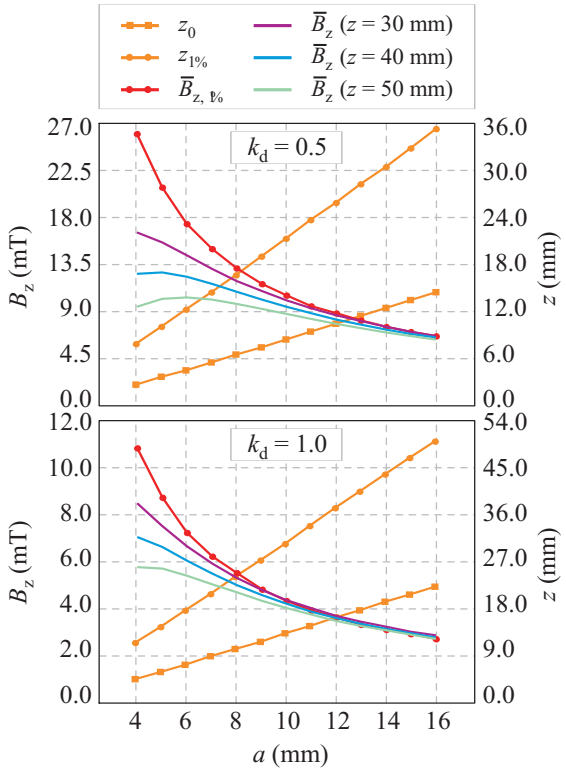

Figure 3. Influence of the magnet side length, a, on several parameters describing the magnetic field above the array, with the relative spacing between the magnets kept fixed at half the side length (upper plot) and whole side length (lower plot)

In Fig. 2, magnetic flux density at the vertical axes through the magnet centers is represented by the dashed lines, and the one between every four magnets (axes where the x-spacings and y-spacings cross) is shown by the dash-dot-dot lines. Mean magnetic flux density in horizontal planes above the array is well approximated as the average of the two (depicted by the solid lines). Up to some low-limit height magnetic flux density along the magnet gap axis is negative as the flux lines close between the magnets. At the same height, right above the magnets the field is strong, so that all in all next to the surface the field intensity is strong, direction of magnetic flux lines alternates, and field gradients are very pronounced. After the limiting height, z_0, magnetic flux densities above the magnets and between the magnets start converging to fast reach the height where the field variation everywhere in the horizontal planes lies below 1% of the mean field level in that plane. For the considered example, magnetic flux density is positive everywhere above the plane z_0 = 10.2 mm. The 1% threshold is $z_{1\%}$ = 24.0 mm, and the B_z value for the strongest neodymium magnets at that height equals $\overline{B}_{z,\,1\%}$ = 5.5 mT. In this particular example, field further decreases almost linearly.

Having in mind average mice height of about 30 mm, experimental volume for *in vivo* experiments can be taken from the height of about 25 mm to 55 mm. For *in vitro* experiments, a range of different field intensities is available by appropriate placement of specimens at different heights above the array. Mean magnetic flux density and its mean gradient in the experimental volume are determined by field averaging between the two limiting horizontal planes.

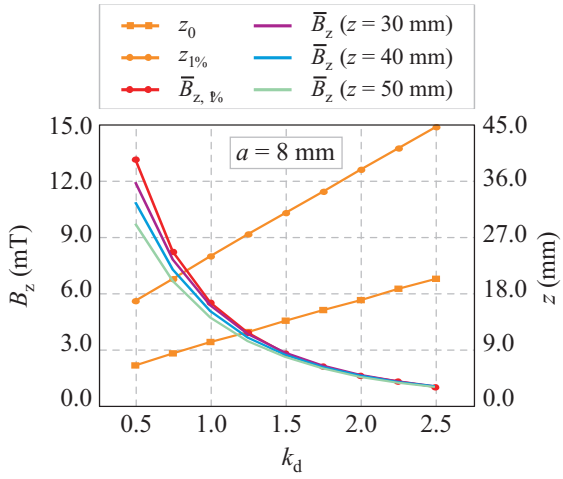

Figure 4. Influence of the gap size, $k_d \cdot a$, between the two neighboring magnets on the parameters describing the magnetic field above the array

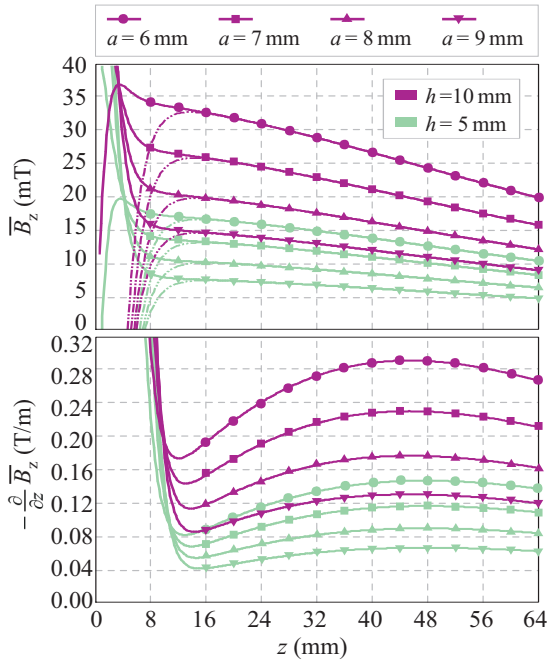

Figure 5. Mean magnetic flux density and its mean gradient for the fixed center-to-center magnet spacing of x_d = 12 mm, for different ratios a versus $k_d \cdot a$, for two magnet heights h

Since the amount of data that could be depicted in Fig. 3 and Fig. 4 is limited, three heights, z = 30 mm, z = 40 mm, and z = 50 mm, were chosen to represent field variations resulting from the changes of input parameters.

Provided that the height of the magnets is relatively small with respect to the size of an array in lateral

directions, doubling the magnet height results in twice the magnetic flux density. Height of the magnets can therefore be used to adjust the field levels. If the more homogeneous magnetic flux density is desired for the experiment, one magnetic array is placed below the experimental volume, and the other one on top. Resultant magnetic flux density is fairly homogeneous. Height of the magnets in Fig. 3 and Fig. 4 is fixed at h = 5 mm and in Fig. 5 it is compared with h = 10 mm.

Data presented in Fig. 3 analyze what are the effects to the field of the changes in magnet side length, a. The ratio gap size versus magnet size is kept fixed at k_d = 0.5 (upper plot) and k_d = 1 (lower plot). Both the low-limit height z_0 and the 1% threshold $z_{1\%}$ show linear dependence on the lateral size of the magnets. Magnetic field is higher and the two limiting heights, z_0 and $z_{1\%}$, are lower for the smaller magnets. Data shown in Fig. 3, Fig. 4 and Fig. 5 correspond to $Nd_2Fe_{14}B$ magnets. For other types of magnetic materials, data need to be scaled by the relative ratio of remanent magnetizations.

Parameters of interest are presented in Fig. 4 as a function of k_d, with the fixed values of other input data. Size of the magnets is kept at moderate a = 8 mm. Similar conclusions are drawn as in the previous example – smaller magnet spacing results in the stronger and higher quality magnetic field (in terms of field homogeneity in horizontal planes).

Figure 5 shows mean magnetic flux density and its mean gradient for the fixed center-to-center magnet spacing of x_d = 12 mm, value of x_d resulting in almost constant gradient about 40 to 48 mm height. Magnetic flux density decrease in that case shows the least variation from the linear one inside the experimental volume recommended for *in vivo* experiments (25 to 55 mm height above the array). It is demonstrated that the increase in height of the magnets results in almost the same relative increase in field intensity.

4. Conclusions

Generic example of the symmetrical two-dimensional magnetic array has been studied using the analytical expressions describing the magnetic flux density above the array. Evaluation of obtainable static magnetic field levels as well as vertical field gradients has been conducted by varying one by one parameter. Input parameters comprised magnet size and spacing (the geometrical parameters) and the type of magnetic material used. The collection of data and results presented can be used for preliminary design of 2D magnetic arrays.

Acknowledgement: *This work was supported by the Ministry of Education, Science and Technological Development of Serbia through the project III-45003.*

References

1. N. Taniguchi, S. Kanai, M. Kawamoto, H. Endo and H. Higashino, "Study on application of static magnetic field for adjuvant arthritis rats", *Evid. Based Complem. Altern. Med.*, vol. 1, pp. 187-191, July 2004.
2. S. Xu, H. Okano, N. Tomita and Y. Ikada, "Recovery effects of a 180 mT static magnetic field on bone mineral density of osteoporotic lumbar vertebrae in ovariectomized rats", *Evid. Based Complem. Altern. Med.*, vol. 2011, Article ID 620984, 8 pages, 2011.
3. H. N. Mayrovitz and E. E. Groseclose, "Effects of a static magnetic field of either polarity on skin microcircula-tion", *Microvasc. Res.*, vol. 69, pp. 24-27, January 2005.
4. A. Ž. Ilić et al., "Analytical description of two-dimensional magnetic arrays suitable for biomedical applications", *IEEE Trans. Magnetics*, vol. 49, pp. 5656-5663, December 2013.
5. J. László et al., "Optimization of static magnetic field parameters improves analgesic effect in mice", *Bioelectromagnetics*, vol. 28, pp. 615-627, December 2007.
6. T. R. Ní Mhíocháin and J. M. D. Coey, "Permanent magnets", in Physical Methods, Instruments and Measurements, vol. III, Y. M. Tsipenyuk, Ed. Oxford, U.K.: Eolss Publishers, 2009 [Online]: http://www.eolss.net., Encyclopedia of Life Support Systems, under the auspices of the UNESCO.
7. I. R. Harris and A. J. Williams, "Magnetic materials", in Materials Science and Engineering, vol. II, R. D. Rawlings, Ed. Oxford, U.K.: Eolss Publishers, 2009 [Online]. Available: http://www.eolss.net., Encyclopedia of Life Support Systems, under the auspices of the UNESCO.
8. W. T. Benecki, "The permanent magnet market – 2015", *Proc. Magnetics 2013 Conf.*, Orlando, FL, USA, 2013.

Универзитет у Београду
Иновациони центар Електротехничког факултета

А. Илић, С. Ћирковић, Ј. Ристић-Ђуровић, Д. Ђорђевић и А. Трбовић

УПОТРЕБА МАДУ ТРАКА У БИОМЕДИЦИНСКИМ ЕКСПЕРИМЕНТИМА

– Техничка документација –

Београд, 2013.

M84: Битно побољшано техничко решење на националном нивоу
УПОТРЕБА МАДУ ТРАКА У БИОМЕДИЦИНСКИМ ЕКСПЕРИМЕНТИМА

Руководилац пројекта: Небојша Ромчевић

Одговорно лице: Анђелија Илић

Аутори: Анђелија Илић, Саша Ћирковић, Јасна Ристић-Ђуровић, Драго Ђорђевић, Александар Трбовић

Развијено: у оквиру пројекта Интегралних и интердисциплинарних истраживања (ИИИ), број ИИИ-45003

Година: 2013.

Примена: 01.03.2013.

Кратак опис

У склопу овог техничког решења, изведене су и дате егзактне формуле за рачунање магнетске индукције произвољног дводимензионог магнетског низа, на основу њих је предложен једноставан начин одређивања средњих параметара магнетског поља који су од интереса за кориснике оваквих низова, написана је процедура за MATLAB која рачуна расподелу поља и средње параметре за произвољан случај. За конфигурације које се уобичајено користе подаци су дати и табеларно, у оквиру "Упутства за употребу МАДУ трака у биомедицинским огледима", припремљеног за студенте и сараднике Медицинског факултета у Београду.

Реализатори:
Иновациони центар Електротехничког факултета, Универзитет у Београду

Корисници:
Медицински факултет, Универзитет у Београду

Подтип решења:
Битно побољшано техничко решење на националном нивоу (М84)

Стање у свету

Стални магнети, као и њихове комбинације у виду површинских низова, користе се већ дуго времена у области физикалне терапије и рехабилитације. Иако сви механизми деловања нису у потпуности разјашњени, емпиријски је утврђен благотворан, односно позитиван, утицај на ублажавање тегоба проузрокованих артритисом, ублажавање запаљења и залечивање рана, ублажавање бола и стреса и побољшање микроциркулације [1]-[6]. Такође, различите комбинације сталних магнета су погодне као извор статичког магнетског поља у биомедицинским огледима *in vitro* или огледима на малим животињама, као у [7]. Овде је потребно нагласити, да током прегледа постојеће литературе нисмо наишли на пример коришћења дводимензионог магнетског

низа као што су МАДУ траке, медицинско средство патентирано за примену у физикалној терапији и рехабилитацији [8]. По три МАДУ траке су употребљене за формирање већих низова који покривају површину испод дна стандардног малог кавеза у нашим експериментима описаним у радовима [9], [10]. Генерички случај дводимензионог магнетског низа је анализиран у раду [1].

Упркос успешној употреби МАДУ трака у медицинској пракси, детаљан опис њихових карактеристика који је неопходан за опис изведених огледа и даље извођење закључака је био недоступан, укључујући и тачну вредност реманентне магнетске индукције материјала. Истраживање спроведено 2007. године је указало на то да непотпун или недовољно прецизан опис употребљених поља представља главни недостатак у великом броју публикација које се баве утицајем електромагнетских поља на живе организме [11]. Дводимензиони магнетски низови имају и велики број немедицинских примена, укључујући микроактуаторске системе, микросензоре, синхроне планарне моторе и магнетску левитацију. Међутим, велики низови се уобичајено анализирају применом Фуријеових низова, док се за конкретан случај низа мањег броја елемената најчешће користи моделовање коначним елементима. Изведени комплетни аналитички изрази за општи случај оваквог низа се могу једноставно применити, а погодни су и за оптимизацију параметара низа. Провера је извршена методом коначних елемената и мерењем.

Опис

На слици 1 је приказан начин употребе МАДУ трака у биомедицинским огледима. Коришћене су МАДУ траке типа L (large), које представљају низ од 5-пута-4 сталних магнета распоређених еквидистантно, у оба правца. За стандардни мали кавез (22,0 mm x 13,5 mm x 15,0mm) потребно је коришћењем три траке формирати низ од 15-пута-4 магнета, док се за стандардни велики кавез (38,0 mm x 21,0 mm x 18,5mm) формира низ од 12-пута-10 магнета коришћењем шест трака. За разлику од магнетских низова са супротно усмереним магнетским моментима суседних елемената, у једној или у обе димензије, или низова са ротираним магнетским моментима као што је то предложио К. Халбах [12], код којих је циљ остваривање што јаче магнетске индукције уз површ низа, скоро паралелне површи, променљивог смера између суседних редова, МАДУ траке спадају у низове код којих сви елементи имају идентичну оријентацију магнетских момената управну на површину низа. Као резултат, добија се магнетска индукција претежно управна на површину низа, изнад неке граничне висине увек истог знака, која споро опада са растојањем од површине низа. Варијације поља у појединачним водоравним равнима су знатно мање од варијација са променом висине, те се и магнетска индукција и градијент вертикалне компоненте магнетске индукције, који се показује довољним за опис промена поља, могу у првој апроксимацији сматрати функцијама само z-координате.

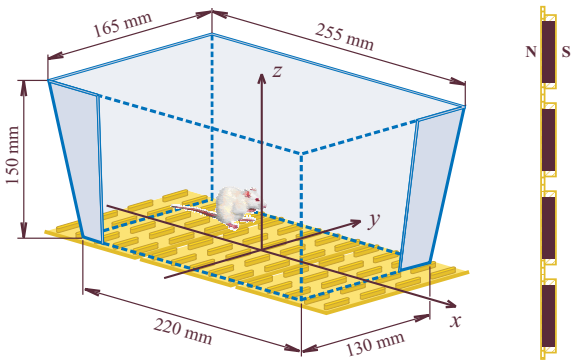

Слика 1. Дводимензиони магнетски низ погодан за коришћење у биомедицинским огледима. Приказан је усвојени референтни координатни систем. Произведено магнетско поље споро опада са растојањем од површине низа и прожима, односно покрива, целу огледну запремину.

Аналитички опис магнетског поља низа

Услед своје примарне намене да лако приањају на делове људског тела, попут магнетског завоја, МАДУ траке су реализоване уграђивањем појединачних магнета у супстрат од еластичног, гумастог дијамагнетика чији се утицај може у потпуности занемарити. Претпостављајући униформну магнетизацију по запремини сваког појединачног магнетића, сваки од њих се може заменити површинским Амперовим струјама, односно еквивалентним кратким соленоидом правоугаоног попречног пресека. На тај начин се проблем своди на одређивање магнетске индукције коначног броја правоугаоних површинских струјних расподела. Магнетска индукција једне правоугаоне траке се може добити коришћењем добро познатог израза за праву струјну нит коначне дужине који следи директно из Био-Саваровог закона:

$$B = \frac{\mu_0 \mathrm{d}I}{4\pi d}\left(\sin\theta_2 - \sin\theta_1\right). \tag{1}$$

Јачина струје $\mathrm{d}I = J_{\mathrm{mS}}\mathrm{d}z$ у нити инфинитезималне висине dz ствара у тачки поља F компоненту магнетске индукције, B, нормалну на раван дефинисану правцем жице и тачком F, смера усклађеног са правилом десне завојнице. Вектор површинске густине струје, $\mathbf{J}_{\mathrm{mS}}$, је повезан са магнетизацијом, $\mathbf{M}$, преко $\mathbf{J}_{\mathrm{mS}} = \mathbf{M}\times\mathbf{n}$, где је $\mathbf{n}$ површинска нормала. Удаљеност тачке F од праве која садржи посматрану нит је означена са d и одговарајућа нормала на нит уједно служи као референтна оса за углове θ_1 и θ_2, при чему индекси 1 и 2 одговарају тачкама уласка струје у нит и изласка из нити, респективно. Најповољнији интеграли за решавање се добијају уколико се угао између потега d и хоризонталне равни која садржи нит означи као ξ, и све остале величине изразе преко овог угла. Након интеграције и сређивања изрази за хоризонталне компоненте магнетске индукције постају

$$\begin{aligned}
B_{\mathrm{x}}(x,y,z) &= \frac{\mu_0 J_{\mathrm{mS}}}{4\pi}\sum_{i=-M}^{M}\sum_{j=-N}^{N-1}\sum_{k=1,3}\sum_{tp=0}^{1}\sum_{tq=0}^{1}\frac{(-1)^{(tp+tq+1)}}{\operatorname{sgn}\left((j+\frac{1}{2})\cdot y_{\mathrm{d}}+(-1)^{m_{\mathrm{S}}+tp+1}\frac{a}{2}-y\right)}\cdot\\
&\qquad\cdot\ln\left(-\left|u_{i,j,k}^{a,tq}\right|+\sqrt{\left(u_{i,j,k}^{a,tq}\right)^2+\left(r_{i,j,k}^{a,tp}\right)^2}\right),\\
B_{\mathrm{y}}(x,y,z) &= \frac{\mu_0 J_{\mathrm{mS}}}{4\pi}\sum_{i=-M}^{M}\sum_{j=-N}^{N-1}\sum_{k=2,4}\sum_{tp=0}^{1}\sum_{tq=0}^{1}\frac{(-1)^{(tp+tq)}}{\operatorname{sgn}\left(i\cdot x_{\mathrm{d}}+(-1)^{m_{\mathrm{S}}+tp}\frac{b}{2}-x\right)}\cdot\\
&\qquad\cdot\ln\left(-\left|u_{i,j,k}^{b,tq}\right|+\sqrt{\left(u_{i,j,k}^{b,tq}\right)^2+\left(r_{i,j,k}^{b,tp}\right)^2}\right),\\
r_{i,j,k}^{a,tp} &= \frac{\left(i\cdot x_{\mathrm{d}}+(-1)^{m_{\mathrm{S}}}\frac{b}{2}-x\right)}{\left((j+\frac{1}{2})\cdot y_{\mathrm{d}}+(-1)^{m_{\mathrm{S}}+tp+1}\frac{a}{2}-y\right)},\qquad r_{i,j,k}^{b,tp} = \frac{\left((j+\frac{1}{2})\cdot y_{\mathrm{d}}+(-1)^{m_{\mathrm{S}}}\frac{a}{2}-y\right)}{\left(i\cdot x_{\mathrm{d}}+(-1)^{m_{\mathrm{S}}+tp}\frac{b}{2}-x\right)},\\
u_{i,j,k}^{a,tq} &= \frac{\left(i\cdot x_{\mathrm{d}}+(-1)^{m_{\mathrm{S}}}\frac{b}{2}-x\right)}{\sqrt{\left(i\cdot x_{\mathrm{d}}+(-1)^{m_{\mathrm{S}}}\frac{b}{2}-x\right)^2+\left(z+t+(1-tq)\cdot h\right)^2}},\\
u_{i,j,k}^{b,tq} &= \frac{\left((j+\frac{1}{2})\cdot y_{\mathrm{d}}+(-1)^{m_{\mathrm{S}}}\frac{a}{2}-y\right)}{\sqrt{\left((j+\frac{1}{2})\cdot y_{\mathrm{d}}+(-1)^{m_{\mathrm{S}}}\frac{a}{2}-y\right)^2+\left(z+t+(1-tq)\cdot h\right)^2}},\quad m_{\mathrm{S}} = \frac{1-\operatorname{sgn}(k-\frac{5}{2})}{2}.
\end{aligned} \tag{2}$$

Дужина, ширина и висина појединачног магнета, елемента низа, су означене као a, b и h, а међусобна одстојања у правцу x- и y-осе као x_{d} и y_{d}. Индекси i и j одговарају елементу i у реду j магнетског низа, док индекс k означава једну од четири струјне траке које одговарају посматраном елементу низа. За k једнако 1, 2, 3, или 4, струјна трака је померена за $\Delta x = -b/2$, $\Delta y = -a/2$, $\Delta x = b/2$, односно $\Delta y = a/2$, у односу на средиште посматраног елемента. Претпостављено је да се низ састоји од $(2M+1)$-пута-$(2N)$ елемената, без губитка на општости. Горњи индекс $tp = 0$ односно $tp = 1$

одговара референтном смеру струје у струјној траци који је увек од 0 ка 1. Горњи индекс $tq = 0$ или $tq = 1$ означава доњу површину, $z = -t-h$, или горњу површину, $z = -t$, магнета, где је t дебљина гуменог омотача МАДУ, траке у коју су уграђени магнети. Вертикална координата $z = 0$ према томе одговара ситуацији када узорак лежи на самој површини траке или трака приања уз узорак.

Вертикална компонента вектора магнетске индукције, која је у случају низа са истоветно оријентисаним појединачним магнетским моментима елемената управним на низ много већа од B_x, B_y, односно доминантна, износи

$$
\begin{aligned}
B_z(x,y,z) &= \frac{\mu_0 J_{mS}}{4\pi} \sum_{i=-M}^{M} \sum_{j=-N}^{N-1} \sum_{k=1}^{4} \sum_{tp=0}^{1} \sum_{tq=0}^{1} (-1)^{(tp+tq+1)} \arcsin\left(p_{i,j,k}^{tp} \cdot q_{i,j,k}^{tq}\right), \\
p_{i,j,k}^{tp} &= \frac{(i\cdot x_d + (-1)^{\left[\frac{k}{2}\right]+tp}\frac{b}{2} - x)^{m_2} \cdot ((j+\frac{1}{2})\cdot y_d + (-1)^{\left[\frac{k-1}{2}\right]+tp}\frac{a}{2} - y)^{m_1}}{\sqrt{(i\cdot x_d + (-1)^{\left[\frac{k}{2}\right]+1+(tp-1)m_2}\frac{b}{2} - x)^2 + ((j+\frac{1}{2})\cdot y_d + (-1)^{\left[\frac{k-1}{2}\right]+1+(tp-1)m_1}\frac{a}{2} - y)^2}}, \\
q_{i,j,k}^{tq} &= \frac{\dfrac{\operatorname{sgn}(i\cdot x_d + (-1)^{m_s}\frac{b}{2} - x)^{m_1}}{(-\operatorname{sgn}((j+\frac{1}{2})\cdot y_d + (-1)^{m_s}\frac{a}{2} - y))^{m_2}} \cdot (z + t + (1-tq)\cdot h)}{\sqrt{(i\cdot x_d + (-1)^{m_s}\frac{b}{2} - x)^{2m_1}((j+\frac{1}{2})\cdot y_d + (-1)^{m_s}\frac{a}{2} - y)^{2m_2} + (z+t+(1-tq)\cdot h)^2}}, \\
m_1 &= (1+(-1)^{k-1})/2,\ \ m_2 = (1+(-1)^{k})/2,\ \ m_s = (1-\operatorname{sgn}(k-\tfrac{5}{2}))/2.
\end{aligned}
\tag{3}
$$

Овде параметри p и q одговарају синусима углова θ_0 и ξ, где смо са θ_0 означили пројекцију угла θ на xOy раван. Оператор [•] означава целобројно дељење.

Са повећањем броја појединачних магнета у оба правца у хоризонталној равни, z-компонента вектора магнетске индукције тежи граничном случају бесконачног низа, када је она периодична са периодом x_d односно y_d, у правцу x- и y-осе, респективно. У случају коначног низа описана расподела вектора магнетске индукције одговара централном делу запремине изнад низа. Сматрајући хоризонталне компоненте вектора магнетске индукције довољно малим да се искључе из разматрања, максимум и минимум магнетске индукције у појединачној посматраној хоризонталној равни се могу изједначити са z-компонентом у одговарајућим тачкама, израчунатом на основу израза (3). Притом максимуму одговара магнетска индукција на вертикалној оси која пролази тачно кроз центар појединачног магнета у централном делу траке, $B_H(z)$. Минимум, $B_V(z)$, се налази као вредност на вертикалној оси која пролази кроз тачку пресека линија које тачно одговарају средини између суседних редова магнета у правцу x- и y-осе. Дефинишимо вертикални градијент магнетске индукције као:

$$
G_z(x,y,z) = -\operatorname{grad}_z B_z(x,y,z) = -\frac{\partial B_z(x,y,z)}{\partial z}. \tag{4}
$$

Тада се средња вредност магнетске индукције и усредњени вертикални градијент магнетске индукције у посматраним хоризонталним равнима могу проценити коришћењем аритметичке средине $B_H(z)$ и $B_V(z)$.

$$
\begin{aligned}
&\overline{B_z}(z) = \frac{B_H(z) + B_V(z)}{2}, \quad \Delta B_z(z) = \frac{B_H(z) - B_V(z)}{2}, \\
&\overline{G_z}(z) = -\operatorname{grad}_z \overline{B_z} = -\frac{1}{2}\left(\frac{\partial B_H(z)}{\partial z} + \frac{\partial B_V(z)}{\partial z}\right) = \frac{G_H(z) + G_V(z)}{2}, \\
&\Delta G_z(z) = \frac{G_H(z) - G_V(z)}{2}, \quad G_H = -\frac{\partial B_H(z)}{\partial z},\ G_V = -\frac{\partial B_V(z)}{\partial z}.
\end{aligned}
\tag{5}
$$

Код овде описаних трака број елемената низа је релативно мали (15 пута 4), док су величине појединачних магнета ($a \times b \times h$ = 24.4 mm×4.8 mm×4.8 mm), однос њихове дужине и ширине (aspect ratio) и растојања између редова (x_d = 19.5 mm, y_d = 36.0 mm) значајни. На неки начин, то је најнеповољнији случај за проверу предложеног приступа. Као што се види из дела (б) Слике 2, и у овом неповољном случају се добија резултат задовољавајуће тачности, који се може искористити за брзу процену средњих параметара магнетског поља у огледној запремини. Такође, израз (5) може да послужи за процену магнетске индукције и њеног вертикалног градијента током прелиминарног дизајна низова са захтеваним средњим параметрима поља.

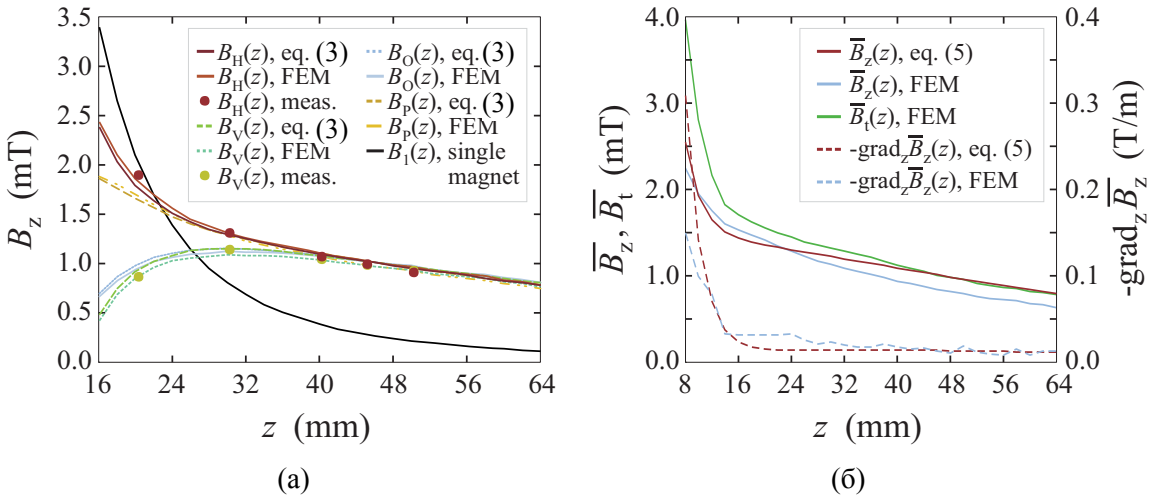

(а) (б)

Слика 2. Поређење аналитички изведених израза са измереним подацима (“meas.”) и подацима израчунатим методом коначних елемената (“FEM”). (а) На већим висинама, z, разлике $B_H(z)$ и $B_V(z)$ постају скоро занемарљиве, а магнетска индукција опада линеарно. (б) Изрази (5) за средњу магнетску индукцију и средњи вертикални градијент индукције показују задовољавајуће слагање са резултатима нумеричког прорачуна (“FEM”), где је приказана и средња вредност укупне магнетске индукције $B_t = \sqrt{B_x^2 + B_y^2 + B_z^2}$. Изрази (5) су погодни за брзу процену параметара поља у огледној запремини, као и приликом прелиминарног дизајна дводимензионих магнетских низова.

Контролна мерења магнетског поља низа

Мерења магнетског поља МАДУ трака имала су двојаку намену. Најпре, подаци о тракама су били веома непотпуни и мерењем је утврђена реманентна магнетизација употребљених магнета. Као друго, мерења су послужила да се потврде изведени аналитички изрази као и да се провере резултати добијени нумеричком симулацијом.

Мерна мрежа се састојала од по двадесет и једне тачке у сваком од три реда, два изнад магнета и трећег између ова два реда, у равнима паралелним xOy равни. Мерни корак у правцу x- и y-осе је износио $x_d/2$ = 9.75 mm, односно $y_d/2$ = 18.0 mm, што одговара максимумима и минимумима магнетске индукције. Мерења су извршена коришћењем дигиталног тесламетра DTM 151 (Group 3, New Zealand), са резолуцијом мерења од 0.005 mT и прецизношћу очитавања од 0.01%, у коришћеном опсегу до 0.3 T [13].

Познато је да су магнети израђени од хексагоналног баријум хексаферита ($BaFe_{12}O_{19}$), једног од најчешће коришћених тврдих магнетских материјала, услед ниске производне цене и веома добрих феромагнетских својстава. Киријева температура је висока и износи T_C = 450°C. Магнетска индукција када је материјал у засићењу износи B_S = 480 mT, што када се узме у обзир густина материјала $\rho = 4.9 \cdot 10^3$ kg/m^3 одговара магнетизацији у засићењу M_S = 78.0 A·m^2/kg. За разлику од ових својстава која не зависе од микроструктуре материјала, реманентна магнетизација може доста

да варира у зависности од производног процеса, посебно времена синтеровања и примењене температуре. Уз коришћење израза (3), довољно је прецизно измерити магнетску индукцију за неколико вредности z-координате (висине), на посматраној вертикалној оси кроз магнет у центру низа. Како смо због провере резултата вршили мерења у већем броју тачака, за карактеризацију материјала мерењем коришћени су усредњени подаци о максимумима и минимумима магнетске индукције за пет хоризонталних равни, $z \in \{19.4, 29.4, 39.4, 44.4, 49.4\}$ mm. За посматрани низ, за пробну вредност реманентне магнетизације M_r, одређене су на основу (3) функције $B_\text{H}(z)$ и $B_\text{V}(z)$, а затим мултипликативна константа која даје најмање средњеквадратно одступање у односу на усредњене мерене податке. Након корекције, добија се $M_\text{r} = 60.0$ A·m^2/kg.

Укупно, изведене су три групе мерења. Најпре, мерењем са једне и друге стране траке на самој површини трака установљена је магнетска индукција (55.70 ± 7.22) mT и (54.34 ± 7.22) mT, дата као (средња вредност ± стандардна девијација). Грешка ручно изведеног мерења, услед јачег или слабијег приањања сонде на мек гумени омотач или благог нагиба у односу на хоризонталну раван, је највећа на површини траке, те су добијене вредности нешто ниже од теоријски предвиђених 59.62 mT. Друга група мерења је изведена са једним слојем, а трећа са по два и три слоја МАДУ трака, за вредности z-координате: $z \in \{4.4, 6.5, 9.4, 19.4, 29.4, 39.4, 44.4, 49.4\}$ mm. Релативна варијабилност резултата, процењена као однос стандардне девијације и средње вредности, је два пута мања за други и трећи скуп мерења у односу на прву групу.

Поређење са нумерички израчунатим подацима

Магнетска индукција МАДУ трака је такође израчуната коришћењем софтверског пакета Mermaid за магнетостатику [14], [15]. Дати програмски пакет, који служи за дизајн делова уређаја од перманентних или електромагнета, користи скаларне коначне елементе првог реда за рачунање магнетостатичког потенцијала. Добијени резултати су показали одлично слагање са аналитичким изразима, што је приказано на Слици 2. Илустрације ради, на Слици 3 је приказана расподела магнетске индукције изнад трака за четири вертикална пресека, укључујући и расипно поље. Доминантна, B_z, компонента чини више од 96% укупне магнетске индукције у делу изнад магнета у центру и више од 80% укупне магнетске индукције свуда у централном делу траке.

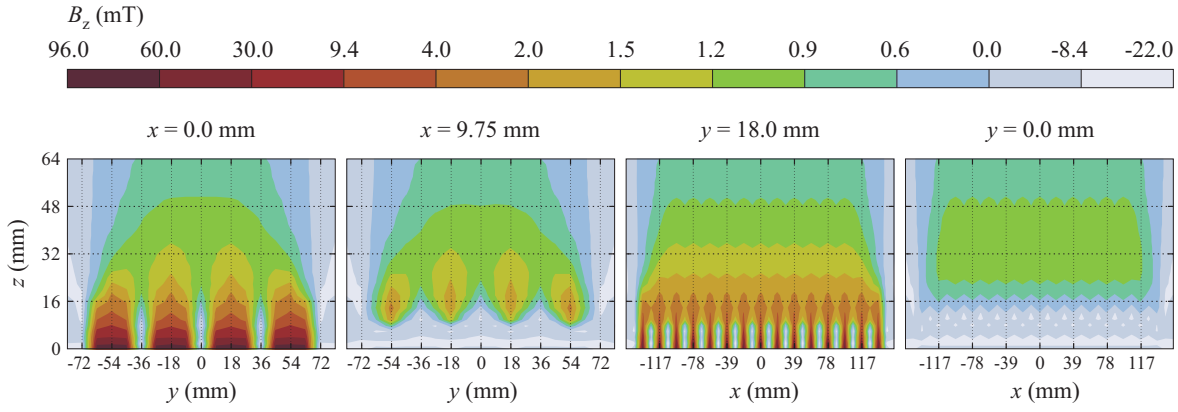

Слика 3. Варијација магнетске индукције у огледној запремини добијена нумеричким прорачуном. Овде је приказана доминантна, B_z, компонента за два пресека паралелна *yOz* равни и два пресека паралелна *xOz* равни, од којих по један полови магнете а други одговара тачно средини између два суседна реда магнета. За пресеке паралелне *xOz* равни расипно магнетско поље се налази изван огледне запремине и претпоставке о периодичности магнетске индукције су потпуно оправдане. У овом конкретном случају, број магнета у правцу y-осе је мали а њихово међусобно растојање значајно, што чини аналитичку процену (5) само апроксимативном.

Модификација поља у огледној запремини

Некада је потребно остварити жељене, захтеване средње параметре статичког магнетског поља у експерименталној запремини. Једноставан начин повећања магнетске индукције за фактор који не зависи од висине изнад низа је употреба више слојева трака, као што је то приказано на Слици 4 (а). За различите комбинације пораста магнетске индукције и њеног вертикалног градијента, изрази (5) се могу употребити као почетан алат у пројектовању новог низа жељених карактеристика. Ово је илустровано у делу (б) Слике 4. За потребе корисника МАДУ трака, на основу горе изложеног, састављено је "Упутство за употребу МАДУ трака у биомедицинским огледима". Такође, написана је процедура за рачунар која за задати низ и огледну запремину ограничену двема хоризонталним равнима $z = h_1$ и $z = h_2$, одређује средње параметре магнетског поља у огледној запремини, као што је за неколико уобичајених случајева приказано у Табели I и Табели II. Тренутно се упутство и поменута процедура у MATLAB-у користе од стране студената и сарадника Медицинског факултета у Београду.

ТАБЕЛА I
СРЕДЊИ ПАРАМЕТРИ МАГНЕТСКОГ ПОЉА
У ОГЛЕДНОЈ ЗАПРЕМИНИ

h_1 (mm)	h_2 (mm)	$\overline{B_z}$ (mT)	$\overline{B_t}$ (mT)	$\overline{G_z}$ (T/m)
0.0 *	10.0	15.4394	16.1613	1.8549
0.0 *	20.0	9.1341	9.6192	1.0302
0.0 *	30.0	6.6632	7.0497	0.7165
16.0	46.0	1.1371	1.3127	0.0223
24.0	54.0	0.9719	1.1476	0.0176
32.0	62.0	0.8442	1.0122	0.0141

* за прва три реда коришћено је $|\overline{B_z}|$

ТАБЕЛА II
СРЕДЊИ ПАРАМЕТРИ МАГНЕТСКОГ ПОЉА
ЗА ВИШЕ СЛОЈЕВА МАДУ ТРАКА

h_1 (mm)	h_2 (mm)	$\overline{B_z}$ (mT)	$\overline{B_t}$ (mT)	$\overline{G_z}$ (T/m)
Два слоја				
16.0	46.0	2.1932	2.5316	0.0431
24.0	54.0	1.8715	2.2096	0.0350
32.0	62.0	1.6214	1.9442	0.0276
Три слоја				
16.0	46.0	3.4402	3.9597	0.0636
24.0	54.0	2.7465	3.2406	0.0518
32.0	62.0	2.3294	2.7931	0.0402

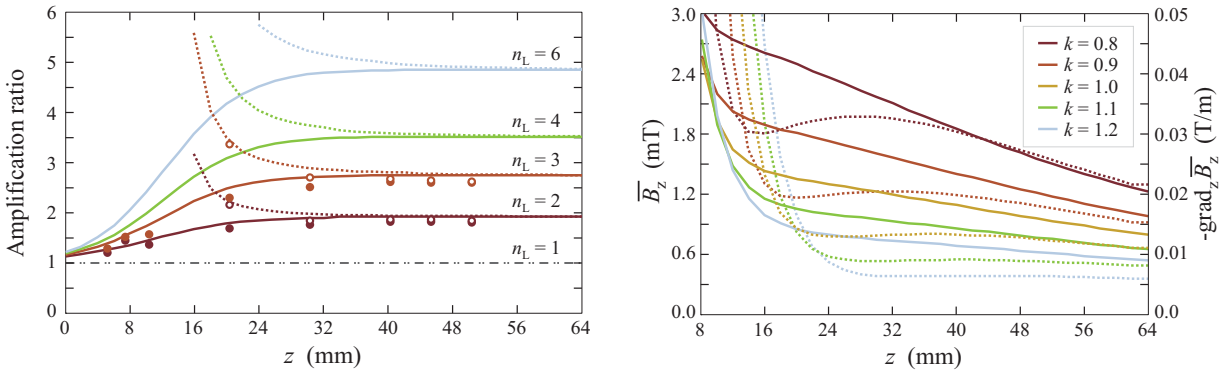

(а) (б)

Слика 4. (а) Повећање магнетске индукције коришћењем више слојева МАДУ трака. Како средња магнетска индукција опада линеарно са висином, значајан фактор увећања поља, скоро једнак броју трака n_L, се добија постављањем једне траке на другу. Пуне линије одговарају максималној индукцији, $B_H(z)$, испрекидане минималној, $B_V(z)$, док су одговарајући измерени подаци приказани пуним и празним кружићима, респективно. (б) Илустрација коришћења приближних израза (5) у прелиминарном дизајну магнетског низа жељених средњих параметара поља. Приказане су промене средње магнетске индукције (пуне линије) и њеног вертикалног градијента (испрекидане линије) са модификацијом растојања између редова магнета за фактор k, овде узет једнак у правцу x- и y-осе.

Закључак

Изведени су комплетни изрази за магнетску индукцију произвољног дводимензионог магнетског низа, који осим осталих примена може да буде погодан извор магнетског поља у биомедицинским експериментима. Мерењем је извршено одређивање реманентне магнетизације материјала, а такође и потврђени аналитички изрази и нумерички прорачуни методом коначних елемената. Припремљена је процедура у MATLAB-у која за потребе корисника рачуна средње параметре поља у огледној запремини, а подаци за најчешће случајеве приказани и табеларно.

Литература

[1] A. Ž. Ilić, S. Ćirković, D. M. Djordjevic, S. R. De Luka, I. D. Milovanovich, A. M. Trbovich, J. L. Ristić-Djurović, "Analytical description of two-dimensional magnetic arrays suitable for biomedical applications," *IEEE Transactions on Magnetics*, vol. 49, No. 12, Dec. 2013.

[2] M. I. Weintraub, G. I. Wolfe, R. A. Barohn *et al.*, "Static magnetic field therapy for symptomatic diabetic neuropathy: a randomized, double-blind, placebo-controlled trial," *Archives of Physical Medicine and Rehabilitation*, vol. 84, no. 5, pp. 736–746, May 2003.

[3] N. A. Segal, Y. Toda, J. Huston *et al.*, "Two configurations of static magnetic fields for treating rheumatoid arthritis of the knee: a double-blind clinical trial," *Archives of Phys. Med. and Rehab.*, vol. 82, no. 10, pp. 1453–1460, Oct. 2001.

[4] C. Vallbona, C. F. Hazlewood, and G. Jurida, "Response of pain to static magnetic fields in postpolio patients: a double-blind pilot study," *Arch. of Phys. Med. and Rehab.*, vol. 78, no. 11, pp. 1200–1203, Nov. 1997.

[5] H. N. Mayrovitz and E. E. Groseclose, "Effects of a static magnetic field of either polarity on skin microcirculation," *Microvascular Research*, vol. 69, no. 1–2, pp. 24–27, Jan. 2005.

[6] Y. Yan, G. Shen, K. Xie *et al.*, "Wavelet analysis of acute effects of static magnetic field on resting skin blood flow at the nail wall in young men," *Microvascular Research*, vol. 82, no. 3, pp. 277–283, Nov. 2011.

[7] A. H. Hashish, M. A. El-Missiry, H. I. Abdelkader, R. H. Abou-Saleh, "Assessment of biological changes of continuous whole body exposure to static magnetic field and extremely low frequency electromagnetic fields in mice," *Ecotoxicology and Environm. Safety*, vol. 71, pp. 895–902, Nov. 2008.

[8] D. Mandic, "Surface magnetised elastic magnetic stripe and application," Patent No. (WO1999060581), available online at: http://patentscope.wipo.int/search/en/WO1999060581 .

[9] D. M. Djordjevich, S. R. De Luka, I. D. Milovanovich, S. Janković, S. Stefanović, S. Vesković-Moračanin, S. Ćirković, A. Ž. Ilić, J. L. Ristić-Djurović, A. M. Trbovich, "Hematological parameters' changes in mice subchronically exposed to static magnetic fields of different orientations," *Ecotoxicology and Environm. Safety*, vol. 81, pp. 98–105, July 2012.

[10] S. R. De Luka, D. M. Djordjevich, I. D. Milovanovich *et al.*, "Subchronic exposure to static magnetic field affects zinc and copper content in mice brain and liver," submitted for publication.

[11] A. P. Colbert, H. Wahbeh, N. Harling *et al.*, "Static magnetic field therapy: a critical review of treatment parameters," *Evidence Based Complem. and Alternative Med.*, vol. 6, no. 2, pp. 133–139, June 2009.

[12] K. Halbach, "Design of permanent multipole magnets with oriented rare earth cobalt material," *Nucl. Instruments and Methods*, vol. 169, no. 1, pp. 1–10, Feb. 1980.

[13] Group3, *DTM-151 Digital Teslameter with serial communications*, User's Manual.

[14] MERMAID 2D and 3D User's Guide, SIM, Novosibirsk, Russia, 1994.

[15] N. A. Dubrovin, E. A. Simonov, S. B. Vorozhtsov, "MERMAID 3D code in ATLAS applications," ATLAS Note ATL-TECH-2001-003, CERN, Geneva 2001.

Техничко решење је развијено у Иновационом центру Електротехничког факултета у Београду, у оквиру пројекта број ИИИ-45003 Министарства просвете, науке и технолошког развоја Србије

Штампано децембра 2013.

ОЦЕНА ТЕХНИЧКОГ РЕШЕЊА

На основу сагласности Наставно-научног већа Електротехничког факултета у Београду датој на својој 758. седници одржаној 22.01.2013. године Комисија за студије трећег степена донела је одлуку да се прихвати техничко решење:

Назив техничког решења: Употреба МАДУ трака у биомедицинским експериментима
Аутори техничког решења: Анђелија Илић, Саша Ћирковић, Јасна Ристић – Ђуровић, Драго Ђорђевић, Александар Трбовић
Врста техничког решења: Битно побољшано решење на националном нивоу
М фактор техничког решења (М81-М86 фактор): М84

Београд, 15.01.2014.

Председник Комисије за студије трећег степена

Проф. др Бранко Колунџија

Република Србија Универзитет у Београду Електротехнички факултет Београд

Рецензија техничког решења

Битно побољшано техничко решење на националном нивоу (М84):

Употреба МАДУ трака у биомедицинским експериментима

Руководилац пројекта: Небојша Ромчевић
Одговорно лице: Анђелија Илић
Аутори: Анђелија Илић, Саша Ћирковић, Јасна Ристић-Ђуровић, Драго Ђорђевић, Александар Трбовић
Развијено: у оквиру пројекта Интегралних и интердисциплинарних истраживања (ИИИ), број ИИИ-45003
Година: 2013.
Примена: 01.03.2013.

Сматрам да су резултати истраживања описани у приложеној техничкој документацији техничко решење и да имају одговарајући стручни и научни допринос. О оригиналности резултата сведочи чињеница да су резултати детаљно описани у раду објављеном у међународном научном часопису *IEEE Transactions on Magnetics*, категорије M_{22}. На основу пружених података може се реализовати произвољан магнетски низ за употребу у биомедицини и прорачунати његови релевантни параметри. Такође, дати изрази су потпуно применљиви за генерички случај дводимензионог магнетског низа произвољне намене и могу послужити приликом пројектовања таквог низа.

Техничко решење припада широј области Примењена електромагнетика, са основном применом у области Биомедицинских наука, што је веома актуелно у светским оквирима. Састоји се од потпуних, егзактних, аналитичких израза којима се описује магнетски низ; приближних израза за брзу процену средњих параметара поља у експерименталној запремини; програма за прорачун електромагнетског поља у разматраној запремини; програма за одређивање жељених средњих параметара и упутства за употребу за кориснике решења. Провера је извршена нумерички и експериментално (мерењем поља).

Решење се засада употребљава од стране студената и сарадника Медицинског факултета у Београду за прецизну контролу и опис примењеног статичког магнетског поља у биомедицинским огледима. У доступној литератури није било примера коришћења дводимензионог магнетског низа у огледне сврхе, иако се сличне конфигурације магнета некада користе у клиничкој пракси али нажалост без прецизног познавања примењеног магнетског поља. У том смислу, решење може бити од користи и у клиничким применама.

У Београду, 20. новембра 2013.

Рецензент

Душко Борка

Др Душко Борка, виши научни сарадник (ВНС)
Лабораторија за атомску физику (040),
Институт „Винча“, Београд

Рецензија техничког решења

Битно побољшано техничко решење на националном нивоу (М84):

Употреба МАДУ трака у биомедицинским експериментима

Руководилац пројекта: Небојша Ромчевић
Одговорно лице: Анђелија Илић
Аутори: Анђелија Илић, Саша Ћирковић, Јасна Ристић-Ђуровић, Драго Ђорђевић, Александар Трбовић
Развијено: у оквиру пројекта Интегралних и интердисциплинарних истраживања (ИИИ), број ИИИ-45003
Година: 2013.
Примена: 01.03.2013.

По увиду у техничку документацију горе наведеног решења, закључујем да оно испуњава услове да буде прихваћено као техничко решење. По мом мишљењу предложено решење има како стручни, тако и научни допринос. Потврду о научном доприносу представља и публикација категорије M_{22} у међународном часопису *IEEE Transactions on Magnetics*, у потпуности посвећена опису техничког решења. У раду је дато довољно смерница за анализу и помоћ у пројектовању произвољног магнетског низа, чиме је омогућена директна примена решења од стране других заинтересованих корисника.

Техничко решење се односи на ширу научну област Примењене електромагнетике, а примена решења је интердисциплинарна и везана за област Биомедицинских наука, која се у свету тренутно веома брзо развија. Решење се заснива на комплетном скупу егзактних аналитичких израза за опис поља изнад дводимензионог магнетског низа, из њега изведених веома једноставних апроксимативних израза за процену средњих параметара магнетског поља и софтверској имплементацији ових теоријских резултата за потребе крајњег корисника.

Суштина техничког решења је да се веома прецизно одреде сви параметри од интереса статичког магнетског поља примењеног у огледној запремини и да се примењено поље веома детаљно опише, што је императив у научно-истраживачком раду. Теоријски резултати могу наћи и ширу примену, будући да су магнетски низови значајни и за микроактуаторске системе и микросензоре, планарне моторе и слично. Сви резултати су потврђени како нумеричком симулацијом тако и директно, мерењем магнетског поља.

Развијено решење се употребљава на Медицинском факултету у Београду.

У Београду, 20. новембра 2013.

Рецензент

Катарина Радуловић

Др Катарина Радуловић, научни саветник (НСВ)
Института за хемију, технологију и металургију,
Београд